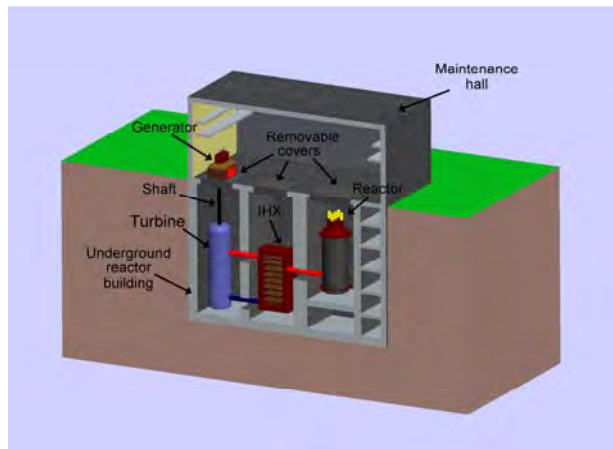


Design of a U-Battery®

Delft, November 2011

PNR-131-2011-014



Authors TU-Delft:

Ming Ding, Jan Leen Kloosterman, Theo Kooijman, Rik Linssen

Authors Manchester University:

Tim Abram, Barry Marsden, Tony Wickham

A study sponsored by Urenco, and Koopman and Witteveen.

Contents

1. Introduction	5
2. Core design	5
2.1 Graphite moderated 20 MW _{th} Design	5
2.2 Graphite moderated 10 MW _{th} Design	7
2.3 Excess reactivity control method	7
2.4 Thorium-fueled fuel block	7
3. Safety characteristics	8
3.1 Graphite moderated 20 MW _{th} design	8
3.2 Graphite 10 MW _{th} BeO reflector design	10
3.3 Beyond design-basis scenarios	10
4. Core Structural Design and Fuel Design	11
4.1 Graphite Moderated 20 MW _{th} Design	11
4.2 Graphite Moderated 10 MW _{th} Design	12
5. Plant Layout and Operation	15
5.1 Fuel Handling System	15
5.2 Energy Conversion System	15
5.3 Control System Design	16
5.4 General Plant Layout	16
5.5 Fuel Transport	17
6. Economic Analysis	18
6.1 Cost of Major Equipment	18
6.2 Markups for direct, indirect cost and contingencies	19
6.3 Working Capital	19
6.4 Resulting total investment	20
6.5 Running costs	21
6.6 Results	21
6.7 Sensitivity Analysis	21
6.8 Conclusions	22
6.9 Still to be addressed, sharing the economic risk	22
Appendices	
A. Core Design of the U-Battery	
B. Reactor Structural and Fuel Design	
C. U-Battery Plant Layout and Operation	
D. Economic Analysis of the U-Battery	

Executive Summary

1. Introduction

In the past fifty years, the size of nuclear reactors has grown from 200 MW_{th} to more than 4.500 MW_{th} in order to make full use of economy of scale. Because large-size nuclear reactors usually require high capital investment and heavily rely on the infrastructure of the nuclear sites, this has motivated designers to develop small modular reactors, especially for developing countries and remote areas off main power grids. Major drawback of most of these small modular reactor designs is that new technology is introduced, which has to be developed and licensed. This will normally take decades in a nuclear environment.

To be economically feasible a small modular reactor should work like a battery. The reactor and the energy conversion system are brought to the purchaser's site as modules, the electricity is hooked up and the reactor will run for 5 years or more with a minimum of operational personnel. This allows the modules to be manufactured in series and transported to the purchaser's site by rail, barge, truck, etc. After operation of 5-10 years, the reactor can be brought back to the factory for refueling or can be directly replaced by a new module. This modular and standardized approach will, with increasing sales, result in significant cost reduction by economy of number. On top of this a user in an industrialized area will save the yearly cost of the power grid infrastructure.

This report presents a feasibility study for the design of an intrinsically safe modular nuclear power generation system that combines quick-developed till commercial design using proven technology with the basic features to profit from economy of number. The investigation shows that the proposed 10MW_{th} U-Battery[®] design is very promising to fulfill all the above requirements.

The study is executed by the Delft University of Technology together with the University of Manchester and is sponsored by URENCO and Koopman & Witteveen.

2. Core design

Different reactor core configurations and thermal power levels of the U-Battery[®] have been investigated for various diameters of the reactor pressure vessels (RPVs). The RPV diameter is one of the important parameters affecting the transportability of the U-Battery[®].

2.1 Graphite moderated 20 MW_{th} Design

Since the main ideas behind the U-Battery[®] are inherent safety, modularity and near-term utilization, the U-Battery[®] has been developed based on currently mature High Temperature Reactor (HTR) fuel blocks utilizing standard TRISO particles as fuel. The reactor core of the U-Battery[®] is composed of hexagonal fuel blocks with reflectors as shown in Fig. 2.1.

The calculations show that the 20 MW_{th} U-Battery[®] can achieve a fuel lifetime of 10 Effective Full Power Years (EFPYs). The annular reactor core Layout 30*4 (meaning a reactor core of 30 fuel blocks per layer and 4 layers on top of each other), as shown in Fig. 2.1, is the recommended configurations for the 20 MW_{th} design.

The cylindrical reactor core Layout 37*4 is a good alternative for comparison. The main difference between the two Layouts is the presence of 28 graphite blocks in the center of the core of Layout 30*4 while these are replaced by fuel blocks in layout 37*4, as shown in Fig. 2.1. The annular reactor core has a longer lifetime than the cylindrical one, because of the extra neutron moderation by the central graphite blocks. The burn up of Layouts 37*4 and 30*4 are 70 and 57 MWd/kgHM, respectively.

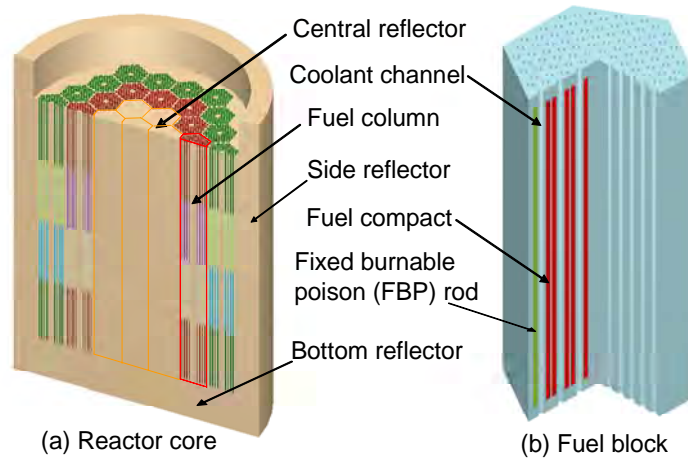


Fig. 2.1: 3D figure of the annular core (Layout 30*4) and fuel block (right); for clarity the top and bottom reflectors have been removed in the core as well as the fuel handling hole in the block.

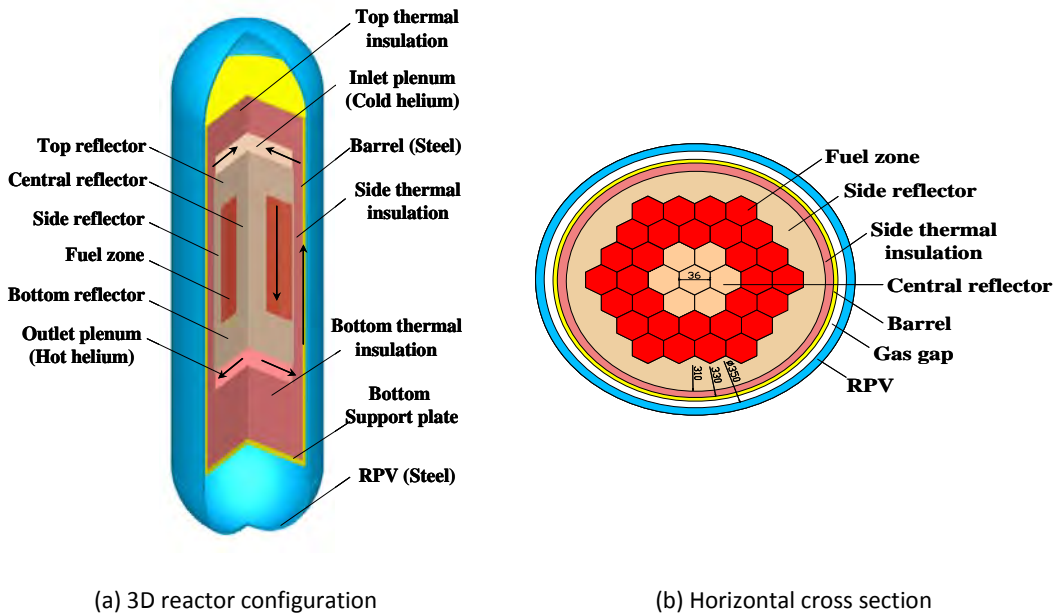


Fig. 2.2: The schematic diagram of Layout 30*4. The coolant channels in the blocks and the auxiliary structures in the reactor have been removed to make the main components of the reactor better visible.

The core configuration and horizontal cross section of Layout 30*4 are shown in Fig. 2.2. The thermal-hydraulic design calculations show that this Layout has preference from thermal-hydraulic point of view. Although it faces slightly higher temperatures for the barrel and RPV, the maximum temperature is 230 °C lower than for Layout 37*4. In conclusion, Layout 30*4 not only decreases fuel cost, but also increases the safety of the U-Battery®.

2.2 Graphite moderated 10 MW_{th} Design

If the thermal power of the U-Battery® decreases from 20 MW_{th} to 10 MW_{th} the inner diameter of the RPV reduces from 3.5 m to 1.8. Using a 25-cm-thick graphite reflector, the fuel lifetime reaches 2 EFPYs. If the side reflector is made of 20-cm-thick Beryllium oxide (BeO), the annular core Layout 6*4, as shown in Fig. 2.3, can achieve a lifetime of 5 EFPYs.

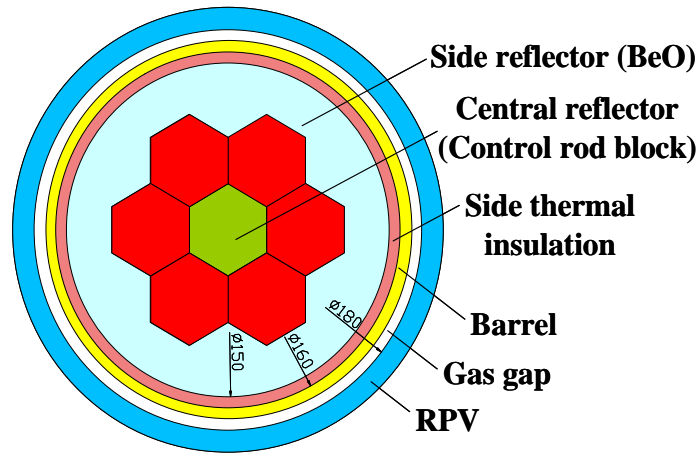


Fig. 2.3: Horizontal cross section of Layout 6*4

2.3 Excess reactivity control method

The geometric parameters of the B₄C fixed burnable poisons (FBP), as shown in Fig. 2.1b, have been optimized to reduce the reactivity swing of the cylindrical core Layout 37*4. Although the reactivity penalty (this is the higher enrichment of uranium needed to compensate for the remaining poison at the end-of-cycle) increases, the use of fixed burnable poisons can be beneficial, because the cost of control rods and driver mechanisms may be higher than the extra fuel costs.

2.4 Thorium-fueled fuel block

Seed-and-blanket (S&B) fuel blocks, as shown in Fig. 2.4, have been investigated for a Thorium-fueled U-Battery® with the aim to reduce the fuel cost of the U-Battery® and to control the reactivity swing without the reactivity penalty inherent to using fixed burnable poisons in a Uranium-fueled U-Battery®.

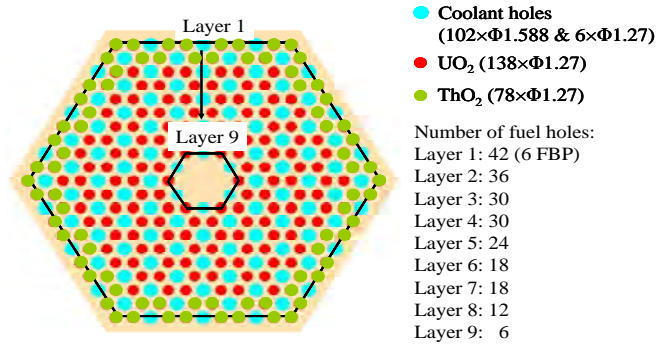


FIG. 2.4: Seed-and-blanket (S&B) fuel block with ThO₂

For fuel blocks with 36, 54 and 78 UO₂ fuel rods in the central regions, the reactivity swing is only 0.1 Δk during 10 EFPYs. The excess reactivity of 0.1 Δk is so small that no fixed burnable poison is needed. Moreover, when thorium is equally expensive as uranium, the S&B fuel block may be about one-third cheaper than that of LEU fuel block.

3. Safety characteristics

3.1 Graphite moderated 20 MW_{th} design

Due to neutronic feedback mechanisms and the thermal-hydraulic performance of the reactor core, the 20 MW_{th} U-Battery[®] is inherently safe.

The negative reactivity feedback coefficients, as shown in Table 3.1, guarantee the automatic shut-down of the reactor when the temperature increases. The values of the reactivity coefficients of the U-Battery[®] are very similar to those of the HTR-10, which has been used to demonstrate this effect.

Table 3.1: Reactivity temperature coefficients of the U-Battery[®].

Configurations	Time [Years]	Fuel [pcm/K]	Moderator [pcm/K]	Reflector [pcm/K]
Layout 30*4	0.0	-3.8	-1.6	+0.5
	5.0	-5.4	-3.1	+0.1
	10.0	-5.3	-3.8	+0.8
Layout 37*4	0.0	-5.4	-2.9	+1.2
	5.0	-7.5	-3.4	+0.4
	10.0	-7.2	-4.1	+0.2

Besides the automatic shut down of the reactor, removing decay heat passively out of the reactor without any fuel damage is an important safety characteristic. When using TRISO fuel particles, the maximum temperature should stay below 1600 °C under all circumstances. The thermal hydraulics analyses show that for loss of forced-cooling scenarios, both pressurized and depressurized, the U-Battery® fulfill these requirements.

Under the assumption that the control rods shut down the reactor two scenarios were investigated:

- A pressurized loss of forced-cooling (PLOFC), In this case, the U-Battery® loses forced-cooling possibly caused by mechanical problems or a loss of power, but the reactor system remains intact, so it does not lose system pressure.
- If the reactor system loses pressure at the same time, for example, because of a broken hot gas duct which connects the reactor pressure vessel with the power conversion system, a depressurized loss of forced-cooling (DLOFC) incident happens.

Both situations are investigated for the cylindrical and annular core configurations. The calculations show that the fuel temperature is higher for a DLOFC incident, because the decay heat can only be removed by conduction and not by natural convection. The maximum temperature of the reactor core (Layout 37*4 and Layout 30*4) decreases immediately, as show in Fig. 3.1, without any violation of the temperature limits. This favorable characteristic is due to the low power density and the large heat capacity of the core.

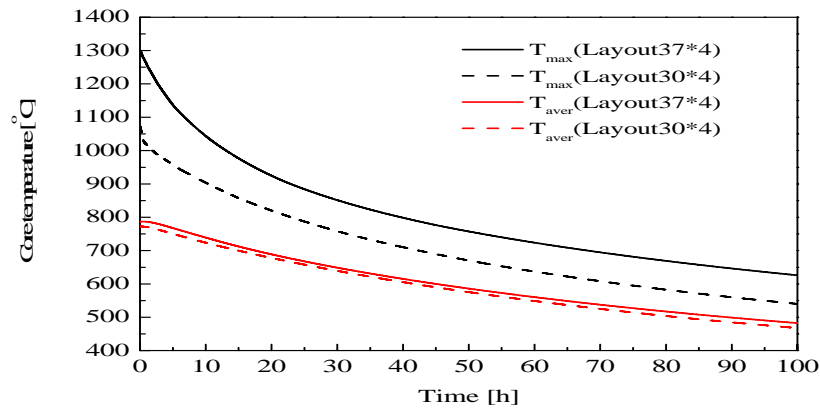


Fig. 3.1: Maximum and volume-averaged temperatures of the fuel zone of the annular (Layout 30*4) and cylindrical (Layout 37*4) core configurations during DLOFC incident.

3.2 Graphite moderated 10 MW_{th} BeO reflector design

Although the 10 MW_{th} U-Battery[®] with BeO reflector was only investigated neutronically, its safety characteristics can be estimated based on the 20 MW_{th} U-Battery[®] design and other large prismatic High Temperature Reactors (HTR), like the USA prototype GT-MHR.

Because the same fuel blocks are used for the 10 and 20 MW_{th} U-Battery[®], the first probably has negative reactivity temperature coefficients as well. Although the power density is higher in the 10 MW_{th} design, which is a challenge for the PLOFC and DLOFC scenarios, it is still one-third lower than for large prismatic HTRs like GT-MHR. This is a strong indication that the decay heat of the 10 MW_{th} U-Battery[®] might be removed by passive means without any violation of the temperature limits. Moreover, the thermal-hydraulic calculation of a 100 MW_{th} U-Battery[®] with an annular core configuration, which has a 50% higher power density than the 10 MW_{th} design, shows a maximum fuel temperature is far below 1600 °C.

3.3 Beyond design-basis scenarios

Besides design-basis scenarios, the U-Battery[®] faces some beyond design-basis scenarios, such as PLOFC and DLOFC without SCRAM (i.e., control rods cannot be inserted into reactors) and control rods withdraw without SCRAM. As shown in Fig. 3.2, tests executed in AVR and HTR-10 showed, that these reactors

- can be shut down immediately by the negative temperature feedback coefficients even if the control rods are not inserted into the cores;
- get re-critical only at a very low power level.

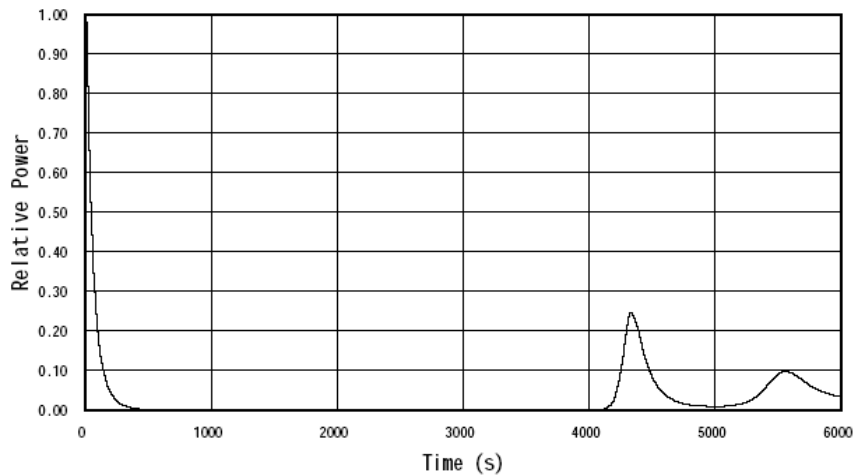


Fig. 3.2: Experimental curve of fission power during PLOFC without scram for the HTR-10 at 3 MW_{th}.

Since the U-Battery[®] has similar values for the temperature coefficients as the Chinese prototype HTR-10, it will also shut down automatically. After the reactor has shut down, the U-Battery[®] can passively remove the decay heat out of the core without violating the fuel temperature limit, as analyzed in Sec. 3.1.

4. Core Structural Design and Fuel Design

Originally the U-Battery® was to be designed to operate in a carbon-dioxide coolant based on the excellent thermal properties of high pressure CO₂. However, investigation, both analytical and experimental demonstrated that this was not practicable due to thermal and radiolytic oxidation. Therefore the design was changed to an inert, high pressure helium system which precludes both radiolytic and thermal oxidation under all normal operation conditions. The design will be such to preclude the accidental ingress of water or air in the system under normal operation and design faults.

The structural designs for two cores is outlined below, the first is a 20 MW_{th} graphite moderated design the second design is a 10 MW_{th} reactor also graphite moderated, but also included a BeO reflector.

4.1 Graphite Moderated 20 MW_{th} Design

The reactor is housed in a steel Reactor Pressure Vessel (RPV) about 100 mm thick designed for a working pressure of 40 bar at 300 °C and a maximum transient temperature about 50 °C higher than the limiting temperature of 395°C during several hours. Transients above this temperature will cause the RPV to vent into the secondary containment (confinement). The RPV design is such that a single main inlet/outlet is situated towards the bottom of the reactor to prevent the “chimney effect” in case of a main inlet/outlet duct failure. The RPV is provided with a removable (bolted) lid that can be removed for refueling. The lid has proved openings to which the control rods mechanisms can be bolted to. All bolted joints are to be “helium tight”.

The design will be such that when the reactor lid is removed for refuelling, the control rods will remain secure in the core.

Inside the vessel a core support structure rests on the bottom of the vessel. The structure provides support for the lower core support plates and the core barrel. The lower core support and core barrel is to be kept as close to the reactor inlet temperature as possible during normal operation.

On top of the core support plates layers of insulation and graphite form the lower inlet/outlet plenums, the detail of which is for further design study but will be based on experience gained at Fort St. Vrain (FSV) and HTTR. The purpose of the lower plenum structure is to direct “cool” inlet gas upwards between the core barrel and RPV and to keep the return “cool” inlet and “hot” return gas separate and direct it outwards to the heat exchanger in the primary circuit.

The lower plenum also supports the main reactor core structure. This consists of a hexagonal array of fuel elements of FSV design, interspersed with other hexagonal blocks with larger holes through which the control and safety shutdown rods can freely pass. The core is four elements high of annular design with outer rings of 18 and 12 elements of fuel elements and a central rings of 6 and 1 hexagonal graphite elements, see Figure 2.1.

The reasoning behind the choice of the FSV fuel block design is that this design of fuel block proved itself in operation for a number of years.

The core is surrounded by an inner (removable) graphite reflector which is surrounded by insulation material. At each fuel block height, tubular “Calder” type restraint bands will be located. These will be designed to facilitate side restraint and will expand/contract with temperature with the same expansion coefficient as graphite ensuring that no “gaps” will appear between reflector and fuel blocks to prevent coolant gas bi-pass and neutron streaming.

Above the core there will be a hexagonal array of tightly clamped graphite reflector bricks, with holes to direct coolant flow downwards from the upper plenum and for control/shutdown rods to pass. The upper core plenum is to be insulated and designed directing the “cool” gas that flows upwards from the lower inlet plenum up between the RPV and core barrel back down through the core (Figure 4.1).

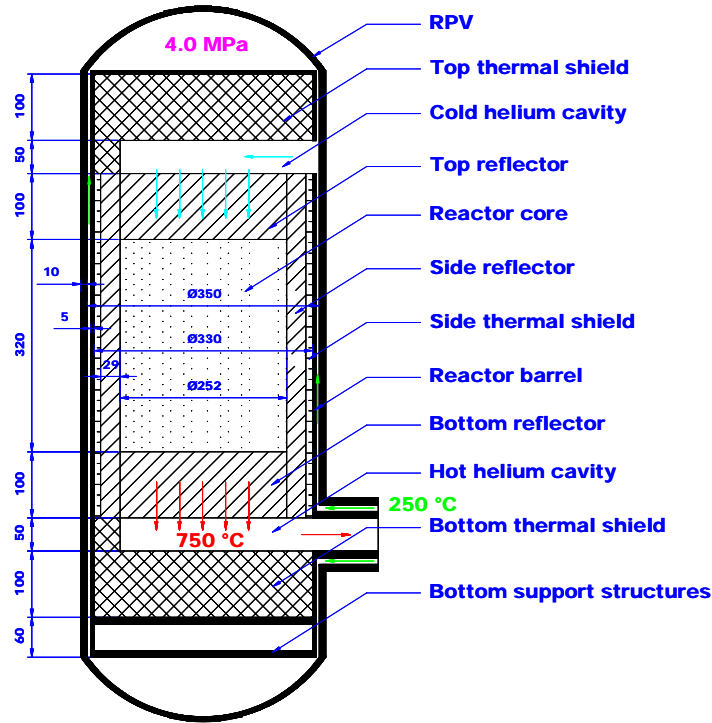


Figure 4.1: Reactor Pressure Vessel and Core Internals - Dimensions

Nuclear graphite property changes will be based on published Material Test Reactor (MTR) data for medium grained graphite obtained over many years. Although there are uncertainties in this data this tends to be the greatest at high fluence and mostly associated with the effect of radiolytic oxidation. The maximum irradiation fluence it is expected that the graphite would experience in the 20 MW_{th} design would be significantly less than one third that AGR would experience in 30 years.

The design will account for:

- Differential thermal expansion between graphite, insulation and steel;
- Differential thermal expansion due to radial and axial thermal gradients;
- Graphite shrinkage.

4.2 Graphite Moderated 10 MW_{th} Design

This design is similar, but physically smaller to that described above. In this case there is one ring of six hexagonal fuel elements by four with a central graphite column by four elements high. However, in this case the active core is surrounded by a beryllium oxide reflector, see Figure 2.3.

Beryllium oxide (BeO) is an excellent neutron reflector. It has very low neutron absorption cross-section, is excellent at moderating fast flux (both due to low mass of Beryllium and the inelastic scattering by oxygen, see Table 4.1).

BeO has a high temperature capability (2840 K). BeO actually improves upon the moderating capabilities of Beryllium alone having a higher neutron scattering cross section and lower absorption cross section at the expense of higher density ($\sim 3.01 \text{ g/cm}^3$ c.f. 1.85 g/cm^3). It also has a high thermal conductivity $\sim 275 \text{ W/m/K}$. The toxicity of BeO make it difficult to handle, however, it has been and still is used in many research reactors and for space applications and there is a significant amount of data concerning the use of beryllium in the nuclear industry.

Table 4.1 Scattering and Absorption Cross Sections for 2200 m/s neutrons (Units barns)

Element	Scattering X-Section	Absorption X-Section
Beryllium	7.63	0.0076
Carbon	5.551	0.0035
Oxygen	4.232	0.00019

It is envisage if this option were chosen that two $10 \text{ MW}_{\text{th}}$ units would supply one power unit.

The layout of the whole plant $20 \text{ MW}_{\text{th}}$ is given in Figures 4.3 - 4.5.

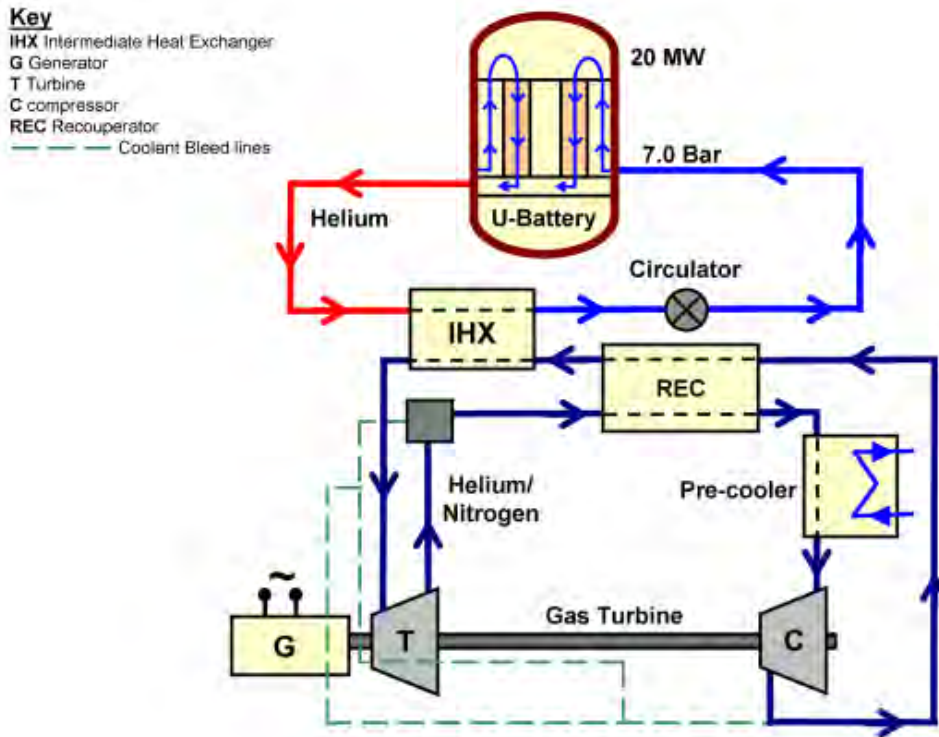


Figure 4.3: Layout of the primary circuit of the $20 \text{ MW}_{\text{th}}$ U-Battery®.

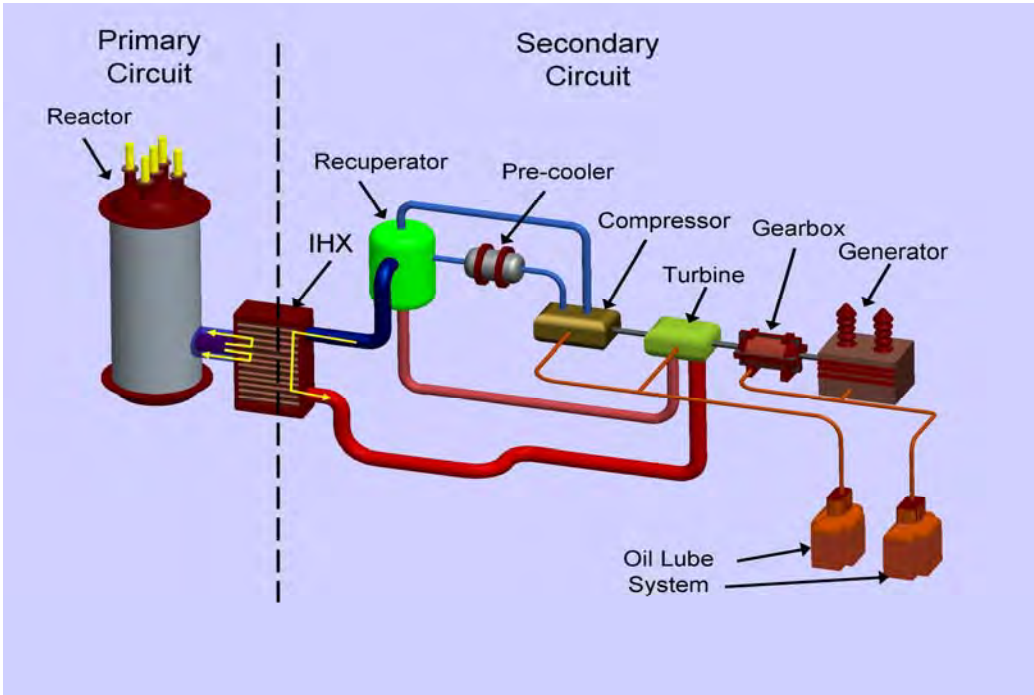


Figure 4.4: Layout of the secondary circuit of the 20 MW_{th} U-Battery®.

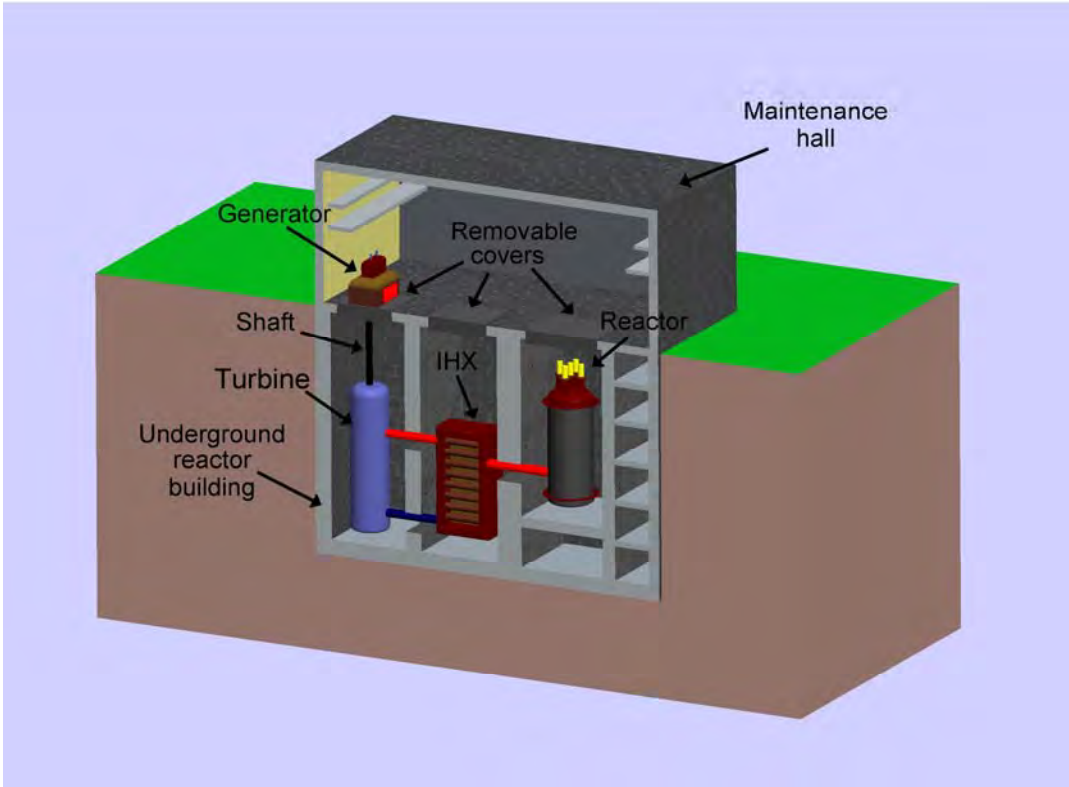


Figure 4.5: Layout of the reactor building of the 20 MW_{th} U-Battery®.

5. Plant Layout and Operation

The original concept for the U-Battery[®] envisaged a simple and robust plant design in which both the reactor and power conversion system would place few constraints on transport, and would require minimal routine maintenance. A long-life core was envisaged that would be capable of being refueled as a single unit and transported away from site immediately after use, requiring very little permanent on-site refueling equipment or fuel storage capacity.

The work conducted over the last two years of the project suggests that whilst some of these objectives can be met, others are not compatible with the current U-Battery[®] concept. A power conversion module based on the concept of an indirect cycle employing a He-N₂ turbine seems feasible, and Rolls-Royce has been identified as a potential supplier of such a system. A plant layout has been developed based on a below-ground reactor cavity and adjacent spent core storage facility, both served by an overhead crane and co-located with the power conversion module in a vented confinement building.

There are no precedents for transporting intact an entire unirradiated reactor core, and regulatory requirements may preclude this option, although transportation of a small number of sub-sections may be possible. In any case the current reference core geometry of the 20 MW_{th} Layout is likely to be too large to allow transportation of an intact irradiated core without developing and licensing a new spent fuel transport container.

5.1 Fuel Handling System

The current reference design for the 20 MW_{th} U-Battery[®] core and fuel elements seems incompatible with a single cartridge-type core module, largely because the dimensions of the active core plus the radial reflector and shielding/packaging requirements may exceed the maximum permissible width for European road transportation.

Currently, all spent fuel shipments take place by rail and/or sea, with very short road transport to the nearest rail head or port facility. The Excellox transport flask is internationally accepted for this purpose, but would impose a limit of 1.8 m on the diameter of the cartridge, and weighs 110 t, making road transport difficult except over very short distances. One of the Sellafield Waste Transport Containers, the SWTC25, has a gross weight of 25 t and may simplify road transport, but in this case the cartridge diameter would be limited to 1.2 m, which is too small to support a feasible core design for the current reference power output.

For these reasons, the current design employs individual fuel elements, which greatly simplifies the transport of fresh and irradiated fuel, but requires the provision of handling equipment suitable for both fresh and irradiated fuel. Fuel handling machines have been developed for previous designs of prismatic HTRs, and these have been reviewed for applicability to the U-Battery[®] design. The simplified single-element design produced by GA for the MHTGR project appears to be well suited to the U-Battery[®].

5.2 Energy Conversion System

The reference concept for the U-Battery[®] is an electricity-generating module, capable of producing around 20 MW_{th}. Several different options have been explored for the energy conversion system, including: an indirect steam (Rankine) cycle with and without reheat; a direct CO₂ turbine; and an indirect gas-turbine, as well as more novel systems such as direct thermal-to-electrical conversion, and an Alkali Metal Thermal-to-Electrical

Converter (AMTEC). Of these, the novel systems and the CO₂ turbine were rejected because they were incompatible with the requirement to employ demonstrated, highly-reliable technologies, and because of their generally poor efficiencies.

A steam cycle with reheat requires a significant increase in the complexity of the steam circuit piping, and the provision of economizers and other additional components, and the small gain in overall efficiency was also considered to be incompatible with the over-riding requirements for plant simplicity and low maintenance. The two preferred options were therefore a steam (Rankine) cycle without reheat, and an indirect-cycle gas turbine. The steam cycle employs proven technology and is reliable and reasonably efficient, but it will require regular maintenance and frequent condition monitoring, for example to ensure an acceptable water chemistry is maintained.

An indirect gas-turbine would require a reasonably large heat exchanger, but avoids the potential safety concern associated with a steam ingress into the primary circuit, and could employ a relatively inert working fluid, minimizing the need for careful control of the secondary coolant chemistry. Rolls-Royce have published a concept for a power conversion module based on their well-established air turbine designs, but employing a He-N₂ mixture which combines the proven aspects of their air turbines with the advantageous thermal properties of helium, allowing a smaller heat exchanger to be used. Moreover, it is possible that Rolls-Royce could design the power conversion module as a separate unit. This would simplify the U-Battery® design process and remove a substantial item of risk from the program, as well as offering the potential for some novel financing options. The U-Battery® investors plan to hold discussions with Rolls-Royce in the near future.

5.3 Control System Design

The control system for the U-Battery® will be based on existing high-integrity control systems available from established vendors such as Siemens. However, it is anticipated that the control requirements for the U-Battery® will be considerably simpler than for corresponding LWRs, allowing a substantial reduction in control system cost.

5.4 General Plant Layout

The layout of the primary circuit and power conversion module fluid systems has already been described in Section 4 (Core Structural Design). A preliminary design for the U-Battery® plant layout is provided in Figure 5.1 below.

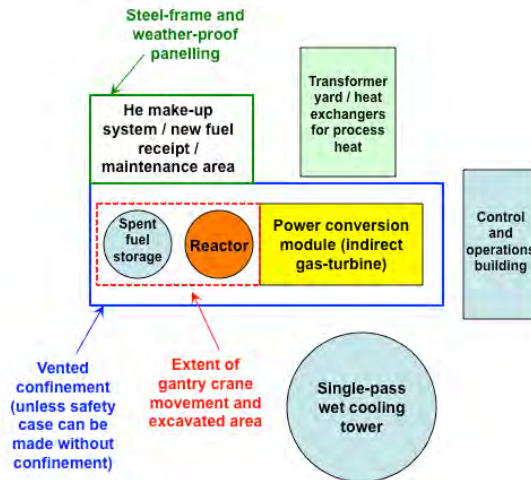


Fig. 5.1: U-Battery® plant layout schematic

The main features are the provision of two adjacent excavated cavities housing the RPV and the spent core storage facility. Locating these major plant items below ground level will assist in radiation shielding and will limit the height of the U-Battery® structure. The power conversion unit is located adjacent to the reactor, sharing the same containment, but at ground level to facilitate access for maintenance. For costing purposes it is assumed that a sealed containment building will be required. However, it is likely that a vented confinement could be justified (similar to the Pebble Bed Modular Reactor concept), with a consequent reduction in cost. The mechanical annex, housing facilities for fuel receipt, maintenance, and He make-up, is also located adjacent to the reactor, but does not need to be accommodated within the containment because it does not house safety-critical systems. It is anticipated that the civil structures outside of the containment can be of steel-frame and weather-proof panel construction to minimize cost.

5.5 Fuel Transport

The original U-Battery® concept envisaged the core being replaced as a single “battery” unit. However, a review of European road transportation regulations has shown that the physical size of the reference U-Battery® core would preclude transport as a single module in a standard ISO freight container package. Moreover, it is considered unlikely that regulatory authorities would accept the transport of an intact reactor core. Instead, it is proposed to transport individual fuel elements, and to build the core structure on site, following conventional practice. Although this approach lacks the simplicity of a single “battery” module, the infrequency of refueling ensures that any additional time taken to refuel the reactor will be inconsequential compared with the regulatory difficulties associated with shipping an intact core. Several existing transport containers are likely to be suitable for U-Battery® fuel elements with only minor modifications, including the current containers for UK Advanced Gas Cooled Reactors. Fresh fuel transport is therefore considered to be feasible with the existing transport infrastructure, and no new development is anticipated.

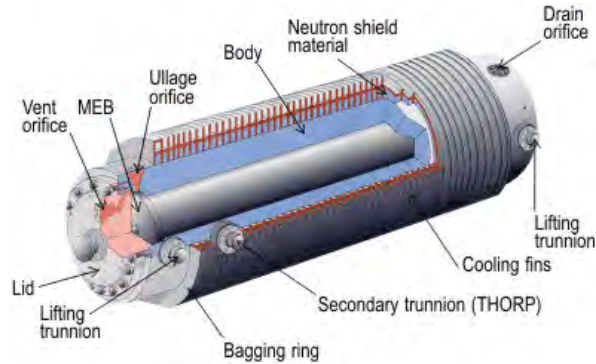


Figure 5.2: Excellox spent fuel transport flask

Spent fuel transport for the reference design is simplified by the use of individual fuel elements, avoiding the need to transport an intact core. For this purpose, several existing spent fuel transport casks already exist.

However, for the 10 MW_{th} design, it may be possible to transport an intact fresh/spent core using an Excellox transport flask, shown in Figure 5.2. Design details for the Excellox-7 flask have been requested from Sellafield Sites Ltd.

6. Economic Analysis

So far, most reactors have been built with economies of scale by increasing the power of the reactor, as the leading principle. The purpose of the U-Battery design however has been to devise an economically feasible micro reactor ($\leq 20\text{MW}_{\text{th}}$) that can be justified by the economics of number. Besides this aspect major cost saving aspects compared to large-scale reactor design have been achieved by the intrinsic safe reactor design with virtually no operating or maintenance expenses and the built in capability for modular design.

Based on the Cost Estimating Guidelines for Generation IV Nuclear Energy Systems, a top-down cost calculation approach is adopted. The analysis consists of an input-throughput-output model to assess the economic parameters of a 20 MW_{th} U-Battery compared with a 2*10 MW_{th} U-Battery. A South African 100MW_{th} HTR case is used as a cost calculation reference.

6.1 Cost of Major Equipment

Starting point of the analysis are the costs of the following equipment, which serves as a base for both cases to be compared (see table 1):

- Reactor Pressure Vessel
 - Vessel (SA-508 steel @ 30€/kg)
 - Reflector material (Graphite @ 65€/kg and BeO @ 230€/kg)
 - Control Rods (scaled down from AP600-CRDM)
- Power Conversion Module (preliminary estimate from Rolls-Royce)
- Miscellaneous Equipment

6.2 Markups for direct, indirect costs and contingencies

Markups on top of the major equipment costs are used for direct field costs, indirect cost and contingencies. For the direct field costs (mechanical, electrical, civil, and instrumentation) the markup is 100% on the cost of major equipment. The markup for indirect cost (engineering, procurement, construction, management) is 50% on top of the sum of cost of major equipment and direct field costs. With the markup for contingency at 30% over the total costs, the total fixed capital expenditures amounts to 76 M€ for the 20 MWth case and 63 M€ for the 2*10 MWth case (see table 6.1).

6.3 Working Capital

Fuel, fuel-handling Costs

At 17% Uranium enrichment for the 20 MWth case and a price (excl. final disposition) per 1,000 kg set at 15,800\$ the cost will be 11.5 M€. Adding handling cost for 0.5 M€ this amounts to 12 M€ for the 20 MWth case for a batch with a lifetime of 10 years. Costs are calculated on 2011 Uranium and fuel enrichment data. Along the same line of reasoning we arrive for the 2*10 MWth case at 6.1 M€ (20% enrichment, 208 kg). This batch will have a lifetime of 5 years.

Construction installation manpower Costs

For both cases the labor costs during construction are set at 4 M€.

Decommissioning Costs

Based upon detailed calculations for the decommissioning of the RID reactor at Delft we estimated that for both U-Battery cases a NPV (Net Present Value) of 10.3 M€ is needed.

6.4 Resulting total investment

Adding up all parts of the capital expenditure we arrive at a cash outflow of 102,4M€ for the 20 MWth U-Battery and 83,2 M€ for the 2*10 MWth:

Table 6.1 Calculation of Total Investment, NPV (both in M€), ROI and PBP

	20 MWth	2*10 MWth
Vessel	2,2	1,1
Reflector Material	5,6	3,0
Control Rods	2,3	2,6
Power Conversion Module	2,9	2,9
Miscellaneous Equipment	6,5	6,5
Cost of Major Equipment	19,5	16,1
Markup for other Direct Costs	19,5	16,1
Direct Costs	39,0	32,2
Markup for Indirect Field Cost	19,5	16,1
Markup for Contingencies	17,6	14,5
Initial Fuel Core Load	12,0	6,1
Labour during Construction	4,0	4,0
Decommissioning Costs	10,3	10,3
Working Capital	26,3	20,4
Total Investment (TI)	102,4	83,2
Net Present Value (NPV)	7	23
Return on Investment (NPV/TI)	7%	28%
Pay Back Period (in years)	18	16

6.5 Running costs

The revenues of both cases are dependent on the availability of the U-Battery, the efficiency and of course the selling price per KWh of the generated electricity. At 96% availability and 40% efficiency, the battery produces 7.7 MW. At a selling price of 0.10 €/KWh and 8.766 hours /year this gives a cash inflow of 6.9 M€.

The cash outflow consists of direct labor 15 FTE (e.g. Operating, Maintenance and Security) and direct materials 350 K€/ year (3% of replacement asset value) which totals 1.4 M€.

These cash flows occur for each year in the lifetime of the U-Battery (set at 60 years) and are accrued with the inflation rate of 2%/year.

6.6 Results

In order to assess both cases, we selected the Net Present Value (NPV), the total Investment (TI), the ROI (defined as the NPV/TI) and the Pay-Back Period (PBP) as measures. The firms cost of capital was set at 5.6%: assuming an equity/debt ratio of 20/80, a return on equity of 12% and the cost of debt at 4%. This results in a NPV of resp. +7 M€ and +23 M€ as shown in table 6.2.

Table 6.2: Resulting measures.

M€	NPV	Investment	ROI	PBP
20 MWth	7	-102	7%	18
2*10 MWth	23	-83	28%	16

In both cases the investment per KWh is approx. 2 euro cent. The total U-Battery electricity producing of 20 MWth would be enough for a community of 20.000 families, consisting of an average of 2.3 persons per family and using on average 3500 KWh per family.

6.7 Sensitivity Analysis

By changing the variables between -100% and +100% we were able to discover the impact of each variable in the end result. Most sensitive for the end result is the price at which a KWh is sold, in our case set at 10 euro cent. This is the lower limit with a positive margin for the 20 MWth U-Battery. A price of 9 euro cent would result in a loss of -9% ROI in the steady state. However the 2*10 MWth U-Battery 9 cent/KWh seems to be still feasible but is the lower limit with a positive margin of 8% ROI.

6.8 Conclusions

This comparison shows that the U-Battery is economically feasible from a KWh price of 9 cent. This result shows that there are opportunities in designing tailor made reactors for large industries or (small) towns. These opportunities lie in modularity and standardization, simple design, serial fabrication of components and building multiple units at one site.

6.9 Still to be addressed: sharing the economic risk

Operating a U-Battery consists of roughly two parts: monitoring the reactor for security reasons and changing the fuel after each 5 or 10-year period. The cost of the monitoring part is dependent on the design of the U-Battery and the deployment of the battery by the end-user. In an industrial environment there might be opportunities to share these tasks either with other companies in the vicinity or within e.g. a production company with similar tasks thereby further improving the economic viability of the case.

The frequent necessity of RPV transport to the producer and changing of the fuel could be heavily reduced when performed by a specialized company that benefits by standardizing this task.

Though the capital investment for a U-Battery is much lower compared to the expenditure for a large reactor; there is still a timing difference between the manufacturing of the battery - up front, and the cash inflows - during the lifetime of 60 years. This would be a problem for a stand-alone situation, in which one or a relatively small number of batteries are produced. By applying serial production the producer can divert part of this economic risk. Alternatively, the timing difference could be a smaller problem for an end-user buying a secure energy solution at a fixed price for the next 60 years. The economic risk of building U-Batteries can thus be shared between producer and end-user.

ANNEX: Main Parameters of the U-Battery®

	10 MW _{th}	20 MW _{th}
Reactor Core		
Reflector composition	BeO	Graphite
Control rods (#)	4	6
Fuel Blocks (#)	6*4	30*4
Enrichment (%)	20	17
Fuel life time (a)	5	10
Fuel block dimension (cm)	36*80	36*80
Fuel mass (kg)	208	1.040
Burn-up (MWd/kg HM)	88	70
Radial dimensions		
Outer diameter (cm)	180	370
Vessel thickness (mm)	<100	100
Reactor core diameter (cm)	108	252
Reflector thickness (cm)	20 (BeO)	29
Insulation thickness (cm)	5 (SiC fiber)	10 (SiC fiber)
Barrel thickness (cm)	2	2
Gap thickness (cm)	5	5
Axial dimensions		
Core Height (cm)	320	320
Top reflector (cm)	20 (BeO)	50
Bottom reflector (cm)	20 (BeO)	50
Top plenum (cm)	20	20
Bottom plenum (cm)	50	50
Top insulation (cm)	30	30
Bottom insulation (cm)	60	60
Core support plate (cm)	10	15
Support structure (cm)	60	60
Vessel height (cm)	590	655
Reflector/Moderator		
BeO mass (kg)	7.900	0
Graphite mass (kg)	8.100	~ 70.000 (incl. Ins.)
Excellox Flasc		
Flask inner diam (cm)	180	
Flask inner height (cm)	>500	

Appendix A

Core Design of the U-Battery[®]

July 2011

Prepared by

Ming Ding

Jan Leen Kloosterman

Delft University of Technology

Contents

List of Figures	V
List of Tables.....	IX
A.1 Introduction	A.1.1
A.1.1 Features of small long-life reactors.....	A.1.1
A.1.2 Status of small long-life reactors	A.1.2
A.1.3 Development trend of small long-life reactors	A.1.5
A.1.4 Main object and structure of the report.....	A.1.7
A.2 Nuclear design of the U-Battery.....	A.2.1
A.2.1 Description of the U-Battery.....	A.2.1
A.2.2 Computer code system for nuclear design	A.2.4
A.2.3 20 MW _{th} designs	A.2.6
A.2.4 5 MW _{th} /10 MW _{th} designs.....	A.2.16
A.2.5 Preliminary design of fixed burnable poison	A.2.23
A.2.6 Thorium utilization in the U-Battery	A.2.30
A.2.7 Summary	A.2.47
A.3 Thermal-hydraulic design of the U-Battery	A.3.1
A.3.1 Coupled neutronic/thermal-hydraulic code system.....	A.3.1
A.3.2 Parametric analysis of two key components	A.3.9
A.3.3 Analysis of LOFC incidents for a cylindrical core	A.3.13
A.3.4 Analysis of LOFC incidents for an annular core.....	A.3.23
A.3.5 Further comparisons of cylindrical with annular designs	A.3.28
A.3.6 Thermal power investigation of the annular design.....	A.3.31
A.3.7 Summary	A.3.33
A.4 Conclusions and recommendations.....	A.4.1
A.4.1 Conclusions.....	A.4.1
A.4.2 Recommendations.....	A.4.3
References.....	A.5.1

List of Figures

Fig. A.1.1 Construction sites and proposed deployment areas of floating nuclear power plants in Russia.	A.1.3
Fig. A.1.2 Russian Power Supply System.	A.1.4
Fig. A.2.1 3D schematic diagram of a cylindrical core and fuel block.	A.2.2
Fig. A.2.2 A schematic of a TRISO coated particle, fuel compacts and fuel block	A.2.3
Fig. A.2.3 3D schematic diagram of an annular core with side and bottom reflectors	A.2.4
Fig. A.2.4 Execution path for the T6-DEPL analytical depletion sequence in TRITON	A.2.5
Fig. A.2.5 Typical cylindrical and annular core configurations	A.2.7
Fig. A.2.6 Four non-cylindrical core configurations	A.2.10
Fig. A.2.7 Induced reactivity as a function of the water/steam density and with time as a parameter for Layout 30*4.....	A.2.15
Fig. A.2.8 Maximum reactivity induced by the water/steam as a function of the burnup time for Layout 37*3 and Layout 30*4	A.2.15
Fig. A.2.9 Reactor core configurations of 5 MWth U-Battery with 3.7 m RPV in diameter	A.2.18
Fig. A.2.10 Reactor core configuration of the U-Battery with 1.8 m RPV in diameter	A.2.20
Fig. A.2.11 Cross section of the fuel block of the U-Battery and main geometric parameters	A.2.24
Fig. A.2.12 k_{inf} of a typical fuel block fueled 12% uranium as a function of time for Layout 37*4	A.2.25
Fig. A.2.13 Reactivity swing and k_{inf} at EOL as functions of initial mass of B-10 for 0.2- mm-diameter FBP kernels	A.2.26
Fig. A.2.14 Reactivity swing and k_{inf} at EOL as functions of initial mass of B-10 for 0.07- mm-diameter FBP kernels	A.2.28
Fig. A.2.15 Reactivity swing and k_{inf} at EOL as functions of initial mass of B-10 for 0.05- mm-diameter FBP kernels	A.2.30
Fig. A.2.16 Seed-and-blanket (S&B) fuel block with ThO ₂	A.2.31
Fig. A.2.17 k_{inf} of the S&B type fuel block as a function of the mass of U-235 and with time as a parameter	A.2.33
Fig. A.2.18 The reactivity swing and mass ratio of fissile isotopes at EOL to at BOL as functions of the number of UO ₂ fuel rods.....	A.2.34
Fig. A.2.19 Mass fractions of main fissile isotopes in the fuel block at EOL as functions of the number of UO ₂ fuel rods.....	A.2.35
Fig. A.2.20 k_{inf} and CR of S&B type fuel block with 36 UO ₂ fuel rods as functions of enrichment of uranium.....	A.2.37
Fig. A.2.21 Mass fractions of fissile isotopes and remaining U-235 at EOL of S&B fuel block with 36 UO ₂ fuel rods as functions of enrichment of uranium	A.2.38
Fig. A.2.22 k_{inf} of the fuel block with 36 UO ₂ fuel rods as a function of N_C/N_{HM} changed by the geometric parameters of ThO ₂ fuel rods	A.2.40

Fig. A.2.23 Reactivity swing of the fuel block with 36 UO ₂ fuel rods as a function of N_C/N_{HM} changed by the geometric parameters of ThO ₂ fuel rods	A.2.41
Fig. A.2.24 Conversion ratios of the fuel block as functions of N_C/N_{HM}	A.2.42
Fig. A.2.25 k_{inf} of the fuel block with 36 UO ₂ fuel rods as a function of N_C/N_{HM} changed by the geometric parameters of UO ₂ fuel rods.....	A.2.43
Fig. A.2.26 Comparison of the k_{inf} of the MOX with S&B fuel blocks at BOL and EOL	A.2.45
Fig. A.2.27 Comparison of the CRs of the MOX with S&B fuel blocks at EOL.....	A.2.47
Fig. A.3.1 Generation methodology of the few-group cross section libraries of the U-Battery.....	A.3.2
Fig. A.3.2 Coupled DALTON/THERMIX code system	A.3.4
Fig. A.3.3 3D schematic diagram of Layout 30*4 of the U-Battery	A.3.6
Fig. A.3.4 A schematic diagram of the horizontal cross section of Layout 30*4 of the U-Battery.....	A.3.7
Fig. A.3.5 Maximum and volume-averaged temperature of the reactor core as functions of time	A.3.10
Fig. A.3.6 Maximum temperatures of the reactor pressure vessel and barrel as functions of time	A.3.11
Fig. A.3.7 Maximum and volume-averaged core temperatures during the PLOFC and DLOFC incidents	A.3.13
Fig. A.3.8 Radial solid temperature distributions of the reactor system during the PLOFC and DLOFC incidents	A.3.15
Fig. A.3.9 Solid temperature responses of the reactor core during the PLOFC and DLOFC incidents	A.3.16
Fig. A.3.10 The volume-averaged temperatures of the reflectors during the PLOFC and DLOFC incidents	A.3.17
Fig. A.3.11 Maximum temperature of the RPV during the PLOFC and DLOFC incidents	A.3.18
Fig. A.3.12 Radial velocity distributions of the coolant in the middle plane (z=130 cm) of the reactor core during PLOFC and DLOPC incidents	A.3.20
Fig. A.3.13 Coolant velocities and densities of two typical channels in the reactor core as functions of time during the PLOFC incident.....	A.3.21
Fig. A.3.14 Coolant velocities and densities of two typical channels in the reactor core as functions of time during DLOFC incident.....	A.3.22
Fig. A.3.15 Maximum and volume-averaged temperature of the fuel zone for Layout 30*4 during the LOFC incidents.....	A.3.24
Fig. A.3.16 Typical axial velocities of two meshes in the fuel zone of the annular core during PLOFC and DLOFC incidents	A.3.25
Fig. A.3.17 Radial solid temperature distribution of Layout 30*4 during the LOFC incidents (z = 130.0 cm)	A.3.26
Fig. A.3.18 Solid temperature responses of the annular fuel zone as functions of time during PLOFC and DLOFC incidents	A.3.28
Fig. A.3.19 Maximum and volume-averaged temperatures of the fuel zone of the annular and cylindrical designs during DLOFC incident	A.3.30
Fig. A.3.20 Maximum temperatures of the barrels and RPVs for the annular and cylindrical designs during DLOFC incident	A.3.30

- Fig. A.3.21 Maximum core temperature of Layout 30*4 as a function of time and with thermal power as a parameter during DLOFC incident..... A.3.32
- Fig. A.3.22 Maximum RPV temperature of Layout 30*4 as a function of time and with thermal power as a parameter during DLOFC incident..... A.3.32

List of Tables

Table A.1.1 Typical small long-life reactors	A.1.8
Table A.1.2 Small long-life reactors at universities	A.1.9
Table A.1.3 Other small and medium size reactors	A.1.10
Table A.2.1 Basic design parameters of the U-Battery	A.2.1
Table A.2.2 Geometric parameters of coated TRISO particles with LEU	A.2.3
Table A.2.3 Reactor core configurations of the U-Battery	A.2.7
Table A.2.4 Fuel compositions of seven core configurations.....	A.2.8
Table A.2.5 k_{eff} of six core configurations with 0.25-mm- radius fuel kernels	A.2.11
Table A.2.6 k_{eff} of six core configurations with 0.3 mm fuel kernel radius	A.2.11
Table A.2.7 Maximum lifetime/burnup of six reactor core configurations.....	A.2.12
Table A.2.8 Reactivity temperature coefficients of U-Battery from 800 K to 1000 K	A.2.13
Table A.2.9 Effective multiplication factors and fuel cost of eight configurations...	A.2.18
Table A.2.10 Fuel cost of different fuel compositions	A.2.19
Table A.2.11 Neutronic results of the reactor configurations for with 1.8 m RPV in diameter (graphite side reflector).....	A.2.21
Table A.2.12 Neutronic results of the reactor configurations for with 1.8 m RPV in diameter (BeO side reflector).....	A.2.23
Table A.2.13 Geometric and composition parameters of fixed burnable poison	A.2.26
Table A.2.14 Excess reactivity control mode of the U-Battery	A.2.30
Table A.2.15 N_C/N_{HM} range caused by geometric parameters of fuel rods	A.2.39
Table A.2.16 Design parameters of the S&B fuel blocks with small reactivity swing	A.2.44
Table A.3.1 Energy boundaries of 26 few-groups structure.....	A.3.3

A.1 Introduction

In the past fifty years, the size of nuclear reactors has grown from 60 MWe to more than 1600 MWe in order to make full use of economy of scale. However, because large-size nuclear reactors usually require high capital investment and heavily rely on the infrastructure of reactor sites, this has motivated designers to develop small and medium-size reactors¹ to provide electricity and heat, especially for developing countries and remote areas off main grids. For example, the area of decentralized energy supply covers about 2/3 of the territory of Russia. Thus small and medium-size reactors can be a reasonable alternative to energy sources based on fossil fuel for Russia. Alaska, USA may have to face the same condition as the north area of Russia. For many developing countries, especially small developing countries, infrastructure and electric grids are not capable to adopt large-size nuclear reactors. Small and modular reactors are preferred for them.

Fortunately, there have been many small-size reactors built for propulsion, research, etc. worldwide, which has already accumulated full operation and design experiences for small-size reactors. For example, Russia is building floating nuclear power plants (FNPPs), which are based on the experiences from reactors well proven in icebreakers. International Atomic Energy Agency (IAEA) and other organizations have been supported the development and employment of small and medium-size reactors^[1, 2, 3]. There are more than 100 small and medium-size reactors operating worldwide. About 60 innovative concepts and designs of the small and medium-size reactors are proposed and analyzed within national or international programs in 13 IAEA member states, including both industrialized and developing countries. Among them, about half of small and medium-size reactors are reactors without on-site fueling^[1].

A.1.1 Features of small long-lifetime reactors

Compared with large-size nuclear reactors, small and medium-size reactors are easier to be modularized, which is a natural advantage. On the other hand, modularization is inherent requirement of small and medium-size reactors in order to reduce the capital cost and compete with large-size reactors, especially for the small-size reactor. For small modular reactors (SMRs), it's possible to fabricate them in a factory and transport them to

¹ According to the classification adopted by IAEA, small size reactors are the reactors with equivalent electric power less than 300 MW, and medium size reactors are the reactors with equivalent electric power between 300 MW and 700 MW.

sites by rail, barge, truck, etc. After a long operation, these reactors can be brought back to factories for refueling or directly replaced by new ones. This would greatly reduce the dependence of nuclear reactors on infrastructure, which means that SMR sites can be chosen more flexibly than large-size reactors'. Moreover, these SMRs are possible to be designed into super secure types like emergency systems free or walk-away safety, since they commonly operate at low power level. It is relatively easier to ensure that these reactors are inherently or passive safer than large-size ones. Because of simplified systems and inherent safety, SMRs can be operated by only a few operators. Thirdly, since these SMRs have a low thermal power, likely less than 100 MWth, it is easy to design them to have a long lifetime, for example, 5 to 10 years or even longer, without fueling. Thus, such SMRs can be used as batteries because of their long lifetime, inherent safety and good transportability; they may usually have different names like nuclear batteries or battery-type reactors. It must be emphasized that some SMRs are designed based on the concepts of passive safety and modularization, but they are not classified into nuclear batteries in this report if they do not have a long lifetime and good transportability. For example, the Pebble Bed Modular Reactor (PBMR) and HTR-PM are two small-size reactors according to the classification of IAEA. However, because they are not designed as transportable reactors with a long lifetime, the PBMR and HTR-PM are excluded out of nuclear batteries in the report.

A.1.2 Status of small long-life reactors

As mentioned above, there are about 30 concepts of innovative SMRs without on-site refueling proposed and analyzed by Russia, USA, Japan, Republic of Korea, Indonesia, etc. Among them, Russia, Japan and United State have possessed relative mature designs of small long-life reactors without on-site refueling. Moreover, these small long-life reactors almost cover all types of exist reactors: water-cooled reactors, gas-cooled reactors, sodium cooled reactors, lead or lead-bismuth cooled reactors and molten-salt cooled reactors.

Some typical small long-life reactors are summarized in Table A.1.1. These designs or projects are developed or supported by national laboratories, research institutes or commercial companies, and they may be demonstrated or commercially operated in the next decades. These designs are relatively mature, and some of them are in the stage of commercialization. Table A.1.2 shows some research projects at universities worldwide. Universities usually play important roles to promote more advanced concepts. These concepts of small long-life reactors are first studied at the universities, and further commercialized by commercial companies. For example, the researchers in Oregon State

University executed the experiment study of MASLWR as shown in Table A.1.2, and its commercialization version is NuScale, as shown in Table A.1.1. Other small or medium size reactors are listed in Table A.1.3. Some of them are small long-life reactors, however because their technologies may not be mature or projects may be terminated because of lacking funding, they are not listed in Table A.1.1. Some of small long-life reactors in Table A.1.3 are also not included in Table A.1.1 because they lack transportability. Although they are excluded as nuclear batteries in the report, the designs and concepts are advanced and can provide experience to the development of nuclear batteries.

The development status of small long-life reactors will be introduced in detail in the following part of this section by taking Russia, Japan and the United States of America as examples, because these three countries have relative mature technologies in the field of the small long-life reactors.

A.1.2.1 Russia

From type and development stage point of view, the technologies of small long-life reactors are the most mature in Russia. The types of small long-life reactors in Russia cover water-cooled reactors, liquid-metal cooled reactors and molten-salt cooled reactors. Russia has developed small and medium-size reactors since 1990s based on the experience of naval reactors, including the VBER150, ABV, KLT20 and SVBR75/100 and so on. The transportable nuclear reactors are usually called in Russia floating nuclear reactors or floating nuclear power plants (FNPPs), because they are transported from factories to sites by barges. Conceptual designs of most reactors have been completed, as shown in Table A.1.1, and some reactors are under construction. For example, Rosatom is planning to build seven or eight FNPP by 2015. The construction sites and proposed deployment areas of FNPP are shown in Fig. A.1.1.



Fig. A.1.1 Construction sites and proposed deployment areas of floating nuclear power plants in Russia

There are mainly two reasons for Russia to develop the small and medium size reactors without on-site refueling. The first reason is that two-third territories of Russia is separated from the country's major electric grid, as shown in Fig. A.1.2. The demand of domestic market is large enough for the small long-life reactors. The second reason is that Russia has accumulated plenty of experience from its naval reactors, especially liquid-metal reactors. For example, operation experience of lead-bismuth cooled reactors amount up to 80 reactor-years. Compared with Russia, there is nearly no mature operation experience for this type of reactors in other countries.

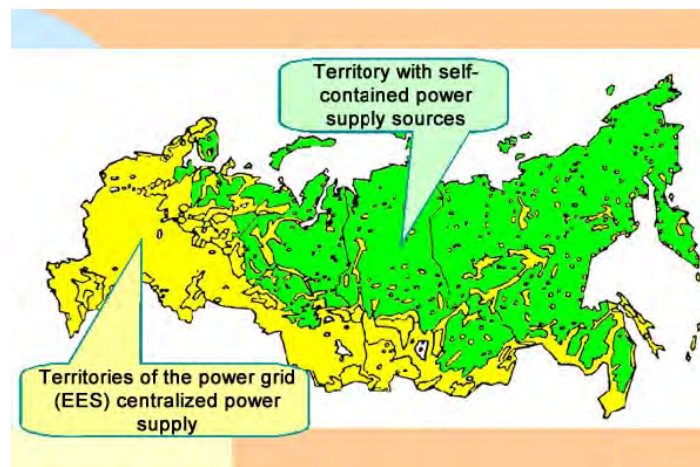


Fig. A.1.2 Russian Power Supply System

A.1.2.2 Japan

Japan is a country lacking of natural resources domestically, such as oil, coal, and gas, so Japan has been developing actively nuclear power. As for small long-life reactors, Japan has been focused on sodium-cooled reactors and lead-bismuth cooled reactors. Toshiba Company Ltd. developed a Super-Safe Small and Simple (4S) Reactor to provide electricity, heat or potable water for remote areas. Since 4S reactor adopts fast reactor technology, it is able to run for 30 years without refueling. The technology of the 4S reactor is almost mature and can enter into demonstration stage or commercial operation currently. The 4S reactor is being reviewed by NRC, USA for design certification because Alaska is pursuing to adopt this type of reactor for electricity. Alaska is separated from the main electrical grid of the United States.

Meanwhile, Tokyo Institute of Technology (TITech) is developing two types of lead-bismuth cooled reactors, Pb-Bi cooled long-life reactor (LSPR) and Pb-Bi Cooled Direct Contact Boiling Water Small Reactor (PBWFR). The former is designed for transportation. JAEA has a similar design as the LSPR. Cooperating with TITech,

Bandung Institute of Technology (ITB) proposed a series of small, long-life, transportable reactor, SPINNOR (Small Power Reactor, Indonesia, No On-site Refueling) and VSPINNOR (Very Small Power Reactor, Indonesia, No On-site Refueling) because Indonesia has thousands of islands where electrical power is generated locally off the major grid.

A.1.2.3 the United States of America

Under the generation IV Nuclear Energy Systems Initiative, the United States of America (USA) has been developed the Secure Transportable Autonomous Reactor (STAR) series by the teams of national laboratories (Argonne, Livermore, Los Alamos, and Idaho) and the Encapsulated Nuclear Heat Source (ENHS) lead by Lawrence Livermore National Laboratory (LLNL) and University of California, Berkeley (UCB). Small Secure Transportable Autonomous Reactor (SSTAR) in the STAR series is a lead-cooled, transportable small size reactor and is targeted to provide electricity or desalination service for countries with small electrical grids, or remote regions where power is generated locally with no connection to the major grids. The ENHS, proposed by UCB, is a lead or lead-bismuth cooled fast reactor and has the same aims as the SSTAR. Both reactors adopt liquid metal cooled reactor technology in the frame of the generation IV nuclear energy system initiative because only the lead or lead-bismuth cooled reactor is proposed to develop small reactors among six generation IV reactor systems. Super critical carbon dioxide (SCO₂) is chosen as the working medium of power conversion systems of the ENHS and SSTAR in order to maintain higher efficient of the systems. Beside of SSTAR, the STAR series includes STAR-LM concept for electricity production and STAR-H₂ concept for hydrogen production. ENHS reactor has a version of Solid-Core Heat-Pipe Nuclear Type Reactor, HP-ENHS. The technology or concept of the HP-ENHS is similar to the space nuclear reactor, SAFE 400. The reactor core is solid and cooled by liquid metal heat pipe.

A.1.3 Development trend of small long-life reactors

In order to maintain maturity of technologies, most of the concepts or designs of small size reactors in the 1990s adopt well-proven technologies. It is common that the primary loop of nuclear reactor systems adopts forced circulation, and meanwhile the secondary loop adopts Rankine cycle (water). For example, the floating nuclear power plant KLT20 employs two pumps in its primary loop. And the 4S reactor of Toshiba Company Ltd. also uses the pool, forced circulation. These two types of reactors current have construction plans. Russia announced to construct a floating nuclear power plant

based on the KLT40S reactor that has the same design of the KLT20 in 2009. And USA and Japan are cooperating to construct the 4S reactor at Galena, Alaska, USA.

However, there are three clear trends of the development of technologies for small-size reactors. The first trend is safer design philosophy, in other words, passive or inherent safety. For the safety of modern reactors, maintaining negative temperature coefficient of reactivity in the entire power range is a basic principle from neutronic point of view. Based on the principle, the safety of reactors relies heavily on thermal-hydraulics design of reactors. A basic challenge of thermal-hydraulics is to safely transfer heat or decay heat out of reactors and keep reactors intact in any conditions, including normal operation and accident conditions. It is preferred to transfer heat out of the reactor by natural laws, like conduction, convection and/or radiation, rather than by forced methods like pumps. Compared with large-size reactors, small-size reactors with passive or inherent safety are easier to be realized.

Since reactors commonly adopt a liquid working medium to transfer heat out of them, natural circulation is a rather popular and natural way to realize heat transfer in the reactor for liquid cooled reactors, and conduction and radiation are also used in high temperature gas-cooled reactors because their large quantities of solid structures and high temperature. In table A.1.1, half designs and concepts of small size reactors use natural circulation as the cooling method of the reactors, including normal operation and accident conditions. If excluded designs and concepts in Table A.1.1 proposed in early the 1990s, for example VBER150, KTL series, 4S series, and LSPR, the ratio of natural circulation cooled reactors will increase largely. For the concepts proposed after 2000 or late of 1990s, almost all designs or concepts adopt the natural circulation at full power as cooling means, including MASLWR (NuScale), SSTAR, ENHS, HP-ENHS. For RS-MHR, it is a high temperature gas-cooled reactor and adopts direct cycle. It means that heat is transferred from the reactor to the power conversion system by forced circulation during normal operation, because the poor natural circulation performance of gas. However, during accidents the RS-MHR can entirely adopt passive cooling ways that has been validated by the experiments of high temperature gas-cooled reactors, such as AVR, HTR10 and HTTR.

The second trend of technology of the small-size reactors is longer life, and sustainable use of uranium source. Therefore, fast neutron reactors dominate most of the concepts of the small long-life reactors, including sodium-cooled reactors and lead or lead-bismuth cooled reactors. Japan has developed sodium-cooled reactors and lead-bismuth cooled reactors, and the United States has focused on the lead-bismuth cooled reactors under the frame of the generation IV nuclear system initiate.

The third trend of technology of the small-size reactors is modular construction. Economy of replication is used to replace the economy of scale that large size nuclear power plants adopt.

A.1.4 Main object and structure of the report

Although a large amount of small long-life reactors are proposed in terms of inherent safety worldwide, most of them are in the stage of the conceptual design, and lack direct experimental validation, especially for the inherent safety principles of the reactors. However, the inherent safety of modular high temperature gas-cooled reactors (HTRs) has been validated directly by experiments over the last 30 years in AVR, HTR-10 and HTTR worldwide. Moreover, few studies have focused on small long-life HTRs. So, this report proposes a small, inherently safe and long-life HTR, called the U-Battery, which can be commercialized in the near future. The term U-Battery is used for this small HTR in order to emphasize its long-life core, transportability and inherent safety.

The second section of the report presents the nuclear design of the U-Battery using the SCALE code system. Different reactor core configurations, like cylindrical reactor cores, annular reactor cores and scatter reactor cores, are proposed in terms of different considerations or design basis, like different thermal power, lifetime and reactor pressure vessels. Because a long lifetime, the initial excess reactivity of the U-Battery is rather large, the geometric parameters of fixed burnable poison are optimized in terms of a typical fuel block of a cylindrical reactor core. Thorium-fueled U-Battery is also analyzed based on the seed-and-blanket fuel block.

The third section of the report presents the thermal-hydraulic design of the U-Battery using the coupled DALTON-THERMIX code system. Two key components, i.e., the reactor cavity cooling system and side reflector, are investigated by in terms of depressurized loss of forced-cooling (DLOFC) incident. Moreover, a cylindrical reactor core and an annular reactor core are evaluated and compared for loss of forced-cooling (LOFC) incident.

The fourth section presents the main conclusions and recommendations of the nuclear and thermal-hydraulic designs of the U-Battery.

Table A.1.1 Typical small long-life reactors

No.	Concept name	Principal designer/Country	Power MWth/MWe	Lifetime (Years)	Design stage	Timeline	Reactor type	Fuel	PCU	Notes
1	NuScale [4]	NuScale Power/ USA	160/45	2.5	Conceptual design/ Pre-application review	<5 years	Integral PWR/Thermal/ Natural circulation	Rod, UO ₂ (4.95%)	Rankine (Water)	LWR
2	UNITHERM [1, 5]	NIKIET/Russia	30/(2.5 or 6)	16.6	Conceptual design completed	5 years	Integral PWR/Thermal/ Natural circulation	Rod, U-Zr metal ceramic	Rankine (Water)	LWR
3	ABV[1]	OKBM/Russia	45/11	8	Conceptual design completed	2-3 years	PWR/Thermal/ Natural circulation	Rod, UO ₂ (16.5%)	Rankine (Water)	LWR, FNPP
	KLT20[1] (KLT-40S)		70/20	8			PWR/Thermal/ Forced circulation	(<20%)		
4	RS-MHR [6]	GA/USA	-/10	6-8	Feasibility study	-	Prismatic HTR/Forced circulation	TRISO UO ₂ (19.9%)	Brayton (Helium)	HTGR
5	4S[1, 7-9] (4S series)	Toshiba/Japan	30/10	30	Conceptual design completed/Pre-application assessment	5-6 years	Pool/Fast/ Forced circulation	Rod, U-Zr metal (17-19%)	Rankine (Water)	SFR
6	SVBR75/100 [1, 10]	IPPE/Russia	280/101.5	6	Conceptual design completed	6-8 years	Pool/Fast/ Forced circulation	Rod, UO ₂ (16.1%)	Rankine (Water)	LFR
7	SSTAR [1, 11-14]	ANL/USA	45/20	20	Early conceptual design	10 years	Pool/Fast/ Natural circulation	Rod, UN TRU-N	Brayton (SCO ₂)	LFR
8	MARS [1, 15]	RRC Kurchatov Institute/Russia	16/6; 16/8.5 (heat)	15-60	Conceptual design	5-8 years	Pebble Bed/Thermal/ Natural circulation	TRISO UO ₂ (10%)	Brayton (Air)	MSR

Table A.1.2 Small long-life reactors at universities

No.	Concept name	Principal designer/Country	Power MWth/MWe	Lifetime (Years)	Design stage	Reactor type	Fuel	PCU	Notes
1	MASLWR [16, 17]	Oregon State University/USA	150/35	5	Feasibility study completed	Integral PWR/Thermal/ Natural circulation	Rod, UO ₂ (8%)	Rankine (Water)	Water
2	ENHS [18, 19]	UC Berkeley/USA	125/50	20	Feasibility study	Pool/Fast/ Natural circulation	Rod, UN or UZr etc	Brayton (SCO ₂)	Pb-Bi
	HP-ENHS [19, 20]	UC Berkeley/USA	125/62.5	20	Feasibility study	Solid/Fast/ Natural circulation	Rod, UN and Pu or TRU	Brayton (SCO ₂)	Liquid metal Heat Pipe
3	LSPR [21-24]	TITech/Japan	150/53	11.5	Feasibility study	Pool/Fast/ Forced circulation	Rod, UN (10-12.5%)	Rankine (Water)	Pb-Bi
4	SPINNOR/ VSPINNO R [1]	ITB/Indonesia	50/20; 27.5/10/ 17.5/6.2 5	15; 25; 35	Feasibility study	Pool/Fast/ Forced circulation	Rod, UN-PuN (10-12.5%)	Rankine (Water)	Pb-Bi
5	UBattery [25,26]	TUDelft/ Netherlands	20/-	10	Feasibility study	Pebble bed&Prismatic/ Thermal/ Natural circulation	TRISO UO ₂ (4-20%)	-	Molten salt
6	BORIS [27-29]	Seoul National University./South Korea	22.2/10.1	20	Feasibility study	Pool/Fast/ Natural circulation	Rod, UN and Pu or TRU	Brayton (SCO ₂)	Pb

Table A.1.3 Other small and medium size reactors

No.	Concept name	Principal designer/Country	Power MWth/MWe	Lifetime (Years)	Design stage	Reactor type	Fuel	PCU	Notes
1	Hyperion [30,31]	Hyperion Power Generation/UUS	70/25	5-10	Feasibility study	Non-conventional	UH ₃	-	Transportable, un-mature, active
2	IRIS [32, 33]	Westinghouse/USA	1000 /335	2.5-4	Conceptual design	Integral PWR/Thermal/ Natural circulation	Rod, UO ₂ (4.95%)	Rankine (Water)	Non-transportable, mature, active
3	mPower [34]	B&W/USA	-/125	5-6	Feasibility study	Integral PWR/Thermal/ Forced circulation	Rod, UO ₂ (<5%)	Rankine (Water)	On-site refueling, active
4	Package reactor [1, 35, 36]	Hitachi and MHI/Japan	25/-	5-10	Feasibility study completed	Integral PWR/Thermal/ Natural circulation	Rod, UO ₂ (<5%)	Rankine (Water)	Transportable, Inactive
5	PFPWR50 [1, 37]	Hokkaido Univeristy/Japan	50/-	10	Feasibility study	PWR/Thermal/ Forced circulation	TRISO UO ₂ (5%)	Rankine (Water)	Non-transportable, un-mature, inactive
6	AFPR [1]	PNNL/USA	300/100	40	Feasibility study	BWR/Thermal/ Forced circulation	TRISO UO ₂ (10%)	Rankine (Water)	Non-transportable, un-mature, inactive
7	FBNR [1]	UFRGS/Brazil	134/40	>10	Feasibility study	PWR/Thermal/ Forced circulation	TRISO UO ₂ , MOX, (U-Th) O ₂	Rankine (Water)	Non-transportable, un-mature, active
8	ACACIA [38]	NRG/ Netherlands	60 /18-23	3	Feasibility study	Pebble bed HTR/Thermal/ Forced circulation	TRISO UO ₂ (9%)	Brayton (N ₂)	Non-transportable, Inactive

A.2 Nuclear design of the U-Battery

The nuclear design of the U-Battery described in this section is executed by the SCALE code system. Different reactor core configurations are investigated in terms of different design requirements like the diameter of reactor pressure vessel (RPV) and thermal power. The first section describes the U-Battery and shows the 3D geometries of the reactor core and a typical fuel block. The second section introduces the SCALE code system, calculation methodology and models of the U-Battery. The third section presents the nuclear design results like the reactor core configurations for the 20 MW_{th} U-Battery, which is the reference design. The fourth section shows that reactor core configurations of the 5 MW_{th} or 10 MW_{th} U-Battery in terms of different-diameter reactor pressure vessels. The fifth section presents the optimized parameters of fixed burnable poison (FBP) which is used to control the excess reactivity of the U-Battery. The sixth section analyzes the neutronic performance of seed-and-blanket (S&B) fuel blocks which aim to reduce the fuel cost and reactivity swing of the low enriched uranium (LEU) -fueled U-Battery.

A.2.1 Description of the U-Battery

The U-Battery is a small, inherently safe and transportable HTR with a long core life, which is designed to provide electricity to residential sites that are not connected to national grids, or electricity and process heat for different industrial costumers. The basic design parameters or design basis of the U-Battery are listed in Table A.2.1.

Table A.2.1 Basic design requirements of the U-Battery

Parameters	Values
Reactor type	Block-type HTR
Thermal power	5-20 MW
Lifetime	5-10 years
Coolant	Helium
Diameter of RPV	≤ 3.7 m
Fuel type	UO ₂ , TRISO coated fuel
Fuel enrichment	≤ 20%
Energy conversion system	Rankine steam cycle
Energy utilization	Electricity, process heat

Since the main ideas behind the U-Battery is inherent safety, modularity and near-term utilization, the U-Battery has been developed based on currently mature block-type HTR technologies, so it inherits the inherent safety which has been validated by experiments. The reactor core of the U-Battery is comprised of a certain number of

hexagonal fuel columns, side, top and bottom reflectors, as shown in Fig. A.2.1 (a), all located inside a reactor pressure vessel (RPV).

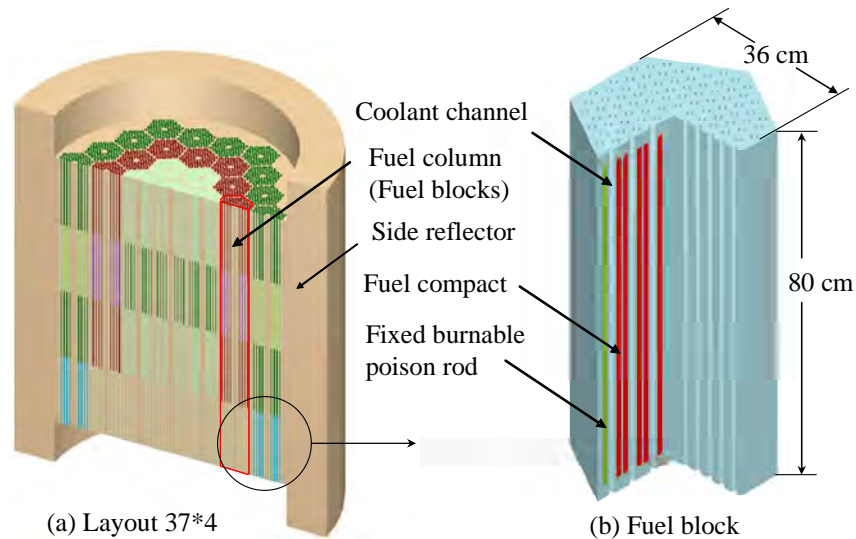


Fig. A.2.1 3D schematic diagram of a cylindrical core and fuel block; for clarity the top and bottom reflectors have been removed in the core, and the fuel handling hole has also been removed in the fuel block.

In the axial direction of the fuel columns, which is also the axial direction of the reactor core, each fuel column consists of several hexagonal graphite fuel blocks including blind holes for fuel compacts and fixed burnable poison (FBP) rods, and full length channels for coolant flow, as shown in Fig. A.2.1(b). The U-Battery uses the fuel blocks developed by General Atomic for the GT-MHR project. The block width cross flats is 36 cm and the height is 80 cm. Each fuel block includes 210 fuel channels, 108 coolant channels (including 6 small coolant channels with the same size as the fuel channels) and 6 FBP channels (which are used as fuel channels for the U-Battery). The diameters of the fuel, coolant and FBP channels are 1.27 cm, 1.588 cm and 1.27 cm, respectively. In each fuel channel, there are 14-15 fuel compacts including coated TRISO particles with fuel kernels. As shown in Fig. A.2.2, each coated TRISO particle consists of a low-enriched uranium (LEU) fuel kernel, buffer layer, IPyC layer, SiC layer and OPyC layer from the inner to outer. The size and density of each component of the TRISO particle are shown in Table A.2.2.

Since the numbers of fuel columns and fuel blocks are two key parameters of a core configuration of the U-Battery, the notation of Layout C*B is used to represent the core configuration of the U-Battery, where C is the number of the fuel columns in the reactor core and B is the number of the fuel blocks in each fuel column in the axial direction. For

example, the configuration of the reactor core shown in Fig. A.2.1(a) is Layout 37*4, which means that the reactor core is comprised of 37 fuel columns and each fuel column has 4 fuel blocks in the height direction or the axial direction of the reactor core. A typical annular core, Layout 30*4, is shown in Fig. A.2.3, which has 30 fuel columns and each fuel column has 4 fuel blocks. Moreover, there are 28(=7*4) graphite blocks in the center regions of the reactor core.

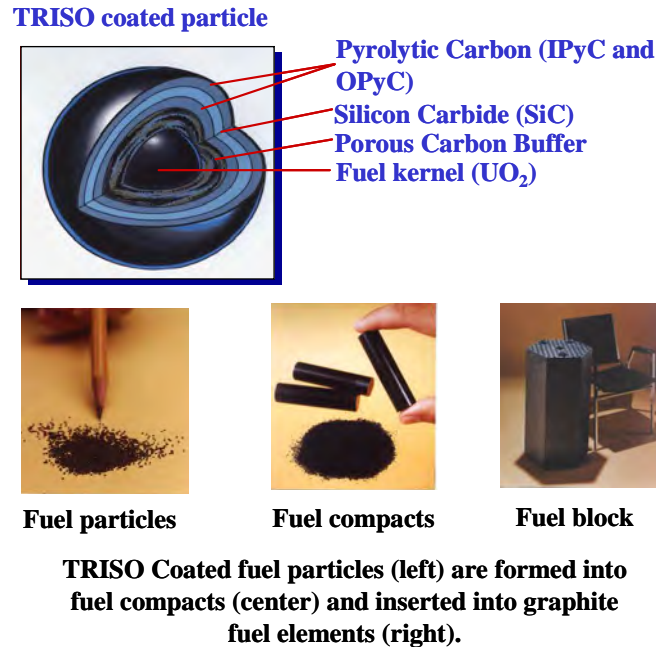


Fig. A.2.2 A schematic of a TRISO coated particle, fuel compacts and fuel block

Table A.2.2 Geometric parameters of coated TRISO particles with LEU

Parameter	Radius or thickness	Density [g/cm ³]
Fuel kernel (UO ₂)	0.25 [mm]	10.5
Buffer layer	100 [μm]	1.0
IPyC layer	35.0 [μm]	1.90
SiC layer	35.0 [μm]	3.2
OPyC layer	40.0 [μm]	1.87

A thermal power of 20 MW_{th} opens up the possibility of using the U-Battery for small industrial process heat applications, as well as for small-scale electricity application. The U-Battery with such thermal power can fill a niche of the market currently not open to nuclear energy. Fuel enrichment higher than 20% U-235 is not feasible since 20% U-235 is the maximum value for commercial applications with LEU. 10% U-235 or lower enrichment would be desirable from a practical point of view. The U-Battery accepts

helium as coolant because it has been used for graphite-moderated reactors over 20 years. The diameter of the U-Battery's RPV is requested to be less than or equal to 3.7 meters so that the U-Battery can be transported as a whole by rail, truck, or barge, etc. The power conversion system of the U-Battery may use a Rankine steam cycle since the U-Battery aims to be commercialized soon and the steam cycle is the most mature technology in the nuclear industry.

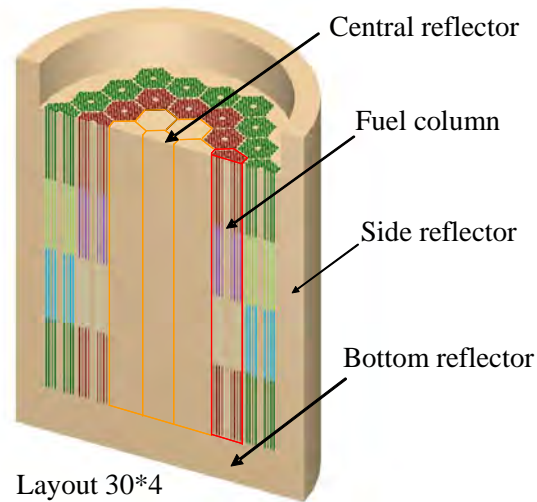


Fig. A.2.3 3D schematic diagram of an annular core with side and bottom reflectors. The top reflector has been removed in the reactor core.

A.2.2 Computer code system for nuclear design

The nuclear design of the U-Battery was executed by the SCALE (Standardized Computer Analyses for Licensing Evaluation) code system, including SCALE 5.1 and SCALE 6.0. The 3D models of the different reactor core configuration designs of the U-Battery, including an assembly of fuel blocks, and central, side, top and bottom reflectors, as shown in Fig. A.2.1 and Fig. A.2.3, were built in SCALE 5.1 or SCALE 6.0, in order to obtain the neutronic performance of the U-Battery, like effective multiplication factor and lifetime.

The SCALE code system has been developed at Oak Ridge National Laboratory for nuclear applications such as problem-dependent resonance self-shielding of cross-section data, criticality safety, radiation and shielding, etc. The SCALE code system is modular and mainly comprised of functional modules and control modules. In the calculations of the U-Battery, two function modules (BONAMI and CENTRM) were used to process the resonance cross section of the mixtures and cells used in the U-Battery. The KENOVI module, a 3D Monte Carlo criticality safety code, was used to calculate the effective multiplication factor of the U-Battery. The ORIGEN-S module was used to perform point

depletion calculations to obtain isotopic concentrations at different burnup times. The TRITON6 module was used to serve as the controller of module sequencing, data transfer, and input/output control for multiple analysis sequences. The modules called by TRITON6 and the T6-DEPL procedure of TRITON6 are shown in Fig. A.2.4 in detail. The whole calculation controlled by TRITON6 can be summarized in the following steps:

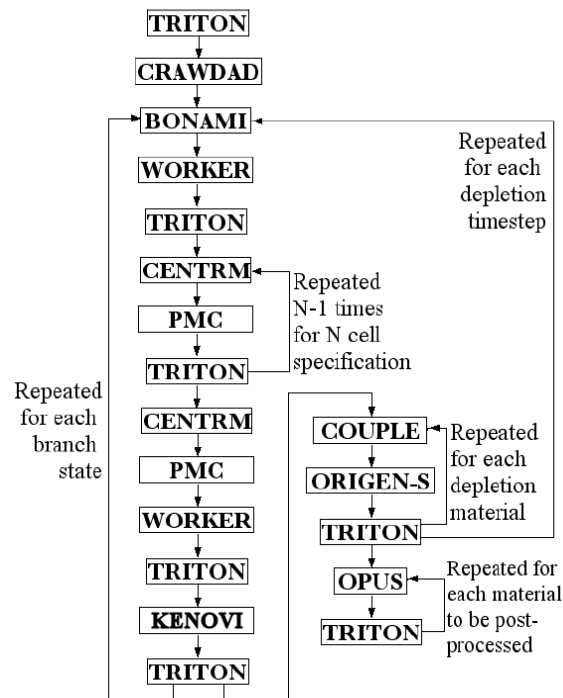


Fig. A.2.4 Execution path for the T6-DEPL analytical depletion sequence in TRITON

(1) Preparing resonance shielded and homogeneous cross sections for given unit cells. In the calculations of the U-Battery, the smallest unit used is a cylindrical homogenized fuel compact without explicit TRISO particles, which is placed in a graphite hexagonal geometry. Resonance cross sections of this unit are generated by the BONAMI and CENTRM modules in this step. Since the heterogeneity of the TRISO particles in the fuel compact is ignored when the cross sections of the unit cells are generated in this step, the results of all calculations in this report are conservative from neutronics point of view because the heterogeneous effect of the TRISO particles can increase the effective multiplication factor of fuel blocks by 2-3%. The conservative model is reasonable for the conceptual design of the U-Battery, which gives certain margins for the detailed design of the U-Battery, for example, impurity in the structure or graphite and reactivity loss caused by long excess reactivity control by fixed burnable poison would reduce the

multiplication factor of the U-Battery. The double heterogeneity of the fuel blocks should directly be included for more detailed design of the U-Battery.

(2) Providing the cross sections generated in step 1 to the 3D Monte Carlo module KENOVI to perform criticality calculations and to obtain the effective multiplication factor and the flux profile of the U-Battery. 3D KENO-VI models were built for the U-Battery with the proper hexagonal block structure, as shown in Fig. A.2.1(b).

(3) Sending the flux profiles and absolute flux values to the ORIGEN-S module that performs the depletion calculations of the U-Battery. A 10-year lifetime is specified for the U-Battery.

(4) Feeding the new material compositions after each ORIGEN burnup step back to step 1 and repeating the whole process until completion of all burnup.

Because the SCALE code system was updated during the nuclear design of the U-Battery, the design of the 20 MW_{th} U-Battery was done by SCALE 5.1, while others were done by SCLAE 6.0.

A.2.3 20 MW_{th} designs

A.2.3.1 Basic designs of the 20 MW_{th} U-Battery

20 MW_{th} is the reference power of the U-Battery. Seven configurations of the reactor core of the U-Battery were built in SCALE 5.1 and compared in this section, including five cylindrical reactor cores and two annular ones, as shown in Table A.2.3. In the third column of Table A.2.3, the first number is the total number of fuel blocks in the reactor core and the second one represents the core configuration of the U-Battery. For example, the notation of Layout 37*4 means that the reactor core of the U-Battery is comprised of 37 fuel columns and each column contains 4 fuel blocks in the axial direction of the core, as mentioned in the Sec. A.2.1. Case 3 in Table A.2.3 (i.e., Layout 37*4) is the reference core configuration of the U-Battery for convenience of the comparisons in this section. Other configurations are considered as its modified versions. Case 1 is the reactor core configuration with the minimum number of fuel blocks, which is comprised of 19 fuel columns, each with 3 fuel blocks.

The horizontal cross sections of the typical cylindrical (e.g., cases 3 and 4 in Table A.2.3) and annular (e.g., cases 6 and 7 in Table A.2.3) reactor cores are shown in Fig. A.2.5. For the cylindrical reactor core configurations, the prismatic fuel columns are placed side by side and surrounded by the side reflector inside the RPV of the U-Battery. A typical reactor core configuration of the cylindrical design with 37 fuel columns is shown in Fig. A.2.5(b). For the annular reactor core configurations, the central fuel columns in the cylindrical reactor cores are replaced by graphite columns. As shown in

Fig. A.2.5(a) , this annular reactor core is comprised of 7 graphite columns in the center and 30 fuel columns surrounding the former.

Table A.2.3 Reactor core configurations of the U-Battery

Case	Type	Number of the fuel blocks/Core configurations
1	Cylindrical	57/Layout 19*3
2		76/Layout 19*4
3		111/Layout 37*3
4		148/Layout 37*4
5		183/Layout 61*3
6	Annular	90/Layout 30*3
7		120/Layout 30*4

The required fuel composition of the seven core configurations in order to achieve 5- or 10-effective-full-power-year (EFPY) lifetime is listed in Table A.2.4 for these reactor core configurations. Except for the packing fraction of coated TRISO particles, other geometric parameters of the fuel block are identical. For example, the radii of fuel kernels and fuel compacts are 0.25 mm and 0.6225 cm, respectively. The third column of Table A.2.4 presents the required fuel composition for the U-Battery with 5-EFPY lifetime, and the fourth 10-EFPY lifetime.

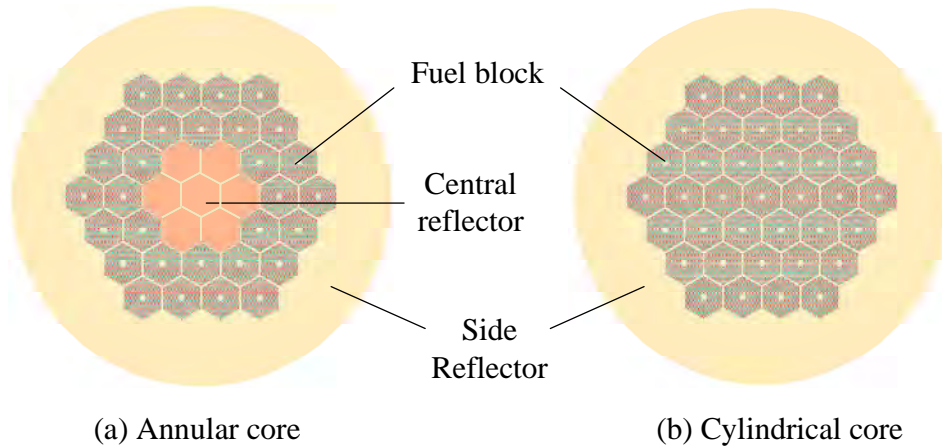


Fig. A.2.5 Typical cylindrical (Cases 4 and 5 in Table A.2.3) and annular core configurations (Cases 6 and 7 in Table A.2.3)

For the reference core configuration, i.e., Case 3, the U-Battery can achieve 10-EFPY lifetime. The required enrichment of the fuel is 16.7% U-235 and the packing fraction of the TRISO particles is 0.3. Case 5 is built by replacing a part of side reflector by 24 fuel columns (i.e., 72 fuel blocks totally) around the reference reactor core, and the required

enrichment of the fuel can reduce by 3% U-235 compared to the reference core configuration. This means that on average adding one fuel block reduces the fuel enrichment by 0.042% U-235. Case 4 is built by adding 37 fuel blocks in the axial direction of the reference reactor core. In this case, the required enrichment of the fuel reduces by 4.6% U-235 (0.124% U-235 per each fuel block on average). Adding the fuel blocks in the axial direction is more effective way than adding the periphery of the reactor core, because the latter method uses thinner side reflector and leads to more neutron leakage from the reactor core.

Table A.2.4 Fuel compositions of seven core configurations¹

Case	Reactor core configuration	5 EFPYs ²	10 EFPYs ²
1	Layout 19*3	6.4 EFPYs ³ /6.9 EFPYs ⁴	
2	Layout 19*4	9.1 EFPYs ³ /9.85 EFPYs ⁴	
3	Layout 37*3	9.55/0.3	16.7/0.3
4	Layout 37*4	6.9/0.3	12.1/0.3
5	Layout 61*3	7.59/0.3	13.7/0.3
6	Layout 30*3	9.8/0.3	17.3/0.3
7	Layout 30*4	7.6/0.3	12.9/0.3

[1] Radii of fuel kernels and fuel compacts are 0.25 mm and 0.6225 cm, respectively.

[2] Enrichment/Packing fraction (PF) of the TRISO particles.

[3] Maximum lifetime when Enrichment=20% and PF=0.3.

[4] Maximum lifetime when Enrichment=20% and PF=0.35.

Besides adding ones, removing fuel blocks may be another good way to build new reactors because the graphite moderated U-Battery is under-moderated from neutronic point of view. Four reactor core configurations in Table A.2.4 are built by reducing fuel blocks (Case 1, Case 2, Case 6 and Case 7) in terms of the reference configuration. For Cases 6 and 7, 7 fuel columns (21 and 28 fuel blocks, respectively) are replaced by the same number of graphite columns in the center of the reactor cores, which leads to annular core configurations. Removing the fuel blocks does not lead to a large increase of the fuel enrichment for Cases 6 and 7. The fuel enrichment of Case 6 increases by 0.6% U-235 compared to the reference configuration. Case 7 has 120 fuel blocks, which is 28 fuel blocks less than Case 4; however, the required fuel enrichment only increases by 0.8% U-235. Although Case 7 uses more 9 fuel blocks than the reference layout, it reduces the fuel enrichment by 3.8% U-235, which means that adding a fuel block can reduce the fuel enrichment by 0.42% U-235. As mentioned in the previous paragraph, adding one fuel block for Cases 4 and 5 reduces the fuel enrichment by 0.042% and

0.124%, respectively. Compared to Cases 4 and 5, the value of 0.42% is 10 and 3.4 times higher than them, respectively. It attributes to a higher moderator-to-fuel ratio and fuel lumping effect. The higher moderator-to-fuel ratio leads to the better neutron moderation, and the fuel lumping contributes to higher resonance escape probability of neutrons. The complex comparisons show that the annular core design, like Case 7, is a good choice for the U-Battery.

Cases 1 and 2 do not achieve 10-EFPY lifetime even though the fuel enrichment is 20% U-235, which is the acceptable maximum value for modern commercial reactors with LEU. If the fuel enrichment is 20% U-235 and the packing fraction of the TRISO particles is 0.3, Case 1 only achieves 6.4-EFPY lifetime. The lifetime of the U-Battery will be 6.9 EFPYs if the packing fraction increases to 0.35. However, for Case 2, the U-Battery achieves 9.1-EFPY and 9.8-EFPY lifetime, respectively, if the packing fractions of the TRISO particles are 0.3 and 0.35. Although Case 2 does not reach the required 10-EFPY lifetime, it needs the minimum number of fuel blocks and has the minimum core volume and weight, which makes the U-Battery easier to transport.

A.2.3.2 Further analysis of scatter core configurations

The configuration comparisons in the previous section show that the required fuel enrichment of the annular Layout 30*4 is slightly higher than that of the cylindrical Layout 37*4, but it greatly reduces the number of fuel blocks from 37*4 to 30*4. There are three advantages for Layout 30*4 over Layout 37*4. Firstly, the U-Battery with annular reactor core improves uranium utilization by loading less fuel into the reactor core and thus a higher burnup of the fuel, which saves on the fuel cost of the U-Battery. Secondly, extra graphite blocks in the center of the reactor core provide larger heat capacity to accommodate the decay heat generated by fission products, especially during loss of forced-cooling accidents. Thirdly, control rods can be placed in these graphite blocks which replace the fuel blocks in the central regions, since the thickness of the side reflector is very small which is limited by the diameter of the RPV.

More non-cylindrical or scatter core configurations with different number and distribution of graphite blocks in the reactor core are investigated in this section. Four different scatter core configurations are shown in Fig. A.2.6. Layouts 30*4B and 30*4C have the same number of fuel blocks (120) and graphite blocks (28) in the reactor core as Layout 30*4 as shown in Fig. A.2.5(a). However, the distributions of these 28 graphite blocks are different from Layout 30*4. For Layout 30*4, all 28 graphite blocks are placed in the central regions of the reactor core, which leads to an annular reactor core configuration. The 28 graphite blocks are evenly dispersed in the fuel zone for Layout

30*4B, and are placed in the outermost and center of the fuel zone for Layout 30*4C. Layouts 24*4A and 24*4B uses more 24 graphite blocks (6 graphite blocks per layer) to replace the same number of fuel blocks than Layouts 30*4, 30*4B and 30*4C.

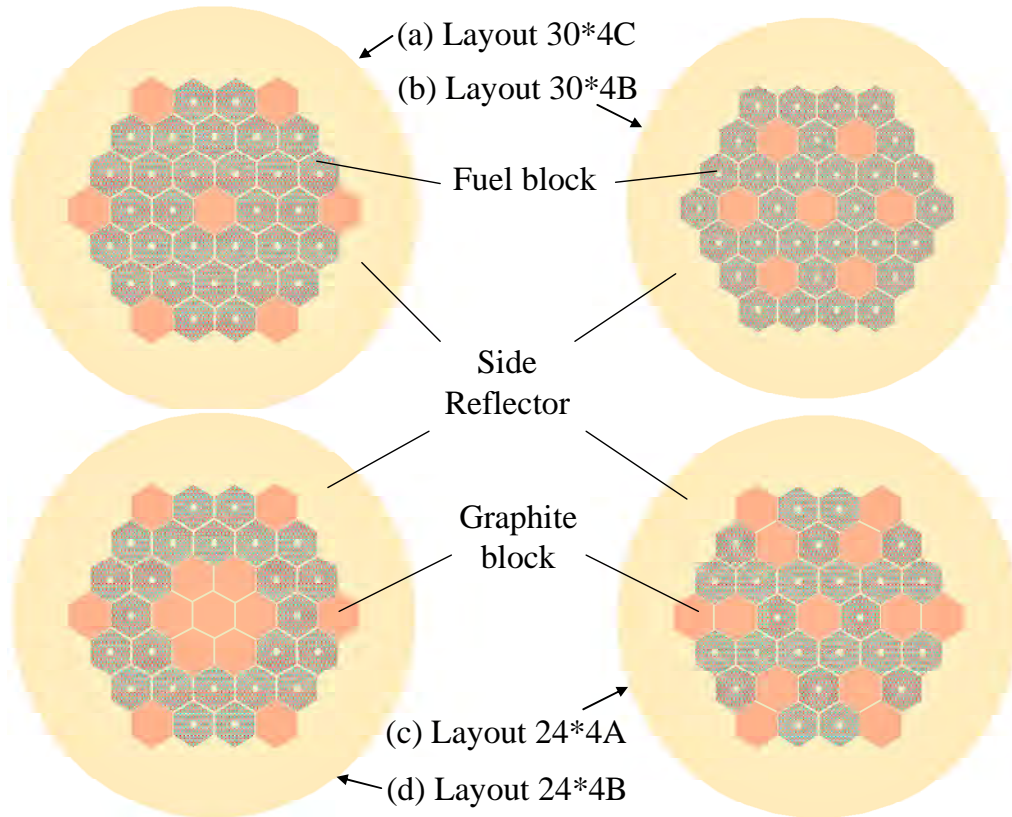


Fig. A.2.6 Four non-cylindrical core configurations

Table A.2.5 and Table A.2.6 present the effective multiplication factor (k_{eff}) of Layouts 30*4, 30*4B, 30*4C, 24*4A and 24*4B with the 0.25 mm and 0.3 mm fuel kernels in radius, respectively. Note that, the fuel enrichment of the configurations in Table A.2.5 and Table A.2.6 has been increased to 20% U-235 in order to investigate the feasibility of a 20-EFPYs lifetime. The k_{eff} of Layout 37*4 is also shown in the two tables as a reference. For 0.25-mm-radius fuel kernel, all five non-cylindrical core configurations (one annular core and four scatter cores) have higher k_{eff} than Layout 37*4 at beginning of life (BOL), i.e., 0.0 EFPYs, and 5.0 EFPYs. At 10.0 EFPYs, Layouts 30*4, 30*4B and 24*4A still have higher k_{eff} than Layout 37*4, and Layouts 30*4C and 24*4B have only slightly lower k_{eff} than Layout 37*4. The larger moderator-to-fuel ratio contributes to the higher k_{eff} of the annular and scatter reactor core because of the under-moderated reactor core of the U-Battery.

Table A.2.5 k_{eff} of six core configurations with 0.25-mm- radius fuel kernels
(Enrichment = 20% U-235; PF = 0.3; fuel compact radius = 0.6225 cm)

Time(EFPYs)	37*4	30*4	30*4B	30*4C	24*4A	24*4B
0.0	1.2980	1.3397	1.3887	1.3242	1.3922	1.3504
5.0	1.1727	1.199	1.2495	1.1787	1.2289	1.1904
10.0	1.0788	1.0941	1.1494	1.0735	1.1049	1.0709
15.0	1.0034	1.0039	1.0508	0.9801	0.9803	0.9508
20.0	0.9304	0.9093	0.9513	0.8955	0.8427	0.8209

The results of the five non-cylindrical reactor core configurations are still quite different, even though some of them have the same number of graphite and fuel blocks. In terms of the results in Table A.2.5, the distribution of the graphite blocks apparently plays an important role for neutronic performance of the configurations. Layout 30*4B has the maximum k_{eff} among all reactor core configurations with 28 graphite blocks in the reactor core from 0.0 EFPYs to 20.0 EFPYs because of the more uniform distribution of the graphite blocks in the reactor core. Compared with the distribution of Layout 30*4B, the distribution of the graphite blocks for Layout 30*4 is over-centralized and Layout 30*4C over-dispersed. More even dispersion contributes to a higher resonance escape probability.

Table A.2.6 k_{eff} of six core configurations with 0.3 mm fuel kernel radius
(Enrichment = 20% U-235 PF = 0.3; fuel compact radius = 0.6225 cm)

Time(EFPYs)	37*4	30*4	30*4B	30*4C	24*4A	24*4B
0.0	1.2706	1.3223	1.3712	1.3012	1.3753	1.3386
5.0	1.1678	1.2045	1.2532	1.1798	1.2376	1.2037
10.0	1.0875	1.1143	1.1643	1.0887	1.1365	1.0994
15.0	1.0159	1.0356	1.0845	1.0082	1.0368	1.0058
20.0	0.9555	0.9613	1.0072	0.9352	0.9407	0.9135

All reactor core configurations in Table A.2.5 do not achieve 20-EFPY lifetime, even though the fuel enrichment is 20% U-235. However, if the radius of fuel kernels in the coated TRISO particles increases to 0.3 mm, as used by the HTTR in Japan, Layout 30*4B achieves 20-EFPY lifetime, as shown in Table A.2.6. The lifetime of the U-Battery is extended only by changing the arrangement of the fuel and graphite blocks, rather than increasing the number of the fuel blocks or reducing the thickness of the internal side reflector. Although the mass of the heavy metal loaded into the reactor core increases slightly (about 2.3 kg per block) when the fuel kernels' radius increase from

0.25 mm to 0.3 mm, its influence is relative small for the total mass of the reactor core or the reactor system of the U-Battery. This means that the height and diameter of the reactor core for the U-Battery with 20-EFPY lifetime maintain as the U-Battery with 10-EFPY lifetime, which is rather positive for the transportability of the U-Battery, and to increase the economy of the U-Battery.

Table A.2.7 shows the maximum lifetimes with k_{eff} up to unity and fuel burnup of the five non-cylindrical reactor core configurations, as well as Layout 37*4 as a reference. As shown in Table A.2.7, compared with the reference configuration, although the lifetimes of some of core configurations decrease slightly, like Layout 24*4B, the fuel burnup greatly increases for all non-cylindrical reactor core configurations, that is, the uranium utilization improves obviously. For example, compared with the burnup of Layout 37*4, the burnup of Layouts 30*4, 30*4B, 24*4A and 24*4B increase by 23.8%, 43.1%, 44.4% and 31.9%, respectively, when the radius of fuel kernels is 0.25 mm. If the radius of fuel kernels increases to 0.3 mm, the fuel burnup increases even more. For example, the burnup of Layout 24*4A increases by 60.5% compared with Layout 37*4. The increase of fuel burnup mainly results from the smaller amount of fuel loaded, which improves the neutron moderation in the reactor core. On the other hand, the longer lifetime also contributes to the increase of the fuel burnup for some core configurations, like Layout 30*4B.

The comparisons of the cylindrical reactor core with non-cylindrical ones show that the reactor core of the U-Battery is under-moderated, and thus increasing the neutron moderation in the reactor core by replacing fuel blocks with graphite blocks is an effective way to extend lifetime and increase the fuel burnup of the U-Battery, or fuel utilization.

Table A.2.7 Maximum lifetime/burnup of six reactor core configurations

Core configuration	Lifetime[EFPYs]/Burnup [GWd/MTU]	
	Kernel radius = 0.25 [mm]	Kernel radius = 0.3 [mm]
Layout 37*4	15.2 /86.6	16.3/73.4
Layout 30*4	15.2/107.3(+23.8%)	17.4/96.8(+31.8%)
Layout 30*4B	17.6/124.0(+43.1%)	20.5/113.5(+54.6%)
Layout 30*4C	14.0/98.8(+14.0%)	15.6/86.3(+17.5%)
Layout 24*4A	14.2/125.1(+44.4%)	17.0/117.8(+60.5%)
Layout 24*4B	13.0/114.2(+31.9%)	15.3/106.2(+44.6%)

A.2.3.3 Two key neutronic characteristics of U-Battery

For the U-Battery, there are two neutronic parameters important for its inherent safety. The first one is reactivity temperature coefficient, and the other one is reactivity change induced by water or steam in the coolant in the reactor core. These two safety-related characteristics of the U-Battery are investigated in this section for two typical core configurations, including cylindrical cores, Layout 37*4 and Layout 37*3, and an annular core, Layout 30*4.

(I) Temperature coefficient of reactivity

One of the important principles of nuclear reactor design is that reactors should have negative reactivity temperature coefficient. Table A.2.8 presents the average temperature coefficients of reactivity of Layouts 37*4 (cylindrical core) and 30*4 (annular core) from 527 °C to 727 °C. The term fuel means the fuel smeared compacts in the fuel blocks; the term moderator means the graphite structure of the fuel blocks excluding the fuel compact; and the term reflector means the side graphite reflector and central graphite reflector (if present). As shown in Table A.2.8, both reactor core configurations keep the negative temperature coefficients of reactivity in the whole lifetime. The fuel and moderator have the negative temperature coefficients of reactivity, while the reflector has a slightly positive reactivity temperature coefficient. The positive reactivity temperature coefficients attributes to the hardened energy spectrum by higher temperature. In fact, the positive reactivity temperature coefficient of the reflector of the U-Battery is smaller than other HTRs like HTR-10 because of a larger neutron leakage.

Table A.2.8 Reactivity temperature coefficients of U-Battery from 527 °C to 727 °C

Configuration	Time [EFPYs]	Fuel [pcm/K]	Moderator [pcm/K]	Reflector [pcm/K]
Layout 30*4	0.0	-3.8	-1.6	+0.5
	5.0	-5.4	-3.1	+0.1
	10.0	-5.3	-3.8	+0.8
Layout 37*4	0.0	-5.4	-2.9	+1.2
	5.0	-7.5	-3.4	+0.4
	10.0	-7.2	-4.1	+0.2

The positive reactivity temperature coefficient of the reflector does not lead to any safety problems for the U-Battery. Firstly, the reactivity temperature coefficients of the fuel and moderator are negative, and the absolute values of the negative coefficients of the fuel and moderator is far larger than that of the reflector. Secondly, the temperatures of the fuel and moderator will increase earlier than that of the reflector, if the power excursion happens because of external reasons, for example, control rods withdraw

without control. In this case, this means negative reactivity will be induced first by the fuel and moderator before positive reactivity may be induced by the reflector. Thirdly, the temperature change of the reflector will be less than those of the fuel and moderator because of the large heat capacity of the reactor core of the U-battery, which means that the positive reactivity possible induced by the reflector can easily be offset by the negative reactivity induced by the fuel and moderator.

(II) Neutronic risk of water ingress

Since the U-Battery may adopt a power conversion system based on a Rankine cycle, the risk of water/steam ingress into the reactor core exists during its operation. Because a water/steam ingress is a design-basis accident for modern HTRs with steam cycles, the effect of water/steam in the U-Battery on the reactivity was investigated in order to make this risk known and provide a reference value for the design of other systems like coolant purification system. The reactivity induced by the water/steam is plotted as a function of the water density in the coolant channel of fuel blocks in Fig. A.2.7 for Layout 30*4, i.e., Case 7 in Table A.2.3. As shown in Fig. A.2.7 the water/steam in the reactor induces positive reactivity during the whole lifetime of the U-Battery. For the water/steam density up to 0.001 g/cm^3 , a small positive reactivity ($\Delta\rho < 0.002 \Delta k/k$) is induced. However, when the water/steam density in the reactor core is larger than 0.001 g/cm^3 , the reactivity induced begins to increase significantly because of the better moderation induced by water/steam, and reaches a maximum value at a water density of 0.4 g/cm^3 for Layout 30*4 at BOL, then drops off rapidly because of the neutron absorption of water. The induced reactivity changes with the same pattern at different fuel burnup time, but with different maximum values in different water/steam densities.

For Layout 37*3, the reactivity induced by water/steam changes in the similar mode as Layout 30*4. However, the maximum possibly induced reactivity of Layout 30*4 is less than that of Layout 37*3 because the central graphite blocks provide more neutron moderation. Although the neutron moderation of Layout 30*4 is better than that of Layout 37*3, Layout 30*4 is still under-moderated. The maximum reactivity possibly induced for Layout 37*3 and 30*4, which is determined by the water/steam density, is illustrated in Fig. A.2.8 as a function of burnup time. As shown in Fig. A.2.8, the maximum possibly induced reactivity for Layout 37*3 increases with the fuel burnup and reaches the maximum value of $0.148 \Delta k/k$ after 6.5 EFPYs, then drops quickly with the fuel burnup. For Layout 30*4, the maximum value and time are $0.119 \Delta k/k$ and 6.0 EFPYs, respectively.

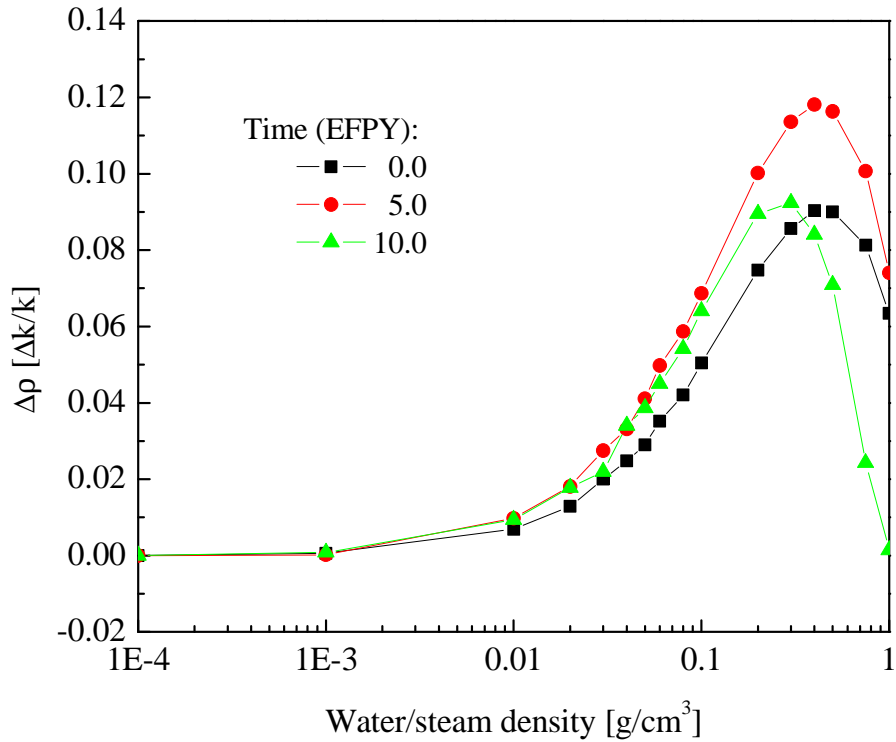


Fig. A.2.7 Induced reactivity as a function of the water/steam density and with time as a parameter for Layout 30*4

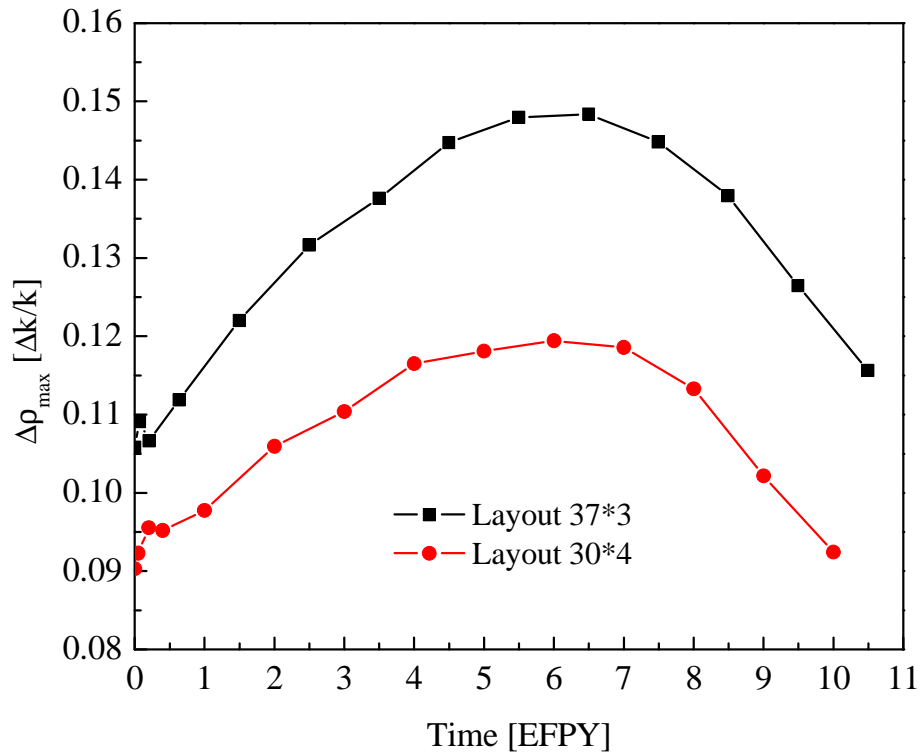


Fig. A.2.8 Maximum reactivity induced by the water/steam as a function of the burnup time for Layout 37*3 and Layout 30*4

Fig. A.2.7 and Fig. A.2.8 indicate that the potential risk of the positive reactivity induced by water/steam does exist for the whole lifetime of the U-Battery. Furthermore, the possibly induced positive reactivity is rather large because the neutron moderation is insufficient in the reactor core of Layout 37*3, as well as Layout 30*4. If a Rankine cycle is adopted by the U-Battery, the high risk of positive reactivity insertion should be considered as the design basis of the U-Battery because it involves safety of the U-Battery, and a coolant purification system should be designed to include a function of limiting the maximum steam density in the reactor. Other gas cycles like SCO_2 , N_2 or He-N_2 are recommended for the U-Battery in order to eliminate water ingress risk.

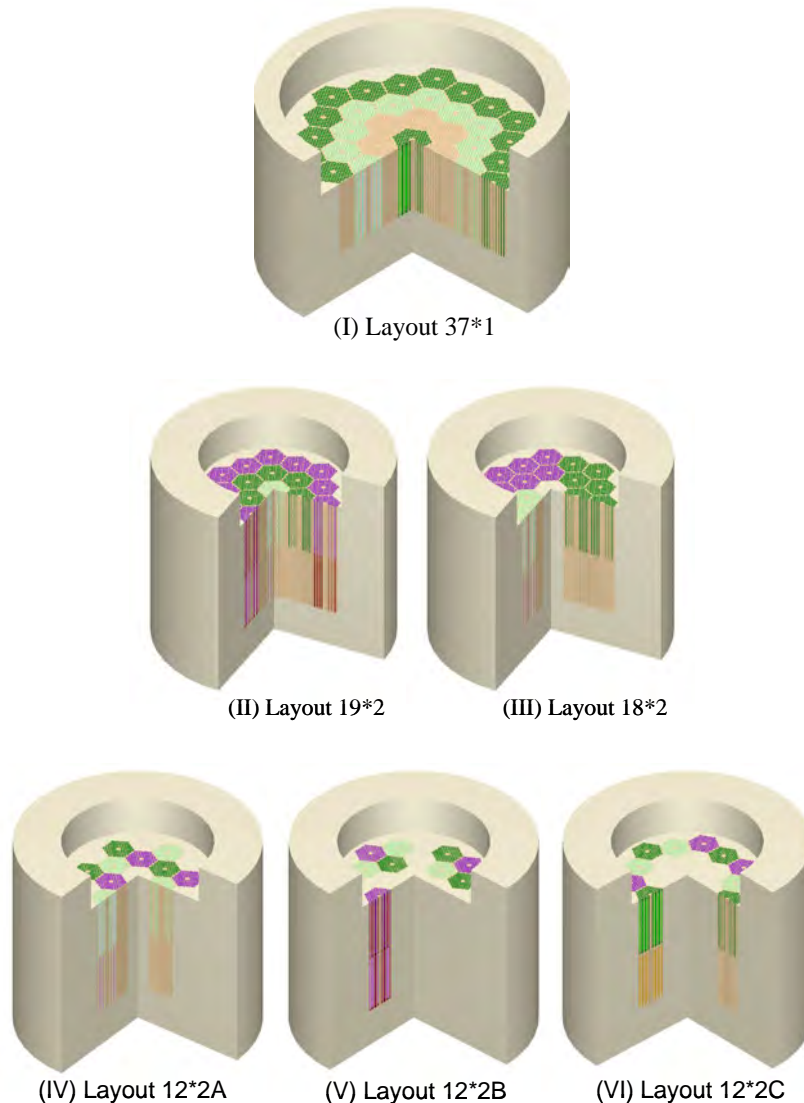
A.2.4 5 MW_{th}/10 MW_{th} designs

Because the U-Battery initially aimed to use CO_2 as coolant, the temperature of the mixtures is 527 °C for the nuclear design of the U-Battery in Sec. A.2.3 since the outlet temperature of the reactor core is limited by CO_2 coolant because of CO_2 -graphite interaction. However, the coolant of the U-Battery switched from CO_2 to He after the irradiation experiments of fuel compact in the CO_2 environment. The outlet temperature of the reactor core was increased up to 750 °C. Moreover, in terms of the initial thermal-hydraulic design of the U-Battery, the volume-averaged temperatures of the reactor core, and top, bottom and side reflectors are about 727 °C, 227 °C, 727 °C and 527 °C, respectively. Thus, the nuclear design of the new reactor core configurations of the U-Battery adopted these temperatures as reference temperature of the mixtures in this section.

For the 20 MW_{th} U-Battery, there are 148(=37*4) blocks for the cylindrical reactor core, as well as 29-cm-thick side reflector, and 50-cm-thick top and bottom reflectors. Although the outer diameter of the reactor pressure vessel (RPV) of the U-Battery is initially limited to 3.7 meters based on the maximum size of road transport in Europe, the weight of the whole reactor core of the 20 MW_{th} U-Battery is quite large number, which decreases the transportable flexibility of the U-Battery. In order to strengthen the transportability of the U-Battery, two types of designs with 5-10 MW thermal powers are proposed in this section, which are in terms of the reactor pressure vessels with different diameters. The first design uses a RPV with 3.7-meter diameter in order to make full use of neutron economy, because very thin side reflector, like 29 cm, is rather uneconomic from neutronic point of view. The second design uses a RPV with 1.8-meter diameter in order to minimize the reactor core of the U-Battery.

A.2.4.1 Nuclear design of the 5 MW_{th} U-Battery with 3.7 m RPV in diameter

Eight reactor core configurations of the 5 MW_{th} U-Battery are shown in Fig. A.2.9 when the outer diameter of the RPV is 3.7 meters. Layout 37*1 has very small height of the reactor core and thus RPV, which has totally 37 fuel blocks in the reactor core. It is calculated because the height of the RPV is a very sensitive parameter for the economy of the U-Battery. Layouts 19*2 and 18*2 have 38 and 36 fuel blocks, respectively. Layout 6*2 is modeled in order to compare with the smaller reactor core designs with very thin side reflectors in the next section. As analyzed in the previous section, the scatter and annular core configurations of 20 MW_{th} U-Battery have better neutronic performance because of a larger mass ratio of graphite and uranium and thus better neutron moderation. Two scatter and one annular core configurations with 24(=12*2) fuel blocks are also shown in Fig. A.2.9.



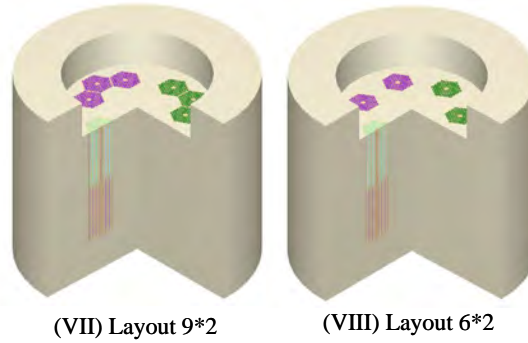


Fig. A.2.9 Reactor core configurations of 5 MW_{th} U-Battery with 3.7 m RPV in diameter
(The top reflectors have been removed in the reactors for illustrating the reactor core)

The results of the neutronic calculations are shown in Table A.2.9 for the eight reactor core configurations. The second column shows the names of reactor core configurations. The third and fourth columns are the effective multiplication factors at BOL and 10 EFPYs, respectively. If the effective multiplication factor of a certain configuration is less than unity, the data in the bracket is the possible maximum lifetime for the specific configuration. The fifth column shows the total uranium mass in the reactor core, and the sixth column shows the fuel cost. The eight reactor core configurations all use 20% enriched uranium.

Table A.2.9 k_{eff} and fuel cost of the eight configurations for the 5 MW_{th} U-Battery

Case	Configuration ¹	$k_{\text{eff,BOL}}$	$k_{\text{eff,EOL}}$	Uranium mass [kg]	Fuel cost ² [M\$]
1	Layout 37*1	1.153	0.964 (7.0)	320.5	5.86
2	Layout 19*2	1.216	1.028	329.2	6.02
3	Layout 18*2	1.238	1.045	311.8	5.70
4	Layout 12*2A	1.243	0.989 (8.5)	207.9	3.80
5	Layout 12*2B	1.270	1.019	207.9	3.80
6	Layout 12*2C	1.249	1.004	207.9	3.80
7	Layout 9*2	1.224	0.889(6.7)	155.9	2.85
8	Layout 6*2	1.193	0.582(4.0)	130.9	1.89

Note: 1. Fuel kernel radius: 0.25 mm; Fuel compact radius: 0.6225 cm; Packing fraction of TRISO particles: 0.3.

2. 20% enriched uranium: 18.281 k\$/kgHM, where manufacture cost is 1200 \$/kgU, and final disposition cost is 1500 \$/kgHM.

3. 10 effective full power years (EFPYs)

Case 2 consisted of 38 fuel blocks has a lifetime of 10 EFPYs, and the k_{eff} is 1.028 at EOL. Case 3 consists of 36 fuel blocks, and the k_{eff} is 1.045 at EOL. Although the

number of fuel blocks of Layout 18*2 is less than that of Layout 19*2, the k_{eff} of the former is larger than the later, because of better neutron moderation. Although the reactor core of Layout 37*1 consists of 37 fuel blocks, which is larger than Layout 18*2, it is not able to reach 10-EFPY lifetime, and the possible maximum lifetime is 7.0 EFPYs, because of 29-centimeter-thick side reflector and thus large neutron leakage. If the number of fuel blocks reduces to 24(=12*2), cases 5 and 6 achieve 10-EFPY lifetime, while case 4 fails to reach it. This means that the reactor core configuration is of importance, even though the number of fuel blocks is identical, as discussed in Sec. A.2.3. Lumping fuel blocks is able to increase resonance escape probability. For Layout 12*2B, the 24 fuel columns are divided into three groups. Each group consists of 4 fuel columns, and is surrounded by graphite. For this configuration, a neutron which escapes from each group of fuel blocks may be moderated in the surrounded graphite blocks, and has a higher probability to have the next collision with uranium in the fuel blocks than Layouts 12*2A and 12*2B. Layout 9*2 and 6*2 are not able to achieve 10-EFPY lifetime because the number of fuel blocks is too few. Compared with the uranium mass of Layout 19*2, the needed mass of uranium for Layout 12*2B decreases by 36.8%, and thus the fuel cost.

Table A.2.10 Fuel cost of different fuel compositions for the 5 MW_{th} U-Battery

Case	Configuration	Enrich.	PF	R_k [mm]	Uranium Mass [kg]	Fuel cost [M\$]
1	Layout 19*2	18.0%	0.30	0.25	329.2	5.48
2	Layout 19*2	20.0%	0.217	0.25	238.1	4.353
3	Layout 19*2	20.0%	0.30	0.20	238.0	4.351
4	Layout 18*2	16.8%	0.30	0.25	311.9	4.82
5	Layout 18*2	20.0%	0.20	0.25	207.9	3.80
6	Layout 18*2	20.0%	0.30	0.19	208.2	3.81
7	Layout 12*2B	20.0%	0.278	0.25	192.6	3.52
8	Layout 12*2B	20.0%	0.30	0.23	186.1	3.40

Note: 1. Fuel compact radius: 0.6225 cm.

2. Fuel costs of 20%, 18% and 16.8% enriched uranium are 18.281 k\$/kgHM, 16.647 k\$/kgHM and 15.668 k\$/kgHM, respectively.

3. 10 effective full power years (EFPYs)

Since the effective multiplication factors of both Layouts 19*2 and 18*2 are larger than unity at 10 EFPYs, there are three ways to improve the economic performance of the two configurations. The first way is to extend the U-Battery to a longer lifetime until the k_{eff} of the reactor is unity, which is not considered for U-Battery. The second way is to reduce further the fuel cost by decreasing the enrichment of uranium, while keeping the

fuel kernel size (R_k) and packing fraction (PF) of the TRISO particles constant, and 10-EFPY lifetime. Cases 1 and 4 in Table A.2.10 are the results of this way. It shows that the enrichments of uranium for Layouts 19*2 and 18*2 reduce by 2% and 3.2%, respectively, thus the fuel cost of them reduces by 9% and 15.4%, respectively.

The third way to increase the economic performance of Layouts 19*2 and 18*2 is to decrease the mass of uranium in the reactor core by reducing the geometric parameters of the TRISO particles, i.e., fuel kernel radius and PF, while keeping the enrichment of uranium constant and keeping the 10-EFPY lifetime. Cases 2 and 3, and case 5 and 6 in Table A.2.10 are the results of this way for Layouts 19*2 and 18*2, respectively. Comparison of case 2 with case 3 shows that reducing the fuel kernel radius R_k and PF of TRISO particles is equivalent from neutronic point of view, because the fuel costs of both cases are almost identical. From the mechanical stress of fuel kernels point of view, keeping the kernel radius 0.25 mm is positive, so it is recommended to keep the fuel kernel radius constant and reduce the PF of TRISO particles. If so, the fuel costs of Layouts 19*2 and 18*2 decrease further by 20.6% and 21.1%, respectively. For Layout 12*2B, reducing the fuel kernel radius is better than reducing the PF of TRISO particles, but the difference between them is rather small.

A.2.4.2 Nuclear designs of the 5/10 MW_{th} U-Battery with 1.8 m RPV in diameter

If the inner diameter of the RPV decreases to 1.8 meters, which is the same as the inner diameter of flasks for the transportation of PWR or BWR spent fuel assemblies, 6 fuel columns is the possible maximum number in the reactor core, as shown in Fig. A.2.10. In this case, the number of fuel blocks for each fuel column in the axial direction and material of side reflector are two key design parameters. If the height of the reactor core is limited to about 4 meters, 4 fuel blocks in the axial direction of the reactor core are the maximum value.

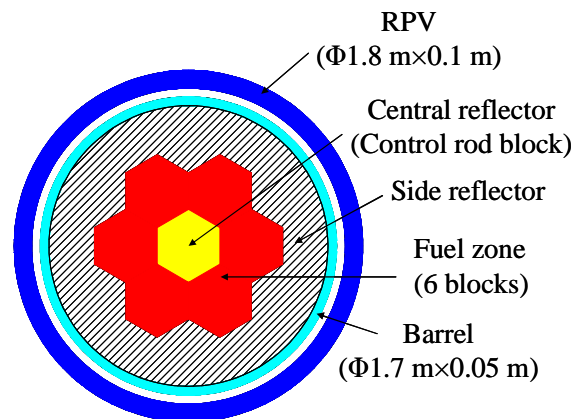


Fig. A.2.10 Reactor core configuration of the U-Battery with 1.8 m RPV in diameter

The results of the nuclear design are shown in Table A.2.11 and Table A.2.12 for the U-Battery with 1.8 m RPV in diameter. The second column shows the reactor core configurations of the U-Battery. The third and fourth columns are the parameters of the side reflectors, i.e., material and maximum thickness, respectively. The fifth column shows the maximum lifetime for each reactor core configuration, and the sixth column shows the total mass of reactor, including the fuel blocks, central, top, bottom and side reflectors, barrel (assumed 5 cm) and RPV (assumed 10 cm). Because the reactor core is very small and the side reflector is very thin, the barrel and RPV were modeled for all cases in this section in order to include their reflection effect.

Group A in Table A.2.11 is three basic cases for 5 MW_{th} U-Battery in terms of 1.8 m RPV in diameter. The number of fuel blocks for cases A.1, A.2, and A.3 are 12, 18 and 24, respectively. The material of the side reflector is nuclear graphite, whose possible maximum thickness is 25 centimeters if thickness of the barrel is 5 centimeters and gas gap between barrel and RPV is 5 centimeters. As shown in Table A.2.11, the maximum possible lifetimes of Layouts 6*2, 6*3 and 6*4 are 0.4, 2.0 and 3.0 EFYPs, respectively. Case A.1 and case 8 in Table A.2.9 have the same number of fuel blocks, but the difference of the effective multiplication factors is very large. If case 8 in Table A.2.9 may be considered to have enough thick side reflector, case A.1 has very poor neutronic performance because a large amount of neutrons leaks from the reactor core though the RPV.

Table A.2.11 Neutronic results of the reactor configurations with 1.8 m RPV in diameter (graphite side reflector)

Cases	Configuration	Material	Thickness	Lifetime	Total Mass ¹
A. Basic design (5.0 MW _{th})					
A.1	Layout 6*2	Graphite	25 cm	0.4 EFYPs	28.4 tons
A.2	Layout 6*3	Graphite	25 cm	~2.0 EFYPs	36.8 tons
A.3	Layout 6*4	Graphite	25 cm	3.0 EFYPs	45.2 tons
B. External side reflector (Thickness = 50 cm)					
B.1	Layout 6*2	Graphite	25 cm	0.4 EFYPs	28.4 tons
B.2	Layout 6*3	Graphite	25 cm	2.0 EFYPs	36.8 tons
B.3	Layout 6*4	Graphite	25 cm	3.0 EFYPs	45.2 tons
C. 1 MW _{th} design					
C.1	Layout 6*3	Graphite	25 cm	10 EFYPs	36.8 tons
C.2	Layout 6*4	Graphite	25 cm	18 EFYPs	45.2 tons

Note: 1. Total mass includes the mass of fuel blocks, reflectors, barrel and RPV without upper and lower heads

Since there is a large neutron leakage for the so the small reactor core, external side reflector (ESR) located outside RPV is considered to be used to reflect neutrons which leak from the reactor core. Group B in Table A.2.11 shows the neutronic effects of the ESR. Compared of group B with group A by pair, the neutronic effects of the 50-cm-thick ESR can be neglected. This means that the RPV and barrel reflect the neutrons back to the reactor cores, as well as reflect the neutrons which are reflected by the ESR outside the RPV. So, it is recommended to model the barrel and RPV for the U-Battery with thin side reflector.

Group C are the results of two configurations for 1 MW_{th} U-Battery. If the thermal power of the U-Battery decreases to 1 MW_{th}, the maximum lifetimes of Layouts 6*3 and 6*4 are 10 and 18 EFPYs, respectively. Compared of cases C.1 and C.2 with A.2 and A.3, an approximately linear relationship between thermal power and lifetime is clear. If so, the maximum thermal power of the U-Battery is about 4 MW_{th} if the lifetime is fixed to 5 EFPYs.

In terms of the results of groups A, B and C, it is impossible to achieve a design of the 5 MW_{th} U-Battery with a lifetime of 5 EFPYs and 1.8 m RPV in diameter when the side reflector is 25-cm-thick graphite. Case 8 in Table A.2.9 shows that a reactor core with 12 fuel blocks is able to achieve 4 EFPYs if there is a enough thick side reflector, even though the model does not include the neutron reflection effect of the barrel and RPV. In other words, the all reactor configurations in Table A.2.11 have very poor neutron economy because of very thin side reflectors, and thus are very bad designs from neutronic point of view. Since the ESR is not effective to reflect the leaked neutrons out of the RPV because of the double blockage of the barrel and RPV, the only way to increase the neutron economy of the U-Battery with 1.8 meter RPV in diameter is to improve the neutronic performance of the side reflector.

Beryllium is a good moderator material from neutronic point of view, which has a larger moderating power and density than graphite. Compared with metallic beryllium, beryllium oxide has a higher melting temperature and density, so beryllium oxide (BeO) is used for the U-Battery with 1.8 m RPV in diameter. Three groups of reactor core configurations are investigated, as shown in Table A.2.12.

The first group (group D) is so-called limit design of the reactor core, because all the space between the reactor core and barrel is filled by beryllium oxide, and a high density of beryllium oxide, 3.0 g/cm³, is used. For the reactor core configurations in this group, the U-Battery is able to achieve a lifetime more than 5 EFPYs. Cases D.1 and D.2 achieve 8 and 10.5 EFPY-lifetime, respectively. The second group, i.e., group E, investigates the influence of the thickness of beryllium-oxide side reflector. Comparing

of case E.2 with case E.3 shows that the 20-centimeter-thick BeO side reflector is enough from neutronic point of view for the side reflector of the U-Battery, even though the density of the beryllium oxide decreases to 2.8 g/cm^3 from 3.0 g/cm^3 . It is really helpful to have 5 cm annular space between the side reflector and barrel from thermal-hydraulic point of view. This means that there is a small space to accommodate side thermal insulation in order to protect the barrel and RPV. Group F shows the results of two reactor core configurations of the U-Battery with 10 MW thermal powers for the same-size RPV. Compared of cases F.1 and F.2 with cases E.3 and E.4, respectively, the lifetime of the reactor core is still linear to the thermal power for the two cases of group F. Of course, from economic point of view, the 10 MW_{th} U-Battery with 5-EFPY lifetime is more economic than the 5 MW_{th} U-Battery with 10-EFPY lifetime.

Table A.2.12 Neutronic results of the reactor configurations with 1.8 m RPV in diameter (BeO side reflector)

Cases	Configuration	Material	Thickness	Lifetime	Total Mass ¹
D. Limit design ($\rho = 3.0 \text{ g/cm}^3$)					
D.1	Layout 6*3	BeO	25 cm	~ 8 EFPYs	45.9 tons
D.2	Layout 6*4	BeO	25 cm	10.5 EFPYs	56.4 tons
E. More realistic design ($\rho = 2.8 \text{ g/cm}^3$)					
E.1	Layout 6*3	BeO	15 cm	6.0 EFPYs	41.7 tons
E.2	Layout 6*3	BeO	20 cm	~7.0 EFPYs	43.2 tons
E.3	Layout 6*3	BeO	25 cm	7.0 EFPYs	44.5 tons
E.4	Layout 6*4	BeO	25 cm	10 EFPYs	54.7 tons
F. 10 MW _{th} design ($\rho = 2.8 \text{ g/cm}^3$)					
F.1	Layout 6*3	BeO	25 cm	3.5 EFPYs	44.5 tons
F.2	Layout 6*4	BeO	25 cm	5.0 EFPYs	54.7 tons

Note: 1. Total mass includes the mass of fuel blocks, reflectors, barrel and RPV without upper and lower heads

A.2.5 Preliminary design of fixed burnable poison

As analyzed in the previous sections, the effective multiplication factors of the different reactor core configurations at BOL is quite large in order to achieve 10-EFPY lifetime for the U-Battery. For example, it is 1.283 for Layout 37*4 fueled 12% enriched uranium. It is not suitable to control excess reactivity by control rods entirely. The excess reactivity is usually controlled by fixed burnable poison (FBP) arranged in fuel blocks for block-type HTRs. The U-Battery also uses this method to manage the excess reactivity at BOL. There are 6 FBP channels in each fuel block of the U-Battery, as show in Fig. A.2.11. The green dots indicate the locations of 6 FBP channels in each fuel block. The

U-Battery uses the coated FBP particles with B₄C kernels proposed by GT-MHR project. The FBP particles mixed with graphite are made into FBP compacts like fuel compacts.

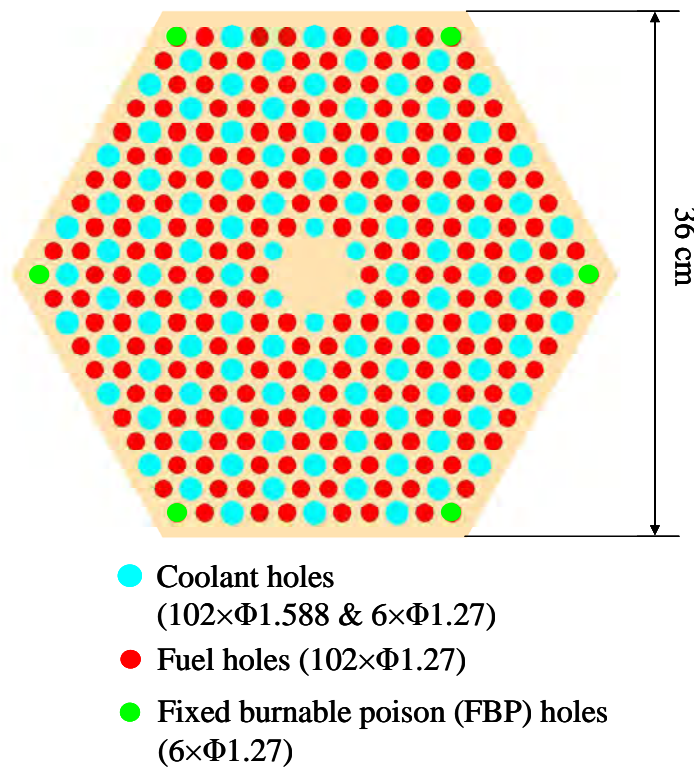


Fig. A.2.11 Cross section of the fuel block of the U-Battery and main geometric parameters

It is very time consuming or expensive to do parametric design calculations of the FBP by the TRITON module directly for a whole reactor core of the U-Battery, so the geometric and composition parameters of the FBP is first optimized in terms of a typical fuel block of Layout 37*4 fueled 12% uranium in this section. Beside the enrichment of fuel, other geometric and composition parameters of the fuel block are the same as Layout 37*4 in Table A.2.4, and the temperature of mixtures is 527 °C. For example, the fuel kernel radius and packing fraction of TRISO particles are 0.25 mm and 0.3, respectively. Because SCALE 6 provides a model of TRISO particles, the coated TRISO particles fueled LEU are modeled explicitly, as well as coated FBP particles, for FBP optimization calculations in this section, rather than the homogenized model used in Secs. A.2.3 and A.2.4. The k_{inf} of this fuel block without FBP is shown in Fig. A.2.12 as a function of time. It is 1.42 at BOL, which is higher than the k_{eff} (1.283) of Layout 37*4, because of infinite geometry of the fuel block and the heterogeneous effect of coated TRISO fuel particles. During 10 EFPYs, the k_{inf} of the fuel block first drops by 0.02 Δk

because of the buildup of the short-lived fission products in the fuel block, and then decreases almost linearly by $0.2 \Delta k/k$ because of burnup, which is the excess reactivity needed to be controlled by FBP. The optimization calculations of FBP aim to reduce the $0.2 \Delta k/k$ reactivity swing during 10 EFPYs to a value as low as possible (for example, $0.05 \Delta k/k$) by adjusting the composition and geometric parameters of the FBP.

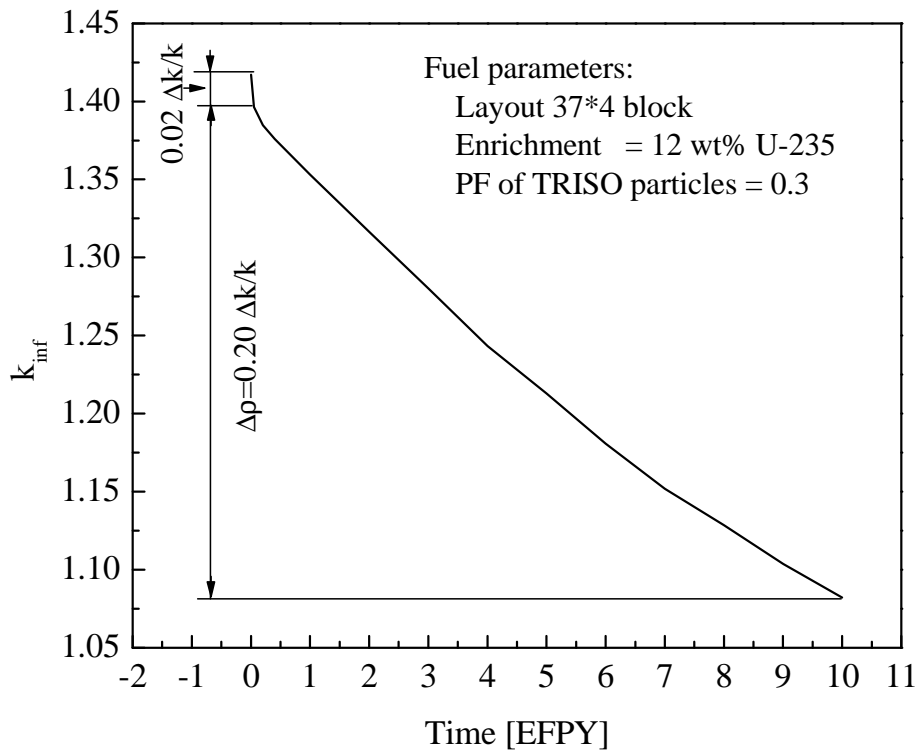


Fig. A.2.12 k_{inf} of a typical fuel block fueled 12% uranium as a function of time for Layout 37*4

Table A.2.13 shows the geometric and composition parameters of FBP used to control the excess reactivity of the reference fuel block of the U-Battery. If the diameter and height of the FBP compacts are constant, a composition and two geometric parameters can be used to adjust the mass of boron in the fuel block. The geometric parameters are the radius of B_4C kernels and the packing fraction of FBP particles, while the composition parameter is the enrichment of boron since there are two stable isotopes for natural boron, i.e., B-10 (18.4%) and B-11 (81.6%). Natural boron is assumed to be used for the long-term excess reactivity control of the U-Battery. If the density of B_4C is fixed to 2.47 g/cm^3 , all geometric parameters determines the mass of boron. If further combined with the constant enrichment of boron, it is convenient to use the mass of B-10 in the fuel block as parameter to compare different designs of the FBP.

Table A.2.13 Geometric and composition parameters of fixed burnable poison

Parameter	Value
Geometric parameters	
Number of FBP rods	6
Diameter of FBP rods	1.143 cm
Length of FBP rods	72.14 cm
Type	Coated B ₄ C particles
Diameter of B ₄ C particles	0-0.1 mm
Thickness of buffer layer	0.018 mm
Thickness of PyC layer	0.023 mm
Composition parameters	
Material	B ₄ C
Density	2.47 g/cm ³
Enrichment	18.4% (natural boron)

The k_{inf} of the fuel block at BOL and EOL, as well as reactivity swing during 10 EFPYs, are shown in Fig. A.2.13 as functions of the initial mass of B-10 when the diameter of FBP kernels is 0.2 mm. Since the diameter of the FBP kernel is constant, the mass of B-10 is changed by the packing fraction of FBP particles. The black and red lines are the k_{inf} of the fuel block at BOL and EOL, respectively, while the blue is the reactivity swing of the fuel block during 10 EFPYs.

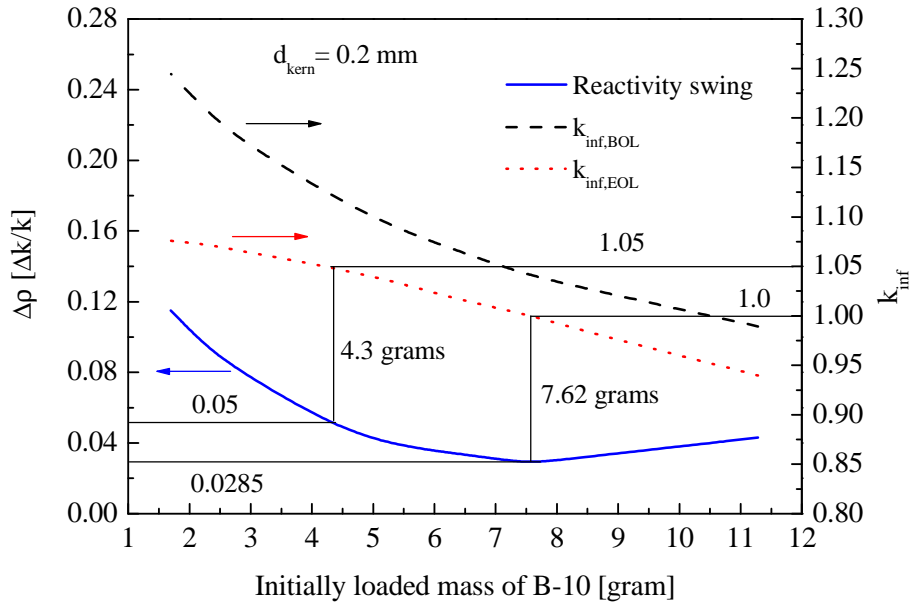


Fig. A.2.13 Reactivity swing and k_{inf} at EOL as functions of initial mass of B-10 for 0.2-mm-diameter FBP kernels

As shown in Fig. A.2.13, the k_{inf} of the fuel block at BOL decreases as initially loaded mass of B-10 increases, and thus the more B-10 initially is loaded into the fuel block. The k_{inf} of the fuel block at EOL also decreases because of the increase of the mass of B-10 remaining in the fuel block. This is so-called the reactivity penalty of FBP. For example, when the k_{inf} at EOL is 1.05, 4.3-gram B-10 is loaded into the fuel block initially, and the remaining mass of B-10 is 0.258 grams. In this case, the reactivity swing during 10 EFPYs is 0.05 $\Delta k/k$. As the initially loaded mass of B-10 increases, the reactivity swing of the fuel block decreases first and then increases, and there is a minimum reactivity swing. As the increase of the initial mass of B-10 in the fuel block, the k_{inf} of the fuel block at BOL decreases rapidly, because of more B-10 loaded and thus the larger effective macroscopic cross section of FBP rods. However, the k_{inf} of the fuel block at BOL decreases more and more slowly after the initial mass of B-10 is larger than 6 grams, because the FBP rods became more and more “black”, and its effective macroscopic absorption cross section starts to be independent on the number density of the B-10, as the initial mass of B-10 increases.

The situation of the fuel block at EOL is completely different from that at BOL. When the initial mass of B-10 is relative small, all B-10 will burn up at EOL. As it increases, more and more B-10 is not burnt up. For example, when initial mass of B-10 at BOL is 4.3 grams, there is about 6% B-10 remaining in the fuel block at EOL; However, when it is 7.62 grams, there is about 11.2% B-10 remaining at EOL. It is the reason that the k_{inf} at EOL starts to accelerate to decrease when the initial mass of B-10 is larger than 9 grams. The trade-off between the k_{inf} at BOL and at EOL leads to possible minimum reactivity swing during 10 EFPYs for the fuel block, which is 0.0285 $\Delta k/k$ for 0.2 mm FBP kernels in diameter.

For 0.07 mm FBP kernels in diameter, the infinite multiplication factors of the fuel block at BOL and at EOL and the reactivity swing as shown in as shown in Fig. A.2.14. The blue line is the reactivity swing as a function of the initial mass of B-10, while the black and red lines are the k_{inf} at BOL and EOL, respectively. As the initial mass of B-10 increases in the fuel block, the change pattern of the k_{inf} at BOL and EOL is the same as the 0.2 mm FBP kernels in diameter. Thus, there is a minimum reactivity swing of the fuel block during 10 EFPYs, which is indicated in Fig. A.2.14. That is, when the initial mass of B-10 is 6.95 grams, the minimum reactivity swing of the fuel block is 0.019 Δk , and the k_{inf} of the fuel block at EOL is 1.012. The minimum reactivity swing of the 0.07 mm FBP kernels in diameter is smaller than that of 0.2 mm FBP kernels in diameter, and the k_{inf} of the former at 10 EFPYs is larger than the latter, because the initial mass of B-10 loaded into the fuel block for the former is less than the latter. If the reactivity swing is

assumed to $0.05 \Delta k$ during 10 EFPYs, the k_{inf} of the fuel block with 0.07 mm FBP kernels in diameter at EOL is 1.061, which is larger than that of 0.2 mm FBP kernels in diameter for the same reason.

Comparisons between the two designs (0.2-mm-diameter and 0.07-mm-diameter kernels) of the FBP kernels show that reducing the radius of FBP kernels is positive to suppress reactivity swing and reduce the reactivity penalty of FBP. For HTRs, coated TRISO particles, matrix, and fuel blocks (fuel pebbles) lead to the so-called double-heterogeneity of fuel blocks, which strengthens the spatial and energy self-shielding effects of the fuel, thus the increase of the resonance escape probability of neutrons. The heterogeneous effect increases the multiplication factor of HTRs. The heterogeneity appears in the coated FBP particles and FBP compacts, which also strengthens spatial and energy self shielding of the FBP rods or compacts. Thus, more neutrons can escape absorption of the FBP rods. For example, when the initial mass of B-10 is 3.4 grams, the k_{inf} of the fuel block at BOL for the 0.2-mm-diameter and 0.07-mm-diameter FBP kernels are 1.154 and 1.139, respectively, and the reactivity swings are 0.093 and 0.077 $\Delta k/k$, respectively. The FBP with larger kernels has a larger heterogeneous effect to reduce the neutron absorption, which also reduces the effectiveness of the FBP.

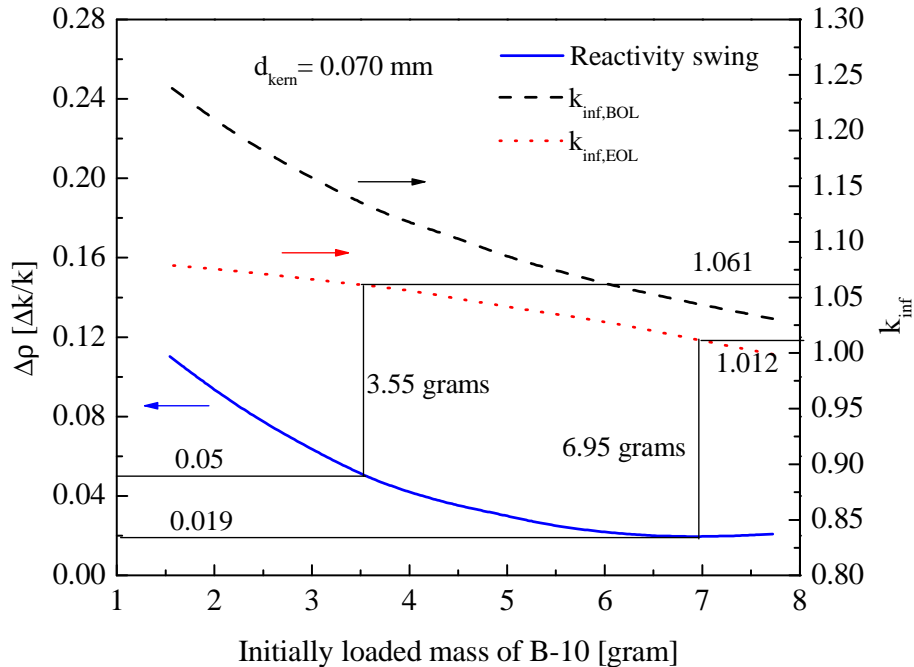


Fig. A.2.14 Reactivity swing and k_{inf} at EOL as functions of initial mass of B-10 for 0.07-mm-diameter FBP kernels

block and thus less B-10 remaining at EOL. Type 3, i.e., 0.07-mm-diameter FBP kernels, achieves the minimum reactivity swing because of the limitation of the packing fraction of FBP particles for smaller FBP kernels. Type 3 is recommended for the long-term excess reactivity control of the U-Battery. If the reactivity swing is allowed to 0.05 $\Delta k/k$ during 10 EFPYs in order to reduce the reactivity penalty of FBP, as indicated as mode B in Table A.2.14, type 4 or designs with smaller FBP kernels are recommended for the U-Battery, because the smaller FBP kernel is, the larger the k_{inf} of the fuel block at EOL is. The final geometric parameters of the FBP are a result of the trade-off between the reactivity penalty and reactivity swing if the cost of other systems like control rod system are not considered. If including the cost of the control rod system of the U-Battery, the minimum reactivity swing mode, i.e., mode A, is recommended for the long-term control of excess reactivity of the U-Battery, because it would reduce the number of control rods in the U-Battery. The cost of control rod system is quite large for reactor systems like PWR.

Table A.2.14 Excess reactivity control mode of the U-Battery

Parameter	Type 1	Type 2	Type 3	Type 4
Diameter of FBP kernels, d_k [mm]	0.2	0.1	0.07	0.05
Mode A: Minimum reactivity swing				
reactivity swing [$\Delta k/k$]	0.029	0.023	0.019	0.026
Initial mass of B-10 [g]	7.6 (PF=14%)	7.4 (28%)	7.0 (45%)	5.2 (60%)
Residual B-10	11.2%	10.0%	9.3%	6.4%
$k_{inf,EOL}$	1.000	1.004	1.012	1.04
Mode B: Reactivity Swing = 0.05 $\Delta k/k$				
Initial mass of B-10 [g]	4.3 (PF=7.6%)	3.9 (15%)	3.6 (23%)	3.4 (40%)
Residual B-10	6.0%	5.0%	4.4%	4.2%
$k_{inf,EOL}$	1.050	1.055	1.061	1.062

A.2.6 Thorium utilization in the U-Battery

During the mid 1950s to the mid 1980s, thorium as forms of (Th,U)O₂ and (Th,U)C₂ was tested and used as fuel in HTRs, like the AVR and THTR in Germany, and Fort St. Vrain in USA. There were several reasons to demonstrate thorium-uranium fuel cycles at that time. Firstly, thorium is three times more abundant in nature compared to uranium. Secondly, Th-232 has an attractive potential for breeding into a fissile isotope, U-233, efficiently in thermal and epithermal neutron reactors. Thirdly, U-233 is considered as the best of the three nuclear fuels, U-235, Pu-239 and U-233, in epithermal or thermal spectrum from neutronic point of view, because the number of fission neutrons per

neutron absorbed, η , is 10% - 20% higher than those of U-235 and Pu-239. Finally, uranium resource was believed to be insufficient to support the development of nuclear industries on a large scale worldwide. Since then, thorium has been an interesting nuclear fuel for various reactor applications, such as HTRs, molten salt reactors, and water-cooled reactors.

In order to extend the potential of thorium and utilize its breeding capacity in thermal and epithermal spectrum, the neutronic performance and breeding capacity of thorium as a nuclear fuel of the U-Battery are investigated in this section.

A.2.6.1 Seed-and-blanket fuel block

A schematic diagram of a fuel block fueled with ThO_2 and UO_2 is shown in Fig. A.2.16. As discussed in the previous sections, each fuel block of the U-Battery consists of 9 layers of fuel channels from the periphery to the center, and different layers are able to adopt different numbers of fuel compacts. The exact number of fuel channels is shown in Fig. A.2.16 for each layer. The 216 fuel channels including 6 fixed burnable poison channels may be filled with UO_2 fuel compacts or ThO_2 fuel compacts, so the number of possible configurations is 2^{210} for the fuel block, which makes it impossible to calculate all of them.

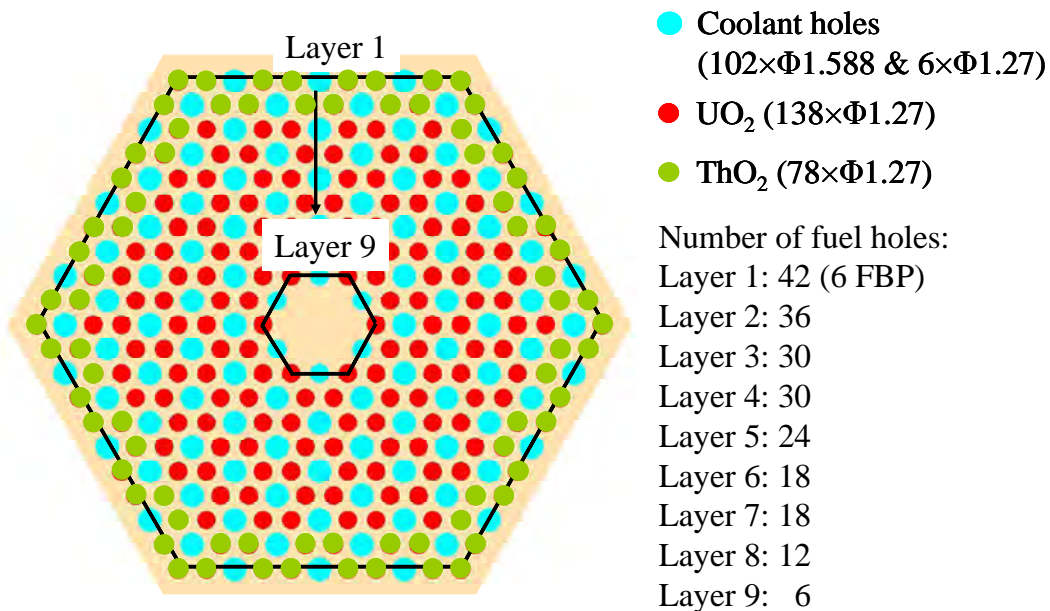


Fig. A.2.16 Seed-and-blanket (S&B) fuel block with ThO_2

In order to simplify the calculations and configurations of fuel blocks with thorium, it is assumed that (1) the same type of fuel compacts is loaded in a fuel channel, as well as

in the same layer of the fuel channels, (2) the six fixed burnable poison (FBP) channels in the corner of the fuel block are all used as fuel channels, (3) fifteen fuel compacts are loaded in each fuel channel, and (4) the ThO_2 fuel compacts are always placed from the periphery to the center of the fuel block. For example, for the fuel block shown in Fig. A.2.16, ThO_2 fuel compacts are loaded in the first and second layers, while UO_2 fuel compacts are loaded in the remaining fuel layers. The uranium used in the fuel block is still low enriched (up to 20%). The fissile U-235 is used as driver material or seed of the fuel block, which starts the fission reactions in the fuel block, while the fertile U-238 and Th-232 are breeder materials. Since each fuel channel has fifteen fuel compacts, the group of fifteen fuel compacts is called a fuel rod in the following analysis for the simplification of expression. Because the uranium is separated from the thorium in space and there are the seed and breeder regions in the fuel block, the pattern or configuration as shown in Fig. A.2.16 is called seed-and-blanket (S&B) fuel block in this report.

A.2.6.2 Neutronic performance of seed-and-blanket fuel block

Three types of geometric parameters were parametrically investigated in order to investigate the neutronic performance of S&B fuel block, including the radii of fuel kernels and fuel compacts, and packing fraction of TRISO particles. The enrichment of uranium is the only composition parameter which is studied in the section. Because the number of UO_2 fuel rods is a typical parameter of S&B fuel blocks and different from other three geometric parameters, it is investigated independently, although it may be considered as a geometric parameter. Because the geometric parameters of the S&B fuel blocks are flexible, the radii of fuel kernel and fuel compacts are 0.25 mm and 0.6225 cm, respectively, and the packing fraction of TRISO particles is 0.3 unless stated otherwise. The thicknesses of the layers of all TRISO particles, including the UO_2 and ThO_2 TRISO particles, in the S&B fuel blocks are the same as the low-enriched uranium (LEU) TRISO particles as shown in Fig. A.2.2. The temperature of all mixtures in the fuel blocks is assumed to be 300 K for all calculations based upon a S&B fuel block.

(I) Number of UO_2 fuel rods

The k_{inf} and conversion ratio (CR) of a seed-and-blanket fuel block are shown in Fig. A.2.17 as functions of the initial mass of U-235 loaded and with time as a parameter. For the S&B fuel block, the enrichment of uranium is 12%, and radii of fuel kernels and fuel compacts are 0.25 mm and 0.6225 cm, respectively, which are the fuel enrichment and geometric parameters of the reference design of the LEU-fueled U-Battery, as discussed in Sec. A.2.3. The top horizontal axis in Fig. A.2.17 shows the number of fuel rods in the

central regions of the fuel block, while the right vertical axis shows the total CR of the fuel block, including U-238 and Th-232. Since the ThO₂ fuel compacts are always placed layer by layer from the periphery to the center of the fuel block, the possible number of UO₂ fuel rods is 215 (assumed 1 ThO₂ fuel rod), 174, 138, 108, 78, 54 and 36 in the fuel block. When the number of UO₂ fuel rods is less than 36, the k_{inf} of the fuel block at BOL is far less than unity, so those results are excluded. The black, red and green lines indicate the infinite multiplication factors at BOL, 5.0 and 10.0 EFPYs. As shown in Fig. A.2.17, as the number of UO₂ fuel rods decreases, the k_{inf} of the fuel block decreases at any time during 0 to 10 EFPYs. Especially, when the number of UO₂ fuel rods is less than 108, the k_{inf} at BOL drops because of the rapid decrease of the area occupied by UO₂ fuel rods and thus a higher leakage probability of neutrons from the regions of UO₂ fuel rods. However, the k_{inf} of the fuel block at EOL only decreases rapidly in the range of middle numbers of UO₂ fuel rods, and it changes slowly in the other ranges. When the number of UO₂ fuel rods is less than 78, k_{inf} at EOL only slightly decreases because of a large CR of Th-232 to U-233, as shown in Fig. A.2.17.

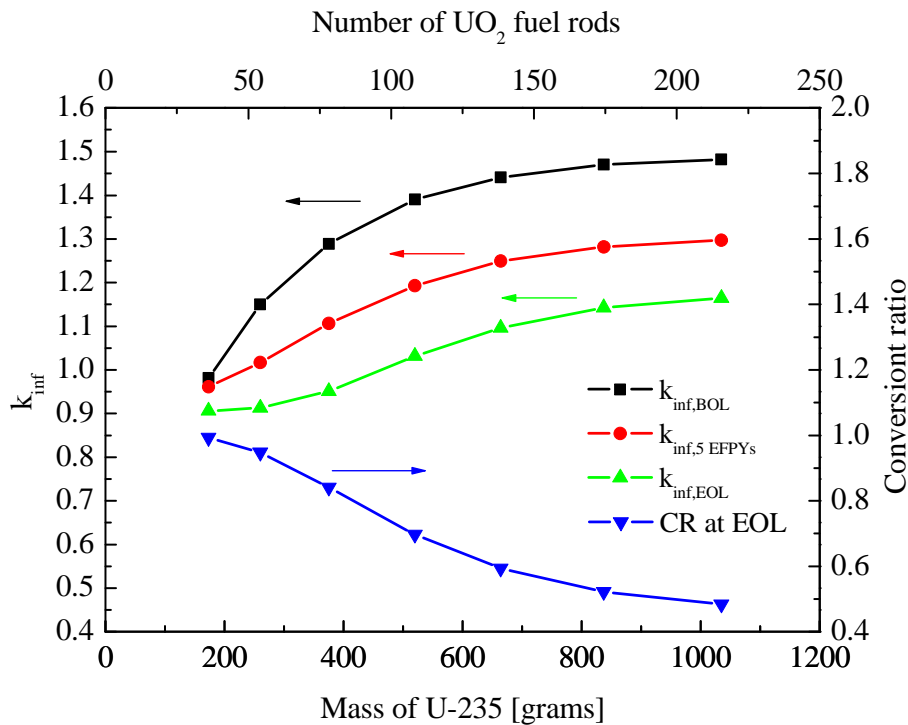


Fig. A.2.17 k_{inf} of the S&B type fuel block as a function of the mass of U-235 and with time as a parameter

The reactivity swing of the fuel block during 10 EFPYs is shown in Fig. A.2.18 as a function of the number of UO₂ fuel rods, as well as the mass ratio of all fissile isotopes at

EOL to at BOL, which is indicated by the black line. The red line is the reactivity swing of the fuel block. The reactivity swing is the difference of the infinite multiplication factors between at EOL and at BOL, that is, $k_{inf,EOL} - k_{inf,BOL}$. The negative reactivity swing means the k_{inf} at EOL is smaller than at BOL. As the number of UO_2 fuel rods decreases, the magnitude of reactivity swing first increases, and then rapidly decreases, especially after it is less than 108, as shown in Fig. A.2.18. When the number of UO_2 fuel rods is 36, the reactivity swing of the fuel block is less than $0.1 \Delta k$, including the first drop because of the buildup of short-term fission products like Xe-135 and Sm-149. However, the fuel block in this case is subcritical because of a small amount of fissile isotopes (U-235) in the fuel block and low enrichment of uranium (12%).

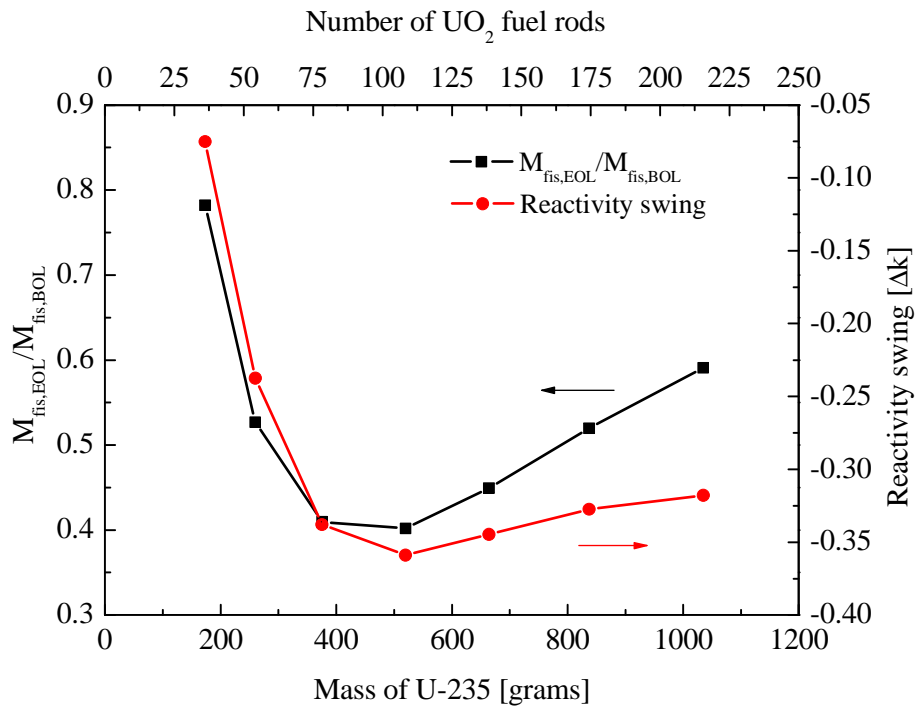


Fig. A.2.18 The reactivity swing and mass ratio of fissile isotopes at EOL to at BOL as functions of the number of UO_2 fuel rods

The reactivity swing of the fuel block depends on the time-dependent total mass of all fissile isotopes in the fuel block. At the BOL, U-235 is the only fissile isotope in the fuel block. After the fission reactions start, the U-238 and Th-232 are transmuted to other fissile isotopes, Pu-239, Pu-241 and U-233, respectively. The mass ratio of all fissile isotopes at EOL to at BOL actually is the mass ratio of all fissile isotopes at EOL to the initially loaded U-235. As the number of UO_2 fuel rods decreases from 215 (1 ThO_2 fuel rod), the mass of fissile isotopes at EOL decreases because of the decrease of initial mass

of U-235 and the low CR of U-238. The mass of thorium in the fuel block is too little to improve the neutronic performance of the fuel block, especially the conversion ratio (CR) of Th-232. In other words, low-enriched uranium fission and the transmutation of U-238 to plutonium dominate the fission reactions in the fuel block, as show in Fig. A.2.19. For example, for the fuel block with 108 UO₂ fuel rods, the mass fractions of U-235, Pu-239 and Pu-241, and U-233 are 45%, 21% and 34%, respectively, at 10 EFPYs.

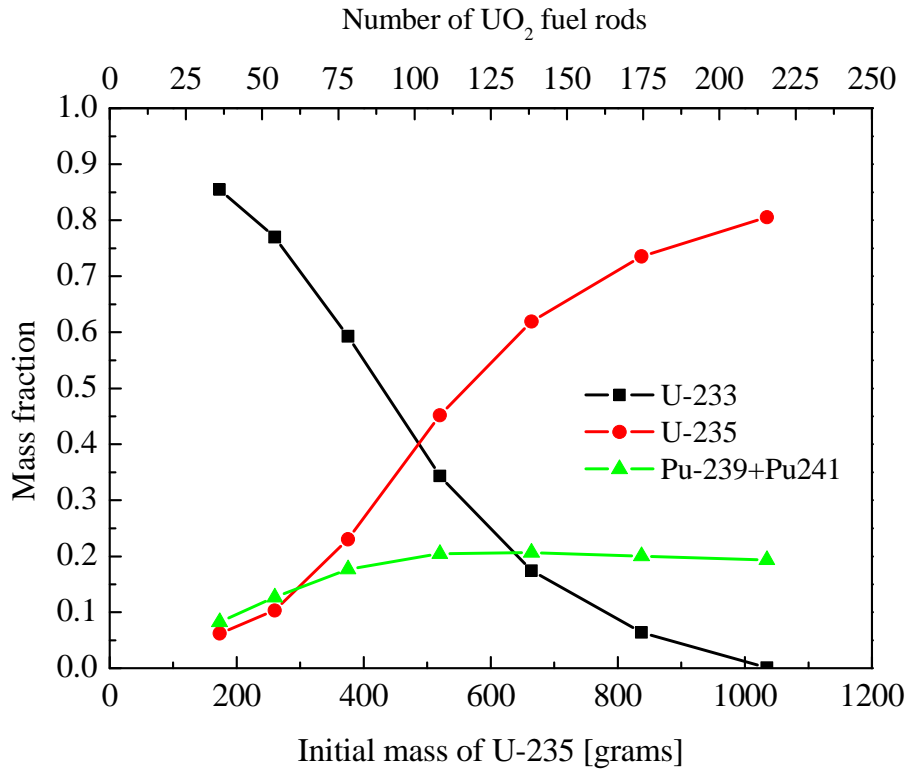


Fig. A.2.19 Mass fractions of main fissile isotopes in the fuel block at EOL as functions of the number of UO₂ fuel rods

However, when the number of UO₂ fuel rods is less than 108 and decrease further, the mass of all fissile isotopes at EOL recovers as shown in Fig. A.2.18 from the minimum value because of the increase of the CR, and thus the decrease of the reactivity swing of the fuel block. The number of ThO₂ fuel rods increases as the number of UO₂ fuel rods decreases, and thus the mass of Th-232 in the fuel block increases. This leads to the increase of the CR of the fuel block because of the larger radiative capture cross section of Th-232 than U-238 and the better neutronic performance of U-233 transmuted from Th-232. As shown in Fig. A.2.19, more U-233, which is the best fissile isotope among all fissile isotopes (i.e., U-235, Pu-239, and Pu-241) in the thermal and epithermal energy

range, is generated by the transmutation of Th-232 as number of UO₂ fuel rods decreases. For example, when the number of UO₂ fuel rods decreases from 108 to 54, the mass fraction of U-233 at EOL increases from 34% to 77%, which means the fission reactions in the fuel block are mainly maintained by the best fissile isotope. As a result, the k_{inf} of the fuel block at EOL decreases slowly when the number of UO₂ fuel rods is less than 54.

Since the configuration with 36 UO₂ fuel rods shows very small reactivity swing and a high CR, the report will focus on this configuration as an example to evaluate the neutronic effects of the composition parameters and geometric parameters of the fuel block in the following sections. The composition parameter only include the enrichment of uranium, while the geometric parameters include the radii of fuel kernels and fuel compacts, the packing fraction (PF) of TRISO particles. The enrichment of uranium changes the mass ratio of U-235 to U-238, while the geometric parameters of the fuel block changes the mass ratio of carbon (i.e., moderator) to heavy metal (i.e., U-235, U-238 and Th-232) in the fuel block.

(II) Enrichment of uranium

The k_{inf} and CR of the fuel block with 36 UO₂ fuel rods are shown in Fig. A.2.20 as functions of the enrichment of uranium. In the top subfigure, different color lines indicate different burnup times, while the conversion ratios of the whole fuel block and thorium region are shown by the green and cyan lines in the bottom subfigure, respectively. As the enrichment of uranium increases, the mass of U-235 increases and mass of U-238 decreases, while the mass of Th-232 and total mass of heavy metal keep constant. In other words, the change of the enrichment of U-235 is actually to replace the U-238 by U-235 while keeping the total mass of heavy metal and mass of Th-232 constant. As the enrichment of U-235 increases, the k_{inf} of the fuel block at BOL rapidly increases because of the increase of the fissile isotope U-235 and decrease of the fertile isotope U-238, when the enrichment of uranium is less than 20%. However, the k_{inf} of the fuel block at EOL only increases slowly in the same enrichment range. The maximum lifetime of the fuel block is only 7 EFPYs if the enrichment of uranium is limited to 20%, which is still less than the aim of 10 EFPYs. When the enrichment of uranium increases from 12% to 20%, because the k_{inf} at BOL increases faster than at EOL, the magnitude of the reactivity swing of the fuel block during 10 EFPYs increases. After that, the k_{inf} at EOL accelerates to increase, so the magnitude of the reactivity swing of the fuel block decreases.

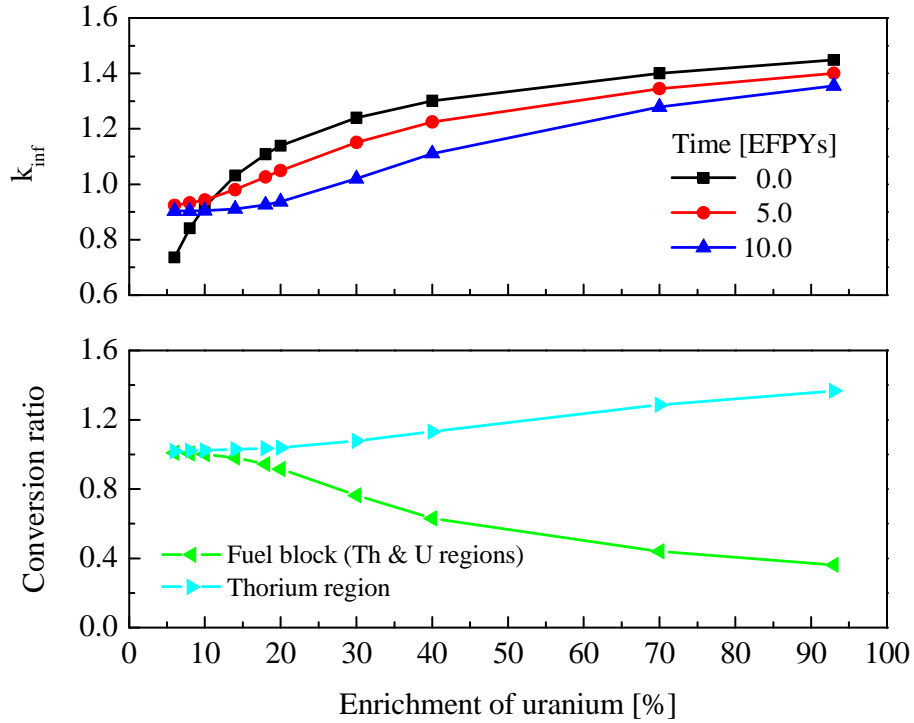


Fig. A.2.20 k_{inf} and CR of S&B type fuel block with 36 UO_2 fuel rods as functions of enrichment of uranium

The mass fractions of all fissile isotopes for the fuel block with 36 UO_2 fuel rods are shown in Fig. A.2.20 as functions of the enrichment of uranium, as well as the remaining fraction of U-235 which is not burnt at EOL. For the fuel block with 36 UO_2 fuel rods, when the enrichment of uranium is less than 20%, the mass fraction of U-233 at EOL is larger than 79% among all the fissile isotopes in the fuel block. It means that the transmutation from Th-232 to U-233 supports the fission chain reactors in the fuel block, and the function of U-235 is mainly to ignite the fission reactions in the fuel block. As a result, the CR of the fuel block is around 1, and the enrichment of uranium hardly affects the k_{inf} of the fuel block at EOL. However, as the enrichment of uranium increases, the mass of U-235 increases rapidly and thus the mass fraction of U-233 decreases. It means that low-enriched uranium dominates the fission reactions in the fuel block. Although the CR of thorium regions increases as the enrichment of uranium increases because of the larger leakage of neutrons from the regions of UO_2 fuel rods, the CR of the whole block decreases along with it because of a large amount of U-235 loaded and left at EOL reducing the influence of U-233.

The mass ratio of U-235 at EOL to at BOL is shown in the bottom subfigure of Fig. A.2.21 as a function of the enrichment of uranium. The mass ratio is actually the mass fraction of U-235 remaining in the fuel block at EOL. As the enrichment of uranium

increases, the remaining fraction of U-235 first decreases and then increases rapidly after the enrichment of uranium is larger than 20%. As discussed in the previous section, the purpose of U-235 is to ignite the fission in the fuel block, so the remaining fraction of U-235 should be as low as possible. From the utilization of U-235 point of view, if the enrichment of U-235 is limited to 20%, the remaining fraction of U-235 in the fuel block remains 7%. Otherwise, more U-235 is left in the fuel block at EOL and the fraction of U-233 transmuted from Th-232 is reduced by U-235.

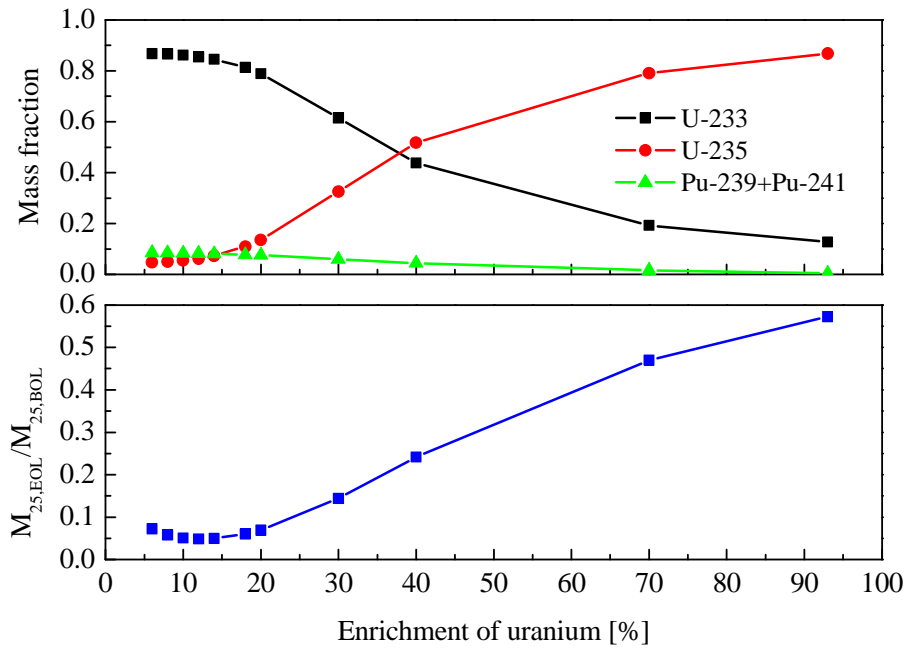


Fig. A.2.21 Mass fractions of fissile isotopes and remaining U-235 at EOL of S&B fuel block with 36 UO_2 fuel rods as functions of enrichment of uranium

(III) Geometric parameters of fuel compacts

If the number of UO_2 fuel rods and enrichment of uranium are 36 and 20%, respectively, the S&B fuel block still has six geometric parameters which may be changed to adjust the mass of uranium and thorium and thus the mass ratio of carbon to heavy metal. Because the UO_2 and ThO_2 fuel rods are independent for the S&B fuel block, each type of fuel rods (i.e., UO_2 and ThO_2 fuel rods) has three geometric parameters: fuel kernel radius, fuel compact radius and the packing fraction of TRISO particles. Although these six geometric parameters only slightly change the mass of carbon in the fuel block, they change the mass of uranium and thorium in the fuel block, and thus the ratio of the number of carbon atoms to the number of heavy metal atoms (i.e.,

uranium and thorium), denoted by N_C/N_{HM} . The N_C/N_{HM} is important parameter for the fuel block because it indicates the neutron moderation performance of the fuel block. Increasing the radii of fuel kernel and fuel rods, and packing fraction of TRISO particles obviously means to obviously increase the mass of heavy metal and slight decrease the mass of carbon in the fuel block, and thus reduce the ratio N_C/N_{HM} , and vice versa. A larger N_C/N_{HM} means better neutron moderation and a softer neutron energy spectrum in the fuel block, while a smaller N_C/N_{HM} means worse neutron moderation and a harder energy spectrum. In order to investigate the neutronic effects of the geometric parameters of UO_2 and ThO_2 fuel rods, the geometric parameters of UO_2 and ThO_2 fuel rods are changed in the ranges shown in Table A.2.15. Moreover, when a geometric parameter changes, other parameters keep constant. For example, when the radius of UO_2 fuel kernels changes from 0.175 mm to 0.5 mm, the radius of UO_2 and ThO_2 fuel compacts is 0.6225 cm, the packing fraction of UO_2 and ThO_2 TRISO particles is 0.3, and the radius of ThO_2 fuel kernels is 0.3 mm. In this case, the ratio N_C/N_{HM} changes from 235.1 to 191.2. In this pattern, there are six groups of geometric parameters totally including three groups of ThO_2 fuel rods and three groups of UO_2 fuel rods, as shown in Table A.2.15.

Table A.2.15 N_C/N_{HM} range caused by geometric parameters of fuel rods

Type	Parameter	Change range	N_C/N_{HM}
UO_2 fuel rods ¹	Radius of fuel kernels	0.175-0.5 mm	235.1-191.2
	Radius of fuel rods	0.45-0.75 cm	237.7-208.6
	Packing fraction of TRISO particles	0.15-0.35	238.3-216.8
ThO_2 fuel rods ²	Radius of fuel kernels	0.175-0.5 mm	418.8-135.7
	Radius of fuel rods	0.45-0.75 cm	460.1-194.9
	Packing fraction of TRISO particles	0.15-0.35	623.9-238.1

1. Geometric parameters of ThO_2 fuel rods: Fuel kernel radius-0.3 mm; PF-0.3; Fuel rod radius-0.6225 cm

2. Geometric parameters of UO_2 fuel rods: Fuel kernel radius-0.25 mm; PF-0.3; Fuel rod radius-0.6225 cm

The k_{inf} of the fuel block with 36 UO_2 fuel rods is shown in Fig. A.2.22 as a function of the ratio N_C/N_{HM} changed by the three geometric parameters of ThO_2 fuel rods and with time as a parameter. The black, red and blue lines indicate the k_{inf} of the fuel block at 0.0, 5.0 and 10.0 EFPYs, respectively. As the ratio N_C/N_{HM} decreases, the k_{inf} of the fuel block decreases at BOL because a larger amount of thorium is loaded in the fuel block, which leads to worse neutron moderation and larger radiative capture rate of the thorium. However, once the fission reaction in the fuel block is ignited by U-235, the

transmutation from Th-232 to U-233, as well as from U-238 to Pu-239 and Pu-241, leads to the increase of the k_{inf} of the fuel block at 10.0 EFPYs as the decrease of the ratio N_C/N_{HM} , because more initial thorium means more U-233 transmuted. It is interesting to see that the k_{inf} of the fuel block at 5 EFPYs changes around unity and is almost independent on the ratio N_C/N_{HM} .

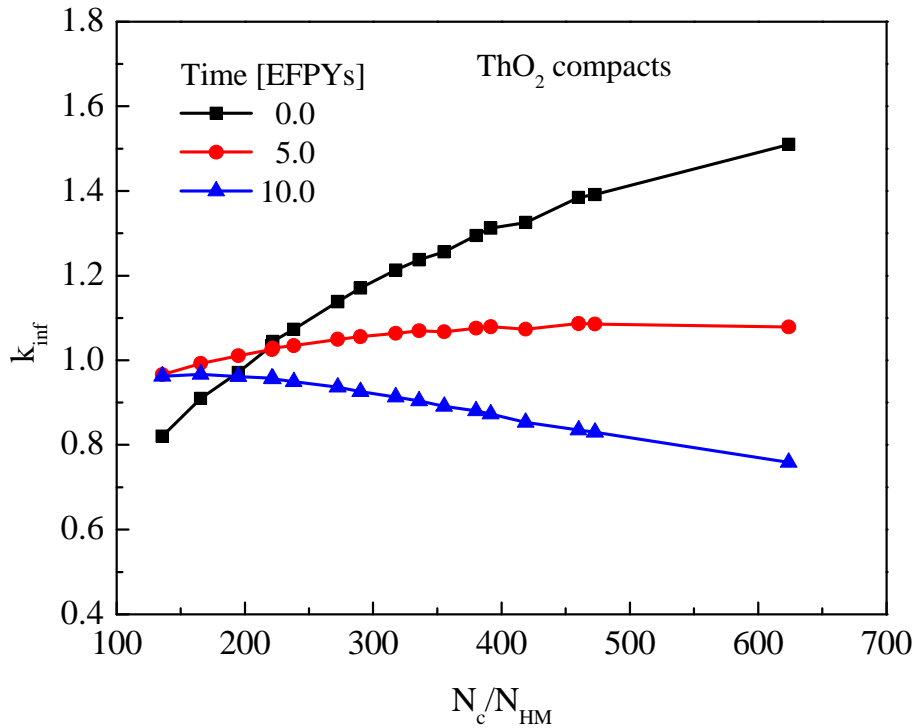


Fig. A.2.22 k_{inf} of the fuel block with 36 UO₂ fuel rods as a function of N_C/N_{HM} changed by the geometric parameters of ThO₂ fuel rods

The reactivity swing and the mass ratio of all isotopes at EOL to at BOL of the fuel block with 36 UO₂ fuel rods are shown in Fig. A.2.23 as functions of the ratio N_C/N_{HM} changed by the geometric parameters of ThO₂ fuel rods. The total mass of all fissile isotopes decreases as the N_C/N_{HM} increases because of the decrease of the mass of Th-232. When the N_C/N_{HM} is less than 150, the fuel block breeds more fissile isotopes than initial U-235 loaded in the fuel block because of the large amount of Th-232. Of course, the k_{inf} of the fuel block at BOL is far less than unity in this case and goes up as the transmutation of Th-232 to U-233 after the fission reactions are ignited, as shown in Fig. A.2.22.

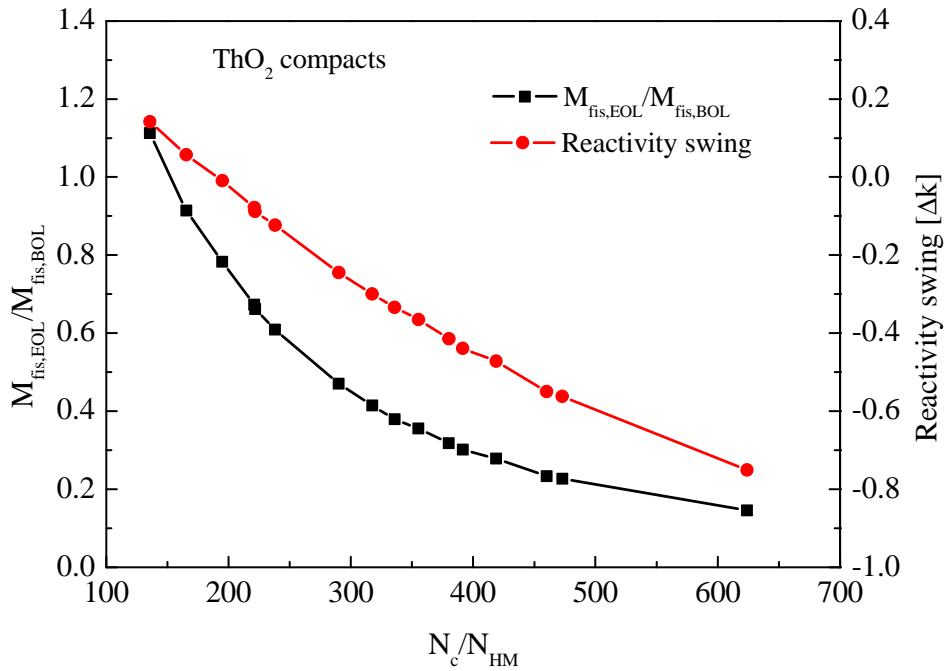


Fig. A.2.23 Reactivity swing of the fuel block with 36 UO_2 fuel rods as a function of N_C/N_{HM} changed by the geometric parameters of ThO_2 fuel rods

The reactivity swing of the fuel block still depends on the time-dependent total mass of all isotopes, as discussed in the previous section. When the N_C/N_{HM} is larger than 200, the magnitude of the reactivity swing increases because a large amount of fissile isotopes is burnt up. When the N_C/N_{HM} is 200, the value of the reactivity swing changes from positive to negative and the reactivity swing during 10 EFPYs reaches the minimum value. However, the fuel block is still subcritical in this case. When the N_C/N_{HM} is about 220, the fuel block achieves at least 5-EFPY lifetime and the reactivity swing is less than 0.01 Δk during 5 EFPYs.

The conversion ratios (CRs) of the S&B fuel block are shown in Fig. A.2.24 as functions of N_C/N_{HM} . In the top subfigure, the black line indicates the CR of the fuel block, including thorium and uranium regions, as a function of N_C/N_{HM} changed the geometric parameters of ThO_2 fuel rods, and the red line indicates that of the thorium regions. As the increase of the N_C/N_{HM} , the CR of the thorium regions decreases down to about 1 because of the softening of the neutron energy spectrum and the decrease of the mass of Th-232. When the N_C/N_{HM} is less than 400, the CR of the thorium regions is larger than 1. Once the N_C/N_{HM} is less than 200, the total CR of the fuel block rapidly increases up to 1, as well as the CR of the thorium regions, because of the hardening of the energy spectrum and the increase of the mass of Th-232. However, the k_{inf} of the fuel

block in this region is less than 1 at 10 EFYPs. If the lifetime of the fuel block is shortened to 5 EFYPs, the fuel block is able to be critical, and the reactivity swing of the fuel block is about 0.01 - 0.04 Δk , when the N_C/N_{HM} is in the range of 221 to 238. Moreover, the total CR of the fuel block is 0.92 to 0.93, while the CR of the thorium regions is 1.06-1.08.

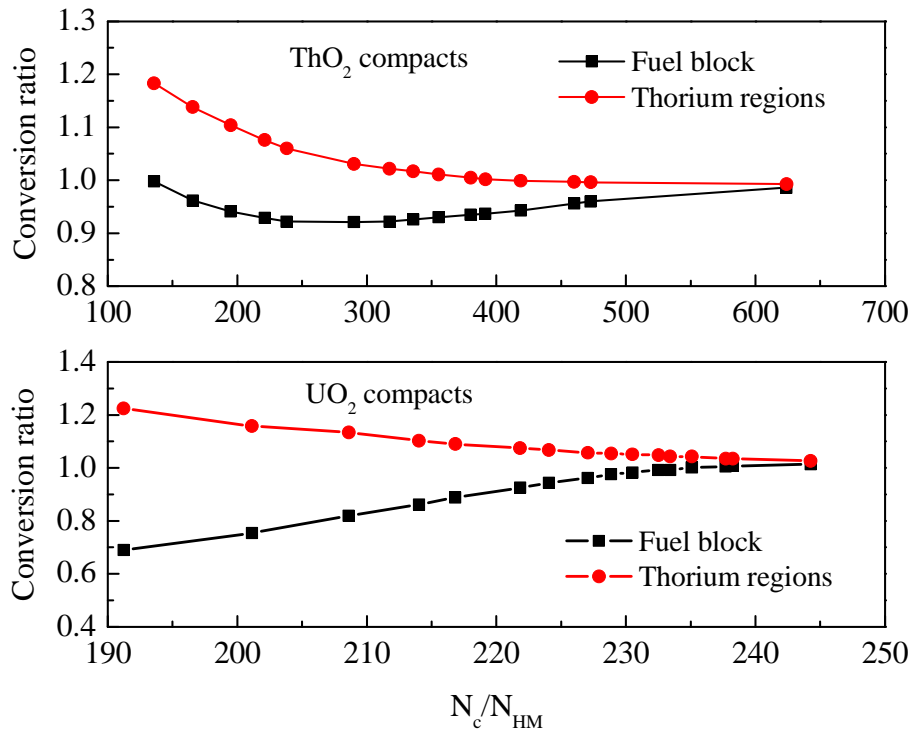


Fig. A.2.24 Conversion ratios of the fuel block as functions of N_C/N_{HM}

The k_{inf} of the fuel block with 36 UO₂ fuel rods is shown in Fig. A.2.25 as a function of N_C/N_{HM} changed by the three geometric parameters of UO₂ fuel rods and with time as a parameter. The black, red and blue lines indicate the k_{inf} of the fuel block at 0.0, 5.0 and 10.0 EFYPs, respectively. Compared with the geometric parameters of ThO₂ fuel rods, those of UO₂ fuel rods only slightly change the ratio N_C/N_{HM} from 190 to 245 because there are only 36 UO₂ fuel rods in the fuel block. Moreover, increasing the N_C/N_{HM} means that the mass of uranium decreases, so the k_{inf} of the fuel block at BOL decreases although it increases the neutron moderation, as well as the k_{inf} at EOL. As shown in the bottom subfigure of Fig. A.2.24, the conversion ratio of thorium regions decreases as the ratio N_C/N_{HM} increases because of the decrease of the fissile isotope U-235 and softer energy spectrum. As the mass of U-235 decreases, the total CR of the fuel block increases because of the decrease of the weight of U-235.

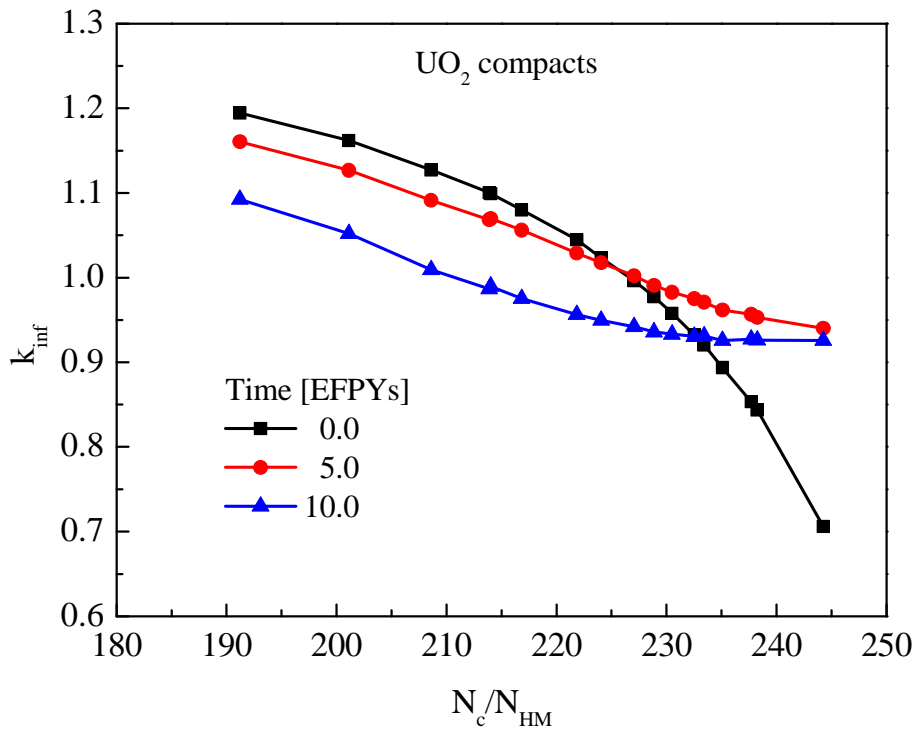


Fig. A.2.25 k_{inf} of the fuel block with 36 UO_2 fuel rods as a function of N_c/N_{HM} changed by the geometric parameters of UO_2 fuel rods

A.2.6.3 S&B fuel block with small reactivity swing

As analyzed in the previous sections, the reactivity swing depends on the time-dependent total mass of all fissile isotopes for the S&B fuel block with a specific N_c/N_{HM} . When the ratio N_c/N_{HM} changes with the geometric parameters of the fuel block, the reactivity swing reaches very small values in the range of N_c/N_{HM} from 200 to 250. For example, when the N_c/N_{HM} is in the range from 221 to 238, the reactivity swing of the S&B fuel block with 36 UO_2 fuel rods is about 0.01 - 0.04 Δk during 5 EFPYs, and the S&B fuel block is still critical. If a larger reactivity swing is allowed for the S&B fuel block, a longer lifetime, like 10 EFPYs, can be achieved. The composition and geometric parameters of the S&B fuel blocks are shown in Table A.2.16 which have about 0.1 Δk during 10 EFPYs, including the early drop because of the buildup of short-term fission products like Xe-135 and Sm-149.

For the configurations of the S&B fuel blocks in Table A.2.16, the excess reactivity is so small that it is not necessary to use fixed burnable poison (FBP) to control it. The FBP is proposed to be used to control the excess reactivity for low-enriched uranium (LEU)

fuel block in Sec. A.2.5. Moreover, for the low-enriched uranium fuel block of the U-Battery, the enrichment of uranium is 8% and the mass of U-235 and U-238 is 0.69 kg and 7.97 kg, respectively, in order to achieve the same lifetime. As shown in Table A.2.16, the total mass of uranium, especially the mass of U-235, is one-fourth to one-third less than that of the LEU fuel block. If the price of thorium is the same as uranium, the S&B fuel block may be about one-third cheaper than that of LEU fuel block. If considering the increase of the enrichment of uranium for the LEU fuel block because of the inclusion of the FBP to control the excess reactivity ($0.2-0.3 \Delta k$), the fuel cost of the S&B fuel block would be even more competitive.

Table A.2.16 Design parameters of the S&B fuel blocks with small reactivity swing

Parameters	Case 1	Case 2	Case 3
Geometric parameters			
Number of UO ₂ fuel rods	36	54	78
$k_{inf,BOL}$	1.112	1.08	1.108
$k_{inf,EOL}$	1.005	1.004	1.000
UO ₂ TRISO particles			
Fuel kernel radius [mm]	0.33	0.25	0.02
Fuel rod radius [cm]	0.6225	0.6225	0.6225
Packing fraction [cm]	0.3	0.3	0.3
ThO ₂ TRISO particles			
Fuel kernel radius	0.3	0.4	0.05
Fuel rod radius	0.6225	0.6225	0.6225
Packing fraction	0.3	0.3	0.3
Composition parameters			
Enrichment of uranium [%]	20	20	20
Mass of U-235 [kg]	0.41	0.43	0.45
Mass of U-238 [kg]	1.64	1.73	1.81
Mass of U-232 [kg]	9.13	11.38	12.01

A.2.6.4 Comparison of MOX with S&B fuel blocks

If thorium is not separated from uranium in space in fuel blocks, that is, UO₂ and ThO₂ are mixed in fuel kernels, the geometry and configurations of the fuel blocks with thorium are the same as the low-enriched uranium fuel blocks of the U-Battery, as used in the previous sections, except for the fuel composition. This type of fuel blocks with mixture of (U,Th)O₂ is called MOX type fuel block because the fuel kernels are a mixture of UO₂ and ThO₂. Typical MOX and S&B fuel blocks are compared in this section. In order to compare them, the enrichment of uranium is 12% for both types of fuel blocks, and the geometric parameters of the fuel rods are identical, for example, the

radii of fuel kernels and fuel compacts are 0.25 mm and 0.6225, respectively, and the packing fraction of TRISO particles is 0.3. The number of the fuel rods for these two types of fuel blocks is 216.

The k_{inf} of a MOX fuel block is shown in Fig. A.2.26 as a function of the initial mass of uranium and with time as a parameter, as well as the k_{inf} of an S&B fuel block. The red lines Fig. A.2.26 indicate the k_{inf} of the S&B fuel block, while the black lines indicate that of the MOX fuel block. For the MOX fuel block, the initial mass of U-238 is determined by the initial mass of U-235 and the enrichment of uranium, so the initial mass of thorium is actually also determined by the mass of U-235 if the total mass of heavy metal is kept the same as the S&B fuel blocks. For the S&B fuel block, the initial mass of U-235 is only adjusted by the number of UO_2 fuel rods. For these two fuel blocks, the total mass of heavy metal is identical, so the ratio N_C/N_{HM} keeps constant as the initial mass of U-235 or Th-232 changes. Since the geometrical parameters of the fuel rods and the enrichment of uranium are also identical for these two types of fuel blocks, the difference of the types of fuel blocks only is the spatial distribution of the UO_2 and ThO_2 in the fuel block, when the mass of U-235 is identical.

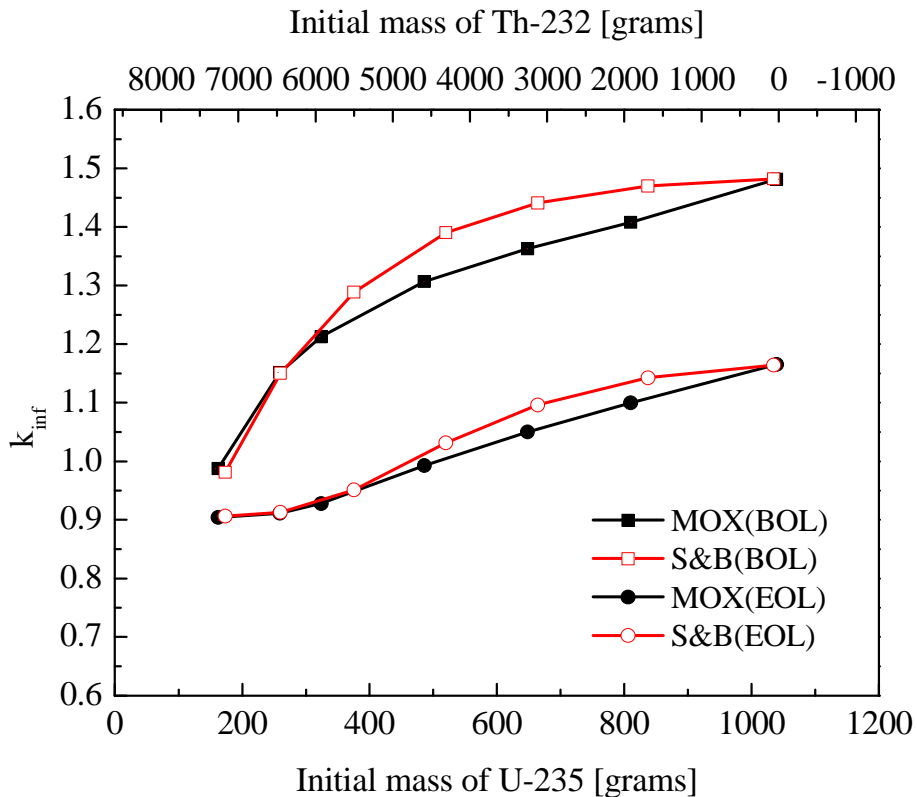


Fig. A.2.26 Comparison of the k_{inf} of the MOX with S&B fuel blocks at BOL and EOL

As shown in Fig. A.2.26, the k_{inf} of the S&B fuel block at BOL is larger than that of the MOX fuel block, when the initial mass of U-235 is larger than 260 grams (corresponding to 54 UO_2 fuel rods for the S&B fuel block). For the S&B fuel block, the UO_2 fuel rods (i.e., uranium) are spatially separated from ThO_2 fuel rods (i.e., thorium). Moreover, the UO_2 is placed in the central regions of the fuel block, while the ThO_2 is placed in the peripheral regions. Compared with S&B fuel block, the uranium and thorium of the MOX fuel block evenly disperse in the whole of the fuel block, including U-235 and U-238. Because the U-238 and Th-232 in the S&B fuel block are more concentrated than in the MOX fuel block, the resonance escape probability of neutrons in the S&B fuel block is higher than that in the MOX fuel block, which leads to the larger k_{inf} at BOL although the mass and composition of heavy metal are the same. The k_{inf} of the S&B fuel block at EOL is also larger than the MOX fuel block when the mass of U-235 is larger than 375 grams (corresponding to 78 UO_2 fuel rods for the S&B fuel block). As shown in Fig. A.2.19, when the mass of U-235 is less than 375 grams for the S&B fuel block, the mass fraction of U-233 transmuted from Th-232 among all the fissile isotopes is higher than 60% at EOL, and increases rapidly as the initial mass of U-235 further decreases. It means that U-233 dominates the fission chain reactions in the fuel block at EOL. In this case, the total mass fraction of Pu-239 and Pu-241 decreases rapidly from 20%. Thus, the spatial distribution of U-235 and U-238 has less influence on the k_{inf} at EOL of the fuel blocks, which causes the k_{inf} of both fuel blocks at EOL to be the same when the mass of U-235 is less than 375 grams.

The conversion ratios (CRs) of both S&B and MOX fuel blocks at EOL are shown in Fig. A.2.27 as functions of the initial mass of U-235. The black lines indicate the total CRs of the fuel blocks. The red lines indicate those of the thorium, that is, it is the CR of the thorium regions for the S&B regions, while it is the CR calculated only in terms of the mass of U-233 generated and burnt for the MOX fuel block. For both types of fuel blocks, as the increase of the mass of U-235, although more thorium is transmuted to U-233, the total CRs decrease because of the higher mass fraction of U-235. Because the thorium disperses in the whole volume of the MOX fuel block, however, it only distributes in a part of volume of the S&B fuel block, so the conversion ratio of Th-232 to U-233 in the former is higher than the latter because of the higher capture probability by thorium.

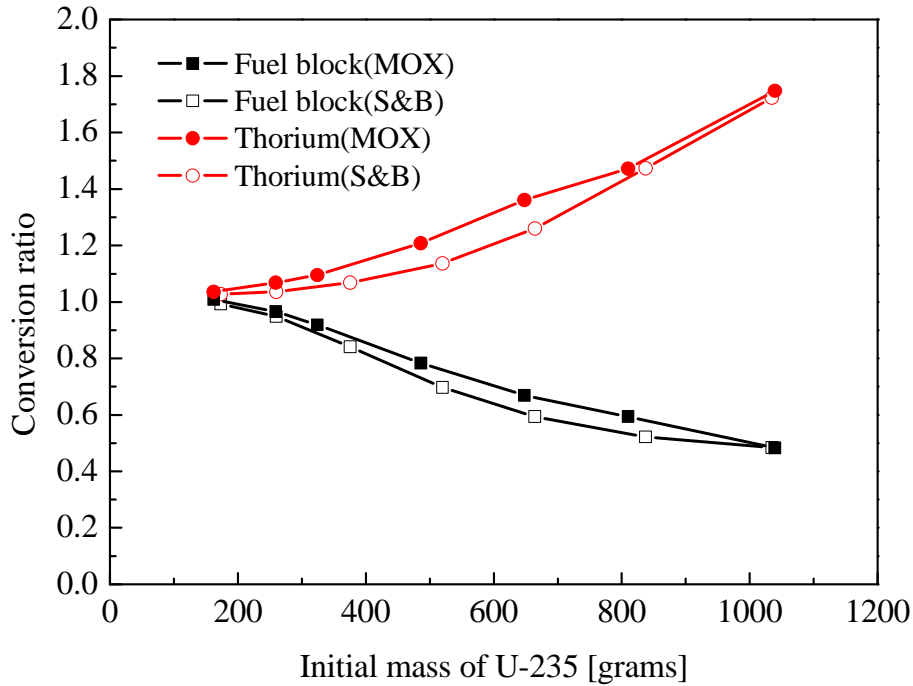


Fig. A.2.27 Comparison of the CRs of the MOX with S&B fuel blocks at EOL

A.2.7 Summary

Nuclear design calculations in this section show that it is feasible and flexible to achieve a design for the 20 MW_{th} U-Battery with a lifetime of 10 effective full power years (EFPYs).

Different reactor core configurations of the U-Battery have been investigated. The results show that the annular reactor core, Layout 30*4, has better neutronic performance than the cylindrical reactor core, Layout 37*4, because of the better neutron moderation and higher resonance escape probability of neutrons attributed to the central graphite reflector (7*4 blocks). The scatter reactor core Layout 30*4B has better neutronic performance than Layout 30*4 because of the more even distribution of the 28 graphite blocks and achieve 20-EFPY lifetime if the radius of fuel kernels increase to 0.3 mm. Because the available thermal-hydraulic code system is not capable to deal with 3D reactor models, the annular reactor core Layout 30*4 and cylindrical reactor core Layout 37*4 are recommended as the reference design of the 20 MW_{th} U-Battery with a 10-EFPY lifetime.

If the thermal power of the U-Battery decrease to 5 MW_{th} and the outer diameter of reactor pressure vessel (RPV) keeps the same size as 20 MW_{th} U-Battery (i.e., 3.7 m), Layout 12*2B is recommended as the reference design of the U-Battery with a 10-EFPY

lifetime. If the inner diameter of the RPV reduces to 1.8 m, it is possible to achieve a lifetime more than 5 EFPYs for the 5 MW_{th} U-Battery. The annular reactor cores Layout 6*3 and Layout 6*4 achieve the lifetime of 7 EFPYs and 10 EFPYs, respectively, when the side reflector is 20-cm-thick Beryllium oxide (BeO). Since the 10 MW_{th} U-Battery with 5-EFPY lifetime is more economic than the 5 MW_{th} U-Battery with 10-EFPY lifetime from economic point of view, the former is recommended for the U-Battery.

The geometric parameters of fixed burnable poison (FBP) have been optimized for a typical fuel block used by Layout 37*4. If the natural boron and coated FBP particles are used, the 0.07 mm FBP kernels in diameter minimize the reactivity swing (0.019 Δk) of the reference fuel block during 10 EFPYs. If the reactivity swing is 0.05 Δk, FBP designs with smaller kernels are recommended for the U-Battery, because the smaller FBP kernel is, the larger the k_{inf} of the fuel block at EOL is. The final design and composition of the FBP is a result of the trade-off between the reactivity penalty and reactivity swing.

Seed-and-blanket fuel blocks are recommended for thorium-fueled U-Battery in terms of the parametric analysis of the composition (the enrichment of uranium) and geometric parameters (the number of UO₂ fuel rods, radii of fuel kernels and fuel compacts, and packing fraction of TRISO particles). The reactivity swing of the S&B fuel blocks depends on the time-dependent total mass of all fissile isotopes for the S&B fuel block with a specific ratio N_C/N_{HM} (the ratio of the number of carbon atoms to heavy metal atoms). When the ratio N_C/N_{HM} changes as the geometric parameters of the fuel block, the reactivity swing reaches very small values in the range of N_C/N_{HM} from 200 to 250. For example, when the N_C/N_{HM} is in the range from 221 to 238, the reactivity swing of the S&B fuel block with 36 UO₂ fuel rods is about 0.01 - 0.04 Δk during 5 EFPYs, and the S&B fuel block is still critical. If larger reactivity swing is allowed for the S&B fuel block, a longer lifetime, like 10 EFPYs, is able to be achieved. Three configurations with different number of UO₂ fuel rods are recommended for the S&B fuel block, whose reactivity swing during 10 EFPYs is about 0.1 Δk, including the early drop because of the short-term fission product like ¹³⁵Xe and ¹⁴⁹Sm.

The excess reactivity of 0.1 Δk is so small that fixed burnable poison (FBP) is not necessary to be used. Moreover, the total mass of uranium of the three recommended configurations of the S&B fuel block is one-fourth to one-third less than that of the low-enriched uranium fuel block. If the price of thorium is the same as uranium, the S&B fuel block may be about one-third cheaper than that of LEU fuel block. If considering the increase of the enrichment of uranium for the LEU fuel block because of the inclusion of the FBP to control the excess reactivity (0.2-0.3 Δk), the fuel cost of the S&B fuel block would be more competitive.

A.3 Thermal-hydraulic design of the U-Battery

For modern modular HTRs, pressurized and depressurized loss of forced-cooling (i.e., PLOFC and DLOFC, or LOFC) are two design-basis incidents. The maximum thermal power of the modular HTRs is limited by maximum fuel temperature, e.g., 1600 °C, during these two incidents. Based on these two incidents, the thermal-hydraulic design and analysis of the U-Battery are carried out by coupled neutronic/thermal-hydraulic code system in this section.

The first section introduces the DALTON/THERMIX code system and coupled calculation methodology. The second section investigates the thermal-hydraulic performance of two key components (i.e., the reactor cavity cooling system and side thermal insulation). The third and fourth sections evaluate a cylindrical design (Layout 37*4) and annular design (Layout 30*4) of the U-Battery, respectively, during the LOFC incident. The fifth section further compares the cylindrical and annular designs directly based on the DLOFC incident. The sixth section simply investigates the potential to increase the thermal power of the U-Battery with the annular reactor core.

A.3.1 Coupled neutronic/thermal-hydraulic code system

A.3.1.1 Cross section generation methodology

In order to do the coupled neutronic/thermal-hydraulic calculations of the U-Battery, the few-group cross section libraries of the reactor core of the U-Battery must be generated first. The cross section libraries of the U-Battery for few-group diffusion calculations are generated by the XSGEN module based on the following 3-step procedure and several modules of SCALE 6.0, like NEWT, XSDRNPM, etc.

(I) Step 1: Unit cell calculation

A typical fuel block of the U-Battery is comprised of 210 fuel channels, 108 coolant channels, and 6 burnable poison channels, as shown in Fig. A.3.1. In order to simplify the model, the 6 burnable poison channels are all assumed to be used for fuel rods or fuel compacts in this design phase, and the fuel handle hole in the center of the fuel block is also neglected. In each fuel channels, there are 15 fuel compacts. The group of 15 fuel compacts is called a fuel rod for simplification. The unit cell of fuel rods is a 2D hexagonal geometry, and consists of the fuel compact, and helium gap and graphite surrounded the fuel compact, as shown in Fig. A.3.1. The unit calculation is mainly executed by the BONAMI and CENTRUM modules to generate the resonance shielding cross sections of the fuel rods. In fact, the unit cell calculation is automatically embedded in the step 2.

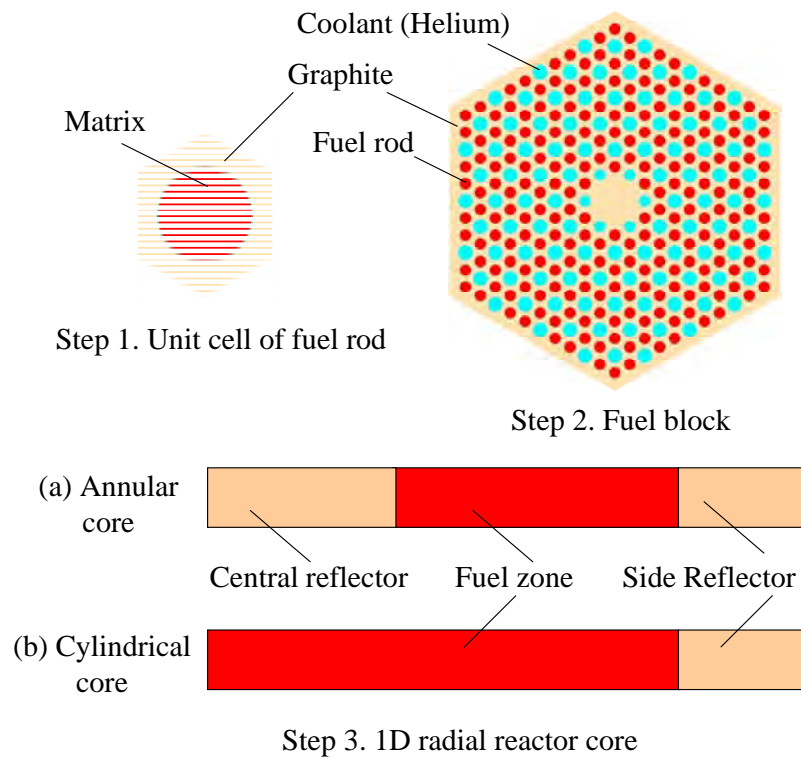


Fig. A.3.1 Generation methodology of the few-group cross section libraries of the U-Battery

(II) Step 2: Fuel block homogenization calculation

After the step 1, a 2D fuel block is modeled by the NEWT module of SCALE 6.0, as shown in Fig. A.3.1. The NEWT module is a 2D discrete-ordinates code system. The cross sections of the matrix (fuel rod), graphite, and helium generated in the step 1 are automatically transferred and used for the fuel block calculations. After the transport calculations of the fuel block, the homogenized cross sections of the fuel block are generated automatically by the NEWT module. Moreover, the energy groups of the cross sections are collapsed from 238 groups into 55 groups during the homogenization of the fuel block.

(III) Step 3: One-dimension reactor calculation

A 1D reactor is modeled in step 3, comprising of the fuel zone, reflector zone and/or central reflector for annular cores, as shown in Fig. A.3.1. 1D discrete-coordinate transport calculations are executed by the XSDRNPM module in SCALE 6.0. The homogenized cross sections of the fuel block generated in the step 2 are used for the fuel zone in this step, and the cross sections of the graphite generated in the step 2 are used for the reflectors of the 1D reactor model. The 1D reactor model is divided into the same

number of meshes as the neutronic model in the later coupled neutronic/thermal-hydraulic calculations. After the calculations, the XSDRNPM module produces the cross sections of the reactor core, or the meshes, which will be used by few-group diffusion calculations. The 55 energy groups are collapsed into 26 energy groups in this step. The structure of 26 energy groups is shown in Table A.3.1.

The 3-step procedure is repeated at different temperatures to generate the corresponding cross section libraries. For the U-Battery, two-temperature cross section libraries are generated, 300 K and 2000 K, respectively.

Table A.3.1 Energy boundaries of 26 few-groups structure

Energy boundaries (eV)	26 energy groups
2.0E+07	1
8.1873E+06	2
3.0E+06	3
6.7E+05	4
1.0E+05	5
1.7E+04	6
3.0 E+03	7
1.55 E+03	8
683.0	9
285.0	10
122.0	11
61.0	12
30.0	13
13.75	14
8.1	15
5.0	16
2.38	17
1.30	18
0.65	19
0.35	20
0.2	21
0.125	22
0.08	23
0.05	24
0.0253	25
0.01	26
1.0E-05	-

A.3.1.2 Coupled DALTON/THERMIX code system

The steady-state thermal-hydraulic design of the U-Battery was carried out by the coupled DALTON/THERMIX code system, as illustrated in Fig. A.3.2, in order to determine the preliminary reactor core configuration of the U-Battery, and provide the initial conditions of the transient thermal-hydraulic evaluations, like power density distribution and steady state temperature distribution of the reactor core of the U-Battery. The coupled code system consists of a diffusion code system (DALTON), a thermal-hydraulic code system (THERMIX), and several other codes or scripts, e.g., the XSGEN module mentioned in the previous section, and MASTER module, etc. The main components of the coupled DALTON/THERMIX code system, especially DALTON and THERMIX, have been validated and verified by experimental data of AVR and HTR-10 or PBMR benchmark problems.

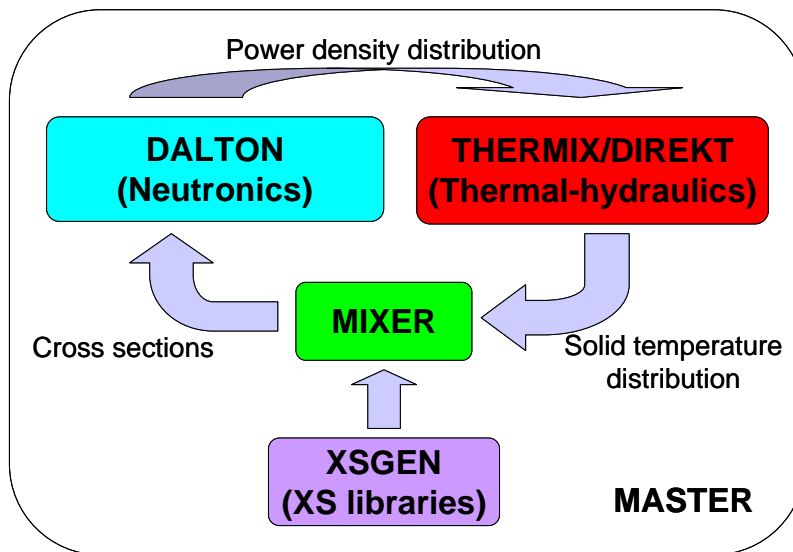


Fig. A.3.2 Coupled DALTON/THERMIX code system

A simple description of each component of the coupled DALTON/THERMIX code system is given as follows:

(1) DALTON is a 2D/3D neutronic code system based on multigroup diffusion theory, which is able to perform diffusion calculations in steady-state and transient modes. It provides the eigenvalues of reactor core models, and also the volume-averaged power density distributions. For coupled neutronic/thermal-hydraulic design of the U-Battery, DALTON is used in 2D (r, z) steady-state mode, since the reactor is cylindrical symmetry. The 2D neutronic model of the U-Battery only includes the fuel zone and top, bottom and side reflectors.

(2) THERMIX is a 2D thermal-hydraulic code system for modular HTRs, and the latest version is called DIREKT, which is able to perform steady-state and transient calculations. For coupled neutronic/thermal-hydraulic calculations, THERMIX uses the power density distribution of 2D reactor core models calculated by DALTON, and does the thermal-hydraulic calculations for the 2D reactor models, which usually includes the reactor core (fuel zone and reflectors), thermal insulations, barrel and RPV.

(3) XSGEN is a PERL script, which calls several modules of SCALR 6.0, such as the XSDRNPM and NEWT modules to generate some cross section libraries of the reactor core at different temperatures. The detail of the cross section generation methodology for the U-Battery is explained in the previous section.

(4) MIXER is a PERL script, which calls some modules of SCALE 6.0. MIXER aims to update the neutron cross-sections of reactor cores used in DALTON by linear interpolation in pre-computed cross-section libraries according to the local solid temperature distribution of reactor cores calculated by THERMIX.

(5) MASTER, a PERL script, is a control script to complete the coupled neutronic/thermal-hydraulic calculations among DALTON, THERMIX and MIXER. MASTER aims to control data exchange among different codes, to choose calculation type (i.e., steady-state or transient), to determine time step control mode (i.e., automatic or fixed time step) during transient calculations.

A.3.1.3 Calculation methodology of the U-Battery

For the U-Battery, two types of reactor core configurations are proposed in Sec. A.2. Layout 37*4 is a cylindrical core configuration, and Layout 30*4 is an annular core configuration. Only one difference between these two designs is the fuel zone configuration in the reactor core, and other configurations, such as the reflectors, thermal insulations, and reactor pressure vessels, are identical. There are extra 28(=7*4) fuel blocks in the central regions of Layout 37*4, which are replaced by the same number of the graphite blocks for Layout 30*4. For each type of reactor design, the procedure of steady-state coupled neutronic/thermal-hydraulic evaluations is identical as follows. Firstly, two few-group (26 groups) cross section libraries at 300 K and 2000 K are generated by the XSGEN module. Secondly, the cross sections of the reactor core (Layout 37*4 or Layout 30*4) are generated by interpolating in the cross section libraries by the MIXER module in terms of an assumed temperature distribution of the reactor core or previous calculation results. Thirdly, the neutronic calculations of the reactor core are executed by DALTON on the base of the assumed cross sections calculated by the assumed temperature distribution. The volume-averaged power density distribution of the

reactor core is generated by DALTON if the diffusion calculations succeed, and is transferred to THERMIX. Fourthly, a new temperature distribution of the reactor is calculated by THERMIX according to the power density distribution. Fifthly, the old cross sections at the beginning of the couple calculation are updated by the MIXER module in term of the latest temperature distribution of the reactor core. The whole calculation procedure is repeated until the convergence (10^{-5}) of the effective multiplication factor of the reactor core. The coupled neutronic/thermal-hydraulic design determines the reference reactor configuration of the cylindrical and annular designs of the U-Battery. The 3D schematic diagram and horizontal cross section of the annular design (i.e., Layout 30*4) are shown in Fig. A.3.3 and Fig. A.3.4, respectively. The cylindrical reactor design Layout 37*4 has the same configuration as Layout 30*4 except the reactor core.

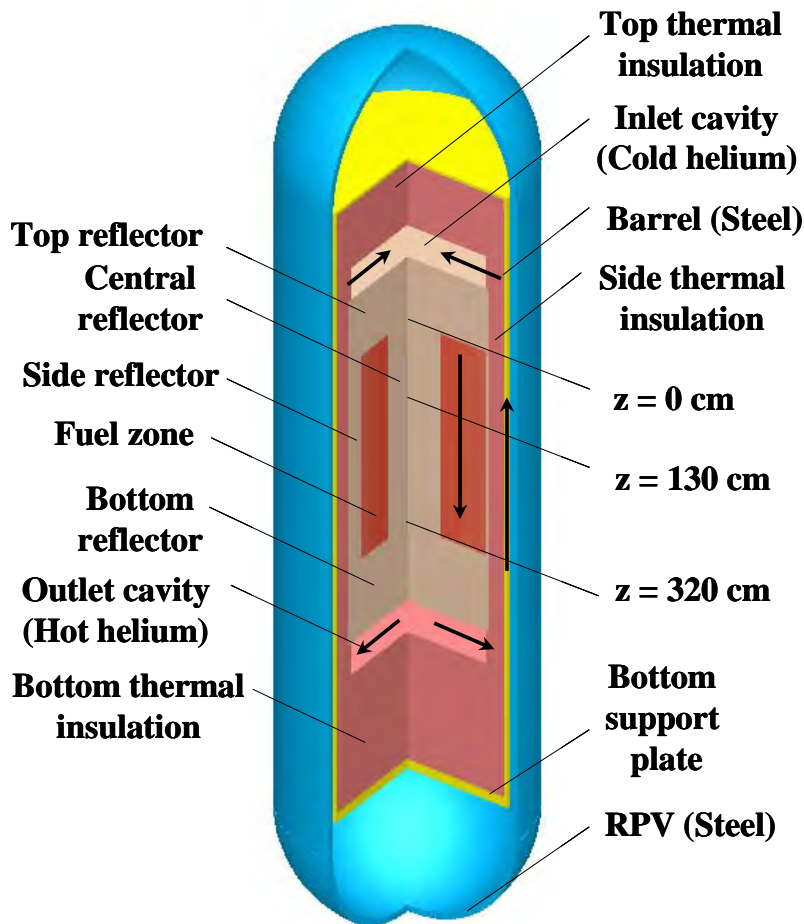


Fig. A.3.3 3D schematic diagram of Layout 30*4 of the U-Battery. The coolant channels in the fuel columns and other auxiliary structures in the reactor have been removed in order to show some main components of the reactor.

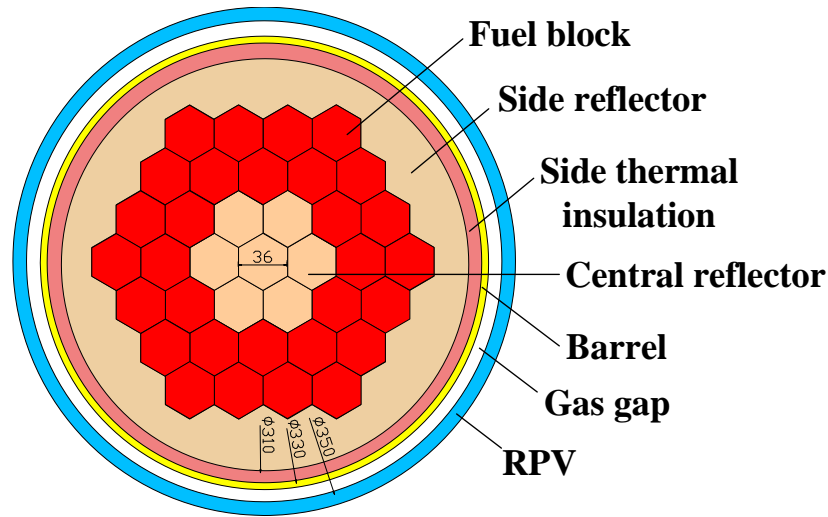


Fig. A.3.4 A schematic diagram of the horizontal cross section of Layout 30*4 of the U-Battery. The coolant channels in the fuel columns have been removed for clarity, and the data are the sizes (unit: cm) of some key components.

After the steady-state coupled neutronic/thermal-hydraulic design calculations of the U-Battery were completed, the reactor configurations were evaluated for PLOFC and DLOFC incidents. A PLOFC incident happens when the U-Battery loses forced-cooling caused by a failure of blower with mechanical problems or loss of power. In this case, the pressure boundary of the reactor system keeps intact, so the reactor system does not lose the system pressure at the same time. If the reactor system of the U-Battery loses the pressure at the same time, for example, because of a broken hot gas duct which connects the RPV with power conversion system, a DLOFC incident happens. During these two incidents, the U-Battery faces severe challenge to remove the decay heat. The maximum thermal power of modular HTRs is usually limited by maximum fuel temperature during these two incidents. So, PLOFC and DLOFC are usually chosen as design-basis incidents for modular HTRs. Moreover, a DLOFC incident was experimentally simulated in AVR in 1988. Based on these two incidents, the thermal-hydraulic characteristics of the U-Battery were evaluated.

However, only the steady-state design of the U-Battery was executed by the coupled neutronic/thermal-hydraulic code system, and all transient thermal-hydraulic evaluations of the U-Battery were executed by THERMIX. There are three reasons for it: (1) the transient thermal-hydraulic evaluations aim to preliminarily verify the feasibility and safety of a certain reactor configuration, to analyze decay heat removal mechanisms in the long term during the PLOFC and DLOFC incidents, and to determine possible

difference caused by some specific configurations of the U-Battery from other HTRs, for example, 29-cm-thick side reflector and 10-cm-thick side thermal insulation. The more detailed design and coupled calculations will be followed in the next design phase in terms of current calculations and design. (2) Coupled transient neutronic/thermal-hydraulic calculations need a long computation time, especially the neutronic calculations. It is very expensive and time consuming to do many times of such calculations, which is a disadvantage for the thermal-hydraulic evaluations of the different designs of the U-Battery. (3) THERMIX is able to use a large time step, e.g., 20 or 50 seconds to do transient calculations, which is very suitable to do long-term transient calculations (e.g., 100 hours) for many times in an acceptable short period.

For the transient thermal-hydraulic evaluations of the U-Battery, it is assumed that the PLOFC and DLOFC incidents happen at the full power of the U-Battery, i.e., $20 \text{ MW}_{\text{th}}$. When the PLOFC incident happens, the reactor system pressure keeps the same as the normal operation, i.e., 4 MPa. It only is 1 bar during the DLOFC incident since the reactor system loses the pressure because of helium leakage. The reactor is also assumed to be shut down immediately by control rods system at the beginning of PLOFC and DLOFC incidents, and the thermal power of the reactor decreases to the decay heat level at the beginning of incidents, in order to simplify the calculations. This assumption is reasonable in this stage, because other calculations showed that there is no big difference for the calculations in the following sections, even through the reactor is assumed to continue to operate more 5 seconds at full power level to include the influence of the drop of the control rods. During the PLOFC and DLOFC incidents, the profile of power density distribution is assumed to be constant, and its magnitude decreases in terms of decay heat level, since the neutronic model of the U-Battery is excluded for the transient thermal-hydraulic calculations. The mass flow of helium decreases from 7.64 kg/s to 0 in 5 seconds.

Because the U-Battery is assumed to use the same fuel blocks with the same specifications and the geometry of the reactor is cylindrically symmetric, a 2D (r, z) reactor core model was adopted for the neutronic part in the coupled calculations. The neutronic model only includes reactor core of the U-Battery in order to save calculation times.

Since THERMIX is a 2D code system, a 2D thermal-hydraulic model was used for the thermal design calculations of the U-Battery. This simplification is enough to keep the main characteristics of the U-Battery based on the same reasons as the neutronic model. The fuel zone in the reactor core of the U-Battery is assumed as a homogeneous porous media. The porosity of the fuel zone is 0.19, which is the ratio of the volume of

the coolant channels to total volume of a fuel block. The thermal-hydraulic model of the U-Battery includes the whole reactor and some important components outside the reactor core, such as the RPV, reactor cavity cooling system (RCCS), and concrete structures (if present). When the RCCS is adopted, it is simplified as a constant temperature (50 °C) boundary. If not, a 1-m concrete wall is modeled, and the thermal-hydraulic model uses the environment as a boundary condition, which is simplified as a constant temperature (30 °C) boundary. This means that the RCCS is the heat sink of the U-Battery if it is present, otherwise, it is the environment.

A.3.2 Parametric analysis of two key components

The thermal power (20 MW_{th}) of the U-Battery is far smaller than some mature designs of inherently-safe modular HTRs, like HTR-module, HTR-PM or GTMHR. Influence of the reactor cavity cooling system (RCCS) on the design of the U-Battery is investigated by simulating DLOFC incident. Moreover, a thin thermal insulation is adopted because of the limited diameter of the reactor pressure vessel (RPV), so material of the side thermal insulation of Layout 37*4 is also investigated.

A.3.2.1 Reactor cavity cooling system

The RCCS, usually placed between RPVs and concrete containment, is a key component for modular HTRs, which is adopted (1) to protect the RPVs and concrete structures surrounded the reactor; (2) to remove the decay heat of reactors during incidents. The RCCS is commonly designed to use natural circulation of air or water, and remove the heat from RPV to environment directly or indirectly. For example, the RCCS uses air-natural circulation for the GT-MHR. For the 20 MW_{th} U-Battery, the amount of decay heat is at least one order smaller than larger HTRs, like HTR-PM and GT-MHR, because of the small thermal power level. The feasibility of the U-Battery without the RCCS is investigated in this section in order to simplify the system configuration of the U-Battery, as well as the costs.

The maximum and volume-averaged temperatures of the reactor core for Layout 37*4 are shown in Fig. A.3.5 as functions of time during the DLOFC incident. The solid black and green lines are the maximum core temperatures of Layout 37*4 with and without RCCS, respectively, while the dashed black and green lines are the volume-averaged temperatures. Comparisons between them show that the RCCS has very limited influence on the maximum core temperature during the DLOFC incident for Layout 37*4. Especially in the first 30 hours of the incident, the maximum temperatures of the reactor core are almost identical. Moreover, the influence of the RCCS gradually appears after 30

hours, which attributes to a better condition for the decay heat removal when the RCCS is adopted, but its function is still very limited. For example, the temperature difference between the black (design with the RCCS) and green (design without the RCCS) lines is only about 20 °C at 100 hours. The solid black and green lines, as well as the dashed black and green lines, show that the reactor core temperature of Layout 37*4 mainly depends on the reactor core configuration for the U-Battery during the DLOFC incident, rather than the configurations outside the RPV. The inherent safety of the U-Battery attributes to the lower thermal power density and the reactor core configuration, for example, the large heat capacity of the fuel blocks and reflectors.

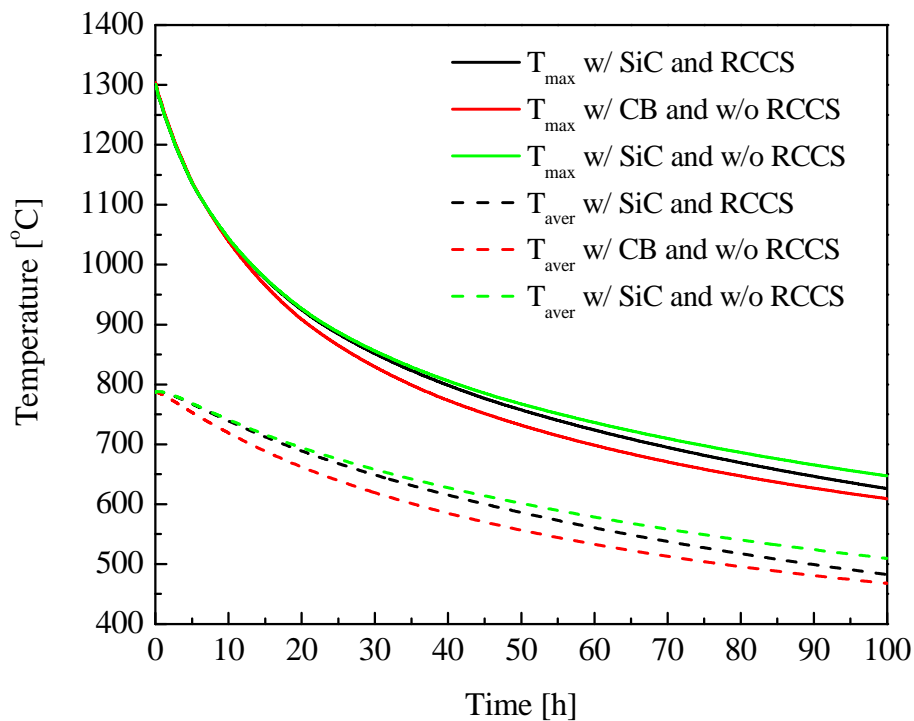


Fig. A.3.5 Maximum and volume-averaged temperature of the reactor core as functions of time

Compared with the core temperature, the maximum temperatures of the barrel and RPV are affected more easily by the RCCS, as shown in Fig. A.3.6. The black lines in the top and bottom subfigures are the maximum temperatures of the RPV and barrel of Layout 37*4 with the RCCS, respectively, while the green lines are those of the RPV and barrel of Layout 37*4 without the RCCS, respectively. As shown in the bottom subfigure, the temperature differences between the black and green lines is 39 °C for the barrel at 100 hours, while that is 56 °C for the RPV, as shown in the top subfigure.

In a word, for the reactor safety of the 20 MW_{th} U-Battery, the RCCS is optional rather than necessary, and the temperatures of the reactor core, barrel and RPV are all below the design limit (i.e., 395 °C), if the decay heat is removed through 1.0-meter concrete wall which is cooled by air in the environment.

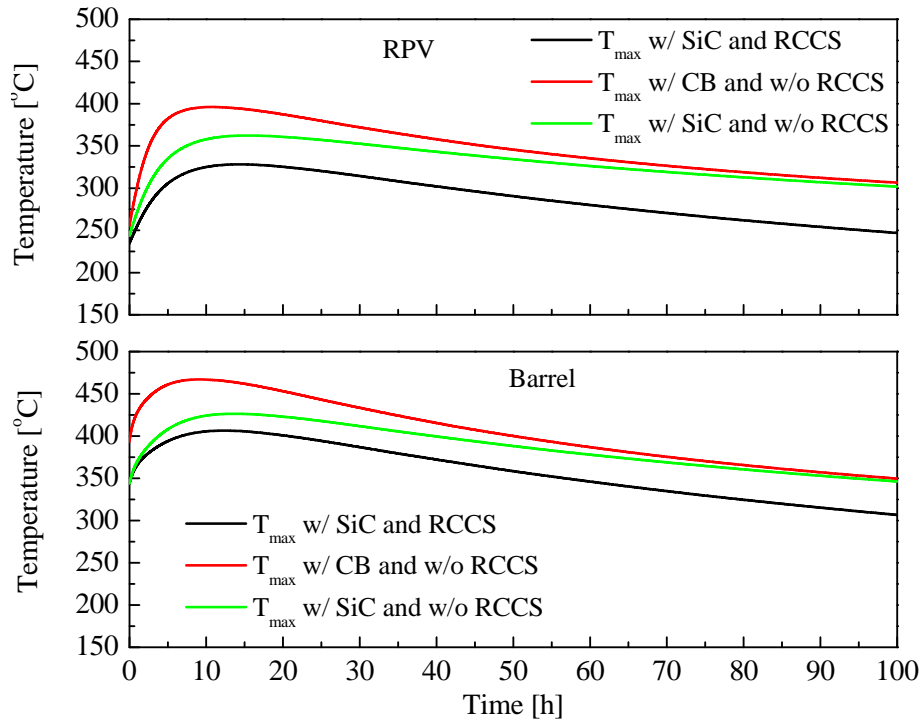


Fig. A.3.6 Maximum temperatures of the reactor pressure vessel and barrel as functions of time

A.3.2.2 Material choice of the side thermal insulation

Carbon brick is widely used in modular HTRs as thermal insulation, and SiC fiber is used in other high temperature applications. For HTRs, thermal insulation aims to protect the barrels and RPVs and reduce heat loss from the reactor core during normal operation because of the high operation temperature like 750 °C to 1000 °C. If the temperatures of the barrels and RPVs are decreased by the thermal insulation as low as possible, it would be possible to use low-temperature steel for these two expensive components. On the other hand, the thermal insulation blocks the removal of decay heat during incidents. The trade-off between the safety of the reactors and cost of the barrels and RPVs determines the thickness and material of the thermal insulation. For the U-Battery, because of the limited diameter of the RPV, and thus the limited thickness of the side reflector and side

thermal insulation, the maximum temperature of the RPV or barrel is a challenge for the thermal design of the U-Battery.

As shown in Fig. A.3.5 and Fig. A.3.6, the solid red lines are the maximum temperatures of the reactor core, and RPV and barrel, respectively, for Layout 37*4 using carbon brick as the side thermal insulation. From reactor safety point of view, the carbon brick as the side thermal insulation is positive because of the lower maximum core temperature (the solid red line in Fig. A.3.5), as well as volume-averaged temperature (the dashed red line in Fig. A.3.5), which means that a larger amount of decay heat is removed to the environment through the RPV. This attributes to the larger heat conductivity of the carbon brick than the SiC fiber. For example, the typical heat conductivities of the carbon brick and SiC fiber are 6.5 W/(m·K) and 2.2 W/(m·K) in the U-Battery at temperature of 500 °C.

However, the carbon brick plays an opposite role on the barrel and RPV for the U-Battery, compared of the maximum temperatures of the barrel and RPV with the reactor core. Because of the larger heat conductivity of the carbon brick, the maximum temperatures of the barrel (the solid red line in the subfigure of Fig. A.3.6) and RPV (the solid red line in the top subfigure of Fig. A.3.6) during the first 10 hours for the configuration with the carbon brick as the side thermal insulation are about 50 °C higher than those with the SiC fiber (the solid green lines in Fig. A.3.6). After the temperatures of the barrel and RPV reach their corresponding maximum values at about 10 hours, the difference of the carbon brick and SiC fiber becomes smaller and smaller, and the maximum temperatures of the barrel and RPV slowly converge to the corresponding temperatures of the configuration without RCCS. This means that the thermal behaviors of the barrel and RPV in the long term mainly depend on the configuration outside the RPV or the removal method of decay heat during the DLOFC incident. However, they depend on both the material of the side thermal insulation and the configuration outside the RPV at the beginning of the DLOFC incident. The maximum temperature of the barrel and RPV is a result of the balance between heat from the reactor core and that removed at the outer boundary.

Although the maximum temperatures of the barrel and RPV for the configuration with carbon brick are higher than the corresponding values of the configuration with the SiC fiber, they are still under the temperature limit of the RPV (i.e., 395 °C) during normal operation. Based on the RPV design requirements of the GT-MHR and HTTR, the maximum temperatures of the RPVs during accidents are 43 °C and 50 °C, respectively, higher than those (495 °C and 500 °C) during normal operation. During the DLOFC incident, the maximum temperature of the barrel of Layout 37*4 is 72 °C higher

than the temperature limit of the RPV for 50 hours, when the reactor does not adopt the RCCS. This means that both barrel and RPV possibly adopt the same material for Layout 37*4, which may be determined in terms of a more detailed requirement of the barrel and RPV for the U-Battery. If the SiC fiber is adopted, it is possible to decrease the thickness of the side thermal insulation, and thus the diameter of the RPV.

A.3.3 Analysis of LOFC incidents for a cylindrical core

The typical characteristics of the cylindrical design (i.e., Layout 37*4) of the U-Battery are analyzed in this section during PLOFC and DLOFC incidents. As mentioned in the previous section, the main aim of the transient thermal-hydraulic analysis is to evaluate the reactor configurations and safety of the U-Battery, and long behavior of the reactor core, especially the removal process and mechanism of the decay heat of the 20 MW_{th} U-Battery. Because the RCCS may have other practical functions, like protecting the concrete structure around the reactor pressure vessel from high temperature and cooling the space near the reactor, the RCCS is still used for the calculations in this and next sections. Since the RCCS has little influence on the thermal-hydraulic performance of the reactor core of the U-Battery, the analysis and results are still capable to the conditions without the RCCS.

A.3.3.1 Features of the cylindrical core during LOFC incidents

The maximum and volume-averaged core temperatures of Layout 37*4 during PLOFC and DLOFC incidents are shown in Fig. A.3.7 as functions of time. The solid lines indicate the temperatures of the reactor core during the PLOFC incident, and the dashed lines indicate those during the DLOFC incident. As shown in Fig. A.3.5, the maximum temperatures of the reactor core decrease immediately at the beginning of both incidents, which attributes to the very low average thermal power level density (1.5 MW/m³) and large heat capacity provided by the reactor core and other structures like reflectors and thermal insulations. They contribute to the inherent safety of the U-Battery from thermal-hydraulic point of view. Because the same compositions like 12% enriched uranium are used for all fuel blocks in the reactor core, the maximum temperature of the reactor core is high than 1300 °C for Layout 37*4. It is very easily decreased by 100-200 °C by flattening the radial power density distribution of the reactor core in the detailed design phase of the reactor, such as lower-enrichment fuel for the central fuel blocks, if the cylindrical core configuration is adopted as the reference design of the U-Battery. However, the paper only focuses on the preliminary or conceptual design of the U-Battery, so the optimization of the power density distribution is not excluded for the

transient thermal-hydraulic calculations. Compared the maximum and average temperatures between the PLOFC and DLOFC incidents, the reactor core is cooled more rapidly during the PLOFC incident than during DLOFC incident. This is the first difference of the thermal-hydraulic behavior of the reactor core between the PLOFC and DLOFC incidents.

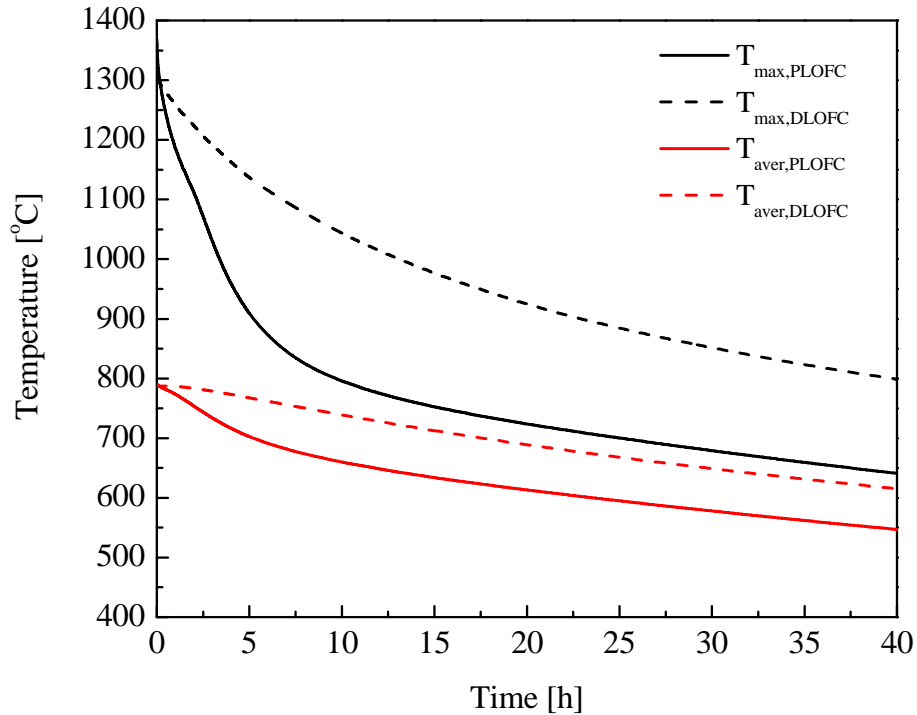


Fig. A.3.7 Maximum and volume-averaged core temperatures during the PLOFC and DLOFC incidents

The second difference of the thermal-hydraulic behavior of the reactor core between the PLOFC and DLOFC incidents is the different temperature distributions of the reactor core during the incidents. The radial solid temperature distribution of the reactor during the PLOFC and DLOFC incidents is shown in Fig. A.3.8 as a function of radius and with time as a parameter. The distribution is the temperature values of the meshes located 130 cm under the top surface of the fuel zone, i.e., in the middle plane of the reactor core, as shown in Fig. A.3.3. The numbers of 1 to 6 in Fig. A.3.8 indicate the regions in the reactor from the center to the periphery: fuel zone, side reflector, side thermal insulation, barrel, and RPV. The top subfigure presents the temperature distribution during the DLOFC incident using the dashed lines, while the bottom one shows that during the PLOFC incident using the solid lines. Different colors correspond to different times. For example, the red lines (solid and dashed) are the radial temperature distributions of the

reactor core at 10.0 hours. Compared each pair of lines with the same colors in the top and bottom subfigures, the radial temperature distributions of the reactor core during the PLOFC incident are far flatter than those during the DLOFC incident. At 10 hours, the temperature difference of the reactor core between central and peripheral regions during the PLOFC and DLOFC incidents are 110 °C and 393 °C, respectively. And at 100 hours, the temperature difference decreases to 207 °C during the DLOFC incident, while it decreases to 37 °C during the PLOFC incident.

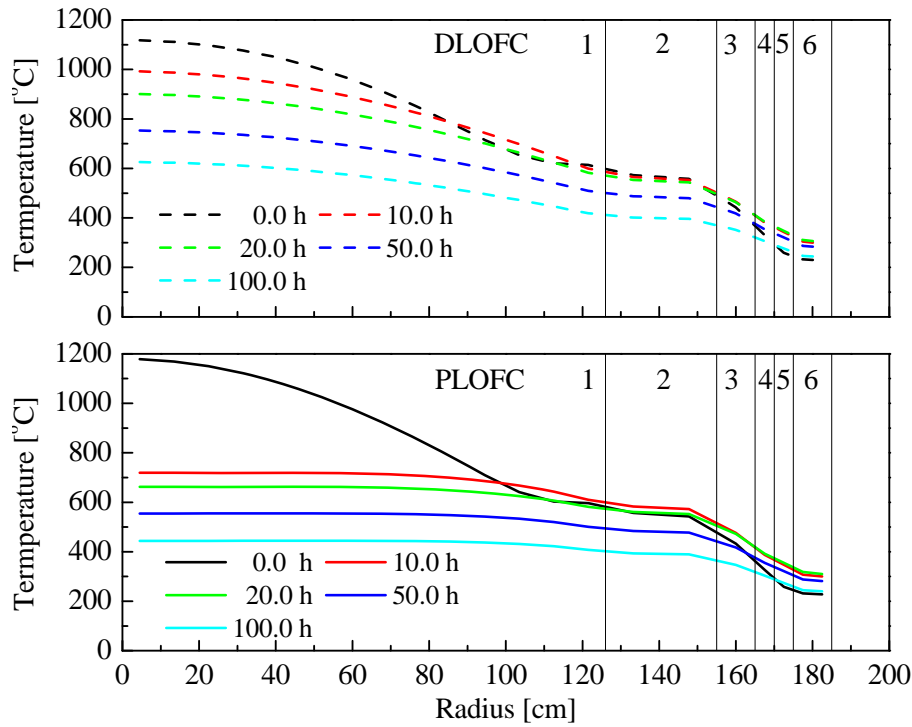


Fig. A.3.8 Radial solid temperature distributions ($z = 130.0$ cm) of the reactor system during the PLOFC and DLOFC incidents (1: Fuel zone; 2: Side reflector; 3: Side thermal insulation; 4: Barrel; 5: Gas gap; 6: RPV)

The third difference of the thermal-hydraulic behavior of the reactor core between the PLOFC and DLOFC incidents is the different temperature responses of the different regions of the reactor core during the incidents. The solid temperatures of the different parts of the reactor core are shown in Fig. A.3.9 during the PLOFC and DLOFC incidents as functions of time. The top subfigure presents the temperature responses of two radial meshes (central and peripheral meshes) in the middle plane ($z = 130$ cm) of the reactor core, and the bottom one shows those of two axial meshes (top and bottom meshes) in the central regions of the reactor ($r = 4.5$ cm). The exact coordinates of the meshes are shown

in the brackets in Fig. A.3.9. Compared of the different-color solid lines, i.e., the temperature responses of the different regions of the reactor core during the PLOFC incident, the temperature of the top region of the reactor core increases rapidly in the first 5 hours, while that of the bottom region decreases at the same period. For example, the temperature of the top central mesh ($r = 4.5$ cm, $z = 10$ cm) (solid green line) increases by 317 °C during the first 2 hours, and that of the bottom central mesh (4.5 cm, 310 cm) (solid blue line) decreases by 412 °C in the same period. The temperature of the middle central mesh (4.5 cm, 130 cm) slightly increases and then rapidly decreases. This means that a large amount of heat immediately accumulates in the top regions of the reactor core during the PLOFC incident, and a large amount of heat in the bottom regions of the reactor core is transferred to the top regions in the first 5 hours. The temperature of the middle peripheral mesh (121.5 cm, 130 cm) decreases at the beginning of the PLOFC incident because of the heat is transferred to the side reflector and further to the RPV, and then it increases because the accumulated rate of the heat is higher than the removal rate at the same time, as heat accumulates in the structures outside the reactor like the side reflector.

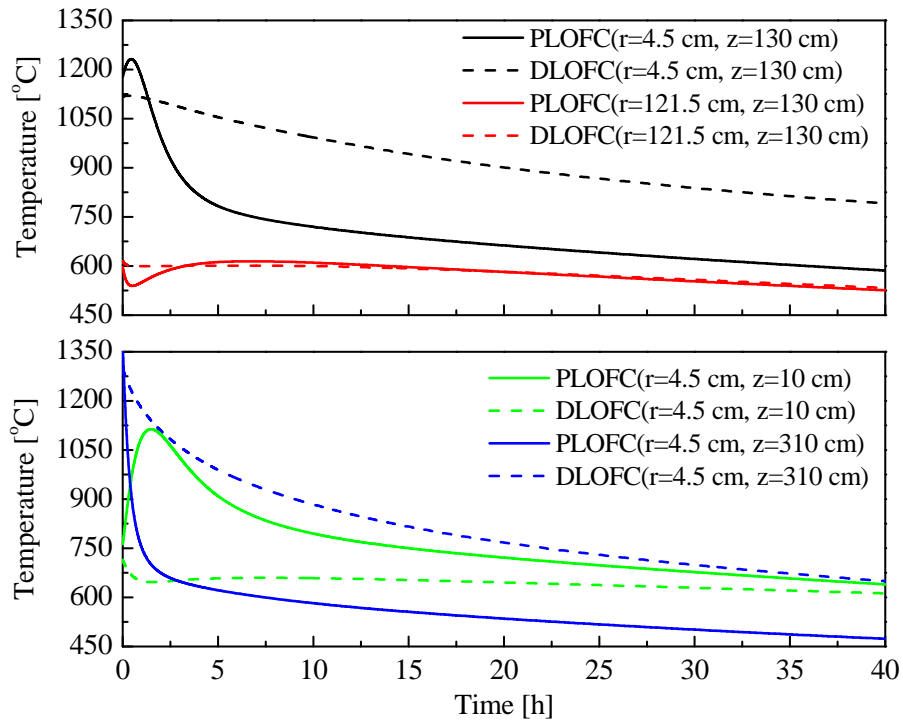


Fig. A.3.9 Solid temperature responses of the reactor core during the PLOFC and DLOFC incidents (The coordinates in brackets are the locations of the meshes)

The rapid temperature change of the different regions of the reactor core, as the solid lines shown in Fig. A.3.9, means that the thermal energy in the reactor core is obviously redistributed during the PLOFC incident. The decay heat and thermal energy absorbed by the solid structures of the reactor core during normal operation is mainly transferred from the bottom of the reactor core (i.e., hot regions) to the top (i.e., cold regions) in the first 2-5 hours. However, the temperature responses of the reactor core during the DLOFC incident are entirely different from those during the PLOFC incident. As the dashed lines shown in Fig. A.3.9, during the DLOFC incident, the temperature of the top central mesh (dashed green line) changes slowly, while that of the bottom central mesh (dashed blue line) decreases far smaller than that of the responding mesh during the PLOFC incident. This means that the heat during the DLOFC incident does not greatly redistribute like the PLOFC incident, and is only slightly transferred from the bottom to the top of the reactor core by conduction.

The temperature redistribution in the top, bottom and side reflectors happens as the reactor core in the similar way for these two incidents. The volume-averaged temperatures of the reflectors are shown in Fig. A.3.10. The same color represents the same component (e.g., top, bottom and side reflectors), and the solid and dashed lines correspond to the PLOFC and DLOFC incidents, respectively. The volume-averaged temperature of the top reflector rapidly increases by 451 °C in the first 3.5 hours during the PLOFC incident, while it only increases by 175 °C during the DLOFC incident in the same period, and slowly up to 503 °C at 30 hours. The volume-averaged temperature of the bottom reflector decreases faster during the PLOFC incident than during the DLOFC incident. The temperature changes of the top and bottom reflectors mean that more heat is transferred from bottom regions of the reactor core during the PLOFC incident than the DLOFC incident. Because the larger amount of heat during the PLOFC incident is transferred to the side reflector outside the reactor core than during the DLOFC incident, the volume-averaged temperature of the side reflector of the former (solid green line) is higher than that of the latter (dashed green line).

As a result of the heat transfer from the bottom to top of the reactor core, the maximum temperature of the top head of the RPV increases by 141 °C during the PLOFC incident, and only 82 °C during the DLOFC incident, as shown in Fig. A.3.11. The maximum temperatures of the side part of the RPV have the similar behavior during the PLOFC and DLOFC incidents because the heat is transferred out of the reactor core.

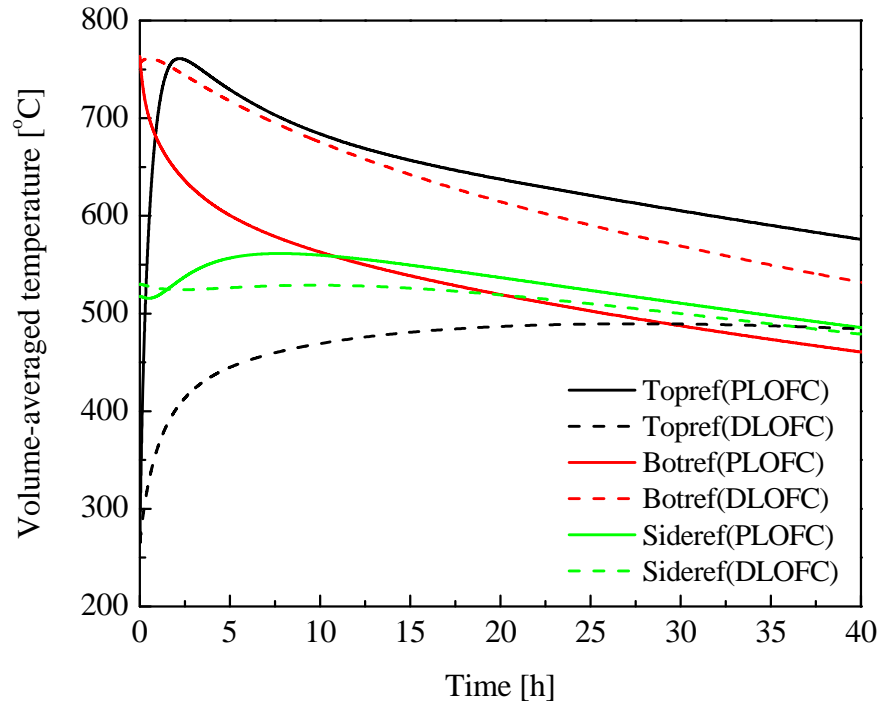


Fig. A.3.10 The volume-averaged temperatures of the reflectors during the PLOFC and DLOFC incidents

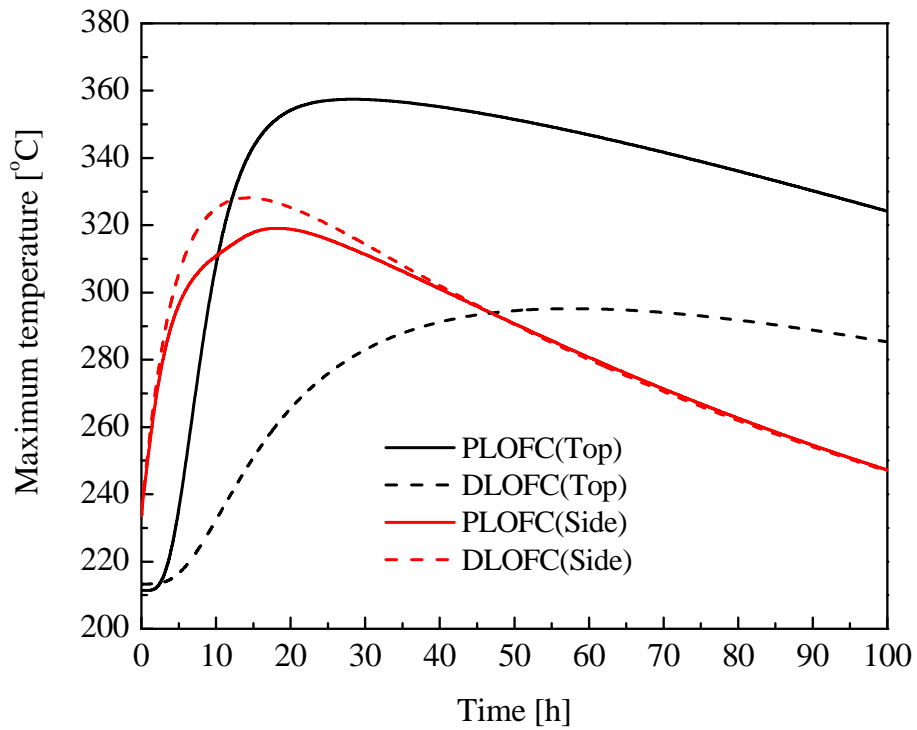


Fig. A.3.11 Maximum temperature of the RPV during the PLOFC and DLOFC incidents

As mentioned in the previous section, the temperature of the side RPV is mainly influenced by the internal structures (e.g., side thermal insulation) in the reactor core and cooling condition of the reactor system in the short term, and by the cooling condition of the reactor system in the long term. The maximum temperature of the side RPV appears at the lower part ($z = 250$ cm) during the normal operation. Because a larger amount of heat is transferred in a faster way from the hot regions to the cold at the first 5-10 hours during the PLOFC incident, the temperature of the bottom regions of the reactor core decreases faster, as well as the bottom peripheral regions of the reactor core. As a result, the maximum temperature of the side RPV during the PLOFC incident is lower than that during the DLOFC incident in the first 40 hours. Since the RCCS is assumed to be used during the PLOFC and DLOFC incidents, the maximum temperatures of the side part of the RPV tend to be identical in the long term. Because a larger amount of heat is transferred to outside during the PLOFC incident, the maximum temperature of the side RPV during the PLOFC incident is slightly higher than that during the DLOFC incident.

A.3.3.2 Discussion of the features of LOFC incidents

For the PLOFC incident, the pressure of the reactor system is the same as the normal operation of the U-Battery, i.e., 4.0 MPa. The simulation of this incident aims to test the inherent safety of the reactor and decay heat removal process, when the primary loop of the U-Battery only loses forced-cooling. For the DLOFC incident, the pressure of the reactor system is assumed to drop to the environment system (i.e., 1.0 bar) in a very short time because of helium leakage, for example, broken hot gas duct which connects the RPV with the power conversion system (PCS) vessel. The simulation of the DLOFC incident aims to test the inherent safety of the reactor and decay heat removal process, when the primary loop of the U-Battery loses not only forced-cooling, but also the system pressure.

The different system pressures lead to the three differences between the PLOFC and DLOFC incidents, as concluded in the previous section. A higher system pressure is positive to build up the natural circulation in the reactor core. The radial velocity distribution of the coolant in the middle plane of the reactor core during the PLOFC and DLOFC incidents are shown in Fig. A.3.12 as a function of radius and with time as a parameter; the top subfigure shows the distribution during the DLOFC incident using the dashed lines, while the bottom one shows those during the PLOFC incident using the solid lines. The positive values in the figure mean the coolant (i.e., helium) in the reactor core flows from the top to the bottom, while the negative values mean it flows from the bottom to the top.

As shown in Fig. A.3.12, the natural circulation does build up in the reactor core during each incident. The coolant naturally flows from the bottom to the top in the central regions of the reactor core, while from the top to the bottom in the peripheral regions. However, the magnitude of velocities during the PLOFC incident is far larger than that during the DLOFC incident because of the higher system pressure. For example, the velocity of the coolant is 0.9 m/s (from the bottom to the top) in the center of the reactor core at 0.1 hours during the PLOFC incident, while the corresponding value is about 0.018 m/s during the DLOFC incident. The natural circulation is driven by the density difference of the coolant between the central and peripheral regions in the reactor core. The density difference depends on the temperature differences and the system pressure. Although the temperature difference between the central and peripheral regions during the DLOFC incident is far larger than those during the PLOFC incident, the system pressure during the PLOFC incident is 40 times larger than that during the DLOFC incident and thus the density difference between the central and peripheral regions during the PLOFC incident is far larger than that during the DLOFC incident.

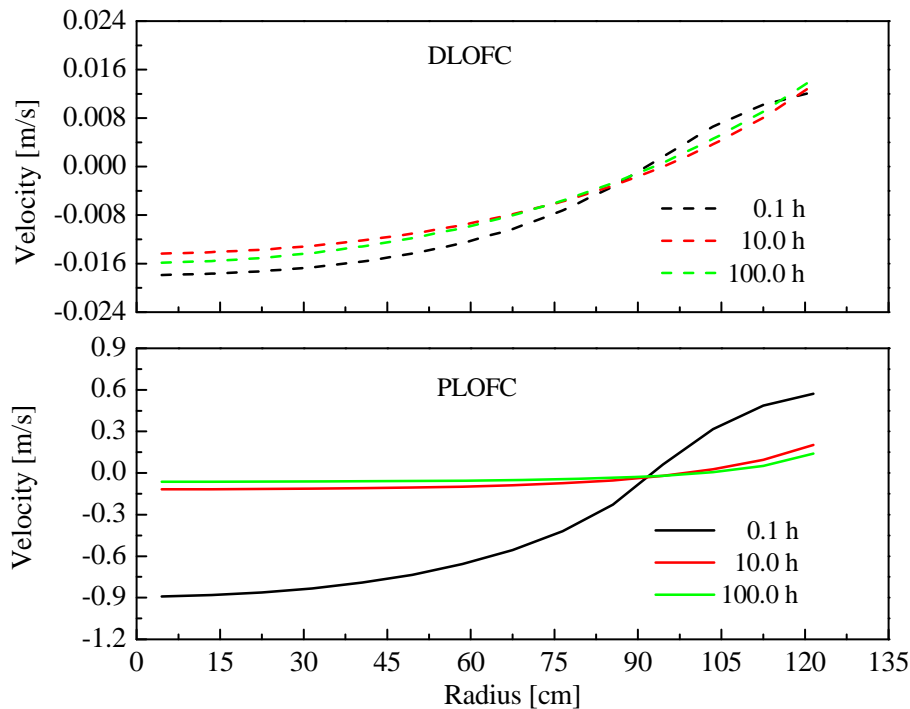


Fig. A.3.12 Radial velocity distributions of the coolant in the middle plane ($z=130$ cm) of the reactor core during PLOFC and DLOFC incidents

The change mode of the natural circulation with time during the PLOFC incident is different from that during the DLOFC incident, as shown Fig. A.3.12. The velocities and

densities of two typical coolant channels in the central and peripheral regions of the reactor core are shown in Fig. A.3.13 as functions of time during the PLOFC incident. It is a more direct illustration of the change mode of the natural circulation with time than Fig. A.3.12.

The red and black lines in the top subfigure represent two typical channels in the central and peripheral regions, respectively. The magnitude of the values in the top subfigure is the magnitude of the natural circulation velocities, while the sign of the values is the flow direction of the coolant. The negative sign means the helium flows from the bottom to the top of the reactor, while the positive one means that it flows from the top to the bottom. During the PLOFC incident, the magnitude of the natural circulation decreases monotonically with time, especially during the first 5 hours, because the density difference of the coolant between the central and peripheral regions decreases rapidly, as shown in the bottom subfigure of Fig. A.3.13. The density difference decreases because of the drop of the temperature difference between the central and peripheral regions. For example, the solid temperature difference of the corresponding meshes drops from 582 °C to 171 °C during the first 5 hours, as shown in Fig. A.3.8.

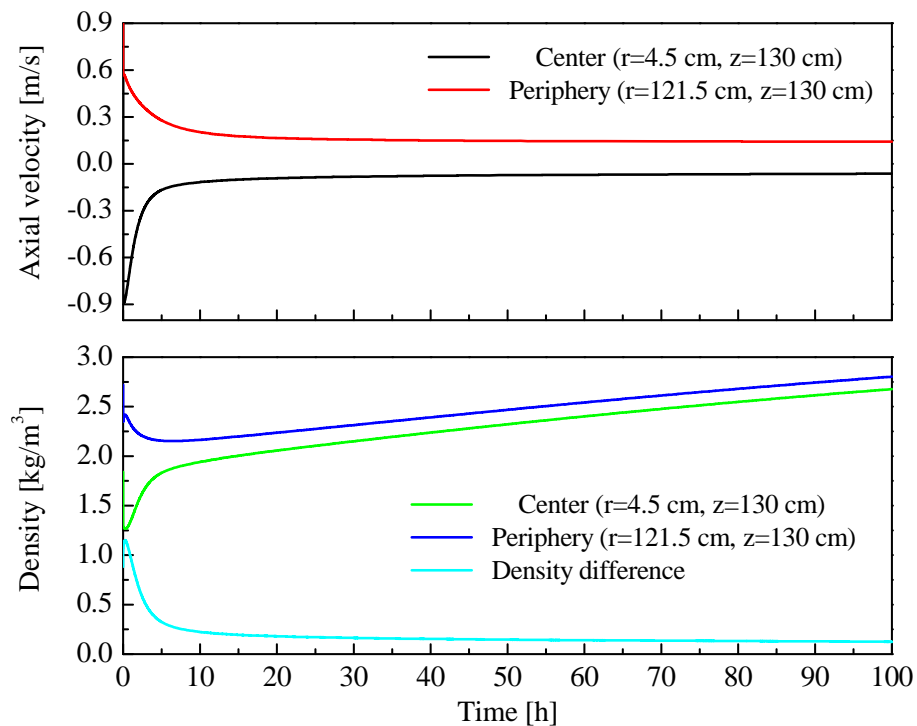


Fig. A.3.13 Coolant velocities and densities of two typical channels in the reactor core as functions of time during the PLOFC incident

Although the natural circulation during the DLOFC incident is so weak that it can not obviously contribute to the removal of decay heat, it is necessary to analyze it because its time-dependent behavior is different from that during the PLOFC incident. The coolant velocities and densities of the same channels as the PLOFC incident in the central and peripheral regions of the reactor core are shown in Fig. A.3.14 during the DLOFC incident. The magnitude of the natural circulation of the DLOFC incident decreases first and then slightly increases after 30 to 40 hours, as shown in the top subfigure of Fig. A.3.14 and Fig. A.3.12. As the bottom subfigure shown in Fig. A.3.14, the first decrease of the density difference weakens the natural circulation, which is caused by the decrease of the temperature difference between the central and peripheral regions. During the DLOFC incident, as the decay heat is transferred to the outside structures mainly by conduction and thus the temperature of the reactor decreases, the coolant density gradually increases with time, as shown in the bottom subfigure of Fig. A.3.14. The large temperature difference remains after 30 to 40 hours between the central and peripheral regions, as shown in Fig. A.3.8, the density difference of the corresponding regions starts to increase slightly, which strengthens the natural circulation after 30 to 40 hours.

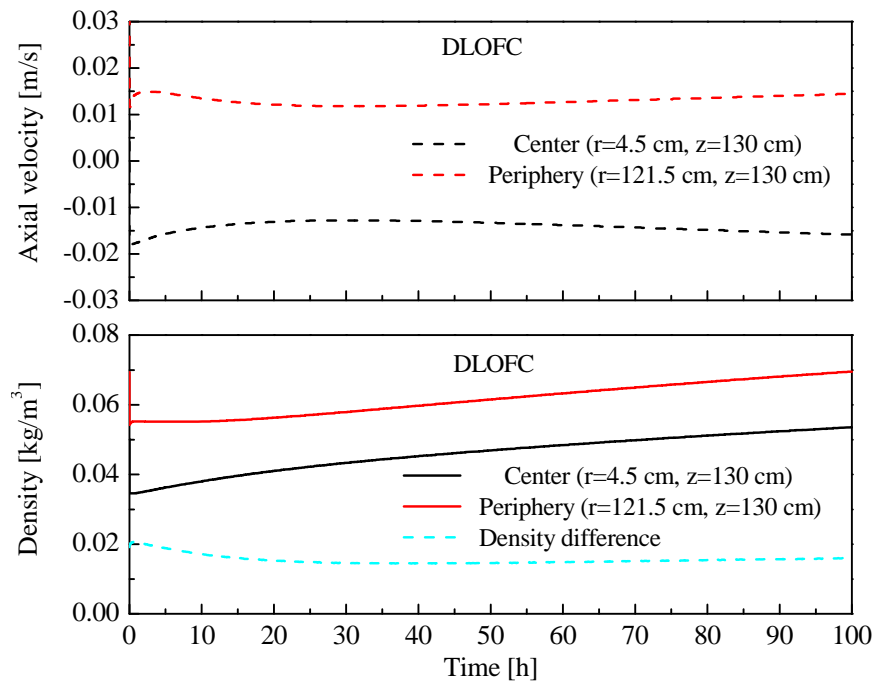


Fig. A.3.14 Coolant velocities and densities of two typical channels in the reactor core as functions of time during DLOFC incident

Although the coolant densities also increase with the decay heat removal during the PLOFC incident, as shown in the bottom subfigure of Fig. A.3.13, the temperature difference between the central and peripheral regions is so small that the density difference continues to decrease. Moreover, the coolant densities are an order larger than the density increase for the PLOFC incident, which is difficult to change the decrease trend of the density difference. However, for the DLOFC incident, the density change itself is almost in the same level as the coolant density, so it does change the change trend of the natural circulation in the reactor core.

The difference of the magnitude of natural circulation leads to the three differences of the thermal-hydraulic behaviors of the reactor core between of the PLOFC and the DLOFC incidents as mentioned in Sec. A.3.3.1. During the PLOFC incident, the strong natural circulation transfers the decay heat and the thermal energy absorbed by the solid structures during normal steady-state operation from the bottom regions to the top regions, which causes the rapid temperature increase of the top regions, e.g., the fuel zone, top reflector, and top head of the RPV, as shown in Fig. A.3.9, Fig. A.3.10 and Fig. A.3.11, respectively. Moreover, because the decay heat is partly transferred from the center to the periphery of the reactor core by the strong natural circulation during the PLOFC incident, which provides a more direct way to discharge the decay heat through the side reflector and the RPV, the reactor core is cooled faster than during the DLOFC incident, as shown in Fig. A.3.7. The radial temperature distribution of the reactor core is also flattened by the strong natural circulation, as shown in Fig. A.3.8. However, the strong natural circulation during the PLOFC incident lasts for 2.5 hours and rapidly decreases as the temperature difference decreases.

During the DLOFC incident, the weak natural circulation does obviously not contribute to the removal of the decay heat from the reactor core to the RPV and environment, which is mainly transferred by heat conduction in the reactor core. As shown in Fig. A.3.8, the radial solid temperature distribution of the reactor core during the whole DLOFC incident is quite similar to that of a pure heat conduction media with an internal heat source, and the weak natural circulation does not obviously change the profile of the heat conduction. Thus, the heat during the DLOFC incident is mainly transferred by heat conduction from the reactor core to the outside structures, and a larger amount of heat accumulates in the reactor center than during the PLOFC incident. The temperatures of the top structures of the reactor core do not also change largely like the PLOFC incident. So, the top structures were designed based on the PLOFC incident for the U-Battery, which is true for other HTRs, especially prismatic HTRs.

A.3.4 Analysis of LOFC incidents for an annular core

Compared with the cylindrical core of the U-Battery (i.e., Layout 37*4), the annular core, i.e., Layout 30*4, has several advantages from neutronic point of view, such as, higher burnup, lower fuel cost, and longer lifetime, etc. The thermal-hydraulic performance of Layout 30*4 will be evaluated in this section by comparing with Layout 37*4. Layout 30*4 is assumed to have the same reactor configuration as Layout 37*4, for example, the same sizes of the reflectors and thermal insulations, and RPV, except the reactor core configuration. Layout 30*4 is built up on the basis of Layout 37*4 by replacing 28 fuel blocks (7 fuel blocks per layer) in the center of the reactor core by the same number of graphite blocks. There are no coolant channels in the central graphite region, or central reflector, so the coolant only flows through the annular fuel zone of the reactor core.

The maximum and volume-averaged temperatures of the fuel zone of Layout 30*4 are shown in Fig. A.3.15 as functions of time during the PLOFC and DLOFC incidents. The solid and dashed lines represent the PLOFC and DLOFC incidents, respectively. The black lines indicate the maximum temperatures of the fuel zone, while the red ones indicate the volume-averaged temperatures.

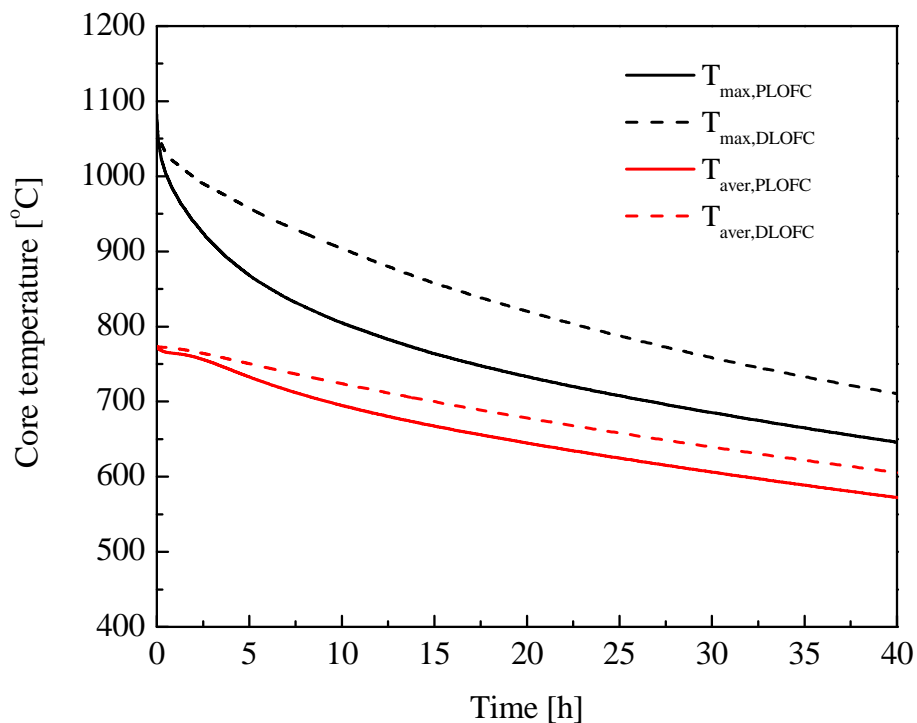


Fig. A.3.15 Maximum and volume-averaged temperature of the fuel zone for Layout 30*4 during the LOFC incidents

Like Layout 37*4, the maximum and average temperatures of Layout 30*4 decrease immediately, after the reactor is shut down, because of a very low thermal power density level. The maximum temperature of the fuel zone of Layout 30*4 is far below 1600 °C during the steady-state operation, and both PLOFC and DLOFC incidents, although Layout 30*4 has a higher power density than Layout 37*4. Moreover, the fuel zone of the annular design during the PLOFC incident is still cooled faster than during the DLOFC incident, which is also the same as the cylindrical design.

As analyzed in the previous section, the stronger natural circulation during the PLOFC incident does contribute to remove the decay heat directly out of the reactor core, and flatten the radial solid temperature distribution for the cylindrical core, as shown in Fig. A.3.8. For the annular core, natural circulation in the fuel zone does also build up during both PLOFC and DLOFC incidents, like the cylindrical core. The typical axial velocities of two meshes in the fuel zone of Layout 30*4 are shown in Fig. A.3.16 as functions of time during the PLOFC and DLOFC incident. Both meshes are located at 130 centimeters under the surface of the fuel zone, i.e., in the middle plane of the reactor core defined in the previous section for the cylindrical core. The position of the middle plane of the annular core is the same as that of the cylindrical core, since the core heights are identical. One mesh (black lines in Fig. A.3.16) is located in the inner regions ($r = 58.5$ cm) of the annular fuel zone, while the other one (red lines) in the outer regions ($r = 121.5$ cm). The top subfigure shows the axial velocities of the two meshes during the DLOFC incident (dashed lines), while the bottom subfigure shows those during the PLOFC incident (solid lines). Positive values mean that the coolant flows from the top to the bottom of the annular core, while negative values mean that it flows in the opposition direction. The data show that the annular core also builds up the natural circulation from the hot regions to the cold regions, i.e., from the inner regions to the outer regions. Moreover, the natural circulation in the annular core decreases with time for the PLOFC incident in the long term, which is also same as the cylindrical core.

However, compared of Fig. A.3.16 with Fig. A.3.14 and Fig. A.3.13, the natural circulation of Layout 30*4 is weaker than that of Layout 37*4 during the PLOFC and DLOFC incidents. For example, the maximum axial velocity of the middle peripheral mesh ($r = 121.5$ cm, $z = 130$ cm) is 0.4 m/s in the middle plane during the PLOFC incident, while the corresponding value of the same position is 0.9 m/s for the cylindrical core. The more flattened radial solid temperature distribution of the annular core weakens the natural circulation, as shown in Fig. A.3.17, since the natural circulation is driven by the temperature difference between the outer regions of the fuel zone and inner regions and thus the density difference, as discussed in the previous sections.

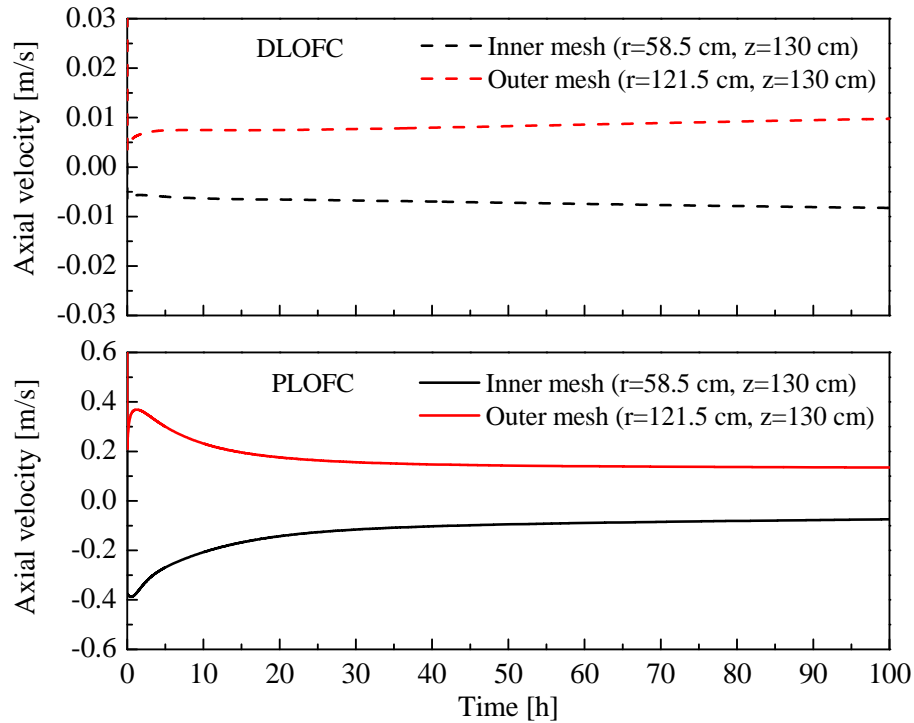


Fig. A.3.16 Typical axial velocities of two meshes in the fuel zone of the annular core during PLOFC and DLOFC incidents

The top subfigure of Fig. A.3.17 shows the radial solid temperature distribution of the reactor core during the DLOFC incident (dashed lines) as a function of radius and with time as a parameter, and the bottom subfigure shows that during the PLOFC incident (solid lines). The number 0 indicates the central reflector of the annular reactor core, and other numbers have the same meaning as the cylindrical reactor core. During the normal steady-state operation (i.e., both black lines) of the reactor, the maximum temperature of the annular core appears in the inner regions of the annular fuel zone, because the central region of the reactor core only consists of graphite blocks. The temperature distribution of the central reflector is uniform because there is no heat source and no coolant as well.

Compared of Fig. A.3.17 with Fig. A.3.8, the radial solid temperature distribution of the fuel zone of the annular core is more flat than that of the cylindrical core at the beginning of the PLOFC and DLOFC incidents. For example, the temperature differences between the middle inner mesh ($r = 4.5$ cm and $z = 130$ cm for the cylindrical core, or $r = 58.5$ cm and $z = 130$ cm for the annular core) and middle peripheral mesh ($r = 121.5$ cm, $z = 130$ cm for both reactor cores) of the cylindrical and annular cores are 582 °C and 174 °C, respectively. Thus the natural circulation of the annular core is weaker than that of the cylindrical core. In turn, the relative weaker natural circulation keeps the temperature

differences between the inner and outer regions of the annular reactor core for a longer time. For example, the temperature differences of the two meshes of the cylindrical and annular cores are 110 °C and 174 °C, respectively, at 10 hours. As a result, the stronger natural circulation of the cylindrical core only lasts less than 5 hours, and dramatically decreases especially in the first 2.5 hours. The axial velocity of the mesh located at position (121.5 cm, 130.0 cm) for the cylindrical core decreases from 0.57 m/s to 0.2 m/s in 10 hours (as shown in Fig. A.3.13), while the value of the same position for the annular core is still larger than 0.23 m/s (as shown in Fig. A.3.16).

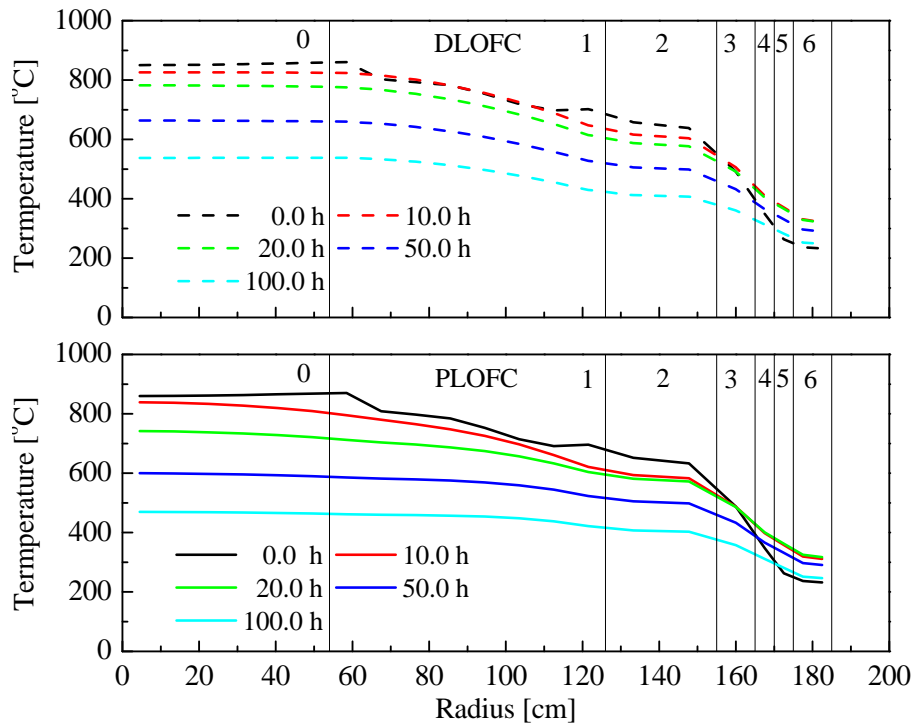


Fig. A.3.17 Radial solid temperature distribution of Layout 30*4 during the LOFC incidents ($z = 130.0$ cm) (0: Central reflector; 1: Fuel zone; 2: Side reflector; 3: Side thermal insulation; 4: Barrel; 5: Gas gap; 6: RPV)

The temperature responses of the different regions of the reactor core or thermal energy redistribution process for the annular design are also similar to those of the cylindrical design. The solid temperature responses of four meshes in the annular fuel zone are shown in Fig. A.3.18 for the annular design during the PLOFC and DLOFC incidents. The data in the brackets are still the coordinates of the four meshes. The top subfigure presents the temperature responses of the two meshes in the middle plane of the reactor core, while the bottom one presents those of the two meshes in the inner region of

the annular fuel zone, located in the top and bottom regions, respectively. The dashed lines still indicate the DLOFC incident, while the solid ones indicate the PLOFC incident.

Similarly to the cylindrical core, the temperature of the top central mesh ($r = 58.5$ cm, $z = 10$ cm) increases rapidly during the PLOFC incident, because the decay heat and thermal energy absorbed by the solid structures during steady-state operation are transferred by the natural circulation of the coolant from the bottom to top of reactor core in the inner regions of the fuel zone; the temperature of the bottom central mesh (58.5 cm, 310 cm) decreases obviously because of the removal of heat by both natural circulation and heat conduction. This also means that the heat is still removed from the bottom hot regions and accumulates in the top cold regions of the reactor by both heat conduction and natural circulation during the PLOFC incident. The temperature of the middle peripheral mesh (121.5 cm, 130 cm) decreases at the beginning of the PLOFC incident because the heat is transferred to the side reflector by heat conduction, and then it increases because the accumulated rate of the heat in the region, which is transferred by both natural circulation and heat conduction, is larger than the removal rate to the side reflectors by heat conduction.

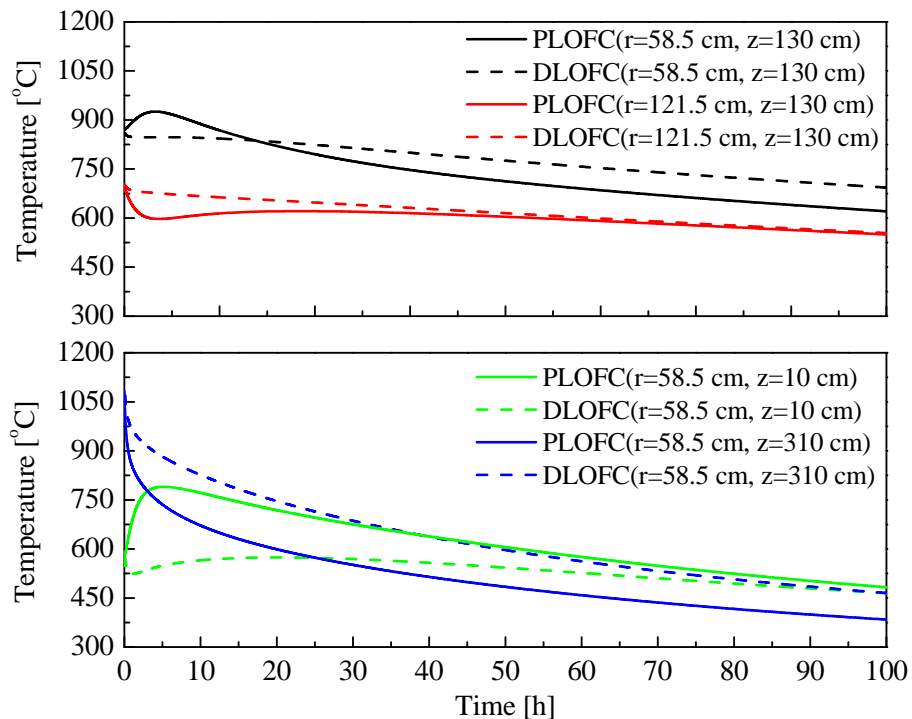


Fig. A.3.18 Solid temperature responses of the annular fuel zone as functions of time during PLOFC and DLOFC incidents
(The coordinates in brackets are the locations of the meshes)

During the DLOFC incident, the temperature of the four meshes changes slowly because the natural circulation of the coolant is so weak that the heat is mainly transferred and redistributed by heat conduction in the solid, and is also removed by heat conduction from the reactor core to the outside structures. If the dashed lines in Fig. A.3.18 are considered as the typical temperature responses of the reactor core by heat conduction, the difference between the dashed and solid lines comes from the natural circulation of the coolant in the fuel zone.

A.3.5 Further comparisons of cylindrical with annular designs

In Sec. A.3.4, Layout 30*4 is analyzed in detail, and is indirectly compared with Layout 37*4, the cylindrical design. Moreover, the comparisons mainly focus on the differences of the temperatures and natural circulations in the reactor core. In this section, Layout 30*4 will be compared directly with Layout 37*4 from the following two points of view: the temperatures of the fuel zone and the maximum temperatures of the barrel and RPV because of the very thin side reflector and thermal insulation for the U-Battery.

The maximum and volume-averaged temperatures of the fuel zone are shown in Fig. A.3.19 as functions of time for Layouts 37*4 and 30*4 during DLOFC incident. The solid and dashed lines are the temperatures of the cylindrical (Layouts 37*4) and annular (Layouts 30*4) designs, respectively. The maximum temperature of Layout 37*4 is 228 °C higher than that of Layout 30*4 at the beginning of incident, and it is about 100 °C during the incident. However, the difference of the volume-averaged temperatures between the cylindrical and annular design is far smaller than that of the maximum temperatures. This means that the solid temperatures of Layout 37*4 are only slightly higher than those of Layout 30*4 in most regions of the fuel zone. The difference of the maximum temperatures between Layouts 37*4 and 30*4 mainly comes from the difference of the power density distributions in the fuel zones. The power density distribution of Layout 30*4 is more uniform than that of Layout 37*4, since there are 7 fuel blocks in each layer replaced by the graphite blocks for Layout 30*4 in the center of the reactor core, as mentioned in the previous sections. For example, the average power factors of the cylindrical and annular designs are 2.39 and 1.34, respectively. This replacement of fuel blocks by graphite blocks flattens the radial power density distribution from neutronic point of view, and thus the radial solid temperature distribution of the fuel zone or the whole reactor core from thermal-hydraulic point of view. It is considered as a thermal-hydraulic advantage of the annular design.

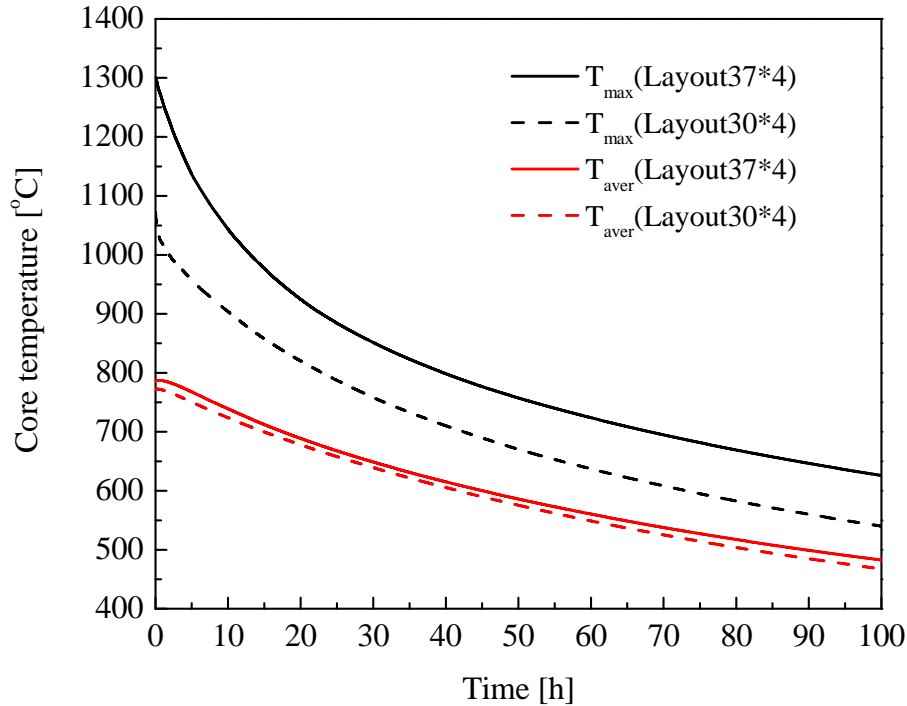


Fig. A.3.19 Maximum and volume-averaged temperatures of the fuel zone of the annular and cylindrical designs during DLOFC incident

All comparisons show that the annular design is better than the cylindrical design, except for the temperatures of the structures outside the reactor core, especially the barrel and RPV. The maximum temperatures of the barrels and RPVs are shown in Fig. A.3.20 for the cylindrical and annular designs during DLOFC incident. The solid and dashed lines represent the cylindrical and annular designs, respectively. The black lines indicate the maximum temperatures of the barrels, while the red ones indicate those of the RPVs. The annular and cylindrical designs adopt the same thick side thermal insulation, i.e., 10-cm SiC fiber. Because the power densities of the fuel regions next to the side reflector for the annular design are 60% higher than those for the cylindrical design, the maximum temperatures of the barrel and RPV of the former are higher than those of the latter. However, the maximum temperature of the RPV is still under the limit value (i.e., 395 °C) for the annular design, and that of barrel is higher than the limit value for about 40 hours.

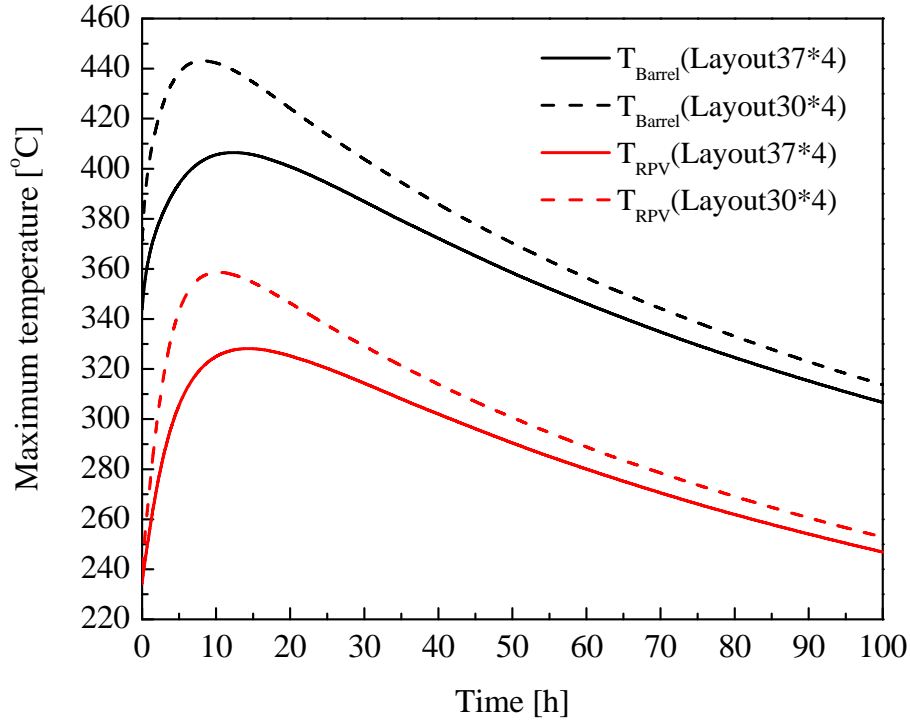


Fig. A.3.20 Maximum temperatures of the barrels and RPVs for the annular and cylindrical designs during DLOFC incident

A.3.6 Thermal power investigation of the annular design

The thermal power of the U-Battery is 20 MW_{th} in the previous thermal-hydraulic analysis. For the 20 MW_{th} U-Battery, the maximum core temperatures of Layout 30*4 and Layout 37*4 monotonously decreases during LOFC incidents because of the low power densities. Moreover, the core maximum temperatures of the U-Battery are far below 1600 °C during the incidents, especially the annular design, Layout 30*4. Thus, the annular core still has a large potential to increase its thermal power.

The possible maximum thermal power of the annular reactor Layout 30*4 is investigated in this section in terms of DLOFC incident. The maximum core temperature of Layout 30*4 is shown in Fig. A.3.21 as a function of time and with thermal power as a parameter. Beside 20 MW_{th}, three higher thermal power levels are investigated, which are 40 MW_{th}, 100 MW_{th} and 150 MW_{th}, respectively, indicated by different color lines. As shown in Fig. A.3.21, because of the low power density, the maximum core temperature of the 40 MW_{th} U-Battery also monotonously decreases during the DLOFC incident. However, it decreases more slowly than that of 20 MW_{th} U-Battery in the long term because of the 2 times larger decay heat level and the same decay heat removal rate by the RCCS. When the thermal power of Layout 30*4 increases to 100 MW_{th}, the

maximum core temperature does increase during the DLOFC incident. The maximum core temperature reaches 1286 °C at 42 hours, and then slowly decreases. Although the power density of Layout 30*4 increases 5 times, the maximum core temperature is still far below 1600 °C because of the large heat capacity provided by the central, top, bottom and side reflectors, as well as fuel zone itself. However, when the thermal power of Layout 30*4 increases to 150 MW_{th}, the maximum core temperature is larger than 1600 °C from 29 to 85 hours.

For the current design of Layout 30*4, especially 10-cm side thermal insulations (SiC fiber), the RPV may face a more severe challenge than the reactor core itself, as the thermal power of the U-Battery increases, as shown in Fig. A.3.22. When the thermal power of Layout 30*4 increases up to 100 MW_{th}, the maximum RPV temperature is larger than 395 °C from 13 hours, and further increases up to 453 °C. In this case, the RPV may still be possible to use the same material of the 20 MW_{th} U-Battery. However, when the thermal power of Layout 30*4 increases to 150 MW_{th}, the maximum RPV temperature reaches 530 °C. In this case, higher-temperature steel may be used for the RPV of the U-Battery if the diameter of the RPV keeps constant. The second way is to increase the thickness of the side thermal insulation. Although the diameter of the RPV may have to be increased, it can decrease the maximum temperature of the barrel at the same time.

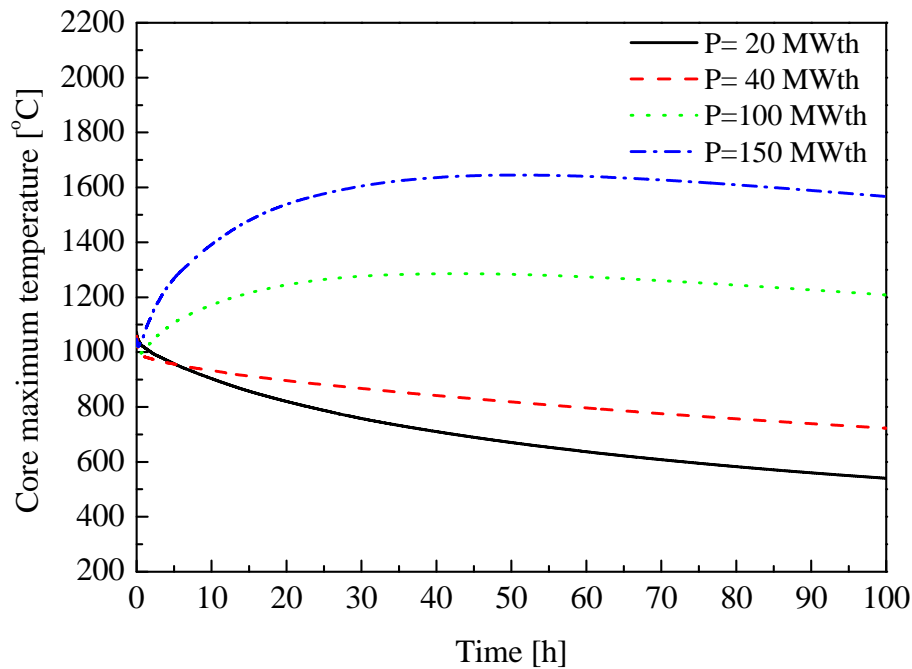


Fig. A.3.21 Maximum core temperature of Layout 30*4 as a function of time and with thermal power as a parameter during DLOFC incident

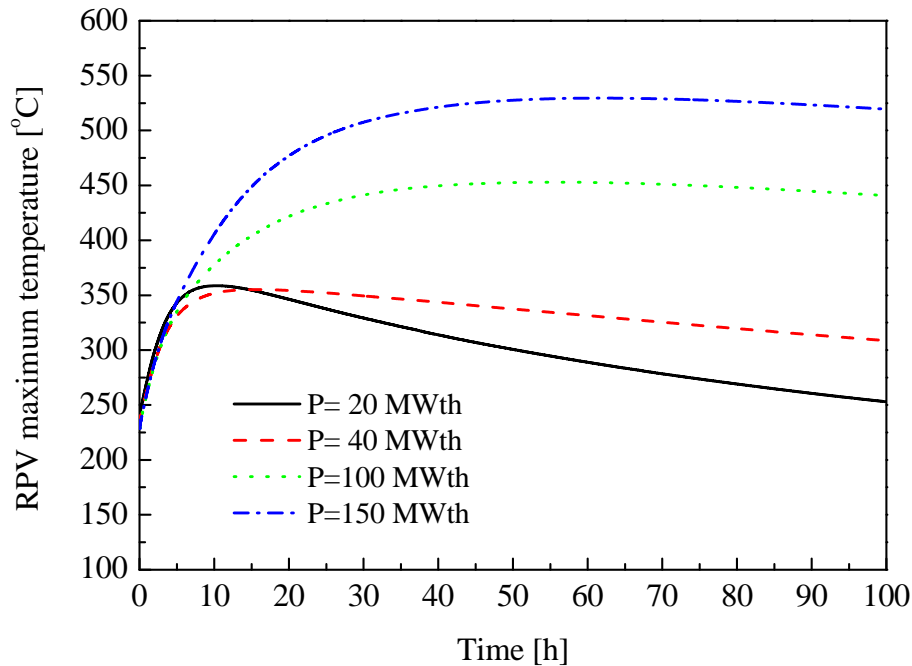


Fig. A.3.22 Maximum RPV temperature of Layout 30*4 as a function of time and with thermal power as a parameter during DLOFC incident

A.3.7 Summary

The coupled DALTON/THERMIX code system has been developed in the report. After the steady-state coupled neutronic/thermal-hydraulic design of the U-Battery using the coupled code system, both a cylindrical design (Layout 37*4) and an annular design (Layout 30*4) are evaluated for pressurized and depressurized loss of forced-cooling incidents. The thermal-hydraulic analysis partly demonstrates the inherent safety of the 20 MW_{th} U-Battery, and the reactor configurations of the U-Battery are safe enough to remove decay heat passively without forced-cooling measures during both design-basis incidents.

During PLOFC incident, natural circulation for both designs does build up to contribute to the removal of decay heat and the thermal energy absorbed by the solid structures during normal operation. Besides heat conduction in the fuel blocks, the strong natural circulation obviously transfers the heat from the bottom high-temperature regions to the top low-temperature regions in the reactor core, and also flattens the radial solid temperature distribution during the PLOFC incident. Although the natural circulation in the reactor core is so weak that it is neglected during the DLOFC incident, the decay heat is removed successfully by heat conduction without any violation of the safety rules for the 20 MW_{th} U-Battery.

Layout 30*4 is a better reactor core configuration than Layout 37*4 from thermal-hydraulic point of view. The maximum temperature of the annular reactor core is 228 °C lower than that of the cylindrical reactor core with the same thermal power, although it faces the slightly higher temperatures of the barrel and RPV. It attributes to the more uniform power density distribution by replacing the 28 fuel blocks by graphite blocks in the central regions of the reactor core. The annular reactor core configuration not only decreases fuel cost, but also increases the safety of the U-Battery.

For the 20 MW_{th} U-Battery, the inherent safety of the reactor, such as the maximum temperature of the reactor, mainly depends on the reactor core configuration and low power density. The reactor cavity cooling system (RCCS) only plays a role to remove the heat in the reactor core in the long term. Since the maximum temperature of the reactor core with different configurations decreases directly during LOFC incidents, the RCCS is optional, rather than necessary, for the U-Battery, if the decay heat may be removed through 1.0-meter concrete wall which is cooled by air in the environment. For the U-Battery, the thermal behaviors of the barrel and RPV in the long term mainly depends on the configuration outside the RPV during DLOFC incident. However, they depend on both the material of the side thermal insulation and the configuration outside the RPV at the beginning of DLOFC incident.

It is possible to adopt the current reactor configuration when the thermal power of the U-Battery increases from 20 MW_{th} to 40 MW_{th}. When it further increases up to 100 MW_{th}, the material of the RPV and barrel may have to use higher-temperature steel (> 395 °C), although the maximum temperature of the reactor core is still far below the limit.

A.4 Conclusions and recommendations

Compared to large-size nuclear reactors, small modular reactors (SMRs) have some inherent advantages. They can be manufactured in modules in factories and transported to operating sites by rail, barge, truck, etc. After a long operation, like 5 - 10 years, these reactors can be brought back to factories for refueling or directly replaced by new modules, which would greatly reduce the dependence of nuclear reactors on infrastructure. More importantly, SMRs can be inherently or passively safe, because they commonly operate at low power density levels. Especially, some SMRs with water or liquid metal as coolant usually adopt passively cooling methods during accidents and/or normal operation.

The report presents a feasibility study on a small long-life high temperature gas-cooled reactor (HTR), which is called U-Battery. The U-Battery aims to provide electricity to residential sites which are not connected to national grids, or electricity and process heat for different industrial costumers. Since the main ideas behind the U-Battery is inherent safety, modularity and near-term utilization, it has been developed based on currently mature block-type HTR technologies, so it inherits the inherent safety that has been validated by experiments.

A.4.1 Conclusions

Different reactor core configurations and thermal power levels of the U-Battery have been investigated by the SCALE code system for different-diameter reactor pressure vessel (RPV), which is one of important parameters influencing the transportability of the U-Battery. Nuclear designs show that it is feasible and flexible to achieve a design for the 20 MW_{th} U-Battery with a lifetime of 10 effective full power years (EFPYs). The cylindrical reactor core Layout 37*4, annular reactor core Layout 30*4 and scatter reactor core Layout 30*4B are recommended reactor core configurations for 20 MW_{th} U-Battery. The annular reactor core Layout 30*4 has the better neutronic performance like higher effective multiplication factor than the cylindrical reactor core Layout 37*4 because of the better neutron moderation and higher resonance escape probability of neutrons attributed to the central graphite reflector (7*4 blocks). The scatter reactor core Layout 30*4B has better neutronic performance than Layout 30*4 because of the more even distribution of the 28 graphite blocks, and achieve 20-EFPY lifetime if the radius of fuel kernels increase to 0.3 mm.

The steady-state coupled neutronic/thermal hydraulic design of the cylindrical design Layout 37*4 and annular design Layout 30*4 has been executed by the DALTON-

THERMIX code system. After the determination of the thermal-hydraulic configurations of the U-Battery in terms of the steady-state design, the transient thermal-hydraulic evaluation of Layout 37*4 and Layout 30*4 is executed for pressurized and depressurized loss of forced cooling incidents, i.e., PLOFC and DLOFC incidents. The sizes of the key components, especially the thickness of the top, bottom and side thermal insulation, are evaluated by analyzing the cylindrical reactor core during DLOFC incident. The thermal-hydraulic analysis and comparison demonstrates the inherent safety of the 20 MW_{th} U-Battery, and the reactor configuration of the U-Battery is designed to remove the decay heat automatically without forced-cooling measures during both design-basis accidents.

During PLOFC incident, natural circulation for both designs does build up to contribute to the removal of the decay heat and the heat stored in the solid during normal operation. Besides heat conduction in the fuel blocks, the strong natural circulation obviously transfers the decay heat from the bottom high-temperature regions to the top low-temperature regions in the reactor core, and also flattens the radial solid temperature distribution during the PLOFC incident. Although the natural circulation in the reactor cores is so weak that it is neglected during the DLOFC incident, the decay heat and the heat stored in the solid structures during normal operation are removed successfully by heat conduction without any violation of the safety goals for the 20 MW_{th} U-Battery.

Layout 30*4 is a better core configuration than Layout 37*4 from thermal-hydraulic point of view. The maximum temperature of the annular design is 228 °C lower than that of the cylindrical design with the same thermal power, although it faces the slightly higher temperatures of the barrel and RPV. It attributes to the more uniform power density distribution by replacing the 28 fuel blocks by graphite blocks. The annular reactor core configuration not only decreases fuel cost, but also increases the safety of the U-Battery.

For the 20 MW_{th} U-Battery, the inherent safety of the reactor, especially the maximum temperature of the reactor core, mainly depends on the reactor core configuration and low power density level in the short term. The reactor cavity cooling system (RCCS) only plays a role to remove the heat in the reactor core in the long term. Since the maximum temperature of the reactor core with different configurations decreases directly during PLOFC and DLOFC incidents, the RCCS is optional, rather than necessary, for the U-Battery. For the cylindrical and annular reactor cores, if the 10-cm-thick SiC fiber is adopted as the side thermal insulations, the current RPV material with limit temperature of 395 °C is capable to be used. Moreover, the barrel of Layout 37*4 may also use the same material as the RPV. However, Layout 30*4 has to use a

higher temperature material if the thickness of the SiC fiber side reflector keeps 10 cm. If its thickness is slightly increased, Layout 30*4 possibly uses the same material as the RPV.

If the thermal power of the U-Battery decrease from 20 MW_{th} to 10 MW_{th} and the inner diameter of RPV keeps the same size as 20 MW_{th} U-Battery (i.e., 3.5 m), Layout 12*2B is recommended as the reference design of the U-Battery with a 10-EFPY lifetime. If the inner diameter of the RPV reduces from 3.5 m to 1.8 m, it is possible to achieve a lifetime 2 EFPYs for the 10 MW_{th} U-Battery, when the side reflector is 25-cm-thick graphite. If the side reflector is 20-cm-thick Beryllium oxide (BeO), the annular reactor cores Layout 6*3 and Layout 6*4 achieve the lifetime of 3.5 EFPYs and 5.0 EFPYs, respectively.

The geometric parameters of B₄C fixed burnable poison (FBP) have been optimized in terms of a typical fuel block of Layout 37*4, which is usually used to control the excess reactivity of HTRs. If natural boron and coated FBP particles are used, the 0.07 mm FBP kernels in diameter minimize the reactivity swing (0.019 Δk) of the reference fuel block during 10 EFPYs. If the reactivity swing is 0.05 Δk during 10 EFPYs, FBP designs with smaller kernels are recommended for the U-Battery, because the smaller is FBP kernel, the larger is the infinite multiplication factor of the reference fuel block at 10 EFPYs. The final design and composition of the FBP is a result of the trade-off between the reactivity penalty and reactivity swing.

Seed-and-blanket (S&B) fuel blocks have been investigated for thorium-fueled U-Battery by parametrically analyzing the composition (the enrichment of uranium) and geometric parameters (the number of UO₂ fuel rods, radii of fuel kernels and fuel compacts, and packing fraction of TRISO particles for UO₂ and ThO₂ fuel compacts). The main aim to analyze thorium-fueled fuel block is to reduce the fuel cost of the U-Battery and control the reactivity swing without the reactivity penalty caused by FBP in the fuel block. The reactivity swing of the S&B fuel blocks during 10 EFPYs depends on the time-dependent total mass of all fissile isotopes for the S&B fuel block with a specific ratio N_C/N_{HM} (the ratio of the number of carbon atoms to heavy metal atoms). When the ratio N_C/N_{HM} changes as the geometric parameters of the fuel block, the reactivity swing reaches very small values in the range of N_C/N_{HM} from 200 to 250. For example, when the N_C/N_{HM} is in the range from 221 to 238, the reactivity swing of the S&B fuel block with 36 UO₂ fuel rods is about 0.01 - 0.04 Δk during 5 EFPYs. If a larger reactivity swing is allowed for the S&B fuel block, a longer lifetime, like 10 EFPYs, is able to be achieved. Three configurations with 36, 54 and 78 UO₂ fuel rods are the recommended S&B fuel

block, whose reactivity swing during 10 EFPYs is about $0.1 \Delta k$, including the early drop because of the short-term fission product like ^{135}Xe and ^{149}Sm .

The excess reactivity of $0.1 \Delta k$ is so small that fixed burnable poison (FBP) is not necessary to be used. Moreover, the total mass of uranium of the three recommended configurations of the S&B fuel block is one-fourth to one-third less than that of the low-enriched uranium fuel block. If the price of thorium is the same as uranium, the S&B fuel block may be about one-third cheaper than that of LEU fuel block. If considering the increase of the enrichment of uranium for the LEU fuel block because of the inclusion of the FBP to control the excess reactivity ($0.2\text{-}0.3 \Delta k$), the fuel cost of the S&B fuel block would be even more competitive.

A.4.2 Recommendations

As mentioned in the previous section, BeO is a better reflector material than graphite from neutronic point of view, and SiC fiber is a better thermal insulation material than carbon bricks from thermal-hydraulic point of view. Adopting BeO as reflector and SiC fiber as thermal insulation provide two potential ways to minimize the volume and weight of the reactor core of the $10 \text{ MW}_{\text{th}}$ U-Battery, as well as the $20 \text{ MW}_{\text{th}}$ U-Battery. Preliminary investigation in the report shows the potential of these two materials, so it is recommended to further investigate the two materials for the application of the U-Battery. For example, for the $10 \text{ MW}_{\text{th}}$ U-Battery with 1.8 m RPV in diameter, the thickness of the side BeO reflector is recommended to be 20 centimeters, while the top and bottom reflectors still use nuclear graphite because of the expensive price of BeO. The feasibility and cost of the BeO top and bottom reflectors should be evaluated coupled the neutronic and economic analysis. Although the side thermal insulation of the $20 \text{ MW}_{\text{th}}$ U-Battery is assumed to use SiC fiber in the thermal-hydraulic evaluation, the top and bottom thermal insulation still adopts carbon bricks in terms of the same reason. The irradiation performance of both materials should also further be evaluated.

Structural design of the U-Battery is recommended to be included to minimize the weight and geometric size of the U-Battery, especially the sizes of the metal structures of the reactor which at least have the half weight of the reactor. Moreover, in order to improve the transportability of the U-Battery, the reactor core configurations of the U-Battery should be optimized in terms of the weight of the reactor and the size of the RPV.

The thermal-hydraulic analysis shows the good safety of the $20 \text{ MW}_{\text{th}}$ U-Battery, and nuclear design of the 5 MW_{th} U-Battery shows that it is able to achieve lower fuel cost by reducing the mass of uranium by reducing the radius of fuel kernels and packing fraction of TRISO particles than the enrichment of uranium. It is recommended to use 20%

enriched uranium for 20 MW_{th} U-Battery and adjust the lifetime of U-Battery by the geometric parameters of coated TRISO particles.

The preliminary FBP analysis shows that it is possible to control the excess reactivity under 0.05 Δk by natural boron. Although the reactivity penalty of the constant reactivity swing mode (e.g., 0.05 Δk during 10 EFPYs) is smaller than that of the minimum reactivity swing mode, it is recommended to adopt the later as a reference of the FBP design of the whole reactor core of the U-Battery, because the cost of control rod systems, especially driver mechanisms, may be higher than the fuel cost.

Since thorium-fueled seed-and-blanket fuel blocks have better neutronic characteristics than low-enriched uranium, like small reactivity swing (i.e., 0.1 Δk during 10 EFPYs), and lower fuel cost, it is recommended to do the whole reactor core design of the U-Battery with seed-and-blanket fuel blocks.

For the 20 MW_{th} U-Battery with a lifetime of 10 EFPYs, the scatter core Layout 30*4B is recommended to do further thermal-hydraulic evaluation because of its better neutronic performance than the annular reactor core Layout 30*4. In order to analyze the Layout 30*4B, a 3D thermal-hydraulic code system should be developed.

References

- [1] International Atomic Energy Agency. Status of Small Reactor Designs Without On-Site Refuelling. IAEA-TECDOC-1536, 2007.
- [2] Kuznetsov V. IAEA Activities for Innovative Small and Medium Sized Reactors (SMRs). Progress in Nuclear Energy, 2005, 47:61–73.
- [3] World Nuclear Association. Small Nuclear Power Reactors, October, 2009. <http://www.world-nuclear.org/info/inf33.html>.
- [4] Reyes J N. Introduction to NuScale Design, July, 2008. <http://www.nuscalepower.com/ot-Nuclear-Power-Presentations.php>.
- [5] Adamovich L, Grechko G, Shishkin V. Self-contained Co-generation Nuclear Power Plant with Integral Nuclear Reactor Designed for Remote and Difficult-to-Access Areas. Nuclear Engineering and Design, 1997, 173:175–182.
- [6] Ueda N, Kinoshit I, Minato A, et al. Sodium Cooled Small Fast Long-Life Reactor 4S. Progress in Nuclear Energy, 2005, 47:222–230.
- [7] Atomic Insights. Nuclear Power for Galena, Alaska, March, 2005. http://www.atomicinsights.com/AI_03-20-05print.html.
- [8] The City of Galena. Overview of Galena S Proposed Approach to Licensing a 4S Nuclear Reactor Based Power Generation Facility, March, 2007. http://www.roe.com/about_techGalena.htm.
- [9] Horie H, Miyagi K, Nakahara K, et al. Safety Performance of the 4S Reactor on the ATWS Events-Statistical Estimation of Uncertainty. Progress in Nuclear Energy, 2008, 50:179–184.
- [10] Zrodnikov A, Toshinsky G, Komlev O, et al. Innovative Nuclear Technology Based on Modular Multi-purpose Lead-Bismuth Cooled Fast Reactors. Progress in Nuclear Energy, 2008, 50:170–178.
- [11] Brown N W, Hassberger J A. New Concept of Small Power Reactor without On-Site Refueling for Non-proliferation. Proceedings of Advisory Group Meeting on Propulsion Reactor Technologies for Civilian Applications, 1998.
- [12] Brown NW, Hassberger J A, Smith C, et al. The Secure, Transportable, Autonomous Reactor System. Proceedings of International Conference on Future Nuclear Systems, 1999.
- [13] Sienicki J, Moisseytsev A, Yang W, et al. Status Report on the Small Secure Transportable Autonomous Reactor (SSTAR)/Lead-Cooled Fast Reactor (LFR) and Supporting Research and Development. Argonne National Laboratory, 2008.
- [14] Smith C F, Halsey WG, Brown NW, et al. SSTAR: The US lead-cooled fast reactor. Journal of Nuclear Materials, 2008, 376:255–259.
- [15] Alekseev P N, Belov I A, Ponomarev-Stepnoi N N, et al. MARS Low-Power Liquid-Salt Micropellet-Fuel Reactor. Atomic Energy, 2002, 93(1):537–546.
- [16] Modro S M, Fisher J, Weaver K, et al. Generation-IV Multi-Application Small Light

- Water Reactor. Proceedings of 10th International Conference on Nuclear Energy, 2002.
- [17] Modro S M, Fisher J E, Weaver K D, et al. Multi-Application Small Light Water Reactor Final Report. Idaho National Engineering and Environmental Laboratory, 2003.
- [18] Greenspan E, Barak A, Buongiorno J, et al. The Long-Life Core Encapsulated Nuclear Heat Source (ENHS) Generation IV Reactor. Proceedings of 2002 International Congress on Advances in Nuclear Power Plants, 2002.
- [19] Greenspan E, Hong S G, Lee K B, et al. Innovations in the ENHS Reactor Design and Fuel Cycle. *Progress in Nuclear Energy*, 2008, 50:129–139.
- [20] Greenspan E. Solid-Core Heat-Pipe Nuclear Battery Type Reactor. University of California, 2008.
- [21] Zaki S, Sekimoto H. Design and Safety Aspect of Lead and Lead-Bismuth Cooled Long-Life Small Safe Fast Reactors for Various Core Configurations. *Journal of Nuclear Science and Technology*, 1995, 32(9):834–845.
- [22] Zaki S, Sekimoto H. Safety Aspect of Long-Life Small Safe Power Reactors. *Annals of Nuclear Energy*, 1995, 22(11):711–722.
- [23] Sekimoto H, Ryu K, Yoshimura Y. CANDLER: The New Burnup Strategy. *Nuclear Science and Engineering*, 2001, 139:306–317.
- [24] Ismail, Ohoka Y, Liem P H, et al. Long Life Small CANDLER-HTGRs with Thorium. *Annals of Nuclear Energy*, 2007, 34:120–129.
- [25] Zwaan S, Kloosterman J, Linssena R, et al. Conceptual Design of a Natural Circulation Cooled Nuclear Battery for Process Heat Applications. Proceedings of International Conference on Non-Electric Applications of Nuclear Power, Japan, 2007.
- [26] Zwaan S, Kloosterman J L, Uiterb G. Parametric Study on a Natural Circulation Cooled U-Battery. Proceedings of International Conference on the Physics of Reactors, 2008.
- [27] Yu Y H, Son H M, Lee I S, et al. Optimized Battery-Type Reactor Primary System Design Utilizing Lead. Proceedings of 2006 International Congress on Advances in Nuclear Power Plants, 2006.
- [28] Son H M, Jeong W S, Suh K Y. Integral Reactor System Analysis of Lead-Cooled Battery BORIS. Proceedings of the 12th International Topical Meeting on Nuclear Reactor Thermal Hydraulics, 2007.
- [29] Kim T W, Kim N H, Suh K Y. Power Conversion System for Lead-Cooled Battery-Type Integral Fast Reactor System BORIS. *Transactions of the American Nuclear Society*, 2007, 96:805–806.
- [30] Peterson O G. Self-regulating Nuclear Power Module. Patent, 2004.
- [31] Peterson O G, Kimpland R H, Coates D M. Compact, Self-Regulating Nuclear Reactor. *Transactions of the American Nuclear Society*, 2008, 98:729–730.
- [32] Carelli MD, Conway L E, Collado J, et al. Integral Layout of the IRIS Reactor.

- Proceedings of 2003 International Congress on Advances in Nuclear Power Plants, Cordoba, Spai, 2003.
- [33] Carelli MD, Conway L, Oriani L, et al. The Design and Safety Features of the IRIS Reactor. *Nuclear Engineering and Design*, 2004, 230:151–167.
- [34] Babcock & Wilcox Company. Modular Nuclear Reactors. [http://www.babcock.com/products/modular nuclear/](http://www.babcock.com/products/modular_nuclear/).
- [35] Hibi K, Takimoto H, Chaki M, et al. Development of the Package-Reactor (1) -Reactor for Pioneering New Nuclear Markets. *Progress in Nuclear Energy*, 2005, 47:115–122.
- [36] Hibi K, Takimoto H, Chaki M, et al. Development of the Package-Reactor (2) -Core Characteristics. *Progress in Nuclear Energy*, 2005, 47:123–130.
- [37] Nagai M, Shimazu Y. Small PWRs Using Coated Particle Fuel for District Heating-PFPWR50. *Progress in Nuclear Energy*, 2005, 47:155–162.
- [38] van Heek A I, Stempniewicz M M, da Cruz D F, de Haas J B M. ACACIA: a Small-scale power plant for near term deployment in new markets. *Nuclear Engineering and Design*, 2004, 234:71-86.

Appendix B

Reactor Structural and Fuel Design

B J Marsden, A J Wickham, G N Hall, T J Abram
The University of Manchester

Core Structural Design and Fuel Design

B1.0 Introduction

Originally the reactor was to be designed to operate in a carbon-dioxide coolant based on the excellent thermal properties of high pressure CO₂. However, investigation, both analytical and experimental demonstrated that this was not practicable due to thermal and radiolytic oxidation. Therefore the design was changed to an inert, high pressure helium system which precludes both radiolytic and thermal oxidation under all normal operation conditions. The design will be such to preclude the accidental ingress of water or air in the system under normal operation and design faults.

The structural designs for two cores is outlined below, the first is a 20MW(t) graphite moderated design the second design is a 10MW(t) reactor also graphite moderated, but also included a beryllium oxide reflector.

B2.0 Reactor Structural Design

B2.1 Graphite Moderated 20MW(t) Design

The reactor and is housed in a steel Reactor Pressure Vessel (RPV) about 100mm thick designed for a working pressure of 40bar at 300°C and a maximum transient temperature about 50°C for several hours. Transients above this temperature will cause the RPV to vent into the secondary containment (confinement). The RPV design is such that a single main inlet/outlet is situated towards the bottom of the reactor to prevent the “chimney effect” in case of a main inlet/outlet duct failure. The RPV is provided with a removable (bolted) lid that can be removed for refuelling. The lid is proved openings to which the control rods mechanisms can be bolted to. All bolted joints are to be “helium tight”

Inside the vessel a core support structure rests on the bottom of the vessel. The structure provides support for the lower core support plates and the core barrel. The lower core support and core barrel is to be kept as close to the reactor inlet temperature as possible during normal operation.

On top of the core support plates layers of insulation and graphite form the lower inlet/outlet plenums, the detail of which is for further design study but will be based on experience gained at Fort St. Vrain (FSV) and HTTR. This purpose of the lower plenum structure is to direct “cool” inlet gas upwards between the core barrel and RPV and to keep the return “cool” inlet and “hot” return gas separate and direct it outwards to the heat exchanger in the primary circuit.

The lower plenum also supports the main reactor core structure. This consists of a hexagonal array of fuel elements of Fort St. Vrain design, interspersed with other hexagonal blocks with larger holes through which the control and safety shutdown rods can freely pass. The core is on annular design.

The reasoning behind the choice of the Fort St. Vrain fuel block design is that this design of fuel block proved itself in operation for a number of years.

The core is surrounded by an inner (removable) graphite reflector which is surrounded by insulation material. At each fuel block height, tubular “Calder” type restraint bands will be located. These will be designed to facilitate side restraint and will expand/contract with temperature with the same expansion coefficient as graphite ensuring that no “gaps” will appear between reflector and fuel blocks to prevent coolant gas bi-pass and neutron streaming.

Above the core there will be a hexagonal array of tightly clamped graphite reflector bricks, with holes to direct coolant flow downwards from the upper plenum and for control/shutdown rods to pass. The upper core plenum is to be insulated and designed directing the “cool” gas that flows upwards from the lower inlet plenum up between the RPV and core barrel back down through the core.

Nuclear graphite property changes will be based on published Material Test Reactor (MTR) data for medium grained graphite obtained over many years. Although there are uncertainties in this data this tends to be the greatest at high fluence and mostly associated with the effect of radiolytic oxidation. The maximum irradiation fluence it is expected that the graphite

would experience in the 20MW(e) design would be significantly less than one third that AGR would experience in 30 years.

The design must account for:

- Differential thermal expansion between graphite, insulation and steel
- Differential thermal expansion due to radial and axial thermal gradients
- Graphite shrinkage

B.2.2 Graphite irradiation database (inert)

1.0 Manufacture and microstructure

Graphite is a versatile material for nuclear technology application. It is used to slow down (*i.e.* moderate) the neutrons released from fission events. The moderator, constructed from graphite bricks, serves as structural component of the core for the full service life of the reactor, *i.e.* they are not replaceable. Graphite presents a high thermal conductivity which is required to remove heat generated in the graphite and from the fuel during normal operation and fault situation. Additionally, graphite is used as a reflector to return neutrons back into the core and also therefore protecting the surrounding structure and pressure vessel from a large proportion of the potential irradiation damage. Finally, the graphite core provides channels to cool the fuel, maintaining the temperature below the melting point of other structural components such as the fuel cladding.

Nuclear graphite is comprised of filler particles and binder. The filler can be petroleum coke, Gilsonite coke (no longer available), metallurgical coke or coal tar-pitch derived. The binder is a mixture of flour (*i.e.* milled coke to a particle size of up to 300 μm) and any hydrocarbonaceous material which leaves a carbon residue upon distillation. The latter should be a thermoplastic material which is solid at room temperature and fluid at higher temperatures. These characteristics allow thorough mixing of the filler with the binder when hot, and yet enable a formed article to hold its shape at room temperature. Coal-tar pitch is one of the most commonly used binders. Other binders include furfuryl alcohol, sugars, phenol formaldehyde, and thermosetting resins ^[1]. In some graphite (*e.g.* Gilsocarbon), the filler to binder ratio is approximately 4:1 ^[2].

Figure B2.2.1 illustrates the nuclear graphite manufacturing process. The coke (filler) is calcined at about 1300°C to remove residual volatile hydrocarbons. Subsequently, the calcined coke is crushed and screened, where the fines are milled to a flour with grain diameters from 2 to ~ 300 μm . The coarser coke filler particles for moderator graphite usually range from 0.4 to 0.8 mm in diameter, and these are mixed with flour in about a 1 to 3 ratio to form a blend. The coke blend is next mixed with a pitch binder at about 165°C, at which temperature the pitch is quite fluid. The resulting mix is pressed, extruded or isostatically moulded into brick form. For the brick to have the proper rigidity, the “green” carbon components are packed tightly in granular coke or a coke-sand mixture to maintain their shape, and heated to about 800-1000°C. This step converts the pitch from a thermoplastic material (softening point ~ 100°C) to an infusible solid, with the evolution of hydrocarbon gases. The bricks are then impregnated, usually with pitch, to achieve desired properties such as strength and density. Finally, the bricks are placed in a high purity coke powder, buried under sand and silicon carbide and then heated to 2600-3000°C. This process takes from

three to four days to reach temperature, a day at temperature and 10 to 14 days to cool before exposure to air. A purification process is also employed to reduce boron content and to remove other heavy metals which could potentially become activated during irradiation, usually as their volatile halides. Modern manufacturing employs magnesium fluoride for this purpose whereas older methods employed chlorine or freons. During the graphitisation process, most of the gases are evolved below 1500°C. Between 1500 and 2500°C, the main process is crystal growth, with the internal structure still imperfect, and above 2500°C, continued minor crystal growth occurs, but crystal perfection is increased due to diffusion and annealing of crystallite imperfections^[1, 3].

Usually when referring to the microstructure of nuclear graphite used in British and French gas-cooled reactors (*i.e.* Magnox, AGRs and UNGG), the matrix refers to the graphitised mixture of binder and the flour, whereas the filler refers to the graphitised large coke particles (*i.e.* grains < 1 mm).

An important characteristic of the microstructure of graphite is the presence of pores. Nuclear graphite contains a wide range of pores from the nano- to the meso-scales. The pores in the nano-micro-scale are dominated by the Mrozowski cracks which are approximately 10 µm in length and ~ 250 Å in width, and a mean periodicity ~ 2 cracks/µm^[4]. These pores develop in the graphite during the cooling from graphitisation temperature (~2800-3000°C). In the micro-meso-scale, cracks (width up to 50 µm) and gas-entrapment-pores, derived from calcination and graphitisation, are found^[5]. In addition, the pore structure can be divided into Open Pore Volume (OPV) and Closed Pore Volume (CPV). The former refers to pores that connect with the external surface of the component, which at the same time can either be connected to other surface region (*i.e.* transport pore) or be terminated within the graphite (*i.e.* blind pore). Regarding CPV, closed macro-pores are probably formed by ‘plugging’ during the impregnation stage of manufacture, whereas, closed micro-pores are developed as a result from shrinkage during graphitisation. These latter pores are expected to be uniformly dispersed throughout the structure^[6].

2.0 Irradiation Damage in Nuclear Graphite

During the controlled nuclear chain reaction in the reactor, free neutrons and charged particles (*i.e.* photons, lighter nuclei) are released. Thus, irradiation damage in graphite occurs when the energetic particles impinge on the crystal lattice and displace carbon atoms from their equilibrium positions, creating a lattice vacancy and an interstitial carbon atom. The displaced carbon atoms recoil through the lattice and produce other carbon atom displacements in a cascade effect.

Neutrons are the energetic species that produces the largest number of displacements due to the large relative mass ratio when compared, for example, with electrons. A 1 MeV electron produces an average of 1.6 atomic displacements and a 1 MeV neutron 500 displacements^[7]. For comparison, Table B2.2.1 shows the atomic displacement by fast particles.

Table B2.2.1. Atomic displacement by fast particles ^[8].

Particles	Energy (eV)	Cross section	Mean number of displacements per collision
Electrons	1 x 10 ⁶	14.5 x 10 ⁻²⁴	1.6
	2 x 10 ⁶	15.0 x 10 ⁻²⁴	1.9
	3 x 10 ⁶	15.5 x 10 ⁻²⁴	2.3
	4 x 10 ⁶	16.0 x 10 ⁻²⁴	2.5
Protons	1 x 10 ⁶	7.8 x 10 ⁻²¹	4-5.5
	5 x 10 ⁶	1.56 x 10 ⁻²¹	4-5.5
	10 x 10 ⁶	7.8 x 10 ⁻²²	4-6
	20 x 10 ⁶	3.9 x 10 ⁻²²	4-6
Deuterons	1 x 10 ⁶	1.56 x 10 ⁻²⁰	4-5
	5 x 10 ⁶	3.12 x 10 ⁻²¹	4-6
	10 x 10 ⁶	1.56 x 10 ⁻²¹	4-6
	20 x 10 ⁶	7.8 x 10 ⁻²¹	4-6.5
α -Particles	1 x 10 ⁶	1.25 x 10 ⁻¹⁹	4-5
	5 x 10 ⁶	2.5 x 10 ⁻²⁰	4-6
	10 x 10 ⁶	1.25 x 10 ⁻²⁰	4-6.5
	20 x 10 ⁶	6.25 x 10 ⁻²¹	4-6.5
Neutrons	10 ³	4.7 x 10 ⁻²⁴	2.83
	10 ⁴	4.7 x 10 ⁻²⁴	28.3
	10 ⁵	4.6 x 10 ⁻²⁴	280
	10 ⁶	2.5 x 10 ⁻²⁴	480
	10 ⁷	1.4 x 10 ⁻²⁴	500

The displacement rate of carbon atoms in the lattice, and thus, the damage to graphite is dependent on the flux spectrum (i.e. the energy spectrum of the neutrons impinging on the graphite ranging from 1eV to ~ 15 MeV ^[9], with an average energy of 2 MeV). It is important to note that the fast neutron flux spectrum differs from reactor to reactor and varies with position in the reactor core. Thus, it is necessary to equate graphite damage to a standard position/flux spectrum. Table B2.2.2 shows the equivalent units of dose and their conversion ^[10].

However, not all of the carbon atoms remain displaced. The displaced carbon atoms diffuse between the graphite layer planes in two dimensions and a high proportion of them will recombine with lattice vacancies. Others will coalesce to form linear molecules, which in turn may form the nucleus of a dislocation loop, in other words, a new carbon plane ^[11]. In addition, adjacent lattice vacancies in the same graphite crystal basal plane are believed to collapse parallel to the basal plane. Recently a new theory has been proposed that involve the buckling of the basal plane resulting in the expansion in the ‘c’ direction and contraction in the ‘a’ direction ^[12].

Crystal lattice defects introduced by fast neutron irradiation increase the energy of the graphite crystals. This stored energy is referred to as Wigner energy ^[13]. If graphite is

irradiated at room temperature, very large levels of stored energy can be accumulated with values up to 645 cal g^{-1} and the release of such energy as heat would lead to temperature rises of approximately 1500°C under adiabatic conditions if the *rate* of release exceeds the specific heat capacity of the graphite ^[8]. The Windscale fire in 1957 was caused by an over rapid release of Wigner energy.

However, irradiation at temperatures in excess of about 300°C does not give rise to large concentrations of the sub-microscopic interstitial clusters and simple lattice vacancies which are the main cause of stored energy, and thus to a large extent it is unimportant. In addition, the overall damage in irradiated graphite is lessened at higher fluxes (at a given temperature and dose) due to irradiation-annealing; the higher rate of defect creation and aggregation is countered by the increased likelihood of the radiation inducing break-up of clusters and vacancy-interstitial annihilation ^[12]. For graphite irradiated at temperatures above $\sim 300^\circ\text{C}$ the total stored energy is about 100 cal g^{-1} ^[3] and, thus, the rate of Wigner energy release and its consequence of fire in the reactor is not a concern.

Table B2.2.2. Conversion factor of neutron flux with different energy spectrum ^[10].

EDND (n/cm^2)	1.0
Equivalent Fission Dose (n/cm^2)	0.547
Calder Equivalent Dose (MWd/At)	1.0887×10^{17}
BEPO Equivalent Dose (n/cm^2)	0.123
$E_{n>0.05 \text{ MeV}}$ (n/cm^2)	0.5
$E_{n>0.18 \text{ MeV}}$ (n/cm^2)	0.67
$E_{n>1.0 \text{ MeV}}$ (n/cm^2)	0.9
dpa (atom/atom)	7.6162×10^{20}

The principal effect of the carbon atom displacements is dimensional change in graphite components. Thus, interstitial defects will cause crystallite growth perpendicular to the layer planes (c-axis direction), in other words, swelling of the graphite block, whereas coalescence of vacancies will cause shrinkage parallel to the layer planes (a-axis direction). As a consequence, the resultant lattice strain causes significant property changes in the graphite.

The following sub-section describes the effect of irradiation on the physical and mechanical properties of medium grained graphite with properties similar to currently available graphites. In other words, the resultant change of properties due to irradiation of such graphite can be taken as a reference and assist with the design of the U-battery[®].

3.0 Effect of Irradiation on the Physical and Mechanical Properties of Nuclear Graphite

As a starting basis typical properties of medium grain graphite available today are given in Figure B.2.2.3.

Table B2.2.2. Properties of a typical medium grained graphite available today.

Density (g/cm ³)	1.8
Dynamic Young's modulus (GN/m ²)	10
CTE (10 ⁻⁶ K ⁻¹) 20-200oC	4.7
Electrical resistivity (mW/m)	10.3
Thermal conductivity (W/m k)	133
Strength (MN/m ²)	
flexural (4 point)	27
tensile	19
compressive	60
Isotropy ratio (a _{AG} /a _{WG})	1.05

The data on irradiation behaviour of ATR-2E are readily available ^[14] and have been used as part of the design database for the Pebble Bed Modular Reactor (PBMR). This type of reactor will operate at high temperatures (~500-900°C) and high neutron doses (up to 200 x 10²⁰ n cm⁻²). Although this graphite is no longer available, its structure and properties are similar to the graphite chosen for future High Temperature Reactor (HTR) design (SGL Carbon's NBG-18 grade).

Considering that the likely to be graphite of the U-Battery[®] would be similar to that of the PBMR and HTR, the design data presented in this report could be used to assist in the reactor design of the U-Battery[®].

Dimensional changes

The ATR-2E graphite shrinks both parallel and perpendicular to the grain during irradiation at the temperatures of interest (300-750°C) as revealed in Figures B2.2.2 and B2.2.3.

Coefficient of thermal expansion

The Coefficient of Thermal Expansion (CTE) is defined as the linear expansion over a temperature range. All the measurements referred to in this report are over the range 20-120°C. Figure B2.2.4 displays the change of CTE of ATR-2E graphite under fast neutron dose at the temperatures of interest.

Young's modulus

During irradiation damage, the resultant imperfections in the crystal structure, such as interstitial atoms and basal plane vacancies, act as dislocation pinning sites causing an increase in the elastic modulus and strength. Additionally, pore closure due to c-axis expansion will cause a gradual increase in Young's modulus and strength. However, at high doses (~ 70 x 10²⁰ EDND), generation of new porosity due to incompatibility of crystal strains causes a reduction in such mechanical properties, leading to the eventual disintegration of the graphite block. This later event is predicted to not occur in the U-Battery since the expected maximum fast neutron dose is 60 x 10²⁰ n cm⁻² EDND, assuming a neutron flux in the range of 1.3-2.0 x 10¹³ n cm⁻² s⁻¹ and a maximum of 10 years of reactor

operation. Figure B2.2.5 displays the change of Young's Modulus of ATR-2E graphite under irradiation with fast neutron doses up to $\sim 65 \times 10^{20} \text{ n cm}^{-2}$ EDND and at the temperature of interest.

Strength

As mentioned previously, fast neutron irradiation increases the strength due to pinning of the dislocations in the basal plane and due to pore closure caused by structural expansion. Assuming that the Griffith failure criteria applied to graphite and that failure would occur at a constant strain energy to failure per unit volume, the strength of graphite is related to Young's modulus by the following equation:

$$\frac{1}{2} \frac{\sigma_o^2}{E_o} = \frac{1}{2} \frac{\sigma^2}{E} \quad (1)$$

where E_o and σ_o are the unirradiated modulus and strength and E and σ are the irradiated modulus and strength. This led to the well-used relationship:

$$\frac{\sigma}{\sigma_o} = \left(\frac{E}{E_o} \right)^n \quad (2)$$

For irradiation temperatures between 300 and 500°C, n is taken as 0.5. However, fittings of experimental data have revealed that a linear relationship between strength and modulus ($n=1$) is more applicable [15].

Thermal conductivity

The ability of nuclear graphite to conduct the heat (i.e. generated internally and by the fuel) and subsequently be removed by the gas-coolant is of prime importance for the operation of the nuclear reactor.

The mechanism by which heat is transferred in graphite, at temperatures above 100 K, is mainly through phonon oscillations along basal planes of crystalline lattice. Therefore, above ambient temperature, thermal conductivity is sensitive to the crystallographic anisotropy and atomic bonding. Thus, defects in the graphite microstructure at the nanometre scale, such as vacancies and interstitials, and at the micrometre scale, such as porosity and grain boundaries, reduces the thermal conductivity of graphite. Such defects reduce the phonon mean free path by phonon scattering and it has been shown that the mechanism that reduces thermal conductivity the most is by pore-phonon scattering [16]. Pores can be formed during irradiation due to large crystal strain originating from the presence of vacancies and interstitial defects.

In graphite technology, thermal resistivity (i.e. the inverse of thermal conductivity) is used instead of thermal conductivity; therefore, the design data is given with respect to the former parameter. Figure B2.2.6 shows the thermal resistivity change with dose for VQMB graphite at a given temperature.

4.0 Section B2.2.References

- [1] D. E. Baker, *Nuclear Engineering and Design* 14 (1970) 413-444.
- [2] G. B. Neighbour, P.J. Hacker, *Materials Letters* 51 (2001) 307-314.
- [3] B. T. Kelly, *Progress in Nuclear Energy* 2 (1978) 219-269.
- [4] K. Wen, J. Marrow, B. Marsden, *Journal of Nuclear Materials* 381 (2008) 199-203.
- [5] I. M. Pickup, B. McEnaney, R.G. Cooke, *Carbon* 24 (1986) 535-543.
- [6] J. Standring, B.W. Ashton, *Carbon* 3 (1965) 157-165.
- [7] P. A. Thrower, R.M. Mayer, *Physica Status Solidi (a)* 47 (1978) 11-37.
- [8] J. H. W. Simmons, "Radiation Damage in Graphite", Pergamon Press (1965) 242.
- [9] D. R. Poulter, "The Design of Gas-Cooled Graphite-Moderated Reactors", Oxford University Press (1963)
- [10] B. T. Kelly, B.J. Marsden, K. Hall, D.G. Martin, A. Harper, A. Blanchard, "Irradiation Damage in Graphite due to Fast Neutrons in Fission and Fusion Systems", IAEA, TECDOC-1154 (2000)
- [11] T. D. Burchell, L.L. Snead, *Journal of Nuclear Materials* 371 (2007) 18-27.
- [12] R. H. Telling, M.I. Heggie, *Philosophical Magazine* 87 (2007) 4797-4846.
- [13] B. J. Marsden, "Specialists Meeting on Graphite Moderator Lifecycle Behaviour", IAEA, TECDOC-901 (1995)
- [14] G. Haag, "Properties of ATR-2E Graphite and Property Changes due to Fast Neutron Irradiation", Forschungszentrum Jülich, Jül-4183 (2005) http://juwel.fz-juelich.de:8080/dspace/bitstream/2128/541/1/Juel_4183_Haag.pdf
- [15] B. J. Marsden, S.L. Fok, T.J. Marrow, P.M. Mummery, "The Relationship between strength and modulus in nuclear graphite", Second International Topical Meeting on High Temperature Reactor Technology (2004) Beijing, 1-9.
- [16] L. Babout, B.J. Marsden, P.M. Mummery, T.J. Marrow, *Acta Materialia* 56 (2008) 4242-4254

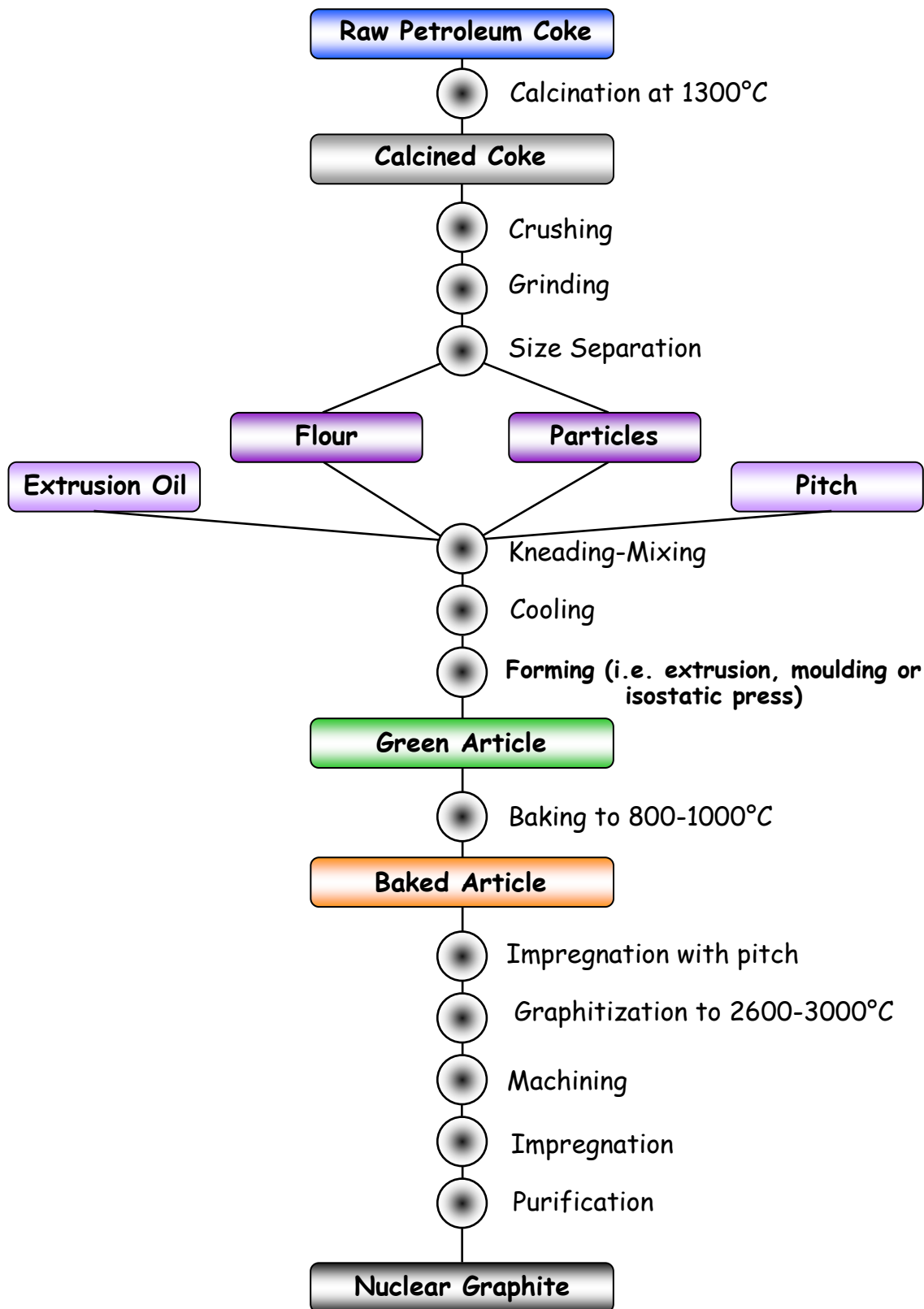


Figure B.2.2.1. Manufacturing process of nuclear graphite.

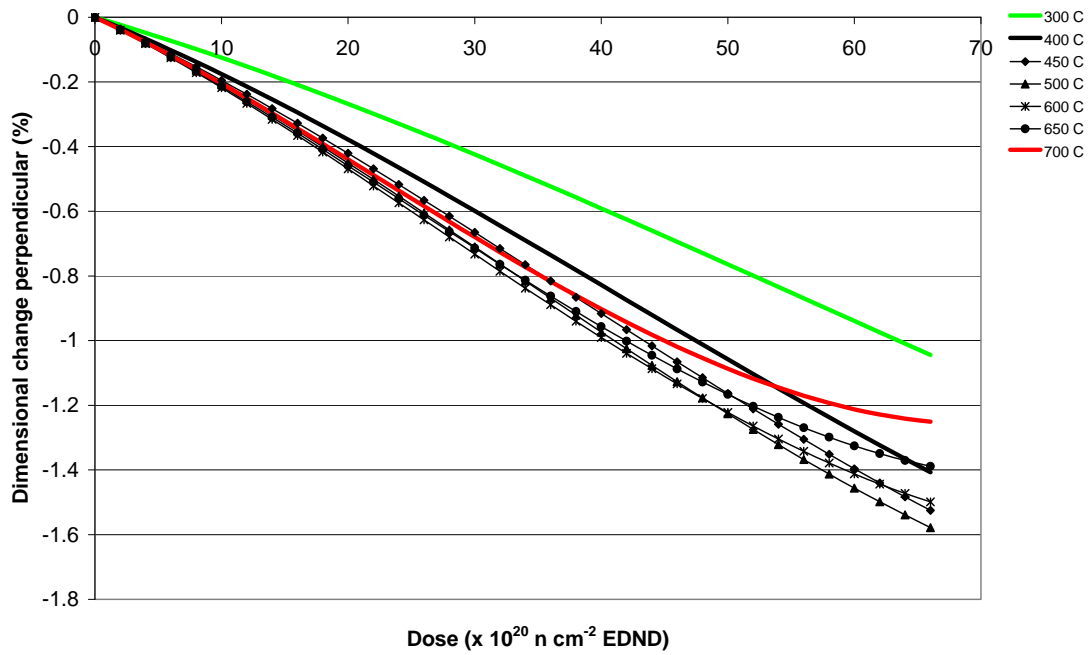


Figure B.2.2.2 Dimensional change in the perpendicular extrusion direction of ATR-2E graphite with respect to fast neutron dose at a temperature range of 300-700 °C.

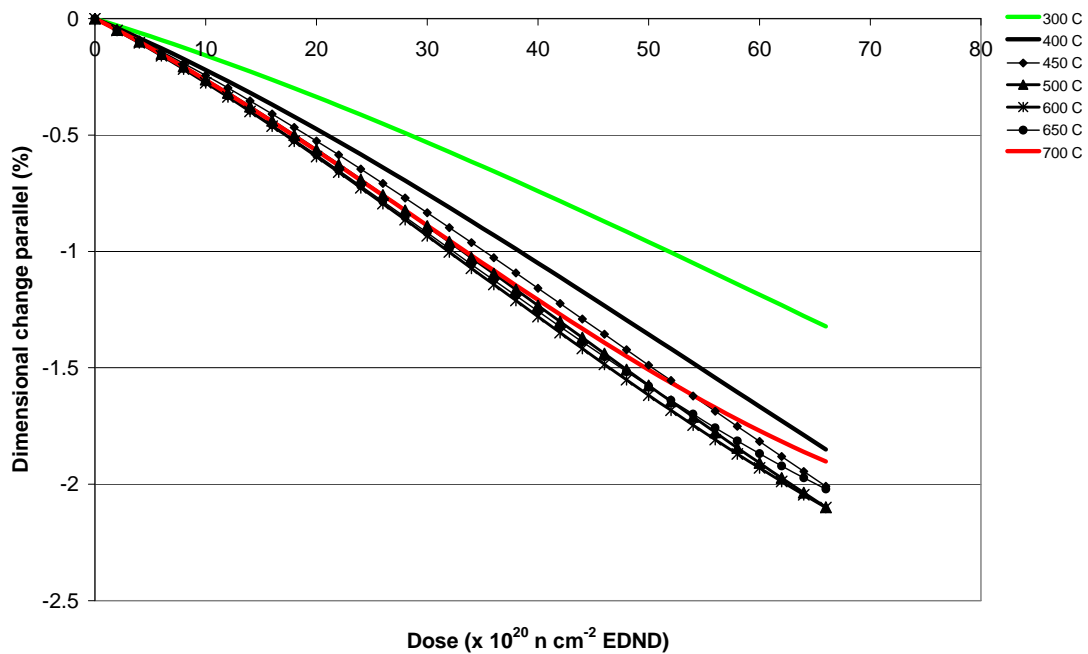


Figure B2.2.3. Dimensional change in the parallel extrusion direction of ATR-2E graphite with respect to fast neutron dose at a temperature range of 300-700 °C.

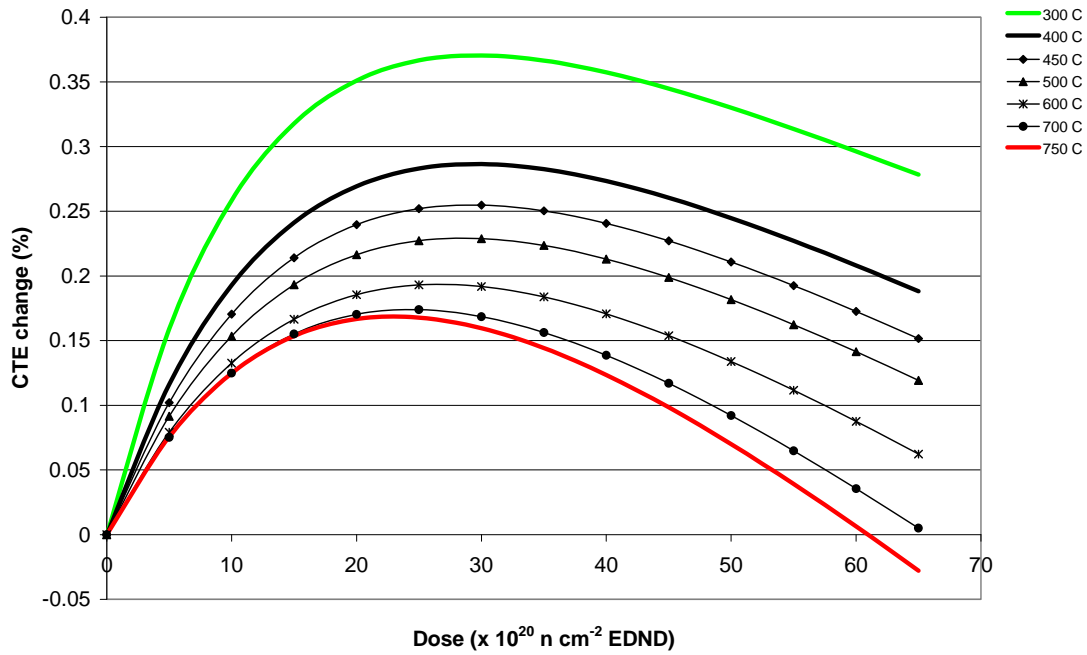


Figure B2.2.4. Coefficient of thermal expansion change of ATR-2E graphite with respect to fast neutron dose at a temperature range of 300-750 °C.

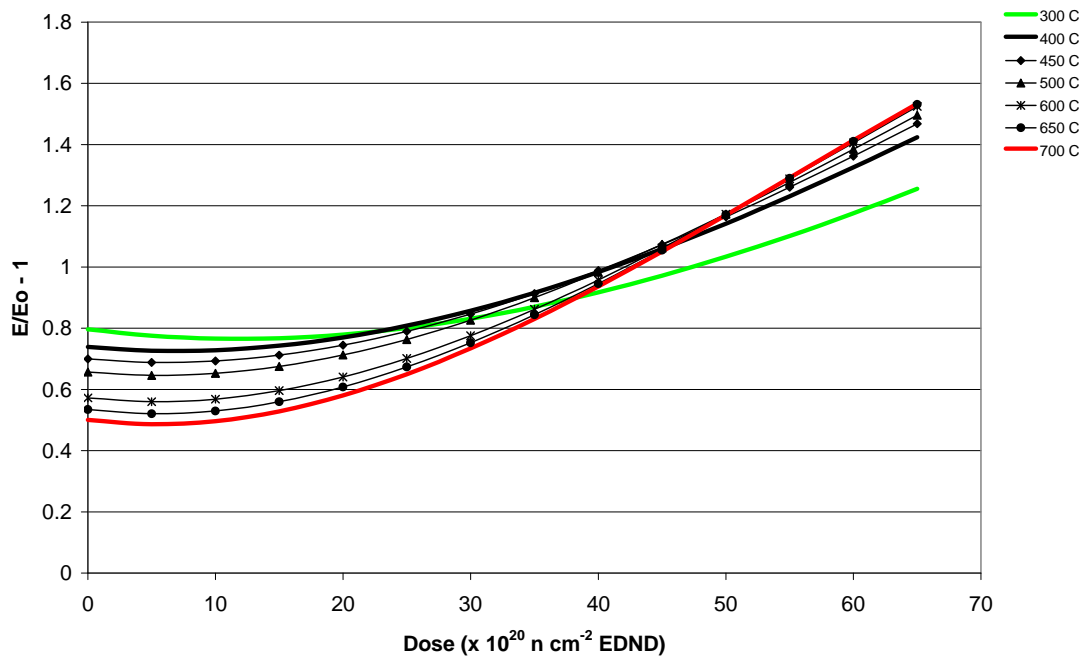


Figure B2.2.5. Young's modulus change of ATR-2E graphite with respect to fast neutron dose at a temperature range of 300-700 °C.

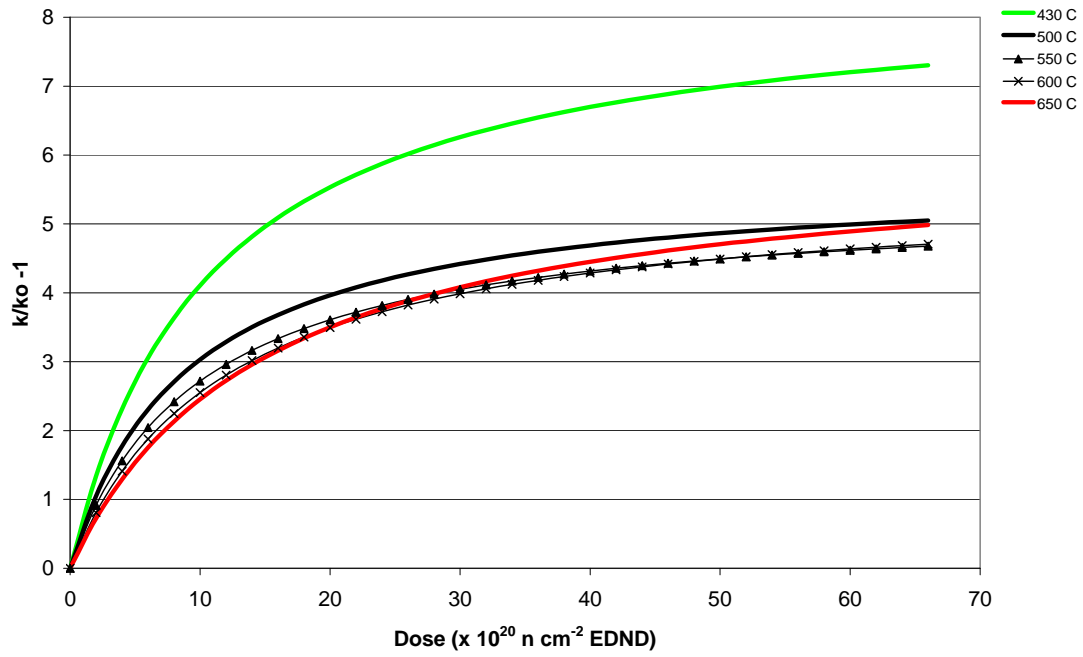


Figure B.2.2.6. Thermal resistivity change of VQMB graphite with respect to fast neutron dose at a temperature range of 430-650 °C.

B2.3 Radiolytic Oxidation of Nuclear Graphite in CO₂ Gas and Related Radiation Chemistry

1. INTRODUCTION

When graphite is used as the moderator in a CO₂-gas cooled reactor, it sustains a radiation induced attack (oxidation) which can lead to significant loss of weight, causing the reduction of integrity of the moderator during the lifespan of the nuclear reactor.

The process of radiolytic oxidation of graphite in nuclear reactors commences with the absorption of ionising-radiation energy in the molecules of the gas within the open-pore structure of the graphite (*i.e.* the accessible pores). The energy absorbed directly by the graphite does not contribute to the radiolytic oxidation and is manifested as heat ^[1]. The simplest description of the oxidation process is by the following reactions:



(2) applies where the activated species drift to the pore walls and react on the surface.

However, the reaction sequence is complicated. The principal oxidising species is considered to be negatively-charged ion CO₃⁻ ^[2, 3, 4].

The energy absorption in the gas within the open pores is considered to be the controlling factor during gasification of graphite ^[5] and the oxidation rate is proportional approximately to the reactor coolant pressure ^[4].

As most of the surface area of nuclear graphite is contained within the graphite pores, the oxidation rate is essentially proportional to the open pore volume (OPV). Thus, the higher the OPV fraction, the higher the oxidation rate of graphite. Evidence of this is displayed in Figure B3.2.1, where at a given gas composition (Table B3.2.1), LIMA graphite (OPV = 20.8%) presents a higher *initial* oxidation rate ($R_0 = 0.56 \times 10^{-8}$ kg/Wh) than GS graphite (OPV = 14.6% and $R_0 = 0.20 \times 10^{-8}$ kg/Wh) and IM1-24 ($R_0 = 0.13 \times 10^{-8}$ kg/Wh). The latter graphite is also known as AGL-mp and is a Gilsonite-coke graphite manufactured by AGL with an OPV variable between ~8-12%.

However, the oxidation rate is also strongly influenced by the pore dimensions. For instance, HDG and IG-50 graphite have a radiolytic oxidation rate at least four times higher than that of IM1-24 (see data in Table B3.2.1, gas coolant # 3) due to a reduced pore size, despite of the former two graphites having similar OPV (8.4 and 8.7% respectively) to that of a particular IM1-24 sample (10.4%). Cumulative open porosity profiles with respect to pore entrance diameter (PED) of the graphite are shown in Figure B3.2.2. Probably, the PED in the IG-50 is due to the manufacturing process, *i.e.* the graphite is made by cold isostatic moulding of extra-fine filler particles, followed by impregnation. The smaller the diameter of the pore, the shorter the distance for the active species to reach the pore walls before being deactivated by collision in the gas phase. For this reason, the gas located externally of the graphite moderator makes negligible contribution to the oxidation ^[5]. In addition, there are

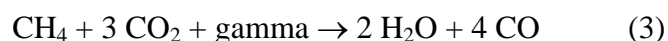
also cases where, in large-pored graphite, oxidising species produced near the centre of a pore may be destroyed by recombination before they can cause gasification ^[6]. In pure CO₂, the minimum pore diameter in which significant neutralisation of oxidising species occurs is of order 24 μm ^[1] and the size of the most reactive pores is less than 5-2 μm ^[7].

Inhibition of the Oxidation of Nuclear Graphite

During radiolytic oxidation, carbon monoxide (CO) is produced and builds up within the pores of nuclear graphite. Carbon monoxide is, in fact, a powerful inhibitor of radiolytic graphite oxidation, and the allowance of up to 1.5 vol % of CO in Magnox reactors reduces oxidation by a factor of approximately two. However, the inhibition efficiency of additional CO is reduced above 1.5 vol % CO. The CO deactivates the oxidising species in the gas phase ^[1].

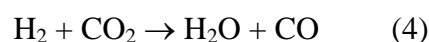
In Advanced Gas-Cooled Reactors (AGRs), the radiolytic oxidation rate requires greater control because of the higher power density and gas pressure (resulting in a much larger ionising-dose rate). This is achieved through the use of a graphite which has open porosity about half of that of the PGA used in Magnox reactors but, more importantly, by the constant addition of methane inhibitor to the CO₂ coolant. . A further increase of CO volume percent (*i.e.* higher than 1.5 vol % CO) would not be sufficient enough to control the oxidation rate and would occasion additional problems through the deposition of carbonaceous materials on fuel cladding.

Methane (CH₄) is therefore added as an inhibitor in AGRs and also reacts with oxidising species in the gas phase ^[8]: previously the mechanism was thought to involve sacrificial carbon deposits on the graphite pore surfaces ^[9] but this is now realised to be a very simplified picture because graphite in Magnox reactors carries much greater carbon deposition in its pores than the graphite in AGRs The simplistic equation for methane reaction is:



However, other by-products are also formed during methane destruction such as ethane (C₂H₆), ethylene (C₂H₄) and the hydrocarbon C₃H₈ ^[10], and these ‘minor organics’ are the principal species responsible for the additional powerful inhibition of graphite oxidation in the presence of methane.

Hydrogen (H₂), which appears as a result of small boiler or oil-seal leaks in some reactors, and is in equilibrium with methane and water in AGR coolant, is also an inhibitor. The classic surface-catalysed water gas shift reaction (4) is strongly affected in the presence of radiation ^[11] with a major shift in the position of equilibrium:



In the specific case of Gilsocarbon graphites in AGRs, the efficiency of inhibition of methane and hydrogen is 8 and 2.5 times higher respectively than carbon monoxide inhibition as shown in Figures B3.2.3 and B3.2.4. These figures also show the dependence of the oxidation rate constant with gas composition.

In inhibited environments, the radiolytic oxidation rate varies across graphite types due to the differing pore shape structures. Thus, pores having a large volume behind a narrow neck could suffer a particularly marked depletion in the methane level and oxidation might proceed rapidly inside such pores, even though the bulk methane concentration is such as to provide adequate protection^[12].

Carbon Deposition under Irradiation

Carbon deposition occurs from the polymerisation and decomposition of carbon monoxide and methane by ionising radiations. The following reaction illustrates the deposition phenomenon from irradiated CO:



The sooty deposits produced end up in the graphite pores which is potentially beneficial for inhibiting oxidation. However, the deposition may also occur on the fuel pins or on the boiler tubes of the AGRs, producing unacceptable temperature rises to the fuel and reducing the efficiency of heat transfer in the boilers.

In Magnox reactors, where only CO was present, rapid deposition was observed with ~ 4% CO in the CO₂ coolant^[13]. As a result, Magnox reactors were operating with a maximum of 1.5%CO in the CO₂. In AGRs, methane is maintained at approximately 230 vppm in the coolant by constant injection in order to inhibit the radiolytic oxidation of the graphite moderator. The potential for carbon deposition from CO and methane under AGR conditions has been investigated in the prototype AGR at Windscale and in rigs in DIDO and PLUTO at Harwell. These studies have been interpreted in terms of two distinct types of fuel-pin deposit^[14, 15].

- (a) *Low temperature deposit (LTD)*: A low density (~ 0.23 g cm⁻³) and irregular fibrous material formed in the region 550 - 720°C.
- (b) *High temperature deposit (HTD)*: regular hollow filaments with higher bulk density than that of LTD of ~ 0.7 g cm⁻³ and formed at temperatures above 720°C.

Coolants that were relatively high in carbon monoxide and low in methane (e.g. 4% CO/350 vpm CH₄) gave LTD exclusively, whereas coolants containing less carbon monoxide but more methane gave mostly HTD and in some cases minor amounts of LTD^[15]. Figure B3.2.5 displayed the carbon deposition threshold with respect carbon monoxide and methane concentration based on the results carried out in the Windscale AGR.

As consequence of deposition experiences, it is clear that this potential problem would need careful study for the U-Battery[®] for a CO₂ coolant and particularly in a sealed coolant system. It is extremely likely that the equilibrium concentration of CO produced by graphite oxidation would significantly exceed 4% in a sealed system, resulting in extensive carbon deposition with potential obstruction of the gas pathways that cooled the fuel. Evidence of the accuracy of this prediction came with the first and second sample sets to be irradiated in pressurised capsules in the TU Delft reactor, each of which showed marked deposition, both on the sample surface and on the quartz containers.

Determination of Radiolytic Oxidation Rate and Weight Loss

The methods that have been used in the prediction of weight loss of graphite in Magnox and AGRs are described in the following sub-sections.

Magnox reactors – Standing equation and Pore-Structure model

For Magnox reactors, it was originally assumed that radiolytic oxidation takes place uniformly throughout the open pore structure of graphite at a rate proportional to the radiation dose rate to the CO₂ contained within the open pores. Standing^[16] originally developed an equation for calculating the *initial* oxidation rate, which formed the basis for all graphite weight loss assessments. The derivation of the equation can be found in^[16], where the final expression for the *initial* oxidation rate (g_0) is given as:

$$g_0 = 4.6 \times 10^{-8} \times \frac{\varepsilon \cdot G_{-C} \cdot D \cdot P}{T} \left(\frac{g}{g \cdot s} \right) \quad (6)$$

or

$$g_0 = 145 \times \frac{\varepsilon \cdot G_{-C} \cdot D \cdot P}{T} (\% \text{ year}) \quad (7)$$

where:

ε = *initial* open porosity of graphite in cm³/g

G_{-C} = G(-C) value for carbon gasification in atoms per 100 eV of energy absorbed by the CO₂

D = radiation dose rate to graphite in W/g

P = CO₂ pressure in lb/in² absolute

T = temperature of CO₂ in K

The previous controlling parameters are described below.

The open porosity term ε

Graphite manufacturers often specify the initial open pore volume (O.P.V in % or π_0 in cm³/cm³) and the bulk (graphite) density (ρ_{B_0} in g/cm³) for their products. Thus, a theoretical open porosity ε can be obtained by dividing the previous terms.

In some manufacturer specifications, only the total porosity is given. Therefore, the following relations might be of use to determine the *initial* open porosity^[6].

$$\text{Total porosity } \pi_T = 1 - \frac{\rho_{B_0}}{\rho_C} (cm^3 / cm^3) \quad (8)$$

$$\text{Open pore volume } \pi_0 = 1 - \frac{\rho_{B_0}}{\rho_{He}} (\text{cm}^3 / \text{cm}^3) \quad (9)$$

$$\text{Close pore volume } \pi_c = \rho_{B_0} \cdot \left(\frac{1}{\rho_{He}} - \frac{1}{\rho_c} \right) (\text{cm}^3 / \text{cm}^3) \quad (10)$$

where ρ_c = crystal density of graphite (2.26 g/cm³)

ρ_{He} = helium density of graphite in g/cm³

Note that the helium density is based on the total volume of crystals and closed pores contained within a given mass of graphite. Helium density is therefore lower than crystal density, but is higher than bulk density.

The G(-C) value

The radiolytic-oxidation rate constant G(-C) is by definition a measure of the number of atoms of carbon gasified by the oxidising species produced adjacent to the graphite surface by the absorption of 100 eV of energy in the CO₂. The presently accepted value of G(-C) in pure CO₂ is 3.0^[4]. However, when one or more inhibitors are present in the coolant, G(-C) value is reduced and the resultant value is characteristic of graphite type (*i.e.* depends on porosity and pore size) and coolant composition.

Best *et al.*^[17] proposed a model that enables G(-C) values to be predicted from knowledge of the pore structure and local gas composition within the pores. This model was used in the POGO'12 code used for estimating weight loss in Magnox reactors^[4]. The model is defined as follow:

$$G(-C) = G(-C)_0 \times F \times P \quad (11)$$

where $G(-C)_0$ is the carbon atoms gasified per 100 eV in pure CO₂ (*i.e.* ~ 2.5-3)

F is the fraction of oxidising species that react with graphite

P is the fraction of graphite surface protected by the effect of inhibitors (*e.g.* CO and CH₄)

The F value is a function of (i) the flux of oxidising species at the pore surface and (ii) the pore geometry (*i.e.* assuming cylindrical or rectangular pore geometry). From Fick's diffusion law, the flux of oxidising species is determined. The following equations defined F_i for each group of pores with a radius ' a ' or half pore width ' l '

Assuming cylindrical pore geometry:

$$F_i = \frac{2\sqrt{D/K}}{a} \cdot \frac{I_1(\sqrt{K/D} \cdot a)}{I_0(\sqrt{K/D} \cdot a)} \quad (12)$$

Assuming slab pore geometry:

¹ "Pore-Opening Graphite Oxidation"

$$F_i = \frac{\sqrt{D/K} \tanh(l \cdot \sqrt{K/D})}{l} \quad (13)$$

where D is the diffusion coefficient of the oxidising species
 K is the rate of removal of oxidising species by CO and CH₄
 I_0 and I_1 are the zero and first order Bessel functions

Thus, the overall efficiency of oxidation (F) for graphite with a known open pore volume (OPV) is obtained as follows:

$$F = \frac{\sum(F_i \cdot OPV_i)}{OPV} \quad (14)$$

The value P is determined empirically from MTRs data and is characteristic for a specific gas mixture.

On the other hand, Ashton *et al.* [18] deduced a simplistic equation to calculate the G(-C) value assuming ideal gas law and that the radiation dose per unit mass of graphite is equal to that received by the gas in the associated pores. The deduction is in [18] and the equation is:

$$G(-C) = \frac{5.02 \times 10^{16}}{8.25 \times 10^{17}} \cdot \frac{wT}{DP \varepsilon_0} \times 100 = 6.07 \frac{wT}{DP \varepsilon_0} \text{ atoms}/100eV \quad (15)$$

where:

D = dose per unit mass of graphite in mWh/g

ε_0 = porosity of graphite in cm^3/g

P = pressure in psi

T = temperature in K

w = weight loss due to oxidation in ppm

The dose rate D term

The energy deposition dose rate term, D , as used here is a measure of the energy absorbed by the CO₂ from the scattering of γ -radiation only (the total energy deposition is the heat generated by fast neutron, gamma rays and secondary gamma rays arising from activation of core components by neutrons). In equation 6 (or 7), the dose rate received by the graphite is the same as that absorbed by CO₂ in the pores of the graphite provided that an appropriate correction is made for relative electron densities of graphite and CO₂ gas [5]. For the mean dose rate to the entire graphite moderator, the following expression can be used:

$$D = \frac{kP}{W} \text{ (W/g)} \quad (16)$$

where: P = reactor thermal power in MW

W = weight of active core graphite (excluding reflectors) in tonnes

k = fraction of thermal power generated in graphite moderator due to neutron and gamma heating. This parameter depends on fuel material, diameter and on the ratio of moderator to fuel volumes. In Magnox reactors, k is typically 0.056 and in AGRs a higher value applies.

However, it is important to note that the dose rate will vary spatially within the graphite such that the rate will decrease in a radial direction away from the fuel element. More importantly, if the nuclear reactor operates at constant thermal power, then the dose rate will increase as radiolytic oxidation (weight loss) proceeds in the core throughout the life-time of the reactor.

The maximum value of dose rate in a peak fuel rating region can be calculated if the radial and axial form factors f_r and f_a are known as followed:

$$D_{\max} = \frac{D}{f_a f_r} \quad (17)$$

Where: $f_a = \frac{\text{mean} \cdot \text{fuel} \cdot \text{rating} \cdot \text{in} \cdot \text{a} \cdot \text{channel}}{\text{maximum} \cdot \text{fuel} \cdot \text{rating} \cdot \text{in} \cdot \text{a} \cdot \text{channel}}$ (18)

$$f_r = \frac{\text{mean} \cdot \text{channel} \cdot \text{rating}}{\text{maximum} \cdot \text{channel} \cdot \text{rating}} \quad (19)$$

As the radiolytic oxidation gasifies the graphite, the open pore volume increases and, additionally, closed pores open up; therefore, in the initial stages, the oxidation rate increases as the weight loss increases. However, the oxidation efficiency of the largest pores is less because there is a higher probability that oxidising species can become deactivated before reaching the graphite surfaces. Thus, it is obvious that the cumulative weight loss is not the simple product of initial oxidation rate (g_0) and time (t). Instead, the cumulative weight loss can be obtained by the following expressions:

- If the dose rate is constant:

$$w_t = A \left[\exp \frac{g_0 \cdot t}{A} - 1 \right] \quad (20)$$

where: w_t = percentage weight loss

t = time in years

g_0 = initial oxidation rate, from equation 7

$$A = \frac{100 \cdot \pi_e}{(1 - \pi_e)}$$

- If the reactor operates at constant power:

$$\frac{A^2}{100 \cdot \pi_e} \ln \left(1 + \frac{w_t}{A} \right) - \frac{A}{100} \cdot w_t = g_0 \cdot t \quad (21)$$

Figures B3.2.6 and B3.2.7 illustrate graphically the relation between cumulative weight loss and initial oxidation rate given in equations 20 and 21.

AGRs – DIFFUSE code and Empirical Equations

Radiolytic oxidation in AGRs is much more complex than that in Magnox reactors due to a more complex gas coolant composition and as a result of a complex distribution of internal coolant flows within the graphite components. Thus, the method of employing Standing equations to estimate the cumulative weight loss is not applicable for accurate prediction of the integrity of the core in AGRs.

The gas coolant chemistry within the pores of graphite in AGRs is very complex. Experimental data indicate that the oxidation rate in the majority of large pores is quite low, with significant oxidation only occurring in smaller pores, especially where the accessibility of methane is restrained due to pore shape and size. Moreover, as methane is destroyed within the graphite pores, its replacement is fundamental to maintain its inhibition efficiency. However, in practice, the rate of destruction of methane is high in relation to the gas flow rates due to permeation and diffusion through the pores. Consequently, there is significant reduction in methane concentration at positions within the graphite blocks which are remote from the external surfaces in contact with the gas coolant flow.

In addition, as methane destruction and radiolytic oxidation result in the formation of water and carbon monoxide (see reaction 3), further concentrations of these constituents builds up to higher levels within the graphite pores. Therefore, methane destruction rate, and consequently the radiolytic oxidation rate, will be a function of all these minor constituents in the coolant gas and their distribution within the graphite pores.

All of the foregoing is moderated by the internal gas flows resulting from the vertical ‘methane holes’ and the lateral differential gas pressures imposed across the components by the pattern of circulating gases.

Thus, the complexity of the situation leads to a differential oxidation rate and weight loss profile within each graphite brick. Moreover, there is an iterative process between local oxidation rate, gas composition and energy dose rate since the oxidation of graphite affects

the local gas composition (and *vice versa*) and consequently the dose rate (and *vice versa*). Therefore, numerical calculations (*i.e.* codes) based on finite element methods or Monte Carlo simulations are carried out to determine the oxidation rate and cumulative weight loss profiles and the controlling factors (e.g. local gas composition, diffusion, and dose rate) which are explained as follow.

For the UK AGRs, a code has been developed to determine the gas coolant composition, specifically the methane (C_1), moisture (C_2) and carbon monoxide (C_3) concentrations, and hence weight loss profiles within an AGR Gilsocarbon graphite brick. In the following paragraphs, a brief description of the formulas used by the code is given. The intention is to demonstrate the complexity of predicting weight loss in graphite subjected to oxidation in presence of inhibitor. This code is largely based on empirical relationships determined from experiments on Gilsocarbon graphite and thus, would require modification and the relevant data to be applicable to the U-Battery[®].

The concentration profiles of the minor constituents (*i.e.* CH_4 , H_2O and CO) in the CO_2 coolant under *impressed flow conditions* (known as “ventilated” condition) are obtained by solving the following second order differential equations:

$$\nabla^T (D_1 \cdot \nabla(C_1)) - \nabla(v \cdot C_1) - K_1 = 0 \quad (22)$$

$$\nabla^T (D_2 \cdot \nabla(C_2)) - \nabla(v \cdot C_2) + STOX \cdot K_1 = 0 \quad (23)$$

$$\nabla^T (D_3 \cdot \nabla(C_3)) - \nabla(v \cdot C_3) + STOX_1 \cdot K_1 + STOX_2 \cdot K_2 = 0 \quad (24)$$

The first term in each equation refers to the pure diffusion contribution of the minor constituents. The second term in each equation is the contribution from porous flow due to permeation and the last term(s) are the destruction and production of methane and carbon monoxide, K_1 and K_2 respectively. $STOX$, $STOX_1$ and $STOX_2$ are the stoichiometry for H_2O formation from CH_4 destruction (reaction 5), the stoichiometry for CO formation from CH_4 destruction (reaction 3) and the stoichiometry for CO formation from graphite (reactions 1-2). These variables are described below:

Diffusion D

The effective diffusion coefficients in graphite of methane in CO_2 (D_1), moisture in CO_2 (D_2) and carbon monoxide in CO_2 (D_3) are obtained from the expression, where methane in CO_2 is taken as example:

$$D_1 = \frac{B \cdot T^{3/2} \cdot \sqrt{\frac{1}{M_1} + \frac{1}{M_{CO_2}}}}{P \cdot r_{1CO_2} \cdot I_D} \times \lambda \quad (25)$$

where:

$$B = \left[10.7 - 2.46 \sqrt{\frac{1}{M_1} + \frac{1}{M_{CO_2}}} \right] \times 10^{-4}$$

T = temperature, K

M_1 = molecular weight of methane in this example (M_2 or M_3 for moisture or carbon monoxide)

M_{CO_2} = molecular weight of CO_2

P = absolute pressure, *atm.*

I_D = collision integral for diffusion

λ = is the ratio of diffusion in graphite to diffusion in free gas. This variable increases with weight loss due to the increase in open porosity

r_{iCO_2} = mean collision diameter for methane and CO_2 in this example, \AA

Permeable flow v

When graphite is subjected to a pressure gradient, gas will permeate through the graphite pores. The flow rate parameter is calculated from the Darcy equation:

$$v = \frac{B_0}{\mu} \nabla P \quad (26)$$

where: v is the CO_2 flow rate through porous graphite

B_0 and μ are permeability and viscosity respectively. In DIFFUSE, the ratio B_0/μ is allowed to vary either linearly or quadratically with either weight loss or dose

∇P is pressure profile obtained by finite element method

Methane destruction rate K_1

Methane destruction rate is proportional to the local dose rate (function of weight loss, fuel rating and burn-up), open pore volume (function of weight loss) and $G(-CH_4)$ value, the latter being known as the number of methane molecules destroyed per 100 eV of energy absorbed by CO_2 gas in the open porosity. Thus, the methane destruction rate, in *vpm/s*, is defined as:

$$K_1 = B_2 \times M \times W \times V \times G(-CH_4) \times 10^6 \quad (27)$$

where: B_2 is a physical constant ($= 1.036 \times 10^{-7} \text{ } 100 \text{ eV Mole} / \text{Joule Molecule}$)

M is the molecular weight of carbon dioxide (CO_2)

W is the dose rate at a particular position (r, θ, z)

V is the open pore volume, which varies with weight loss according to the following relationship:

$$V = V_{t=0} + \frac{x}{100}(1 - V_{t=0}) \quad (28)$$

$G(-\text{CH}_4)$ is defined as follows:

$$G(-\text{CH}_4) = \frac{2.2[\text{CH}_4]}{[\text{CH}_4] + k_5 \cdot \exp\left(\frac{4900}{R_c T}\right) \cdot [\text{CO}] + k_6 \cdot \exp\left(\frac{4900}{R_c T}\right) \cdot [\text{H}_2\text{O}]} \quad (29)$$

Carbon monoxide production rate K_2

The production of CO from graphite oxidation, K_2 , has been defined as:

$$K_2 = B_2 \times M \times W \times V_0 \times G(-\text{C}) \times f \times 10^6 \quad (30)$$

where: V_0 is the initial open pore volume (known also as OPV)

f is the factorial increase in rate of weight loss, defined in equation 37

Dose rate

The dose rate to graphite, in W/g , at a particular position (r, θ, z) in the reactor core is given by the expression:

$$W = \frac{H\alpha_r\alpha_z}{W_m} k' d(r, \theta) \quad (31)$$

where: H is the reactor power in MW

α_r and α_z are radial and axial power form factors

$d(r, \theta)$ is the dose rate factor in the brick

k' is the proportion of heat generated by ionising radiation deposited in the graphite

W_m is the weight of graphite

k' is given by:

$$k' = \mu' + \nu' \frac{W_m(t)}{W_u(t)} \quad (32)$$

where: $W_u(t)$ is the weight of fuel in the reactor

W_m is given by:

$$W_m = W_{m0} \left(1 - \frac{\bar{x}}{100}\right) \quad (33)$$

The cumulative heating dose rate, in $kWh.g^{-1}$, is obtained from:

$$\frac{\partial D}{\partial t} = W \quad (34)$$

Weight loss

The predictive route DIFFUSE 6 for AGR Gilsocarbon graphite radiolytic oxidation is described by the following expression^[19]:

$$\frac{\partial x}{\partial t} = \left[9.92076 \cdot AR_{t=0} \times 10^8 \times W_{t=0}\right] \times \frac{P}{T} \times f \quad (35)$$

or, otherwise;

$$\frac{\partial x}{\partial t} = Rate_{t=0} \times \frac{P}{T} \times f = Rate \quad (36)$$

where:

the numerical constant 9.92076 is derived from empirical fits to AGR-graphite oxidation data from rig experiments (from^[19]);

$Rate$ has units %/year;

$AR_{t=0}$ is the initial oxidation rate;

$W_{t=0}$ is the initial dose rate;

P and T are pressure and temperature

f is the factorial increase in rate of weight loss, which is calculated as follows:

$$f = \frac{RPV}{RPV_0} \times \frac{W}{W_{t=0}} \times \frac{AR}{AR_{t=0}} \quad (37)$$

where:

$\left(\frac{RPV}{RPV_0}\right)$ term is the factorial increase in reactive pore volume (RPV) over the time increment. It is a function of initial open pore volume (OPV), initial oxidation rate, weight loss, pore entrance diameter (PED) and the rate of pore closure due to fast neutron irradiation.

$\left(\frac{W}{W_{t=0}}\right)$ term is the factorial increase in dose rate over the time increment.

$\left(\frac{AR}{AR_{t=0}}\right)$ term is the factorial increase in oxidation rate due to changes in coolant composition.

It is important to note that the data inputs, such as $AR_{t=0}$ and constants, have been derived from fitting and experimental results obtained in materials test reactors (MTRs) and in the AGRs themselves. Therefore, the previous code is ONLY applicable for the weight loss predictions of the AGRs graphite, *i.e.* Gilsocarbon. The methodology could be extended to include other graphites, but would require further experimental work.

Nevertheless, for the initial design purposes of Magnox and AGRs, the weight loss prediction was carried out by using Standring and empirical equations (38 and 39) from MTRs results, respectively.

$$w_t = R_0 \cdot d_1 \left[\exp\left(\frac{D_t}{d_1}\right) - 1 \right] \quad \text{for } D_t < 1.099d_1 \text{ MWh/kg} \quad (38)$$

$$w_t = R_0(3 \cdot D_t - 1.30 \cdot d_1) \quad \text{for } D_t > 1.099d_1 \text{ MWh/kg} \quad (39)$$

where: w_t is the cumulative weight loss

R_0 is the initial oxidation rate (also known as AR_0) in 10^{-8} kg/Wh

D_t is the cumulative dose in MWh/kg

$d_1 = 18.58 \times (41/P) \times (T/673) \text{ MWh/Kg}$, where P is pressure in Bar and T is temperature in K

These empirical equations for forecasting the weight loss (for different types of graphite) with cumulative dose give excellent agreement with the measured weight loss when a measured initial oxidation rate (R_0^{Exp}) is used in the equations 40 and 41 [20].

Several measured initial oxidation rates of different types of graphite under several CO₂-gas coolant composition were obtained in one of the largest MTR projects carried out in an experimental loop facility in the Siloe reactor at CEN Grenoble. The joint project between France and United Kingdom was known as the BFB experiment (**B**oucle **F**ranco-**B**ritannique) and it consisted of 30 experiments under varying coolant compositions, graphite type and flow conditions (*i.e.* ventilated and unventilated). Only three of the experimental results are provided in Table B3.2.1 for illustrative purposes.

The results obtained in the BFB loop (Table B3.2.1) illustrate the effect of the open pore volume (OPV) on the radiolytic oxidation rate. The higher the OPV, the higher the oxidation rate of graphite. However, the OPV is not always the “sole” factor to be relied on for graphite selection. For example, comparing the OPV of EK-78 and IM1-24 graphite from Table B3.2.1, one could expect that the initial radiolytic oxidation rate would be similar or even lower for the former graphite. Thus, the second and very important microstructural factor to be considered is the pore size distribution. From Table B3.2.2, it is clear that EK-78 presents many more open pores that are highly reactive (pores with entrance diameter of less than 5 µm) than the IM1-24 (90% vs. 39% respectively).

Generally, the manufacturer only gives the total porosity or the OPV. However, for the selection of the graphite to be used in U-Battery[®], it is necessary to obtain or determine the PED distribution of all graphite candidates should an oxidising coolant be chosen.

As observed in Table B3.2.1, the radiolytic oxidation data were obtained in rigs where the assembly permitted either the gas coolant to flow without restriction through the specimens (unventilated condition) or within a section with imposed pressure drop (ventilated condition), generally about 35-75 mbar. In the latter assembly, the coolant was forced through the graphite, resulting in a constant supply of inhibitors to remote pores. Thus, when comparing the oxidation rates of graphite placed in ventilated and unventilated conditions, the rate in the latter condition was and will always be expected to be higher because the rate at which methane is depleted is greater than the rate at which the inhibitor is replenish within the pore.

Summary of Modelling Radiolytic Graphite Oxidation

The following models have been utilised in modelling the radiolytic oxidation of graphite:

Standing Model: It assumed that the oxidation rate is proportional to OPV and that G(-C) is constant. Additionally, the model presumed that 40% of close pore volume (CPV) opens up during the first few percentage of weight loss. This model was employed for PGA graphite used in Magnox reactors.

Pore-Structure Model: It was developed based on studies carried out at the BNL Gamma Irradiation facility, where G(-C) value is taken as the oxidation rate. The G(-C) value depends on the pore size and geometry and the local gas composition within the pore, which changes during oxidation and it is influenced by irradiation damage. POGO12, a code that predicts the

weight loss for Magnox reactors, is based on this model. It has also been used to facilitate a better understanding of the behaviour of Gilsocarbon graphite in AGRs.

RPV Model: “The Reactive Pore Volume” model was developed based on results of radiolytic oxidation rates of Gilsocarbon obtained in the ‘Boucle Franco-Britannique’ (BFB) series of experiments, where an empirical fit-to-data equation was derived.

DIFFUSE: It is a semi-empirical code based on the RPV model. This code considers methane distribution effects (diffusion), pore geometry, dose rate profile on graphite brick, and the irradiation damage from fast neutrons. This code is used to predict graphite weight loss in AGRs.

Effect of Radiolytic Oxidation on the Physical and Mechanical Properties of Nuclear Graphite

The strength and Young’s modulus of nuclear graphite are controlled by the amount and shape of the porosity in the material ^[21] and are very sensitive to the distribution of large pores ^[16]. Regarding pore shape, pores of high aspect ratio (*i.e.* slit-shaped, elongated) reduce modulus to a greater extent than pores of low aspect ratio (*i.e.* spherical).

Empirical equations have been derived to determine the change in mechanical property with weight loss of different graphite in various CO₂ gas mixtures ^[22, 23].

For **Young’s modulus**: $E = E_o \exp(-bx)$ (40)

where E_o is the Young’s modulus with zero weight loss, *x* is fractional weight loss and *b* is a constant that can be 4.6 for PGA graphite ^[22] or 3.4 for Gilsocarbon moderator graphite and AGR fuel-sleeve graphite. These *b* values were obtained in a gas coolant composition of 0.2%CO/CO₂.

For **thermal conductivity**: $\frac{1}{K} = \frac{1}{K_o} \exp(-bx)$ (41)

where K_o is thermal resistivity at zero weight loss and *b* is a constant that can be -3.1 for PGA graphite, -2.7 for Gilsocarbon moderator graphite and -2.3 for AGR fuel-sleeve graphite. Previous values are independent of CO₂ gas coolant composition ^[23].

For **strength**: $S = S_o \exp(-bx)$ (42)

where S_o is the strength at zero weight loss and *b* is a constant that can be 5.2 for PGA graphite, 3.7 for Gilsocarbon moderator graphite and 3.9 for sleeve graphite. These *b* values were obtained in a gas coolant composition of 0.2%CO/CO₂.

Recombination Unit for the Control of Carbon Monoxide

There is considerable experience in the UK of using recombination units to re-oxidise carbon monoxide in a reactor coolant to carbon dioxide. Thus, should it be decided to proceed with a forced-circulation CO₂-cooled system, the UK experts could provide a relatively simple design for the U-Battery[®]. It is almost certainly the case however that forced circulation would be necessary. It is also obvious that a reliable supply of compressed oxygen is available, in order to facilitate the chemical reaction.

The recombination units at Magnox-reactor stations in some cases operated at a rather low temperatures (~220C), with a palladium on alumina catalyst. These did suffer from catalyst poisoning, but the demand on them was low so they were just adequate with very occasional catalyst changes during scheduled maintenance outages. The instrumentation provided was extremely limited.

Given the probable operating temperature regime of a CO₂-cooled U-Battery[®], a more sensible model is the Advanced Gas-Cooled Reactor versions although these are extremely large units compared with what would be required for this project. They utilise platinum on gamma alumina catalysts. In almost all cases these are 0.5% Pt surface loaded although, because the catalyst beds on the final reactors at Heysham 2 and Torness are huge and hence can operate with more poisoning (notably from carbonyl sulphide), tests showed that they could use a reduced Pt content of 0.3%. Replacement of a catalyst charge is rare, providing the bed size is adequate (those at Hartlepool and Heysham 1 reactors are a little small). The Hinkley Point B units, for example, are still operating with their original charge. The main reason that catalyst has had to be replaced in some reactors (*e.g.* Dungeness B) is that it has been soaked in gas-circulator lubricating oil due to operational failures.

Costing is fairly straightforward and is here based on a Hinkley Point B unit, which can be scaled down more or less *pro rata* with the relative reactor thermal power. In addition, a further scaling down compared with an AGR unit will be made on the assumption that no methane is used as a graphite oxidation inhibitor. Where this *does* take place (AGRs), it should be assumed that all of the carbon in the added methane ends up as CO and must also be re-oxidised. The basic AGR plant data which follow are based upon the maintenance of approximately 230 vpm methane in the coolant. The data which follow have also been kindly provided by that organisation.

Other parameters for the Hinkley Point B design:

CO₂ mass in circuit ~ 120 te;

Proportion of mass of CO₂ in primary circuit flowing through bed at full flow ~13% hr⁻¹;

Temperature (inlet) ~280°C;

Volume of catalyst ~ 1.0 m³;

Mass of catalyst ~ 1000 kg;

Pellets are cylinders with height and diameter approximately 3 mm;

Theoretical temperature rise (no heat losses) = 60°C per 1% CO conversion across the bed;

Maximum CO₂ flow ~ 4.4 kg.sec⁻¹ = 15840 kg.hr⁻¹ (this was the design value: in practice, it will be reduced by filter blockage, valve problems and so forth and hence the initial efficiency will fall off);

Estimated methane feed rate at 1600 MW(th) $\sim 3.46 \text{ kg.hr}^{-1}$ (maximum value for design purpose which is not actually required to maintain 230vpm methane: current feed rates are not immediately available but could be obtained from EdF Energy if required);
 Oxygen feed rate to recombination unit $\sim 4.2 \text{ g.sec}^{-1}$ (allowing an amount of CO production from graphite corrosion);
 At full flow, conversion of CO across the unit $\sim 0.26\%$ (ignoring small amounts of hydrogen oxidation).

The cost of the catalyst may be estimated from the current world price for platinum, plus 10%.

The recombination unit generally needs no attention, although it is, of course, monitored - especially outlet oxygen concentrations and temperatures (usually not measureable - much less than 1 vpm). Some operational problems (including significant oxygen breakthrough) have been experienced in the AGR units, particularly the rather under-sized units at Hartlepool and Heysham 1.

As part of the AGR coolant-bypass plant, one circulator provides the differential pressure across the whole plant of ~ 2.5 bar (max). Only a proportion ($<20\%$) of the bypass gas flow passes through this unit, and the differential pressure across the packed bed itself is negligible.

Prediction of Cumulative Weight loss due to Radiolytic Oxidation in a CO₂ Coolant

The following basic data are used in this analysis (as agreed at TU Delft on the 27th May 2009):

Thermal power (P)	20 MWth
Weight of graphite (W)	4.6 tonnes: There are 61 blocks in the reference design assumed at the time of this study, where the volume of graphite in each block is 2107187.94 cm^3 and taking the density of structural graphite 1.85 g cm^{-3} , the total weight is 3.9 tonnes. Assuming that the total mass of carbon in compacts is $\sim 10.8 \text{ kg}$ per block, the total weight of graphite is 4.6 tonnes
Mean graphite temp. (T)	800 K (527°C)
CO ₂ -coolant pressure (p)	41 bar (594.7 psi)
CO ₂ -coolant bulk composition	pure CO ₂ with a G(-C) = 3 (worst case, neglects all inhibition from CO)
Type of graphite for the prismatic block	graphite with OPV = 6% ($\pi_0 = 0.06 \text{ cm}^3 \text{ cm}^{-3}$), bulk density, $\rho_B = 1.85 \text{ g cm}^{-3}$, and open porosity, $\epsilon = 0.03 \text{ cm}^3 \text{ g}^{-1}$

Operation time of the U- 5, 7 or 10 years
Battery®

Since no measured initial radiolytic oxidation (g_0) has been obtained for prospective or currently manufactured graphites in pure CO₂, Standing equation 7 will be used to calculate g_0 and then inserted in equation 38 (or 39) to predict the cumulative weight loss at the 5th, 7th and 10th year of U-Battery® operation. For this, the mean dose rate D to the entire graphite moderator is first determined from equation 18. However, bearing in mind that the overall thermal power (*i.e.* 20 MWth) is generated by fast neutrons and gamma radiation and that the latter, which causes radiolytic oxidation, accounts for approximately 70% of the total thermal power, the term P in equation 16 (below), has to be multiplied by 0.7:

$$D = \frac{kP}{W} = \frac{0.086 \times 20 \times 10^6 \times 0.7}{4.6 \times 10^6} = 0.262 \text{ W/g}$$

In addition, let assume that the axial and radial flux factors at the peak position in a flattened zone core are 1.8 and 1.3 respectively. Superimposing these two factors, the dose at the peak-rated region would be approximately 2.3 times higher than the mean dose. These estimated factors are specific to some British reactors and may not apply to the finalize U-Battery®. In addition, the variation of flux within the unit cell is not considered as yet.

(1) The mean initial oxidation rate for the entire moderator is (from equation 6):

$$R_0 = 4.6 \times 10^{-8} \times \frac{\varepsilon \cdot G_c \cdot D \cdot P}{T} = 4.6 \times 10^{-8} \times \frac{0.03 \cdot 3 \cdot 0.262 \cdot 5947}{800} \times \frac{3600}{0.262 \cdot 1000} = 1.11 \times 10^{-8} \text{ kg/Wh}$$

(2) The mean initial oxidation rate in peak-rated regions is:

$$R_0 = 1.11 \times 10^{-8} \times 2.3 = 2.55 \times 10^{-8} \text{ kg/Wh}$$

(3) To obtain the cumulative weight loss from equation 40, firstly, the cumulative dose D_t is determined. In principle, the cumulative dose in the in-core graphite would be the simple multiplication of the initial dose rate (D) and the time of reactor operation (*i.e.* 5, 7 or 10 years). This would apply if the reactor works at constant dose rate. However, if the reactor operates at constant power, the dose rate increases as the weight loss increases.

Thus, for a reactor operating at **constant dose rate**:

The total cumulative dose is: $D_t = D \times t$ in *MWh/kg*

where $D = 2.62 \times 10^{-4} \text{ MWh/kg}$ and $t = 43829.06 \text{ h}$ (5 years), 61360.69 h (7 years) or 87658.13 h (10 years)

$$D_t \text{ in 5 years} = 11.48 \text{ MWh/kg}$$

$$D_t \text{ in 7 years} = 16.08 \text{ MWh/kg}$$

D_t in 10 years = 22.97 MWh/kg

Secondly, the constant d_1 from equation 38 is determined as follows:

$$d_1 = 18.58 \times (41/41) \times (800/673) = 22.1$$

Finally, the cumulative weight loss is determined using equation 40:

- For $R_0 = 1.11$ and $D_t = 11.48$ MWh/hg

$$w_t = R_0 \cdot d_1 \left[\exp\left(\frac{D_t}{d_1}\right) - 1 \right] = 1.11 \cdot 22.1 \left[\exp\left(\frac{11.48}{22.1}\right) - 1 \right] = 16.7\%$$

- For $R_0 = 1.11$ and $D_t = 16.08$ MWh/hg

$$w_t = 26.3\%$$

- For $R_0 = 1.11$ and $D_t = 22.97$ MWh/hg

$$w_t = 44.8\%$$

- For $R_0 = 2.55$ and $D_t = 11.48$ MWh/hg

$$w_t = 38.4\%$$

- For $R_0 = 2.55$ and $D_t = 16.08$ MWh/hg

$$w_t = 60.3\%$$

- For $R_0 = 2.55$ and $D_t = 22.97$ MWh/hg

$$w_t = 100\%$$

The following Table B3.2.3 will provide a summary of the data obtained in this section.

The reader should understand that these are very preliminary estimates, but nonetheless indicative of the challenge posed by radiolytic oxidation in the U-Battery[®] in a CO₂ coolant. These weight losses are also the upper limit values, since the equations used to predict the weight losses do not consider the change in coolant composition. As graphite oxidises, carbon monoxide is produced and hence, inhibition of the oxidation reaction proceeds, reducing the radiolytic oxidation rate with time.

References to Section B3.2

- [1] J. V. Best, W.J. Stephen, A.J. Wickham, *Progress in Nuclear Energy* 16 (1985) 127-178.
- [2] B. T. Kelly, B.J. Marsden, K. Hall, "Appendix 1 - Radiolytic Oxidation in Graphite", IAEA, TECDOC-1154 (2000)
- [3] A. J. Wickham, J.V. Best, C.J. Wood, *Radiation Physics and Chemistry* 10 (1977) 107-117.
- [4] P. C. Minshall, I.A. Sadler, A.J. Wickham, "Radiolytic Graphite Oxidation Revisited", IAEA, TECDOC-901 (1995)
- [5] V. Y. Labaton, B.W. Ashton, R. Lind, J.N. Tait, *Carbon* 7 (1969) 59-75.
- [6] J. Standring, B.W. Ashton, *Carbon* 3 (1965) 157-165.
- [7] C. Berre, S.L. Fok, P.M. Mummery, J. Ali, B.J. Marsden, T.J. Marrow, G.B. Neighbour, *Journal of Nuclear Materials* 381 (2008) 1-8.
- [8] B. T. Kelly, P.A.V. Johnson, P. Schofield, J.E. Brocklehurst, M. Birch, *Carbon* 21 (1983) 441-449.
- [9] B. T. Kelly, *Progress in Nuclear Energy* 16 (1985) 73-96.
- [10] P. Campion, "Carbon Formation Processes Relevant to Advanced Carbon Dioxide-Cooled Reactors in *"Gas Chemistry in Nuclear Reactors and Large Industrial Plants"* edited by A. Dyer", HEYDEN (1980)
- [11] J. C. Fessler, "A Study of Water-Gas Shift Reaction Equilibria under Gamma Radiation", PhD Thesis, University of Grenoble, (1971). Available in English translation by P. Campion, UKAEA, report TRG Memorandum 6680(S), (1974).
- [12] J. D. Clark, P.J. Robinson, *Journal of Materials Science* 17 (1982) 2649-2656.
- [13] A. J. Wickham, *Personal Communication*.
- [14] B. T. Kelly, *Nuclear Energy* 25 (1986) 225-233.
- [15] P. A. V. Johnson, *Nuclear Energy* 24 (1985) 381-395.
- [16] J. Standring, *Journal of Nuclear Energy Parts A/B* 20 (1966) 201-217.
- [17] J. V. Best, C.J. Wood, *Carbon* 13 (1975) 481-488.
- [18] B. W. Ashton, J. Standring, M.T. Jaquiss, *Journal of Nuclear Energy* 21 (1967) 871-882.
- [19] M.A. Davies, "A Theory Manual for DIFFUSE 6"; AEA Technology Report AEA-RS-5117, February 1991

[20] J. Ketchen, P. Schofield, "Graphite Oxidation Results from BFB Experiment 30. December 1983 to September 1984", UKAEA, ND-M-2970(w) (1984)

[21] P. Quagne, G.B. Neighbour, B. McEnaney, *Journal of Physics D: Applied Physics* 38 (2005) 1259-1264.

[22] J. E. Brocklehurst, R.G. Brown, K.E. Gilchrist, V.Y. Labaton, *Journal of Nuclear Materials* 35 (1970) 183-194.

[23] J. E. Brocklehurst, M. Birch, R.G. Brown, P. Champion, "The Effect of Radiolytic Oxidation in 2%CO/0.02% CH₄/ CO₂ on the Physical and Mechanical Properties of Graphite", UKAEA, ND-M-1473(S) (1981)

Table B3.2.1. Initial radiolytic oxidation data from BFB loop experiments for various type of graphite oxidized in various CO₂-coolant compositions at 41 Bar and 673 K.

#	CO ₂ - coolant composition				Graphite [†]	ρ (g/cm ³)	O.P.V (%)	C.P.V (%)	$R_0^{Exp.}$ (x10 ⁻⁸ kg/Wh)
	CO (%)	CH ₄ (vpm)	H ₂ (vpm)	H ₂ O (vpm)					
1	2.00	130	200	200	LIMA	1.69	20.8	4.2	0.56 ± 0.04 0.66 ± 0.04*
					GS (sleeve graphite)	1.81	14.6	5.1	0.20 ± 0.02 0.27 ± 0.02*
					AGLMP	1.80	12.1	8.2	0.13 ± 0.01 0.15 ± 0.01*
					LIMA	1.69	20.8	4.2	2.58 ± 0.27
					BAEL Sleeve	1.80	13.2	7.4	1.08 ± 0.25
					Pechiney Sleeve 2	1.89	7.6	8.6	0.66 ± 0.14
2	1.03	6-43 (mean 7)	65	10	AGLMP	1.80	12.1	8.2	0.65 ± 0.04
					Pechiney Sta. Maria Coke	1.58	24.9	5.4	2.24 ± 0.25
					POCO	1.80	17.6	3.0	1.92 2.10*
					Carbon Lorraine 1116	1.77	11.6	10.3	1.56 ± 0.27
3	0.5	150	270	260	IG-80	1.94	7.9	6.6	1.31
					IG-50	1.87	8.7	8.7	1.29 ± 0.22
					HDG	2.01	8.4	2.9	1.28 ± 0.27 1.34*
					Ringsdorff EK-78	1.87	7.8	9.7	1.26 ± 0.21
					Ringsdorff EK-76	1.84	8.8	9.9	1.14 ± 0.07 1.19*
					Union Carbide Outer Sleeve (OS)	1.84	9.8	8.8	0.72 ± 0.11
					Pechiney OS	1.76	12.4	9.8	0.61 ± 0.02

		(Gilsocoke)				
--	--	-------------	--	--	--	--

Table B3.2.1 (continued). Initial radiolytic oxidation data from BFB loop experiments for various type of graphite oxidized in various CO₂-coolant compositions at 41 Bar and 673 K.

#	CO ₂ - coolant composition				Graphite [†]	ρ (g/cm ³)	O.P.V (%)	C.P.V (%)	$R_0^{Exp.}$ (x10 ⁻⁸ kg/Wh)
	CO (%)	CH ₄ (vpm)	H ₂ (vpm)	H ₂ O (vpm)					
3					Pechiney inner sleeve (IS)	1.86	9.1	8.9	0.48 ± 0.03
									0.70 ± 0.08*
					Pechiney OS	1.87	8.5	8.5	0.48 ± 0.05
									0.52 ± 0.02*
					GCMB 2	1.82	9.9	9.6	0.39 ± 0.05
									0.46 ± 0.08*
					GCMB 1	1.82	9.2	10.5	0.29 ± 0.03
									0.40 ± 0.06*
					IM1-24	1.81	10.4	9.5	0.28 ± 0.07
									0.37 ± 0.04*

[†] The dimensions of the graphite specimens for ventilated condition were 36 mm outer diameter with a central hole of 16 mm and 12 mm long, and for unventilated condition solid cylinder of 6.2 mm diameter.

* Unventilated condition

Table B3.2.3. Microstructural characteristics of different type of graphite and their initial measured radiolytic oxidation rate for the bulk CO₂ -coolant composition 0.5%CO/150 vpm CH₄/270 vpm H₂ /260 vpm H₂O in ventilated condition (pressure drop in the range of 35-75 mbar, corresponding to the bottom and top rig assembly respectively).

Graphite	OPV (%)	CPV (%)	PED < 5 μm (OPV %)	PED < 5 μm (%)	R ₀ ^{Exp.} (x10 ⁻⁸ kg/Wh)
IM1-24 (Gilsocarbon)	10.4	9.5	4	39	0.28
GCMB 1 (Gilsocarbon)	9.2	10.5	4	44	0.29
GCMB 2 (Gilsocarbon)	9.9	9.6	5	51	0.39
Pechiney OS	8.5	8.5	7	82	0.48
Pechiney OS (Gilsocoke)	12.4	9.8	9	73	0.61
Union Carbide OS	9.8	8.8	8	82	0.72
EK-76	8.8	9.9	8	91	1.39
EK-78	7.8	9.7	7	90	1.26
HDG	8.4	2.9	8	95	1.28
IG-50	8.7	8.7	8	92	1.29
IG-80	7.9	6.6	7	89	1.31
Carbon Lorraine 1116	11.6	10.3	11	95	1.56
POCO	17.6	3.0	17	97	1.92
Pechiney Sta. Maria Coke	24.9	5.4	14	56	2.24
NBG-10					
NBG-17	9-10				
NBG-18	6				
NBG-25	11				
IG-110					
IG-430					
2124 PT	8				
2320 PT	10				
2160 PT	7				

Some graphite candidates with no information on the PED

Table B3.2.3. Summary of predicted weight losses due to radiolytic oxidation in the entire graphite core and in peak-rated regions

Years	Predicted radiolytic weight loss (%)	
	Mean	Peak-rated regions
5	16.7	38.4
7	26.3	60.3
10	44.8	100

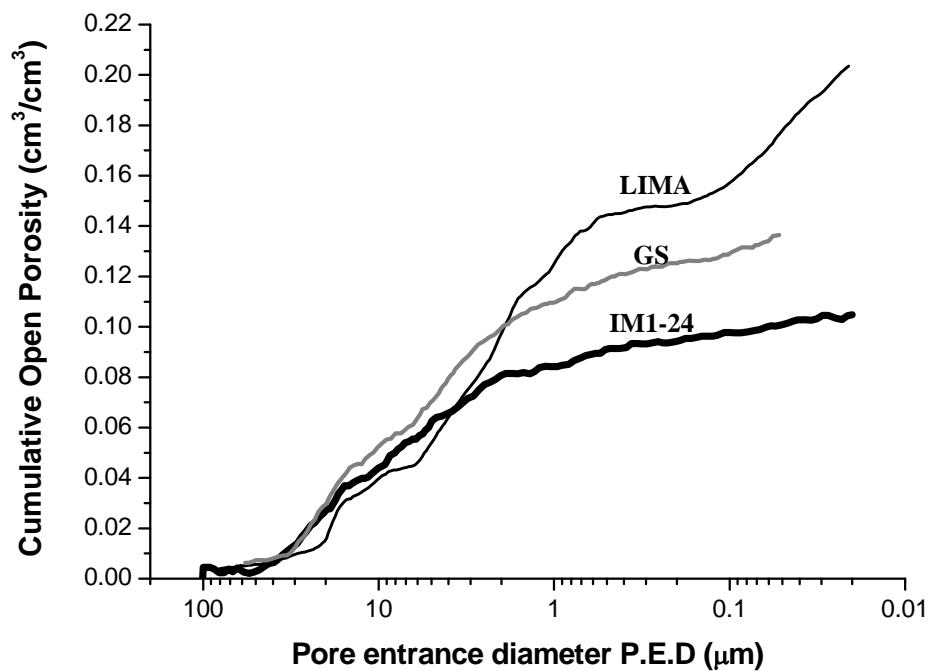


Figure B3.2.1. Mercury pore size distribution curves for virgin LIMA, GS and AGLMP graphite.

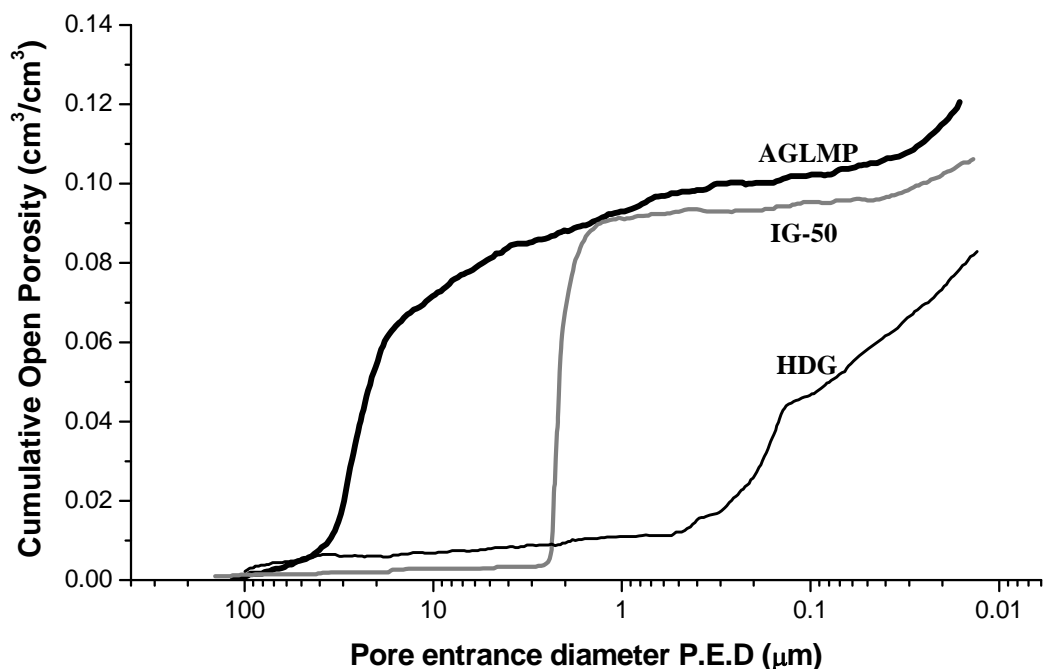


Figure B3.2.2. Mercury pore size distribution curves for virgin AGLMP, IG-50 and HDG graphite.

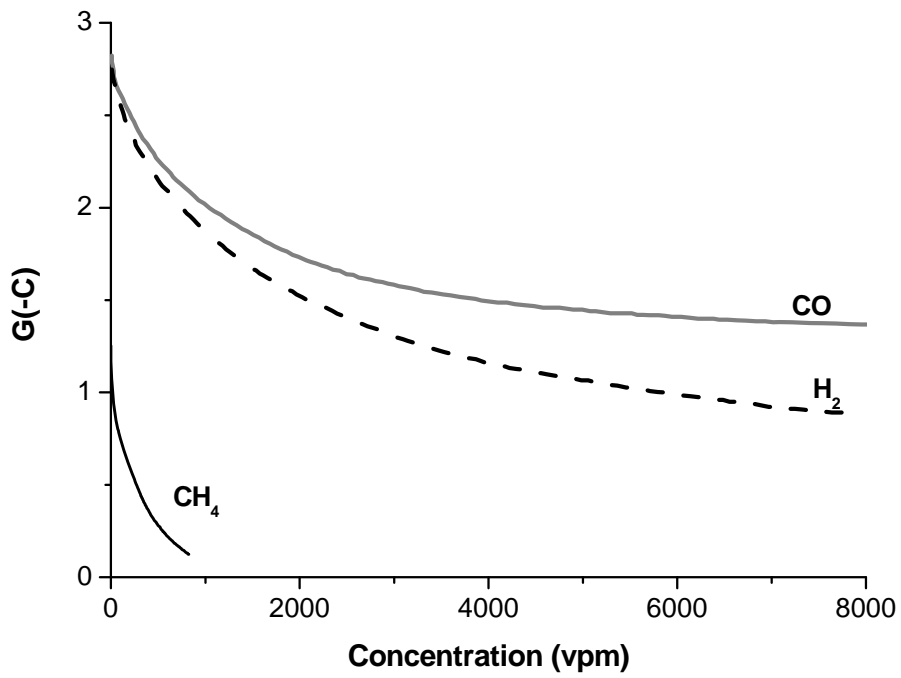


Figure B3.2.3. The gas-phase inhibiting effect of carbon monoxide, hydrogen and methane on graphite oxidation.

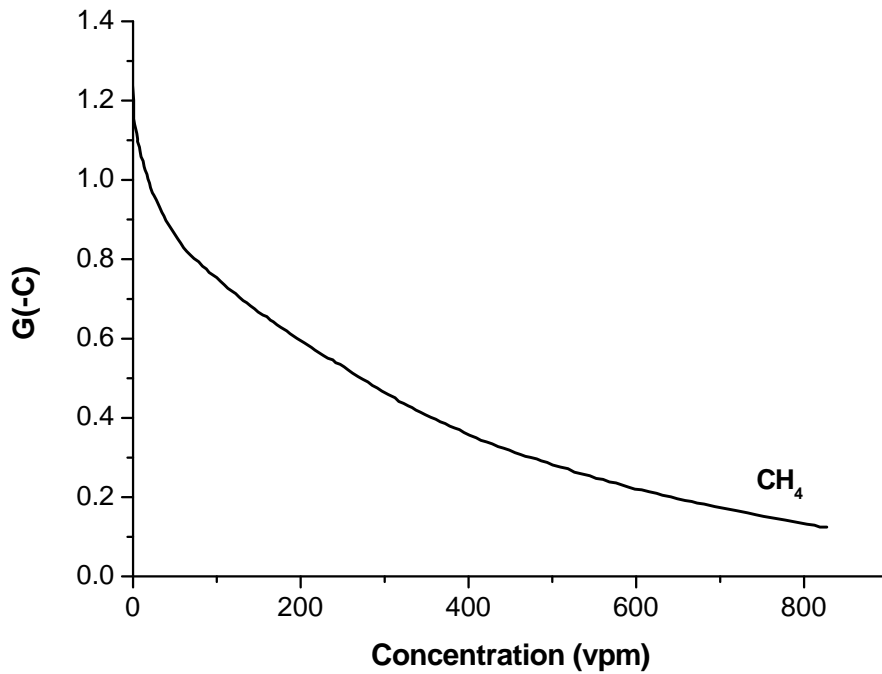


Figure B3.2.4. The inhibiting effect of methane on graphite oxidation for a 1.2% CO/CO₂ gas mixture.

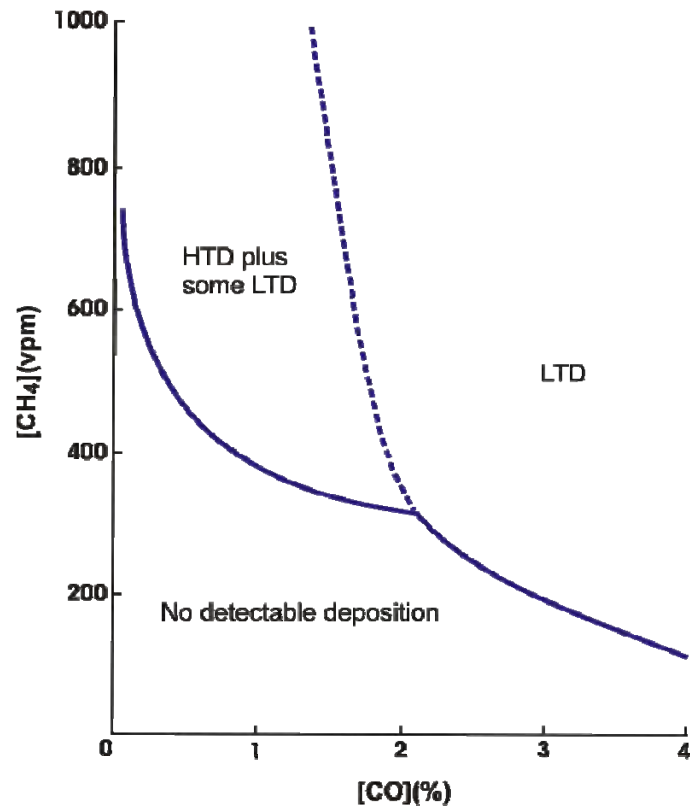


Figure B3.2.5. Relative initial deposition rates in WAGR coolant tests indicating a probable deposition threshold (solid line) and HTD/TD boundary (broken line).

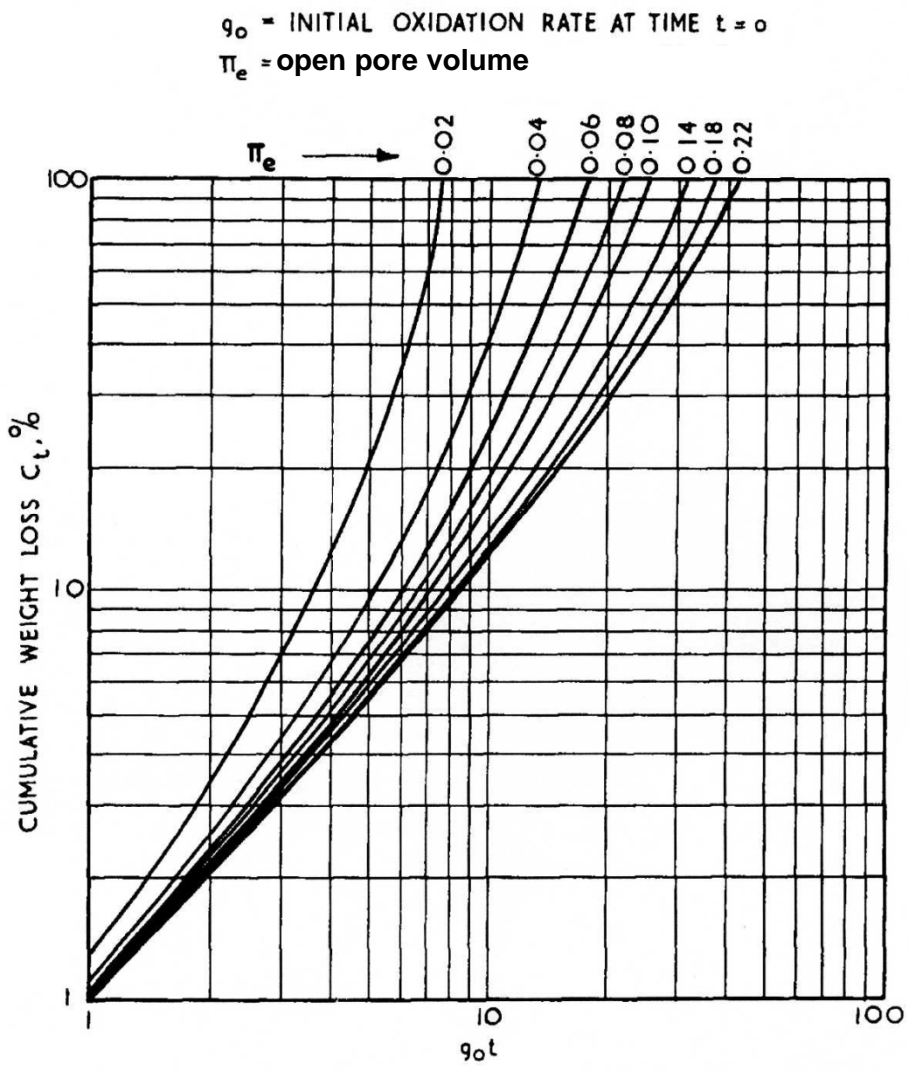


Figure B3.2.6. Effect of increase in porosity on cumulative weight-loss when dose rate to gas is constant.

g_0 = INITIAL OXIDATION RATE AT TIME $t = 0$

π_e = open pore volume

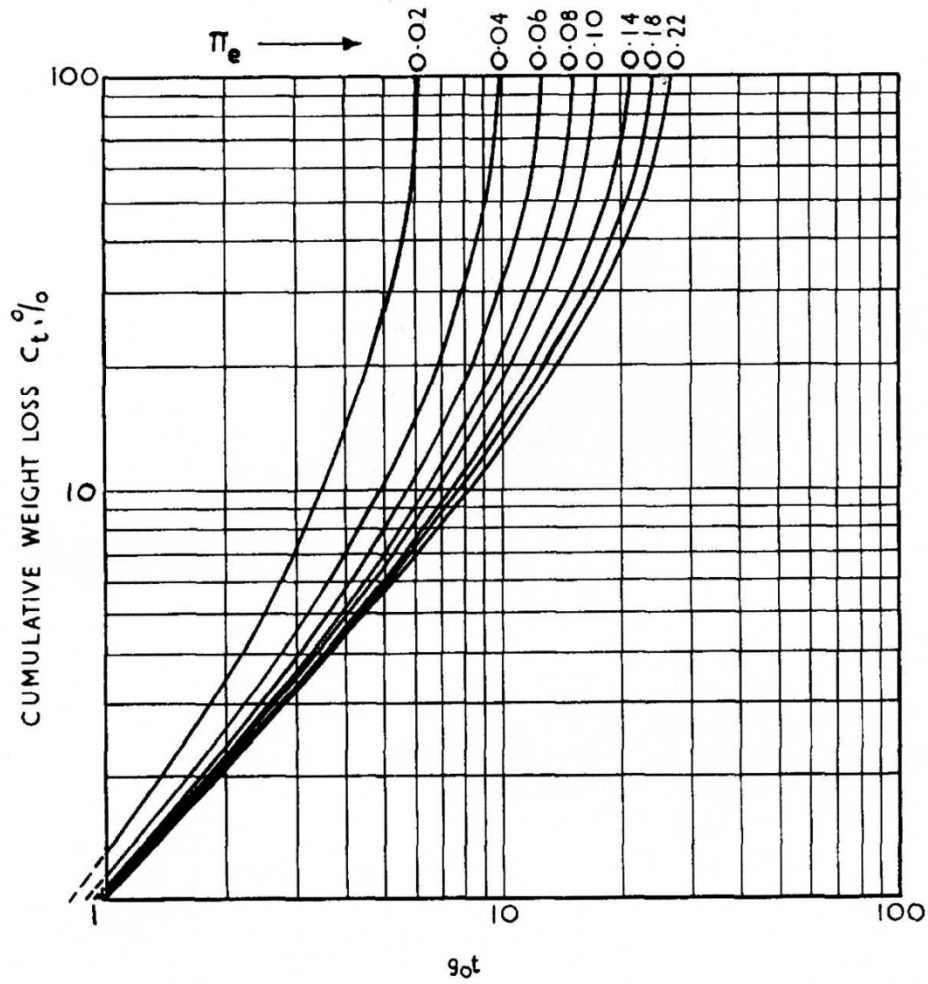


Figure B3.2.7. Effect of increase in porosity on cumulative weight-loss for a reactor operated at constant power.

B2.4 Thermal Oxidation of Nuclear Graphite

The thermal-oxidation reaction of potential interest in the U-Battery[®] concept is the simple chemical reaction between graphite and CO₂ and it becomes important only at temperatures above about 450°C.

The oxidation of graphite at different temperatures is governed by three regimes: the chemical-control regime, the in-pore diffusion-controlled regime and the boundary-layer controlled regime. At lower temperatures (Mode I), the oxidation rate is solely controlled by chemical kinetics (reactivity). The reaction between oxidising gas and graphite occurs relatively slowly. The concentration of oxidising gases is nearly uniform through the depth of penetration although different parts of the graphite microstructure may react at different rates. For example, the binder is more reactive than the grit particles, and edge atoms are more reactive than basal plane atoms^[1, 2]. Further, the reactivity of graphite varies depending on the source coke type; graphite made of petroleum coke shows faster weight loss than that made of pitch cokes^[3].

On the other hand, at high temperatures (Mode III), the rate of consumption of oxidant is so high that all the oxidising gases react at the surface of the component or sample. The concentration gradient of oxidising gases at the graphite surface is high. The oxidising attack is severe at the exterior surface of the graphite block and changes the geometry of the graphite body without significantly changing the material in the interior.

In the in-pore diffusion-controlled regime (Mode II), which is between the chemical regime and the boundary-layer controlled regime, the oxidation rate is controlled by a combination of in-pore diffusion and chemical kinetics. In this regime, the concentration of reactant and therefore burn-off varies exponentially in depth, giving rise to what is known as an oxidation burn-off (weight loss) profile^[4, 5]. For integrity purposes of the nuclear graphite, the thermal oxidation mechanism or regime that affects the most is the chemical regime, where higher weight loss in the interior of the graphite than at the surface is encountered.

The temperature limits for each regime depends on the oxidising gas, pressure, sample size, density and type of graphite^[5, 6]. Nevertheless, in text books it can be found that for the carbon dioxide-graphite system, Mode I conditions prevail from about 650°C, where the thermal reaction becomes ‘significant’, to 900 or 950°C^[7]. The transition from Mode I to Mode II is gradual and extends to approximately 1250°C for spectroscopic carbon in CO₂ at 1 atm. Additionally, we should note that references to “threshold oxidation temperature” can be found in the literature (and in manufacturer’s literature, and, for general purpose graphite in CO₂, is nominally quoted as 900°C. However, this “threshold oxidation” refers to a graphite sample losing approximately 1% of its weight in 24 hr^[8], which implies a rather high oxidation rate of 416.66 μg g⁻¹ h⁻¹, and is therefore not a threshold at all. This rate is excessively high for purposes of integrity of graphite in a nuclear reactor with a desired operation of at least 5 years.

During thermal oxidation in CO₂-based gas mixtures, most graphites exhibit an increase in reactivity (*i.e.* oxidation rate) during the first 1-2% weight loss^[9].

The most significant change in the microstructure of anisotropic and isotropic nuclear graphite during thermal oxidation is the development of narrow, slit-shaped pores in the

binder phase and the enlargement of already existing cracks. The development of slit-shaped pores is attributed to the difference in reactivity of the carbon atoms located at the edges of basal planes compared with those carbon atoms within the basal planes ^[10]. Thus, the oxidation of the basal planes exposed at the walls of the pores is very much slower than oxidation of the edge carbon atoms exposed at the ends of the pores, resulting in elongation of the pores rather widening during thermal oxidation.

It has been found that thermally oxidised graphite to ~ 6% weight loss contain three times more small pores of about $5 \mu\text{m}^2$ than the unoxidised material ^[10].

Thermal Oxidation Rates of various Graphites in CO₂ Gas

The thermal oxidation rate of graphite increases with graphite weight loss and thus, the surface area increases with time. However, it has been observed that the rate is relatively constant at a given temperature when a weight loss of 10% is reached ^[9, 11].

Several researchers have carried out experiments of thermal oxidation of graphite in CO₂ with and without the presence of CO. Stephen ^[12] obtained oxidation rates (Tables B2.4.1 and B2.4.2) of a unipore graphite (Morganite Grade EYC9106) with pore size ranging from 5-8 μm at a temperature range of 851-987 °C, pressure of 41 bar and gas compositions of 5.6 and 22.5%CO/CO₂. The oxidation behaviour of the graphite was fitted to the Arrhenius equation. Thus, the parameters of the Arrhenius equation can be obtained for each CO/CO₂ composition and subsequently, extrapolate the data for a composition of CO₂ gas containing 0.5, 1 and 1.5% CO. Higher CO contents are to be expected to build up in a closed system. The thermal oxidation rates for 0.5, 1 and 1.5% CO at 41 bar between 750 and 900°C are depicted in Table B2.4.3.

In addition, Board ^[13] obtained oxidation rates for PGA at ~ 15 Bar, from 700-800°C in pure CO₂ and 0.7% CO/CO₂ (Table B2.4.4). Two additional sets of tests were carried out to determine the effect of CO content and pressure on the oxidation rate. The inhibiting power of CO is clearly shown in Table B2.4.5 and, at pressures above 3 bar, the oxidation rate is relatively similar (Table B2.4.6).

At higher temperatures, Turkdogan *et al.* ^[11] found that the oxidation of an electrode graphite (density: 1.69 g cm^{-3} , porosity $\epsilon = 0.19$ and O.P.V= 0.11) with a weight loss of 10% at 900°C and 40 bar was $8400 \mu\text{m g}^{-1} \text{ h}^{-1}$.

Similarly to the results of Board ^[13], Turkdogan data ^[6] revealed that the oxidation rates were similar at pressures of 10, 20 and 30 bar, in other words, the oxidation rate was independent of pressure at high operating pressures (> 10 bar). It was suggested that at high pressures molecular diffusion predominates and that the lack of gas diffusion through the pores becomes the rate-controlling process.

It is important to note that the oxidation rates given in Tables B2.4.1-6 are comparable amongst the nuclear graphites (*e.g.* unipore graphite and PGA) since the specific surface areas are in the range of $0.16\text{-}0.20 \text{ m}^2\text{g}^{-1}$. Note that values of thermal oxidation rate for a given temperature of about five times higher than that given in the present report can be found in the literature ^[11, 14]; however, the values correspond to graphite granules with a geometric surface area of five times higher than that of nuclear graphites.

Effect of Thermal Oxidation on the Physical and Mechanical Properties of Nuclear Graphite

It is well known that, for a given weight loss, the thermal oxidation of nuclear graphite in Mode 1 conditions causes a greater change in mechanical properties than radiolytic oxidation^[15]. This is illustrated by the mechanical strength, since graphite samples with a thermal weight loss of ~ 40% frequently crumble away when gently handled^[16]. In addition, the change in property value for a given weight loss is independent of the oxidising gas used^[16]. Radiolytically oxidised samples to the same weight loss retain a greater residual strength.

The mode of failure of thermally oxidised graphite is the same as for the unoxidised material up to a weight loss of 5%. Fracture occurs by the linking of pores by cracks through the large grains, resulting in the failure of graphite at a constant strength/strain rate. However, at higher burn-off the preferential attack of the fine-grained material (*i.e.* binder) results in cracks propagating through the binder and more particularly along grist-binder boundaries. This change in the mechanism of crack propagation is not reflected in the change in the strain to failure; instead, it appears to remain relatively constant up to weight losses of ~ 20%^[2].

The empirical equations that provide the tendency of a mechanical property to change with thermal weight loss are given below.

Young's Modulus

The effect of thermal weight loss on the dynamic Young's Modulus can be fitted the Knudsen equation with a b value of 7^[15]. Note that this value is higher than that obtained for the effect of radiolytic weight loss on the modulus (*i.e.* $b=3.4-4.8$).

Compressive Strength

The predictive equation for the strength change in AGR moderator graphite is described by the Knudsen relationship (B2.2 equation 42) of the form:

$$\frac{\sigma}{\sigma_0} - 1 = \exp(-bx) - 1 \quad (1)$$

where σ_0 is the compression strength for zero weight loss, b is an exponent (determined experimentally) and x is the fractional weight loss.

Neighbour *et al.*^[17] found that b is 6.4 for IM1-24 and 8.4 for GCMB. The results are within 3 % uncertainty.

References to Section B2.4

[1] A. Blanchard, "Appendix 2 - The Thermal Oxidation of Graphite", IAEA, TECDOC-1154 (2000)

- [2] J. A. Board, R.L. Squires, "The effect of oxidation in CO₂ on graphite strength", Proceedings Second Conference on Industrial Carbon and Graphite (1966) London, Soc. Chem. Ind., 289-298.
- [3] S.-H. Chi, G-C. Kim, *Journal of Nuclear Materials* 381 (2008) 9-14.
- [4] Y.-S. Lim, S-H. Chi, K-Y Cho, *Journal of Nuclear Materials* 374 (2008) 123-128.
- [5] L. Xiaowei, R. Jean-Charles, Y. Suyuan, *Nuclear Engineering and Design* 227 (2004) 273-280.
- [6] E. T. Turkdogan, J.V. Vinters, *Carbon* 7 (1969) 101-117.
- [7] R. E. Nightingale, "Nuclear Graphite", Academic Press (1962) pp. 402.
- [8] C. L. Mantell, "Carbon and Graphite Handbook", John Wiley & Sons (1968) pp. 350.
- [9] W. J. Stephen, T. Swan, "The Influence of Structure on the High Temperature Thermal Oxidation of Reactor Graphites", Central Electricity Generating Board, RD/B/N4063, RPC/CGC/M2/P(77)45 (1978)
- [10] I. M. Pickup, B. McEnaney, R.G. Cooke, *Carbon* 24 (1986) 535-543.
- [11] E. T. Turkdogan, V. Koump, J.V. Vinters, T.F. Perzak, *Carbon* 6 (1968) 467-470.
- [12] W. J. Stephen, "The "Compensation Effect" in the Graphite/CO₂ Reaction", Central Electricity Generating Board, TPRD/B/0248/N83 (1983)
- [13] J. A. Board, "The thermal oxidation of nuclear graphite in carbon dioxide", Proceedings Second Conference on Industrial Carbon and Graphite (1966) London, Soc. Chem. Ind., 277-288.
- [14] J. D. Blackwood, *Australian Journal of Applied Science* 13 (1962) 199-206.
- [15] T. D. Burchell, I.M. Pickup, B. McEnaney, R.G. Cooke, *Carbon* 24 (1986) 545-549.
- [16] C. Rounthwaite, G.A. Lyons, R.A. Snowdon, "Influence of thermal corrosion on the strength, permeability and frictional properties of nuclear graphite", Proceedings Second Conference on Industrial Carbon and Graphite (1966) London, Soc. Chem. Ind., 299-318.
- [17] G. B. Neighbour, P.J. Hacker, *Materials Letters* 51 (2001) 307-314.

Table B2.4.1. Oxidation rates of a unipore graphite (pore size range 5-8 μm) with weight loss of 10% at 41 bar in a gas mixture of 5.6 %CO/CO₂^[12].

Temperature (°C)	Oxidation Rate ($\mu\text{g g}^{-1} \text{h}^{-1}$)
851	57
866	101
885	182
902	374
913	551
914	657

Table B2.4.2. Oxidation rates of a unipore graphite (pore size range 5-8 μm) with weight loss of 10% at 41 bar in a gas mixture of 22.6 %CO/CO₂^[12].

Temperature (°C)	Oxidation Rate ($\mu\text{g g}^{-1} \text{h}^{-1}$)
920	303
932	446
934	557
955	790
967	1193
987	3700

Table B2.4.3. Extrapolated oxidation rates of a unipore graphite (pore size range 5-8 μm) with weight loss of 10% at 41 bar in a gas mixtures 0.5 %CO/CO₂, 1 %CO/CO₂ and 1.5%CO/CO₂.

T (°C)	Oxidation rate in 0.5%CO/CO ₂ ($\mu\text{g g}^{-1} \text{h}^{-1}$)	Oxidation rate in 1%CO/CO ₂ ($\mu\text{g g}^{-1} \text{h}^{-1}$)	Oxidation rate in 1.5%CO/CO ₂ ($\mu\text{g g}^{-1} \text{h}^{-1}$)
750	6.7	3.4	2.3
800	65	33	22
820	152	77	52
850	515	261	176

900 3441 1743 1177

Table B2.4.4. Oxidation rates of PGA graphite at ~ 15 Bar in pure CO₂ and 0.7%CO/CO₂^[13].

T (°C)	Weight loss (%)	Oxidation rate in Pure CO ₂ (µg g ⁻¹ h ⁻¹)	Oxidation rate in 0.7%CO/CO ₂ (µg g ⁻¹ h ⁻¹)
700	0.50		2.48
	10	48	
750	0.50		13
	7	161	
800	2.5		62
	3	533	

Table B2.4.5. Oxidation rates of PGA graphite at ~ 15 Bar and 800°C in 2.8%CO and 7.8%CO/CO₂^[13].

%CO/CO ₂	Weight loss (%)	Oxidation rate at 800°C (µg g ⁻¹ h ⁻¹)
2.8% CO	1.5	30
	10	94
7.8% CO	1.7	15
	5	27

Table B2.4.6. Oxidation rates of PGA in pure CO₂ at 800°C and various pressures^[13].

Pressure (bar)	Oxidation rate at (µg g ⁻¹ h ⁻¹)
3	510
7	490
10	620
14	510

B2.5 Graphite Waste

Introduction

Given the generally large delays in planned waste repositories capable of receiving irradiated graphite wastes, it is appropriate here to record the present status of planning and research in relation to the potential disposal of graphite blocks and fuel compacts from the U-Battery.

From those nations with graphite-moderated reactors, only France has formally considered the disposal of graphite as a specific waste stream, initially planning a shallow burial site for the graphite from the UNGG and earlier development reactors along with ‘radium-bearing wastes’. This formal intention, thoroughly investigated by ANDRA at the behest of the French government, has run into difficulties in two respects: (i) concerns about the potential movement within the environment of weak beta emitters (^{36}Cl , which arises from the purification process of older graphite stocks, and ^{14}C , whose production is inevitable even in a helium coolant through the reaction $^{13}\text{C}[\text{n},\gamma]^{14}\text{C}$); and unwillingness on the part of local communities to sanction suitable sites. As a consequence, French officials have admitted in EU FP7 project meetings that either a ‘deeper’ solution must be adopted, or an alternative process which in some way takes ‘advantage’ of the specific chemical and physical properties of graphite.

Ironically, at the same time, the UK authorities (NDA) are considering a move in precisely the opposite direction for graphite, and it is felt that this is extremely unlikely to succeed. However, this plan would not be a short-term solution, since the official UK position remains to leave the graphite within the pressure vessels of the former commercial reactors for up to 130 years, although there are powerful arguments to avoid this strategy. Russia is taking the same view and proposing long-term ‘safe storage’, whilst at the US Hanford site, initial plans to bury the graphite within the Hanford reservation have met with objections related to the quantities of radioisotopes contained within the material: several reactors have been secured for long-term review, whilst the recent plan to fully dismantle one reactor (KE) as a demonstration has now been set back at least one year.

Noting these positions, and also the lack of progress for the Japanese and Italian Magnox reactors and plant in other countries of the former Soviet Union, the only country which is pressing ahead with a determination to achieve full reactor dismantling is Lithuania. One of the present Manchester team (AJW) is closely engaged with this process, along with a number of other important initiatives which have been taken to secure ‘lateral thinking’ and alternative strategies for dealing with graphite wastes.

In the specific case of U-Batteries which have been active for a number of years and the cores then decommissioned, it is presumed that, in common with other ‘prismatic HTR’ designs, the fuelled and un-fuelled blocks can all be removed with relative ease from the vessel by a mechanical process. This does not rule out some other options which are discussed below, but intimates that the blocks from this project would not introduce any specific problems relating to the design: indeed, the smaller scale of the vessel implies a relatively simple task (and reasonable costs) in comparison with a full-scale plant.

We therefore give here a brief review of the various initiatives which have taken place – and will continue to take place – in this topic area, along with a list of the options for disposal and subsequent treatment, of the graphite.

Graphite Dismantling and Disposal Initiatives

In addition to the research and development programmes within individual nations, three important international organisations have involved themselves with this issue.

Firstly, the International Atomic Energy Agency has commissioned a number of meetings and activities relating to the graphite irradiation and disposal lifecycle. The first activity was a general discussion meeting in 1995 held in the UK^[1], and this was followed by a further conference more focussed on the disposal issues, hosted by Manchester University in 1999^[2]: at this meeting a number of very useful papers were discussed. The meeting served to highlight areas in which essential knowledge was poor – such as in the leaching behaviour of graphite in aqueous environments – and introduced some alternative options for treatment and disposal. With the benefit of hindsight, some assertions made in papers presented there have been shown to be inaccurate, but this was nonetheless a most valuable meeting which was followed up in 2007 by a further meeting, also held in Manchester^[3], which debated the ability to speed up the decommissioning process and also had the benefit of focussed discussions on both alternative technologies, their relative economic benefits, along with environmental and public-opinion issues.

In parallel with these activities, an IAEA review report on dealing with radioactive graphite was produced which drew together the deliberations of a Technical Meeting held in October 1999 and those of a subsequent technical discussion held at IAEA Vienna in 2000: this report was subsequently re-edited and issued in 2006^[4]. This was the first significant document which reviews options other than deep-repository disposal for irradiated graphite and, after a period in which these and other options have been further considered and investigated, the IAEA has now established a Collaborative Research Programme with the title “Treatment of Irradiated Graphite to Meet Acceptance Criteria for Waste Disposal” which one of us (AJW) will lead as Chief Scientific Investigator. It is expected that this activity will commence at the end of 2011 and will last for four years.

The second major activity, in which Manchester University is one of 29 participating organisations from within Europe and the wider community, is the EU FP7 ‘CARBOWASTE’ project. This seeks to identify and characterise existing wastes, whilst exploring a number of potential ‘treatments’ which will include the treatment and disposal of ‘TRISO’ fuel particles and compacts or ‘pebbles’ containing them as well as conventional irradiated-graphite stocks. This project is now in its third year (of four) and has made important advances in areas such as the mobilisation of radioisotopes from graphite (particularly ¹⁴C), the use of microbiological processes to release activity, and the identification and investigation of other potential retrieval processes. This work will eventually be published through the EU route.

Finally, there is the EPRI ‘Graphite Decommissioning Initiative’, in which (again) one of us (AJW) has been closely involved. This commenced in 2006 with the publication of a general review document^[5] on potential options and has been followed with detailed investigations of graphite dust explosibility and its relevance in plant dismantling^[6] (there is also a key paper on this in^[3] which also has direct relevance to the U-Battery and is here referenced

separately^[7]); graphite leaching issues^[8]; pressure-swing absorption and other techniques for improving the efficiency of the recovery of isotopes from irradiated graphite^[9]; a detailed investigation of the nature and potential release of ¹⁴C in graphite^[10] (a similar investigation relating to ³⁶Cl and ³H is now in progress); and finally the so-called ‘nibble-and vacuum’ process for graphite recovery from within the plant^[11] (on the basis that if intact blocks are not required for a subsequent process, then crumbling the material and literally ‘hoovering it up’ is an efficient and cheap means to recover the material from the reactor). Trials utilising concrete and individual graphite components have already been successfully completed, and it is intended that a trial with a larger assembly of graphite will be conducted shortly. Moving the graphite as a suspended foam has also been mooted^[12].

This last topic also raises the issue of how intact blocks should be retrieved, if that is the intention. Three graphite reactors have so far been dismantled. Two of these were in the UK – the very low energy GLEEP pile, which was (effectively) dismantled by hand and is non-representative of a power reactor, and the Windscale prototype AGR, which was dismantled mechanically with the blocks removed through the pressure vessel into containers which were then retrieved through the building dome and transferred to a temporary storage in a newly-constructed building. This was a very successful demonstration of direct mechanical dismantlement, but it could be argued that, with no subsequent onward route for the material, ‘risk’ would have been minimised by leaving the graphite within the pressure vessel.

The Fort St. Vrain HTR-reactor graphite and fuel blocks were also recovered mechanically^[13], but with water used as a radiation shield (the vessel being so filled). This was not as a consequence of radiation from the graphite components, but from other internal components. These items are also now in a temporary store. The underwater route is planned for some of the French UNGG plant. It is believed that this decision was originally taken upon the spurious grounds of graphite-dust explosibility risks, but the most recent justification relates to radiation shielding and cost savings, although this is difficult to equate with the additional water-treatment plant, inclusive of resin beds, which must be disposed of, and the complications of short-term leaching of radioisotopes from the graphite still in-core.

It should be noted that other chemical methods for removal of graphite might be considered, such as utilisation of oxidation by high-temperature steam^[14]. This reaction to produce carbon monoxide and hydrogen is endothermic, which means that the rate can easily be controlled since a constant input of energy is required to maintain it. However, that in turn implies a high energy cost overall although, once dealt with this way, there are obviously no on-going storage and disposal costs for the graphite.

It appears very clear that the chosen route for dismantling of U-Battery components should strongly depend upon the preferred options for subsequent handling of the graphite.

Graphite Treatment and Utilisation

Direct incineration of graphite was investigated nearly twenty years ago by Framatome, who constructed a successful pilot plant^[15] operating on the fluidised-bed principle. This methodology has fallen out of favour, largely based upon concerns about the consequent ¹⁴C emissions, despite a very favourable calculation indicating that the consequences of incinerating one Magnox-reactor core per year for 20 years would impact upon the global ¹⁴C concentration by less than one part in 1000^[16]. Of course, local dose issues arise close to the site of any incineration plant.

Interestingly, it has subsequently been noted that ^{14}C (and ^3H too) can readily be mobilised from irradiated graphite by heating in various atmospheres, and this offers both a means towards reducing the activity of graphite ahead of disposal and also an option to recycle the ^{14}C rather than produce new supplies from the irradiation of aluminium nitride. Use of this property has been made of in disposal of graphite from the GLEEP reactor at Harwell UK, and the process is being investigated thoroughly at Forschungszentrum Jülich as part of the CARBOWASTE project.

Misplaced concern over weak beta-emitting nuclides extends to ^{36}Cl which, with a half-life of 300,000 years, is unlikely to contribute significantly to background dose or to personnel dose unless highly concentrated in certain organisms or vegetation (as is alleged). Ironically, it was demonstrated recently that this isotope is already highly mobile in irradiated graphite, being lost to the atmosphere upon grinding and even upon standing in air^[17].

In the unlikely event of fuel failures in the U-Battery leading to significant contamination of irradiated graphite, two different vitrification techniques have been developed in Russian institutions using direct chemical reactions of the irradiated material, although these lead to overall volume increases in material. The full range of techniques available was recently summarised^[18] but will again be reviewed and investigated further as part of the forthcoming IAEA Collaborative Research Programme.

Recycling of irradiated graphite, probably via an amorphous carbon intermediate, has been under investigation by two major graphite manufacturers as part of the CARBOWASTE programme. A number of different carbonaceous materials for the nuclear industry (not only graphite for future HTRs) may possibly be produced in the future in this manner, avoiding the creation of stocks of new material to add to the overall waste burden.

Conclusions

As with any new-build nuclear plant, it is necessary to demonstrate a clear plan in advance to deal with reactor decommissioning. It is considered on the basis of existing information and experience that the U-Battery graphite core can safely be dismantled, and that the graphite and carbon-containing fuel wastes will not present any particular issues in handling and disposal which will not be addressed by the wider national and international programmes in support of dealing with the existing quarter-million tonnes of irradiated graphite materials.

References to Section B2.4

- [1] IAEA, "Graphite Moderator Lifecycle Behaviour"; Proceedings of a Specialists' Meeting, Bath, United Kingdom, September 1995, IAEA-TECDOC-901 (pub. 1996)
- [2] IAEA, "Nuclear Graphite Waste Management"; Proceedings of a Technical Committee Meeting, Manchester, United Kingdom, October 1999, IAEA-NGWM/CD (pub. 2001)
- [3] IAEA, "Progress in Radioactive Waste Management"; IAEA-TECDOC-1647, 2010

- [4] IAEA, “Characterization, Treatment and Conditioning of Radioactive Graphite from Decommissioning Nuclear Reactors”; IAEA-TECDOC-1521, 2006
- [5] D. Bradbury and A.J. Wickham (*principal investigators*), “Graphite Decommissioning: Options for Graphite Treatment, Recycling or Disposal, including a discussion of Safety-Related Issues”; EPRI, Palo Alto, CA, 2006, 1013091
- [6] D. Bradbury and A.J. Wickham (*principal investigators*), “Graphite Dust Deflagration: A Review of International Data with Particular Reference to the Decommissioning of Graphite Moderated Reactors”; EPRI, Palo Alto, CA, 2007, 1014797 and “Graphite Dust Deflagration: Ignition and Flame-Propagation Data – Supplement to EPRI Technical Report 1014797”; EPRI Palo Alto CA, 2007, 1015460
- [7] A.J. Wickham and L. Rahmani, “Graphite Dust Explosibility in Decommissioning – A Demonstration of Minimal Risk”; *in [3] (CD supplement of presented papers)*
- [8] D. Bradbury and A.J. Wickham (*principal investigators*), “Graphite Leaching: A Review of International Aqueous Leaching Data with Particular Reference to the Decommissioning of Graphite Moderated Reactors”; EPRI, Palo Alto CA, 2008, 1016772
- [9] D. Bradbury and R. Mason (*principal investigators*), “Program on Technology Innovation: Graphite Waste Separation”; EPRI, Palo Alto Ca, 2008, 1016098
- [10] A.J. Wickham (*principal investigator*), “Carbon-14 in Irradiated Graphite Waste: A Study of the Formation and Distribution of C-14...”; EPRI, Palo Alto CA, 2010, 1021109
- [11] D. Bradbury (*principal investigator*), “Innovative Graphite Removal Technology for Graphite Moderated Reactor Decommissioning: ‘Nibble and Vacuum Feasibility Study’”, EPRI Palo Alto CA, 2010, 1021110
- [12] L. Rahmani and A.J. Wickham, “Irradiated Graphite Waste Disposal by Aqueous Foam Injection into a Geological Formation”; paper presented at INGS-10, West Yellowstone, USA, 2009 (available from IAEA International Knowledge Base on Nuclear Graphite, www.iaea.org/NuclearPower/Graphite)
- [13] M. Fisher, “Fort St. Vrain Decommissioning Project”; *in* “Technologies for Gas-Cooled Reactor Decommissioning, Fuel Storage and Waste Disposal: Proceedings of a Technical Committee Meeting, Jülich, Germany, September 1997”, IAEA-TECDOC-1043, pub. 1998, pp. 123 – 131
- [14] R. Mason and D. Bradbury, “Pyrolysis and its Potential Use in Nuclear Graphite Disposal”; *Nuclear Energy*, **39**, 2000, pp. 305 – 310
- [15] J.J. Guirouy, “Graphite Waste Incineration in a Fluidised Bed”, *in* “Graphite Moderator Lifecycle Behaviour”, IAEA-TECDOC-901, 1996, pp. 193 – 203
- [16] S. Nair, “A Model for the Global Dispersion of ^{14}C Released to the Atmosphere as CO_2 ”; *J. Radiological Protection*, **3**, 1983, pp. 16 – 22

[17] L. Rahmani, “Chlorine Degassing from Nuclear Grade Graphite”; paper presented at INGS-6, Chamonix, France, 2005 (available from IAEA International Knowledge Base on Nuclear Graphite, www.iaea.org/NuclearPower/Graphite)

[18] A.J. Wickham, “New Directions in Treatment Options for Irradiated Graphite Waste”; presented at Nuclear 2011, Institute for Nuclear Research, Pitești, Romania, May 2011 (available on Proceedings CD)

B2.6 Non-graphite components - Beryllium

Introduction

Due to its low thermal neutron absorption cross-section, large scattering cross-section (Table B2.6.1), high melting point, and good strength, beryllium (Be) has been a candidate material for moderators and reflectors in a number of reactor designs. However, because of the high cost and issue of toxicity, beryllium has only been used in research reactors in the Netherlands, Russia, US, France, and Japan. Beryllium oxide (BeO) has larger scattering and absorption cross-sections (Table B2.6.1) and has previously been considered as a suitable material for moderators and fuel matrix; it is currently being considered as a reflector in the 5 MWth U-Battery, a moderator and reflector material in the Compact High-Temperature Reactor (CHTR)^[2], and as a reflector in the Sected Compact Space Reactor (SCoRe)^[3].

Table B2.6.1 Neutron properties of common solid moderators/reflectors^[1].

Property	Beryllium (Be)	Beryllium oxide (BeO)	Graphite (C)
scattering cross-section σ_s (10^{-24} cm ²)	6.15	11.2	4.75
absorption cross-section σ_a (10^{-24} cm ²)	7.6	9.0	3.53

Manufacture

Beryllium oxide (also known as beryllia, and historically as glucina or glucinium oxide) is a refractory material that can be obtained through the processes used to extract beryllium from beryllium ores. There are two main processing routes; one using fluoride^[4] and one using sulphuric acid^[5]. Both routes produce beryllium hydroxide that can be reduced to beryllium oxide by heat-treating at 1800°C. As the resulting product is not suitably pure for use in a reactor, the oxide is purified by dissolving it in sulphuric acid, removal of the impurities by precipitation, crystallisation of beryllium sulphate, and then a final calcination at 1150°C to produce a high purity oxide. An alternate process is to convert the beryllium hydroxide to beryllium acetate using acetic acid, and then to distil and decompose this to give oxide powder.

Beryllium oxide components can be manufactured using standard powder metallurgy processes, although care must be taken as beryllium oxide powder is a carcinogenic. Components can be formed from the beryllium oxide powder using hot or cold pressing techniques (plus sintering in the case of cold pressing) and a pre-firing binder agent. If the components require machining, pre-firing temperatures range from 1200 to 1500°C, and after machining, there is a final heat treatment to 1700 to 2000°C. The process temperature, time at temperature, and pressure used have been shown to have an effect on the grain size and/or density of the material^[6,7]; an increase in time or temperature increases the grain size, and an increase in pressure, increases the density. This has consequences on the unirradiated and irradiated material properties and behaviours.

Unirradiated properties

Typical unirradiated material properties for beryllium oxide (compared with graphite) are shown in Table B2.6.2. However, these properties can be highly dependent upon the final density of the component. Young's modulus and thermal conductivity increase with increasing density, strength decreases with increasing density, and CTE is insensitive to changes in density^[8]. It has also been shown that larger grain sizes reduce the strength and modulus of the material^[12,13] but do not affect the CTE^[13].

Table B2.6.2 Typical unirradiated properties for beryllium oxide and graphite at room temperature.

Property	Beryllium oxide ^[1,8,10,11]	Graphite ^{[1,9]†}
	(BeO)	(C)
density (g/cm ³)	2.86	1.81
thermal conductivity (W/m k)	93	131
coefficient of thermal expansion (10 ⁻⁶ K ⁻¹)	5.5	4.3
dynamic Young's modulus (GN/m ²)	379	11
flexural strength (MN/m ²)	151	23
tensile strength (MN/m ²)	98	18
compressive strength (MN/m ²)	784	70

†Graphite grade IM1-24 (Gilsocarbon) was used as a "prototypic" graphite.

The material properties, including CTE, are temperature dependent. The Young's modulus exhibits a gradual decrease at lower temperature and then a rapid reduction at ~1200°C^[10]. Thermal conductivity initially reduces with increasing temperature and then there is a reduction in the rate of change and the thermal conductivity starts to increase^[10]. CTE shows a non-linear increase with increasing temperature^[10,13]. The flexural strength behaves similarly to Young's modulus with there being a small change at lower temperatures and a rapid decrease at higher temperatures^[10,13,14].

At higher temperatures (1200°C and above) beryllium oxide has been shown to exhibit creep in compression, tension, and bending^[10,13,15,16]. In compression, the creep rate increases as the temperature or applied load increases, and decreases if the grain size of the material increases^[13,15]. In tension, experiments have shown the creep rate to be similarly dependent upon temperature and applied load i.e. an increase in either will increase the creep rate^[10]. In bending, experiments^[16] have demonstrated the creep rate to also be a function of temperature, applied load, and grain size as per compression.

Irradiated properties

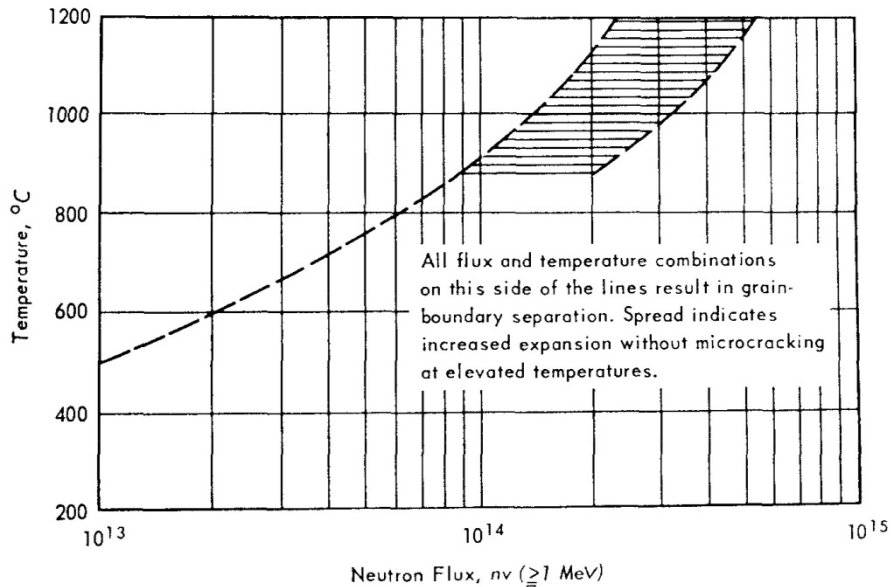
When irradiated with fast neutrons, the volume of beryllium oxide expands almost linearly with an increase in the irradiation temperature, reducing the rate of expansion and the overall magnitude of the expansion^[17-20]. At lower temperatures (100°C and below) there is a slower rate of expansion at lower fluences, followed by a higher, steady rate of expansion^[18]. At higher temperatures (100 to 1000°C) there is an initial expansion at lower fluences followed by a reduction in expansion rate, and possibly saturation^[18]. Material with larger grain sizes exhibited larger expansion than smaller grain material at comparable fluences and temperatures^[18,20]. Hot pressed beryllium oxide was also shown to expand more than cold pressed and sintered beryllium oxide^[19].

The anisotropic expansion of the beryllium oxides grains that cause the volume expansion can also lead to crumbling and cracking of the material due to the intergranular stresses^[21]. This microcracking is dependent upon the microstructure, particularly the grain size^[17,18], and the irradiation temperature^[8]. Increasing the grain size causes cracking to occur at a lower fluence but increasing the irradiation temperature increases the fluence at which cracking occurs. It has also been found that cold pressed and sintered beryllium oxide is more resistant to microcracking compared to hot pressed beryllium oxide, possibly because the latter tends to have microcracks even before it is irradiated^[8]. The separation of the grain boundaries is assumed to be the dominant cause of the irradiation-induced changes in the material properties of beryllium oxide^[19,20].

The microcracking causes a significant reduction in strength (bending and compressive)^[17-19] but there is a small but significant increase in bending strength at lower temperatures (~100°C) prior to cracking^[22]. There is reportedly little change in Young's modulus and shear modulus before microcracking^[18] but sparse information on the elastic properties after microcracking. The coefficient of thermal expansion does not change with irradiation at 100 or 1000°C but the data for this only goes to a maximum of ~1 dpa^[18]. Microcracking significantly reduces the thermal conductivity of beryllium oxide^[23] with increasing fluence decreasing the thermal conductivity and reducing the temperature dependence^[24]. Irradiation at higher temperatures (500 to 600°C) causes changes in thermal conductivity considerably smaller than those at lower temperatures (75 to 100°C).

Recommendations

It has been stated^[8] that due to irradiation-induced microcracking, beryllium oxide is only usable as a solid moderator for a limited range of fast neutron fluences and temperatures, with fine-grained material having greater irradiation resistance than coarse-grained material^[17]. In the proposed design, beryllium oxide would be used as a reflector material where the fluences and temperatures are significantly lower than those in the moderator regions. However, when the predicted fluence and temperature ranges are available, the first step should be to compare these ranges with those identified as being safe i.e. no microcracking (Figure 1). If the predicted ranges are within the non-microcracking ranges, the next step should then be to conduct a full analysis of the irradiation changes of the beryllium oxide reflector components and their interaction with the graphite moderator components.



Estimated minimum irradiation temperature to avoid grain-boundary separation in BeO of 20-micron grain size and 2.9 g·cm³ density

Figure 1 Predicted irradiation temperature and fluence ranges to avoid microcracking in beryllium oxide^[25].

References to Section B2.6

- [1] *Thermophysical properties of materials for nuclear engineering: a tutorial and collection of data*. International Atomic Energy Agency, 2008.
- [2] I Dulera & R Sinha. High temperature reactors. *Journal of Nuclear Materials*, **383** (1-2), pp. 183-188, 2008.
- [3] S A Hatton & M S El-Genk. Sectored Compact Space Reactor (SCoRe) concepts with a supplementary lunar regolith reflector. *Progress in Nuclear Energy*, **51** (1), pp. 93-108, 2009.
- [4] H C Kawecki in *The metal beryllium* in (eds D W White & J E Burke) pp. 63-70 (American Society for Metals, 1955).
- [5] C W Schwensfeier in *The metal beryllium* in (eds D W White & J E Burke) pp. 71-101 (American Society for Metals, 1955).
- [6] M J Bannister. The kinetics of sintering and grain growth of beryllia. *Journal of Nuclear Materials*, **14** pp. 315-321, 1964.
- [7] B R Steele, N S Hibbert, F Rigby, B Oldfield & F S Martin. The preparation and characterisation of ceramic grade BeO. *Journal of Nuclear Materials*, **14** pp. 310-314, 1964.
- [8] B T Kelly in *Nuclear Materials, Part 1 in Materials Science and Technology: A Comprehensive Treatment, v10A* (eds R W Cahn, P Haasen & E J Kramer) pp. 365-417 (VCH Verlags GmbH, Weinheim, Germany, 1994).
- [9] B T Kelly, B J Marsden, K Hall, D G Martin, A Harper & A Blanchard. *Irradiation damage in graphite due to fast neutrons in fission and fusion systems*. IAEA, IAEA-TECDOC-1154, 2000.
- [10] S Carniglia & J Hove. Fabrication and properties of dense beryllium oxide. *Journal of Nuclear Materials*, **4** (2), pp. 165-176, 1961.
- [11] A Karklit & L Tikhonova. Thermomechanical properties of some oxide refractories. *Refractories and Industrial Ceramics*, **11** (11), pp. 727-730-730, 1970.

- [12] S C Carniglia, R E Johnson, A C Hott & G G Bente. Hot pressing for nuclear applications of BeO; process, product, and properties. *Journal of Nuclear Materials*, **14** pp. 378-394, 1964.
- [13] R Fryxell & B Chandler. Creep, strength, expansion, and elastic moduli of sintered BeO as a function of grain size, porosity, and grain orientation. *Journal of the American Ceramic Society*, **47** (6), pp. 283-291, 1964.
- [14] G Bente & R Kniefel. Brittle and Plastic Behavior of Hot-Pressed BeO. *Journal of the American Ceramic Society*, **48** (11), pp. 570-577, 1965.
- [15] R R Vandervoort & W L Barmore. Compressive creep of polycrystalline beryllium oxide. *Journal of the American Ceramic Society*, **46** (4), pp. 180-184, 1963.
- [16] W L Barmore & R R Vandervoort. High-Temperature Plastic Deformation of Polycrystalline Beryllium Oxide. *Journal of the American Ceramic Society*, **48** (10), pp. 499-505, 1965.
- [17] B S Hickman & A W Pryor. The effect of neutron irradiation on beryllium oxide. *Journal of Nuclear Materials*, **14** pp. 96-110, 1964.
- [18] C G Collins. Radiation effects in BeO. *Journal of Nuclear Materials*, **14** pp. 69-86, 1964.
- [19] G W Keilholtz, J Lee, J.E. & R E Moore. The effect of fast-neutron irradiation on beryllium oxide compacts at high temperatures. *Journal of Nuclear Materials*, **11** (3), pp. 253-264, 1964.
- [20] G W Keilholtz, J Lee, J.E., R E Moore & R L Hamner. Behaviour of BeO under neutron irradiation. *Journal of Nuclear Materials*, **14** pp. 87-95, 1964.
- [21] B Hickman, T Sabine & R Coyle. X-ray diffraction studies of irradiated beryllium oxide. *Journal of Nuclear Materials*, **6** (2), pp. 190-198, 1962.
- [22] F Clarke, G Tappin & T Ghosh. Some irradiation induced property changes in beryllium oxide. *Journal of Nuclear Materials*, **4** (2), pp. 125-132, 1961.
- [23] R Dullow. Thermal resistance due to microcracking in neutron-irradiated beryllium oxide. *Journal of Nuclear Materials*, **17** pp. 83-85, 1965.
- [24] M Cooper, A Palmer & G Stolarski. The effect of neutron irradiation on the thermal conductivity of beryllium oxide. *Journal of Nuclear Materials*, **9** (3), pp. 320-326, 1963.
- [25] R S Wilks. Neutron-induced damage in BeO, Al₂O₃ and MgO -- a review. *Journal of Nuclear Materials*, **26** (2), pp. 137-173, 1968.

B.3 Fuel Design

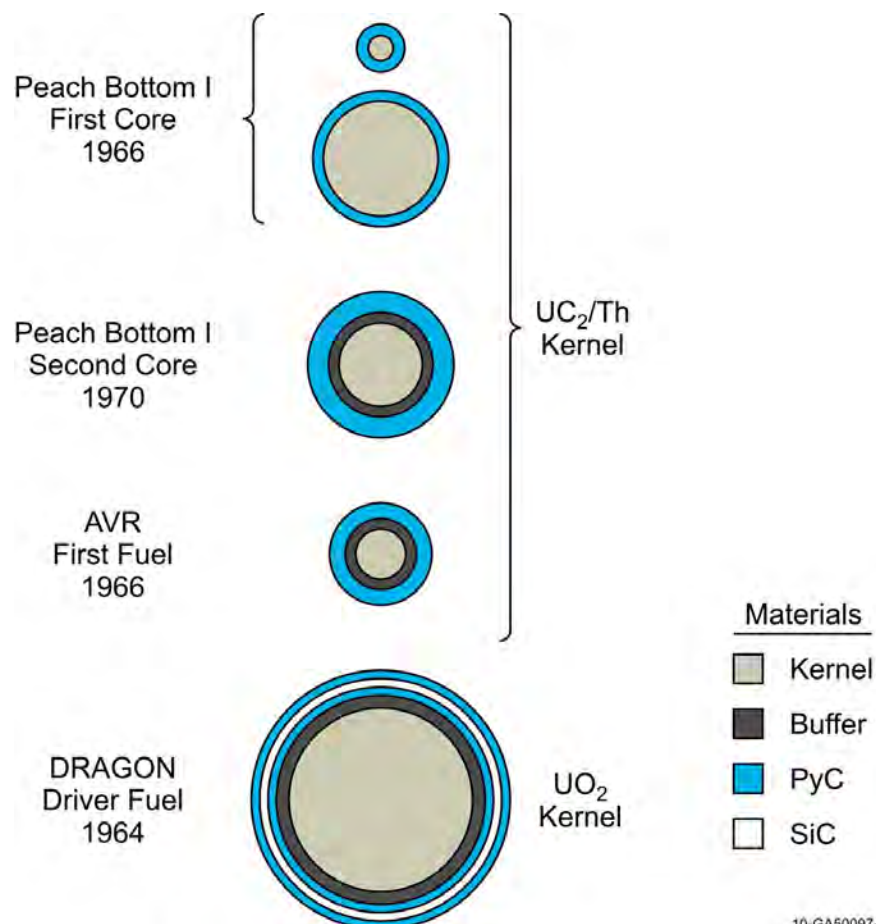
Introduction

No new experiments have been carried out on TRISO particles in CO₂. This is because the graphite experiments gave such poor results that the CO₂ option was abandoned before the experiments were conducted. In addition there is overwhelming evidence that TRISO performs exceptionally well in an Helium environment.

The PhD Student is investigating oxidation rates in carbon matrix materials but this will not be reported until he produces his thesis in about 12 months time. This thesis will be made available to the sponsors.

Experience with TRISO Coated Particle Fuel in Helium-cooled Reactors

Coated particles start with a spherical kernel of fissile or fertile material which is surrounded by one or more ceramic coatings. By the early 1960s, coated particle fuel development for graphite moderated helium cooled High Temperature Gas-Cooled Reactors (HTGRs) was well under way in the United Kingdom in support of the DRAGON research reactorⁱ, and was followed by development work in the United States in support of the Peach Bottom Unit 1 prototype power reactorⁱⁱ and in Germany in support of the Arbeitsgemeinschaft Versuchsreaktor (AVR) research and power reactor. Coated particle designs for these reactors varied considerably as illustrated in Figure B3.2 (the AVR fuel loadings evolved through many designs in the course of over two decades of plant operation, including the LEU TRISO design relevant to the U-Battery[®]).



10-GA50097-07

Figure B3.2. Early coated particle designs.

Coated particle fuel development programs have also been conducted in France, Russia, Japan, China South Africa and the Republic of Korea. The development of coated particle fuel technology for both pebble bed and prismatic HTGR designs has drawn from an extensive international background of coated particle fuel fabrication and testing experience spanning more than 50 years and covering a broad range of parameters as summarised below:

- Kernel characteristics
 - Diameter – 100 to 800 μm .
 - Fissile/fertile materials – uranium, thorium, plutonium (mixed and unmixed).
 - Chemical forms – oxide, carbide, oxycarbide.
 - Enrichment – ranging from natural to high enriched uranium and plutonium.
- Coating characteristics
 - BISO – variations in buffer and PyC coating thicknesses and properties.
 - TRISO – variations in buffer, PyC and SiC (or zirconium carbide) thicknesses and properties.
- Fuel forms
 - Spheres – multiple geometries and fabrication methods.
 - Compacts – cylindrical and annular shapes with variations in particle packing fractions and fabrication methods.
- Irradiation facilities
 - Materials Test Reactors – HFR (Netherlands), FRJ 2 DIDO (Germany), IVV-2M (Russia), Siloe (France), R2 (Sweden), BR2 (Belgium), HFIR (U.S.), ATR (U.S.), with wide variations in spectra and degree of acceleration.
 - Research and Demonstration Reactors – DRAGON (United Kingdom), Peach Bottom I (U.S.), AVR (Germany), FSV(U.S.), THTR (Germany), HTTR (Japan), HTR-10 (China).
- Irradiation and testing conditions
 - Burnup – ranging from below 1% to above 70% fissions per initial metal atom (FIMA).
 - Fluence – ranging from below 1×10^{21} to above 10×10^{21} n/cm^2 .
 - Irradiation Temperature – ranging from 600°C to 1,950°C.
 - Accident Simulation Temperature – ranging from 1,400°C to 2,500°C.

This broad range of experience and data has supported development of a detailed understanding of the parameters and phenomena of importance in the fabrication and performance of coated particle fuel. Extensive bilateral and multilateral international information exchanges facilitated the incorporation of this broad experience base into the German and other modern coated particle fuels. The evolution of the German fuel design is summarised in Section 2.4 of a report on the AVR.ⁱⁱⁱ A broader range of international experience, focused mainly on LEU TRISO fuel, was addressed in an International Atomic Energy Agency (IAEA) coordinated research project conducted in the early 1990s.^{iv} In considering this experience and data, the international community has converged on common LEU TRISO particle design, having very similar coating thicknesses and properties with variations in kernel diameter, enrichment, and composition (UO_2 and UCO), depending on the specific service conditions and requirements. This highly successful design, underpinned by many years of excellent performance in HTGR environments, is the reference TRISO particle design for the U-Battery[®] project. Experience with manufacturing coated-particle fuel has demonstrated the feasibility of producing large quantities of fuel with low as-manufactured defect levels (approaching defect fractions of 10^{-5}). This was first demonstrated in Germany with the production of reload fuel batches for the AVR, and subsequently confirmed in fuel production campaigns in Japan for the HTTR first core and in China for the 10 MW High Temperature Gas-Cooled Reactor (HTR-10) first core. The manufacture and performance in helium-cooled reactors of TRISO coated particle fuel is therefore considered to be extensively validated, and is not a feasibility issue for the U-Battery[®] project.

-
- i. R. Simon, P. Capp, "Operating Experience with the Dragon High Temperature Reactor Experiment", HTR-2002, The Netherlands, April 2002.
 - ii. INEEL/EXT-03-00103, "Fuel Summary for Peach Bottom Unit 1 High-Temperature Gas-Cooled Reactor Cores 1 and 2", April 2003.
 - iii. IAEA-TECDOC-978, "Fuel Performance and Fission Product Behaviour in Gas Cooled Reactors," November 1997.
 - iv. IAEA-IWGGCR/8, 'Specialists' Meeting on Gas-Cooled Reactor Fuel Development and Spent Fuel Treatment,' Moscow, October 1983

B.4 Conclusions

1. An initial design for the U-Battery core has been established.
2. The use of CO₂ as a coolant is impractical due to high oxidation rates and formation of carbonaceous deposits
3. Nuclear graphite data and assessment methods for the U-Battery have been established.
4. Scoping calculations show that the design is feasible.
5. If beryllium oxide is used as a reflector, life time prediction for these components will be necessary
6. The next stage requirement is a detailed design of the core structures

Appendix C

U-Battery[®] Plant Layout and Operation

November 2011

Prepared by

Tim Abram

with contributions from

Edward Woodhouse, Azrudi Mustapha, and Mengqi Bai

University of Manchester

Contents

C.1	Introduction	3
C.2	Fuel Handling System	4
C.3	Energy Conversion System	6
C.4	Control System Design	8
C.5	General Plant Layout	8
C.6	Fuel Transport	11
C.7	Conclusions and Recommendations	12
C.7.1	Conclusions	12
C.7.1.1	Fuel Transport.....	12
C.7.1.2	Plant Layout.....	12
C.7.1.3	Energy Conversion System	12
C.7.1.4	Fuel Handling System.....	13
C.7.1.5	Reactor Control System	13
C.7.2	Recommendations	13
C.7.2.1	Fuel Transport.....	13
C.7.2.2	Plant Layout.....	13
C.7.2.3	Energy Conversion System	14
C.7.2.4	Fuel Handling System.....	14
C.7.2.5	Reactor Control System	14
C.8	Annex 1: Study of Fuel Transport and Handling Systems for the U-Battery, by Edward Woodhouse	15
C.9	Annex 2: Study of Power Conversion Systems for the U-Battery, by Azrudi Mustapha	15
C.10	Annex 3: Extract from a Shielding Study for Excellox Transport Flasks, by Mengqi Bai	15

C.1 Introduction

Appendix C addresses the balance of plant for the U-Battery, including the power conversion system and the fuel handling system. It also describes the recommended strategy for plant control, the proposed plant layout, and the arrangements for fuel transport.

The original concept for the U-Battery® has been described in detail in Appendix A. A simple and robust plant design was envisaged, in which both the reactor and the power conversion system would be constructed from modules that would be suitable for road and rail transport within Europe, and which would require minimal routine maintenance. A long-life core was envisaged that would be capable of being refuelled as a single unit. This fuel unit would comprise a compact cartridge or “battery” that would be road-transportable, and would have required only simple fuel handling equipment. Ideally, the spent fuel “battery” would have been suitable for transport away from the reactor site immediately after use, using an existing licensed spent fuel transport flask, such that no permanent on-site fuel storage capacity would be required.

The work conducted over the last two years of the project suggests that whilst some of these objectives can be met, others are not compatible with the current U-Battery® concept. An initial review of power conversion technologies, included here in Section C.9 (Annex 2), suggested that a steam Rankine cycle without re-heat would offer the best combination of well-established, robust technology; a reasonable thermal efficiency; and minimal maintenance, even though the operational requirements of a steam cycle plant would likely require the presence of an on-site maintenance team. Since this initial technology review was conducted, further research has highlighted the potential availability of an alternative power conversion system, based on an indirect cycle gas turbine employing a He-N working fluid. Rolls-Royce have been identified as a potential supplier of such a system, and discussions are underway between the U-Battery® partners and Rolls-Royce to determine the likely development costs and timescales.

It is recommended that the U-Battery® control system be based on existing licensed control systems employed for LWR plant. These are likely to be considerably more complex than would be required for the U-Battery® plant, but in respect of demonstrating concept feasibility, it is clear that currently available systems offer a capability that comfortably exceeds the U-Battery® requirements.

Fuel transport arrangements for a variety of different fuel and reactor systems are summarised in Section C.6, based on a more detailed review provided in Section C.8 (Annex 1). No precedents have been found for the road or rail transport of an entire un-irradiated reactor core, and it is concluded that regulatory considerations are likely to preclude this option, although transportation of a small number of sub-sections may be possible. For this reason, a conventional core layout composed of individual fuel elements has been adopted. Several different fuel handling systems for prismatic HTR fuel elements have been developed, and it is recommended that the design produced by General Atomics for the M-HTGR is adopted. Similarly, the current reference 20

MW_{th} U-Battery® core geometry is too large to allow transportation of an intact irradiated core without developing and licensing a new spent fuel transport container, which is considered to be prohibitively expensive, and could in any case delay the introduction of the U-Battery. Instead, at least two existing spent fuel transport flasks have been identified as being suitable for the transport of U-Battery® fuel elements, although some modest re-design of the flask internals is likely to be required.

A plant layout concept has been developed based on a below-ground reactor cavity and adjacent spent core storage facility, both served by an overhead crane and co-located with the power conversion module in a vented confinement building. Preliminary drawings of the proposed system and plant architecture have been developed, and are provided in Section C.5.

Finally, in order to support the most recent investigations into a small 10 MW_{th} U-Battery® variant, shielding calculations have been performed for TRISO coated particle fuel inside an Excellox spent fuel transport flask. Although this work is at a preliminary stage, it suggests that the transport of an entire core composed of TRISO U-Battery® fuel would be feasible using an existing transport flask.

C.2 Fuel Handling System

The current 20 MW_{th} reference design for the U-Battery® core and fuel elements, described in Appendix A, is incompatible with a single cartridge-type core module, largely because the dimensions of the active core plus the radial reflector and shielding/packaging requirements exceed the maximum permissible width for European road transportation, as described in Section C.6. Similarly, the constraints imposed by spent fuel transport also preclude the use of a single cartridge-type core. Several internationally-licensed transport flasks exist for spent fuel movements, such as the Excellox series, but Excellox flasks impose a limit of 1.8 m on the diameter of the cartridge. Moreover, the weight of 110 t eliminates the possibility of road transport except over very short distances. One of the Sellafield Waste Transport Containers, the SWTC25, has a gross weight of 25 t and could therefore be used for road transport, but in this case the cartridge diameter would be limited to 1.2 m, which is too small to support a feasible core design for the current 20 MW_{th} reference power output.

For these reasons, the current U-Battery® design employs individual fuel elements, which greatly simplifies the transport of fresh and irradiated fuel, but requires the provision of handling equipment suitable for both fresh and irradiated fuel. Fuel handling machines have been developed for previous designs of prismatic HTRs, and these have been reviewed for applicability to the U-Battery® design, as described in Section C.8 (Annex 1). The simplified single-element design produced by General Atomics for the Modular High Temperature Gas Reactor (MHTGR) project appears to be well suited to the U-Battery. The estimated cost was \$17M in 1986, but it is expected that this cost could be reduced on the basis of the small number of elements needed for the U-Battery® and the relatively infrequent need for fuel handling.

Figure C.2.1 Fuel Handling Machine Designed by General Atomics for the Modular High Temperature Gas Reactor

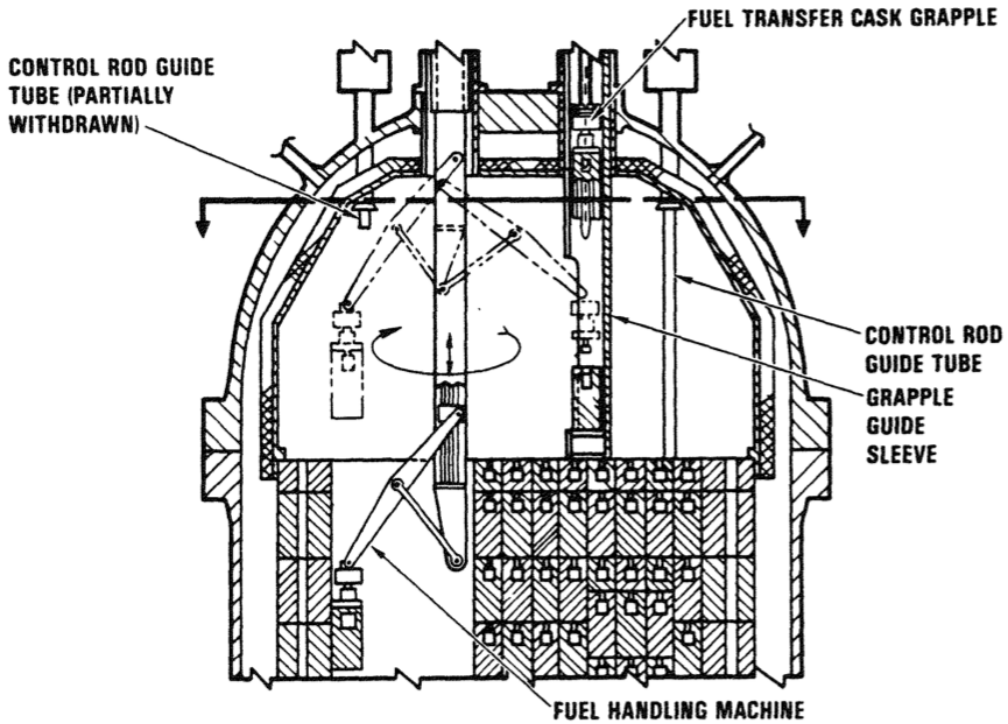
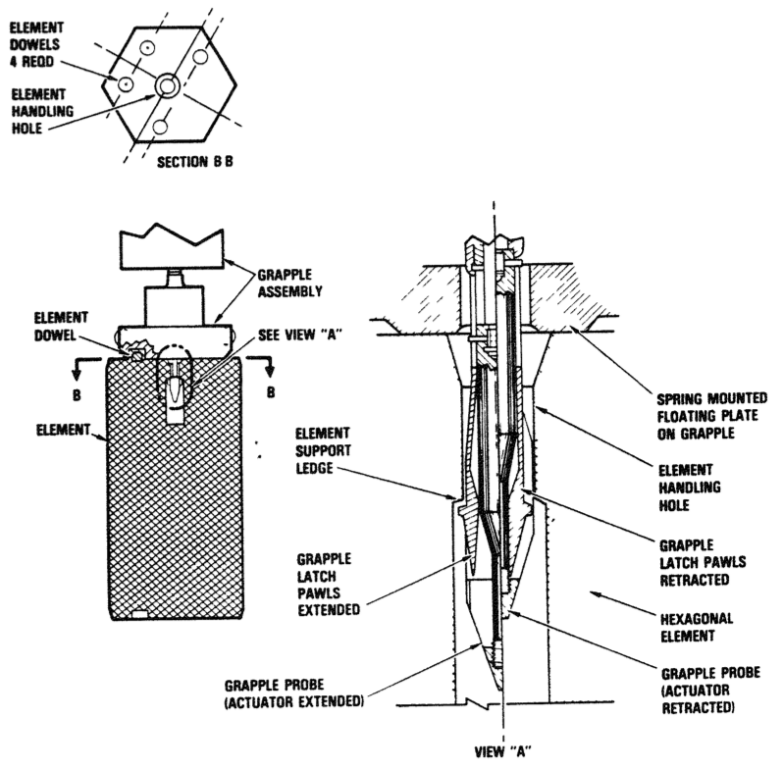


Figure C.2.2 Details of the GA MHTGR Fuel Handling Machine Grab Arrangement



C.3 Energy Conversion System

The reference concept for the U-Battery® is an electricity-generating module, capable of producing around 20 MWth. Several different options have been explored for the energy conversion system, including:

- an indirect steam (Rankine) cycle with and without reheat;
- a direct CO₂ turbine;
- an indirect gas-turbine;
- novel systems such as direct thermal-to-electrical conversion, and an Alkali Metal Thermal-to-Electrical Converter.

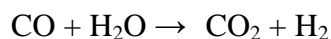
A review of potential energy conversion systems for the U-Battery® has been undertaken, and is provided in Section C.9 (Annex). The main findings of this review are presented below, and are augmented by additional information obtained on indirect gas-turbine cycles.

Most commercially-available direct thermal-to-electrical conversion systems employ the Seebeck effect, where a temperature gradient across a metal junction produces a voltage. Older devices operate with silicon-germanium elements and have only low thermal efficiencies (typically around 5%), but more modern designs based on bismuth telluride semiconductor *p-n* junctions offer better efficiencies (10-15%), albeit at greater cost. The principal advantage of a direct thermal-to-electric converter for an autonomous reactor system is the complete absence of moving parts and the very low (effectively zero) maintenance requirements, but this advantage is offset by the low power outputs available, which typically range from 10⁻³ W (for low-power electronics) to a few kW. More advanced systems have been proposed, such as the Alkali Metal Thermal-to-Electrical Converter (AMTEC), that offer the prospect of up to 40% thermal efficiency. However, the AMTEC is still at a very early stage of development, and would therefore entail significant development costs (and clearly has no established record of satisfactory industrial-scale performance). Moreover, the system requires the use of a liquid alkali metal such as sodium, and would therefore present significant safety concerns when incorporated into a compact plant design such as the U-Battery.

A direct-cycle CO₂ turbine has the advantage of avoiding the need for a secondary circuit. However, conventional CO₂ turbines have never found application in power generation applications: partly because of thermal stability problems at elevated temperatures, and the prospect of carbonaceous deposits on the turbine blades, and partly because of the availability of well-established steam and helium-based cycles. Super-critical CO₂ has been used as an industrial solvent for many years (for example, in the freeze-drying of coffee), and offers the prospect of a highly-efficient gas-turbine Brayton cycle, with efficiencies in excess of 40%. Although there is considerable industrial experience with super-critical CO₂, and the temperature needed to operate an efficient Brayton cycle is comparable with that produced by the U-Battery® design (circa. 550°C), the working pressure of around 20 MPa is considerably higher. This would introduce major additional costs associated with plant safety, notably a considerable increase in the thickness of the RPV and coolant pipework, as well as the availability of nuclear-grade components such as gas circulators and valves that can operate at such pressures. The development costs and

uncertainties associated with a super-critical CO₂ turbine preclude its selection for the U-Battery® concept.

The steam Rankine cycle has been adopted almost exclusively for large-scale power generation in both fossil-fired and nuclear plants. The technology is extremely well established, and the supply chain for steam-cycle components is extensive. In most applications, cycle efficiency is improved by bleeding high pressure steam to re-heat the exhaust steam from the high- and intermediate-pressure turbine stages, and by employing feedwater heaters, although these measures require increased pipework complexity and additional plant items such as economisers. In applications where plant simplicity and reliability is important, such as nuclear-powered naval vessels, a simple Rankine cycle without reheat is often preferred. The study of power cycle options provided in Annex 3 recommended a steam Rankine cycle without reheat for the U-Battery® because it offers a well-established, proven and robust technology with good thermal efficiency and a globally established supply chain. A disadvantage of the Rankine steam cycle is the need to maintain acceptable water chemistry and the need for regular maintenance. However, the energy conversion system is not a safety-critical element of the U-Battery® design, and it is therefore believed that remote condition monitoring could be used to inform an off-site monitoring centre of the need for maintenance or plant chemistry control. The heat exchanger would also need to be of a robust design in order to avoid the possibility of water ingress into the primary circuit, and the potential for hydrogen generation via the water-gas shift reaction:



Experience with operation of the AGRs in the UK has shown that the consequences of water ingress into the primary circuit at temperatures close to those of the U-Battery® system are, whilst undesirable, at least manageable from a safety perspective. Nevertheless, this is a potential drawback of the steam Rankine cycle for the U-Battery.

An indirect gas-turbine cycle based on a Brayton cycle would avoid the potential safety concern associated with a steam ingress into the primary circuit, and could employ a relatively inert working fluid, minimizing the need for careful control of the secondary coolant chemistry. The cycle would, however, require a reasonably large heat exchanger, and experience with indirect gas-turbines is limited. However, Rolls-Royce have published a concept for a power conversion module based on their well-established air turbine designs, but employing a mixed He-N₂ working fluid. This design combines the proven aspects of their air turbines with the advantageous thermal properties of helium, allowing a smaller heat exchanger to be used. Moreover, it is possible that Rolls-Royce could design the power conversion module as a separate unit. This would simplify the U-Battery® design process and remove a substantial item of risk from the program, as well as offering the potential for some novel financing options. The U-Battery® investors plan to hold discussions with Rolls-Royce in the near future, subject to the conclusion of a satisfactory non-disclosure agreement.

C.4 Control System Design

Although design of the U-Battery® control system is clearly beyond the scope of a conceptual design study, it is important to verify that an appropriate control technology is available, and that the plant parameters will not challenge the capabilities of currently available control and safety systems.

The design of the Westinghouse AP600 reactor control and safety systems has been taken as a reference point for the U-Battery® study. Appendix A provides a comprehensive description of the reactivity control systems that have been investigated for the U-Battery. It is immediately apparent that the reactivity control systems are considerably simpler than those that are necessary for PWR plant. In particular, the adoption of TRISO coated particle fuel eliminates the need for complex and diverse systems for residual heat removal, because the plant characteristics are such that temperatures that could threaten fuel integrity cannot be reached in the U-Battery. For this reason, existing high-integrity nuclear-qualified control systems available from vendors such as Siemens and Westinghouse already offer substantially greater capability than is necessary for the U-Battery. Consequently, the availability of appropriate reactor control systems is not considered to be a feasibility issue for the U-Battery, and it is anticipated that the control requirements for the U- Battery® will be considerably simpler than for corresponding LWRs, allowing a substantial reduction in control system cost.

C.5 General Plant Layout

The structural design of the U-Battery® core is described in section B.2, and is also illustrated in Figure A.3.3. This work has been extended to investigate potential layouts for all of the major components of the U-Battery, and to produce a conceptual layout for the entire plant. The plant layout concepts are illustrated in Figures C.5.1 to C.5.4 below.

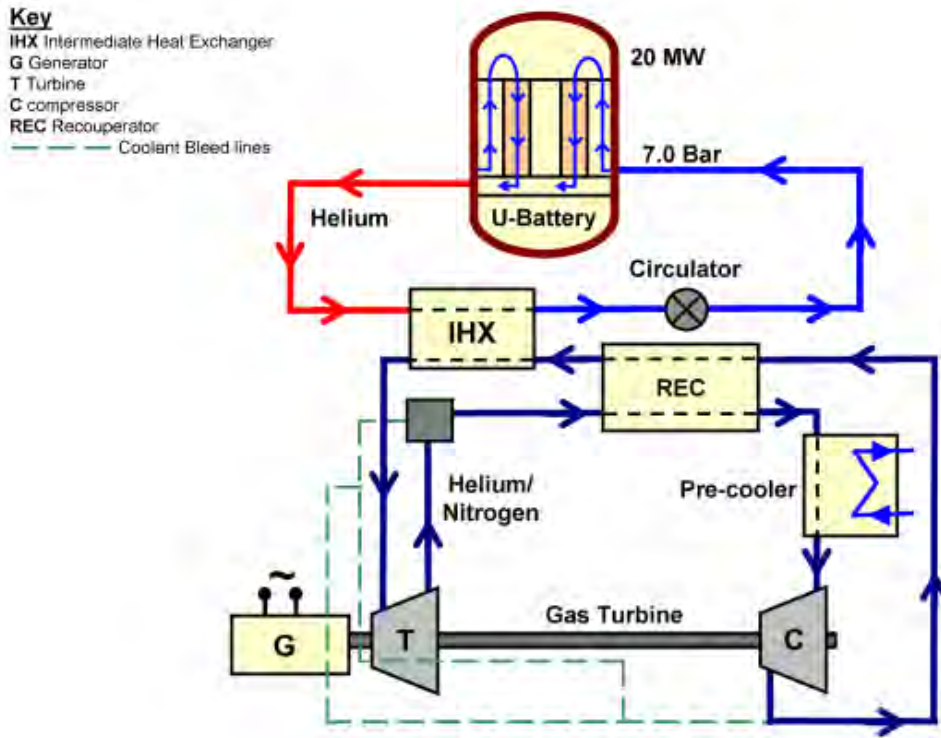


Figure C.5.1 Schematic layout of U-Battery® Primary and Secondary Circuits for an Indirect Gas-Turbine Power Conversion Unit

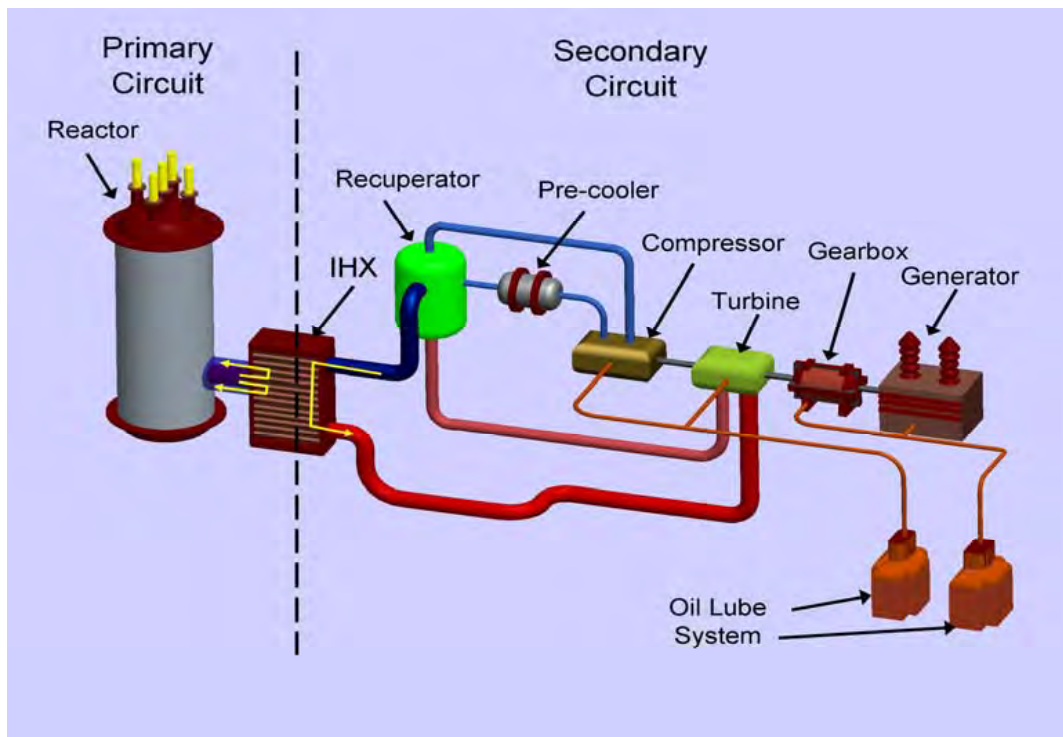


Figure C.5.2 Isometric layout of the U-Battery® Primary and Secondary Circuits for an Indirect Gas-Turbine Power Conversion Unit

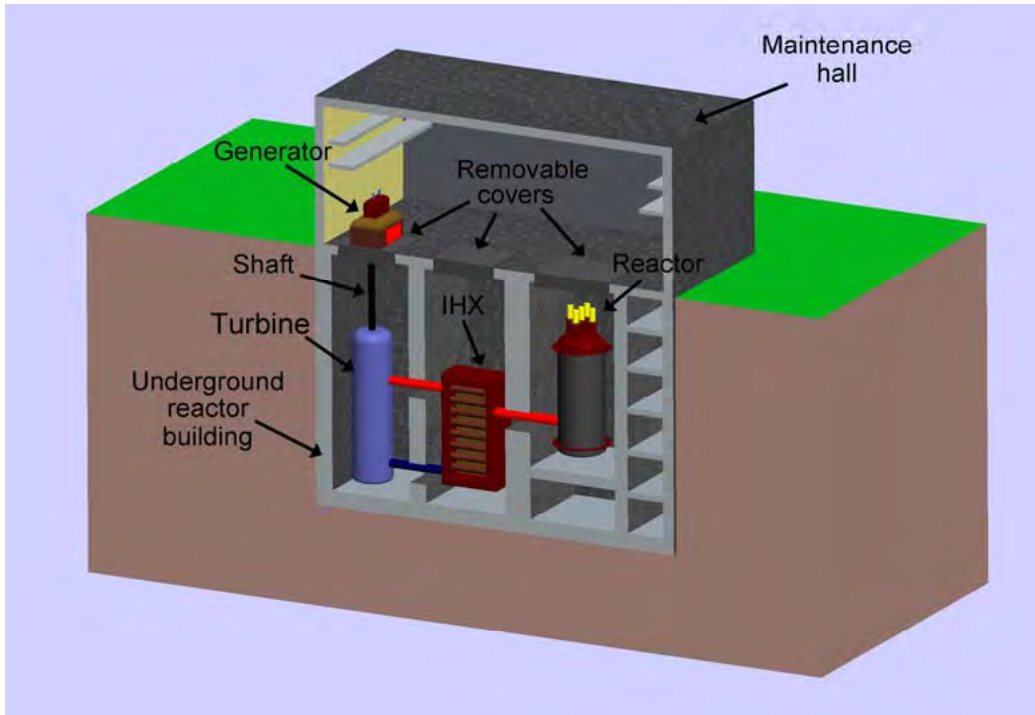


Figure C.5.3 Schematic layout of the U-Battery® Reactor Building

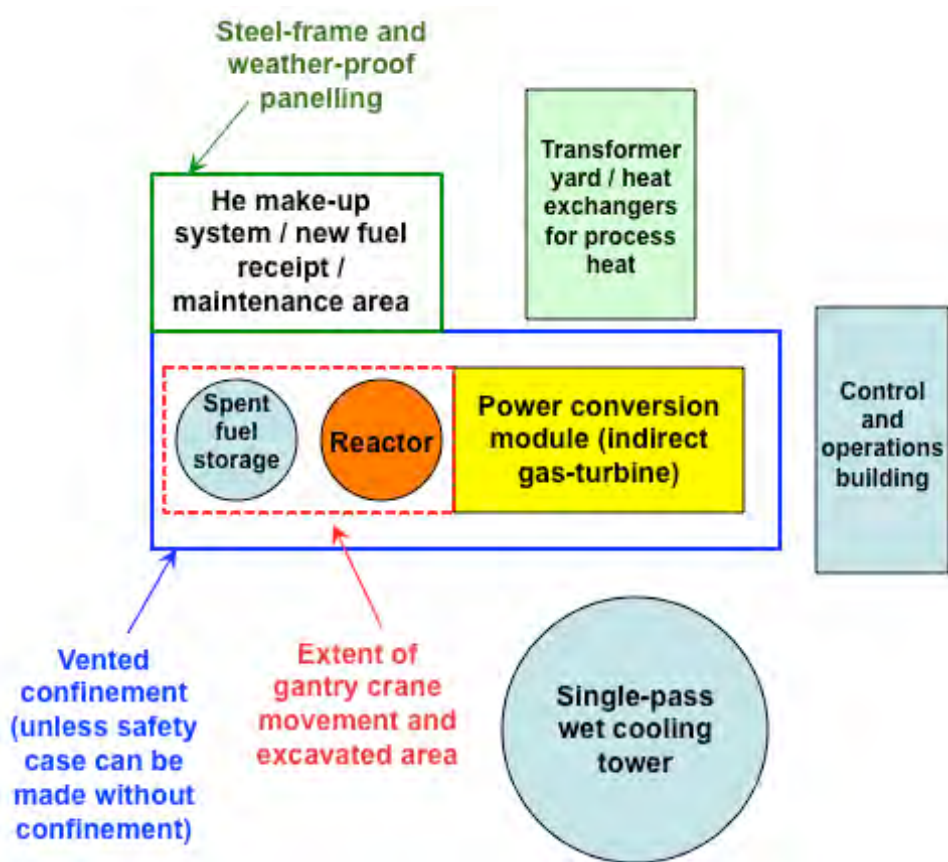


Figure C.5.4 Conceptual layout of the U-Battery® Site Installation for an Inland Location

C.6 Fuel Transport

The original U-Battery® concept envisaged the core being replaced as a single “battery” unit. In order to evaluate the feasibility of this approach, a review of the fuel transport arrangements for a variety of different fuels and reactor systems has been conducted, and is reproduced in Section C.8 (Annex 1). In addition, a supplemental review of European transport regulations has been conducted, and is included here in Section C.9 (Annex 2).

No precedents have been found for the road or rail transport of an entire un-irradiated reactor core, either in the civilian or military sectors. Moreover, a review of European road transportation regulations has shown that the physical size of the reference 20 MW_{th} U- Battery® core would preclude transport as a single module in a standard ISO freight container package. It is concluded that regulatory concerns over the ability of the core to remain sub-critical under all potential accident conditions, together with the costs associated with transporting an over-sized nuclear load, are likely to preclude this option, although transportation of a small number of sub-sections may be possible. For this reason, a conventional core layout composed of individual fuel elements has been adopted, with the core structure being built on site, following conventional practice. Although this approach lacks the simplicity of a single “battery” module, the infrequency of refueling ensures that any additional time taken to refuel the reactor will be inconsequential compared with the regulatory and logistical difficulties associated with shipping an intact core.

Several existing transport containers are likely to be suitable for unirradiated U-Battery® fuel elements with only minor modifications, including the current containers for UK Advanced Gas Cooled Reactors. Fresh fuel transport is therefore considered to be feasible within the existing transport infrastructure, and no new development needs are anticipated.

Currently, all spent fuel shipments take place by rail and/or sea, with very short road transport to the nearest rail head or port facility. Spent fuel transport for the reference 20 MW_{th} U-Battery® design is simplified by the use of individual fuel elements, avoiding the need to transport an intact core. For this purpose, several existing spent fuel transport casks already exist, including the internationally licensed Excellox LWR flasks, and several Sellafield site Waste Transport Containers (licensed for the UK, but not elsewhere). The availability of internationally-licensed transport flasks that could accommodate U-Battery® fuel elements ensures that the off-site transport of U-Battery® fuel is feasible, although additional licensing work will be required to verify that flasks suitable for transporting LWR and/or AGR fuel are also suitable for U-Battery® elements.

For the 10 MW_{th} U-Battery® design, it may be possible to transport an intact spent core using an Excellox transport flask. A preliminary study has been made to assess the shielding requirements for such a transport, based on the use of TRISO coated particles in an assembly of a similar geometry to a PWR assembly (representing a limiting case for the U-Battery). This study has concluded that the Excellox flask would prove suitable for the transport of spent U-Battery® fuel, and that it may also be suitable for the transport of an entire core module.

C.7 Conclusions and Recommendations

C.7.1 Conclusions

C.7.1.1 Fuel Transport

It has not been possible to meet the original target of designing the core of the 20 MW_{th} U-Battery® core to be easily road-transportable as a single “cartridge”. In part, this is because the core and shielding exceed the maximum dimensions and weight for which unescorted road transport is feasible. Road transport over limited distances would indeed be possible, even within existing transport regulations, but no precedent has been found for either road or rail transport of intact reactor cores, and it is likely that licensing considerations would effectively preclude this option. Instead, the reference U-Battery® concept employs conventional HTR fuel elements of the prismatic design. This greatly simplified transport of both fresh and irradiated fuel, and existing licensed transport containers have been identified that would be suitable for such transports with minimal modification.

Very preliminary work on the smaller 10 MW_{th} U-Battery® plant suggests that it may be possible to incorporate such a unit into the envelope provided by an Excellox transport container, and preliminary shielding calculations suggest that this may be a feasible solution.

C.7.1.2 Plant Layout

Layout schemes have been developed for the main plant components, and for the site architecture. The component layout scheme follows a similar approach to other small modular concepts, notably the PBMR plant, and provides a compact footprint. The site layout is based on a minimal amount of civil construction in order to minimise costs. If the U-Battery® is incorporated into an existing industrial site, then it is anticipated that the functions of some of the auxiliary buildings (such as the control and operations building) could be provided by existing site infrastructure, offering further cost reductions.

C.7.1.3 Energy Conversion System

Several alternative energy conversion systems have been examined for the U-Battery. Currently, the most promising solution appears to be an indirect cycle gas-turbine, based on demonstrated air-turbine technology, but employing a N₂/He working fluid in order to minimise the size of the primary-to-secondary heat exchanger. Rolls-Royce have been working on such a concept, and it seems likely that this could be provided as a separate (though integrated) module. Discussions between the U-Battery® partners and Rolls-Royce to further explore this concept are ongoing. As a back-up solution, a steam Rankine cycle without re-heat is recommended, on the basis that it offers a well-established and robust technology with good thermal efficiency and an extensive global supply chain. The disadvantage of a steam Rankine cycle is that it requires regular maintenance and water chemistry control, but remote condition

monitoring technology (similar to that employed in aero-engines) could enable this function to be performed by a centralised off-site team.

C.7.1.4 Fuel Handling System

The use of individual fuel elements for the U-Battery® core requires the availability of a fuel handling system capable of manipulating individual elements. The fuel handling arrangements employed by previous and current prismatic HTR designs have been reviewed, and the solution adopted by General Atomics for the MHTGR concept has been preferred. This is based on the demonstrated Fort St. Vrain fuel handling machine, but with a simplified design, resulting in cost savings. At present, the fuel handling machine is anticipated to remain within the reactor building as a permanent installation. However, given the infrequency of refuelling operations, there is scope for investigating a mobile solution that could be shared between several U-Battery® plants.

C.7.1.5 Reactor Control System

The high level of inherent safety offered by the U-Battery® will greatly simplify the complexity of the plant control and safety systems relative to LWRs. Existing LWR control systems are therefore expected to be readily adaptable for the U-Battery, and will likely provide far greater capability than is required. Nevertheless, the availability of a demonstrated and licensable control system from global suppliers such as Siemens or Westinghouse is assured, and is not a feasibility issue for the U-Battery® system.

C.7.2 Recommendations

C.7.2.1 Fuel Transport

For the 20 MWth U-Battery® design, it would be helpful to verify that the transport solutions recommended for both fresh and irradiated fuel can be adapted for the prismatic U-Battery® element.

For the 10 MWth design, the prospect of mounting the entire core inside an existing licensed spent fuel transport flask, such as the Excellox-7 design, should be further explored. This could allow a return to the original U-Battery® concept, although the implications for road transport would need to be better understood.

C.7.2.2 Plant Layout

Further elaboration of the 20 MWth U-Battery® design would allow a more detailed plant layout to be developed. In particular, a more detailed exploration of the response of the plant to a range of accident conditions would provide a clearer indication of the safety systems that need to be provided, and in particular of the need for a sealed and

reinforced containment building. This could justify a further simplification of the site architecture.

For the 10 MW_{th} U-Battery® design, novel plant layouts could be envisaged if the core can be accommodated within a spent fuel storage flask. In this case, a very simplified site layout could be developed that could significantly reduce costs.

C.7.2.3 Energy Conversion System

Assuming that an appropriate agreement can be concluded with Rolls-Royce, it is recommended that a joint review be undertaken to determine how the Rolls-Royce concept can be optimised for the two U-Battery® systems under investigation. The aim of this work should be to reach an integrated reactor and power conversion system concept for both systems.

C.7.2.4 Fuel Handling System

For the 20 MW_{th} U-Battery® design, the possibility of adopting a shared, off-site fuel handling system should be further explored, because of the potential for significant cost reductions.

For the 10 MW_{th} design, an on-site fuel handling system may not be required if the module can be located in a transportable flask. In this case, the only design consideration required is the means of exchanging core modules once the core has reached the end of its useful life.

C.7.2.5 Reactor Control System

The feasibility of employing currently available reactor control systems does not seem in doubt, so no near-term work on the reactor control system is proposed.

C.8 Annex 1: Study of Fuel Transport and Handling Systems for the U-Battery

Extracted from a Dissertation by Edward Woodhouse, University of Manchester

C.9 Annex 2: Study of Power Conversion Systems for the U-Battery

Extracted from a Dissertation by Azrudi Mustapha, University of Manchester

C.10 Annex 3: Extract from a Shielding Study for Excellox Transport Flasks, by Mengqi Bai

Extracted from a Dissertation by Mengqi Bai, University of Manchester

**C.8 Annex 1: Study of Fuel Transport and Handling Systems
for the U-Battery**

Extract from a dissertation by Edward Woodhouse

**Review of Nuclear Fuel Transport and Handling
Systems for Application to a Small Scale HTGR**

2009

Edward Woodhouse

Contents

List of Figures	3
Abstract	4
Declaration	5
Copyright Declaration	5
Acknowledgments	6
Aim	7
1.1 Introduction	8
1.1.1 Justification of Objectives	8
1.2 The Initial Reactor Conceptual Design	10
2. Transport Safety and Management (Both Spent and Fresh)	12
2.1 International Regulations for the transport of Radioactive Material	13
2.1.1 Transporting Radioactive Material	14
2.1.2 Design and Testing Requirements	15
2.1.3 Regulations Relevance to Reactor Cartridge Design	20
2.2 Transport Regulations in the UK	21
2.2.2 Rail Constraints	25
2.2.3 Restraints Imposed on the Reactor Cartridge Design by UK Transport Network Regulations	27
2.3 Security Requirements for the Transportation of Nuclear Material	30
2.3.1 Security Requirements for all carriers of Nuclear Fuel	31
2.3.2 Determination of Threat	32
2.3.3 Security Relevance to the Cartridge Design	33
2.4 Transport Containers Currently In Operation	34
2.4.1 Fresh Fuel Containers	35
2.4.2 Excellox Transport Flasks	36
2.4.3 Generic Road Transport Containers	37
2.4.4 TN International Flasks	38
2.4.5 Sellafield Waste Transport Containers (SWTC)	40
2.4.6 Naval Nuclear Propulsion Engine Transports	41
2.5 Discussion of Constraints Imposed by Transport	42
3. Fuel Handling	45
3.1.1 Advanced Gas Reactor Fuel Handling	46
3.1.2 High Temperature Test Reactor (HTTR)	48
3.1.3 Naval Propulsion Reactors	51
3.1.4 Discussion of the Considerations for Cartridge Fuel Handling System	53
4. Discussion of Cartridge Design	54
5. Conclusion and Recommendations	57
6. Future Work	59
7. References	60

List of Figures

Figure 1.1: Thermal Resilience of the TRISO particle	11
Figure 2.1: Nuclear Fuel Cycle	12
Figure 2.1: Thermal Testing	18
Figure 2.2.1: Notification for different weight and width/length categories	24
Figure 2.2.2: Train Carriage Dimensions are limiting Factor	27
Figure 2.4.1: ANF-18 Transport Containers	36
Figure 2.4.2: Excellox (7/7) Container	37
Figure 2.4.3: TN24 Family Transport Container	39
Figure 2.5.2: Change in Surface Dose Rates of TN24 Container	45
Figure 3.1.1: AGR Fuel Stringer	47
Figure 3.1.2(a): HTTR Fuel and Core Assemblies	49
Figure 3.1.2(b): HTTR Fuel Handling Unit	50
Figure 4.1: Separation of 'Battery' in to more transport friendly segments	56

Abstract

The University of Manchester is working in collaboration with the Technical University of Delft in the Netherlands and the funding partners Urenco and K&W to develop a conceptual design of a High Temperature Gas Reactor with an electrical power of around 10-15 MW, where the reactor core can be refuelled like a battery. This project is one of several which are all looking at the initial concept for such a reactor and on the completion of these, it will be decided whether to take the design forward to the next stage of development, the feasibility study.

This project specifically reviews the transportation and fuel handling systems currently in operation at similar facilities to those that would be required for the battery like HTGR design and discusses their applicability. The project also sets out an initial set of weight and dimension constraints imposed if the reactor battery is to be transported on the road and rail networks without onerous restrictions.

The report finds that it is possible to transport radioactive material of any size by road and rail, however, it becomes more difficult to transport after the container that the material is being transported in exceeds the ISO standards for road and rail. These restraints are discussed in greater detail in this report.

Aim

This report hopes to review the transport containers and fuel handling systems currently used and their applicability to the proposed 'cartridge' reactor design. The transport regulations are to be used to find an initial set of size and weight constraints that will be the building blocks of the reactor design, and any potential 'show stoppers' are to be identified throughout the review.

1.1 Introduction

The University of Manchester in collaboration with the University of Delft is undergoing the conceptual design of a small scale high temperature, carbon dioxide cooled, graphite moderated nuclear reactor. This nuclear reactor is to be designed with the following key objectives:

- The design should require minimum human interaction during operation, ideally with no operator contact;
- The design is to have a high fuel burn-up and a reactor life approaching 10 years without re-fuelling;
- The design is to be easily transportable, as far as practicable;
- The reactor power is to be approximately 10-15 MWe;
- The design has to have the ability to be easily re-fuelled;
- The enrichment is to be as low as practicable.

1.1.1 Justification of Objectives

The design of the reactor module has to minimise the need for human interaction from the operator at all times to control the risk of proliferation and operating costs. The IAEA favours a nuclear security approach that reduces the number of stages at which the material is exposed, therefore reducing the number of opportunities for proliferators.

This reactor is to be commercially competitive with other power generating devices currently on the market. To achieve this, the reactor has to operate for a long period of time to overcome the high capital costs. The design is intended to require no routine maintenance for the foreseeable life of the reactor and the operation costs are minimal

due to the self sustaining power generation nature of nuclear fuel. The operating and maintenance costs will therefore be restricted to times of refuelling in an effort to minimise costs.

The end user intends the reactor to be attractive to oil refineries and other large plants that require significant power to operate. The design should therefore be able to accommodate the need for access to remote areas where processing plants are usually located. These remote areas are unlikely to have rail access to them and will require road access, and in an attempt to reduce the number of fuel handling interactions during the transport of the cartridge to minimise the risk of proliferation and to soften the security requirements of such a shipment, the design should hope to be transportable on the local road networks without the need for exceptional circumstances.

The total reactor power of this cartridge is to be around 10-15 MWe. This amount of electrical power would not be enough to power an average sized oil refinery alone but an array of such reactors would be. This is an advantage because the refinery would then have the energy capacity to remain in operation in the event of a malfunction in one or more of the reactors. The low electrical power output increases the range of industries the reactor is applicable to.

The ability to re-fuel the reactor creates the potential for indefinite operation, certainly until the end of life of a processing plant for which it is generating electricity for. The overall cost of such a reactor decreases with the prolongation of its operational life, because the bulk cost of nuclear energy is the initial start-up costs.

The ideal nuclear would be water moderated with a natural uranium fuel at atmospheric pressure. However, in reality criticality is only achievable with higher enrichments of ^{235}U and for a practical small reactor design high enriched fuel is required to reach

criticality. The cost of the enrichment process increases with higher enrichments, therefore the design should be made with the lowest enrichment possible that generates the required power.

1.2 The Initial Reactor Conceptual Design

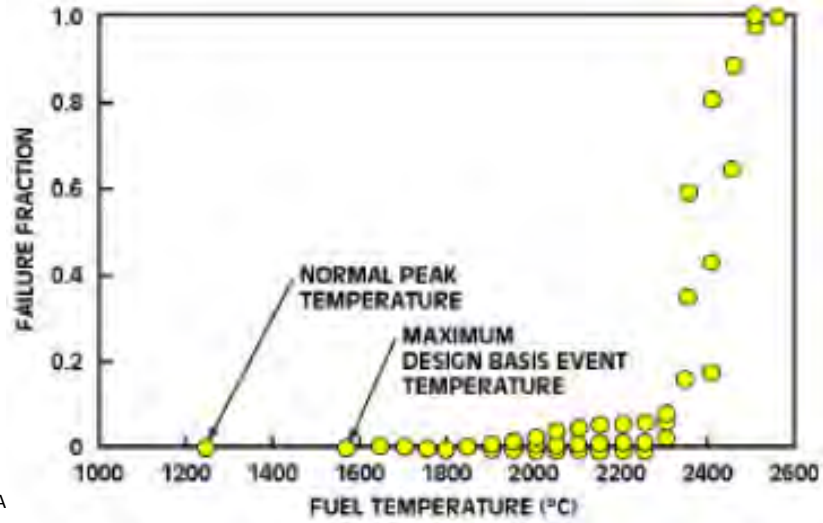
High Temperature Gas Reactors have the capability of reaching much higher temperatures than other reactor designs and as a result can operate with higher thermal efficiencies making them attractive for high fuel burn-up. Graphite has a factor of magnitude less absorption than water, therefore increasing the reactivity of the system and reducing the amount of fissile material required in the reactor and therefore reducing the overall weight and size of the reactor.

The choice of coolant is therefore restricted to a gas, other high temperature reactors that have been in operation have been helium cooled. Helium has high thermal conductivity properties for a gas but has a tendency to leak from the system, and in smaller systems the proportion of helium leaked from the system can be significant. Therefore, considering that the cost of helium is much higher than carbon dioxide, and carbon dioxide has been successfully used as a coolant in the British Advanced Gas Reactor series, the initial conceptual design is carbon dioxide cooled.

The reactor fuel will be made from tri-structural isotropic particles (TRISO) which consist of a fissile kernel (usually Uranium Oxycarbide) surrounded by multiple resistant layers. The different layers consist of pyrolytic carbon (PyC) and SiC which essentially makes the particle a highly corrosion resistant pressure vessel where the fission products are unable to escape. Figures 1.1 above illustrates the thermal properties of the TRISO particles which offer much greater resistance to thermal changes than conventional fuel used in current reactor designs and far exceeds the maximum temperatures that would

be reached in accident conditions. TRISO fuel eliminates the possibility of a core meltdown.

Figure 1.1: Thermal Resilience of the TRISO



particle^A

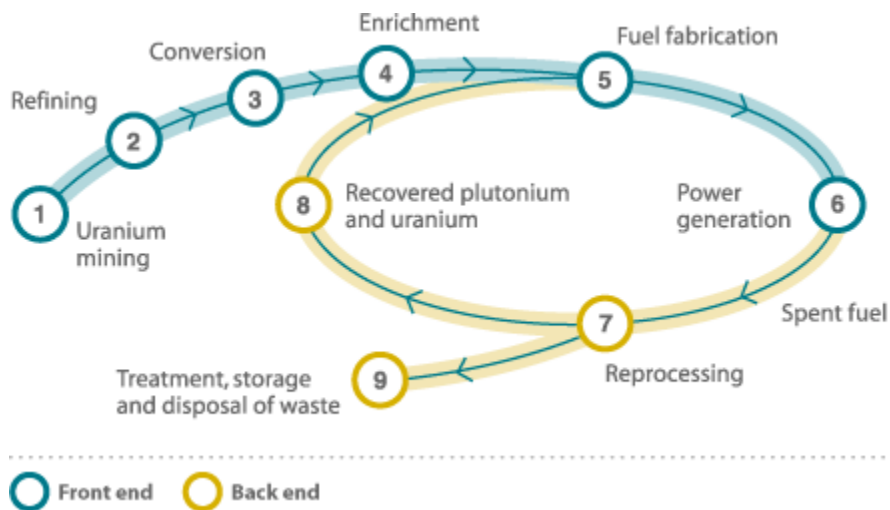
The TRISO particles satisfy the high fuel burn-up requirements that will produce a longer reactor operating life without re-fuelling than conventional systems in operation today. They also reduce the activity of the primary coolant because of their capability to retain the fission products within their structure. These particles are to be fabricated into prismatic fuel elements that will make a core.

The prismatic core assembly offers advantages in fuel handling systems because the shape allows shorter control arms to be used, in the sense of manoeuvring individual fuel element around a core, however, the cartridge design is to allow the movement of an entire core rather than individual fuel blocks. By reducing the number of handling locations a reduction in core access requirements and increasing the size of the fuel block the fuel handling times should be minimised and the complexity of the system reduced. However, the handling system will be required to handle a larger load difficulties may arise during transport in terms of weight and dimension restrictions. Enrichments that are higher than conventional civil power plants are to be used in an attempt to minimise the weight and dimensions of the reactor core.

2. Transport Safety and Management (Both Spent and Fresh)

The nuclear fuel cycle is the generic term given to describe the activities involved in the production of electricity from a nuclear fuel, such as Uranium. It covers the entire life of the Uranium from being mined out of the ground, through fuel fabrication and power generation to disposal of the nuclear waste, shown in figure 2.1 below. These activities are based in different locations around the world and the various forms of uranium have to be transported between process facilities.

Figure 2.1: Nuclear Fuel Cycle^B



The fuel cycle is separated into two categories:

- **the front end** where the processes involve fresh, non-irradiated material and;
- **the back end** where the activities involve processing spent, irradiated, highly radioactive material.

The two different categories pose different challenges during the transportation of the nuclear material and therefore have a different set of requirements from each other. In general, front end material has a low radioactivity and does not require excessive

thermal and radiation protection, in contrast the back end material is highly radioactive and at high temperatures making it necessary for significant radiation shielding and cooling systems.

The small scale, high temperature gas cooled reactor cartridge design described in this report is to be delivered to the operating site by road, as a complete, fresh reactor core including some of the moderator and control rods. For this journey the nuclear material being transported will be front end material, thus will be required to meet the same regulatory requirements. Similarly the spent cartridge that will have to be transported from the operator site to a disposal or re-processing facility will have the same regulatory requirements as back end nuclear fuel.

This chapter will look at the International regulations associated with transporting both fresh and spent fuel to determine a preliminary design envelope for the reactor 'cartridge' design. The design envelope is to be further refined through an evaluation of the dimensional and weight restrictions imposed on the UK transport network.

2.1 International Regulations for the transport of Radioactive Material

Radioactive material is transported around the world every day whether it is to be used for medical, inspection or energy purposes. The International Atomic Energy Agency (IAEA) have set international standards which national regulatory authorities incorporate into law to ensure the safety of persons, property and the environment from radiological hazards that arise during the transport of radioactive material. These standards are outlined in the IAEA *'Regulations for the Safe Transport of Radioactive Material: Safety Requirements No. TS-R-1'*^C.

2.1.1 Transporting Radioactive Material

These regulations set specific requirements for the person or organisation that is transporting the radioactive material to adhere to protect people, the environment and property from the damaging effects of radiation exposure. There are four key requirements that will ensure this protection^A;

1. the containment of the radioactive contents;
2. control of external radiation levels;
3. prevention of criticality;
4. prevention of damage caused by heat.

The adopted method of meeting these requirements is to classify the *radioactive contents* of a *package* into different groups dependent on their activity and physical state. *'The philosophy of these regulations is that the safety is ensured primarily by the package whatever mode of transport is used'*^D. This package is comprised of a containment system whose integrity is maintained for the required transport conditions for a given classification of radioactive material.

A graded approach is then used to impose regulatory constraints upon the packages dependent on the potential hazards. These *packages* are specifically designed to meet the above requirements. The higher the potential radiological hazard the radioactive contents present the more robust the safety controls of the package have to be.

The integrity of the containers is demonstrated through demanding testing techniques. The IAEA set standard impact and fire tests to ensure that there is no radioactivity released during even the most powerful of accidents. The severity of the test depends

on the contents of the container and takes into account not only the potential radiological hazards but also the chemical and thermal risks.

The *packaging* itself acts as a physical barrier between the radioactive material and the environment and it is a key design feature in the effort to control the hazards to acceptable levels during different conditions expected to be experienced during transport. The IAEA takes into account three different conditions of transport;

1. routine transport conditions (vibrations)
2. normal transport conditions (minor mishaps)
3. accident conditions (severe crashes, explosions)

The design and testing of the containers are developed around these three conditions to create the following criteria for the different packages used for the transport of radioactive material.

2.1.2 Design and Testing Requirements

All packages

The safe handling of any package should be easily achieved through the design ensuring that it can be secured properly to withstand the acceleration and vibration forces that are likely to be experienced in any mode of transport.

Excepted Packages

The radiological hazards associated with the contents of the package are so low that they are deemed insignificant and therefore only need to be able to withstand the

minimum baseline of disturbances. There is no requirement for testing the containment or shielding of the container.

Industrial Packages

Industrial packages are used to transport materials with low radioactivity. These are for both material with low specific activity (per unit mass) and material with low levels of surface contamination. The industrial packages are split into three different groups, IP1, IP2 and IP3 with increasing capability of withstanding minor mishaps respectively.

IP1 packages have to satisfy the requirements for that of excepted packages, IP2 packages have to be also able to withstand a drop test and a compression test whilst IP3 packages have to further withstand a penetration drop test and water spray testing.

The drop test simulates the container falling from height off the transport vessel. The test itself is a drop from a height between 0.3-1.2 metres, depending on the weight of the container and its contents, onto a solid concrete block so that all of the maximum force is directed back to the container. The compression test involves stacking a weight of 5 times the container itself for a period of 24 hours.

For the penetration test a 3.2 cm diameter bar weighing 6kg is dropped from a height of 1 metre directly on to the weakest part of the containment system of the container. Finally, the water spray test simulates the presence of rain using a rate of 5cm of water per hour. Table 2.1.1 below has been extracted from reference E to show the increasing intensity of testing required with the increased severity of potential hazards.

Industrial packages include steel drums used for transportation in chemical industries but also include purpose built transport flasks. IP-3 packages can be used to transport uranium ores.

Table 2.1.1. Design and Test Requirements for Industrial Packages^E

Criteria	IP-1	IP-2	IP-3
Design Requirements	<ul style="list-style-type: none"> ▪ General Requirements for all packages ▪ Additional pressure and temperature requirements if transported by air 	<ul style="list-style-type: none"> ▪ General Requirements for all packages ▪ Additional pressure and temperature requirements if transported by air 	<ul style="list-style-type: none"> ▪ General Requirements for all packages ▪ Additional pressure and temperature requirements if transported by air ▪ Type A additional requirements
Test requirements		<ul style="list-style-type: none"> ▪ Free drop(from 0.3 to 1.2 metres, depending on the mass of the package) ▪ Stacking or compression 	<p>Each of the following tests must be preceded by a water spray test:</p> <ul style="list-style-type: none"> ▪ Free drop(from 0.3 to 1.2 metres, depending on the mass of the package) ▪ Stacking or compression ▪ Penetration (6kg bar dropped form 1m)

Type A Packages

These packages are used for small but significant quantities of radioactive material. The risks from external radiation and contamination in the event of a release are limited by the amount of material in the container. These limits are set by the IAEA and ensure safety even in the most severe of accident. These packages have the same design and test requirements as the IP-3 package to withstand the effects of normal transport conditions but in addition to this, they have to be able to maintain their integrity in accident conditions, described below.

The IAEA testing regime is much more intensive than that of any real credible accident and is therefore a conservative approach. The requirements are met if the integrity of the container still remains with no significant radiological release after the container has been subject to the following cumulative test sequence;

1. Mechanical Impact Testing^A(para727)

- i. The container will drop a height of 9 metres on to a solid concrete surface in a manner that exposes the weakest part of the container to the maximum impact.
- ii. The container will then be dropped from a height of 1 metre on to a rigidly mounted perpendicular steel bar in a manner that will exert the most damage to the container.
- iii. The container is the subject to a dynamic crush test where a 500 kg steel plate, 1 by 1 metre is dropped from a height of 9 metres.

2. Thermal Testing^A(para 728)

- i. The container is then subject to thermal testing equivalent to engulfing the entire container in fossil fuel flames with an average temperature of at least 800°C for 30 minutes.

~ 2.1: Thermal Testing^F



- ii. The container is then allowed to cool without the aid of cooling systems so that all of the combustion mechanisms fade out naturally.

3. Water Immersion^A (para 729, 730 or 733)

The container is then immersed in at least 15 metres of water, equivalent to a gauge pressure of 150kPa for eight hours.

These containers are used to transport front end nuclear fuel cycle materials (nuclear fuel materials from mining directly up to power generation).

Type B Packages

These packages are used for the transport of highly radioactive material. The radioactive material transported is far more hazardous than that transported in Type A packages and therefore the design and testing requirements of Type B packages must satisfy and exceed those of Type A packages.

Type B packages have to undergo the same mechanical and thermal testing as Type A packages but a more strenuous water immersion test in a head of at least 200m of water, equivalent to 2 MPa for at least 1 hour.

Type B packages are tested thoroughly to ensure that there is no release of containment even in the most severe of accidents. Such containers provide the assurance and confidence for the safe transportation of highly radioactive materials, such as spent fuel and high level waste, by land or sea.

Type C Packages

Type C packages are to be used for small amount of highly radioactive materials when being transported by air. Such containers require even more extensive design and testing requirements than that of type B containers and as to date there are no licensed type C containers in operation.

Transporting Fissile Materials

In addition to the impact and thermal requirements of packages, when transporting fissile material, there is a requirement to ensure subcriticality during all transport conditions. Special consideration shall be taken in developing contingencies for ^A (para 671);

- Leakage of water in or out of the container;
- Loss of efficiency in neutron absorbers, moderators and reflectors;
- Re-arrangement of the contents of the package and the array spacing;
- Temperature changes and;
- Containers being immersed in water or snow.

The requirements are justified through the implementation of mechanical, thermal and water immersion testing for accident conditions. The specific requirement given to fissile packages, particularly those in an array formation where the leakage of water in or out of the container is likely to increase criticality, a water immersion test with a head of at least 0.9 metres is required over a duration of 8 hours.

2.1.3 Regulations Relevance to Reactor Cartridge Design

The reactor cartridge will require two separate package designs, one for the delivery of the fresh core to the operating site and another for the shipment of the spent core away from the site. Both packages contain fissile material and are therefore required to at least be subject to the fissile water immersion test.

The spent core will be a Type B fissile package and have to remain structural integrity and containment of the radioactive contents after being subjected to the most strenuous of the tests described above. The high radioactivity of the spent core and the fission products make it necessary for this package to be heavily shielded to prevent radiation exposure outside of the package.

The fresh core will have to 'survive' the same mechanical impact and thermal testing as the spent fuel packaging but because it has a much lower radioactivity it can be transported in a Type A fissile package as fresh fuel assemblies are today. The water immersion testing is therefore less strenuous and additional shielding is not required. However, the reactor cartridge is planned to be transported as a full core, with the ability to reach criticality if no control rods are used, therefore it is dissimilar to most transport packages used today, with packages used for the nuclear naval propulsion reactors being the only similar concept. The package will have to be designed in such a way that the control rods remain effective in all transport conditions.

Both of the packages are required to demonstrate that they will remain in a state of sub-criticality at all times according to the IAEA Criticality Safety Index^C and this is achieved by modeling the contents and their arrangement within the package using an accepted criticality safety management code.

2.2 Transport Regulations in the UK

The regulations for the transportation of nuclear fuel in the UK is derived from the IAEA's Regulations for the Safe Transport of Radioactive materials, as are the EU directives. In addition to the requirements explained in section 2.1, transport is also governed by the UK Department for Transport (DfT) under the Highways Agency and the

Rail authorities, which impose size and weight restrictions for loads. These regulations do not restrict the packaging directly but they do concern the overall load it is a part of.

The operational objective of the reactor 'cartridge' design is to be road transportable whilst remaining economical and practical. This section will concentrate on the constraints imposed for a design that will minimise both transportation and fuel handling costs however, the maximum limits for these constraints will be considered along with the operational penalties associated with them.

A similar review of the safe transport of radioactive material by road and rail, but instead looking at the constraints transport imposes on the *Phased Disposal Concept* was carried out in the 2002 Nirex Report.⁶ The constraints below are roughly based on the template of this report but with additional resources.

2.2.1 Road Constraints

The constraints imposed by road transportation are derived from a combination of size and weight restrictions defined by:

- a. the highways agency for the classification of road vehicles and;
- b. the chosen route (i.e. bridge restrictions).

The route to be taken for the transport can be changed to suit the specific load of a package with the permission of the Office of Civil Nuclear Security which will be discussed later in section 2.3. The restrictions imposed on road vehicles from the highways agency are less easy to overcome, although there is no definite limit to the size and weight of a load that can be transported on the roads, as from time to time large vessels can be seen being transported with an escort but there are costs dependent on the type of load.

The highways agency adopts a graded approach to the classification of loads ranging from that of the normal 'Heavy Goods Vehicle' where no restrictions apply and through to 'abnormal loads', which is further divided into four different classifications.

An abnormal load is defined in the *Road Vehicles (Authorisation of Special Types) (General) Order 2003* as a load that is unable to be divided into smaller fragments without undue expense and risk of damage and exceeds the nominal dimensions of width 3 m or length 18.75 m or exceeds the maximum gross weight for a HGV of 44 tonnes or 11.5 tonnes per axle. Figure 2.2.1 below shows the different categories of loads and the different regulatory bodies that need to be notified of the transportation before it is authorised.

Figure

2.2.1^H

Notification required for different weight and width/length categories *					
Gross vehicle weight	Individual axle weight	Width < 2.9m and Rigid length < 18.65m	Width 2.9 to 5.0m or Rigid length > 18.65m	Width 5.0 to 6.1m	Width > 6.1m or Rigid length > 30.0m ◇
Under 18t (2-axle) Under 26t (3-axle) Under 32t (4-axle rigid) Under 36t (2+2 axle artic) Under 40t (5-axle) Under 44t (others)	Under 11.5t	No special requirements	Police notification †	HA AIL team & Police notification	HA AIL team, Police & Highway authority notification
Between limits above and 80t (STGO category 1 & 2‡)	Between 11.5t and 12.5t	Highway authority notification	Police & Highway authority notification	HA AIL team, Police & Highway authority notification	
Between 80t and 150t (STGO category 3)	Between 12.5t and 16.5t	Police & Highway authority notification			
Over 150t	Over 16.5t	HA AIL team, Police & Highway authority notification			

- * Note that there are other factors, e.g. total combination length and overhangs that also affect the notification requirements
- ◇ Loads with a rigid length over 27.4 m are also in this category if the load is below the STGO weight limits
- † Loads wider than 4.3m are subject to STGO regulations
- ‡ STGO category 2 is over 50 tonnes gross weight, category 1 is under 50 tonnes

Key to classifications:

	C&U abnormal load
	STGO
	STGO VR1 category
	Special Order

Figure 2.2.1 displays the graded approach to the classification of abnormal loads. No special requirements exist for loads within the HGV weight and dimension limits but as you the weight and dimensions increase the level of classification increases.

- A Construction and Use (C&U) load has a weight under 44 tonnes but exceeds the dimensions of a HGV, with a width between 2.9 and 5 m or a length exceeding 18.75 m.
- A Special Type General Order (STGO) category 1 load has a weight not exceeding 50 tonnes or 11.5 tonnes per axle.
- A STGO category 2 load has a weight between 50 and 80 tonnes and a category 3 load is between weights of 80 and 150 tonnes
- Weights exceeding 150 tonnes can be transported but under a Special Order but at extra effort and cost.

The higher the category of load, the higher the penalties are in terms of effort and cost. C&U loads are much less restricted than STGO loads, however they do differ from HGV loads and the police have to be notified of the transport in advance to assess if any special measures are needed. The 44 tonnes limit for HGV and C&U loads translates to a payload limit of about 26 tonnes¹.

STGO category 1 and 2 loads are all subject to speed restrictions and travel times to minimise the chance of an accident and to minimise traffic congestion respectively. STGO category 3 loads and above will also have to be accompanied by an escort thus incurring additional costs.

2.2.2 Rail Constraints

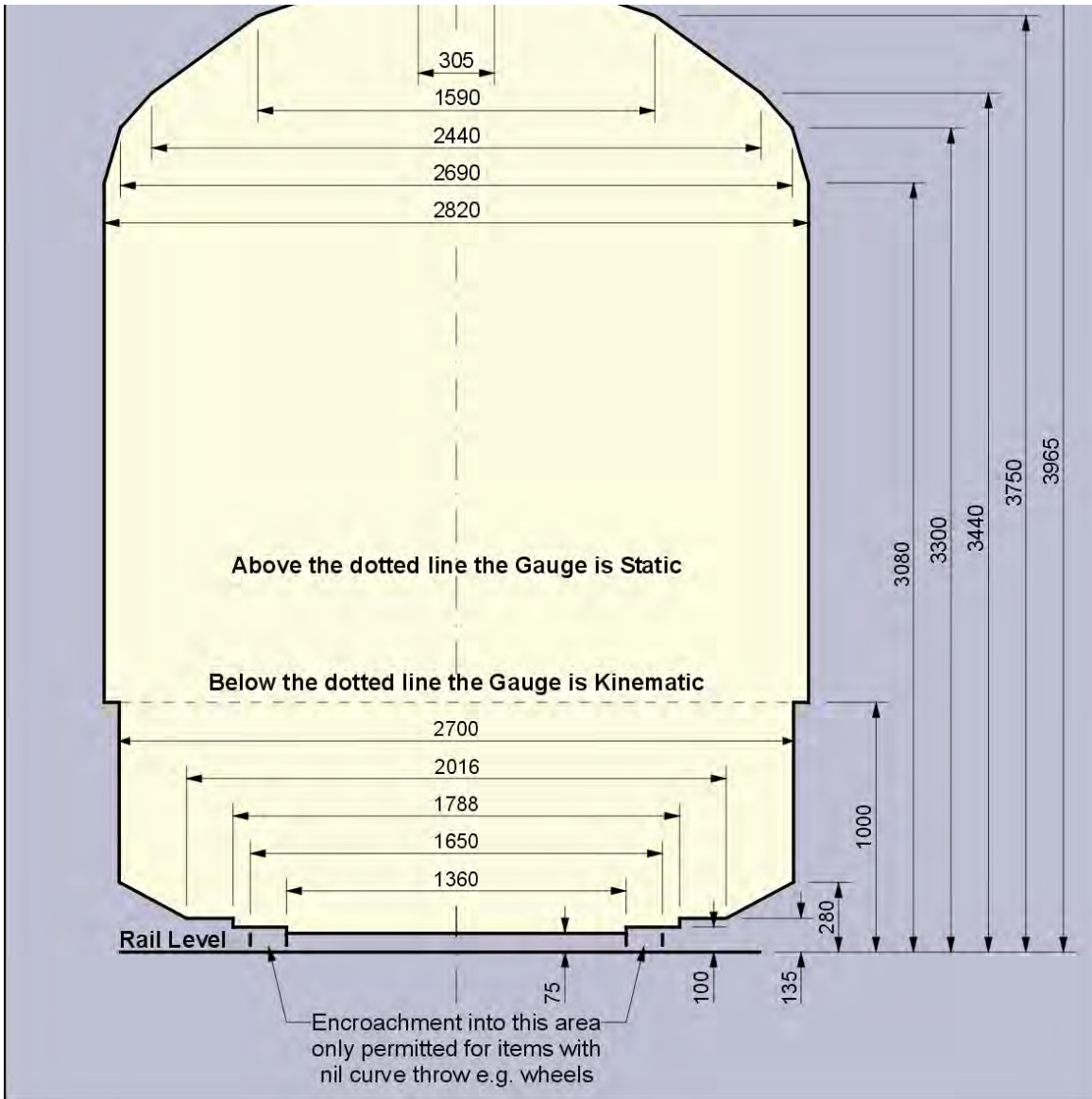
The design objectives of the nuclear 'cartridge' do not currently include the need to be road transportable but it is something that should be considered, especially when considering where the spent core will eventually be disposed of. In the UK, currently all the spent fuel elements that are to be re-processed, arrive at Sellafield by rail in Type B flasks that can exceed 100 tonnes, after being moved only short distances by road

because of the slow speeds the special heavy vehicles transporting them are restricted to.

There is an additional bonus to designing the transport flasks to meet the UK rail network requirements, in that the UK has the smallest dimensional limits for historic reasons, making a flask designed to maximum external dimensions of 2450 mm x 2450 mm x 2360 mm height acceptable in all other countries. Figure 2.2.2 below shows the maximum dimensions of a rail carriage and initial estimates of the maximum available dimensions for the package.

The weight restrictions applying to the rail network in the UK are classified in terms of 'Route Availability'¹ (RA) rated from 1 to 10. An RA of 10 translates to the maximum weight availability, applying to mostly main lines and some specifically designed track for heavy transports. The maximum loaded weight of a trailer is 102 tonnes but this is assuming the rail route is of all RA 10 rating but in reality it averages out to be an RA of 6 which is comparable to 22.5 tonnes per axle and a payload exceeding 65 tonnes (that equivalent to a Sellafield Waste Transport Container with a lead shielding of 285 mm for high level waste). However, the current transport flasks (Excellox) used for transporting spent PWR fuel elements to THORP at Sellafield weigh in excess of 100 tonnes and these are transported by sea in a specially designed double hull boat operated by Pacific Nuclear Transport Limited.

Figure 2.2.2: Train Carriage Dimensions are limiting Factor¹



2.2.3 Restraints Imposed on the Reactor Cartridge Design by UK Transport Network Regulations

The initial objective of the reactor cartridge concept was to design it to be road transportable to allow access to remote locations and to transport it as an entire core

that easily fits in a power generation module. To achieve this it is clear that the spent core is the limiting factor because it will produce more significant thermal stresses and radiation than a fresh core.

For the spent core to be easily road transportable it must not exceed the conditions of a C&U load. This package design must therefore provide adequate radiation shielding and withstand the high temperatures of the spent core, after it has been cooled for an adequate amount of time at the operating site, within the following weights and dimensions:

- A width of 5 m or less and a length less than 18.75 m.
- A weight of 44 tonnes or less.

These dimensional constraints at first glimpse seem to be manageable but it should be recognised that these are the requirements of the total load being transported and not just the package. It will not be until the neutronics of the core design has been completed before a definite solution is known. The weight of such a package appear to be a more significant problem as some current spent fuel assemblies exceed 100 tonnes but this will be looked at in further detail in a later section.

The ideal reactor core design would have slightly smaller dimensions and fit in an adequate package that does not exceed the ISO standard freight container. This would allow the reactor core to be transported almost anywhere within the restrictions imposed on the bridges and road for a chosen route.

If it becomes apparent that these constraints are not practical it does not necessary mean that the reactor cartridge design is not economically viable. The special order categories allow larger and heavier loads to be transported on the road network but at

greater expense. A feasibility study will have to be performed at a later date if the design is to be taken further.

Spent fuel containers are currently only travelled short distances by road because of the size and weight of them restricts the speed they are allowed to travel. They are usually only transported to the nearest rail link where it is possible to transport loads exceeding 100 tonnes. The proximity of the proposed operating sites to the rail links should be considered as it may reduce logistical costs if rail transport was to be used in addition to road transport. This would increase practicability of heavy transport packages whilst only imposing dimensional constraints shown in figure 2.2.2.

2.3 Security Requirements for the Transportation of Nuclear Material

The security surrounding nuclear materials has always been high profile because of the potential catastrophic consequences of it being used in intentional malicious acts. The most vulnerable operation involving nuclear materials in terms of proliferation is probably the transportation of it. Therefore a well devised protection strategy is necessary to minimise the opportunity for proliferation.

The Physical Protection of Nuclear Material and Nuclear Facilities^K legislation advises that an effective protection strategy for transporting nuclear materials should seek to:

- Minimise the total journey time of a transport;
- Minimise the number of material transfer interfaces, i.e from a rail carriage to a road vehicle;
- Provide adequate protection in line with the categorisation of the nuclear material;
- Avoid the over use of regular routes;

- Ensure pre-determined trustworthy and responsible individuals are used for the transport; and
- Keep the number of individual with advance knowledge of a transport to a minimum.

The UK independent security regulator for the transportation of civil nuclear material is the Office for Civil Nuclear Security (OCNS) which conduct their duties in accordance with the Nuclear Industries Security Regulations 2003. It should be recognised that the UK conducts more shipments of highly sensitive nuclear material than any other nation and it is the OCNS's responsibility to ensure the security measures are adhered to.

The overriding aim of the OCNS is to:

To ensure that nuclear material, whether in the course of transport or on sites, and sensitive nuclear information held by the civil nuclear industry is subject to effective security protection.^L

This aim in itself makes it difficult for the OCNS to share information about the security of nuclear transports and is prohibited from sharing information that might prejudice the security of any nuclear site or nuclear material under section 79 of the UK's Anti-Terrorism, Crime and Security Act 2001. As a result of these restrictions to information this section is a more general and simplistic review of the security for nuclear transport than real life transports require. The following information has been sources from the WNTI, a conversation with the Principal Inspector of the OCNS and a paper he has written on the security of civil nuclear transports.

2.3.1 Security Requirements for all carriers of Nuclear Fuel¹

Nuclear material is given a classification varying from Category I-III, category I materials require the most security measures because it is potentially dangerous material that proliferators are most interested in. Table 2.3.1 shows the classification of the fissile nuclear materials that are being considered for the nuclear cartridge design.

Table 2.3.1: Categorisation of the Nuclear Material^M

Form	Category I	Category II	Category III
Unirradiated Fuel enriched between 10–20 % ²³⁵ U	5 kg or more	Less than 5 kg but more than 1 kg	1 kg or less but more than 15g
Unirradiated Fuel enriched between natural & 10% ²³⁵ U		10 kg or more	Less than 10 kg but more than 1 kg
Irradiated Fuel ²		Depleted or natural uranium, thorium or low enriched fuel (less than 10% fissile content)	

The un-irradiated reactor cartridge core is likely to be a category II or III design if it has enrichment between 10-20% and more than 10 kilograms of ²³⁵U are being transported^N. If a shipment contains less than 10 kilograms of ²³⁵U it is a category III nuclear material.

Similarly, the spent reactor core will be a category II material because of the ²³⁵U burn-up reduced the enrichment of the material and the contents is less desirable to

¹ **Civil Nuclear Transport Security Regulation Paper**
Presentation by Bryan Reeves, the Principal Inspector at the OCNS, at a Radiation Transport Conference.

² Based on international transport considerations and OCNS guidelines.

proliferators because of the dangers and hazards associated with irradiated fuel. From a security point of view spent fuel is unlikely to cause a threat.

The OCNS set the following key requirements:

- A carrier must be approved by the OCNS before transporting Category I-III material. Approval is obtained through a Transport Security Statement (TSS) written to the OCNS detailing the carrier's capability of personnel security, information security, transportation security (escorts, route planning etc), container tracking and contingency planning;
- The preparations for the transport must adhere to the approved TSS;
- Ensure that those responsible with access to the sensitive information of the transport are appropriately vetted;
- Notify the OCNS of anything that veers from the initial plan;
- A Transport Plan for each shipment of category I or II material has to be approved by the OCNS and the OCNS has to be notified of the date of transport at least 7 days before;
- For category III materials the OCNS has to be given a brief outline of the details of the transport.
- Comply with all OCNS recommendations regarding nuclear security.

2.3.2 Determination of Threat

The security measures that are required for a transport are determined through an evaluation of the threats that the material poses to a state. This is achieved through a 'Design Basis Threat' (DBT) document, where appropriate protection systems are developed to ensure the adequate defense of the transports in the event of an attack from armed terrorist groups intent on stealing a shipment of nuclear material. The DBT assumes the threat from different terrorist groups operating in different areas and

across different transport modes, hence the minimum requirements for the protection of the nuclear material varies from state to state.

The threat posed to the state from the transport can vary in magnitude over time and therefore the minimum requirements can vary over time. The OCNS interact closely with national and international authorities to effectively manage this change of requirements, and because the OCNS have to be notified of any transport of category I-III material, they can react quickly to any change of threat and increase the security or even stop the transport of the nuclear material.

2.3.3 Security Relevance to the Cartridge Design

The security requirements for transporting the reactor cartridge will vary dependent on the classification of the nuclear material in the final design. Table 2.3.1 shows the classification for all of the nuclear materials that are being considered for the design.

In keeping with the original design objectives of the design project, the costs and effort of transport should be kept to a minimum. Therefore, it would be desirable to design the reactor core so that it does not become classified as a category I nuclear material. Category I nuclear materials require significantly more security measures than category II and III transports including armed guards (unless in a country that does not have them).

The spent core will also be of category II nuclear material, making the security requirements for both journeys of the core, to and from the site, of the same level. The exact requirements will not be exactly the same as they are based on an evaluation of the threat the nuclear material poses to a state dependent on the geographical route and mode of transport.

The key requirements that will have to be met for the category II transport of the nuclear cartridge design are:^K

- Notification to the receiver of the exact time of handover;
- The selection of a route which poses the least risk due to known threats;
- The transport container must be locked and sealed to make it clear when unauthorised access has occurred;
- The transport vehicle should be inspected to ensure there are no sabotage devices present prior to loading;
- The individuals involved carrying out the transport should be given written instructions that have been approved by the OCNS; and
- Frequent contact should be made between the transport vehicle and the organisation responsible for the transport.

The security measures that need to be in place before the nuclear cartridge design would be able to be transported should not be difficult to overcome providing that the transport routes are developed with collaboration with the competent authority for nuclear security in the states that are involved with the transport. Providing that the design remains within the category II classification the approval of transport by the security authority is almost guaranteed as this classification of nuclear material is transported today on a routinely basis in various different containers.

2.4 Transport Containers Currently In Operation

Nuclear material of all classifications and grades is transported routinely between nuclear facilities on a day to day basis. The safe transport of this material has been successfully completed for the past fifty years without any significant incidents. This has

been achieved primarily through containing the radioactive contents in a sealed package, which act as a containment system and a physical barrier between the potential hazards of the material itself and the environment.

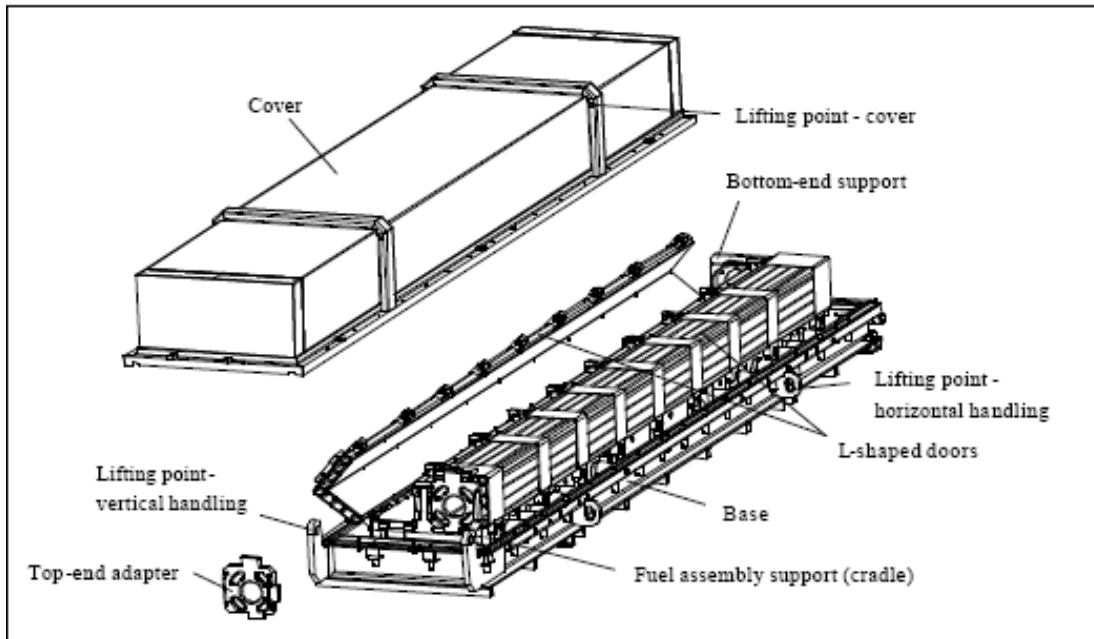
2.4.1 Fresh Fuel Containers

Fresh Fuel has a relatively low activity and can therefore be transported without onerous restrictions. PWR fuel can be transported around in ANF containers which are of a box shape. The PWR fuel assemblies are wrapped in the ANF package which provides adequate protection from the hazards associated with transport. The packages have been successfully tested to ensure they meet the tough IAEA criteria.

The ANF-18 package has been in operation since 2002 and consists of an outer steel casing that shrouds a fuel assembly support that is suspended in place through rubber shock absorbers. Figure 2.4.1 below shows the schematic of the container. The container can carry two PWR assemblies and has outer dimensions of 5866 mm x 1136 mm x 792 mm and has a maximum loaded weight of 4.7 tonnes, therefore a standard ISO vehicle, with a typical payload of 25 tonnes, can carry 5 of these containers.

Spent fuel provides a much more difficult challenge for transport than fresh fuel because of the increased radioactivity from the fission products created during power generation. The packaging requirements for spent fuel packaging are therefore much more intensive, in particular radiation shielding. In most instances, fresh fuel can be transported without any additional shielding than that provided by the casing where as spent fuel requires up to 300 mm of gamma shielding⁰. Gamma shielding tends to be lead lined stainless steel blocks and therefore add significant weight to a load.

Figure 2.4.1: ANF-18 Transport Containers^P



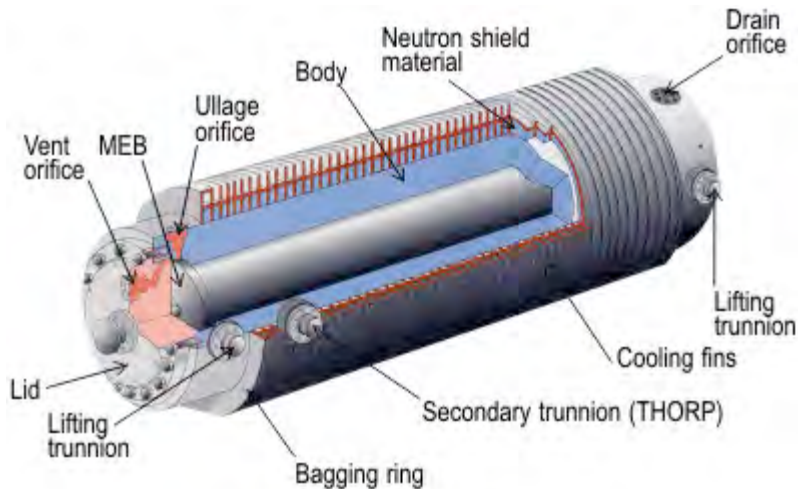
2.4.2 Excellox Transport Flasks

The Excellox 6 and 7 containers, shown in figure 2.4.1 below, are used for the transport of light water reactor fuel assemblies. They are cylindrical in shape and approximately 6 m in length and 2.5 m in diameter and are re-usable. The outer shell is made from mild steel and it is finned circumferentially to aid cooling, and the gaps are filled with neutron absorbing materials, such as cadmium, to reduce the reactivity of the contents and ensure sub-criticality.

There is a cavity on the interior of this shell, approximately 5.2 m in length and between 1700 - 1800 mm in diameter. This is traditionally filled with a multi-element bottle (MEB), which is a sealed container usually containing 12 LWR fuel assemblies, the equivalent to 6 tonnes of fuel, in an array. The MEB simplifies the fuel handling and keeps the loose fission products contained in one vessel. The array is held in position by

a boronated stainless steel rack, where the spacing has been carefully selected using criticality safety modelling that ensure sub-criticality in all transport modes.

Figure 2.4.2: Excellox (7/7) Container^Q



The total weight of this Excellox flask is around 110 tonnes, far exceeding the acceptable weight for road transport using HGVs or C&U vehicles. As a result they are only transported short distances by road, from the operating site to the closest rail link, using special order vehicles and appropriate escorts.

The Excellox flask would allow a cartridge design with a maximum length less than 5.2 m, diameter less than 1.8 m and a weight less than 8 tonnes.

2.4.3 Generic Road Transport Containers^R

There is a generic design for spent fuel transport used today which is similar but simpler designs of the Excellox transport flasks. They consist of outer and inner cylindrical steel shells, with additional lead gamma shielding in-between. The inner steel shell is lined with a neutron shielding material and a container of the nuclear fuel sits in the centre, with impact limiters on either end of the flask.

The inner diameter of this flask is 1200 mm with 70 mm of gamma shielding and the overall length of the container is 6 m. The PWR assemblies tend to have a length of 1.4 m with 100 mm spacing between each other. These flasks can typically carry up to 4 PWR assemblies or 9 BWR assemblies, with a gross fully loaded weight of 25 tonnes.

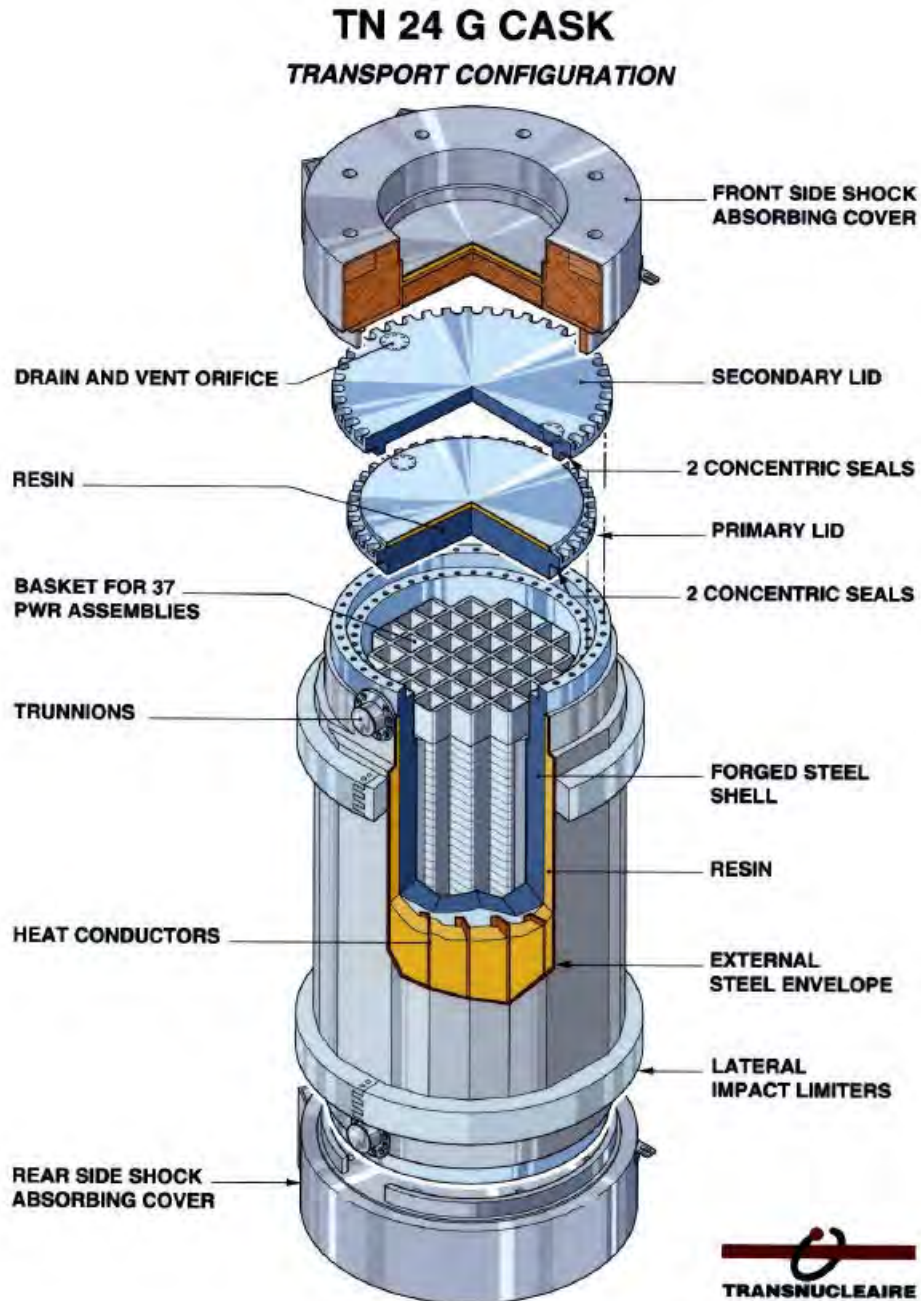
Larger containers are also used which are transported by rail, the largest of which weighs 125 tonnes. The inner diameter of the flask is 2400 mm and the length approaches 8 m. These flasks can accommodate up to 26 PWR assemblies which make the fully loaded weight so much higher and as a result can only be transported by road effectively over short distances using a special order vehicle.

The smaller container is the most appropriate container for the cartridge design because it would allow remote access to sites by road with little regulatory restrictions or additional costs. For the cartridge to be transported in this it would be restricted to a maximum length of 6m and diameter of 1.2 m. These dimensions can be increased but the larger and heavier containers require rail transport.

2.4.4 TN International Flasks

Transnuclear have been developing transport containers for nuclear fuel for over 20 years and have developed containers for both transport and storage. They have several series of flasks which can be adapted to different specifications dependent on the contents. Figure 2.4.3 below shows the layout of a typical TN24 container.

Figure 2.4.3: TN24 Family Transport



Container^s

The TN families of transport flask are essentially the same as the generic flasks describe in section 2.3.3 with a cylindrical central shell, with an impact limiter on either end and neutron and gamma shielding along the length of the cylinder. The TN flasks are used to transport spent LWR fuel assemblies in an array, where the fuel elements rest in a

basket in the cavity of the flask. The basket has neutron shielding to maintain subcriticality, where the neutron absorber is an intricate part of the aluminum basket itself to prevent any accidental displacement. The basket also acts as a series of coolant channels with the aluminum providing high thermal conductivity.

The maximum cavity dimensions of the TN series of flasks and the maximum enrichments the flasks are designed to ensure subcriticality are given in Table 2.4.3.2 below.

Table 2.4.3.2: TN Series Parameters^T

Container	Cavity Length (mm)	Inner Diameter (mm)	Weight (tonnes)	Max. Enrichment (²³⁵ U%)
TN24	4150	1600	110	3.5
TN32	4150	1750	117	4.05
TN32A	4180	1750	117	4.05
TN32B	4150	1750	117.5	4.05
TN40	4140	1830	-	3.85

The TN series of transportation flasks does not appear to offer an option for transporting higher enriched spent fuels but this may be because of the fuel basket design to ensure subcriticality. TN international have the necessary expertise to adapt one of their existing containers or develop a new package that would be able to be used for the cartridge design.

2.4.5 Sellafield Waste Transport Containers (SWTC)

SWTC flasks are used to transport intermediate level waste with varying thickness of gamma shielding depending on the activity of the contents. Currently the waste is packaged in drums and then secured in an array inside the reusable SWTC. It may be possible to place the spent reactor battery core into one of these flasks.

SWTCs are cubical in shape and come in three different sizes dependent on the amount of shielding uses. There are three different thicknesses of shielding, 70 mm, 150 mm and 285 mm but the internal dimensional are the same for each one.

Only one of the STWCs can be transported by road within the standard ISO limits of a HGV and this is the SWTC70. This has a maximum payload of 28 tonnes, but the other packages can still be transported by road but with more onerous restrictions. The maximum gross weight of the heaviest package is 65 tonnes.

2.4.6 Naval Nuclear Propulsion Engine Transports

Due to the highly sensitive nature of the naval propulsion systems there is not much information about the transportation of the fresh or spent cores released by the UK Ministry of Defence (MoD). The propulsion systems themselves are a highly kept secret but it is fair to assume that they contain highly enriched material, far exceeding that used in any current or foreseeable future civil nuclear reactor. The core is likely to be built up of smaller blocks which are transported separately with control rods locked in place. For these reasons it is the most similar fuel transport arrangement to that of the cartridge design and any information regarding naval reactor transport could prove to be the most relevant.

The British Nuclear Group (BNG) developed an approved package for the transport of spent naval fuel elements which transferred 13 core modules at a time by rail with a fully loaded weight of 75 tonnes^U. This is too heavy for the desired package design for the cartridge design but provides evidence that it is possible to transport spent fuel with the control rods included as a complete package.

2.5 Discussion of Constraints Imposed by Transport

The transportation of nuclear fuel is an integral part of the nuclear fuel cycle. In the context of the Nuclear Cartridge concept it sets an initial design envelope which is most desirable for economic and practical purposes. This envelope can be broadened but with a penalty in the form of additional costs.

There are three main categories that restrict the movement of nuclear material, which all have the interest of the public and environment as a priority. These are;

1. The ability to maintain containment during all required modes of transport;
2. Size and weight of a load using the established transportation networks; and
3. The ability to provide adequate protection against any threats of un-authorised removal or sabotage of nuclear materials.

When transporting radioactive material the carrier must be able to ensure that there will be no radiation exposure or damage caused to person, property or the environment as a result of the transport. This is ensured through the use of packages which are tested thoroughly to ensure that the risks and hazards are as low as reasonably practicable (ALARP).

The cartridge design will need to be transported in at least a fissile Type A package when fresh fuel and a fissile Type B package when irradiated. There are transport flasks that are currently in operation that would allow the transportation of both the fresh and spent cartridge but to transport it as a single entity would require the dimensions and weight to be within that of the current flasks described in section 2.4. Further for the ability of effectively transporting the cartridge by road the cartridge is restricted to the smaller generic cylindrical package whose maximum parameters are shown in table 2.5.1 with other containers.

Table 2.5.1: Maximum parameters provided by current transport flasks

Type of Container	Max Internal Diameter (mm)	Max Internal Length (mm)	Fully Loaded Weight (tonnes)
Small Generic Package	1200	6000	25
Large Generic Package	2400	8000	125
Excellox 6	~1700	5200	110
BNG Naval Flask	-	-	75
TN32A	1600	4150	110

For the purpose of meeting the objectives of the design the classification of the nuclear fuel to be used, in terms of security should not reach a category I material before or after power generation. The classification of nuclear materials is given in table 2.3.1.

If the intended users are large chemical processing plants, the extra cost of transporting the cartridge as an exception may be proportional to the capital saving these companies will receive over their operational life. The cartridge may therefore still be attractive if it exceeds all of the desirable classifications and falls in to the category I for nuclear materials and is required to be transported as a special order load.

The cartridge may prove applicable to a number of smaller industries than it was initially intended for if it remains within the constraints of a category II, HGV or C&U load. The security restrictions will in this instance be placed on the organisation that it is providing electrical power for, as they will have to provide the regulatory body that they have the protection in place, as a nuclear facility, to prevent sabotage and proliferation. This may make it favourable for the manufacturer of this reactor to also act as the operator at the operating site on behalf of the plant it is providing energy to. This is a study that will have to be carried out at a future date when looking at the regulations surrounding nuclear facilities.

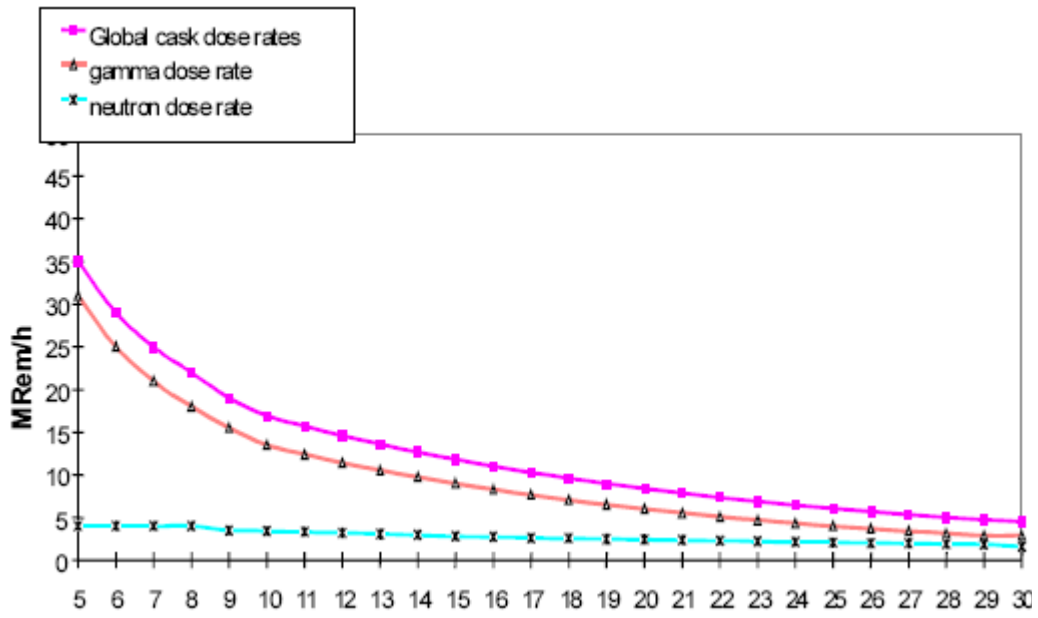
In a conversation with a principal engineer at the transport package division of BNFL the challenges with extending the internal radius close to 2 m were discussed. The maximum outer diameter for rail transport is less than 2.7 m due to bridge and tunnel requirements on the track bearing in mind that the weight of such a flask would be significantly large. The gamma shielding required will be 285 mm of heavy steel, which reduces the internal diameter to 2 - 2.1 m and a fully loaded container would have trouble meeting the weight requirements for both road and rail.

Alternatively, a lead liner has been used in the past which, when placed close to the core can reduce the thickness of gamma shielding required and potentially reduce the weight of the package. This use of the lead liner has been vacant from the most recent design of containers because of the difficulty to manufacture a thin layer in the inner side of the steel shell and the contamination of the gap between the two materials.

The new Excellox 8 transport containers for the transport of spent PWR fuel assemblies is designed to have a larger payload than previous designs by using the benefit of longer on-site cooling before transportation for re-processing. Figure 2.5.2 below shows the reduction in gamma and neutron radiation over time. It is debatable to how much of the shielding thickness that will be saved over a period of time, perhaps only several mm over a year.

The identification of possible transport containers allows the initial weight and dimensional constraints of the reactor core to be determined. However, these constraints will be influenced by every aspect of the construction, operation, maintenance and decommissioning of the power plant before design is finalised.

Figure 2.5.2: Change in Surface Dose Rates of TN24 Container^T



3. Fuel Handling

The engineering design of any project involves compromises between different aspects of a products life. This chapter will look at the fuel handling systems currently in operation, looking at the loading and unloading of the fuel assemblies and discuss their applicability to the cartridge design and attempt to identify any potential 'showstoppers'.

3.1.1 Advanced Gas Reactor Fuel Handling

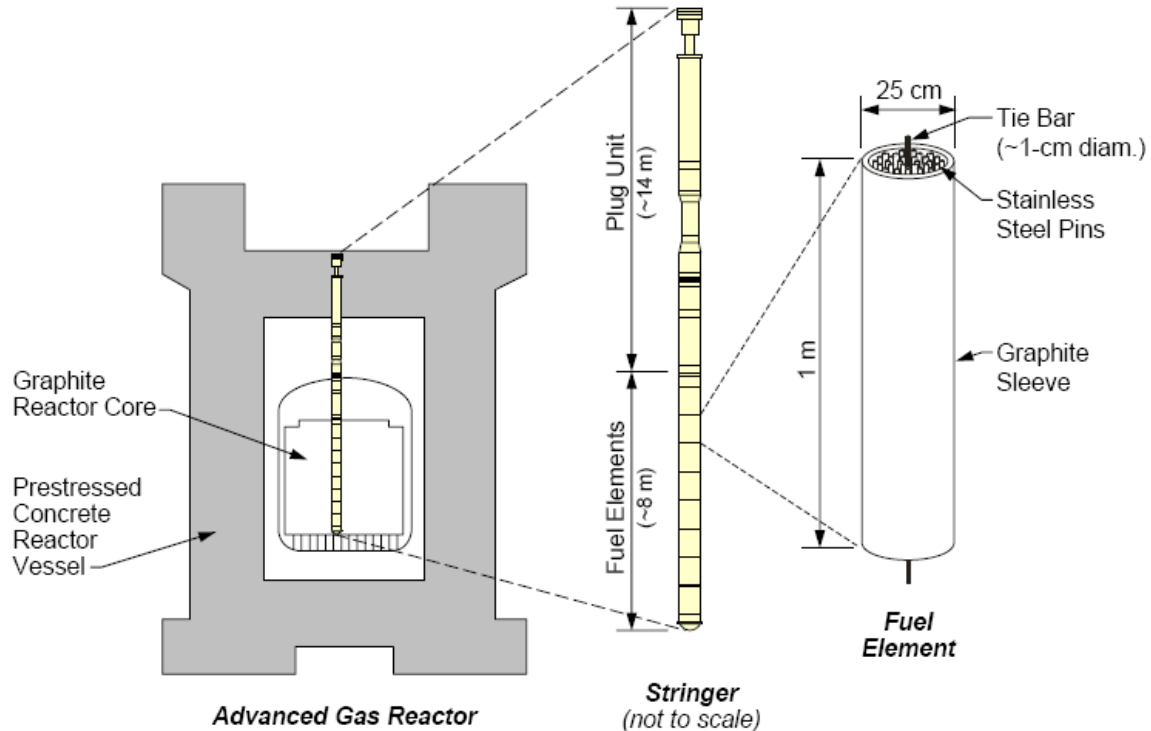
The British designed AGR is similar to the conceptual cartridge reactor in that it is a graphite moderated and carbon dioxide cooled. The AGR uses Uranium Oxide fuel pellets, enriched to about 3 % ^{235}U , assembled in a graphite sleeve fuel element. The AGR reactor is a much larger design than the cartridge, producing up to 660 MWe.

The AGR fuel elements are around 1 m in length, 25 cm in diameter and consist of uranium oxide fuel pellets in a graphite sleeve, with a central hole. They arrive at the power stations in cuboid, Type A transport containers, in which several fuel elements are loaded vertically. The fuel elements are removed from the containers and inspected visually to ensure that they are undamaged.

The AGR fuel elements are moved to a new build facility at the operating site, where the fuel stringer is assembled. Figure 3.1.1 below shows the stringer used for the re-fueling of the core, which can be achieved online. The stringer consists of (in ascending order from the bottom) a nose unit that mates with a seat on the diagrid at the bottom of the reactor, eight fuel elements, a top reflector and anti-gapping unit, and a plug unit. The components located below the plug unit are all replaced after each fuel channel is re-fueled.

Figure 3.1.1: AGR Fuel

Stringer^v



The plug unit is the largest component of the stringer and consists of a flow control unit named the 'gas gag', a burst can detection system, gas outlet temperature thermocouples, and thermal and radiation shielding. The components of the stringer are held together by a slender central tie bar, approximately 1 cm in diameter and made from a high nickel alloy, PE16.

The re-fueling machine collects the new fuel stringers from the new build facility and holds them in a carousel. The re-fueling machine is then moved to the pile gap above the fuel channel to be re-fueled before being connected to the fueling standpipe to become an integral part of the primary cooling circuit. The empty fuel stringer is then slowly withdrawn into a vacant position in the carousel which then moves around to

place the new fuel stringer into the now empty fuel channel. The channel is then closed, allowing the re-fueling machine to be disconnected.

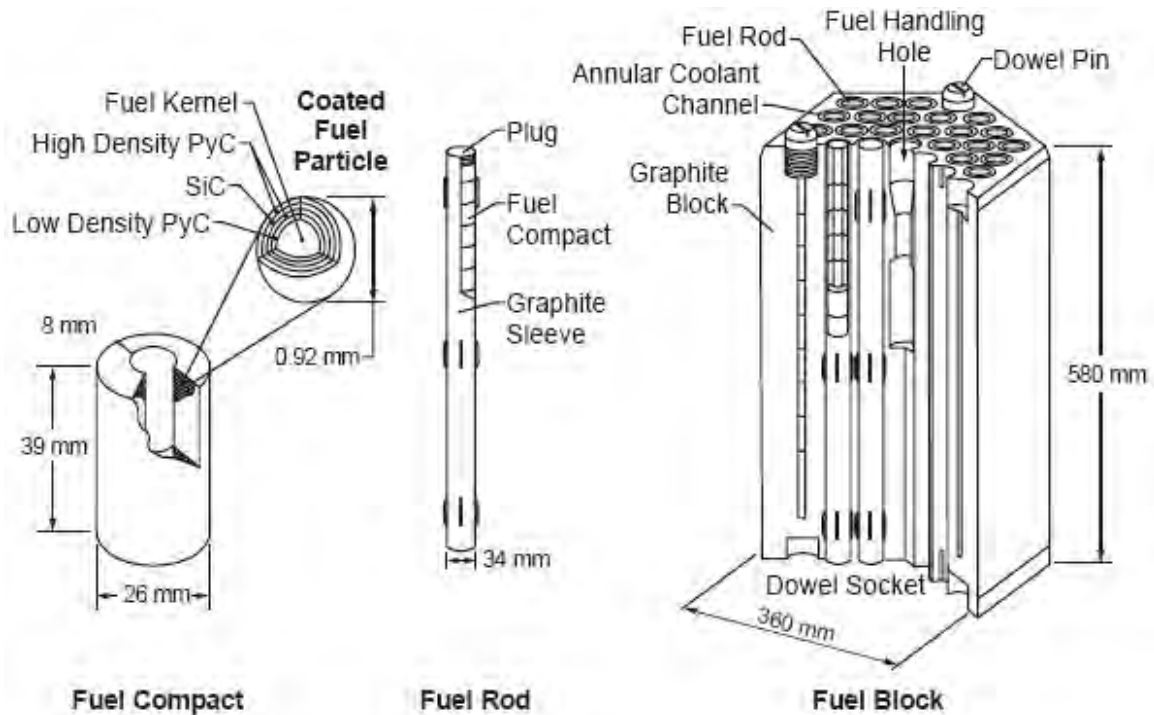
The refueling machine then moves the spent stringer to an on-site intermediate storage facility for spent fuel where it is cooled for several weeks until it is cool enough to be disassembled by cropping the tie bar. The gag unit is conditioned for reuse whilst the spent fuel elements are transferred to an on-site cooling pond, where they will remain until they have sufficiently cooled to be transferred to Sellafield for reprocessing. The non-fuel components are re-located into a storage vault where they will remain until they are eventually moved to a medium-level waste storage facility.

The AGR reactor design and re-fuelling machine differ significantly from the proposed cartridge designs and do not provide much guidance in terms of core or fuel handling specifications. The stringer design may pose some use if it is found infeasible to transport the core as one single entity and instead it needs to be divided into smaller sections, where the carousel could pick up the different sections and then move to a spent fuel cooling storage facility on-site, however significant changes would have to be made to the design, as from operating experience the AGR stringer is prone to malfunction.

3.1.2 High Temperature Test Reactor (HTTR)^W

The Japanese HTTR is the most similar design to the cartridge in terms of the core arrangement and fuel composition. The HTTR is a 30 MWt^X, graphite moderated, helium gas cooled reactor with a prismatic block core made up from low enriched TRISO particles. Figure 3.1.2(a) below shows the HTTR core assembly and details the contents of the TRISO particles.

Figure 3.1.2(a): HTTR Fuel and Core Assemblies^W



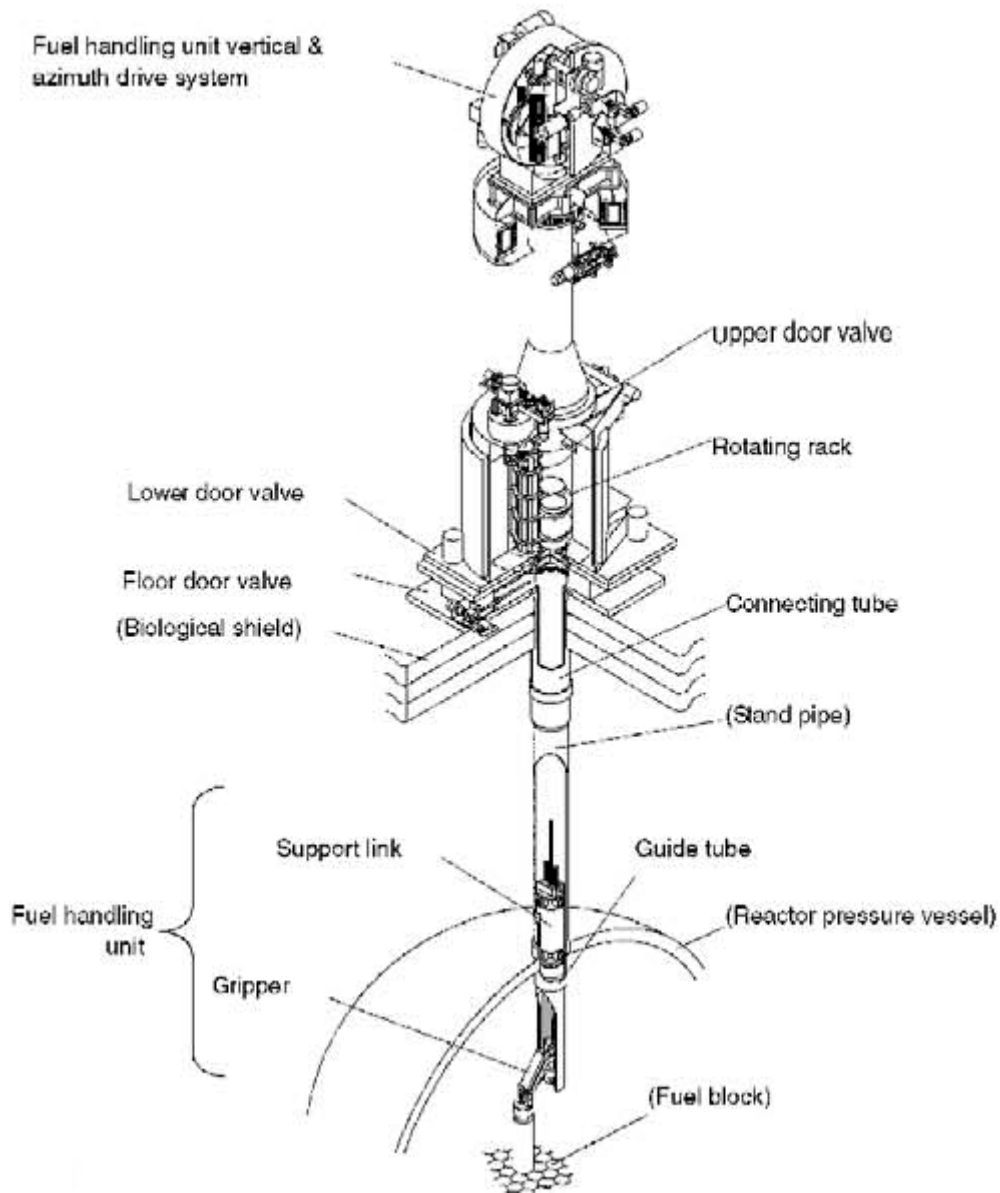
The fuel handling machine used for the HTTR was designed and manufactured by Fuji Electric and its objective is to load, unload and re-fuel the prismatic fuel blocks in the core. Radiation shielding is provided by a sealed cask, and the entire fuel handling unit has a height of 11 m and weighs 150 tonnes, with a capacity to store a maximum of 10 fuel blocks.

The fuel handling mechanism is similar to that of an AGR where the re-fueling unit is attached to a standpipe on the fuel element, but for the HTTR the standpipe is located at the top of the reactor pressure vessel and the gripping mechanism can access 13 separate columns per standpipe. The gripping mechanism that holds the fuel blocks is assisted by a support link that helps guide the lifting and horizontal movement of the fuel block. The gripper connects to the fuel blocks, of about 200 kg in weight, by hooking onto a 30 mm diameter grip hole machined into the fuel block.

The fuel handling unit, shown in figure 3.1.2(b) below, has been designed to:

- Ensure that the gripping mechanism remains in tact even in the event of a single failure to the system, so that the fuel block does not fall and damage the reactor;
- Have automatic, precise positioning of the gripper; and
- Remove the fuel handling mechanism from the reactor in the event of a failure of the arm folding mechanism.

Figure 3.1.2(b): HTTR Fuel Handling Unit^W



The fuel handling unit in this case transfers fuel from three separate locations, the fresh fuel storage facility, the core and the spent fuel storage facility. This is a total of three locations, which is the same number of different locations as the proposed cartridge design; the only difference being the intricacy of the gripping unit for the HTTR is much higher because it has to manoeuvre between 13 separate fuel block locations instead of the single cartridge location.

Although the fuel itself is almost identical to that being considered for the cartridge design, only differing in dimensions and enrichment, the fuel handling requirements are significantly different. The HTTR fuel handling unit is designed to lift a maximum of 13 individual fuel blocks, a total of 2.6 tonnes, which is significantly different to the cartridge design which proposes to lift an entire core as one unit, with a weight that could be an order of magnitude heavier.

3.1.3 Naval Propulsion Reactors

There is little detailed information released about the nuclear fuel cycle of naval nuclear propulsion reactor because of the interest of national security. Naval reactors are of the PWR type but much smaller than civil reactors for obvious reasons and have very high enrichments. Newer submarine reactors have high enough enrichments and enough fissile material to operate for the submarine life to remove the need for submarine re-fuelling. However, the older class of submarines requires re-fuelling and the following is a vague description of the re-fuelling process adopted at the Davenport facility, the UK facility for the handling of spent naval reactors, as described by Malcolm Smith in an Ingenia magazine article^Y.

He describes the dry dock facility at Devonport that is used for the refit and refueling of nuclear Vanguard class submarines. The submarine is directed into a flooded dock that is then sealed with a caisson before the submarine is lowered onto suitable supports by removing the water from the dock. Electrical and cooling water systems are then connected to the onboard systems and the reactor plant to ensure that all of the safety systems remain operational throughout the re-fuelling process.

A chemical process is used to decontaminate the primary coolant circuit and hence reduce the potential radiation exposure to maintenance workers. Access holes are cut into the submarine to allow access to the reactor. A protective reactor access house is

erected around the hole to control radiation releases. The next stage is to remove the reactor lid and install a water shielding tank before the reactor components and fuel elements can be removed and placed into shielded containers for transport to the on-site storage facilities. The fresh fuel elements are then inspected before being installed into the submarine and the hull is sealed before being re-commissioned. The whole re-fuelling process takes at least 2 years to complete.

The spent components are then left to cool in the on-site temporary storage facilities until they can be transported to Sellafield in dedicated transport containers for re-processing. The cores for the newer class of submarines will not be tampered with until the submarines are retired from service and decommissioned at Devonport with the same process for removing the spent core.

The naval propulsion systems are similar to the cartridge design in that they are small reactors where the fuel is not re-fuelled for a long period of time. However, they are still very different from the proposed cartridge design as the core is transported in smaller parcels and assembled in a purpose built building in Barrow, whereas the fuel handling for the cartridge will be completed on a much smaller site.

3.1.4 Discussion of the Considerations for Cartridge Fuel Handling System

All fuel handling machines are designed to a set of principal considerations, including²:

- The configuration of the fuel during handling and storage;
- Type and condition of fuel;
- Size of store and fuel movement schedule;

- Seismic considerations;
- Safety philosophy;
- Operating philosophy; and
- Maintenance and inspection requirements.

The cartridge design proposes to have the fuel as a complete reactor core, with moderation and control rods already in place on arrival to the operating site. The fuel will be enriched between 10 - 20 % and the cartridge will have to be easily fitted into the power generation module. The cartridge is intended to be operated in various different worldwide locations and the seismic conditions will have to be assessed in each case.

The safety philosophy will be in line with IAEA regulations of providing a physical barrier between the radioactive contents and the environment. This will be achieved through a containment system, which is the packaging during transport and the pressure vessel during operation. The operation of the reactor is for prolonged life with a high fuel burn-up which would make the spent fuel element very hot on removal. There is therefore a need for a cooling storage facility on-site which could be dry or wet, where the spent core will be cooled for an appropriate amount of time before being transported in a purpose built transport container to a re-processing or storage facility dependent on which fuel cycle is selected for operation of the reactor.

The maintenance regime is to be scheduled to ensure the safe operation of the reactor but also minimise the need for interference. Ideally the only inspection and maintenance times will be during the re-fuelling and decommissioning of the reactor.

The fuel handling system will therefore have to be able to lift a substantial load from three positions; the arrival/departure position of the transport container, the reactor position in the power generation module and the on-site spent fuel cooling storage

facility. To maximise the efficiency of such a fuel handling machine the heights of the lifts should be kept to a minimum.

Of the fuel handling machines discussed above, the most suitable would be an adaption of the HTTR design where the dexterity of the machine is reduced to allow the maximum loading to increase to a magnitude equivalent to at least the weight of the fresh cartridge if not the spent cartridge.

4. Discussion of Cartridge Design

Through the review of the transport regulations and the current transport regulations it has become apparent that the cartridge will be able to be transported on the road and rail networks but not necessarily without onerous restrictions. The transport of fresh fuel is the most likely of the transports to comply within the road restrictions to allow the shipment without special arrangements having to be made. This is because much less shielding will be needed and therefore the required container will be a much lighter Type A package.

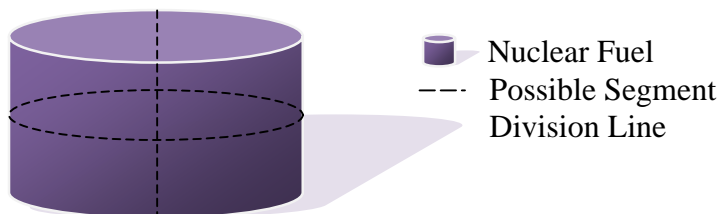
The spent core will be much heavier because not only does it require additional gamma and neutron shielding to the fresh core, but also cooling systems to dissipate the enormous decay heat, even after several years of cooling. The current containers will limit the diameter of the core to less than 2 m and the internal cavity is unlikely to be appropriate for the cartridge design, therefore it is likely that a new package will have to be developed. After a conversation with a member of the UK Department for Transport (DfT) it takes around 2 years to get the approval of a Type B package design, including testing and criticality modeling. The DfT provide assistance throughout the application and currently do not provide charge for this.

There are several developers of packages and once the neutronics have been calculated to give a minimum diameter of core, required to reach criticality, they could be contacted to see if they can adapt one of their current transport containers to accommodate the cartridge design. Alternatively they could begin to design a new flask that is specific for the core design, such transport package developers are BNFL and TN International.

After the first iteration of this review, with the knowledge that the initial core diameter is about 2 m it would appear that even with a specifically designed flask, the spent fuel may have to be transported in more than one package, in that the core would have to be disassembled into more than one piece. This would be deterring away from the initial design but would not necessarily be a 'show stopper'. The core could be designed to be one complete section on arrival that can be separated into smaller sections after irradiation in the core, so that it can be transported more easily.

Figure 4.1 below shows a simple diagram that highlights how the core could be divided up into smaller sections. More thought would have to be put into the number and orientation of the divisions as although simply cutting it in half would provide a solution to the weight restrictions the spent fuel would still have a length or height equivalent to that of the diameter, which is too large for the container.

Figure 4.1: Separation of 'Battery' into more transport friendly segments



The fuel handling systems that are currently in operation are all dissimilar to that of the desired cartridge design in that they are all designed to handle individual fuel columns, with the prismatic HTTR fuel handling machine requiring high dexterity. The advantage to having one large load for loading and unloading is that the re-fuelling can be completed quickly and in minimal steps. Lifting the entire cartridge would only require the fuel handling unit to index to three locations, furthermore the orientation of the three deposits could be designed such that, the height that the cartridge has to be lifted is minimised to reduce the required strength.

The division of the cartridge into smaller, more manageable sections would affect the fuel handling unit in two ways; a smaller load would be being moved and the frequency of the operation will be multiplied by the number of sections the core has been divided up into. The disadvantages to dividing the core into smaller sections come from proliferation risks and the increased operating costs because of the additional time taken to disassemble the core. However, the proliferation risk can be minimised by only having the disassembly of the core divided into smaller sections, because it is much more difficult to steal irradiated fuel.

5. Conclusion and Recommendations

To keep the transport restriction to a minimum the size and weight limits have to be within the limits of a standard ISO container, with a maximum weight of 44 tonnes and a payload around 25 tonnes. The dimensions can be increased slightly without onerous restrictions impacting the shipment of the container, where the maximum width is less than 5 m.

The transport containers can be increased in both size and weight but with logistical penalties, whether this be lower speed limits, time restrictions or the accompaniment of a police escort and special permission from the highways agency. The maximum dimensions and weights allowed for transport are determined by the choice of roads used on the route of a shipment. For rail transport the weight restrictions are of around 100 tonnes and the maximum dimensions are restricted by the rail width and tunnel and bridge restrictions imposed on the length of track being used.

It appears that a new transport package will have to be designed for transport of a complete core for both spent and fresh fuel because the sub-criticality of the reactor has to be ensured during all transport conditions. Current designs tend to prevent criticality through the use of neutron absorbers, the spacing of the fuel elements/assemblies or simply by restricting the amount of fissile mass to a limit lower than the critical mass. This will come at an additional cost to the reactor and it will take around two years to receive approval from the competent authorities.

The organisation responsible for the transportation of nuclear material has to be in possession of an approved licence. The organisation must have the relevant expertise and resources to hand to ensure the safety and security of the transport before any nuclear material can be transported. It may prove that the transportation of the fresh and spent core has to be outsourced to an approved carrier.

The fuel should be designed to be within the category II classification of nuclear materials so that the regulatory authorities only need to be notified of the transport route taken, and the appropriate safety measures are in place. The cartridge should aim never to reach a category I material as an armed guard would also be required to accompany the shipment.

The most suitable fuel handling unit is that of the Japanese HTTR reactor, with a few modifications to the current design. The dexterity of the HTTR fuel handling unit would be replaced by a more robust and stronger unit that only has to be indexed between the core, the temporary onsite cooling storage and the transport vehicle.

There appears to be show stoppers surrounding the transport and fuel handling of the cartridge. As far as the transport regulations are concerned you can transport a package of any size along as you can prove that there will be no damage to the road network, the surrounding environment or those using the network. Therefore it is recommended to continue researching the cartridge design.

6. Future Work

The natural extension to this work is to review the regulations surrounding the operation of nuclear power plants in terms of nuclear facilities. It may turn out that it is not possible to operate such a reactor module in remote locations without significant security and costs that exceed the viability of the project.

It would be interesting to look at a mechanism for dividing the core into smaller sections during and after irradiation, to allow the transportation of the spent core in smaller packages that are much easier to transport.

7. References

- A **The Gas Turbine – Modular Helium Reactor: A Promising Option for Near Term Deployment** Malcolm P. LaBar *General Atomics* GA-A23952
- B **WNTI Nuclear Fuel Cycle Diagram**
<http://www.wnti.co.uk/nuclear-transport-facts/what-is-transported-and-how>
- C **Regulations for the Safe Transport of Radioactive Material: Safety Requirements**
No. TS-R-1; 2009 Edition
- D **Nuclear Fuel Cycle Transport: Information paper no. 3**
World Nuclear Transport Institute
http://www.wnti.co.uk/UserFiles/File/public/publications/informationpapers/wnti_info-3.pdf
- E **Package Types Used for Transporting Radioactive Materials**
World Nuclear Transport Institute
http://www.wnti.co.uk/UserFiles/File/public/publications/factsheets/wnti_fs-2.pdf
- F
- G **Foundations of the Phased Disposal Concept: Radioactive Waste Transport**
Nirex Report N/022 October 2002
<http://www.nda.gov.uk/documents/upload/Foundations-of-the-phased-disposal-concept-radioactive-waste-transport-Nirex-Report-N-022-2002.pdf>
- H **Review of the management of C&U and STGO abnormal loads** TRL
Published Project Report **PPR370**
E J Hardman, N B Taylor, J Weekley, S Notely, R Smith, N Bourne and J Ritter
- J **UK Transport Risks and Logistics Associated with BNFL Waste Substitution**
March 2003 Nirex Number: 490680
<http://www.nda.gov.uk/documents/upload/UK-transport-risks-and-logistics-associated-with-BNFL-waste-substitution-Technical-Note-March-2003.pdf>
- K **The Physical Protection of Nuclear Material and Nuclear Facilities:** INFCIRC/255/Rev.4
http://www.iaea.org/Publications/Documents/Infcircs/1999/infcirc225r4c/rev4_transport.html
- L **Civil Nuclear Transport Security Regulation Paper**
Presentation by Bryan Reeves, the Principal Inspector at the OCNS, at a Radiation Transport Conference.
- M **Categorisation of Nuclear Material:** Paragraph 5 of **The Physical Protection of Nuclear Material and Nuclear Facilities:** INFCIRC/255/Rev.4
http://www.iaea.org/Publications/Documents/Infcircs/1999/infcirc225r4c/rev4_categ.html#5.1
- N **NISR 2003: Schedule**
<http://www.opsi.gov.uk/si/si2003/20030403.htm#sch>

- O **Private Conversation with a member of the nuclear transport packaging team at BNFL**
- P **A New Transport Container for Fresh PWR Assemblies According to IAEA Regulations**
W. Jahreib, U Phillipczyk, W. Paulinyi, T. Quercetti
<http://www.tes.bam.de/ram/pdf/33297.PDF>
- Q **Materials Used in Nuclear Fuel Reprocessing**
Figure 2: Excellx 7/7 container
<http://www.azom.com/details.asp?Articleid=627>
- R **Nuclear Fuel Cycle: NTEC Module Chapter 10**
- S **RATIONALIZING TRANSPORT OPERATIONS: THE TN 24 TRANSPORT STORAGE CASK APPROACH**
V. ROLAND, P. SAMSON Transnucléaire, Paris, France
IAEA-SM-357/34
http://www-pub.iaea.org/MTCD/publications/PDF/csp_006c/PDF-Files/paper-34.pdf
- T **Characteristics of Spent Fuel Transportation Packages**
NRC Cask Info
http://www.csgmidwest.org/About/MRMTP/Committee/Meetings/Columbus07/NRC_Cask_Info.pdf
- U **British Nuclear Group: Waste Packaging Solutions: Project Services Brochure 05/06**
<http://www.projectsolutions.com/UserFiles/File/Waste%20Packaging%20Product%20Booklet.pdf>
- V **Re-fuelling Options for LS-VHTRs Based on High-Temperature Reactor Experience**
Presentation by Charles Forsberg of the Oak Ridge National Laboratory
<http://www.ornl.gov/~webworks/cppr/y2001/pres/124827.pdf>
- W **The role of Japan's Industry in the HTTR design and its construction**
I. Minatsukia, M. Tanihiraa, Y. Mizokamib, Y. Miyoshih, H. Hayakawac,
F. Okamoto, I. Maekawad, K. Takeuchie, H. Kodamaf, M. Fukuiegi,
N. Kanh, S. Katoj, K. Nishimurai, T. Konishij
Nuclear Engineering and Design, 233 (2004) 377–390
- X **Present status of energy in Japan and HTTR project**
Masuro Ogawa & Tetsuo Nishihara
Nuclear Engineering and Design 233 (2004) 5–10
- Y **The D154 project – Redevelopment of the Submarine Support Facilities at Devonport Royal Dockyard**
Malcolm Smith, Former technical director Devonport facilities redevelopment programme
Article - Issue 13, Aug 2002
<http://www.ingenia.org.uk/ingenia/articles.aspx?Index=180>
- Z **Fuel management and handling: proceedings of the international conference by British Nuclear Energy Society 1995**
http://books.google.co.uk/books?id=Pv5UjoJMIwEC&dq=agr+fuel+stringer&source=gbs_navlinks_s

C.9 Annex 2: Study of Power Conversion Systems for the U-Battery

Extract from a dissertation by Azrudi Mustapha

A Study of Potential Power Conversion Systems
for a Small Autonomous Nuclear Reactor

2009

Azrudi Mustapha

Contents

i.	Abstract	4
ii.	Acknowledgements	4
iii.	Declaration	5
iv.	Copyright Statement	5
1.	Introduction	6
2.	The Nuclear Battery Concept	6
2.1	Description of the general concept	7
2.2	Potential applications	7
2.3	Constraints	8
2.4	Key Assumptions	9
3.	Review of Potential Power Conversion Technologies	10
3.1	Civil Nuclear Power Systems	10
3.1.1	Gas-cooled Reactors	12
3.1.1.1	Magnox Reactors	12
3.1.1.2	Advanced Gas-cooled Reactors	14
3.1.2	Pressurized Water Reactors	17
3.1.2.1	The Reactor Vessel	18
3.1.2.2	The Heat Exchanger	19
3.1.2.3	Reactor Coolant Pumps	20
3.1.2.4	Pressurizer	21
3.1.2.5	The Secondary Steam System	23
3.1.3	High Temperature Gas Reactors	25
3.1.3.1	The Indirect Cycle High Temperature Gas Reactor	26
3.1.3.2	The Direct Cycle High Temperature Gas Turbine	29
3.2	Fossil-fired Power Stations	31
3.2.1	Coal-fired Power Stations	31
3.2.2	Gas-fired Power Stations (Combined Cycle Gas Turbine)	33
3.3	Space Reactors	36
3.3.1	Thermionic Emission Reactor	36
4.	Analysis of Potential Systems	38
4.1	Plant Efficiency	40
4.2	Plant Flexibility	41
4.3	Plant Complexity	42
4.4	System Reliability	45
4.5	Maintenance Requirements	47
4.6	Plant Size	50
5.	Design Considerations	52
5.1	Power Conversion System Components	52
5.2	Safety Considerations	55
5.3	Heat Exchangers	56
5.4	Power Conversion Technology Considerations	59
5.5	Potential Applications	60
5.5.1	District Heating	60
5.5.2	Hydrogen Production	63
6.	Conclusions and Recommendations	66
7.	Suggestions for Further Work	68
8.	References	69
9.	Appendix	71

[Final Word Count : 21,082 words]

List of Figures

Figure 1	Layout of a Generic Nuclear Power Station	11
Figure 2	Schematic Diagram of a Magnox air-cooled reactor (Wikipedia)	13
Figure 3	Schematic of the Advanced Gas-cooled Reactor	15
Figure 4	The layout of main systems in a Pressurized Water Reactor	18
Figure 5	Detailed description of reactor pressure vessel components in a PWR	18
Figure 6	The components of the PWR Pressurizer	21
Figure 7	Schematic diagram of the Pressurizer and the Pressurizer Relief Tank	23
Figure 8	Schematic diagram describing the components in the secondary system	24
Figure 9	Pre-stressed concrete vessel for the high temperature gas-cooled reactor (<i>Oak Ridge National Laboratory, US Department of Energy</i>)	27
Figure 10	Schematic diagram of the high temperature gas-cooled reactor steam cycle	28
Figure 11	The layout of the GT-MHR reactor module located in an underground containment building. (Baxi et al., 2008)	30
Figure 12	Schematic diagram of a coal power station	31
Figure 13	The open cycle gas turbine power station	33
Figure 14	The closed cycle gas turbine power station	34
Figure 15	The combined cycle gas turbine power station	35
Figure 16	Schematic diagram showing the principles of a thermionic converter (Generator)	36
Figure 17	Factors governing the design of the autonomous reactor	38
Figure 18	T-s Diagram of a typical Rankine cycle with highlighted saturated point at 270°C and 6.02 kJ/kgK enthalpy	44
Figure 19	Tube failure probabilities for stress corrosion, creep transition joints and oxidation expressed as a function of half-unit mean temperatures	49
Figure 20	Schematic diagram comparing existing power conversion technologies on a Rankine cycle	53
Figure 21	Schematic diagram comparing existing power conversion technologies on a Rankine cycle with reheat	53
Figure 22	The functional arrangement of primary system components in an integral primary system reactor (IRIS design courtesy of Westinghouse Electric Company)	55
Figure 23	Possible schematic diagram of a small autonomous nuclear station with district heating with HX3 connected to the secondary steam system to transfer heat into the district heating piping.	62
Figure 24	Schematic of the sulphur-iodine (S-I) thermo-chemical cycle	63
Figure 25	Efficiency of the sulphur-iodine process versus temperature	64
Figure 26	Simplified Diagram of Sulphur-Iodine, Ispra Mark 13 and Westinghouse Cycles (Forsberg et al., 2003)	66

List of Tables

Table 1	Comparison between early and late Magnox design parameters	13
Table 2	Key Parameters in CO ₂ gas-cooled reactors	17
Table 3	Reactor outlet/turbine inlet temperatures and thermal efficiencies of existing power conversion technologies.	41
Table 4	Key design parameters comparing air-based compressors and helium-based compressors.	51
Table 5	Comparison of estimated thermal efficiencies of established steam-cycle nuclear technologies	54
Table 6	Operating conditions of compact heat exchangers, Thonon & Breuil (2000)	57
Table 7	Table summarizes the comparison between existing nuclear technologies to be adopted for the autonomous reactor	59

Acronyms

Magnox	Magnesium no-oxide
AGR	Advanced Gas-cooled Reactor
LWR	Light Water Reactor
PWR	Pressurized Water Reactor
BWR	Boiling Water Reactor
HTGR	High Temperature Gas Reactor
CCGT	Combined Cycle Gas Turbine
HP	High Pressure
LP	Low Pressure
IHX	Intermediate Heat Exchanger
PCR/V	Pre-stressed Concrete Reactor Vessel
EPR	Evolutionary Pressure Reactor
AP1000	Advanced Passive 1000 MWe
GTG	Gas Turbine Generator
LOCA	Loss-Of-Coolant Accident
LOFC	Loss-Of-Forced-Convection
SCRAM	Super Critical Reactor Axe Man (describing emergency reactor shutdown)
EM	Electromagnetic
DSR	Deliberately Small Reactors
IPSR	Integral Primary System Reactor
DPR	Deep Pool Reactor
GT-MHR	Gas Turbine – Modular Helium Reactor
GT-HTR	Gas Turbine High Temperature Reactor

Abstract

A small and autonomous power source based on established nuclear technologies, known as the U-Battery, is explored to provide electrical power in the range of 10 MW to 25 MW for off-the-grid applications. The aspiration of this endeavour is to assemble a transportable reactor that is able to take care of itself without the reliance on water supply, natural gas, external electrical source or manned operators at a reasonable cost. This report details the review of current conventional nuclear and fossil-fuel technologies to select the most viable option. The findings of this investigation reveal a number of potential technologies to be practical according to its proposed industrial application, among which the CO₂ gas-cooled reactor technology and the thermionic emission reactor technology.

Acknowledgements

I would like to express my heartiest gratitude to Professor Tim Abram for invaluable guidance, recommendations and initiative. I am also grateful to Professor Jonathan Billowes and my colleagues for all the support I have received whilst researching and writing up this dissertation. Finally, I am grateful to the U-Battery partners for the opportunity to contribute to the project (Technical University of Delft, The University of Manchester, K&W, and Urenco).

1 Introduction

A mobile energy source can play a large role in shaping the world's future. The nuclear battery as a form of mobile energy source has opened up enormous possibilities to power small towns, offshore oil platforms, or remote small-scale mining operations.

Today, these applications require the installation of small diesel-based or gas-based generators to power their industrial needs. However, current implementations to address these issues are not without their own problems. The price of fuel, the required maintenance, transportation and size are among the most critical concerns with existing implementations. Thus, any new technology that is proposed will have to specifically address these unsettled concerns.

The proposed nuclear battery should be able to satisfy the criteria to provide a safe, clean, and effective solution to the needs of commercial and industrial applications and be able to further provide significant reduction in operating costs to further encourage growth in the sectors these units are employed.

2 The Nuclear Battery Concept

The nuclear battery describes the concept of a small, autonomous, standalone nuclear reactor which is transportable by road and installed in a remote location. The service life of the device starts when it is transported to the proposed site where its services are required. The device is then installed and connected to the small electrical distribution network where it is then powered up. It is then left alone to service the application in the range of years. If the device runs low on power, maintenance personnel will transport a new fuel block replace the existing depleted fuel block within the device, and the device will then continue its service for many more years. At the end of its required application, the device will be disconnected and transported back to the factory where it will be serviced awaiting its next service demand.

This overview illustrates the implementation of an industrial battery, which is the base concept of the small, autonomous nuclear reactor.

2.1 Description of the general concept

The small autonomous nuclear reactor in its normal operating state functions just like a typical battery. From these ideals the small autonomous nuclear reactor must be designed to provide a full and reliable solution to the required applications. In most cases, the applications include the ability to provide electrical power to a remote location that is off the grid.

To be able to achieve these aims, the autonomous nuclear reactor must be designed to be assembled modularly so that the different modules of the complete system can be transported by existing transport technologies such as trailers, rails or tug boats. The modularity of design also has another significant advantage in that it can be manufactured in factories instead of on site, thus benefitting from higher quality from industrial inspection, monitoring and quality control procedures and technologies.

Upon its installation at the site of application, the device will operate under design conditions but it will also operate under reduced efficiencies during unexpected environment or external conditions. The reduced efficiency is expected to ensure that the device continues to operate safely and reliably. At the end of the fuel service life, the entire spent fuel block will be removed from the device and replaced by a new fuel block that is transportable by road. This spent fuel block will also include all the radioactive fission products where it can be taken back to the factory to be reprocessed, or treated under radioactive waste management programmes.

At the end of the required application, the entire device can be disassembled back into its fundamental modules and transported back to the factory to be inspected, serviced, and stored.

2.2 Potential applications

A very large portion of world energy consumption is in the form of thermal energy. The production of this form of energy is traditionally sourced from conventional fossil-fuels, while the product of nuclear energy is conventionally limited to electricity generation. The application of thermal energy differs however from typical electricity generation as it requires certain conditions such as:

- Various ranges in temperature
- Capacity of heat source
- Distance of heat transport

Jiafu et al (1998) thus claims that it is for these reasons that there exists some difficulty in the penetration of nuclear energy into the heat market. However, current developments in the nuclear industry allow for a safe and durable power source with benefits that far outweighs other existing implementations into these markets.

Power grid connections to remote locations such as villages or islands are mediocre, if not lacklustre. This is due to the relatively high cost to install long range transmission or submarine cables to these sites from existing grid points. Without government intervention, the cost to transport power from the grid to these remote locations will far outweigh the revenues potentially accrued from the residents.

The nuclear battery can also replace existing power sources on remote mobile barges or oil and gas platforms. With the soaring prices of fossil fuel today, it makes more economical sense to employ a small reliable battery based on nuclear technologies than by self consuming the product fashioned and refined by their own industrial processes.

The drive towards employing the nuclear battery resides from the economics of today, where the cost of generating power is dictated by the supply and demand of such power. The potential applications of the nuclear battery are therefore endless, limited only by cost and technology constraints.

2.3 Constraints

The primary constraint in the deployment of full-scale nuclear applications is the regulations involved with the nuclear industry. Nuclear industries are recognized to be one of the riskiest fields in the power industry. Past accidents within the nuclear industry do much to enforce this perception. In most countries, a nuclear installation must be sited from a distance of kilometres from the nearest population bloc. This constraint, while succeeds in promoting safety, places a challenge to transport the electricity generated by the plant to the consumers.

Other constraints involve the reliability, availability and size of the product. No reactor that is operating today is entirely autonomous and unmanned, therefore true

autonomous reliability is still unproven in the field. Sizing of the reactor is important as it needs to be small enough to be fashioned in factories and assembled on site. This involves the use of compact equipment and systems to achieve the necessary design parameters. The availability of technology is also a concern for the development of the autonomous nuclear reactor. While the technology is possible and proven, there has not been much market drive in the industry to necessitate the production of these technologies. Thus, the nuclear reactor will not be able to capitalize on the benefits of these technologies until there is enough demand to induce capital injection into the production of said technologies.

2.4 Key Assumptions

To achieve the required specifications of nuclear battery concept, several key assumptions must be made. These assumptions start from the availability of factories to produce and assemble the product modules to the final operational conditions including the postulated accident conditions.

Among the key assumptions in this report are:

- Power conversion system components designed for a large civil power station are available in smaller scales
- Reactor system monitoring and automated reactivity control is available
- Turbine, compressor, and pump losses are negligible compared to energy produced
- Fission products produced by the fission process stay within the graphite fuel block without affecting coolant fluid, primary pumps and circulators.
- The reactor fuel block can be transported out taking with it all the fission products and replaced with a new block without affecting coolant sealing qualities.
- The reactor core is built with the best available technologies to reduce negative response to operational transients
- The modularity of the reactor allows for the removal of the secondary circuit condensers, pumps, turbines for service and maintenance while a new replacement component is attached to replace the component under maintenance.
- All possible major accident conditions are recognized and prepared for.

For the last assumption in the least above, a further explanation is necessary. In the event of a loss of forced circulation of the primary coolant, mechanisms must be provided for removal of the residual power that continues to generate heat in the reactor core from the decay of radionuclides. The conduction of heat through the core material and

the natural convection of the primary coolant transfer the excess heat to the reactor vessel boundary. However, additional external cooling of the vessel is needed to transfer the heat to the ultimate heat sink which is typically the atmosphere. Ingersoll (2009) claims that small plant designs are able to accommodate this heat transfer better than large plants for a number of reasons. Firstly, a lower core operating power will result in lower decay power. Secondly, the smaller core volume enables more effective conduction of the decay power to the reactor vessel. Thirdly, the removal of heat from the external surface area of the vessel is more effective.

The third advantage of small reactor designs warrants further explanation. Ingersoll (2009) describes this feature of smaller reactors resulting from the fact that core power (and decay power) is proportional to the volume of the core, which varies as the cube of the effective core radius. However, heat removal from the vessel is proportional to the vessel surface area, which varies roughly as the square of the core radius. As the power level is reduced, the core volume decreases faster than the surface area of the vessel, which consequently increases the relative effectiveness of external heat removal. As a result, most small reactor designs are able to easily accommodate removal of the decay heat using fully passive, natural convection air ventilation systems.

These benefits work in the favour of the small autonomous nuclear reactor as it needs to be reliable and able to take care of itself even in unexpected conditions.

3 Review of Potential Power Conversion Technologies

To understand the possibilities of the small autonomous nuclear reactor, firstly a critical review of existing power conversion technologies must be undertaken. The basis of these technologies comes from civil nuclear, fossil-fuel and space based power stations.

3.1 Civil Nuclear Power Systems

Figure 1 below illustrates the layout of a generic nuclear power station. The reactor core is made up of fuel elements and moderator. For a reactor consisting of a solid moderator such as graphite, the reactor coolant flows in between the gaps or annular channels between the fuel and the moderator, meanwhile for a reactor with liquid moderator such as water, the moderator could also serve as a coolant and flow through the core, or the coolant could be separate and flow in pressure tubes in between the fuel and moderator.

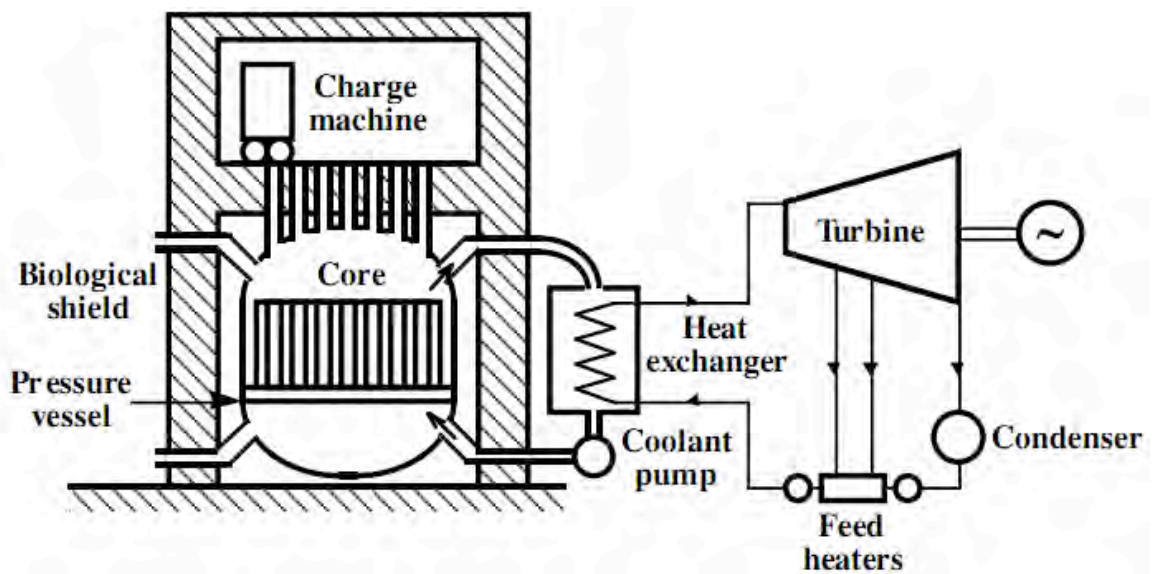


Figure 1: Layout of a Generic Nuclear Power Station (Courtesy of University of Cambridge, Department of Engineering)

The reactor core and most of the primary system are enclosed within the pressure vessel that is made from steel lined pre-stressed concrete that acts as the biological shield for the core as well as containment for the coolant. For air-cooled reactors, the system pressure could be up to 40 bar, meanwhile in water-cooled reactors, the system pressure could be as high as 150 bar. The biological shield is designed to prevent radioactive release into the environment, usually made of several feet thick concrete as concrete has good shielding properties in addition to its well accepted structural qualities. Submarine reactors get their biological shields from a combination of steel and water, because space comes at a premium for these modular applications.

The power conversion system in a generic nuclear reactor works by passing the heat generated in the reactor core to the turbine which drives a generator to produce electricity. The nuclear reaction in the reactor core generates energy in the form of heat which is transferred to the coolant flowing across the coolant channels. This heated coolant exits the core through the hot leg at the top of the reactor and enters the heat exchanger which transfers heat from the primary coolant system to the secondary system fluid. The secondary system fluid expands in the heat exchanger and flows to drive the turbine. The secondary system fluid is then cooled from a feedwater system before being pumped back to the heat exchanger. The primary system fluid, which is now cooled by the secondary system fluid, is pumped out of the heat exchanger and enters the reactor core through the cold leg at the bottom of the reactor. In most reactor designs, the secondary system fluid is composed of water and steam while the primary

system fluid is composed of either liquid coolants such as water and heavy water, or gas coolants such as helium and carbon dioxide.

Understanding the generic design is important to appreciate the different approaches reactor designers have taken in the past to address heat transfer. This led to a number of established designs, of which many new reactors systems are based upon. These different approaches are discussed further in detail in the following sections, along with a discussion on other existing power conversion systems not directly related to nuclear technology.

3.1.1 Gas-cooled Reactors

All commercial reactors in the UK were moderated by graphite and cooled by carbon dioxide before the construction of the first British Pressurized Water Reactor (PWR) at Sizewell B. These commercial nuclear power stations were built in the late 1950's and were developed throughout the years reaching a total number of eleven built stations including two in Japan and one in Italy. These reactors were fuelled by natural uranium and clad with Magnox (magnesium-aluminium no-oxide alloy).

3.1.1.1 Magnox Reactors

Magnox reactors are fuelled by natural un-enriched uranium, cooled by pressurised carbon dioxide, moderated by graphite, and clad by Magnox alloy. Control of the neutron flux is achieved using B_4C loaded control rods. Early Magnox reactors were made with steel pressure vessels with working pressure between 6.9 to 19.35 bar while the later designs in Oldbury and Wylfa were made of reinforced concrete with working pressure between 24.8 and 27.57 bar. The reason for the variation is because there were no British construction company that was big enough at the time to construct all the power stations, thus various competing manufacturers were involved and contributed to the differences between the reactor stations. However, the underlying principles of the Magnox reactor remained the same. *Figure 2* describes the primary circuit components that make up the Magnox reactor.

The reactor core is built from graphite bricks incorporating a large number of vertical channels to accommodate the fuel, which also acts to moderate the energy of the neutron flux in the core. The heat generated inside by the fissile material is removed by a flow of pressurized carbon dioxide coolant gas which is circulated by blowers. This

heated gas then passes through the steam generators to produce steam to drive the turbines.

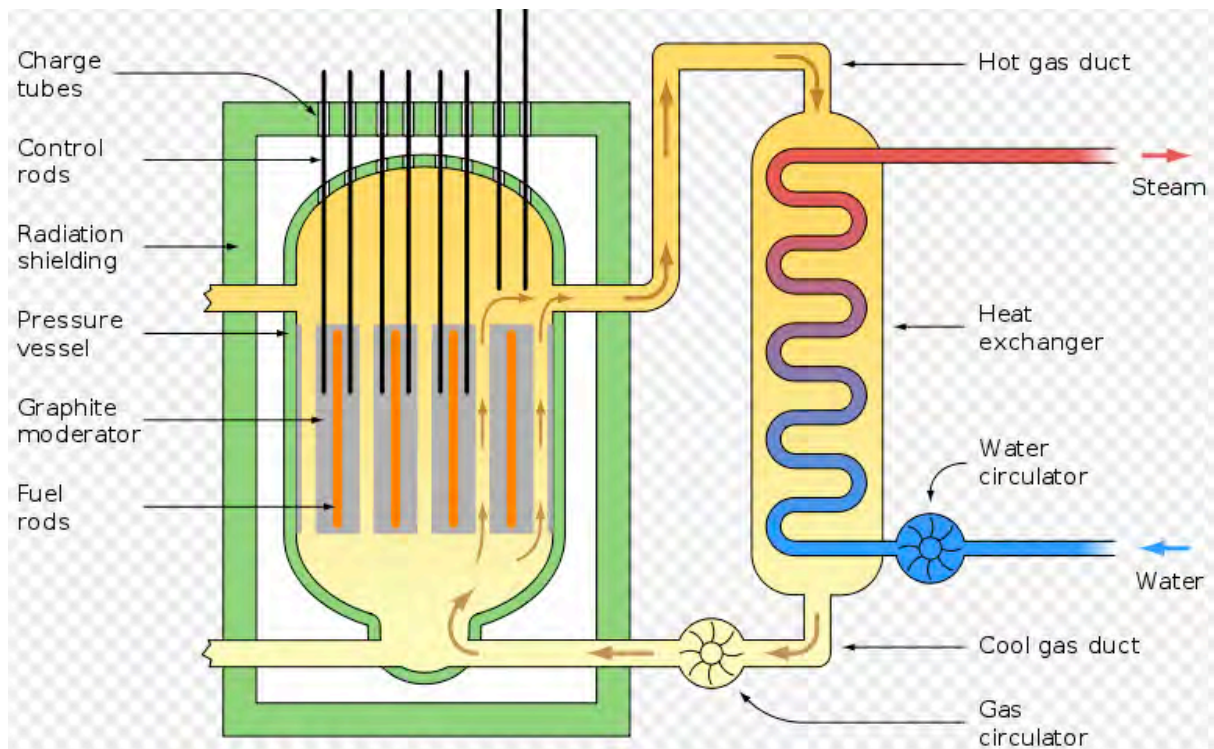


Figure 2: Schematic Diagram of a Magnox air-cooled reactor

(Image courtesy of Wikipedia)

The Table 1 below compares the key parameters of the Magnox design that evolved over the years, depicting the first station built in Berkeley and the last station built in Wylfa.

Area	Parameter	Berkeley	Wylfa
General	Gross Station Output	320 MW(e)	1310 MW(e)
	Gas Inlet Temperature	160 °C	247 °C
	Gas Outlet Temperature	345 °C	414 °C
	Net Thermal Efficiency	24.6%	31.4%
Pressure Vessel	Material	Steel	Concrete
	Geometry	Cylinder	Sphere
	Internal Diameter	15.2 m	29.3 m
	Internal Height	24.2 m	-
	Working Pressure	9.65 bar	27.57 bar
Core	Active Diameter	13.1 m	17.4 m
	Active Height	7.4 m	9.1 m
	Number Of Fuel Channels	3265	6150
Fuel	Element length	482 mm	1067 mm
	Number Of Elements/Channel	13	8
Boilers	HP Steam Pressure	21.4 bar	45.9 bar
	HP Steam Temperature	320 °C	400 °C

Table 1: Comparison between early and late Magnox design parameters

The key difference to take notice between the two designs is that the efficiency of the plant increased significantly from 24.6% at the Berkeley station to 31.4% at the Wylfa station. This is due to the higher gas outlet temperature from the core which results in higher HP steam temperature. Although the maximum temperature of the CO₂ coolant can be higher at around 650°C, the maximum temperature of the Magnox reactor is limited by the melting point of the magnox cladding at around 410°C, resulting in the low efficiency of the station.

The Magnox reactors benefit from a considerable degree of inherent safety due to its sturdy design, low power density and gas coolant. Loss of coolant accidents (LOCA) were considered in the design but would not lead to a large-scale fuel failure as the Magnox cladding were able to retain the bulk of the radioactive material under a SCRAM. Considering that the coolant is already a gas, pressure build-up from boiling would not risk an explosion, in contrast to the steam explosion at Chernobyl station.

3.1.1.2 Advanced Gas-cooled Reactors

During the early 1960's, work began on the concept of Advanced Gas-cooled Reactors (AGR) with the aim of achieving a higher gas coolant temperature than that of the Magnox designs, to accomplish a higher thermodynamic performance of the station. The AGR was constructed in the late 1980's at the Heysham and Torness site, with each twin unit station producing an output of 1320 MWe. Beech & May (1999) claimed that the reactors operated at core coolant outlet temperatures of 650°C.

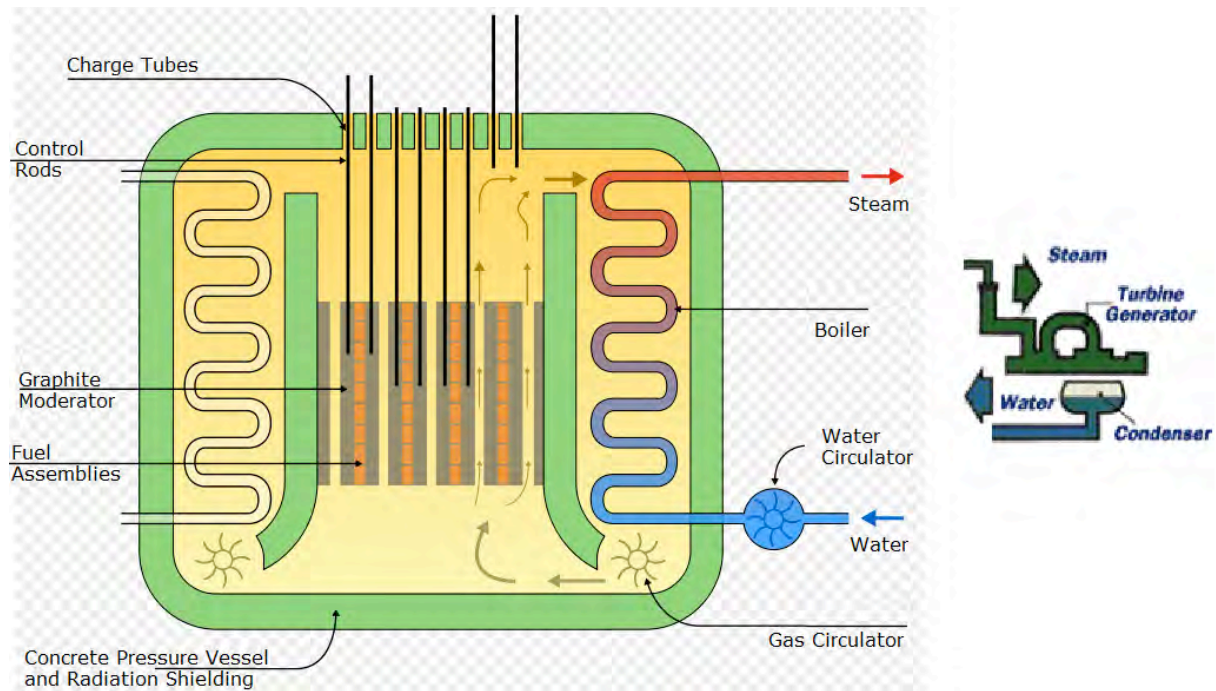


Figure 3: Schematic of the Advanced Gas-cooled Reactor (Image courtesy of Wikipedia)

The Advanced Gas-cooled Reactor (AGR) is a second generation British gas cooled reactor design using graphite as the moderator, enriched uranium dioxide as fuel and carbon dioxide gas as coolant.

The limitation of the first generation design was that the Magnox stations could not be operated at a high enough temperature for good thermal efficiency without risking the melting of the magnesium cladding. Stainless steel was found to be more stable in high temperature environments and thus replaced Magnox as the cladding material. However, due to the higher neutron absorption cross-section of stainless steel, the fuel element requires enriched uranium instead of the natural uranium used in the Magnox design. The fuel element was designed to be the oxide form of uranium, UO_2 , to benefit from the higher melting point of the oxide fuel of 2865°C as compared to 600°C for uranium metal fuel.

The AGR design also benefitted from other Magnox developments, such as the design of the gas circulation system where the steam generators were now mounted on the inside of the pre-stressed pressure vessel. Since now the CO_2 reactor coolant can be heated to high temperature, the steam generators can be designed to provide steam under conditions similar to those found in the most efficient fossil fuel plants, i.e. 560°C steam at 170 bar.

The AGR was designed to have the final steam conditions at the boiler to be equivalent to those in conventional coal fired power stations, such that the existing conventional turbo-machinery systems could be used. Understanding that graphite oxidises readily in CO₂ at high temperatures, coolant re-entry into the core was made at a temperature of 278°C to cool the graphite core. This ensures the graphite core temperatures are within the range of industrial experience seen in the Magnox reactors as *Table 1* above.

The AGR employs boilers to transfer the heat from the reactor through the primary circuit to heat up the secondary circuit which is a steam-based circuit. The heated carbon dioxide coolant in the primary circuit gives off its energy to turn the water in the boiler into superheated high pressure steam. A key difference to note here between the AGR station and the Magnox station is that the AGR station includes the boiler within the concrete pressure vessel, enclosing the entire primary circuit within the concrete shield.

This superheated steam coming out of the boilers will be pushing against the high pressure turbine's blades thus causing the turbine to rotate. The steam then is routed back to the boilers to be reheated, and then directed to the intermediate pressure turbine and consequently to the low pressure turbine to ensure every little available kinetic energy is converted into the corresponding electrical energy.

This steam is then passed onto a condenser where it is cooled down to become water before it is returned to the boilers. The condenser directs steam over the surface of thousands of tubes containing cold filtered water pumped from the sea, and results in condensed water which is then cleaned and heated before it is returned to the boilers. The condensed water has its impurities removed by running through a chemical plant and then through heaters to be mixed with warm steam from the turbines to increase its temperature. It is then pumped into a large de-aerator to remove any gases before being pumped back into the boilers.

The *Table 2* below compares the key parameters between the last Magnox station commissioned at Wylfa to the last AGR station at Torness.

Area	Parameter	Wylfa (Magnox)	Torness (AGR)
General	Gross Station Output	1310 MW(e)	1344 MW(e)
	Gas Inlet Temperature	247 °C	334 °C
	Gas Outlet Temperature	414 °C	635 °C
	Net Thermal Efficiency	31.4%	40.0%
Pressure Vessel	Material	Concrete	Prestressed concrete
	Geometry	Sphere	Cylinder
	Internal Diameter	29.3 m	20.25 m
	Internal Height	-	21.87 m
	Working Pressure	27.57 bar	43.6 bar
Core	Active Diameter	17.4 m	9.5 m
	Active Height	9.1 m	8.3 m
	Number Of Fuel Channels	6150	332
Boilers	HP Steam Pressure	45.9 bar	171 bar
	HP Steam Temperature	400 °C	541 °C

Table 2: Key Parameters in CO₂ gas-cooled reactors (Parks, University of Cambridge)

The AGR achieved a thermal efficiency of about 41%, which is better in comparison to modern pressurized water reactors at about 34%, largely due to the higher coolant outlet temperatures in the advanced gas-cooled reactors.

3.1.2 Pressurized Water Reactors

The Pressurized Water Reactor (PWR) as in *Figure 4* is a light water reactor (LWR) design utilizing light water as their coolant. In contrast to the Boiling Water Reactor (BWR) design, the PWR primary coolant is pressurized to prevent film boiling on the fuel pin walls within the reactor, in effect increasing heat transfer between the core and the coolant. Throughout history, a number of light water reactor designs have been implemented, utilizing various materials for the moderator material. However, the most prominent PWR design today is based on light water for both coolant and moderator, allowing for control of the reactivity through a feedback effect – the more water gets converted to steam in between the fuel pins, the less moderator density will become available, hence reducing the core reactivity because fast neutrons will not be moderated as much as before. The *US-NRC Reactor Concepts Manual* on the PWR describes this reactor technology in much detail.

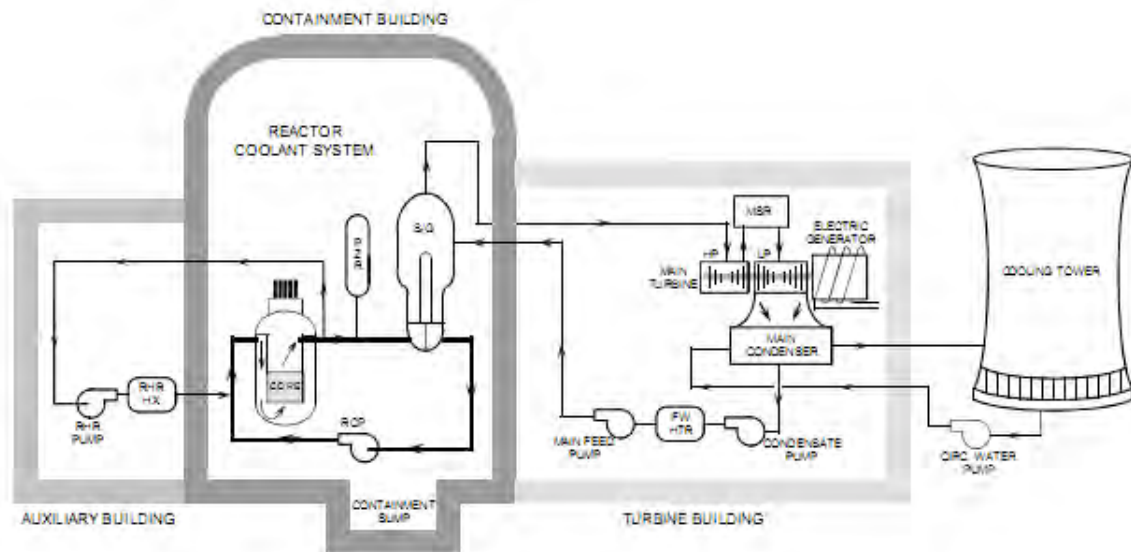


Figure 4: The layout of main systems in a Pressurized Water Reactor (USNRC)

3.1.2.1 The Reactor Vessel

The reactor core and all associated support components are housed within the reactor vessel as shown in *Figure 5*. The major components in this design are the reactor vessel, the core barrel, the reactor core, and the upper internals.

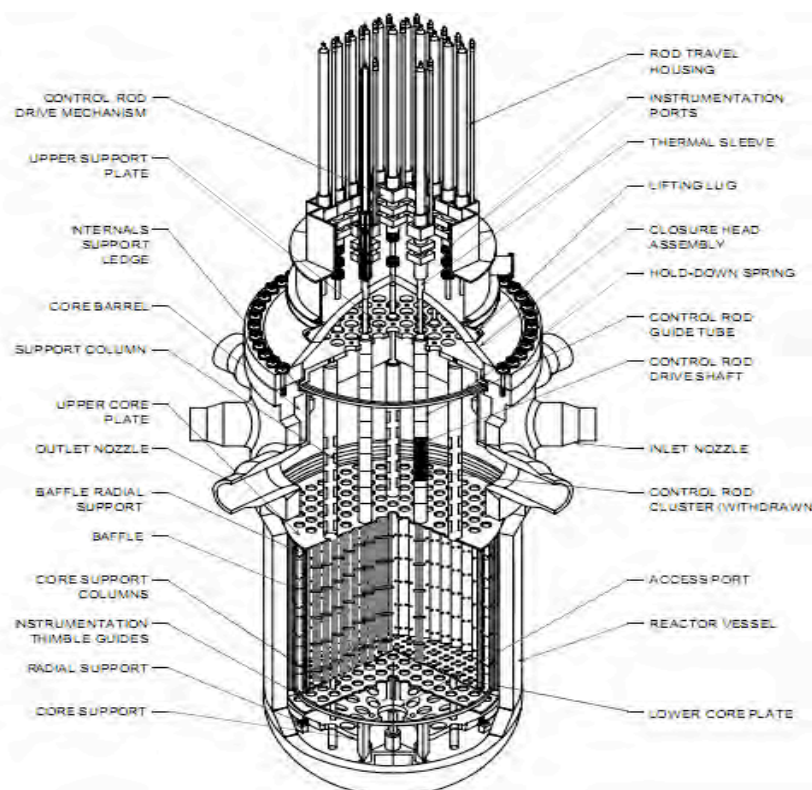


Figure 5: Detailed description of reactor pressure vessel components in a PWR (USNRC)

The reactor vessel is a cylindrical vessel with a hemispherical bottom head and a removable hemispherical top head to allow for the refuelling of the reactor to take place. The reactor vessel is constructed from manganese molybdenum steel, although for all parts that come into contact with the reactor coolant will have a cladding made with stainless steel to reduce the effects of corrosion. For each reactor coolant loop, there will be a cold leg inlet and a hot leg outlet.

The core barrel houses the fuel and slides down the inside of the reactor vessel. Nearing the bottom of the core barrel, there is a core support plate where the fuel assemblies rest. The core barrel and all of the lower internals in fact hangs from the internals support ledge. On the outside of the core barrel, some samples of the material used to manufacture the vessel will be placed as irradiation specimens, which will periodically be removed and tested to analyse how much the irradiation from the fuel has affected the quality of the material.

The upper internals package is located on top of the fuel. This contains guide columns to guide the control rods when they are pulled and inserted into the fuel. The upper internals package prevents the core from moving upwards during operation due to the force from the coolant flowing through the fuel assemblies below.

The flow path of the reactor coolant through the reactor vessel would be:

- The coolant enters the reactor vessel at the inlet cold leg nozzle and hits against the core barrel.
- The core barrel forces the coolant to flow downward in the space between the reactor vessel wall and the core barrel
- The coolant reaches the bottom of the reactor vessel and flows upwards to pass through the fuel assemblies, absorbing the heat produced by the fission process.
- The now hot coolant enters the upper internals region, where it is then routed to the hot leg outlet nozzle which then flows to the heat exchanger.

3.1.2.2 The Heat Exchanger

The hot coolant enters the heat exchanger through the inside of many tubes. The secondary coolant, in this case also water, flows through the outside of these tubes, absorbing heat from the hotter primary coolant. As this occurs, the secondary coolant starts to absorb enough heat to start boiling and form steam. From this point, manufacturers of heat exchangers employ a number of approaches in their design of the

secondary cycle. Although the water boils into steam, moisture rises along with it and this needs to be separated from the dry steam. The moisture content of the steam needs to be as low as possible to prevent damage to the turbine blades.

The approach used by Westinghouse and Combustion Engineering requires the water/steam mixture to pass through multiple stages of moisture separation. One of these stages causes the mixture to spin which results in water accumulating on the outside wall while the steam stays at the centre. The water at the walls is then drained back to the heat exchanger to produce more steam. The dried steam from the centre of the first stage is routed to the second stage of the operation, where the mixture is forced to make rapid changes in direction. Steam is able to change directions with ease as compared to water, thus water accumulates at the walls of the second stage and is drained back to the heat exchanger, while steam exits the heat exchanger on the other side. This two-stage process of moisture separator is very efficient in removing water, resulting in water content of less than 0.25 pounds for every 100 pounds of steam.

The approach used by Babcock and Wilcox employs the use of a once through steam generator. The flow of the primary coolant comes in from the top of the steam generator to the bottom, as compared to the Westinghouse and Combustion Engineering designs where the coolant goes through U-shaped tubes. The steam is heated above the boiling point, or superheated, so that the steam exiting the once through steam generator contains no moisture due to the heat transfer achieved by this design.

For all of the said designs, the steam is then piped to the main turbine system, while the primary coolant is routed to the suction of the reactor coolant pumps.

3.1.2.3 Reactor Coolant Pumps

The reactor coolant pumps provide forced primary coolant flow to remove the heat generated by the fission process in the reactor core. Without this pump, there will still be a natural circulation flow throughout the reactor; however, this natural flow is usually not sufficient to remove the heat when the reactor is at power. When the reactor is shutdown, however, the natural flow is sufficient in removing the decay heat from the reactor.

As the primary coolant leaves the heat exchanger, the coolant enters the pump from the suction side and has its velocity increased by the pump impeller. This velocity increase is converted to pressure in the discharge volute. The reactor coolant pump has three major

components: the air cooled electric motor, the hydraulic section which consists of the impeller and discharge volute, and the seal package which prevents any water leaks.

After the coolant leaves the discharge side of the pump, it enters the cold leg inlet of the reactor vessel, where it will then pick up heat from the fission process in the core. This completes the primary coolant cycle.

3.1.2.4 Pressurizer

The pressurizer is a major component that differentiates the PWR from other reactor designs. The PWR requires the primary coolant pressure to be high enough to prevent film boiling in the core, with most designs setting this system pressure at about 150 bar. The purpose of the pressurizer is thus to provide a means to control the system pressure. The pressure is controlled in the pressurizer by the use of electrical heaters, pressurizer condenser spray, power operated relief valves and safety valves.

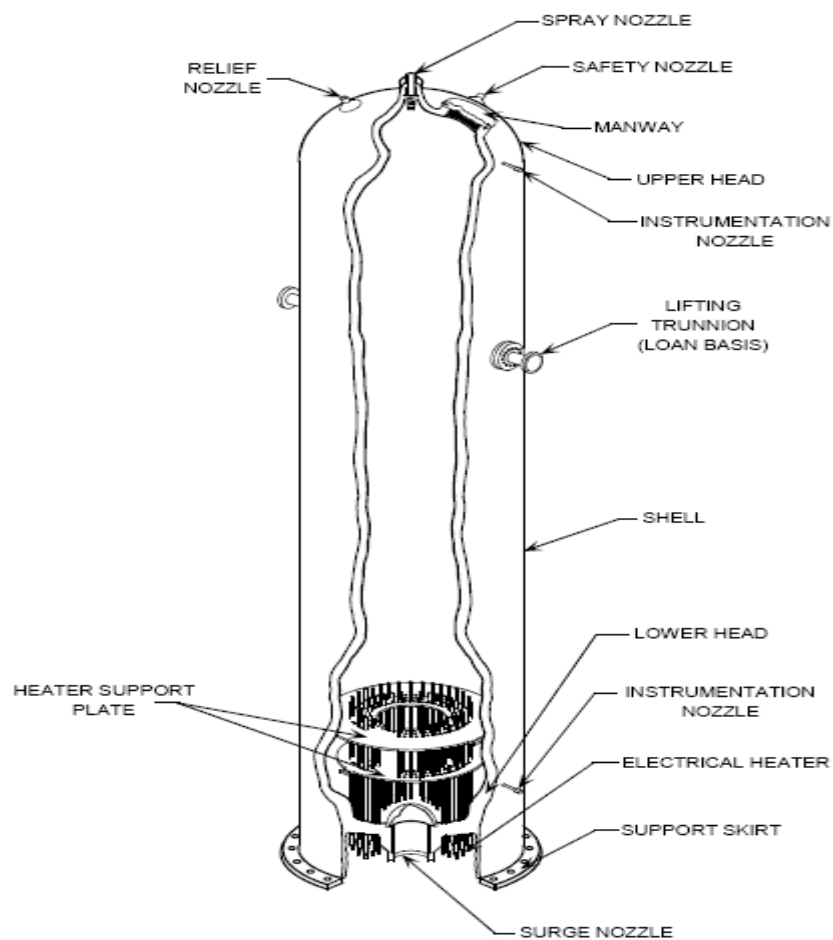


Figure 6: The components of the PWR Pressurizer (USNRC)

The pressurizer works with a blend of steam and water in equilibrium. If the system pressure starts to drop or rise from the set value, the various components in the pressurizer starts to function to restore the system pressure back to its normal operating conditions. Usually pressure changes in the system are due to a change in the temperature of the reactor coolant system. As the reactor coolant system temperature increases, the density of the reactor coolant will decrease, resulting in the water taking up more space. Since the pressurizer is connected to the reactor coolant system on the surge line, the water will expand up into the pressurizer connected above. This causes the steam in the top of the pressurizer to be compressed and hence the system pressure starts to increase.

In contrast, if the reactor coolant system temperature decreases, the water will become denser and hence occupy less space. The water level in the pressurizer will therefore drop down which will cause a decrease in system pressure.

For an increase or decrease in pressure, the pressurizer starts to work to return the system pressure back to normal operating conditions. For example, if pressure starts to increase above the normal operating condition, the pressurizer spray starts to discharge cold water from the reactor coolant pump to be sprayed into the steam space, leading the steam to condense into water. This will reduce the pressure because steam takes up to about six times more space than the same mass of water. If lets say the pressure continues to increase beyond control of the pressurizer sprays, the pressurizer relief valves will open and unload steam to the pressurizer relief tank. If this still does not relieve the pressure, the safety valves will open, also releasing to the pressurizer relief tank.

If the pressure starts to decrease, however, the electrical heaters will start to operate to boil more water into steam, hence increasing pressure. If the pressure continues to decrease, and reaches a preset point, the reactor protection system will trip the reactor to stop the fission process. This is important because if the primary coolant system pressure drops, it could result in film boiling in the reactor core coolant channels and therefore could damage the reactor assemblies.

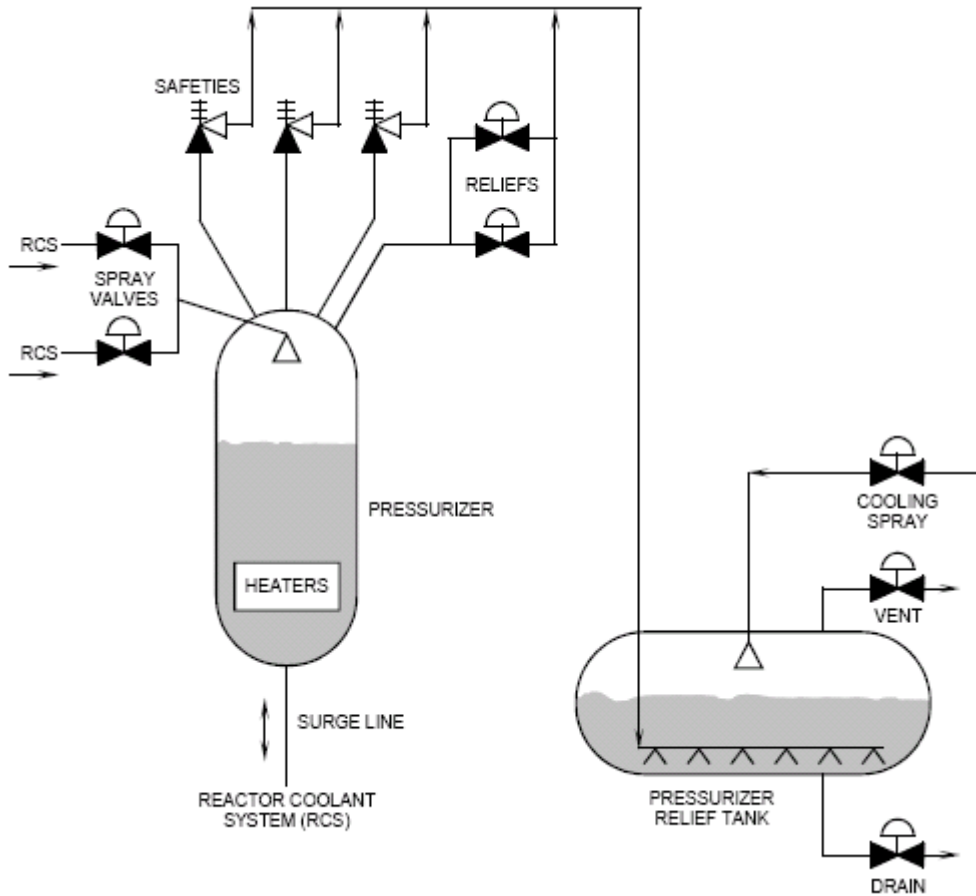


Figure 7: Schematic diagram of the Pressurizer and the Pressurizer Relief Tank (USNRC)

The pressurizer relief tank (*Figure 7*) is made up of a large tank containing water with a nitrogen atmosphere. The purpose of the water is to condense any steam discharged by the relief valves or the safety valves of the pressurizer. The nitrogen atmosphere is used to prevent hydrogen from existing in a potentially explosive environment, as the reactor coolant system contains hydrogen.

3.1.2.5 The Secondary System

The primary and secondary system of the PWR is separated from each other by the heat exchange tubes inside the heat exchanger/steam generator. A benefit of this separation is that there will be little to no radioactive contamination in the secondary system, allowing for simpler and safer maintenance of the secondary system. The secondary system is described by the main steam system and the feedwater system as pictured in *Figure 8*.

This separation results in a typical reactor vessel outlet temperature of 320 degrees Celsius at 150 bar and steam temperature of about 270 degrees Celsius at 50 bar. Newer Generation III plants such as the Areva EPR is able to output reactor outlet temperatures as high as 327.2°C at 155 bar and steam temperatures of 293°C at 78 bar.

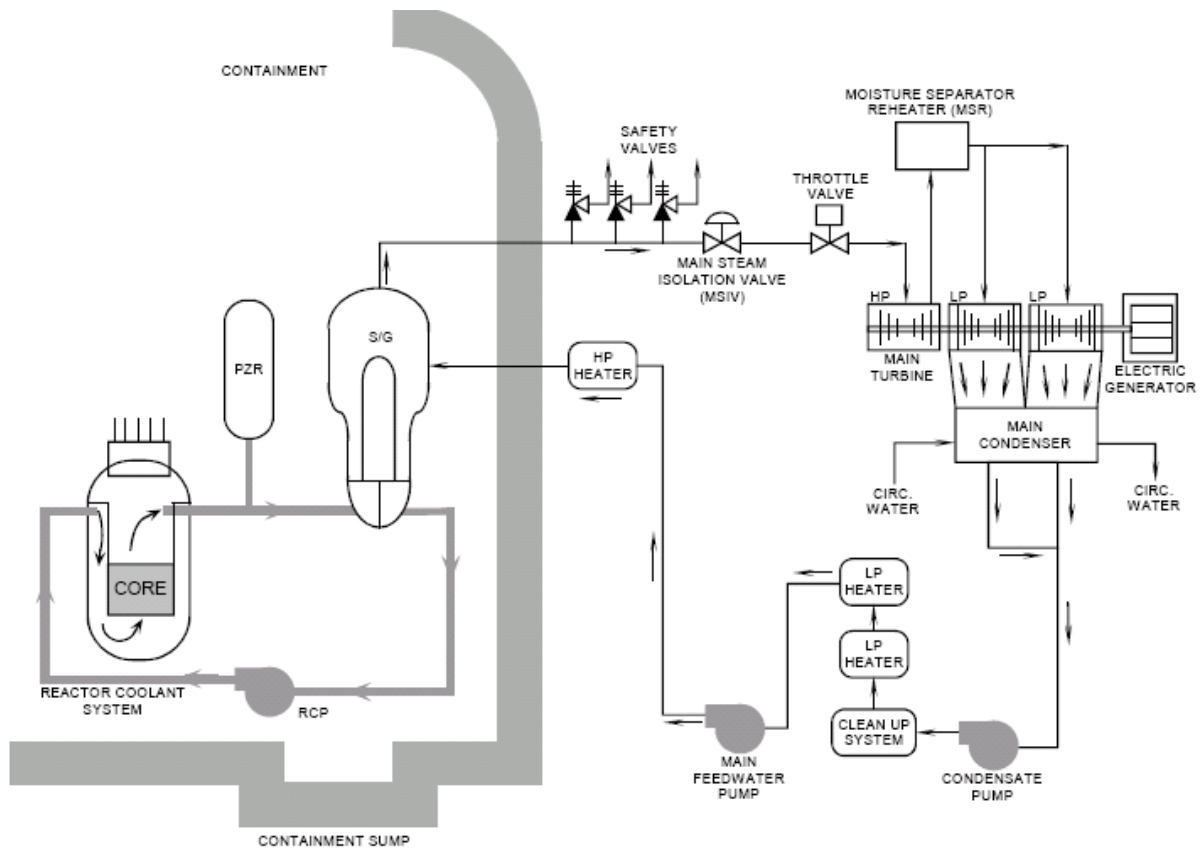


Figure 8: Schematic diagram describing the components in the secondary system (USNRC)

The main steam system begins at the outlet of the heat exchanger/steam generator where the steam is routed to the high pressure main turbine. After exiting the high pressure turbine, the steam is then routed to the moisture separator and reheater (MSR) system where the steam is dried with moisture separators and then reheated. From the MSR system, the steam is then routed to the low pressure turbines to squeeze even more energy out of the excess steam from the high pressure turbines into turning the main generator shaft. The steam from the low pressure turbines then enter the main condenser which is operated at a vacuum to promote greater removal of energy from the steam by the low pressure turbines. The steam is then condensed into water by the flow of circulating water through the condenser tubes, which is really another heat exchanger between the secondary system and the circulating water system.

The condensed steam accumulates in the hotwell area of the main condenser. The condensate pumps then pump from the hotwell to increase the pressure of water hence reducing the quality of the steam and turning excess condensed steam into even more water. The condensate then passes through a cleanup system which removes any impurities in the water. These impurities, if not removed, could accumulate in the heat exchanger tubes and damage it. After passing through the cleanup system, the condensate passes through some low pressure feedwater heaters where the temperature of the condensate is increased in the heaters by using excess steam from the low pressure turbines. The condensate is then pumped by the main feedwater pumps where the pressure of the condensate is increased high enough to be able to enter the main heat exchanger. The feedwater then passes through the high pressure feedwater heaters which are heated by extraction steam from the high pressure turbine. The heating of the feedwater before entering the main heat exchanger allows for greater efficiency of the power conversion system.

The pressurized water reactors are very stable due to its negative void coefficient properties. As the reactor temperatures increase, the reactor tends to produce less power. This allows for stability in control and ease of operation. Another advantage of the PWR is that there is a wide wealth of experience world wide in operating these reactors, and therefore the wisdom and understanding gained from the operation of existing PWR reactors can contribute to better PWR designs as proposed by the Westinghouse AP1000 and Areva EPR Generation III designs.

3.1.3 High Temperature Gas Reactors

The most significant limitation of the PWR type reactors is of its lower efficiency as compared to fossil-fuelled power stations mainly as a result of its lower turbine inlet temperature. The high temperature gas reactor (HTGR) is designed to address this issue, employing gas coolant instead of water to allow for higher operating temperatures. The HTGR with a typical efficiency of approximately 40% as compared to a typical PWR (30%) are comparable to the thermal efficiency of fossil-fuelled power stations, driving the motivation to further look into this technology to be introduced as the next generation of nuclear power stations.

The attraction of the HTGR is due to its high power conversion efficiency, while also being able to utilize the high temperatures that these reactors operate to embark on some

industrial applications and chemical processes that requires such high temperatures for example, the production of hydrogen to facilitate a hydrogen economy.

Currently there are two different paths undertaken by HTGR designers, both featuring its own advantages. The indirect cycle HTGR employs the use of an intermediate heat exchanger (steam generator) to provide power for a steam cycle to power a steam turbine, splitting the power conversion system into two circuits; primary and secondary circuits. The direct cycle HTGR in contrast utilizes the helium coolant from the reactor core to directly drive a gas turbine, thus eliminating the use of the intermediate heat exchanger and all its supporting components altogether. Another design worth mentioning is the combination of both through employing the use of gear boxes to synchronize the gas turbine with the steam turbines.

3.1.3.1 The Indirect Cycle High Temperature Gas Reactor

The indirect HTGR power stations utilize a steam turbine-generator power conversion cycle to generate electricity. The indirect HTGR power station is comprised of a single reactor system that provides an energy source in the form of steam for a single turbine generator. In all indirect HTGR designs, the reactor core is housed under a pre-stressed concrete reactor vessel (PCRVR).

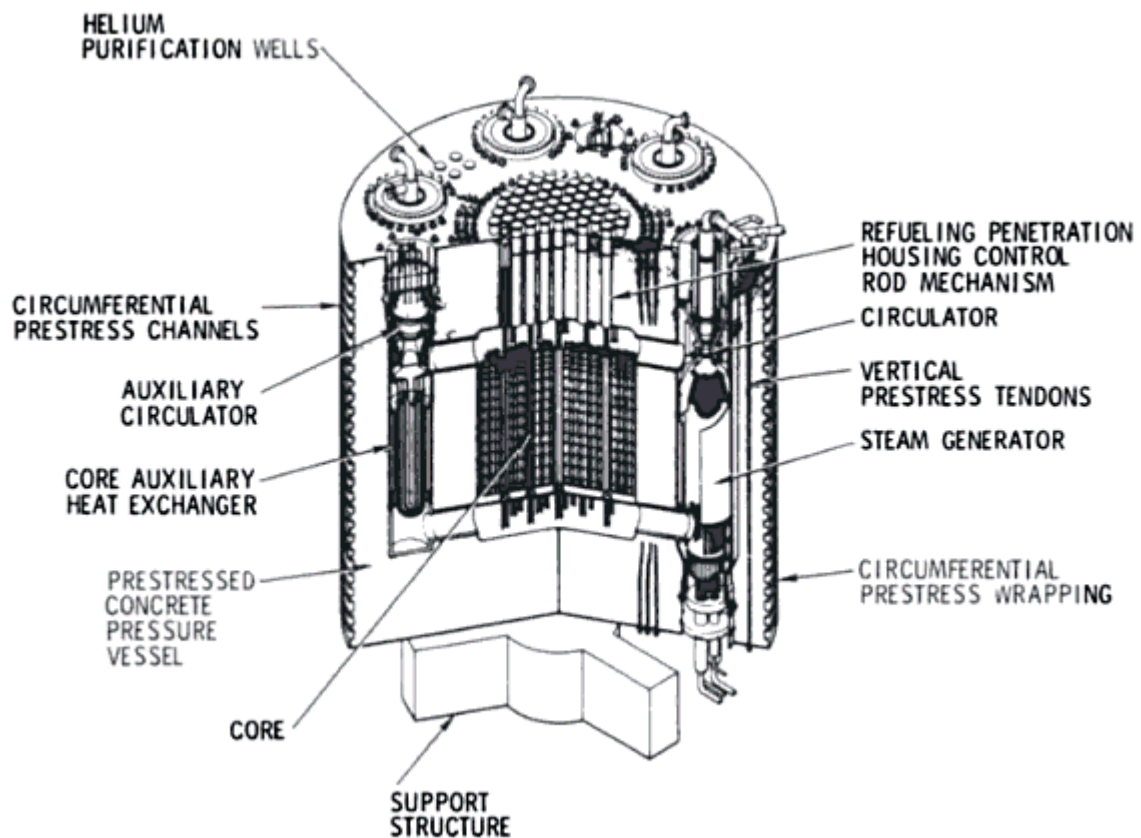


Figure 9: Pre-stressed concrete vessel for the high temperature gas-cooled reactor (ORNL, US DoE)

The reactor containment is a steel-lined reinforced concrete, circular cylindrical structure with a hemispherical dome on top. It houses the pressure vessel, nuclear steam supply system auxiliaries and a polar crane which is used to service the PCRV and fuel handling components.

Knief R.A. (1992) describes the indirect cycle HTGR in further detail. The HTGR power station is a thermal reactor moderated by graphite and cooled by helium within a multi-cavity RPV. The fuel is concentrated in rod form and is located in vertical holes in hexagonal cross-section graphite elements. These graphite elements include vertical, full-length channels for coolant flow. Some of these channels also become channels for the insertion of control rods.

The core, control equipment, primary coolant, primary coolant circulators, heat exchangers, and decay heat removal equipment are all contained within the pre-stressed concrete reactor vessel. The PCRV is a vertical cylinder of varying dimensions. The core is located in a central cylindrical cavity. On one side of the core cavity, there are two or four vertical cavities containing the heat exchanger and the helium circulator for the primary coolant loops. Horizontal ducts exist to connect the primary and auxiliary loop

cavities with the core inlet and outlet plenums. The PCRV is designed for a maximum cavity pressure of 78 bar, and it has a water-cooled steel liner with a thermal barrier on the gas-side surfaces.

The helium coolant enters above the core and flows downward through the fuel assemblies and enters the intermediate heat exchanger. Provisions are also made within the PCRV for control-rod drives, refuelling penetrations and helium purification.

The HTGR has two heat transport loops comprising of a heat exchanger/steam generator, which is a once through unit with helical coils in the evaporator section and a straight tubes in the superheater section, and a main helium circulator which is a single-stage, water lubricated, and centrifugal compressor with variable speed electric motor drive. Another HTGR design has four heat transport loops comprising of a heat exchanger/steam generator, but uses a down-hill boiling characteristics. Feedwater traverses the upper series of coils and leaves through an axial tube in the form of superheated steam. A reheat cycle uses the lower series of coils below the helium inlet. Each helium circulator is installed with a shutoff valve to allow the reactor to operate with the heat transport loop not in service.

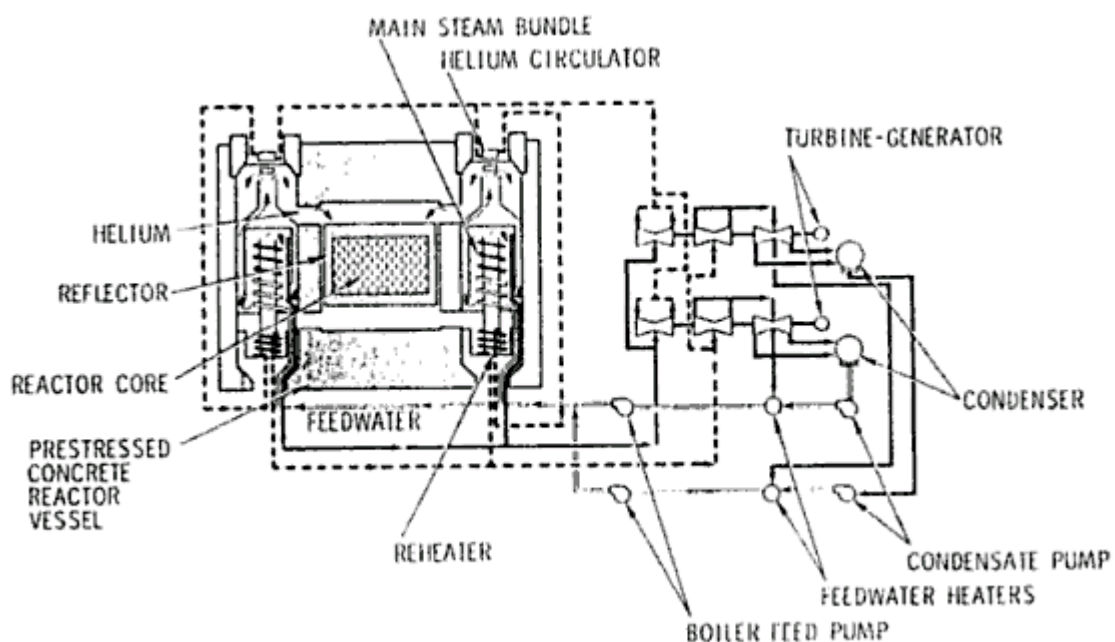


Figure 10: Schematic diagram of the high temperature gas-cooled reactor steam cycle.

The power conversion cycle for the HTGR is given in *Figure 10*. The primary loop is contained entirely within the pre-stressed concrete pressure vessel (PCRV). The helium circulators pump the helium coolant through the core which is then piped to the entrance

of the intermediate heat exchanger at a temperature of 740°C with a system pressure of 49 bar.

The intermediate heat exchanger receives feedwater and converts it to steam at a temperature of 510°C and 172 bar. This steam supplies energy into the high pressure conventional turbine. Steam exiting from the high pressure stage drives the primary helium circulators before it goes back into the intermediate heat exchanger to be reheated in the lower section of the intermediate heat exchanger, providing a steam output of 540°C at 40 bar. This steam is then fed into the intermediate-pressure turbine and then to the low-pressure turbine sections. This reheat cycle serves to increase the thermal efficiency up to about 40 percent.

3.1.3.2 The Direct Cycle High Temperature Gas Turbine

Baxi et al. (2008) claimed that the High Temperature Gas Reactor (HTGR) is the only demonstrated nuclear technology that can achieve a reactor coolant hot leg outlet temperature of up to 1000°C. This allows the HTGR to benefit from the implementation of the high-efficiency Brayton gas-turbine cycle reaching 50% efficiency or more when coupled with a conversion system based on the direct closed gas turbine cycle. Another advantage with the direct cycle HTGR design is the simplification due to reduction in the required amount of equipment and systems involved in the indirect cycle high temperature gas reactors. These include the elimination of the turbine hall with steam generator, steam pipelines, condenser, de-aerator and other systems. This makes the entire power conversion system more compact and reduces capital costs.

The power plant consists of two interconnected units: the modular high-temperature reactor and the direct gas turbine cycle power conversion unit. The primary system components are housed within two metallic pressure vessels that are connected with each other by a cross-vessel. Both the reactor vessel and the power conversion unit vessel are laid in vertical configuration, among the reasons for the latter being to prevent the bowing of the turbine shaft by gravitational forces. However, this configuration introduces extra axial load on the electromagnetic bearings. The entire system is located in an underground containment building as shown in *Figure 11*.

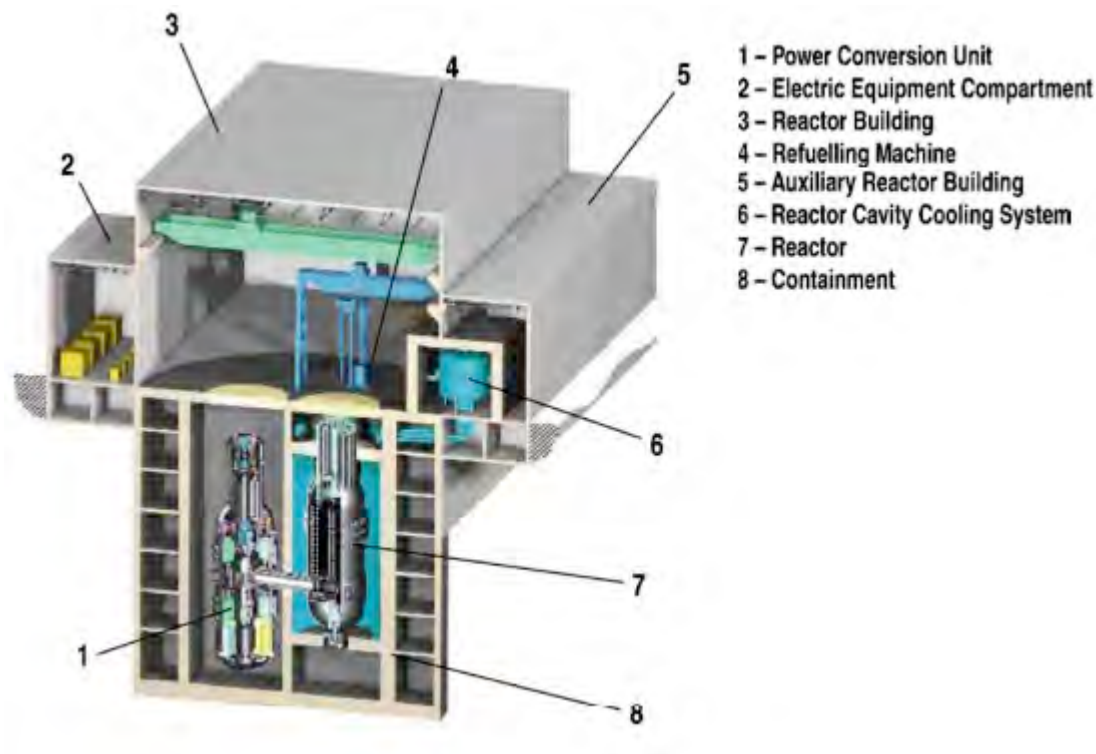


Figure 11: The layout of the GT-MHR reactor module located in an underground containment building. (Baxi et al., 2008)

The power conversion unit was designed based on a recuperated direct gas-turbine cycle that is optimized for high efficiency. Under operation, the heated high pressure helium coolant leaves the core and is routed via the hot duct inside the cross-vessel to the turbine where it expands to produce mechanical energy to drive the generator and two compressor stages located on the same shaft. The recuperator recovers residual thermal energy from the reduced pressure but hot gas stream coming out of the turbine. The helium gas then enters the pre cooler which provides the main heat sink for the cycle. The cool low-pressure helium is then compressed in two stages with an intermediate cooling in the inter cooler. The helium gas is then directed to the high-pressure side of the recuperator, where it is preheated using thermal energy recovered from the exhaust of the turbine. Now, the helium is routed to the cold leg of the core via the annular passage between the outer shell of the cross-vessel and its internal hot duct.

Although the reactor can be designed to produce helium at temperatures of up to 1000°C at the outlet of the reactor core, a helium temperature of 850°C was chosen as the design temperature as a compromise between efficiency and material limitations. Baxi et al (2008) also discussed that by using the direct Brayton energy conversion cycle, the system is able to achieve higher efficiency than if an indirect cycle was used. Employing an intermediate heat exchanger for the indirect cycle meant that the additional piping will

be a potential for leaks, as well as an increase of pressure losses in the system. There will also be a temperature drop across the intermediate heat exchanger as the inlet turbine temperature will be lower by around 15-50°C, thus reducing conversion efficiency by around 2-3%.

The implementation of the direct cycle HTGR system has been faced with numerous obstacles, however. Although the power station design is sound, the fabrication of the plant includes systems that are not yet available in the world today in terms of capacity. This includes the availability of the helium turbines, frequency converter, the gear box of 300 MW capacity and electromagnetic bearings at such high capacity. The designers have compensated for this by extrapolation and the introduction of two power conversion units instead of one to allow for existing available technologies to be used. However, for the reference nuclear battery concept with a power estimated only around 15 MW, this may not prove to be so much of an obstacle.

3.2 Fossil-fired Power Stations

3.2.1 Coal-fired Power Stations

A coal power station generates its power from boiling water into steam which drives a steam cycle to produce power. The coal power station functions from three primary components: the furnace, the boiler, and the steam turbine. A schematic of a typical coal power plant is show in the *Figure 12* below.

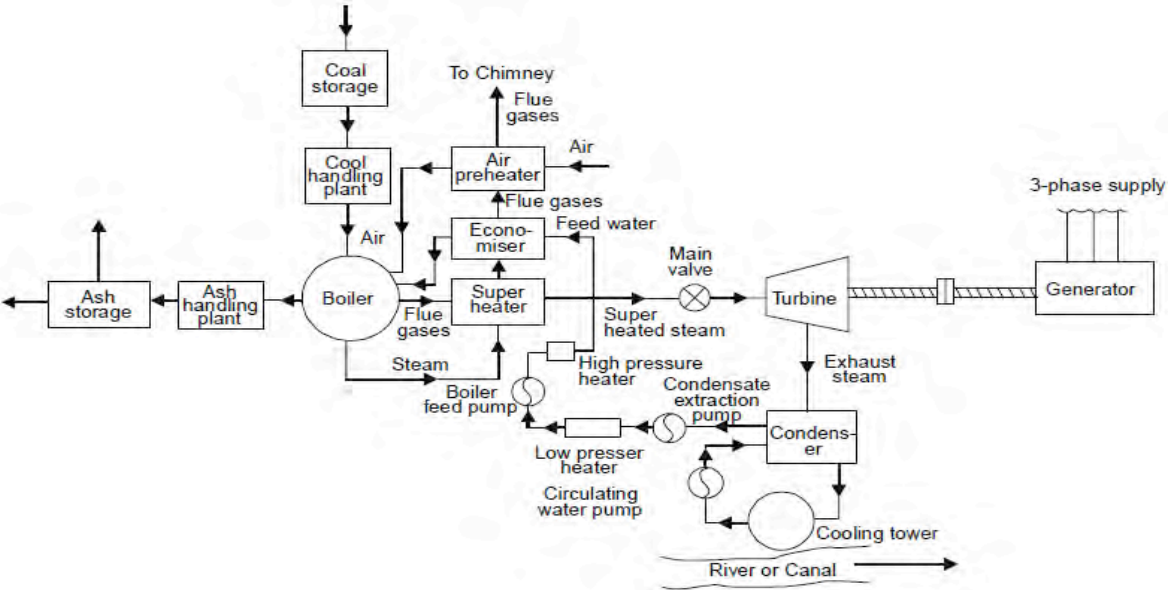


Figure 12: Schematic diagram of a coal power station

As described in *Figure 12*, the flow sheet of a coal power station consists of four circuits: the feed water and steam flow circuit, the coal and ash circuit, the air and gas circuit, and the cooling water circuit. The coal power station operates by employing steam as the working substance which is based on the Rankine cycle.

Raja et al (2006) describes in their book the process of these four circuits in the coal power station. Coal is received from the coal storage yard of the power station and is transferred to the furnace by the coal handling unit. To burn the coal, air is taken from the atmosphere and is first passed through the air pre-heater where it is heated by flue gases. The hot air then passes through the furnace, where it then passes over the boiler through superheater tubes as flue gases. The air then flows through the dust collector, and then through the economiser, air pre-heater, and finally exhausted to the atmosphere through the chimney. The burned coal produces heat, which is utilized to convert water in the boiler drum into steam at a suitable pressure and temperature. The steam generated is then passed to the superheater where the superheated steam produced then passes through the steam turbine. After doing turbine work, the steam exits with reduced pressure, and passes through the condenser which maintains the low pressure steam at the exhaust of the turbine. The steam pressure at the condenser depends on the flow rate and temperature of the cooling water and the effectiveness of the air removal equipment. The circulating water in the condenser is sourced from a nearby body of water, and if unavailable, the hot water coming out of the condenser can be cooled in cooling towers and then circulated again through the condenser. The excess steam from the turbine can be sent to the low pressure and high pressure water heaters to squeeze out as much available energy as possible to increase the plant efficiency in a regenerative configuration.

Schilling (2005) notes that coal plant efficiencies were only 5% at 275°C and 13 bar pressure around 1910. This further developed to around 38% average efficiency in the mid 1980's. The world's best achieved coal fired plant efficiency of 47% was in Denmark which was constructed using the best modern technologies. Schilling also goes further to claim that the average efficiency of coal fired power plants in the world are only 31%. Taking into account that coal fired plants have been erected almost a century and that any new coal fired plant constructed today will surpass the average efficiency, it is safe to assume that coal fired technologies can achieve plant efficiencies of around 38% at 600°C temperature.

3.2.2 Combined Cycle Gas Turbine Power Stations

The gas turbine power station utilizes the energy obtained from burnt gases and air, which is at high temperature and pressure, and converts it to power by letting the gases expand through several rings of fixed and moving blades in the form of a turbine. To obtain the high pressures necessary of the order of 4-10 bar which is essential for the expansion of gas, a compressor is required. The compressor allows for a higher speed and quantity of the working fluid, in this case a gas, to accept energy from the heat source.

A simple gas turbine consists of a compressor, a combustion chamber, and a turbine. The turbine shaft is coupled to the compressor; hence the compressor absorbs some of the power produced by the turbine thus lowering the energy output slightly. The combustion chamber of the gas turbine is able to use from a number of fossil fuel sources such as oil, natural gas, coal gas, producer gas, blast furnace and pulverized coal.

The gas turbine power station comes in three configurations. The open cycle gas turbine compresses the air from the atmosphere and feeds it to the combustion chamber. The product gas at high temperature comes out of the combustion chamber and then passes through to the turbine where it expands and performs mechanical work by spinning the turbine. The turbine main shaft powers the generator but it also expends energy to power the compressor. Since the cycle extracts air from the atmosphere and exhausts it back into the atmosphere after work has been done, the working medium must be replaced continuously. This is what defines the open cycle gas power station, which is further described in the *Figure 13* below. Raja et al. (2006) claims that in general, a simple open cycle gas turbine achieves about 16-23% thermal efficiency as most of the energy is lost as exhaust gases.

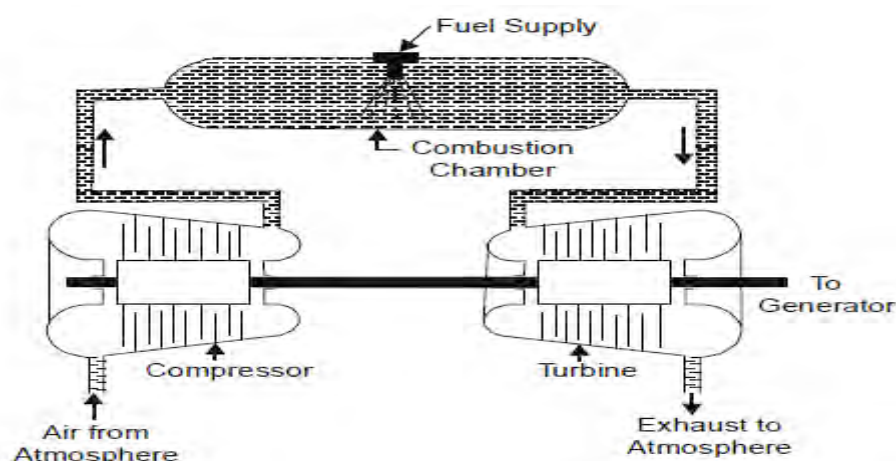


Figure 13: The open cycle gas turbine power station

In a closed cycle gas turbine power station the working fluid, which is either air or any suitable gas, comes out of the compressor to be heated in a heater by an external source at constant pressure. The high temperature and high pressure air coming out of the heater is passed through to the gas turbine. The gas coming out of the turbine is then cooled to its original temperature in the cooler using an external cooling source before being passed back to the compressor. Thus, the primary working fluid is continuously used in the system in a full cycle without experiencing a change of phase. The component arrangement of a closed cycle gas turbine power station is described as a schematic the diagram as in Figure 14.

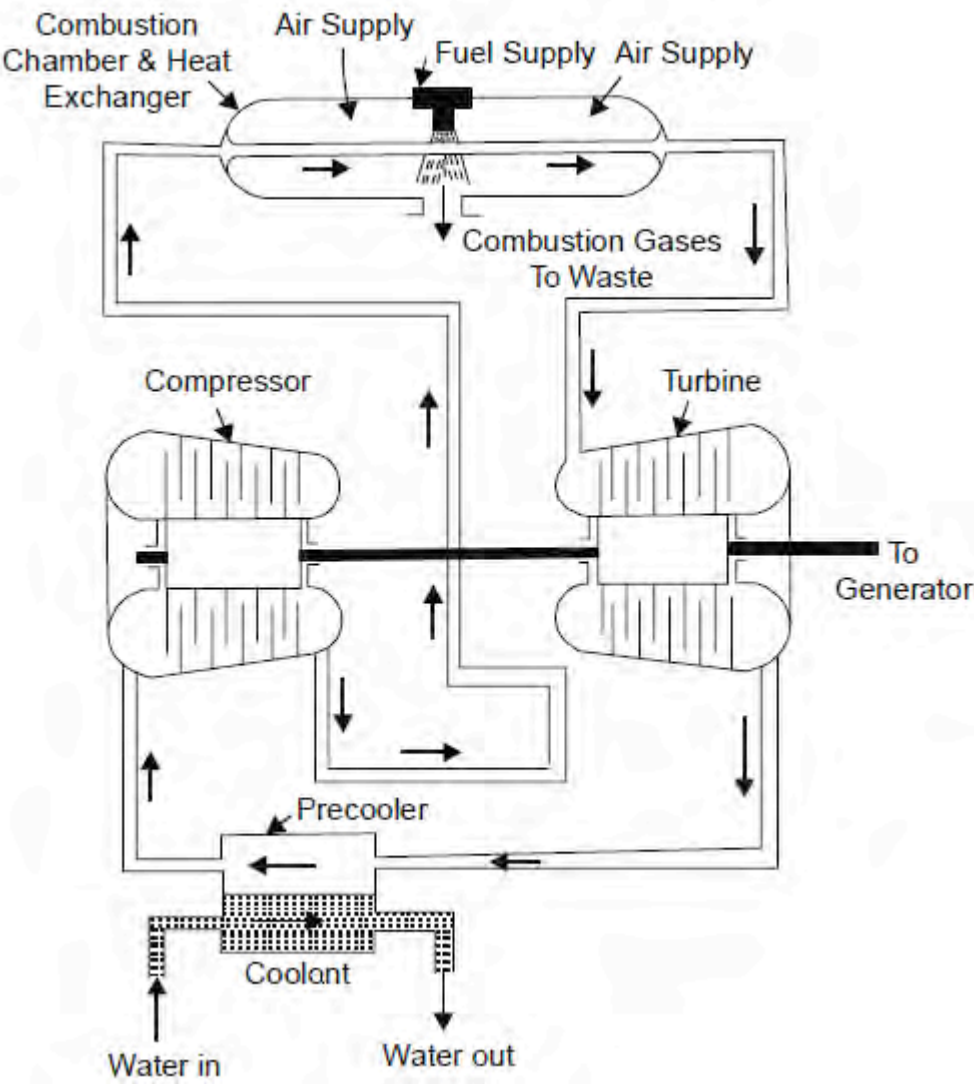


Figure 14: The closed cycle gas turbine power station

The closed cycle gas turbine opens new doors to the choice of the primary working fluid as opposed to air in the open cycle which includes argon, carbon dioxide or helium. However, helium based gas turbines with a large enough energy output capacity are far from the reality at the moment due to the unavailability of such a helium turbine technology in the present day.

The primary disadvantage of a closed cycle gas turbine over an open cycle gas turbine is that because it is a closed system, the feedwater system in the cooler needs to be operational at all times to ensure heat is removed from the heating source. In contrast, the open cycle gas turbine does not face this problem because the air is input from the atmosphere. This results in some required maintenance and monitoring of the circulating feedwater equipment such as pumps and piping.

Noticing that a considerable amount of excess heat energy is released as exhaust, a new approach was undertaken with the objective of utilizing as much energy as technologically possible. This requires the utilization of heat energy in a power system at different temperature levels at which it can be used to produce work, or steam, or the heating of the water before entering the heat exchanger. This approach results in the conception of the combined cycle gas turbine. *Figure 15* describes the schematic diagram of the combined cycle gas turbine.

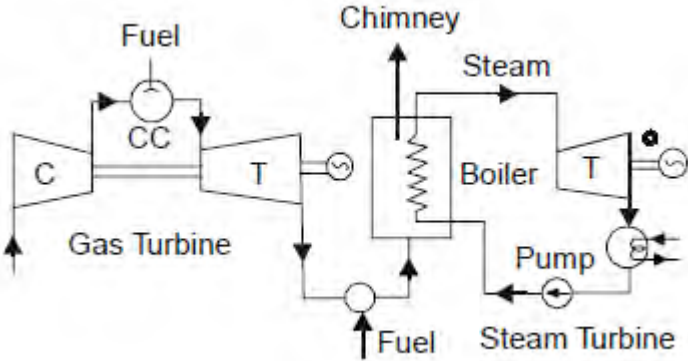


Figure 15: The combined cycle gas turbine power station

The gas at the exhaust of the gas turbine is utilized as inlet gas to the steam generator where the combustion of additional fuel takes place. Raja et al (2006) comments that this combination allows for nearer equality between the power outputs of the gas and steam turbines than what is obtained with a simple recuperative heat exchanger. For a given power output, the energy input is reduced. In other words, the combination cycle exhibits higher thermal efficiency although at a cost of higher complexity of the design.

Combined cycle gas turbines can achieve turbine inlet temperatures as high as 1250°C. Depending on the employed design, utility scale generation can accommodate different efficiency compromises through a range of established designs. The range starts from single shaft machines with simple steam cycles to multiple shaft arrangements with triple pressure steam cycles and reheat. Heppenstall (1997) alleges that this allows combined cycle gas turbine power stations to achieve plant efficiencies of up to 55% and more.

3.3 Space Reactors

3.3.1 Thermionic Emission Reactors

Thermionic power converters are a class of device that converts thermal power to electricity using thermionic emission directly without converting it to another form of energy in between. All metals and oxides have free electrons which are released on heating. These electrons then travel through space and collected on a cooled metal, and then can return to the hot metal through an external load therefore completing the circuit and produce electrical power.

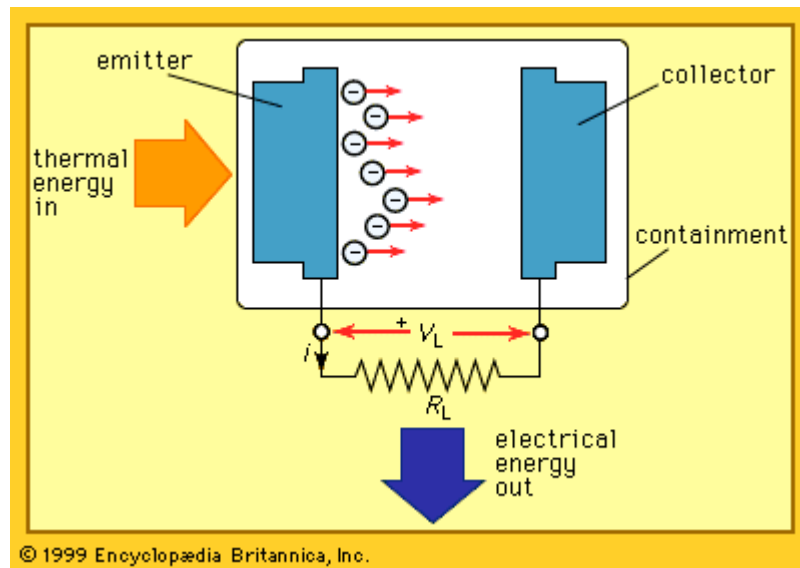


Figure 16: Schematic diagram showing the principles of a thermionic converter
(Generator)

A thermionic power converter as shown in *Figure 16* has two electrodes enclosed in a tube. One of these, the cathode, is raised to a sufficiently high temperature to become a thermionic electron emitter, or "hot plate." The other electrode, called a collector

because it receives the emitted electrons, is a cooled metal anode and operates at a significantly lower temperature. The space between the electrodes is sometimes a vacuum but is normally filled with a vapour or gas at low pressure to minimize energy losses. The gap size is only about one millimetre. The thermal energy may be supplied by chemical, solar, or nuclear sources. Thermionic converters are solid-state devices with no moving parts. They can be designed for high reliability and long service life. Thus, thermionic converters have been used in many spacecraft designs.

Emission of electrons from a hot plate is analogous to the liberation of steam particles when water is heated. These emitted electrons flow toward the collector, and the circuit can be completed by interconnecting the two electrodes by an external load. Part of the thermal energy that is supplied to liberate the electrons is converted directly into electrical energy, while some of the thermal energy heats the collector and must be removed.

The thermionic generator is like a cyclic heat engine and has a maximum efficiency that is limited by Carnot's law. Raja et al (2006) asserts that the thermionic device is a low-voltage, high-current device where current densities of 20-50 A/cm² have been achieved at a voltage between 1 to 2V, with realized thermal efficiencies of between 10-20%.

Although the thermionic converter is able to convert energy from thermal to electrical, to apply this technology to a nuclear reactor still requires that the excess heat be removed from the reactor to avoid structural and fuel meltdown. Thus, a cooling system still needs to be employed to ensure the reactor operates within accepted temperatures. The paper presented by Andreev et al (1991) discussed the principles and characteristics of a thermionic space nuclear power system. The power unit within the device includes a thermal reactor, radiation shielding, heat removal system, cabling system, sensors and load-bearing members. The coolant used for this reactor is a eutectic alloy of sodium and potassium, and the neutron moderator is made of zirconium hydride. The core is contained within a steel vessel which separates it from the side reflector which has twelve revolving control elements. The maximum coolant temperature is limited to 600°C and special coatings are done on the surface of the moderator and core structural elements to decrease hydrogen leakage. The thermionic devices are setup to function at an average specific conversion power of up to 3 W/cm² with temperatures not more than 1600°C. Such a limit is chosen to ensure a long service life of the thermionic devices. It is estimated that the conversion efficiency of the thermionic system to be equal to not less than 8% at the end of the service life.

Thermionic generators are currently being further developed. Raja et al (2006) also revealed that practical working prototypes have been built and feasibility of these prototypes has been proved. The results revealed that with an anode of low work-function material such as barium oxide or strontium oxide coupled with a cathode of high work-function material such as tungsten impregnated barium compound, a power output density of 6 W/m can be achieved at cathodic temperatures of around 2000°C. The efficiency of this system is about 35%.

The primary advantage of using thermoelectric and dynamic conversion systems are the compactness and the long service life of the product. Achieving an efficiency of 35% would make it comparable to gas-cooled reactors, however to reach such high temperatures would be a heavy challenge to satisfy with current nuclear technologies.

4 Analysis of Potential Systems

The design of the small autonomous nuclear reactor is defined by three key factors. These factors are size, reliability and availability, and their relationship is as in the figure below:

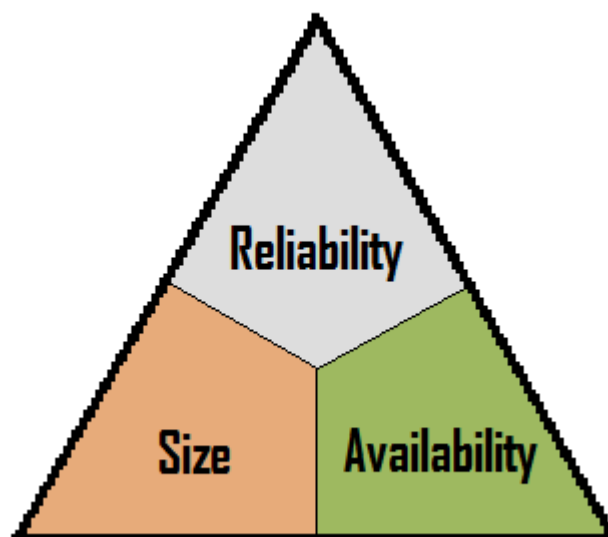


Figure 17: Key Factors governing the design of the autonomous reactor

The size of the reactor directly influences the overall cost to be incurred in the deployment of the reactor. The two main questions directly relating to the size factor is how it can be transported and where it can be deployed. If the size is too big to be transported, then it will need to be built on site instead of in a factory, and there are costs to be incurred to transport equipment and personnel to the construction site. Similarly, the size limits the sites where the autonomous reactor can be deployed. Should the autonomous reactor become too large, it may have to be deployed outside the required work area and hence necessitating power cables to be laid into the working area; this may also incur licensing costs to run the reactor outside the small permissible area. Both these concerns relate directly to overall costs, thus it is imperative that the size of the autonomous reactor be kept as compact as technologically and safely possible.

Reliability of a power source is one of the most important things to consider, especially if it is to be an autonomous source. To provide a stable and consistent power supply in the grid-connected power system is a heavy task for the grid operators, as they understand that energy consumers need the power source to be available all the time as power interrupts or even a slight transient in the quality of the power delivered could become very costly. For an autonomous source, there will be no operators. The autonomous source must be able to take care of itself, tripping when necessary and restoring power once the fault condition is removed. It needs to achieve this without human input. Hence, the design must be extremely reliable to ensure the power supply is given consistently and dependably. The autonomous supply must be designed with as little reliance on moving parts as possible to reduce the influence of wear-and-tear. Any possible avenue of degradation must be identified and tackled before the power source leaves the factory. For a nuclear-grade power source, reliability becomes even more important: a fault in an important component such as the heat removal system could cause the reactor core to melt down. A worst-case scenario would be a meltdown of the reactor core breaching the outer radioactive containments and thus contaminate the geological environment.

To achieve both the above factors, remarkable designs have been discussed to ensure the compactness and the reliability of the energy source to be at its optimum point. Unfortunately, available technology has not caught up with the requirements of these designs. This does not mean that the technology has not been proven on a lab scale; it simply means that although technically possible, the technology does not exist yet today because it does not make economical sense for the manufacturers to have these technologies ready when there is currently little demand for them. For the manufacturers to launch a one-off product, the costs incurred will be tremendous. Hence, the availability

factor here describes the availability of such technology in the market. The design of the autonomous nuclear reactor needs to take into account the available technologies in the market to capitalize on existing strengths to ensure a low cost but effective solution.

The design of the small autonomous nuclear reactor is therefore dependant on the balance of these three key factors. The analysis for the potential systems best established to provide the power conversion system for the small autonomous reactor will be benchmarked against a base system. I have chosen the AGR as the base system for this purpose.

4.1 Plant Efficiency

To compare the operating costs on existing potential power conversion systems, we will first look at the thermal efficiencies of the station. The thermal efficiencies give a figure that translates how much useful energy can be harvested from the fuel, which relates to how much uranium fuel must be purchased to keep the reactor running at its designed power output.

For the gas-cooled Magnox reactor, the plant efficiency is rated at 31.4% as compared to 40.0% efficiency of the base reactor design. The AGR design was devised to outdo the success of the Magnox reactor design and hence the results are hardly surprising. The Magnox design did not reach optimum reactor coolant outlet temperatures because of the low temperature limit of the Magnox alloy cladding.

The PWR plant efficiency is rated at 30% for a typical PWR although newer designs are estimated to reach 37% for the Areva EPR 1600 MWe PWR station as reported by Ellia G. (2006). This places the PWR within reach of the benchmark AGR design nonetheless still falling a little bit short. The reason for this is the reactor outlet temperature of pressurized water reactors could not reach the temperatures achievable by gas cooled reactor stations.

The Indirect Cycle HTGR design is rated at 40% thermal efficiency which is comparable to the base AGR design. Both designs employ the steam cycle for the secondary circuit to capitalize on the reheated Rankine cycle concept thus this is to be expected. However, the Direct Cycle HTGR, which is based on the Brayton cycle, is able to achieve thermal efficiencies of up to 50% or more. This places the Direct Cycle HTGR to be the only nuclear reactor concept that outperforms the benchmark design.

Thermal efficiencies of the thermionic reactor lie around the range of 10-20 percent, which places this technology as the least efficient of all current technologies under consideration. However, the high reliability and long product life could compensate for the low thermal efficiencies.

The table below compares the thermal efficiencies of the different nuclear reactor types and other power conversion systems.

Power Conversion Technology	Reactor Outlet Temperature	Plant Thermal Efficiency
Magnox	414°C	31.4%
AGR	635°C	40.0%
PWR	320°C	30-35%
Indirect Cycle HTGR	740°C	40.0%
Direct Cycle HTGR	850°C	50.0%
Coal Power Stations	(Turbine Inlet) 600-700°C	38.0%
Gas CCGT Power Stations	(Turbine Inlet) 1250°C	50-55%
Thermionic Conversion	600°C	10.0%

Table 3: Reactor outlet/turbine inlet temperatures and thermal efficiencies of existing power conversion technologies.

4.2 Plant Flexibility

The small autonomous nuclear reactor must also be flexible in its applications. The market for the deployment of this reactor is in locations where it is too far to be connected to the power grid. Another concern in the deployment of the reactor is its application, either for electricity generation or industrial applications.

The Magnox and AGR stations were built on the site it was to be erected on. Each of the main components was too big to be built in factories of that age and so they were constructed from the ground up. The PWR stations were also built in a similar way but recent designs such as the Westinghouse AP1000 and the Areva EPR allowed for the bulk of its main components to be designed in factories and shipped to the site by rail. The high temperature gas reactors were also designed with modularity in mind.

The modularity of modern designs are important as quality of the product can be better ascertained when it is built in factories. The assembly of modular equipment on site could also be better performed as they are laid and connected to each other. This also

allows for better maintenance philosophies, where a heavily defective module could be removed from the site and replaced with an upgraded module. In addition, reactors can also be flexible enough to be able to perform various applications by adhering to the modularity concept. For example, a module to generate hydrogen thermally could be replaced by another module for district heating just by interfacing with the heat sinks or condensers of the nuclear station.

Although the AGR was never constructed as a modular system, the technological developments of today will allow the AGR to be designed in such a way like its PWR and HTGR counterparts.

The thermionic reactors will not benefit as much from the modularity of design. This is because the thermionic converters are all lined up inside the reactor itself, thus any upgrade in the thermionic converters will require the entire reactor to be rebuilt. This means any efficiency declared in an erected thermionic reactor station is likely to stay as much and not differ. However, thermionic reactors will still benefit overall from any improvements in reactor coolant safety systems.

4.3 Plant Complexity

One of the main focuses of the small autonomous nuclear reactor is that the design must be reliable. The addition of many systems to safeguard the reactor's operations and to increase the reactor's efficiencies will lead to design complexity. Complex designs have more components, and each of these components has a chance of failing. For a reactor that is designed to be deployed as a self-sustaining power source, it is not economically feasible to send a team over to the site to replace a malfunctioning part each time a component fails. Thus, simple, reliable designs are preferred.

The Magnox reactor has its steam heat exchangers on the outside of the pressure vessel, thus increasing the amount of piping and the potential for a primary loop break. However, this allows the heat exchanger to be accessed for services much simpler as compared to the base AGR. The Magnox design incorporates 4 heat exchangers but the volume of the heat exchangers is also larger than the base AGR. CO₂ leakage problems were prevented by lining the internal face of the vessel with steel of 25 mm thickness at a pressure of 29 bar. Complexity arises due to the control of corrosion. Methane was introduced with the coolant gas to reduce the effect of radiolytic corrosion by carbon monoxide and the oxidizing free radicals formed by the irradiation of the CO₂.

The AGR reactor improvised on the Magnox design to achieve higher power density. It also incorporates 12 steam heat exchangers inside the pressure vessel.

The PWR design is one of the most developed designs in the nuclear industry. The negative void coefficient present in pressurized water reactors helps make it much more safely controllable. However, the PWR needs to run at high pressures and the presence of water results in possible high temperature corrosion in the pipes. The pressurizer, a unique component only available in the PWR, requires the actions of heating elements and condensation sprays to maintain the pressure within the primary system. In the event of a Loss-Of-Coolant-Accident (LOCA), the pressurized water within the primary coolant system may experience film boiling at the fuel channels hence leading towards core meltdown. There are many backup cooling systems designed to operate for such an accident and these add to the complexity of the design. The Areva EPR, for example, has 4 times the redundancy to ensure operational accidents do not occur. The Westinghouse AP1000, in contrast, takes a revolutionary approach to tackle this problem by introducing passive circulation and switches to ensure the AP1000 remains in the safe state. The AP1000 removes dependence on pumps and electrical systems and replaces them with passive equipment such as those reliant on gravity, springs and pressurized cans to operate the safety mechanisms. The secondary system also presents a potential concern with regards to the complexity of the PWR design. PWR reactor coolant outlet temperature is only around 320°C, and at 270°C (assuming a drop of 50°C in the heat exchanger) and 50 bar secondary pressure results in an enthalpy of 6.02 kJ/kgK, and this puts the thermodynamic point on the T-s diagram to be just above the saturation point (*Figure 18*). When the steam enters the HP turbine at this temperature, the output steam quality drops to less than 80% and this excess moisture could damage the turbine blades. Thus, the PWR employs the use of moisture separators in the steam generators to ensure only gaseous steam enters the turbine. The turbine design is also more complex to address the water drop erosion problem of the rotating turbine blades, according to Leyzerovich (2005).

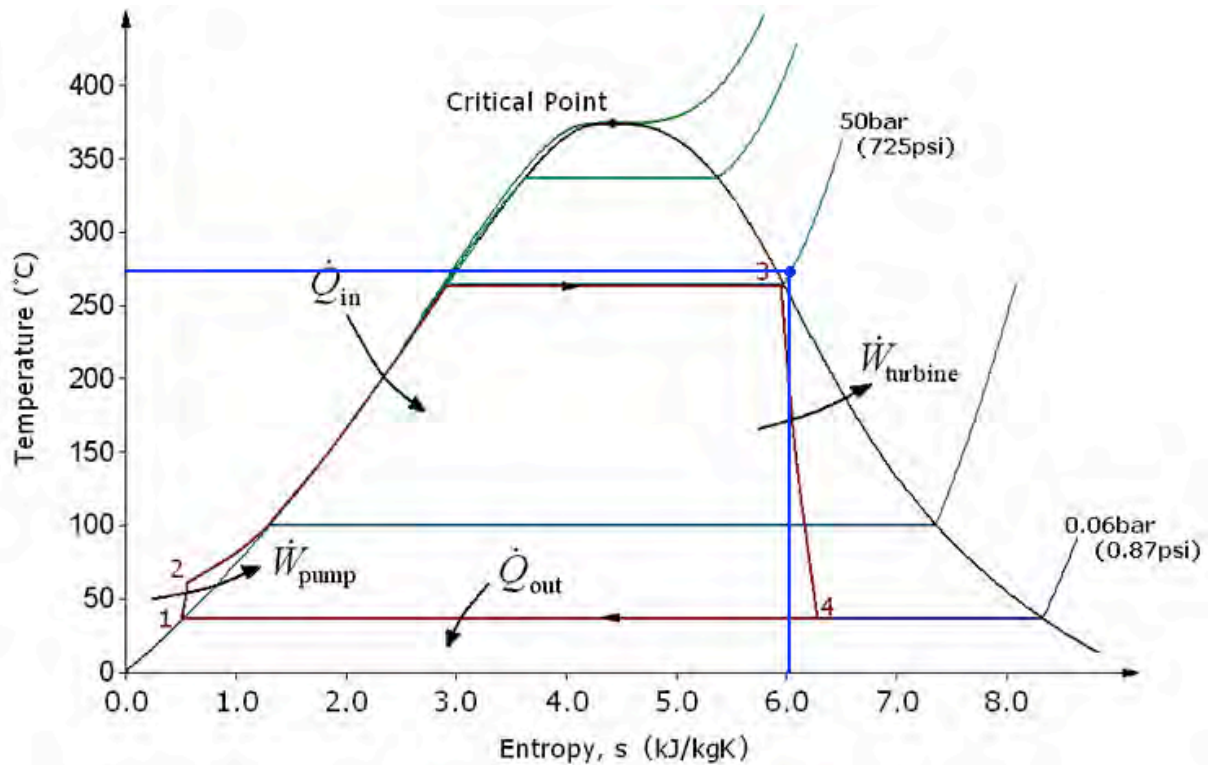


Figure 18: T-s Diagram of a typical Rankine cycle with highlighted saturated point at 270°C and enthalpy of 6.02 kJ/kgK.

The indirect cycle HTGR such as the GT-HTR consists of three subsystem modules: the prismatic core reactor, the standalone Gas Turbine Generator (GTG) and the Intermediate Heat Exchanger (IHX). The design of the HTGR was made to be modular, so that the construction of each individual module can be done in factories and erected on site in parallel. Kunitomi et al (2001) discussed that the GT-HTR 300 benefits from the non-intercooled design as compared to the intercooled design although it costs about 3% efficiency. This is due to the complexity of operations and maintenance of the system. The authors noted that the savings in operations and maintenance of the intercoolers far outweighs the benefits from the extra efficiency. The intercooler also requires a sophisticated inspecting machine because heat transfer tubes composing the primary boundary in the intercooler are required to be inspected by regulations. The design also compels the use of feedwater heaters and reheaters to maximize efficiency, thus adding to the complexity of the design.

The drive towards simplicity led to the conception of the direct gas turbine energy-conversion cycle. Kostin et al (2007) noted that this greatly simplifies the layout of the energy unit as compared to the steam cycle. The design benefits from the reduction of the number of equipment and systems required and the elimination of some equipment relevant to the steam cycle such as the steam generator, the machine room, the steam

pipes, the condenser, the de-aerator. This allows for a more compact gas-turbine energy conversion unit which lowers the overall costs. The use of electromagnetic bearings eliminates the requirement for complex seals for the shaft and expensive systems for distributing the helium and oil. This simultaneously decreases the requirements for the helium purification system. However, there still exist some challenges in the availability of active magnetic bearings to hold the rotor of the turbo-machinery in place. Another problem with the design is that the number of stages of the helium turbines is large, requiring about 19 stages to achieve the promoted efficiencies. Helium is not very dense and this results in a turbine design with a large diameter with many stages and small change in flow area through the turbine. It also requires many blades for each stage and unconventional mechanical designs of the blades.

Persson & Donaldson (2009) reiterated that both the turbine and compressor designs for the indirect cycle are closely related to the well established conventional designs. This allows for reduced risks and promotes confidence in the design.

In summary, the direct gas turbine energy-conversion cycle is the simplest design out of the nuclear reactor types discussed, however it is upset by the unavailability of the technology necessary at the scale it requires, hence not fulfilling a major item outlined as a key factor in the pyramid of *Figure 17*.

4.4 System Reliability

All the nuclear reactor types discussed have had their fair share of problems but the consequent reviews of their design have managed to iron out most of their inherent issues. However, some of these issues require constant monitoring and operator interaction to ensure the constant operation of the plant.

The Magnox and AGR reactor uses carbon dioxide as the coolant and this coolant may react with the graphite moderator present in the AGR reactors under high temperature and radiation fields to produce carbon monoxide through the reaction $\text{CO}_2 + \text{C} \rightarrow 2\text{CO}$. This reaction corrodes the graphite core and reduces its strength. To control this reaction, the water vapour content and the addition of methane was performed in small concentrations, which allows for the minimization of the rate of attack on the graphite. The precise control is important, because the over-concentration of methane and carbon monoxide could lead to carbon formation on the fuel elements itself which will reduce

heat transfer efficiency. Thus, constant monitoring of the fuel temperature and radiation needs to be performed to maintain operation of the reactor.

The PWR benefits from the negative void coefficient inherent in all light water moderated and cooled reactor designs. This allows for better control of the core reactivity. If there is an increase in power, the primary water coolant will start to boil and turn to steam, hence reducing in density. The reduction in water density at the reactor coolant channels decreases the neutron moderation, thus reduces the fission rate of the fuel. This in turn lowers the heat generated, hence allowing for the primary water coolant in the channels to return to liquid water and commence normal heat transfer. However, the PWR also suffers from corrosion of its stainless steel pipes from water at high temperature and high pressure. This condition is mitigated in a number of ways, but with modular construction and design, the power conversion system including the steam generator could be replaced on site simply, albeit costly.

In HTGR stations, leaking of the working fluid can easily occur due to the helium's low molecular weight. Thus, No et al (2007) notes that it is imperative that there is a reliable sealing of the system. Hence, helium gas turbines differ somewhat from other gas turbines using air or combustion gases.

The leaking of helium usually occurs at the turbine and compressor seals and there have been many innovative proposals to minimize the problem, unfortunately helium leakage problems will still occur. Wright et al (2006) explains that leaking could result in the mole fraction of helium to decrease over the life of the system and this could result in increased viscosity and lower conductivities of the helium working fluid. Therefore helium population needs to be consistently monitored and replenished. Although this maintenance requirement is satisfactory for most civil nuclear power station designs, it is however a major concern for an autonomous reactor design. It is unacceptable for the unmanned autonomous nuclear reactor that has a fuel load in the periods of years but compelling helium replenishment in periods much more frequent.

However, although helium leakage is hard to control, it also is non corrosive and does not become radioactive due its properties as an inert gas. This eases out on the maintenance requirements on the piping, steel lining of reactor components and the steam generators. The direct cycle helium cooled reactor also benefits from not having a heat exchanger in between the reactor and the turbine. The elimination of the heat exchanger saves the reactor from typical problems with heat exchangers such as tube ruptures, corrosion or water ingress from the steam circuit into the primary circuit.

Verfondern (2007) explains that the modular design of the HTGR, although lacking the advantage of economies-of-scale, is much more fascinating, because such designs like the tall and slim core geometry promotes a self-acting decay heat removal which works through heat conduction, free convection and radiation. This ensures that the maximum fuel temperature in the core to stay below 1600°C in loss-of-forced-convection accident conditions (LOFC) which are equivalent to LOCA in water reactors.

In the thermionic space reactors, the electromagnetic pumps used on liquid metals have no moving parts unlike the mechanical pumps for gases. This allows for even higher reliability compared to conventional nuclear stations as there are less moving parts in the thermionic reactors. However, in case there is fire or explosions within the core, the phase change of liquid metal could cause a catastrophe similar in concept to the Chernobyl disaster. These explosions could not happen with a single phase coolant such as those present in the gas-cooled reactors although this scenario is highly unlikely as it will take an extreme temperature to change the liquid metal into a gas phase. Also to be noted is that the high core power density, high operating temperatures and significant radiation environments of thermionic reactors pose major material and configuration design challenges to provide both efficiency and operating reliability over extended periods. The US Department of Energy, Office of Defense Energy Projects and Special Applications (1986) reports that the fuel element includes an emitter, collector, insulators, spacers, sheath, cladding, and fission product purge lines and all these elements must be held to tight tolerances or fuel swelling leading to structural deformation or radiation leakage could start to pose problems.

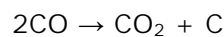
4.5 Maintenance Requirements

The CO₂ based power stations require the installation of a heat exchanger in between the primary and secondary coolant circuits. The presence of a heat exchanger or steam generator requires more maintenance to ensure proper operation of the power conversion system. James D.W. (Central Electricity Generating Board) noted that although most of the early difficulties associated with Magnox steam generators have been reported, most of these problems are now solved. However, there is still the problem of oxidation of mild steel components in steam generators, which is undoubtedly the most severe problem encountered with the Magnox stations. The Magnox steam generators are made from mild steel which are readily available, low cost, easy to fabricate and high heat transfer compared to higher alloy steels. The material suffered

breakaway oxidation under service conditions, and is peculiar to high pressure CO₂. It is understood that carbon monoxide is produced under the oxidation reaction:



The porous breakaway oxide is then filled with the carbon monoxide produced in the above reaction which had diffused through the protective oxide and coalesce to form pores. Once the carbon monoxide fills these pores, the Boudouard reaction occurs:



The carbon produced then diffuses into the steel producing cementite, which acts as a catalyst for the reactions above. The CO₂ causes further oxidation with the mild steel and thus is self sustaining.

Laboratory scale findings have shown that to reduce this behaviour, the maximum gas temperature should be reduced to 360°C and water levels should be reduced in the CO₂ coolant. The application of gas phase inhibitors were to act as catalytic poisons were also performed to predict the probabilities of failure of critical components under a set of operating conditions. More precise understanding of oxidation kinetics today has allowed for the initial restriction of the maximum temperature to be relaxed under carefully controlled circumstances.

The AGR steam generators initially suffered from stress corrosion cracking but research has found that the austenitic superheater tubes could be wetted for a short period of time as long as the periods coincide with normal operating conditions i.e. not during a severe condenser leak period. Small defects were also found in the root run of the transition welds. The replacement of these joints would be an extremely difficult and costly task, and this led to the quantification methods on the possibility of a joint failure in service. James D.W. further described that the steam generator control is based on the boiler "half-units", each half-unit containing 44 transition joints of which 3 thermocouples were installed, from which a half-unit "mean" temperature is derived. The temperature is then controlled by adjusting the boiler feed flow valve for each half-unit. Combining these probabilistic methods, the following curve was produced in *Figure 19*.

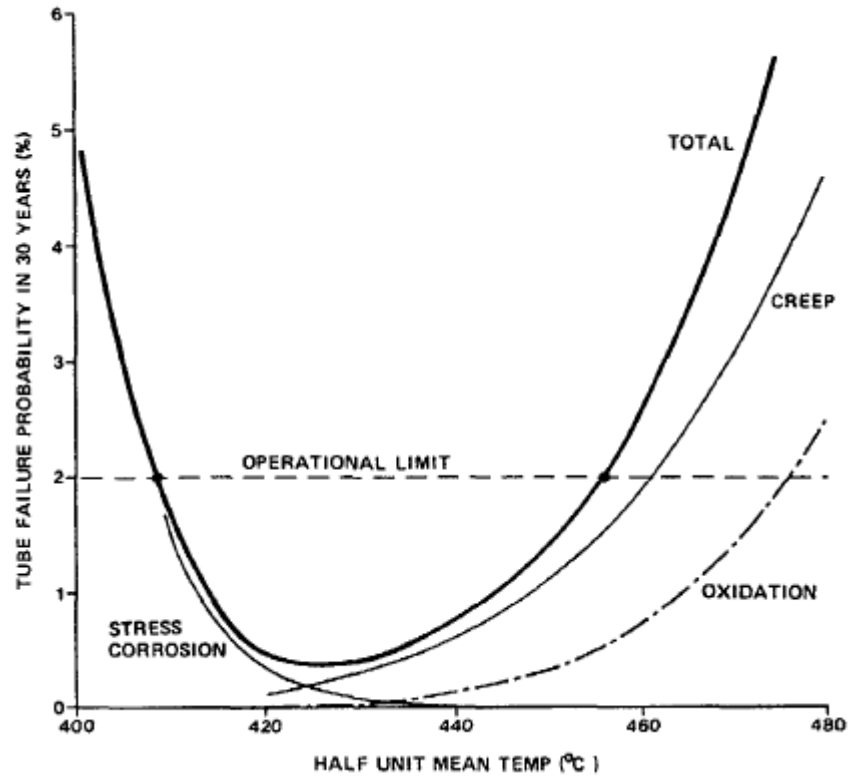


Figure 19: Tube failure probabilities for stress corrosion, creep transition joints and oxidation expressed as a function of half-unit mean temperatures (James D.W.)

This probabilistic approach to the boiler operation led to improved control systems and it led to arrange for feedback of half-unit mean temperatures to adjust the position of the half-unit feed flow control valve, allowing for fully automated boiler controls within the limits defined by material constraints.

The pressurized water reactors require the same maintenance and inspection on the steam generators, but attention must also be given to more system components than the Magnox or the AGR. Although advances have been made to ensure safe passive operation in some PWR designs, the number of components to ensure an operable system introduces more risk of malfunction. For example, the heater and condenser spray in the pressurizer requires constant operation to ensure the primary coolant pressure is within operational limits. The PWR, operating under lower turbine inlet temperatures compared to other designs, also face risks of operating the turbine under wet steam. This requires more maintenance of the moisture removal equipment and the turbine itself to ensure water droplets have not caused damage to the turbine blades. Overall, remarkable concepts such as the Westinghouse AP1000 PWR design allows for little maintenance as compared to other designs because of its designed passivity, such

as less maintenance on electrical systems and pumps as it does not require them to ensure safe operations.

Overall, maintenance of steam generators is among the most critical jobs to be performed especially on PWR stations. Although typically the tube wall thickness may be degraded up to 40 percent of initial wall thickness before the tube must be repaired thus affording adequate margin before bursting, the US NRC emphasized the importance of performing comprehensive examinations of steam generator internals to ensure that structural integrity is maintained indicating that the potential for degradation to damage tube supports and damage tube bundle wrappers. Among the initiatives taken by US NRC is the reporting of significant steam generator operating experience which is publicly available online on the US NRC website.

The direct cycle high temperature reactors do not use steam generators in its design, thus severely reducing maintenance activities especially those related to steam generators and its support systems. The use of steam generators also causes several problems such as the possibility of water ingress which needs to be monitored. The direct cycle HTGR stations also use only one coolant circuit, thus reducing the number of coolant pumps and gas circulators as compared to typical indirect cycle stations. However, maintenance of the turbo-machinery is much harder and more expensive with direct cycle systems as the turbo-machinery can be contaminated with radioactivity.

The thermionic reactors operate under the least maintenance requirements compared to all of the compared power conversion systems, as there are no moving parts in the thermionic converter itself. However, Genk & Paramonov (1994) noted that thermionic reactors still require a cooling mechanism and these will include systems such as the electromagnetic (EM) pumps, the volume accumulator and also the radiator for the rejection of heat. Other equipment requiring inspection and maintenance will include the start-up batteries for the EM pump, the caesium reservoir assembly and also the helium gas system.

4.6 Plant Size

Reactors which employ steam turbines such as the Magnox, AGR and PWR are generally quite large. The turbine itself, operating on superheated steam or wet steam, requires the blade sizes to be larger than 1 m. In contrast, the blade size of the helium gas turbine used in the direct cycle HTGR can be only around 0.1 m. However, steam based turbines benefit from only needing a few turbine and compressor stages as compared to

helium turbines and compressors. The heat exchangers used with the steam cycles are also larger as compared to helium based gas turbines which can be more compact because of the helium specific heat properties which are better than air. It is also important to note that any usage of a heat exchanger will at least require an extra pump.

No et al (2007) also noted that the heat exchanger design is also advantageous due to the thermal conductivity and heat transfer coefficient properties of the helium coolant being higher than air. These strongly influence the size and geometries of the gas turbine. Helium compressors need a large number of stages, however, to achieve the required pressure ratio thus reducing performance of the turbine. The Table 4 below shows the design parameters comparison between air breathing compressors and HTGR helium compressors:

Unit	Air-Breathing Compressors			Helium Compressors		
	C135	C141	NACA	GTHTR300	GT-MHR	
					LP	HP
Number of stages	2	4	8	20	14	19
Design pressure ratio	1.88	2.95	10.26	2.00	1.70	1.70
Inlet hub-to-tip ratio	0.38	0.69	0.48	0.88	0.87	0.90
Exit hub-to-tip ratio	0.57	0.81	0.90	0.91	0.88	0.90
Mass flow/unit annulus area (kg/s.m ²)	207	189	189	447	591	1141
Blade tip speed (1 st , m/s)	423.0	362.0	356.0	321.0	301.7	245.8

Table 4: Key design parameters comparing air-based compressors and helium-based compressors.

The first and largest helium turbine with a capacity of 50MWe at 750°C was constructed at Germany in 1968, operating pressure 1 MPa. A high temperature test plant (HHV) was built in 1981 consisting of a 2-stage turbine and an 8-stage compressor on a single shaft arrangement. The compressor required 90 MW of power, of which the turbine produced 46 MW. Helium leakage occurred but later rectified.

The sodium potassium cooled thermionic reactors can be even more compact than the helium cooled direct cycle gas turbine. This is because the heat transfer of liquid metals is much better than gases, leading to the reduction in surface area required for heat transfer. This results in a smaller sized reactor vessel. Thermionic reactors do not require compressors or turbines but instead dumps its excess heat into radiator structures thus saving some more space as compared to typical nuclear reactors.

5 Design Considerations

To determine the optimal design for the small autonomous nuclear reactor, a revision of the potential applications and its requirements against the capabilities of the autonomous reactor is necessary.

The potential technologies and components to be utilized must first be established for the basis of further discussion into the design of potential applications.

5.1 Power Conversion System Components

The design of the small autonomous nuclear reactor will need to balance the benefits of each technology against design constraints. Although the benefits and challenges of established nuclear technologies have been discussed in Section 4, it must be understood that these reviews are based on existing erected stations. Existing stations are more directed towards the cost of generating electricity and achieving high thermal efficiency. Although these factors are important, it is not as critical as the three key parameters described in Section 4. An exception to this is the thermionic reactor design which, like the small autonomous reactor, also focuses on long term low maintenance use.

Therefore, it is important to note that these established reactor designs combine complicated arrangements of reheaters, regenerators, pressure-based turbines to squeeze as much useful energy out of the system coolant as possible and these results in a gain of between 3-4% efficiency. Although even 1% thermal efficiency could translate into millions of pounds per year, it may not be the optimum choice as the addition of these components result in more components that has the probability of breaking down and also has an impact on the final size of the system. The purpose of this analysis is to compare the power conversion system efficiency instead of the entire system efficiency including the steam cycle optimizations; the thermal efficiencies of these reactor power conversion technologies with the indirect cycle will be estimated only by employing the Rankine cycle and the reheated Rankine cycle. This will give us a better picture of what to expect when porting the established designs to be used on the small autonomous nuclear reactor.

The thermodynamic modelling of the system was performed using the PC-based analysis code CyclePad v2 (written by K D Forbus & P B Whalley). The schematic of the complete Rankine Cycle system is shown in Figure 20 and 21 below:

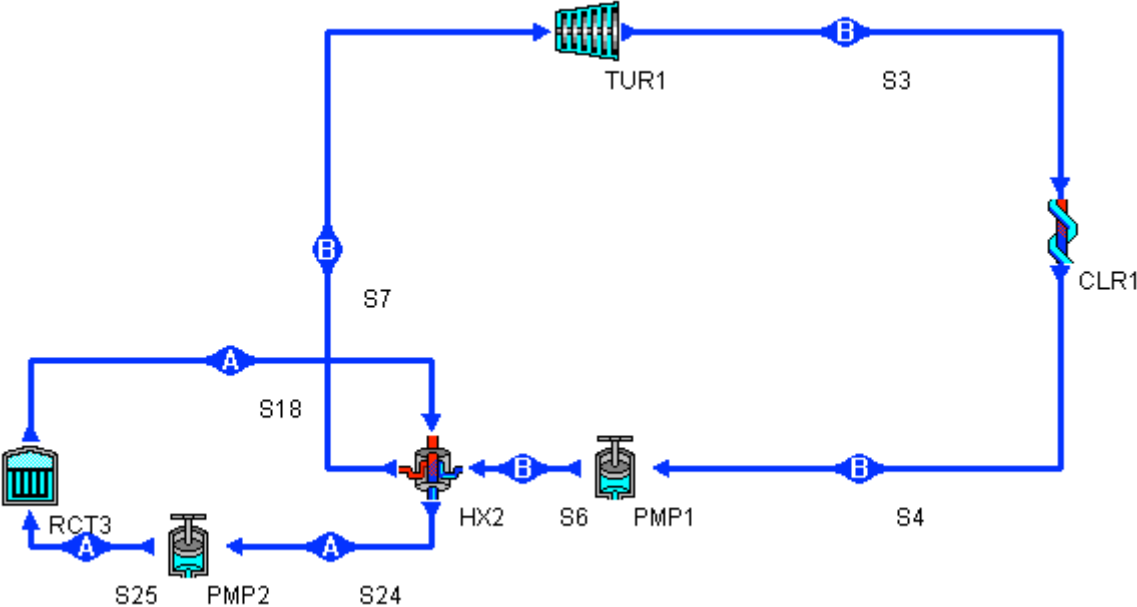


Figure 20: Schematic diagram comparing existing power conversion technologies on a Rankine cycle (CyclePad v2)

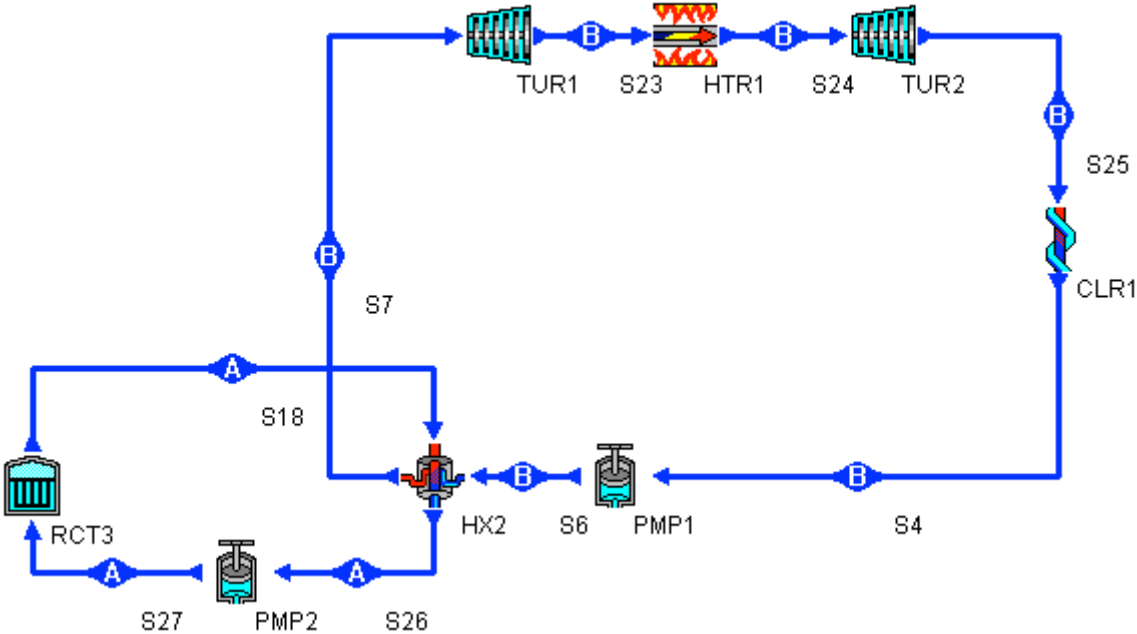


Figure 21: Schematic diagram comparing existing power conversion technologies on a Rankine cycle with reheat (CyclePad v2)

For the system as above, RCT is the reactor source, PMP is a pump/circulator, CLR is the condenser/cooler, TUR is the turbine, HX is the heat exchanger and HTR is the reheater which reheats the turbine outlet steam to reactor temperatures. The full parameters of the simulation are described in the Appendix. The steam generator is assumed to cause a temperature drop of 50°C between the primary and secondary cycles to be consistent with the models employed by Perrson & Donaldson (2009). The secondary system pressure is assumed to be 50 bar and the condenser inlet pressure is assumed to be 0.1 bar.

The calculation of the Rankine cycle without reheat efficiency results in a turbine pressure ratio of 500 which is very large. Redesigning the circuit to include a reheat and a low pressure turbine allows the pressure ratio to drop to 15.87 which is still large but acceptable.

The results of the thermal efficiency calculations are produced in the table below:

Reactor Type	Rated Efficiency	Rankine Efficiency	Rankine with Reheat Efficiency	Steam Turbine Outlet Quality (Rankine, HP Reheat)
AGR	40.00 %	38.91 %	41.10 %	87.42 %, 100.00 %
PWR	33.00 %	34.67 %	33.26 %	71.59 %, 81.88 %
HTGR (Indirect)	40.00 %	40.72 %	43.24 %	91.19 %, 100.00 %

Table 5: Comparison of modelled thermal efficiencies of established steam-cycle nuclear technologies using CyclePad v2.

From *Table 5* we note that the indirect cycle HTGR achieves the highest efficiencies of all the three technologies compared. Although the temperatures achievable by the indirect cycle HTGR is much higher than that achievable by the AGR, the final efficiencies are not much different. These results, coupled with the discussions in Section 4, concludes that although the indirect cycle HTGR is able to achieve a higher efficiency than the AGR, the obstacles involved with helium upkeep rules out the HTGR in the consideration to be adapted to the small autonomous nuclear reactor design.

Also important to note that from the results in the Appendix, the quality of the steam at the PWR turbine exit for the simple Rankine cycle is only 71.59%. Although this improves to 81.88% after the HP turbine and 94.71% after the reheat and LP turbine, the quality of the steam is still too low (< 85%) to discard moisture separation technologies to prevent damage to the turbine blades. This increases complexity and risk when employing the PWR technology to adapt to the small autonomous reactor design.

5.2 Safety Considerations

During the development of commercial nuclear power plants, the most challenging accident scenario for designers was the double-ended break of the largest diameter coolant piping. This was typically the main pipe connecting the primary reactor vessel to the steam generator vessel. A break at this section could very quickly isolate coolant fluid from the reactor vessel and thus result in the uncovering of the reactor core. This could cause major damage to the fuel and assemblies within the core.

To mitigate the severe consequences of such an accident, designers have added complex water injection systems into the plant designs. These safety systems add significant capital and maintenance costs but are never expected to be used on successfully operated plants.

Therefore, to eliminate these systems, it will require that the vulnerability be eliminated beforehand. In this case, all the large primary coolant pipes must be eliminated from the power conversion design.

This approach has been employed in the past for Advanced Gas-cooled Reactor designs in the UK and is now being considered by a number of novel new reactor designs. A number of DSR designs integrate the entire primary coolant system into a single integral vessel. An example of such a design is the IRIS integral primary system reactor depicted in *Figure 22*.

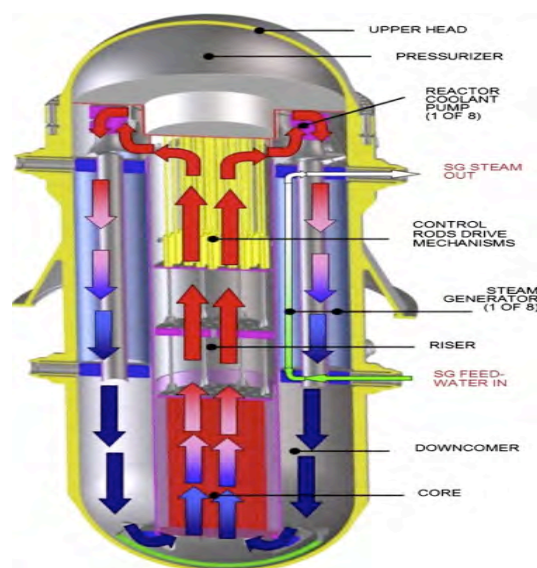


Figure 22: The functional arrangement of primary system components in an integral primary system reactor (IRIS design courtesy of Westinghouse Electric Company).

An integral primary system reactor (IPSR) consists of the reactor core, steam generators, and pressurizer into a single common pressure vessel. The integral design is only viable for smaller sized reactors, however, otherwise the size of the vessel would be prohibitively large to manufacture and transport. This has not been a problem for AGR stations in the past because the AGR stations in the UK were built from the ground up on the site.

Ingersoll (2009) noted that packing all of these components into a single vessel has a number of advantages:

- All large coolant pipes are eliminated. Only small feed water and steam outlet pipes penetrate the vessel wall. For typical PWR, this will result in 5 cm diameter pipes as opposed to 90 cm diameter pipes.
- The heat capacity and thermal inertia of the system is increased because the total inventory of the primary coolant in the reactor vessel is much larger as compared to conventional designs. This yields a better response to core transients.
- The heat exchangers are placed above the core creating a vertical system that promotes more effective natural circulation of the primary coolant in the case of a coolant pump failure especially for light water reactors.
- The extended riser area provides the possibility for internal placement of the control rod drive mechanisms. This prevents another potentially serious accident scenario where the control rod can be ejected due to temperatures and pressures in the core.

The Advanced Gas-cooled Reactor design in the UK already incorporates the heat exchangers into the main pressure vessel (*Figure 3*), thus to rework the base AGR design to adapt to a similar system such as the IRIS (*Figure 22*) should not require as much effort and analysis as compared to other typical reactor designs.

5.3 Heat Exchangers

To develop an integral primary system reactor, the heat exchanger must be included within the reactor pressure vessel. This requires for the installation of a compact heat

exchanger but with enough surface area to extract the heat out of the primary coolant and into the secondary coolant.

In a heat exchanger, the heat exchanger surface is where heat transfer takes place from one fluid to another. The fundamental characteristic of a heat exchanger surface is therefore the surface area per unit volume occupied by the surface. Thus, a compact heat exchanger means having a large surface area per unit volume. The design analysis by Northern Research and Engineering Corporation (1965) notes that any surface with an area density greater than $328 \text{ m}^2/\text{m}^3$ is defined as a compact surface heat exchanger.

Technology	Max. pressure (MPa)	Max. temperature (°C)	Fouling
Stainless steel plate fin heat exchanger	8	650	No
Aluminum plate fin heat exchanger	8-12	70-200	No
Ceramic plate fin heat exchanger	0.4	1300	No
Spiral heat exchanger	3	400	Yes
Diffusion bonded heat exchanger	50	800-1000	No
Brazed plate heat exchanger	3	200	No
Welded plate heat exchanger	3-4	300-400	Yes/no
Gasketed plate heat exchanger	2-2.5	160-200	yes

Table 6: Operating conditions of compact heat exchangers, Thonon & Breuil (2000)

Table 6 notes the typical types of compact heat exchangers available in the industry. For the application of a medium temperature reactor, only the stainless steel and ceramic plate fin heat exchangers or the diffusion bonded heat exchangers are usable at the temperatures required.

Plate fin type heat exchangers have been utilized in a number of industries such as natural gas liquefaction, large scale production of petrochemicals and hydrocarbon separation. The heat exchanger consists of a core block constructed of alternating layers of corrugated sheets (or fins) and flat parting sheets. Each layer is then bound by bars and provided with inlet and outlet distributors. Headers with nozzles are welded onto the bars covering the distributors or ports. Hesselgreaves (2001) wrote in his book that these heat exchangers have secondary surfaces, or fin structures, between stream separation plates. The fins have two functions, to act as the secondary heat transfer

surface and to contain the pressure differential between the streams. For temperatures of over 200°C, aluminium becomes unsuitable as it rapidly loses strength in addition to being incompatible with many process chemicals. Therefore, the stainless steel and the ceramic based plate fin heat exchangers are instead considered for the application in the small autonomous nuclear reactor.

The diffusion bonded heat exchangers were developed for applications involving corrosive and reactive chemicals as a compact alternative to shell and tube heat exchangers. The heat exchanger is formed by the diffusion bonding of flat plates. The element is formed by diffusion bonding three sheets of material with the inner sheet to finally form the fin at high temperature. Similar elements formed in the same way are then diffusion bonded together to form a core. This heat exchanger is fabricated from titanium and thus is very suitable for offshore oil and gas applications due to its corrosion resistance and low weight.

These compact heat exchangers should integrate well into the design of the integral primary system reactor in the small autonomous nuclear reactor. A quantitative study of the heat transfer area and the compatibility of the working coolant fluid will still need to be undertaken to investigate the necessary parameters depending on the specific heat of the coolant of choice.

5.4 Power Conversion Technology Considerations

From the discussions in the previous section, it has been determined that only a few of the potential technologies as reviewed will be adaptable to the small autonomous nuclear reactor concept. This is summarized in the *Table 7* below with a score between 1 (best) to 3 (unsatisfactory).

From *Table 7* below, we conclude that the most attractive technologies to be adapted to the small autonomous nuclear reactor are:

- The Advanced Gas-cooled Reactor design; high reliability, available technology and proven track record
- The Thermionic Reactor design; small, compact, reliable design. However the technology may need to be developed further for higher efficiencies in converting thermal power to electricity

Technology	Size	Availability	Reliability	Justification
Magnox	3 (fuel capacity)	1	3 (external heat exchanger, fuel capacity)	The Magnox reactor is fitted with heat exchangers on the outside of the pressure vessel, increasing the chance of a primary system break. It is also loaded with natural uranium fuel, thus to operate for an extended duration will require the fuel capacity to be too large.
AGR	2	1	2 (temperature control)	The AGR drawback is with the CO ₂ coolant not being able to reach high enough temperatures without interacting with the fuel graphite to become carbon monoxide and weakening the core structure.
PWR	2	1	2 (steam explosions, pressurizer, active & passive pumps, corrosion of piping at high pressure)	The PWR is inconvenienced with the requirement to be equipped with a pressurizer and the maintenance problems involving corrosion of stainless steel piping at high temperature and pressure.
Indirect HTGR	2	1	3 (helium leakages in the primary circuit)	The indirect cycle HTGR has the potentially disastrous problem of primary coolant leakage which is a major risk in an unmanned deployment.
Direct HTGR	1	3 (helium turbines, magnetic bearings)	3 (helium leakages)	The direct cycle HTGR has problems with the unavailability of helium gas turbines and compressors in the market, and also faces helium leakages in the main coolant circuit.
Coal	3	1	2	Coal-fired stations need to be large to contain all the fuel required for extended deployment and requires constant monitoring of boiler temperatures and air intake.
Gas CCGT	3	1	2	Combined-cycle gas-fired stations are large to incorporate both gas and steam cycle boilers, and also require a large feed source to generate power for an extended period of time.
Thermionic	1	2 (high efficiency conversion)	1	Thermionic reactors are small, compact, but none exist on the commercial scale. The low efficiency of these reactors also prohibits large scale deployment especially once uranium demand picks up resulting in higher prices. These reactors are also not upgradeable to increase efficiency once the technology becomes available.

Table 7: Table summarizes the comparison between existing nuclear technologies to be adopted for the autonomous reactor. (Scored lower the better)

5.5 Potential Applications

As noted in section 2.2, the thermal applications of nuclear reactors are bound by several key constraints. This may indicate that it is advantageous to make a specific design for each thermal application of the source reactor. For a design that is based on the modular concept, thermal applications could also be designed in a modular form and be retrofitted to the main reactor or power conversion system that provides the source of heat for these thermal applications.

Verfondern (2007) agrees that the modular arrangement will be necessary for redundancy, reliability and reserve capacity reasons. In a modular design, the nuclear circuit is separated from the chemical process by an intermediate heat exchanger thus creating a chemical island for applications such as hydrogen production. This prevents the direct access of primary nuclear coolant to the chemical plant and in the reverse direction, the product gases into the reactor system. This allows for the chemical plant to function as a conventional facility and to have maintenance works conducted under non-nuclear conditions.

Here, consideration is given to utilize the reactor energy not only to generate electricity, but also to thermal applications. These applications are:

- District Heating
- Hydrogen Production

5.5.1 District Heating

The potential market for district heating appears in climatic zones with relatively long and cold seasons. The challenges faced by the power industry in supplying energy for consumption include the scarcity of fossil-fuel sources to be dependable in the long run. A potential solution to address these challenges includes the employment of nuclear resources to provide the thermal power required for these applications. However, the drawback to using nuclear technologies is the high capital investment. To explore this possibility even further, it may be possible for a small power station to provide both electricity and district heating to communities residing far off the grid.

Typically, any modern discussion involving the operation of a nuclear reactor to supply heat for district heating is addressed by the use of a deep pool reactor (DPR). The DPR core is put in a deep pool where static water pressure on the coolant is triggered. Even with a light pressure, Tian (2001) explains that the DPR will be able to meet the temperature demands of heat supply for district heating. Tian even claims that the feasibility studies of DPR in some cities in China results in the overall costs to be only one third of coal and one tenth of natural gas. This provides an economically competitive solution to satisfy the demands of district heating.

Historically, however, district heating was supplied using water reactors. Kupitz & Podest mentioned that the decoupling of heat for district heating from nuclear power plants from Soviet WWER-440 or WWER-100 PWR based reactors have achieved good results for many number of years. The challenges faced were that the nuclear plants must be placed quite far from the population centres, using somewhere between 30 to 80 kilometre transmission lines due to safety requirements. The PWR reactors, being able to achieve steam temperatures of up to 320 degrees at pressures of 150 bar, are naturally the prime candidate for district heating applications which requires temperature ranges between 100°C to 150°C.

Losev et al (1989) described that the design features of heat delivery systems from nuclear power stations are based on standard radiation safety requirements for thermal energy consumers. The heating water circulates in a tertiary circuit in relative to the reactor core circuit with an intermediate heat exchanger placed in between the turbine extraction and the condenser. Safety requirements suggests that the pressure in the tertiary circuit is kept higher than the maximum possible circuit pressure in the secondary coolant cycle to prevent any radioactive product from getting into the heating water in case there is a small rupture in the heat exchange surfaces.

Under the modular design concept, addition of a tertiary circuit in addition to the two primary and secondary coolant circuits in Rankine cycle systems could be implemented. A schematic diagram of this is proposed in *Figure 23*. The real challenge however is the steam transport to heavily populated areas. Losev et al. notes that in the old USSR, the safe distance between a nuclear station and a populated area varies between 25 km for population density of between 100,000 to 500,000, to 100 km for population density of over 2 million.

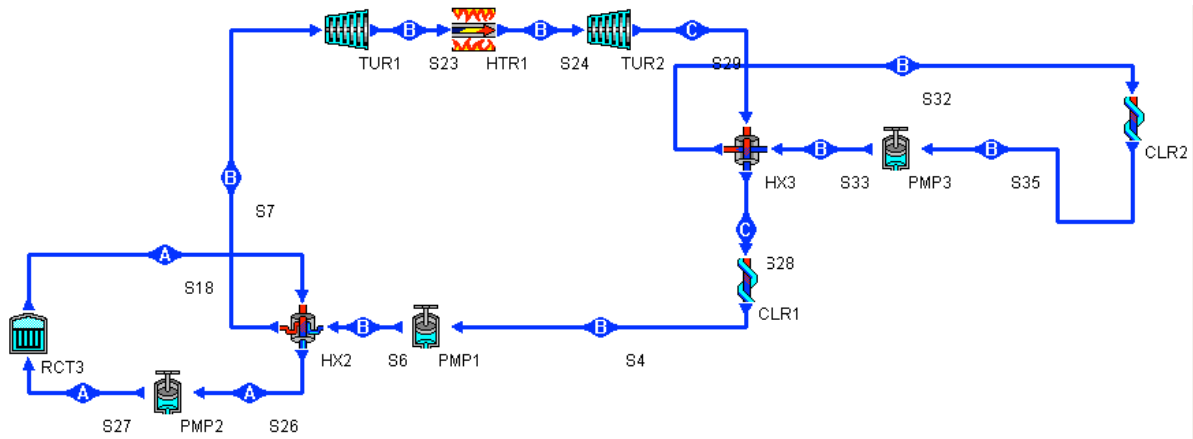


Figure 23: Possible schematic diagram of a small autonomous nuclear station with district heating with HX3 connected to the secondary steam system to transfer heat into the district heating piping.

For the purposes of our small autonomous nuclear reactor with rated power of between 10-25 MWe, assuming an average of 5 KW maximum demand for each house, this results in the range of between 2000 to 5000 houses. This should allow the small autonomous nuclear reactor to be installed much closer to population centres, hence permitting the delivery of heated steam through district heating networks without many losses.

Two reactor technologies that must be ruled out at this point are the pressurized water reactor and the thermionic reactor. The PWR based reactor requires heavy monitoring and maintenance of the primary circuit to ensure that reactor heat is removed and controlled without causing film boiling in the fuel channels. The boiling of the main coolant could cause the water to change phase and pose the risk of steam explosions. As the reactor needs to be located near population centres, such risk need to be minimized. This, coupled with concerns of wet steam problems with PWR secondary turbines, as discussed in Section 5.1, indicates that the PWR design requires much complexity and maintenance problems.

The thermionic reactor design, while novel, reliable and attractive, simply could not produce the power required for the installation in a small community. The thermal efficiencies yielded would make the system not economically feasible for the purposes of both generating electricity and district heating.

The only design that has the potential to be deployed in a remote location disconnected from the grid would be the AGR based reactor which is both reliable and cheap. The AGR achieves higher efficiencies than light water reactors and only employs single phase

coolant within the reactor core. Hence, this makes the Advanced Gas-cooled Reactor technology the ideal candidate to be deployed as a small autonomous nuclear reactor providing both electricity and district heating.

5.5.2 Hydrogen Production

Currently, the splitting hydrocarbons are among the most popular methods of hydrogen production. The industrially established methods are steam reforming of natural gas, extraction from heavy oils, and the gasification of coal.

Nuclear energy can play an essential role in this process by acting as CO₂ emission free energy sources. This involves thermo-chemical cycles which are composed of several reaction steps which leads to the decomposition of water into hydrogen and oxygen. Verfondern (2007) explained that ideally, the supporting chemical substances involved in this cycle are regenerated and recycled, and remains in the system. This means that the only inputs into the system are water and heat. The sulphur-iodine (S-I) process has been touted to be the choice process to base the hydrogen production cycle. The S-I thermo-chemical cycle is represented in Figure 24 below:

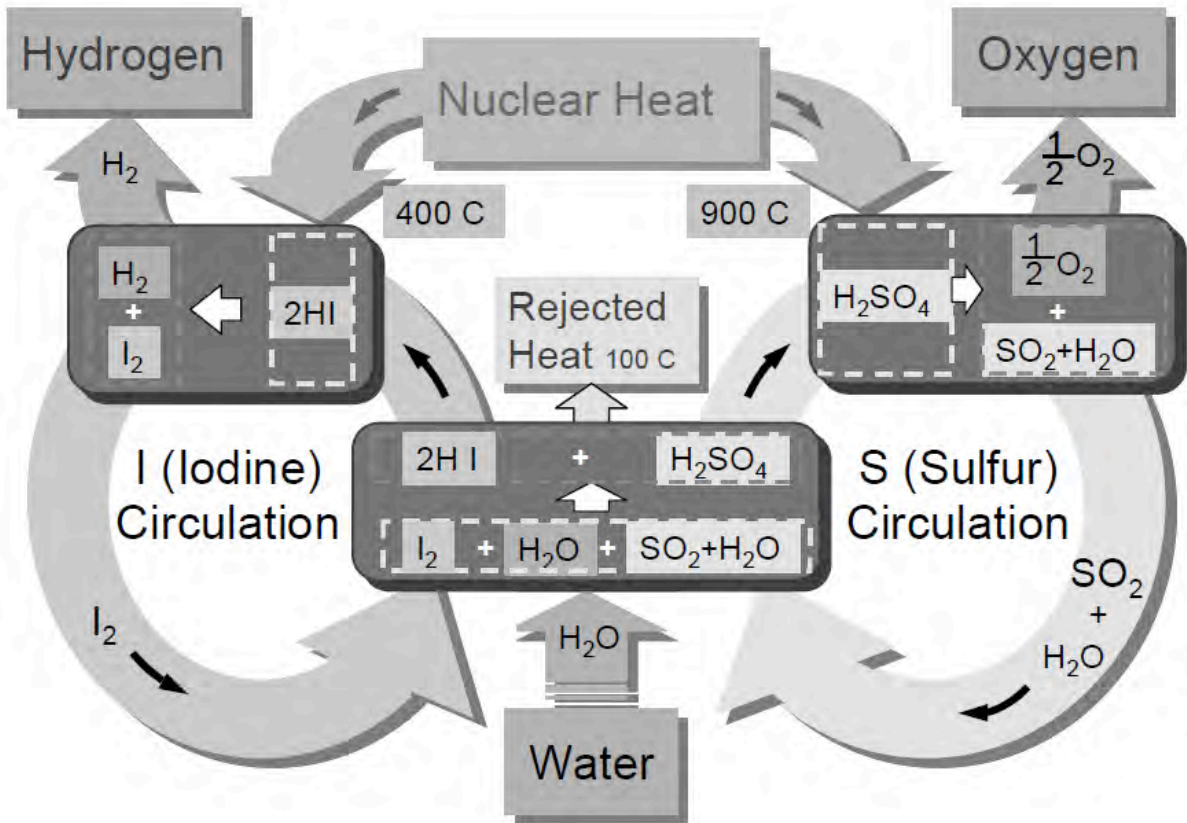


Figure 24: Schematic of the sulphur-iodine (S-I) thermo-chemical cycle

The problem with the integration of the above cycle with the small autonomous nuclear reactor is that the temperatures required for the process is at the limits of current nuclear technologies (900°C). This condition presents a major challenge as the nuclear reactor must operate at significantly higher temperatures to be able to allow for the transfer of heat from the reactor to the thermal process at this temperature. Comparing the thermal heat required for this application with established nuclear technologies we realize that only the direct closed Brayton HTGR cycle technology is able to achieve high enough temperatures for hydrogen production.

At lower temperatures, it is still possible to continue the chemical process but it will be both very inefficient and uneconomic process. This is shown in *Figure 25* below where the overall efficiency is plotted against temperature. Process efficiency decreases rapidly with decreasing temperature such that the process can no longer produce hydrogen at temperatures below 700°C.

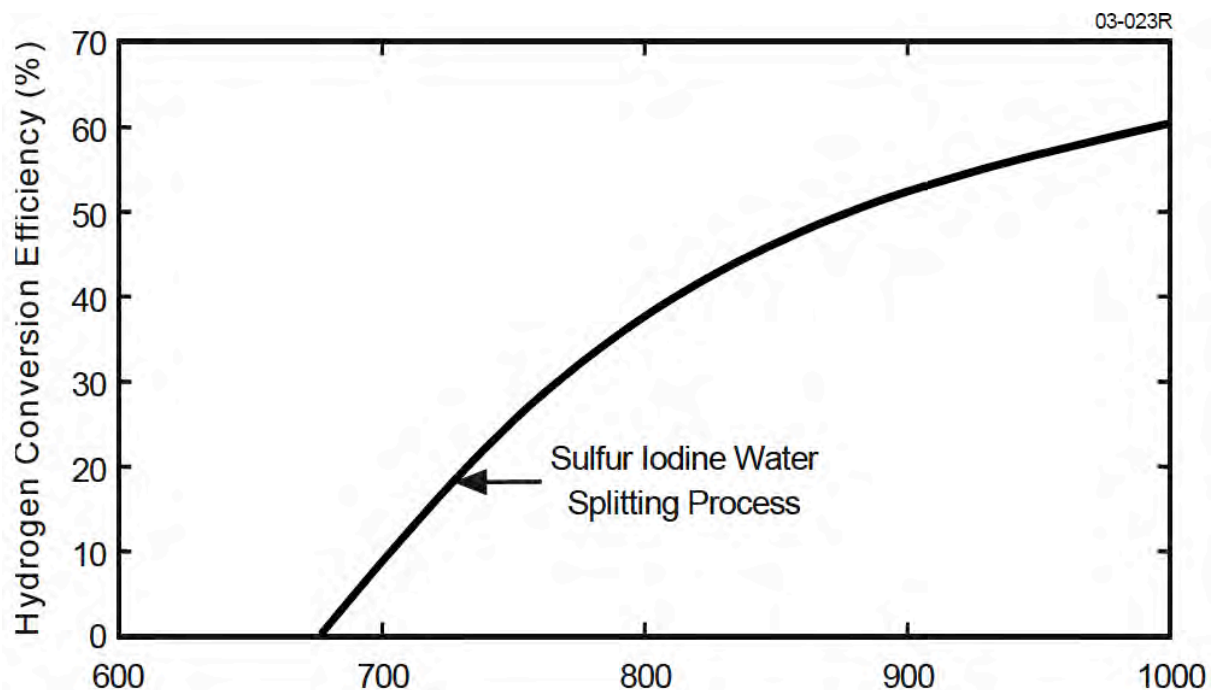


Figure 25: Efficiency of the sulphur-iodine process versus temperature

There are works underway to investigate the possibility of hydrogen production at a lower temperature by employing the Westinghouse or Ispra Mark 13 cycle that allows for the process to transpire at temperatures of around 700°C which allows the production to be achievable by nuclear technologies. The comparison between Westinghouse and Ispra Mark 13 cycle against the sulphur-iodine cycle are depicted in *Figure 26*. However, these

processes require the use of inorganic membranes. The inorganic membranes can promote the separation of SO_2 , H_2O , and O_2 from the SO_3 and selectively remove the reaction gases and drive the whole process towards completion (Forsberg, 2003). However, this study is still under investigation and based on experimental results and theory, new custom membranes will be fabricated and tested in an iterative process. Be that as it may, this approach does appear to be particularly fascinating.

Understanding the thermal requirements of the chemical processes involved in producing hydrogen, and the potentials of the small autonomous reactor, we can conclude that it is not economical, if not possible, to use the current iteration Rankine-cycle based small autonomous reactor to drive a chemical process for producing hydrogen. To be able to do so would require to bring into play the helium-based direct Brayton cycle systems design to achieve such high temperatures required by this process.

There may be a possibility of employing the thermionic reactor system for the purpose of producing hydrogen. Thermionic converters are able to reach temperatures high enough to utilize the heat for chemical thermal applications and are simple, compact and robust. The main drawback is that the reactor coolant for this system is limited to 600 degrees Celsius but this may change in the future. Therefore, thermionic reactors are ruled out based on the unavailability of the technology required for it to be feasible as a hydrogen production thermal source.

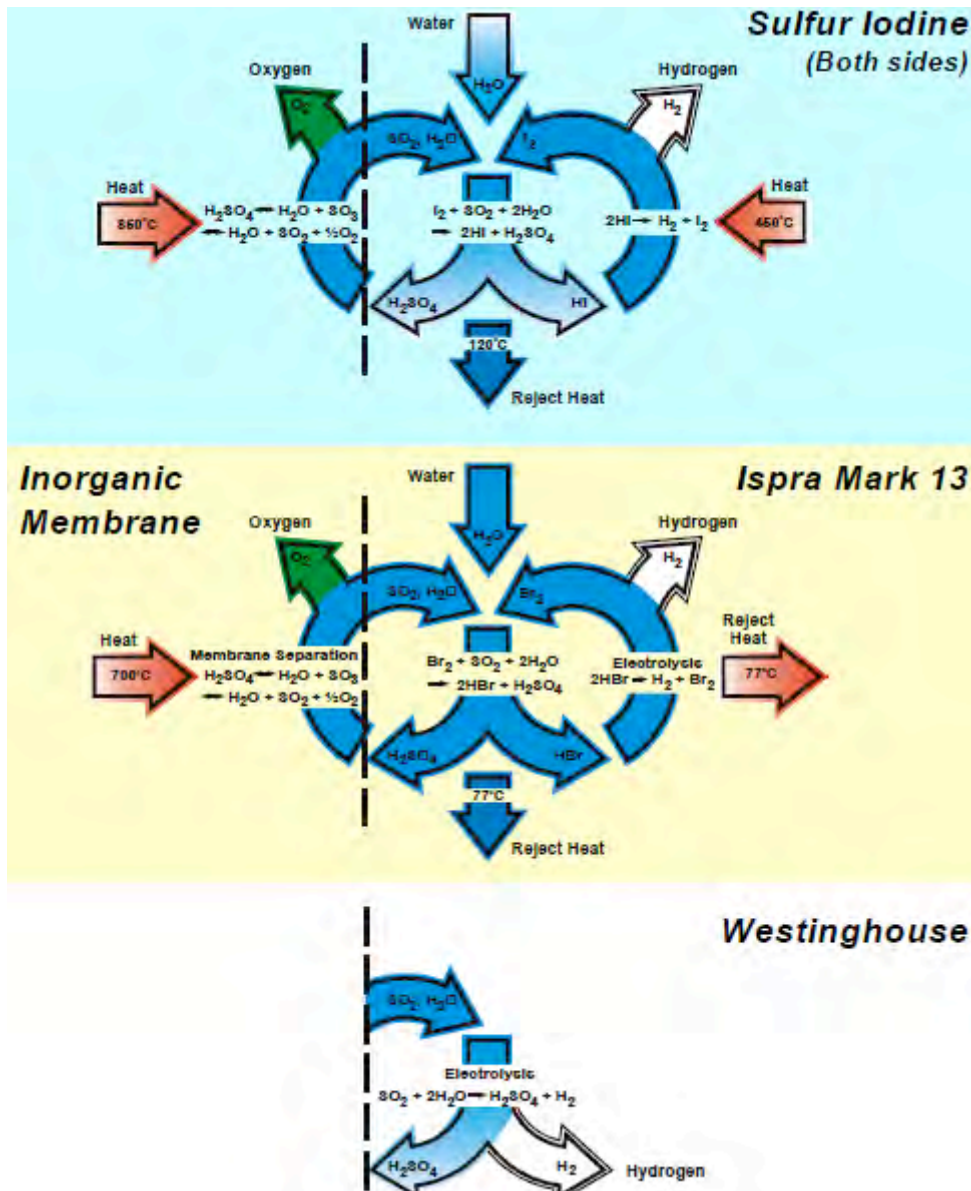


Figure 26: Simplified Diagram of Sulphur-Iodine, Ispra Mark 13 and Westinghouse Cycles (Forsberg et al., 2003)

6 Conclusions and Recommendations

From the discussions above the conception of a small autonomous nuclear reactor as a mobile energy source is entirely possible. It has been examined through the analysis of required demands against known features that the solution is available, small and reliable.

The small autonomous nuclear reactor requires the technology to be available. In this sense, there are many potential novel designs being proposed however current technology and financial limits constrain designers to build only on technologies available

off-the-shelf. These unavailable technologies, while theoretically possible, have not been developed in the industry because there is little demand for them thus resulting in a lack of investment into further developing these concepts. Thus, once the market permits, such novel technologies could be available off-the-shelf in the near future.

The reactor also needs to be small enough to be modularly constructed and transportable to the proposed site. For example, it does not make much sense to erect a nuclear station near off-shore oil and gas platforms. Open cycle heat sources have the prominent advantage in being compact and simple, but only closed cycle systems have the inherent flexibility to be deployed anywhere in the world because all the required fluids and systems are already built-in. Thus, the reactor faces a challenge to be able to generate enough energy to power the consumer for many years but still be small enough to be reliable and transportable.

Perhaps the most important parameter of the small autonomous nuclear reactor is that it must be reliable. The reactor must be able to operate under unexpected conditions without the need for an operator to be on site. The reactor must also be able to take care of itself, either through passive safety systems and natural circulation. Nuclear accidents provide one of the most horrific scenarios in the world today and steps must be taken to ensure that any vulnerability in the system is designed out.

From the discussions presented in this thesis, the small autonomous nuclear reactor can be built according to the above constraints reproduced from two possible technologies. Nevertheless, to attract interest and achieve economic feasibility, the proposed design should be able to be flexible enough to be deployed as a thermal source with more than one application.

Therefore, the proposed applications are:

- Electricity Generation with District Heating
- Electricity Generation with Hydrogen Production

The small autonomous nuclear reactor can fulfil the requirements of electricity generation with district heating by employing the concepts refined from the UK AGR programme.

The reactor consists of:

- enriched uranium fuel moderated by graphite
- CO₂ based primary coolant
- Integral primary system reactor vessel with built-in heat exchangers
- Secondary steam Rankine cycle with reheat

- Modularity of design
- Tertiary steam/condensed water circuit and module for district heating.

Regrettably, the small autonomous nuclear reactor is not able to fulfil the requirement of hydrogen production with the technologies available today.

An alternative to the AGR-based autonomous reactor will be the compact thermionic reactor. Electronic development has seen much growth in the last decade and depending on further maturity of the thermionic emitter design efficiencies, it could be possible to take advantage of this progress by replacing the AGR-based autonomous reactor with a thermionic converter based autonomous reactor.

7 Suggestions for Further Work

It would be interesting to attempt to analyse the potential for a different coolant fluid than those that are available from established nuclear reactor technologies. Perrson & Donaldson (2009) made an interesting observation about employing the nitrogen/helium mixture in the secondary cycle to replace the secondary steam cycle to take advantage of both the nitrogen and helium atomic properties. The use of nitrogen makes the mixture much closer to air so that existing conventional turbo-machinery technologies can be employed to generate electricity. The addition of helium in the mixture on the other hand allows the cycle to take advantage of helium's specific heat capacity to expand and compensate for the nitrogen's low specific heat capacity.

Unfortunately, the version of CyclePad used in this report was unable to combine helium and nitrogen as a mixture to model the secondary cycle based on this gas combination. It would be intriguing to attempt this with another thermodynamic simulation software package.

A further analysis should also be undertaken to explore the possibilities of gas leakage and the rate of leakage, should there be, of using the nitrogen/helium gas combination. Provided that the rate of leakage is slow and the period for gas replenishment can be coincided with reactor refuelling intervals, it could be very well possible to employ the use of this gas combination to increase secondary cycle temperatures which may lead to the possibilities of hydrogen production in a remote location.

8 References

Knief, Ronald Allen, *Nuclear engineering: theory and technology of commercial nuclear power*, 2nd Edition, 1992.

Parks, Geoffrey T, *Reactor Design*, Nuclear Power Course, University of Cambridge

Beech DJ & May R, *Gas Reactor and Associated Nuclear Experience in the UK Relevant to High Temperature Reactor Engineering*, Overviews of High Temperature Engineering Research in Each Country and Organization, OECD/NEA, France, 1999

US NRC Technical Training Center, *Pressurized Water Reactor (PWR) Systems, Reactor Concepts Manual*, United States Nuclear Regulatory Commission. Online version available at: www.nrc.gov/reading-rm/basic-ref/teachers/04.pdf

Leyzerovich & Alexander, PennWell Corporation, *Wet Steam Turbines*, 2005, ISBN 1-59370-032-6

Kunitomi K, Yan X, Tachibana Y, Saikusa A, Shiozama S, *Design Study on Gas Turbine High Temperature Reactor (GT-HTR300)*, SMiRT 16 Washington DC, 2001

VI Kostin, NG Kodochigov, SE Belov, AV Vasyaev, VF Golovko, A Shenoy, *Development of a design for the GT-MHR Energy Conversion Unit*, Atomic Energy Vol 102 No 1, 2007

CB Baxi, A Shenoy, VI Kostin, NG Kodochigov, AV Vasyaev, SE Belov, VF Golovko, *Evaluation of Alternate Power Conversion Unit Designs for the GT-MHR*, Nuclear Engineering & Design, Elsevier B.V., 2008

Raja AK, Srivastava AP, Dwivedi M, *Power Plant Engineering*, New Age International Publishers, 2006, ISBN (10) : 81-224-2333-7, ISBN (13) : 978-81-224-2333-4

Hans-Dieter Schilling, Sealnet, *How Did the Efficiency of Coal-Fired Power Stations Evolve, and What Can Be Expected In The Future?*, Published Feb 2002 at www.energie-fakten.de and translated by sealnet.org on Jan 11 2005.

No HC, Kim JH, Kim HM, *A Review of Helium Gas Turbine Technology For High Temperature Gas Cooled Reactors*, Nuclear Engineering and Technology, Vol. 39, No. 1, KAIST, Korea, Feb 2007

S Wright, M Vernon, P Pickard, *Concept Design for a High Temperature Helium Brayton Cycle with Interstage Heating and Cooling*, Sandia National Laboratories, New Mexico USA, 2006

Karl Verfondern, *Towards a Cleaner Planet, The Clean and Safe Nuclear Reactors of the Future*, Environmental Science & Engineering, ISBN (Online) 978-3-540-71345-6, 2007

Gérard Ellia, *Introduction to the EPR design*, Institute of Physics & Institution of Chemical Engineers, London, June 13, 2006

T. Heppenstall, *Advanced Gas Turbine Cycles for Power Generation: A Critical Review*, Applied Thermal Engineering 18 (1998) pg 837-846, Elsevier Science Ltd, 27 Nov 1997

US Department of Energy, Office of Defense Energy Projects and Special Applications, *Strategic Defense Initiative Multimegawatt Space Nuclear Power Program – Summary*, April 1986, pg 26

J Perrson & A Donaldson, *Power Conversion System (PCS) Options For Generation IV Nuclear Plant*, 17th International Conference on Nuclear Engineering, ICONE 17, Belgium, 2009.

James DW, *Steam Generator Materials Constraints In UK Design Gas-Cooled Reactors*, Bristol, United Kingdom. Online version available at : www.iaea.org/inisnkm/nkm/aws/htgr/fulltext/iwggcr15_15.pdf

US NRC, Generic Communications, Online Bulletin available : www.nrc.gov/reading-rm/doc-collections/gen-comm/index.html

EI Genk MS & Paramonov DV, *An Analysis of Disassembling the Radial Reflector of a Thermionic Space Nuclear Reactor Power System*, Nuclear Safety, Vol 35, No 1, 1994

Northern Research and Engineering Corporation, *The design and performance analysis of compact heat exchangers*, 1965

B Thonon, E Breuil, *Compact heat exchanger technologies for the HTRs recuperator application*, IAEA TCM, Palo Alto California USA, 2000

J Hesselgreaves, *Compact Heat Exchangers: Selection, Design and Operation*, Pergamon, Oxford, United Kingdom, 2001, ISBN 0080428398

Ingersoll D.T., *Deliberately Small Reactors and The Second Nuclear Era*, Progress in Nuclear Energy 51 (2009) pg. 589-603, Elsevier Ltd.

Forsberg, C., Bischoff, B., Mansur, L., Trowbridge, L., Tortorelli, P., *A Lower Temperature Iodine-Westinghouse-Ispra Sulphur Process for Thermochemical Production of Hydrogen*, Global 2003 Manuscript number 87682 by Oak Ridge National Laboratory, 2003

Forsberg C., *Lowering Peak Temperatures For Nuclear Thermochemical Production of Hydrogen*, Safety and Economy of Hydrogen Transport: Second International Symposium, August 2003.

Jiafu Tian, *Economic Feasibility of Heat Supply From Simple and Safe Nuclear Plants*, Tsinghua University, Beijing, China, 2001.

Kupitz & Podest, *Nuclear Heat Applications: World Overview*, IAEA Bulletin Vol. 26, No. 4. Online version available at : www.iaea.org/Publications/Magazines/Bulletin/Bull264/26404781821.pdf

VL Losev, MV Sigal, GE Soldatov. *Nuclear District Heating in CMEA Countries*, IAEA Bulletin, 3/1989. Online version available at: www.iaea.org/Publications/Magazines/Bulletin/Bull313/31304794649.pdf

Appendix

Modelling on the simple Rankine Cycle and Reheated Rankine Cycle was performed on the AGR, PWR and HTGR steam conditions to investigate the thermal efficiencies and steam qualities at the exit of the HP and LP (where available) turbines. For saturated steam with quality/dryness of less than 0.85, it could indicate potential moisture damage to turbines blades. Also of interest is the Pressure Ratio (PR) of the turbine(s).

Stated assumptions are coloured in green.

Label	Description
RCT	Reactor
HX	Heat Exchanger
PMP	Pump
TUR	Turbine
CLR	Cooler/Condenser
HTR	Reheater

1. AGR Rankine Cycle

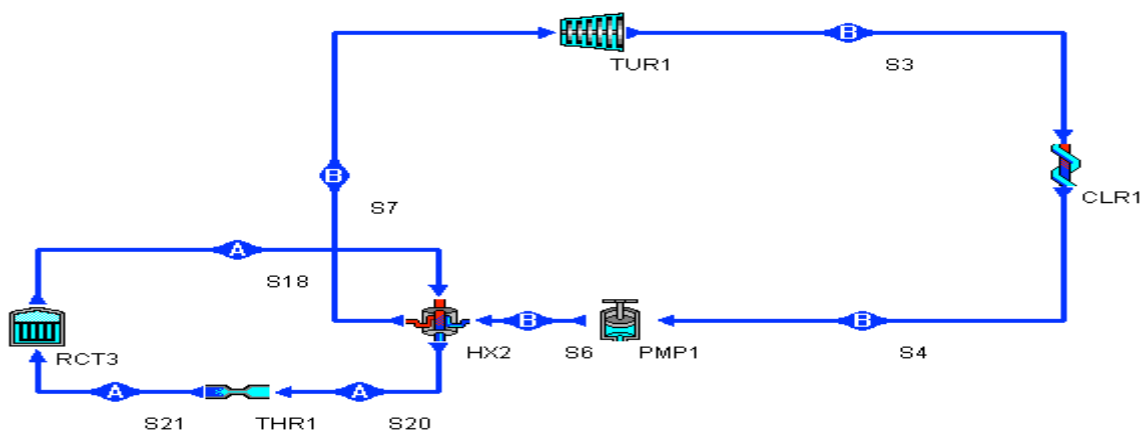
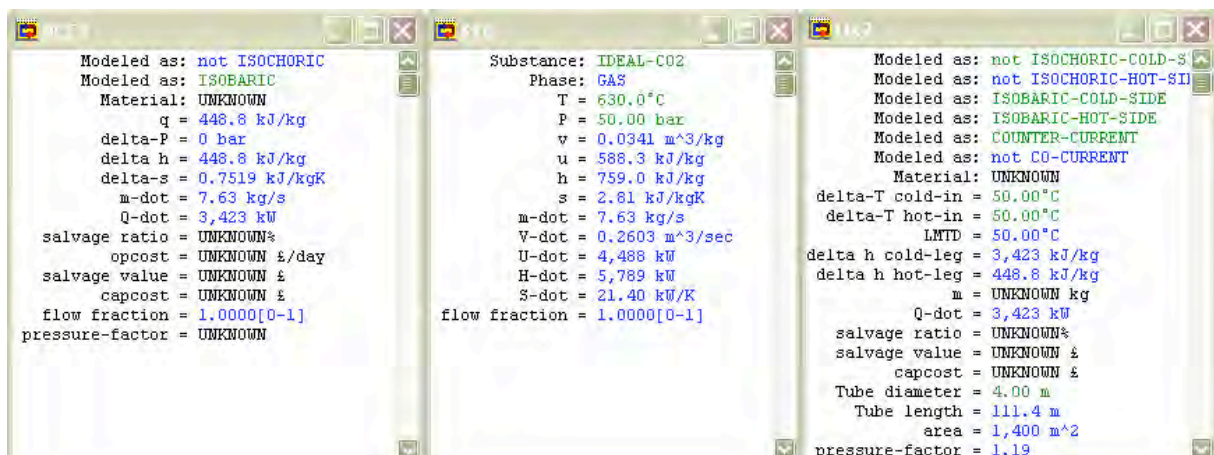
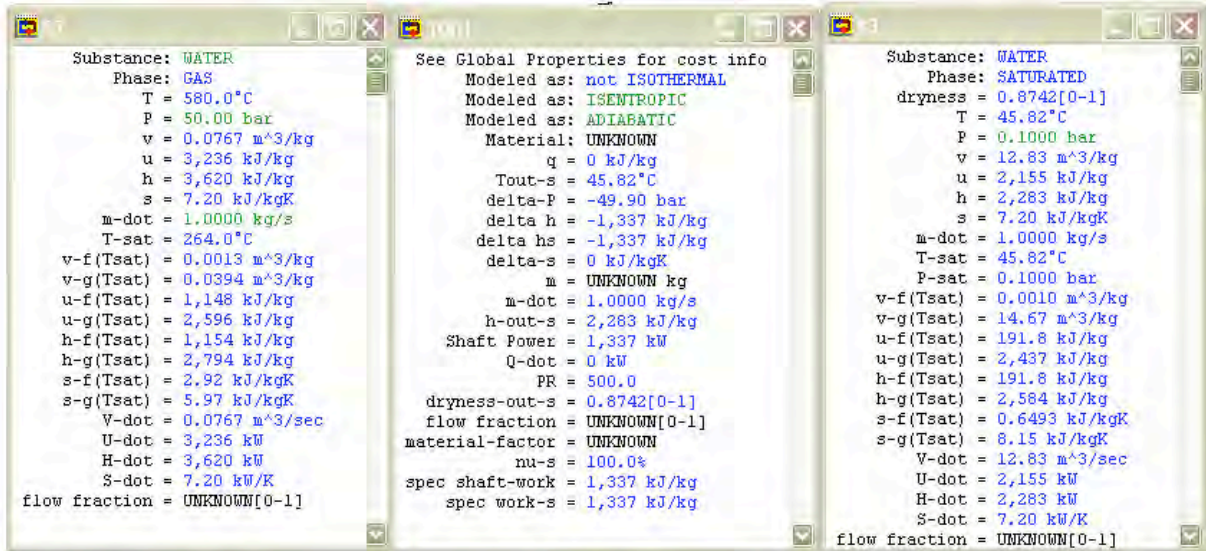


Figure A1: AGR Rankine Cycle schematic.

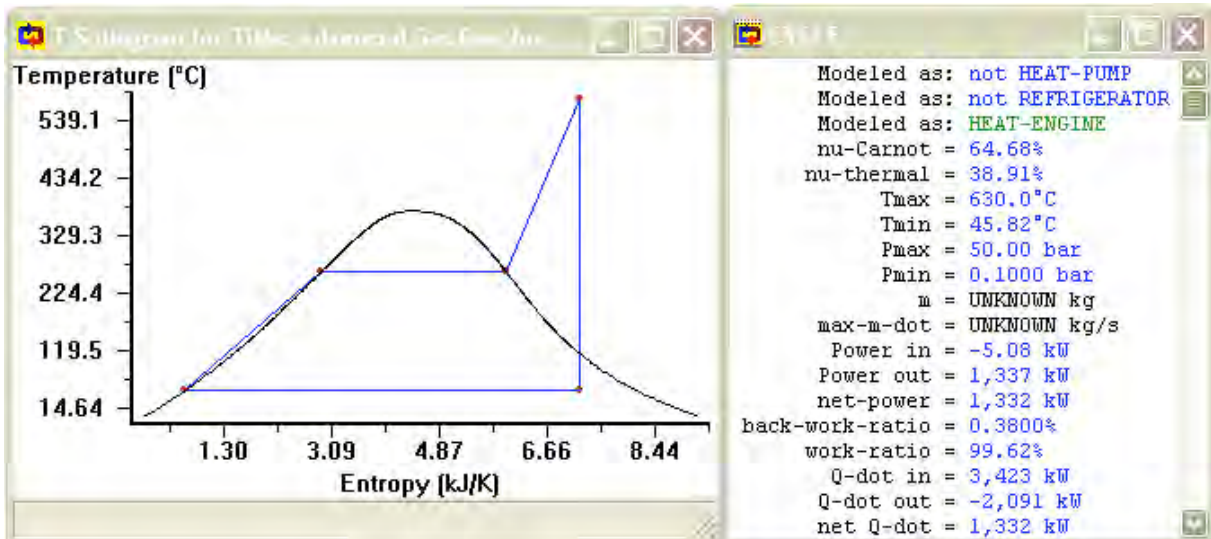
Primary System Component Parameters
(Parameters in green are assumed)

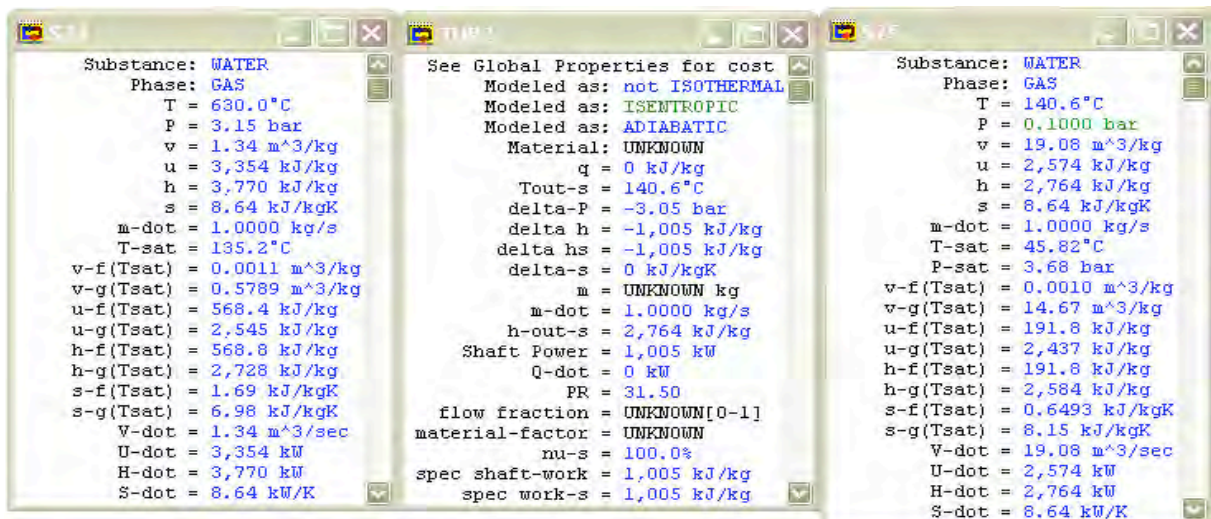
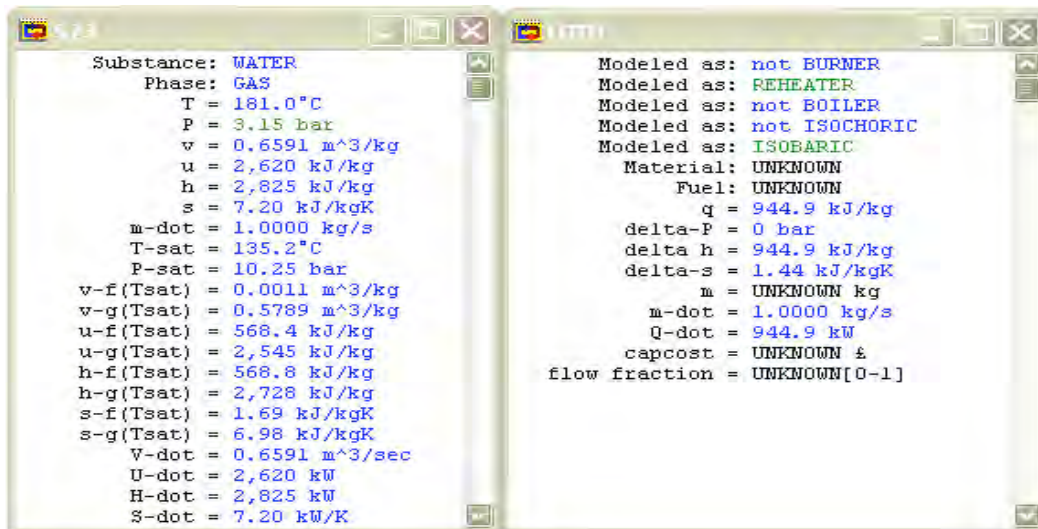


Secondary System Parameters
 (Parameters in green are assumed)

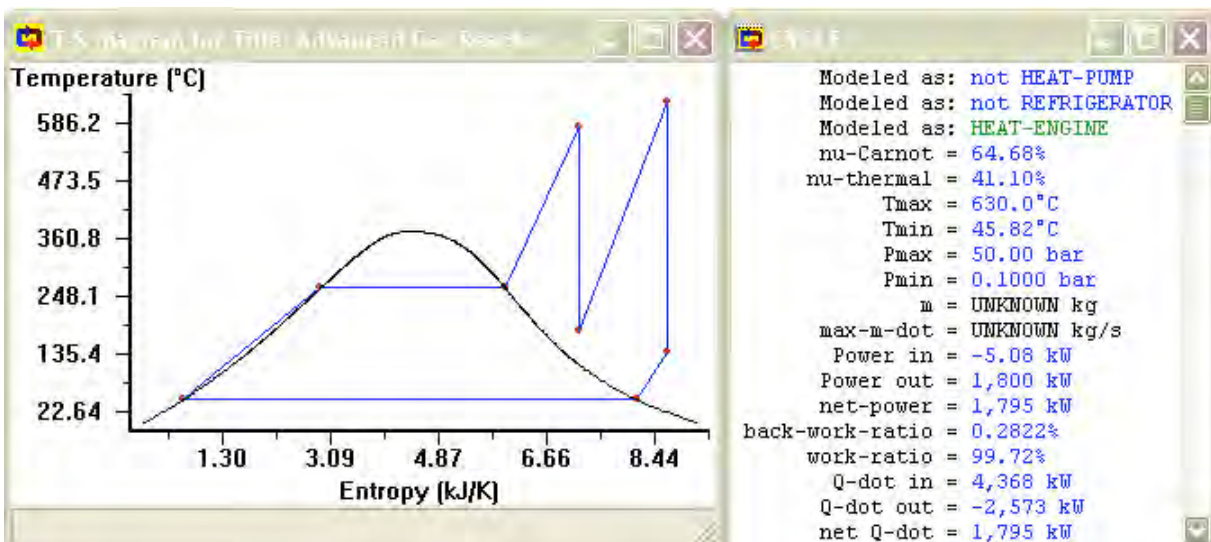


T-s Diagram and Cycle Properties
 (Final thermal efficiency of system is noted as *nu-thermal*)





T-s Diagram and Cycle Properties
(Final thermal efficiency of system is noted as *nu-thermal*)



3. PWR Rankine Cycle

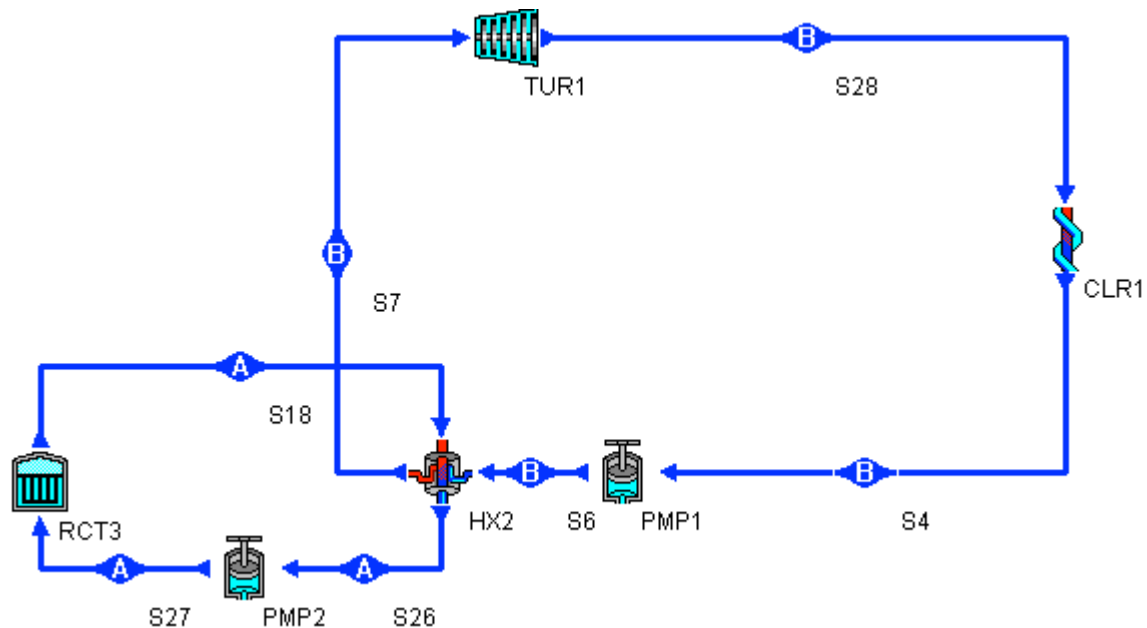
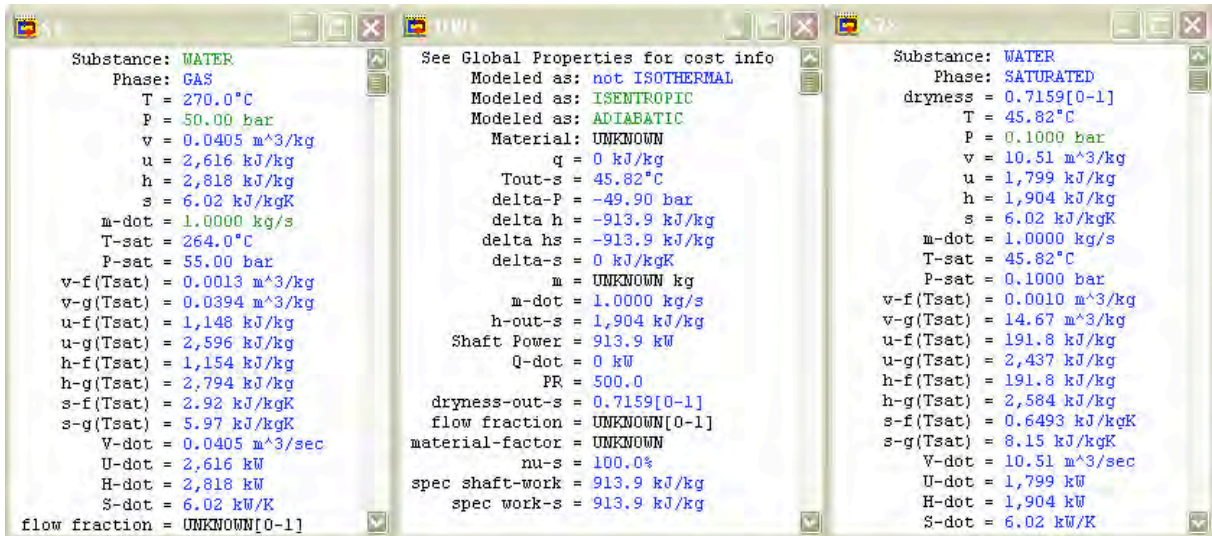


Figure A3: PWR Rankine Cycle schematic.

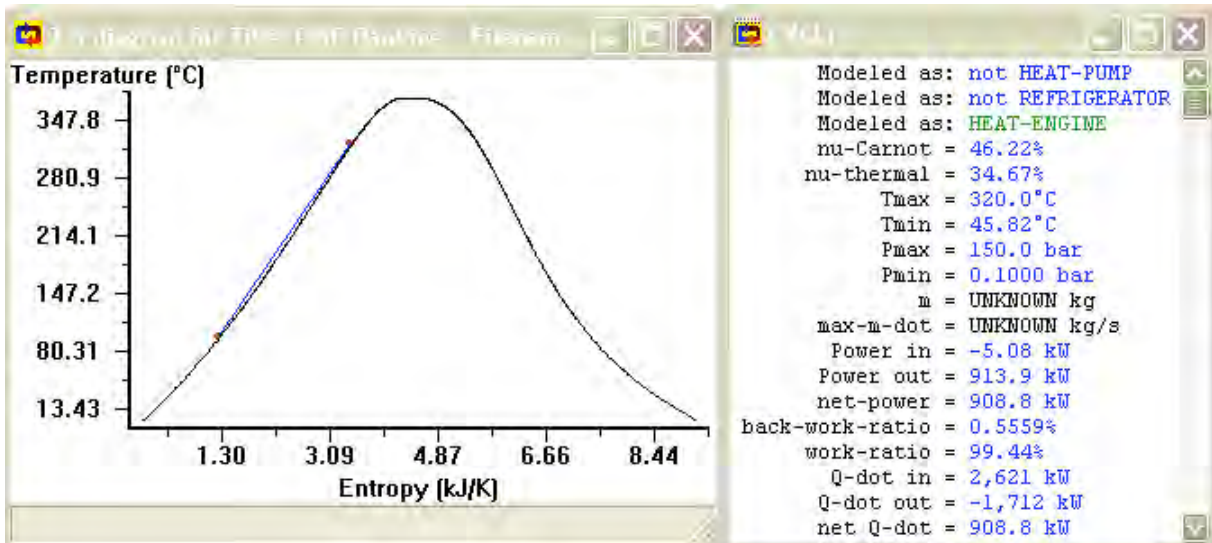
Primary System Component Parameters
(Parameters in green are assumed)

Component	Parameters
RCT3	Modeled as: not ISOCHORIC Modeled as: ISOBARIC Material: UNKNOWN $q = 1,040 \text{ kJ/kg}$ $\Delta P = 0 \text{ bar}$ $\Delta h = 1,040 \text{ kJ/kg}$ $\Delta s = 2.18 \text{ kJ/kgK}$ $\dot{m} = 2.52 \text{ kg/s}$ $\dot{Q} = 2,621 \text{ kW}$ salvage ratio = UNKNOWN % opcost = UNKNOWN $\text{\$/day}$ salvage value = UNKNOWN $\text{\$}$ capcost = UNKNOWN $\text{\$}$ Flow fraction = 1.0000[0-1] pressure-factor = UNKNOWN
HX2	Substance: WATER Phase: LIQUID $T = 320.0^\circ\text{C}$ $P = 150.0 \text{ bar}$ $v = 0.0015 \text{ m}^3/\text{kg}$ $u = 1,432 \text{ kJ/kg}$ $h = 1,454 \text{ kJ/kg}$ $s = 3.43 \text{ kJ/kgK}$ $\dot{m} = 2.52 \text{ kg/s}$ $T_{\text{sat}} = 342.2^\circ\text{C}$ $P_{\text{sat}} = 112.8 \text{ bar}$ $v\text{-f}(T_{\text{sat}}) = 0.0017 \text{ m}^3/\text{kg}$ $v\text{-g}(T_{\text{sat}}) = 0.0103 \text{ m}^3/\text{kg}$ $u\text{-f}(T_{\text{sat}}) = 1,585 \text{ kJ/kg}$ $u\text{-g}(T_{\text{sat}}) = 2,455 \text{ kJ/kg}$ $h\text{-f}(T_{\text{sat}}) = 1,610 \text{ kJ/kg}$ $h\text{-g}(T_{\text{sat}}) = 2,610 \text{ kJ/kg}$ $s\text{-f}(T_{\text{sat}}) = 3.68 \text{ kJ/kgK}$ $s\text{-g}(T_{\text{sat}}) = 5.31 \text{ kJ/kgK}$ $\dot{V} = 0.0037 \text{ m}^3/\text{sec}$ $\dot{U} = 3,608 \text{ kW}$ $\dot{H} = 3,664 \text{ kW}$ $\dot{S} = 8.63 \text{ kW/K}$ Flow fraction = 1.0000[0-1]
CLR1	Modeled as: not ISOCHORIC-COLD-SID Modeled as: not ISOCHORIC-HOT-SID Modeled as: ISOBARIC-COLD-SIDE Modeled as: ISOBARIC-HOT-SIDE Modeled as: COUNTER-CURRENT Modeled as: not CO-CURRENT Material: UNKNOWN $\Delta T_{\text{cold-in}} = 50.00^\circ\text{C}$ $\Delta T_{\text{hot-in}} = 50.00^\circ\text{C}$ LMTD = 50.00°C $\Delta h_{\text{cold-leg}} = 2,621 \text{ kJ/kg}$ $\Delta h_{\text{hot-leg}} = 1,040 \text{ kJ/kg}$ $\dot{m} = \text{UNKNOWN kg}$ $\dot{Q} = 2,621 \text{ kW}$ salvage ratio = UNKNOWN % salvage value = UNKNOWN $\text{\$}$ capcost = UNKNOWN $\text{\$}$ Tube diameter = 4.00 m Tube length = 3.57 m area = 44.80 m^2 pressure-factor = 1.48

Secondary System Parameters
(Parameters in green are assumed)



T-s Diagram and Cycle Properties
(Final thermal efficiency of system is noted as *nu-thermal*)



4. PWR Rankine Cycle with Reheat

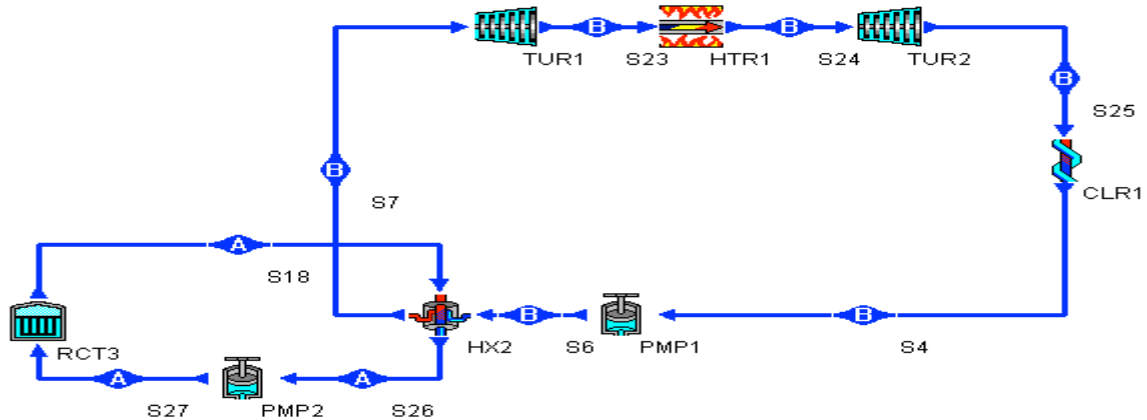
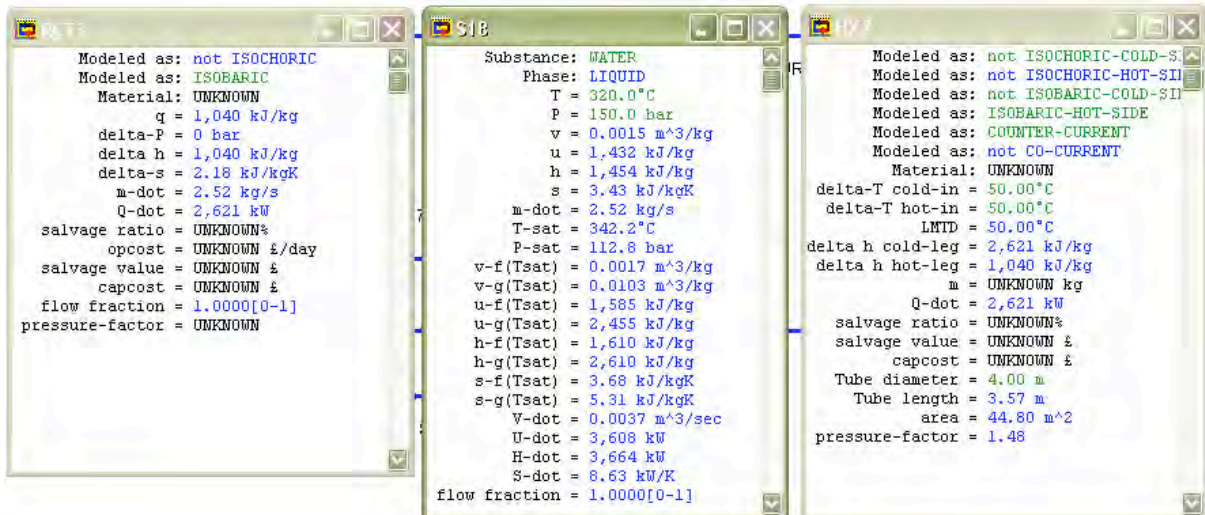
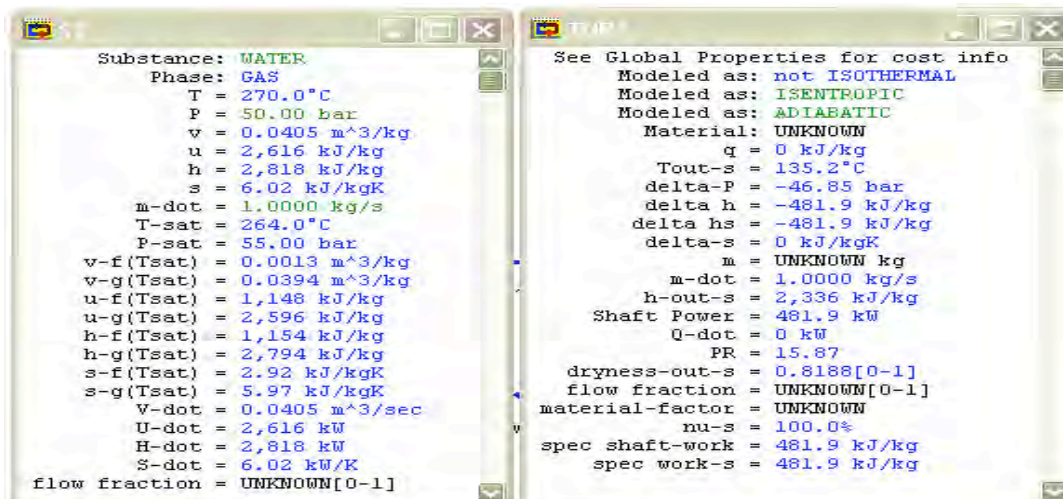


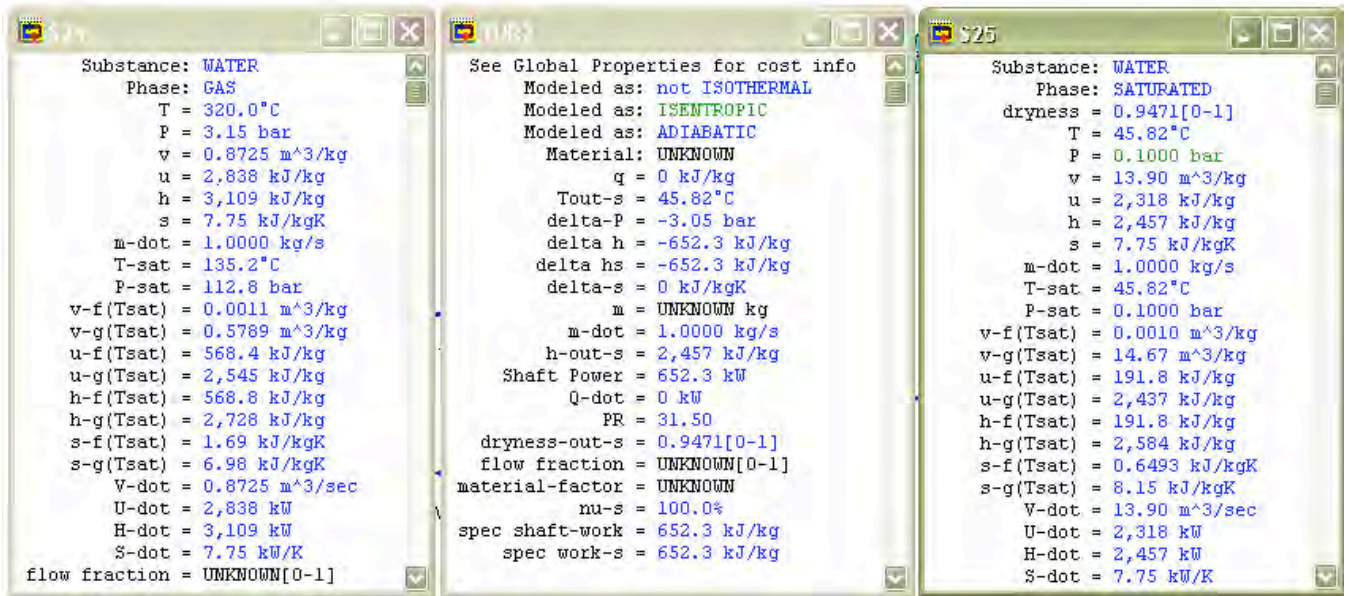
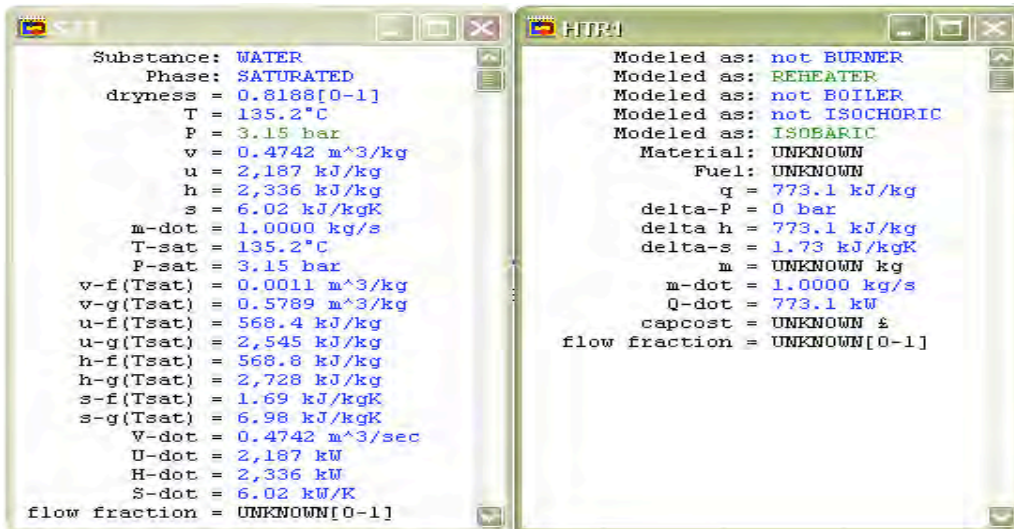
Figure A4: PWR Rankine Cycle with Reheat schematic.

Primary System Component Parameters
(Parameters in green are assumed)

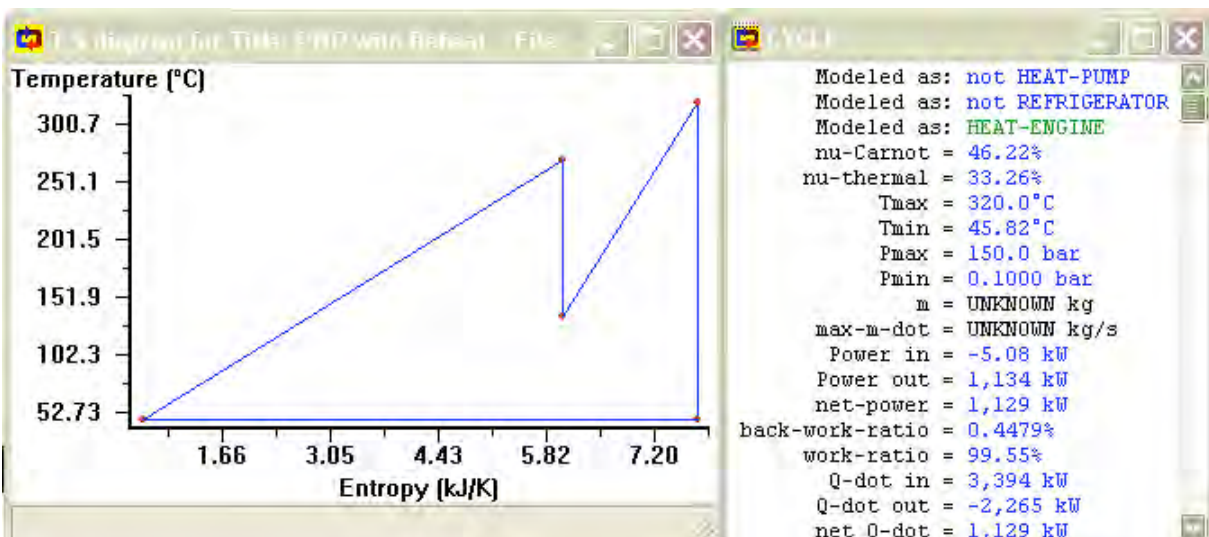


Secondary System Parameters
(Parameters in green are assumed)





T-s Diagram and Cycle Properties
 (Final thermal efficiency of system is noted as *nu-thermal*)



5. Indirect HTGR Rankine Cycle

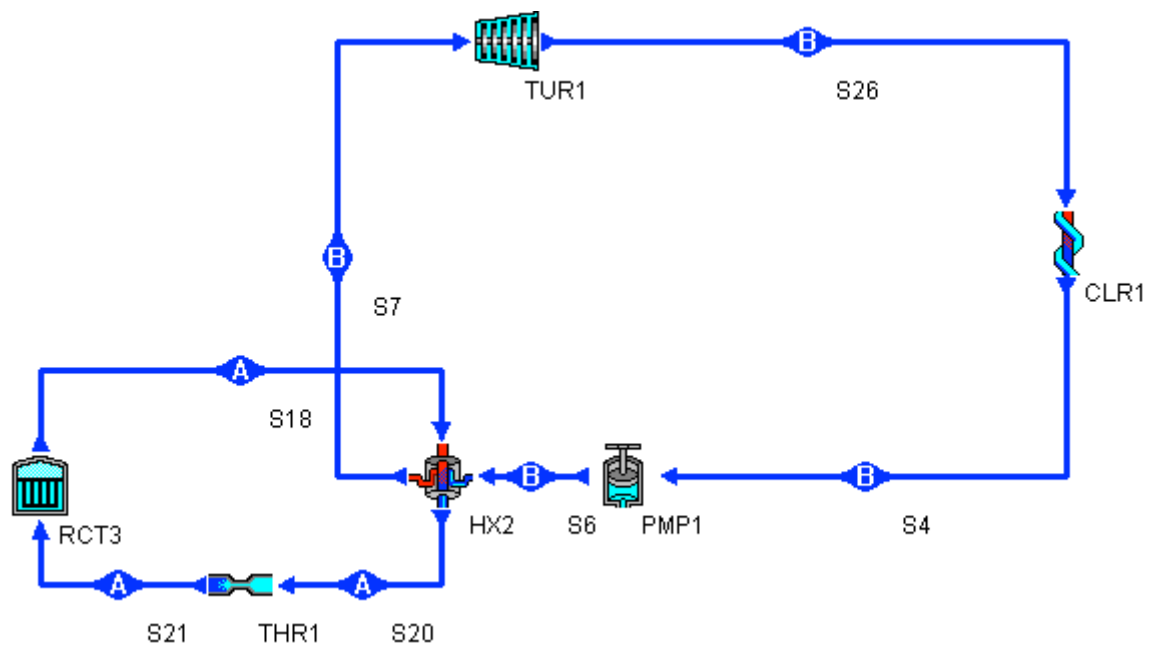
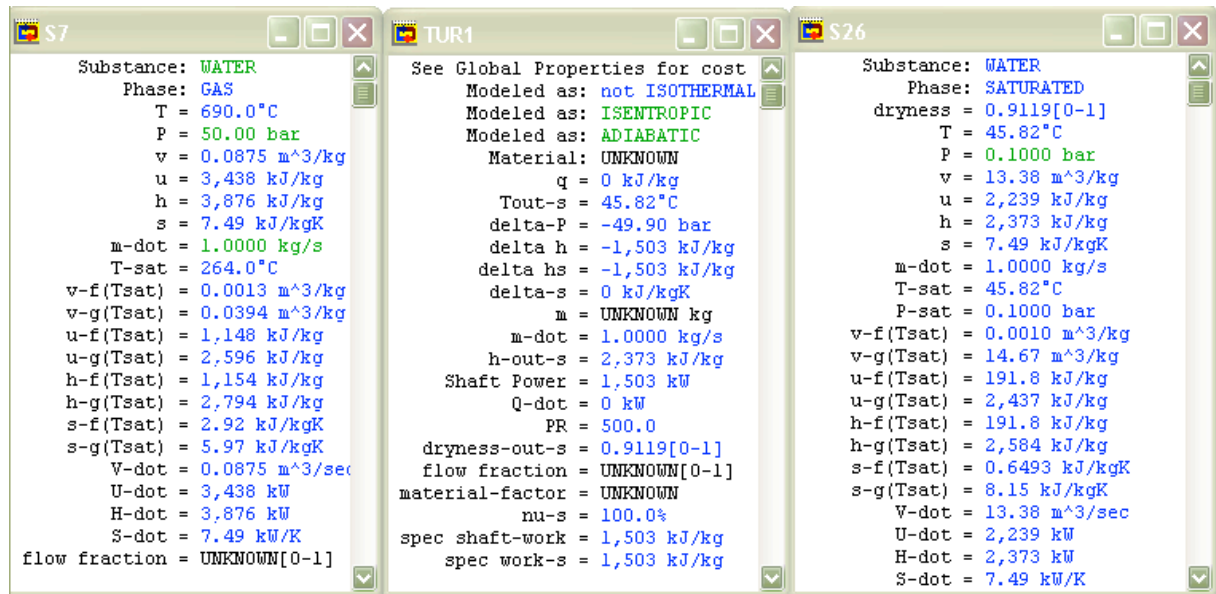


Figure A5: Indirect HTGR Rankine Cycle schematic.

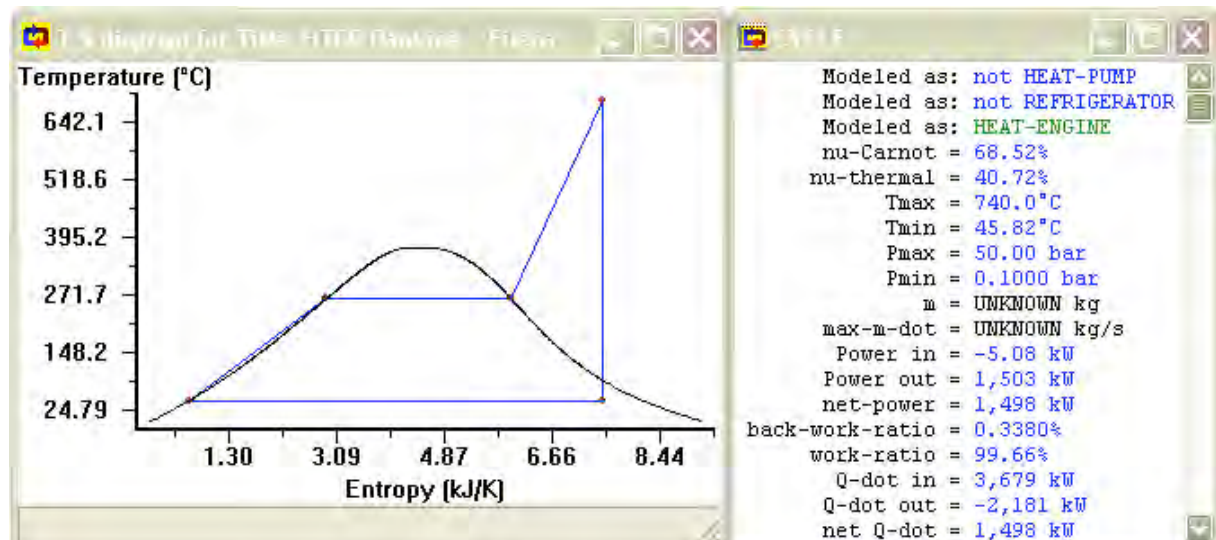
Primary System Component Parameters
(Parameters in *green* are assumed)

Component	Parameters	Component	Parameters
HTGR	Modeled as: not ISOCHORIC Modeled as: ISOBARIC Material: UNKNOWN $q = 3,334 \text{ kJ/kg}$ $\Delta P = 0 \text{ bar}$ $\Delta h = 3,334 \text{ kJ/kg}$ $\Delta s = 5.23 \text{ kJ/kgK}$ $\dot{m} = 1.10 \text{ kg/s}$ $\dot{Q} = 3,679 \text{ kW}$ salvage ratio = UNKNOWN% opcost = UNKNOWN \$/day salvage value = UNKNOWN \$ capcost = UNKNOWN \$ flow fraction = 1.0000[0-1]	HX1	Substance: HELIUM Phase: GAS $T = 740.0^\circ\text{C}$ $P = 50.00 \text{ bar}$ $v = 0.4209 \text{ m}^3/\text{kg}$ $u = 3,141 \text{ kJ/kg}$ $h = 5,245 \text{ kJ/kg}$ $s = 3.79 \text{ kJ/kgK}$ $\dot{m} = 1.10 \text{ kg/s}$ $\dot{V} = 0.4644 \text{ m}^3/\text{sec}$ $\dot{U} = 3,466 \text{ kW}$ $\dot{H} = 5,788 \text{ kW}$ $\dot{S} = 4.18 \text{ kW/K}$ flow fraction = 1.0000[0-1]
Condenser	Modeled as: not ISOCHORIC-COLD-SIDE Modeled as: not ISOCHORIC-HOT-SIDE Modeled as: ISOBARIC-COLD-SIDE Modeled as: ISOBARIC-HOT-SIDE Modeled as: COUNTER-CURRENT Modeled as: not CO-CURRENT Material: UNKNOWN $\Delta T \text{ cold-in} = 50.00^\circ\text{C}$ $\Delta T \text{ hot-in} = 50.00^\circ\text{C}$ $\text{LMTD} = 50.00^\circ\text{C}$ $\Delta h \text{ cold-leg} = 3,679 \text{ kJ/kg}$ $\Delta h \text{ hot-leg} = 3,334 \text{ kJ/kg}$ $m = \text{UNKNOWN kg}$ $\dot{Q} = 3,679 \text{ kW}$		

Secondary System Parameters
(Parameters in green are assumed)



T-s Diagram and Cycle Properties
(Final thermal efficiency of system is noted as nu-thermal)



6. Indirect HTGR Rankine Cycle with Reheat

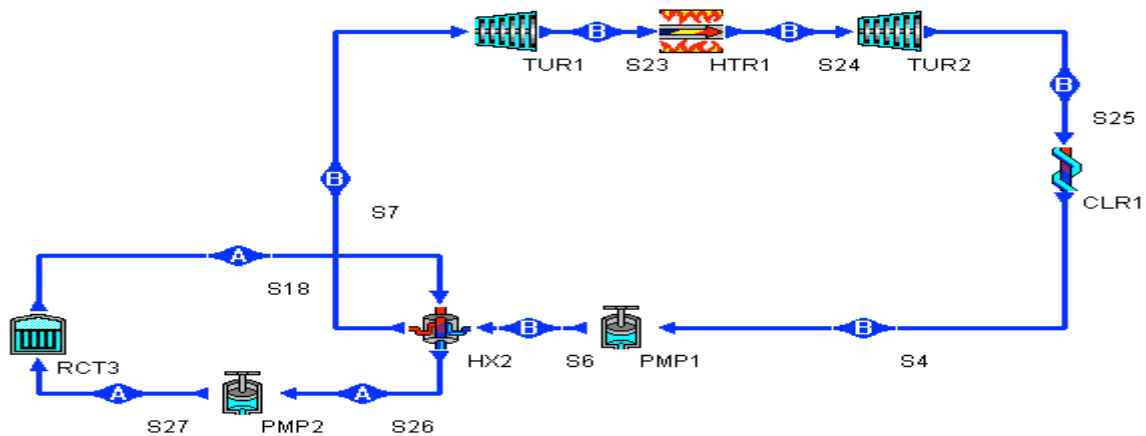
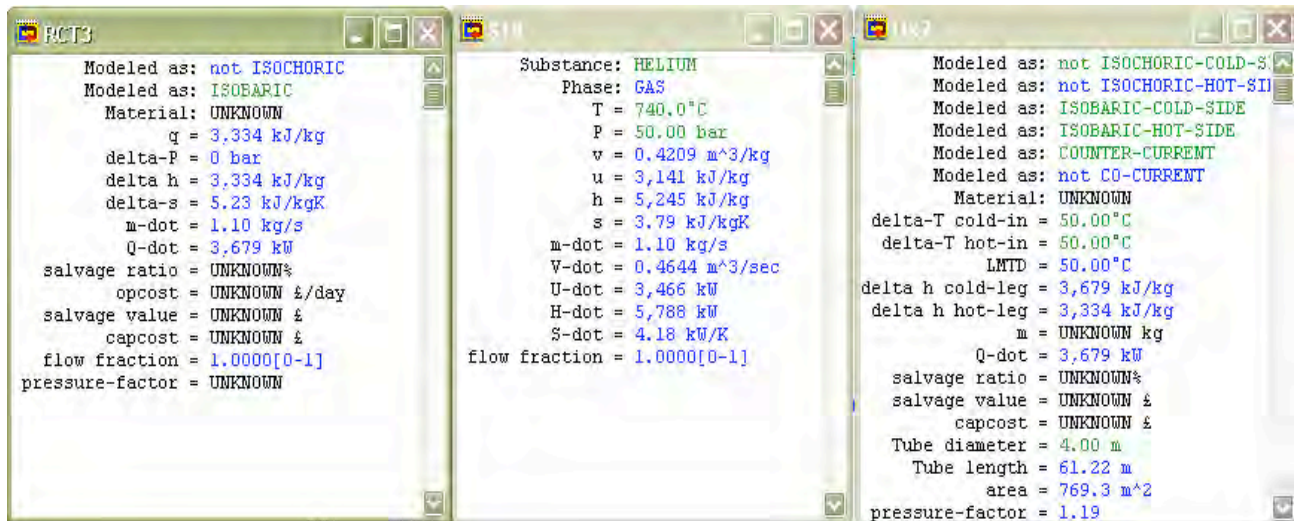


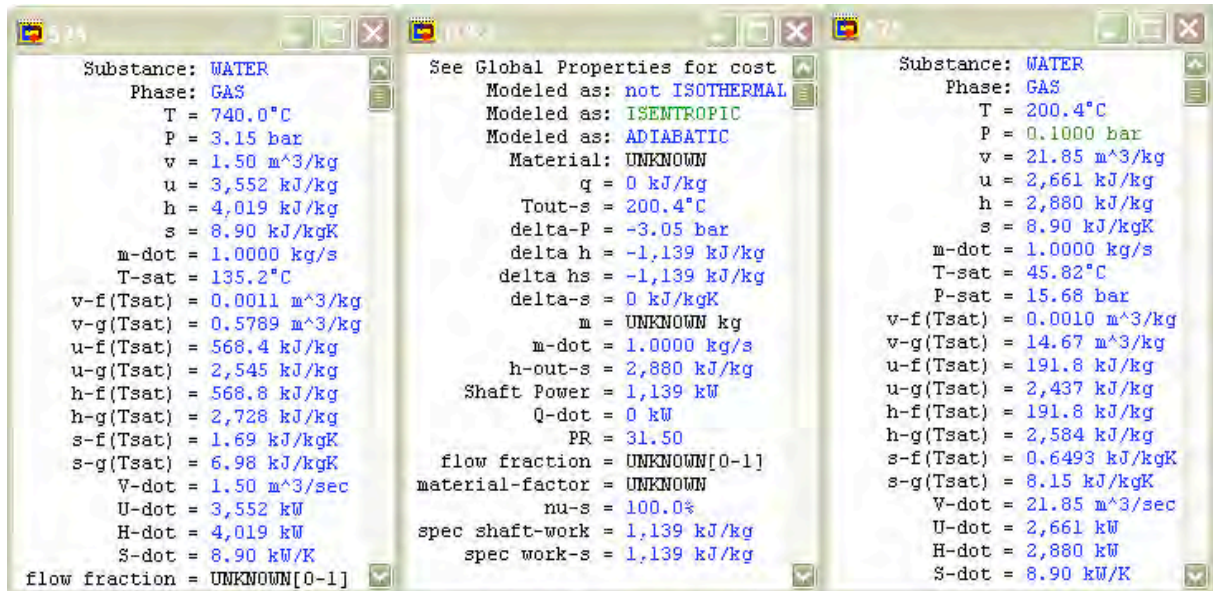
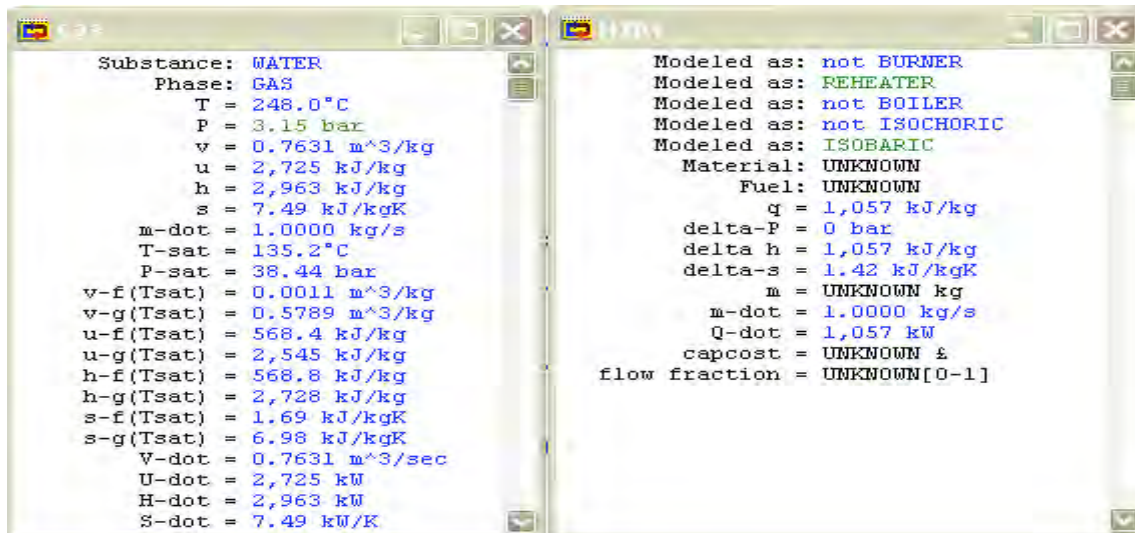
Figure A6: Indirect HTGR Rankine Cycle schematic.

Primary System Component Parameters
(Parameters in green are assumed)



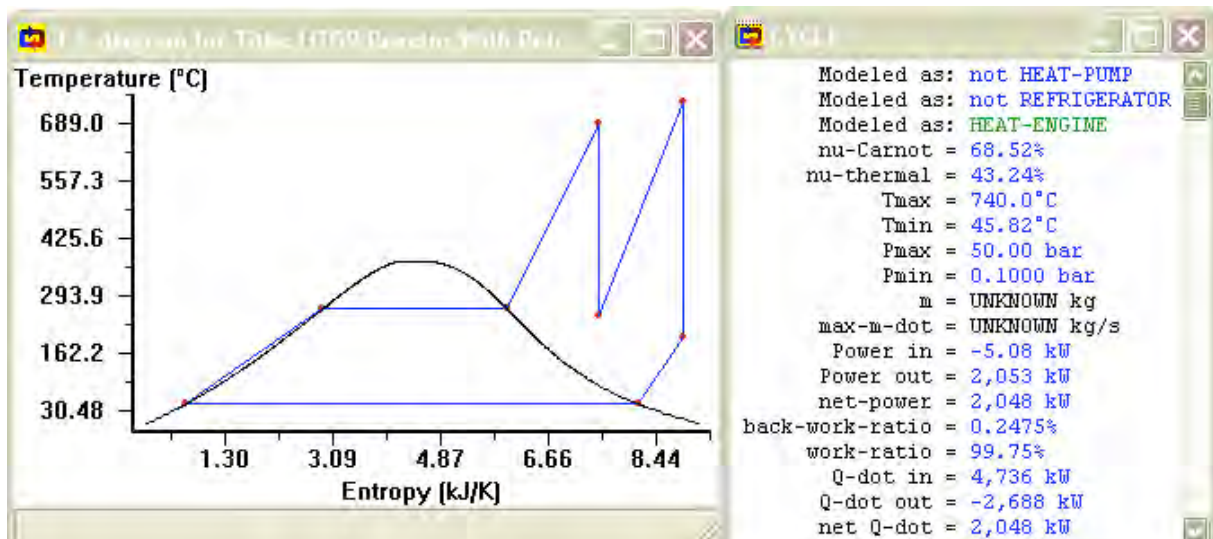
Secondary System Parameters
(Parameters in green are assumed)





T-s Diagram and Cycle Properties

(Final thermal efficiency of system is noted as *nu-thermal*)



MCBEND Shielding Calculation for Excellox Spent Fuel Flask Design

A dissertation submitted to The University of Manchester for the degree of Master of
Science in School of Physics and Astronomy

2011

Mengqi Bai

School of Physics and Astronomy

University of Manchester

DECLARATION

No portion of the work referred to in the dissertation has been submitted in support of an application for another degree or qualification of this or any other university or other institute of learning.

Signed 

COPYRIGHT STATEMENT

- i. The author of this dissertation (including any appendices and/or schedules to this dissertation) owns certain copyright or related rights in it (the “Copyright”) and s/he has given The University of Manchester certain rights to use such Copyright, including for administrative purposes.
- ii. Copies of this dissertation, either in full or in extracts and whether in hard or electronic copy, may be made only in accordance with the Copyright, Designs and Patents Act 1988 (as amended) and regulations issued under it or, where appropriate, in accordance with licensing agreements which the University has entered into. This page must form part of any such copies made.
- iii. The ownership of certain Copyright, patents, designs, trade marks and other intellectual property (the “Intellectual Property”) and any reproductions of copyright works in the dissertation, for example graphs and tables (“Reproductions”), which may be described in this dissertation, may not be owned by the author and may be owned by third parties. Such Intellectual Property and Reproductions cannot and must not be made available for use without the prior written permission of the owner(s) of the relevant Intellectual Property and/or Reproductions.
- iv. Further information on the conditions under which disclosure, publication and commercialisation of this dissertation, the Copyright and any Intellectual Property and/or Reproductions described in it may take place is available in the University IP Policy (see <http://documents.manchester.ac.uk/display.aspx?DocID=487>), in any relevant Dissertation restriction declarations deposited in the University Library, The University Library’s regulations (see <http://www.manchester.ac.uk/library/aboutus/regulations>) and in The University’s Guidance for the Presentation of Dissertations.

Abstract

Excellox type flasks are especially designed for transporting BWR and PWR spent fuels for BNFL since the late 1960's. Shielding calculation for both neutron and primary gamma radiation of this type flask utilizes Serco software MCBEND is presented in this research paper. The dose rates outside the flask which is closely relevant to the shielding thickness employed by the flasks are calculated for the flask design. Radius and axial dose rate distribution near the flask, water level effect, burnup effect, cooling time and initial enrichment effect to dose rate are also discussed. In addition, a conceptual TRISO PWR fuel is compared with the normal PWR fuel to show the superiority of the new design.

Acknowledgements

I would like to thank my supervisor professor Timothy Abram for his support and advice during the course of this project. I would also like to thank Tim Ware for his time, patience and assistance in helping me to understand of MCBEND.

Contents

Abstract	3
Acknowledgements	4
Abbreviations	7
List of Figures	8
List of Tables.....	10
1. Introduction	12
2. MCBEND.....	12
3. Excellox Flask	13
4. MCBEND model Building up	15
4.1. Control Function.....	15
4.2. Geometry Function.....	16
4.2.1. PWR fuel assembly.....	17
4.2.2. Multi Element Bottle (MEB).....	19
4.2.3. Excellox 7 flask	21
4.3. Material specification.....	24
4.4. Energy Data Unit	29
4.5. Unified Source Data.....	30
4.6. Variance Reduction Technique.....	32
4.7. Scoring Function.....	34
5. MCBEND Result.....	37
5.1. Neutron Dose Rate Varying With the Shielding Thickness.....	37
5.2. Gamma Dose Rate Varying With Shielding Thickness.....	43
5.3. Radius and Axial Dose Rate Distribution	49

5.4.	Water Level	56
5.5.	Burnup, Cooling Time and Initial Enrichment Effect to Spent Fuel Dose Rate.....	58
5.6.	Distance Effect.....	62
6.	TRISO Type Fuel Utilized in PWR.....	64
6.1.	TRISO Type Fuel Rod Geometrical Description	64
6.2.	Material Specification.....	65
6.3.	The Building up of Model	66
6.4.	Calculation Result	68
7.	MCBEND Calculation Error.....	69
8.	Conclusion.....	70
9.	Reference	71
10.	Appendixes.....	74
10.1.	Appendix 1 Input Data for 32.5 cm thick gamma shielding	74
10.2.	Appendix 2 Partial input Data for TRISO PWR fuel.....	83
10.3.	Appendix 2 Input Data for Axial score region.....	84
10.4.	Appendix 4 Detailed Tables	86
10.5.	Appendix 5 Extra Figues	94

Total Words: 19143

Abbreviations

AGR	Advanced Gas-Cooled Reactor
AP	Activation Product
BBS	Basic Safety Standards
BWR	Boiling Water Reactor
BNFL	British Nuclear Fuels
CPU	Central Processing Unit
CR	Control Rod
FG	Fractal Geometry
FP	Fission Product
LWR	Light Water Reactor
MEB	Multi Element Bottle
NDA	Nuclear Decommissioning Authority
PWR	Pressurized Water Reactor
S/R	Splitting/Russian Roulette
TRISO	Tristructural-Isotropic (Fuel)
TRU	Transuranic
VAR	Variation
VR	Variance Reduction

List of Figures

Figure 1. Excellox 4 (left) and 7 (right) flask with shock absorber.....	14
Figure 2. MEB Fuel assembly layout of different PWR fuel enrichment for Excellox 7 flask (left 3.8 enrichment limit, right 4.5 enrichment limit).....	14
Figure 3. Typical PWR Fuel assembly lay out (left) and typical PWR fuel rod (right) ..	17
Figure 4. Cutaway views of a PWR fuel pin and a guide tube with/without control rod	18
Figure 5. MEB detail illustration.....	21
Figure 6. Comparison of real and modeled MEB	21
Figure 7. Excellox 7 spent fuel flask	24
Figure 8. Excellox 7 flask global geometry in MCBEND model.....	24
Figure 9. Excellox 7 flask with and without splitting mesh	33
Figure 10. Illustration of score region in modeling	36
Figure 11. A warning in MCBEND output	37
Figure 12. Elastic and radioactive capture cross section for 1H. (Sources From: http://www.dne.bnl.gov/CoN/index.html .).....	39
Figure 13. Neutron dose rate varying with Neutron shielding thickness in normal coordinate	40
Figure 14. Neutron dose rate attenuated with Neutron shielding thickness in logarithmic coordinate	41
Figure 15. Eviews fitting result of neutron dose rate variation	42
Figure 16. Different energy gamma-ray exponential attenuation in lead	46
Figure 17. Gamma dose rate attenuated with Neutron shielding thickness in logarithmic coordinate	47
Figure 18. Eviews fitting result of photon dose rate variation	48
Figure 19. Radius dose rate distribution at the upper shock absorber	53
Figure 20. Axial dose rate distribution around Excellox 7 flask in normal coordinate ...	53

Figure 21. Axial dose rate distribution around Excellox 7 flask in logarithmic coordinate	54
Figure 22. Measured and calculated gamma ray source distributions along fuel rod for Cs134 and Ru106 distribution	55
Figure 23. Measured and calculated neutron emission distributions along fuel rod (Sources from: Akihiro Sasahara et al., 2004. Neutron and gamma ray source evaluation of LWR high burn-up UO ₂ and MOX spent fuels)	55
Figure 24. Flask cut views of water levels change for modeling	56
Figure 25. Dose rate variation with respect to water levels in flask.....	57
Figure 26. Radioactivity per ton initial heavy metal (IHM) versus time after discharge	59
Figure 27. Neutron and gamma dose rate varying with spent fuel Burnup	61
Figure 28. Change of predominant nuclides in typical PWR spent fuel with respect to different initial enrichment	61
Figure 29. Dose rate varying with distance from flask in normal coordinate axes	62
Figure 30. Simplified Cask Geometry Modeling of 2 x 5 array and Photon dose rates within the array (left); Photon dose rates for the array (right) (Byeong-Soo Kim et al., 2007).....	63
Figure 31. Illustration of TRISO particles and TRISO PWR fuel rod	65
Figure 32. Space remaining when modeling a single fuel rod with TRISO fuel particles in real dimension	67
Figure 33. Illustration of geometrical details for two modeling cases (Left for TRISO type fuel and right for ordinary type fuel; upper for case 1 and lower for case 2) ..	67
Figure 34. Comparison of TRISO PWR and Normal PWR spent fuel dose rate outside flask	68
Figure 35. Burnup effect to spent fuel composition	94
Figure 36. Cooling time effect to spent fuel composition	94

List of Tables

Table 1. Comparison of four different types of Excellox flask	13
Table 2. Typical fuel load parameter of Excellox 6/7	15
Table 3. Fuel assembly detailed geometrical description	18
Table 4. Geometry description of the MEB in Modeling	20
Table 5. Excellox 7 flask dimension for modeling	23
Table 6. Material description for modeling	25
Table 7. Excellox 7 flask side face neutron dose rate varying with Neutron shielding thickness	40
Table 8. Gamma dose rate varying with the gamma shielding thickness	47
Table 9. Gamma dose distribution at lid surface and 1m away from lid surface of 32.5 cm thickness of gamma shielding	50
Table 10. Neutron dose distribution at lid surface and 1m away from lid surface of 14 cm thickness of neutron shielding	50
Table 11. Axial gamma and neutron dose rate distribution along the flask for 32.5cm Gamma shielding and 14 cm neutron shielding	51
Table 12. Axial gamma and neutron dose rate distribution along the flask for 22.5cm Gamma shielding and 24 cm neutron shielding	52
Table 13. Gamma dose rate varying with water level in the Excellox 7 Flask	57
Table 14. Neutron dose rate varying with water level in the Excellox 7 Flask	57
Table 15. High burnup PWR spent fuel case	59
Table 16. Gamma and neutron dose rate scoring at 14 cm from cooling fins for different burnup	60
Table 17. Gamma and neutron dose rate scored at side face of different distance	62
Table 18. Comparison of TRISO PWR fuel and normal PWR fuel	65
Table 19. Description of TRISO fuel particle for modeling	66

Table 20. Calculation results for two cases	68
Table 21. Atom densities for dominant absorbers in spent fuel, atom/barn-cm (PWR typical irradiation history 4.0% enrichment, 2 years cooling).....	86
Table 22. Atom densities for dominant absorbers in spent fuel, atom/barn-cm (PWR typical irradiation history 4.0% enrich, 45 GWd/MTU)	87
Table 23. Atom densities for dominant absorbers in spent fuel, atom/barn-cm (PWR typical irradiation history 2 years cooling, 45 GWd/MTU)	88
Table 24. Excellox 7 flask 14cm away from side face gamma dose rate varying with gamma shielding thickness.....	89
Table 25. Excellox 7 flask 1 meter away from side face gamma dose rate varying with gamma shielding thickness.....	89
Table 26. Excellox 7 flask shock absorber surface gamma dose rate varying with gamma shielding thickness.....	90
Table 27. Excellox 7 flask 1 meter away from lid surface gamma dose rate varying with gamma shielding thickness.....	90
Table 28. Excellox 7 flask 14 cm away from side face neutron dose rate varying with Neutron shielding thickness	91
Table 29. Excellox 7 flask 1 meter away from side face neutron dose rate varying with Neutron shielding thickness	91
Table 30. Gamma dose rate varying with spent fuel burnup.....	92
Table 31. Neutron dose rate varying with spent fuel burnup	92
Table 32. Gamma dose rate varying with distance.....	92
Table 33. Neutron dose rate varying with distance	92
Table 34. TRISO PWR fuel case 1 dose rate scoring at 14cm from the cooling fins	93
Table 35. TRISO PWR fuel case 2 dose rate scoring at 14cm from the cooling fins	93

1. Introduction

The requirements for radiation protection established in the BSS (IAEA, 1996), which underlie the Transport Regulations, set a limit on the effective dose for members of the public of 1 mSv/a and for workers of 20 mSv/a averaged over five consecutive years (IAEA, 2007). Shielding calculation for transport flask is particularly important due to the high reactivity of spent fuel and the necessity of considering possibility of accident. Similar study also been reported (M Coeck et al., 2002). Accurate shielding calculation results obtained by using computational code MCNP and SCALE have been discussed in previous study. Excellox 7 flask loading PWR and TRISO PWR (A. Hussain et al., 2010) spent fuel have been calculated using ANSWERS latest software MCBEND 10 in this article to provide reference and comparison together with the previous achievement for later study and design. Detailed geometrical parameters of Excellox type flask are collected from previous relevant articles (R. Gowing et al., 1994) and (G. Ellcock et al., 1981). MCBEND code including the calculation error and Excellox flask application and development history are briefly presented. Modeling and calculation results are discussed in detail, especially material geometry and material specification units in modeling section and gamma/neutron shielding thickness variation in calculation result section.

2. MCBEND

MCBEND is a radiation shielding code which can calculate neutron, gamma photon, charged particle and coupling of different types of radiation transport in subcritical systems. It models the transport of individual particles accurately by using a very fine energy group representation of nuclear data and a flexible geometry modeling package. In effect the code simulates what happens in practice, and performs a numerical experiment of the system under study (Serco, 1994). It has evolved through thirty years of continuous development from its origin as a basic shielding code for simple geometries (Serco, 1994). The latest release MCBEND 10 is capable of

modeling realistic geometries in great detail and is a major launch of the code with many new and enhanced features which focus on the key areas of improving accuracy, understanding of uncertainties, efficiency and user friendliness (Serco, 1994).

3. Excellox Flask

In the late 1960's BNFL undertook the reprocessing of oxide fuel from certain American BWR and PWR type reactors, principally situated in Europe, and also in Japan. BNFL developed a type of flask suitable for transporting BWR and PWR fuel known as the Excellox flask (C. J. Edney et al., 1977). (Figure1.) This is of a cylindrical flask about 5m long and about 1.5m diameter, with a loading capacity of 2 or 3 tonnes of spent fuel (depending on fuel type). The fuel is immersed in water and the flask has a total weight of about 90 tonnes. The design of the Excellox flask is different from that of the Magnox flask due to the greater lengths of the fuel elements and to the higher neutron irradiation levels of the fuel (C. J. Edney et al., 1977). BNFL has developed a series of Excellox flask until now. The latest Excellox 8 flask has ability of loading higher rating spent fuel with a total weight around 100 tonnes. Dimensions and loading capacities of four different types of Excellox flasks are given in Table1.

Table 1. Comparison of four different types of Excellox flask

flask type	Spent fuel contains	Dimension (mm)	Weight(metric ton)
Excellox 4	7 PWR element	5512*1676	75
Excellox 6	7 PWR element	6605*2130	94
Excellox 7	7 P/17B	6095*2130	89
Excellox 8	12 PWR element	6300*2500	115

Figure1 below gives the illustration of Excellox 4 and 7 flasks. The main difference between Excellox 4 and 7 flasks is that the lead liner stainless steel gamma shielding

used in Excellox 4 is replaced by a monolithic carbon steel body. The new design of Excellox 7 flask also allows increased pre-irradiation enrichment, using the conventional rectilinear arrangement of fuel compartments, to cater for the maximum BWR enrichment, While a new arrangement with the compartments grouped radially around the centre allows for a major increase in enrichment for PWR fuels (R. Gowing et al., 1994).(Figure2.) These increases will also for the transport of MOX fuels. The design of Excellox 7 flask is very similar to that of Excellox 6 flask except that Excellox 6 can carry fuel assemblies up to 5.0 m long and Excellox 7 for 4.5 m fuel. The flasks have maximum loaded weights of 94 and 89 tonnes respectively. Table2 gives the basic loaded fuel parameters of these two types of flask. Excellox 7 is chosen for geometry modeling and shielding calculation in this article. Detail geometry description can be found in the ‘Geometry building up chapter’.

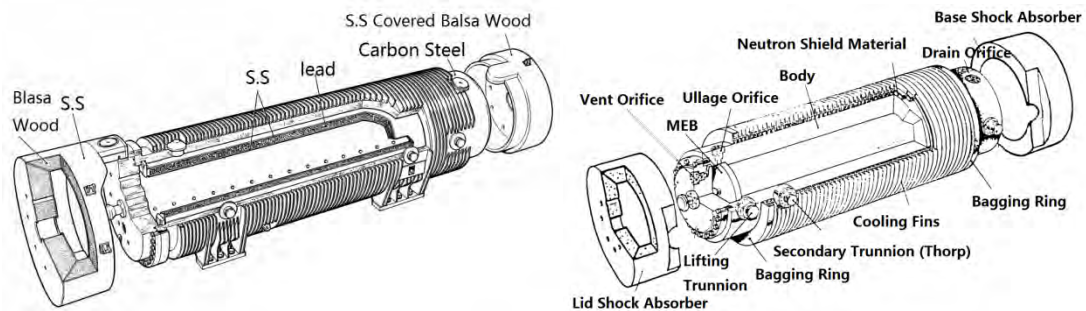


Figure 1. Excellox 4 (left) and 7 (right) flask with shock absorber

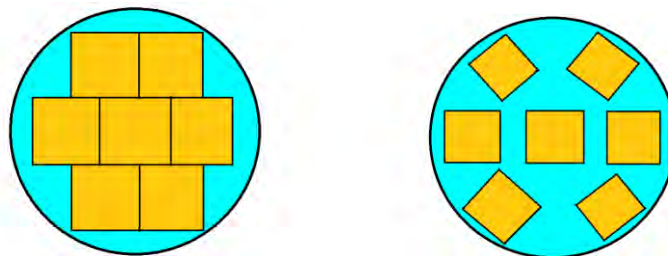


Figure 2. MEB Fuel assembly layout of different PWR fuel enrichment for Excellox 7 flask (left 3.8 enrichment limit, right 4.5 enrichment limit)

Table 2. Typical fuel load parameter of Excellox 6/7

Parameter	Excellox 6	Excellox 7	
	PWR	PWR	BWR
Maximum enrichment (%)	4.5	4.5	3.8
Maximum fuel element length (m)	5.0	4.5	4.5
Max. fuel element cross-section (mm)	230	216	140
Maximum irradiation (MWd/tU)	50,000	50,000	40,000
Maximum specific power (MW/tU)	40	40	33
Maximum weight of U per assembly (kg)	551	458.4	200

Sources from R. Gowing et al., Introduction of new flasks for high burnup spent fuel.

4. MCBEND model Building up

All the involving programming function including control function, geometry function, material function, physics function, source function, acceleration function and scoring function that used in our modeling are explained in this chapter. The calculation function, typical features and modeling process are discussed in each unit. Sectional input files are included in each unit and the entire input data can be found in appendixes.

4.1. Control Function

Control Function unit controls the duration of a Monte Carlo calculation and the type of processing. The calculation ends when a CPU time/sample limits or a specified standard deviation has been reached. An internal random number generator built in the program produce random samples to get close to reality of natural feature of radioactive particles and to achieve reproducible results. Control data must always be included in an executable MCBEND calculation (Serco, 1994). A simple example of input data is given below:

```
*****  
BEGIN CONTROL DATA  
RUN  
TIME LIMIT 3600  
SEEDS 12345 54321  
END  
*****
```

In the above example, the program process is controlled by CPU time limit of one hour. 'RUN' means execution of Monte Carlo calculation. Other options are 'READ' and 'CHECK'. Initial two seed values for the random number generator are set. More detailed function and options are stated in the MCBEND 10 manual and not discussed here.

4.2. Geometry Function

This unit is a major part of the input data which takes about 75% effort of the whole input data. The MCBEND 10 geometry modeling and tracking package (N.R.Smith et al., 1994) comprises a simple body component, known as Fractal Geometry (FG) using conventional ray tracing and the additional power of Hole Geometries employing Woodcock tracking (Serco, 1994). In this paper of shielding calculation, only Fractal Geometry is used to build up the Geometry of flask.

Fractal Geometry is a system of geometry modeling where the problem geometry is subdivided into zones of uniform material. These zones are defined as the intersections and differences of simple mathematical bodies such as cuboids, cylinders and spheres. The bodies are assembled into structures called parts. Parts are self contained to simplify the model construction. Parts may be included within other parts to any depth of nesting and a given part may be included more than once within the geometry. The combination options for parts of different shape and material are 'NEST', 'CLUSTER', 'OVERLAP' and 'GENERAL'. The ability to break down complex models into parts, each separately described in its own local co-ordinate

system, simplifies the preparation and checking of the input data (Serco, 1994). In addition, parts can be replicated and subdivided to satisfy different requirement.

4.2.1. PWR fuel assembly

Pressurized water reactor (PWR) is the major type of LWR widely used all over the world. The fuel used in typical PWRs is UO_2 , so dose in BWRs. The spent fuel composition of PWRs and BWRs are very similar, both of these two kinds of spent fuel are suited for Excellox type flask. In our modeling, PWRs are chosen for shielding calculation because that plentiful valuable reference about PWRs is available.

Figure3 gives the illustration of typical PWR fuel rod and fuel assembly lay out. Figure4 shows the detail structure of fuel pin and guide tube associated in the assembly. The geometry of modeling is accurately based on the dimension numbers and structure given in Table3, Figure3 and4 except that some hardware (e.g. grid spacers) in the fuel assembly is ignored. For the fuel rod end hardware, there are two methods can be adopted, mock up the hardware as a region of smeared water and stainless steel or use the rough nuclides density in Atoms/barn-cm. The latter option is chosen in this paper (Anne Barreau, 2006). This is presented in detail in Material specification unit.

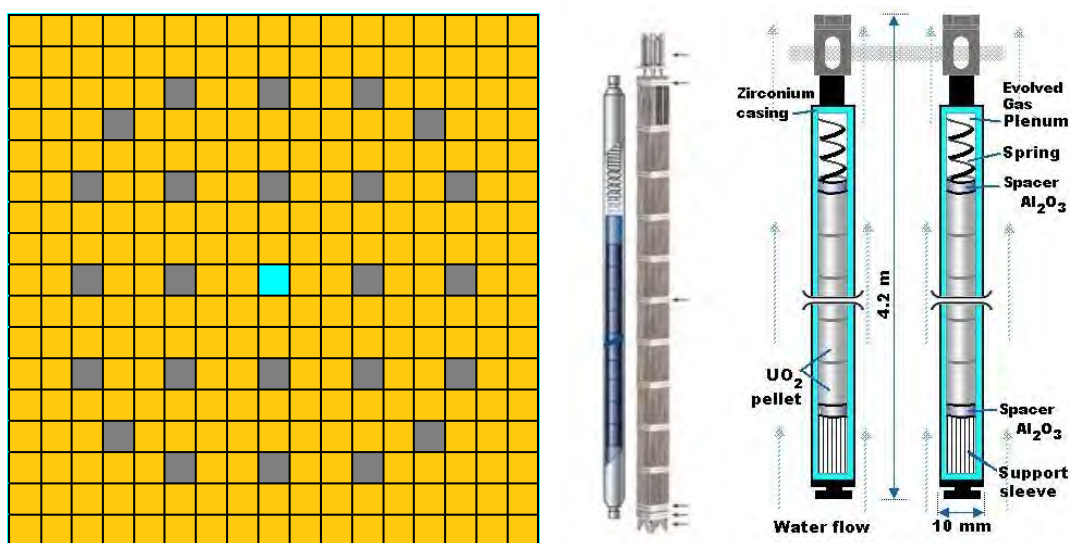


Figure 3. Typical PWR Fuel assembly lay out (left) and typical PWR fuel rod (right)

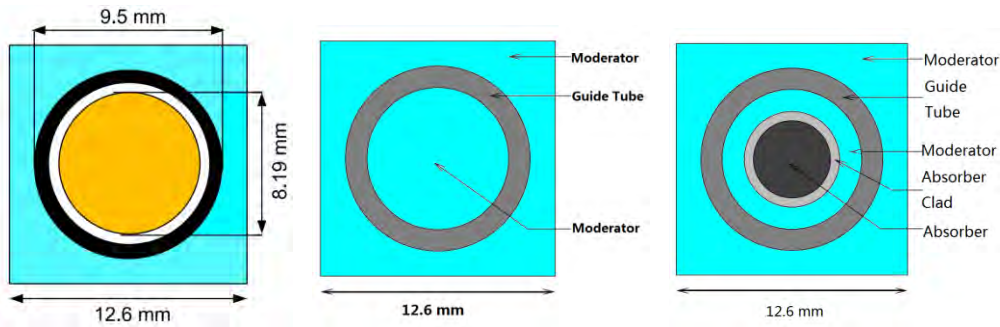


Figure 4. Cutaway views of a PWR fuel pin and a guide tube with/without control rod

Table 3. Fuel assembly detailed geometrical description

Parameter	Dimension or Number for modeling
Total Fuel assembly	21.42 *21.42*409.2(cm)
Matrix	17*17
No. of fuel rods	264
No. of control rods/guide tube	25
Guide tube Inner radius	0.573 cm
Guide tube Outer radius	0.613 cm
Absorber clad Outer radius	0.486 cm
Absorber (AIC) radius	0.436 cm
fuel pellet radius	0.4095 cm
Fuel Cladding outside radius	0.475 cm
Fuel Cladding Inner radius	0.418 cm
Pitch	1.26 cm
Active fuel length (fuel/G.T)	365.7 cm
End plug	1.75 cm
Upper hardware	30.0 cm
Lower hardware	10.0 cm
Upper water region	7.0 cm
Lower water region	0.0 cm

Sources from: M.Q. Huda et al., Design studies of a typical PWR core using advanced computational tools and techniques

4.2.2. Multi Element Bottle (MEB)

MEBs are stainless steel tubes with a welded base, removable lid, internal grid for criticality control or holding fuel and integrated pipes for flushing, venting and ullaging. They are used both in spent fuel transport flask and for interim fuel storage. There are several benefits of using MEBs, for example, preventing crud migration within wet transport casks, reducing the dose rate during operation, reducing dose in pool water activity levels, minimized volume of contaminated water to be handled and faster flask turnarounds.etc (IAEA, 1997). The MEB discussed in this paper is fit for flask such as Pollux and Excellox, both normal and borated water can be adopt but it is only certified for storage and transport of intact fuel assemblies (NDA, 2010).

The list below gives main geometry feature of MEB for modeling (G. Ellcock et al., 1981).

1. The MEB is comprised of a one end closed tube vessel (1) made of stainless steel
2. The MEB lid (2) is a removable stainless steel disk with bolts, lifting pintles and valves mounted on it and secured to a flange at one end of the vessel.
3. Valves (5) are used for water level adjustment and flushing operations during normal fuel handing operations.
4. The whole vessel (1) comprises two chambers: Fuel chamber (7) and ullage chamber (10).
5. Fuel chamber (7) contains a number of separate compartments (8)
6. The separate compartments (8) are made of boronated stainless steel to receive nuclear fuel element assemblies. They are supported at one end by the flange (3) and by support plate intermediate the lid and the plate (6) and can be arranged both in the form of a cruciform and encompassment. (Figure5.)
7. The ullage chamber (10) is designed as an additional safety precaution to accommodate the expansion of the water and thereby largely relieve the pressure in both the fuel chamber of MEB and flask cave in the event of an accident resulting in fire.

8. Bursting discs are mounted in two positions inside the vessel. One is in the lid which will break at a certain predetermined pressure to allow the water in the bottle to mix with the water in the flask. The other one is in plate (11) at bottom of the vessel which will rupture or collapse at higher pressure and release the additional ullage in chamber (10) to reduce the overall pressure within the flask and the MEB. The bursting disc in plate (11) is protected by disc (12) and supported by leg (14).

Table 4. Geometry description of the MEB in Modeling

MEB component	NO. in Figure	Dimension for modeling (cm)
Total Vessel	1	45.5(outer)*468 (height)*2(thickness)
Removable lid	2	45.5 (dia)*3(thickness)
Flange	3	Ignored in modeling
Bolts	4	Ignored in modeling
Valves	5	Ignored in modeling
Fixed plate	6, 11	1 cm thickness
Fuel chamber	7	43.5 (dia)*450 (height)
Separate compartment	8	22.5*22.5*450*7 (assembly NO.)
Bounded sheet	9	22.5*22.5(inner) 23.5*23.5 (outer)
Ullage chamber	10	43.5 (dia)*10 (height)
Bursting disc	12	Ignored in modeling
Bursting disc cover	13	Ignored in modeling
Supporting leg	14	Ignored in modeling
Lifting pintle	26	Ignored in modeling
Lifting keyways	27	Ignored in modeling

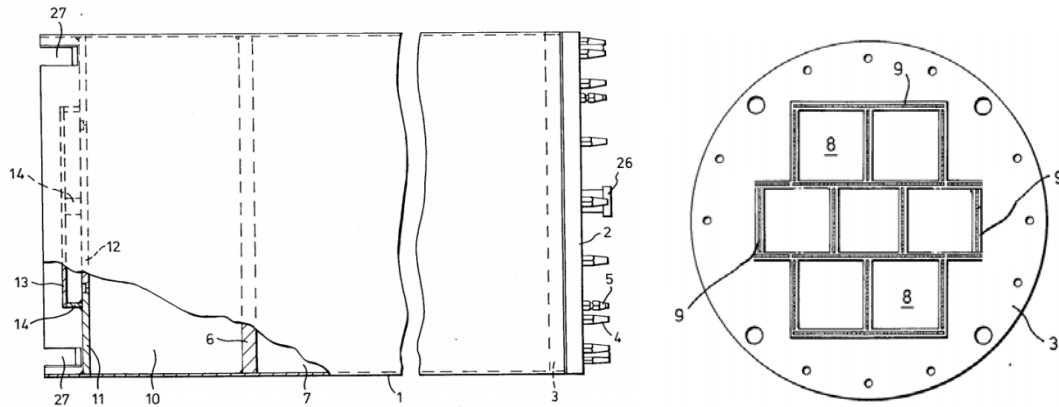


Figure 5. MEB detail illustration

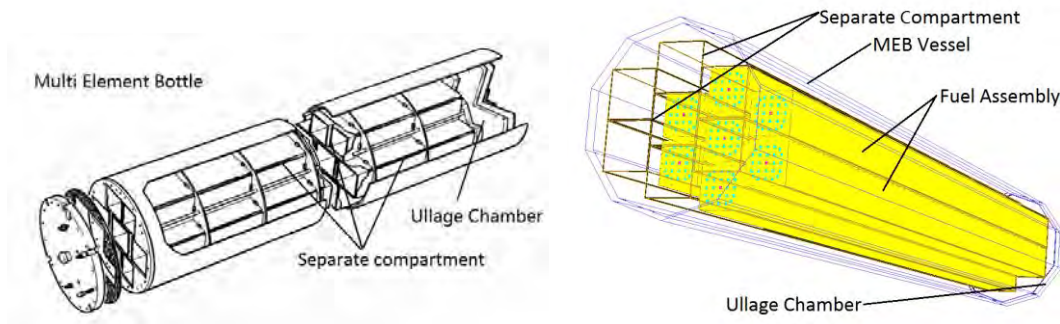


Figure 6. Comparison of real and modeled MEB

Table 4 gives the geometry parameters of the MEB in Modeling as geometry feature described above. Figure 6 is a comparison of real and modeled MEB illustration. Some of the dimension and materials are assumed in the modeling due to technical security reasons.

4.2.3. Excellox 7 flask

As mentioned above, Excellox 7 is chosen for geometry modeling and shielding calculation in this research article. The detailed dimension of Excellox 7 is given in Table 5. Some of the dimensions are also assumed. The main geometry features of Excellox 7 flask are given below (R. Gowing et al., 1994).

1. A monolithic body which is a one end closed tube made of forged carbon steel shell with about 32.5 cm thick wall and stainless steel cladding overlaid on both

the internal and outer surfaces around it providing all the gamma shielding (replaced the thinner containment shell with a separate lead-in-steel liner for gamma shielding as used in the Excellox 4 flask designs).

2. Flask lid is made of stainless steel and is bolted directly into the thick forged carbon steel shell (gamma shielding), which improves the strength of the flask and protection of the lid joint.
3. Discarding the lead liner makes the flask easier to decontaminate and maintained
4. The snug fit of the multi element bottle (MEB) or inner fuel container transfers the ullage to the space between MEB and flask lid when the flask is standing vertical. This enables the water level valve to be placed securely under the protection of the lid shock absorber.
5. Balsa-in-steel shock absorbers enclose the lid and base ends and all penetrations
6. Three pairs of lifting trunnions are designed for flask transportation. Particularly the pair of lifting trunnions among the cooling fins are designed to fit BNFL's THORP receipt facility.
7. Neutron shielding material (boroned silicon rubber) is filled in the gaps of the external circumferential cooling fins. (Compare with that in the Excellox 4 designed a water annulus outside a lead linear provides neutron shielding).
8. The cylindrical surfaces at each end, the base and the locations for the three pairs of trunnions are not be covered by cooling fins.
9. These are 12 mm thick annular plates set at 50 mm pitch along the flask, which 85 made of carbon steel provided as cooling surface and 2 in stainless steel at each end closed by stainless steel hoops to form bagging rings. Pairs of holes in all fins except the end ones were also drilled to provide an escape for the off-gases, especially in the event of a fire accident.
10. Tungsten alloy shielding block is used as compensation at orifice.

Table 5. Excellox 7 flask dimension for modeling

Parameter	Dimension for modeling (cm)
Overall length with shock absorber	609.5
Overall length	562
Cavity length	472.5
Body radius	106.5
Cavity radius	46.5
Lift to secondary Trunnion distance	75.5
Upper trunnion height (to ground)	462.2
Lower trunnion height (to ground)	29
Ullage in flask when stand vertically	4.5 (height)
Assumption of dimensions	
Shock absorber	115(diameter)*56.25 (height)
Neutron shield material thickness	14
Gamma shielding material thickness	32.5
MEB(outer diameter*height)	45.5*468
Lid(dia*h)	*32.5(height)*79 (dia)
Lifting pintle	29.75 (height)*6.5-10 (dia)
Lifting trunnion	21 (height)* 5.5-10 (dia)
secondary trunnion (THORP)	13.5 (height)* 5.5-10 (dia)
cooling fins height	27.5
space between cooling fins	5 cm
cooling fins thickness	1 cm
bagging ring	Ignore in modeling
Drain /Ullage/ Vent orifice	Ignore in modeling

Data from: E. G. Nisbett et al., Steel Forgings, American Society for Testing and Materials

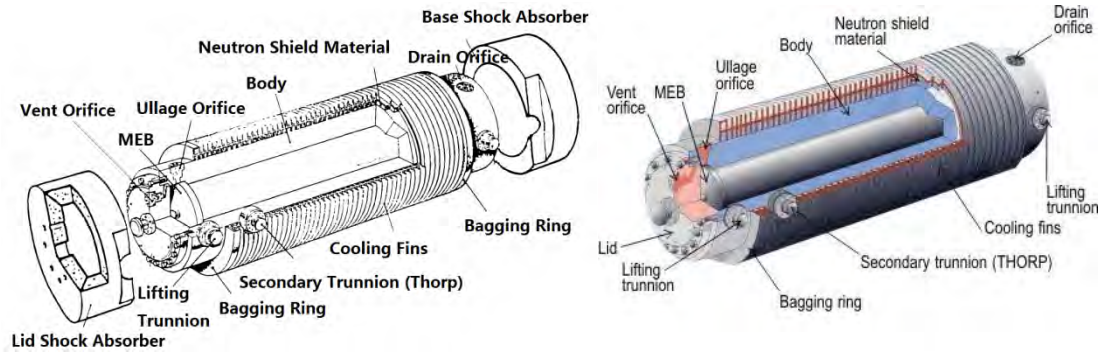


Figure 7. Excellox 7 spent fuel flask

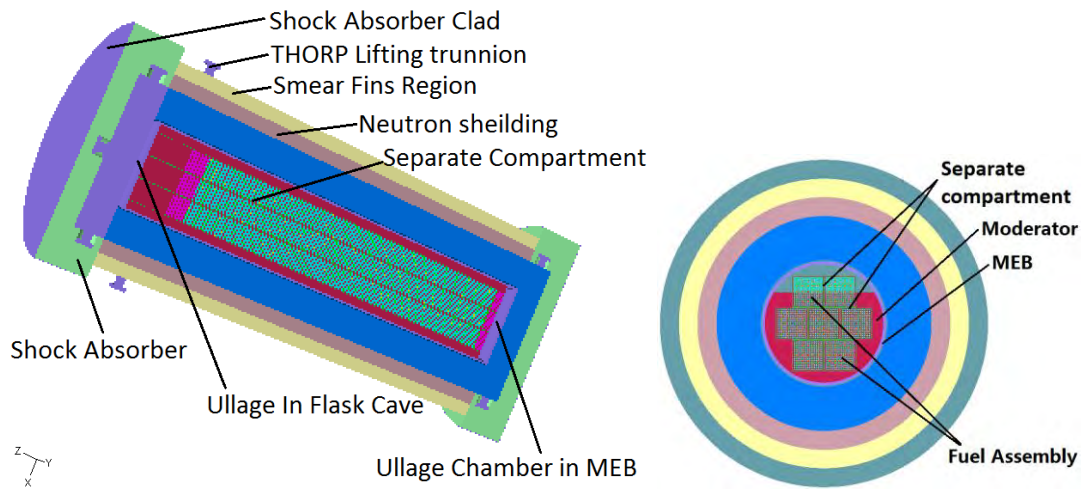


Figure 8. Excellox 7 flask global geometry in MCBEND model

4.3. Material specification

The material function in MCBEND 10 defines the chemical composition of material present in the problem. It allows material compositions to be defined in terms of the volume, weight, atoms proportions and atom density in atom/barn-cm. A concept of mixtures is introduced in order to increase the flexibility of defining material composition of various situations. For example, the smear region of cooling fins can be readily defined with the help of the concept of mixtures. To set up the material specification properly, particle type must be chosen to tell the module which cross section library is to be used. The number of material defined in this unit must equal or exceed the highest number that specified in material geometry function (Serco, 1994). In addition, the module also has the ability of taking account the temperature

influence between material and specific cross section. Normally, this unit must be included in any shielding calculation of MCBEND.

Table6 gives the detailed material description for modeling. There are totally 12 different material are specified in this model. These materials including all kind of the materials used in Excellox 7 flask component except these will greatly increase the complexity of modeling but has little influence on the result, such as drain/ullage/vent orifice, tungsten alloy shielding blocks, bursting disc, bolts and valves in MEB. It is wise to ignore these components in the modeling because they can largely slow down the calculation speed and take up too much CPU resources. Detailed modeling of cooling fins will take a lot of CPU time and obtain the result with little difference of calculating the volume fractions of air and smearing the cooling fins region. The details of each material in the model are listed in the table below including the material composition and density.

Table 6. Material description for modeling

Material In Model	Material composition	Density
Fuel Pellet Material M1	Irradiated PWR fuel composition See Table21.	No need
Fuel-Cladding Gap Material M2	Helium (Atoms) HE 1.00	1.786E-4
Fuel Cladding Material Upper And Lower End Plug Guide Tube M3	Zircaloy-4 (Number Density in Atoms/Born-cm ²) FE 1.383E-4 CR 7.073E-5 O 2.874E-4 ZR 3.956E-2	No need

Continued		
Upper And Lower Hard Wares M4	50% stainless steel, 50% H ₂ O (by volume) (Number Density in Atoms/Born-cm ²) CR 8.714E-03 MN 8.682E-04 FE 2.968E-02 NI 3.860E-03 H 3.338E-02 O 1.669E-02	No need
Moderator M5	Water/Boron Water (Atoms) H 2.00 O 1.00 B10 0.00018	0.79
Control Rods/ Absorber M6	Gd ₂ O ₃ (Atoms) GD 2.00 O 3.00	7.41
Absorber Clad Entire MEB Vessel Flask Lid Flask Lifting Pintle Shock Absorber Clad M7	Stainless Steel (Number Density in Atoms/Born-cm ²) CR 1.743E-02 MN 1.736E-03 FE 5.936E-02 NI 7.721E-03	No need

			Continued
Assembly Basket In MEB M8	Borated stainless steel (1 wt.% boron) (Number Density in Atoms/Born-cm ²) CR 1.691E-02 MN 1.684E-03 FE 5.758E-02 NI 7.489E-03 B10 7.836E-04 B11 3.181E-03		No need
Gamma Shielding Material M9	Carbon steel (Weight) FE 0.9926 C 0.002 MN 0.0045 P 0.0004 S 0.0005		7.872
Neutron Shielding Material M10	Boron-silicon rubber (Number Density in Atoms/Born-cm ²) H 4.49E-2 B 9.40E-4		No need
Smeared Region Of Cooling Fins M11	30% stainless steel MN 0.01 NI 0.09 CR 0.175 FE 0.725	70% air (by volume) (Weight) N 7.65172E-1 O 2.34828E-1	7.905 1.225E-3
Shock Absorber M12	Balsa Wood (Vol.) H 0.06545 O 0.40175 C 0.5328		0.64

All the material composition and density are fixed with time if flask and fuel assembly type is specified. For material one, the spent fuel, further discussion is necessary because it is the priority research areas where the radiation come from and also because its complexity due to material composition variation with time.

For a typical fresh PWR fuel, only U234, U235, U236, U238, O16 exist in the composition. As a reactor operates, the composition of the fuel changes due to fission (depletes U and generates fission products), neutron capture, (n,γ) , other neutron reactions: (n,p) , $(n,2n)$, (n, α) .etc and radioactive decay (α , β). The reaction products include fission products, actinides and activation products. 30 to 40 different chemical species, each of them with a range of isotopes, in total two to three hundreds of different radionuclide are created as fission products. All of them are beta or gamma emitters with half-lives vary from less than 1 second to 1000 years. Fortunately, not all FPs are important, some of them have very short half-lives that they decay to zero before loaded in spent fuel flask. Actinides are actinium and the 14 elements to its left in the periodic table (uranium and plutonium are actinides). Most actinides are produced via neutron capture on uranium isotopes and followed by beta decay. The presence of actinides in spent fuel reduces the reactivity and meanwhile increases the activity. Most actinides are alpha emitters and many of them are very long lived (million years). As a result actinides are important in shielding calculation although some of them are of trace amounts. Activation products (APs) are created by neutron capture in clad and structural materials. The most significant are C14, Fe55, Ni63 and Co60 (stainless steel clad includes Co). APs are ignored in the modeling due to its small amount and not significant activity.

All reaction products can be classified as fission products and activation products which are responsible for decay heat (mainly from α , β), radiation emission (mainly γ), and potential contamination. As a result, inventory calculations are important to

obtain relatively accurate spent fuel composition for either decay heat estimation or shielding calculation.

A number of computer codes have been created which can be used to solve the fuel inventory equation including ORIGEN (Oak Ridge, US), CINDER (Los Alamos, US) and FISPIN (UK). In this paper, inventory calculation results obtained from reference ([S. P. Cerne et al., 1987](#)) are directly used for shielding calculation. Detailed spent fuel compositions are listed in Table 21 of Appendix 4.

After irradiation, 96 wt% Uranium with average enrichment about 1 wt %, 3 wt% fission Products, 1 wt % plutonium (about 70% fissile crucial for criticality safety), plus about 0.1 wt% other actinides and activation Products constitute the typical PWR spent fuel composition. The composition varies with several parameters including:

1. Fuel type (AGR, PWR, MOX or TRU.etc)
2. Reactor type (thermal or fast reactor)
3. Operation histories of the assemblies
4. Fuel enrichment
5. Fuel burn up
6. Cooling time after irradiation in reactor
7. Control rod influence during irradiation.(CR in or out during irradiation)

4.4. Energy Data Unit

The energy data unit form the main part of the physics function. Items gathered into this unit are strongly inter-related within the code ([Serco, 1994](#)). The physics function is used to define the particle type (neutron, photon or electron) and calculation type, the time of birth of the source particle, the speed of the source particles and energy group structure for splitting (importance function) or scoring and source module used to define source (energy distribution for simple source). This unit must always be included in an executable MCBEND program ([Serco, 1994](#)). For the flask shielding

modeling in this paper, the unified source module are selected (see the example input given below).

```
*****  
BEGIN ENERGY DATA  
  
GAMMA  
SPLITTING GROUPS 17 4.0 3.0 2.5 2.0 1.66 1.44 1.22 1.0 0.8  
0.6 0.511 0.4 0.3 0.2 0.1 0.05 0.02 0.01  
SCORING GROUPS 8 4.0 3.0 2.0 1.5 1.0 0.5 0.2 0.1 0.01  
UNIFIED SOURCE  
END  
*****
```

In the above example, an energy group scheme for an important map of 17 energy groups are adopted which gives the energy splitting data for Splitting/Russian roulette variation reduction technology. 8 energy group boundaries for scoring are also included.

4.5. Unified Source Data

This unit defines the starting parameters of the particles emitted from the source including the starting position, initial direction, initial energy and weight of the source particle. It must be included if a ‘Unified Source’ has been selected in the Energy Data Unit. Historically, there are two methods of modeling a source in MCBEND. One is simple source which offers simple geometry but with a sophisticated range of spectra and weighting options. The other one is complex source which offers a more general geometry with relatively simple energy and weight distributions. In MCBEND 10, these two modeling options are superseded together by ‘Unified Source’ (See Energy Data Unit) ([Serco, 1994](#)).

In the Unified Source module, surface, point and lines source can be modeled. Different source build-in-code spectra are available. Automatic source weighting can also be provided by the importance map. For a point source emitting photons/neutrons

at a rate Q per second in all directions, the flux (ϕ) at distance 'R' is the number of photons/neutrons passing through unit area (m^2) per second (s^{-1}), so the inverse square law obtained:

$$\Phi = \frac{Q}{4\pi R^2} \text{ Or } D = \frac{ME}{6R^2} \dots\dots\dots(1)$$

Where,

D is the dose rate in $\mu\text{Sv}/\text{hour}$

M is the activity of the source in MBq

E is the total gamma energy per Bq in MeV

R is the source/detector distance in m

The source function also include collision source data and angular data, which define the production of secondary gamma rays from neutron collision files and provide special angular weight options respectively. In our case, secondary gamma rays and angular weighting distribution are not taking into consideration. The source modeling input files are given below:

```

*****
BEGIN UNIFIED SOURCE DATA
GEOMETRY
FGBODY x2 1 IN PART 1
ENERGY LINES
3.5 2.9 2.5 2.2 1.55 1.0 0.76 0.51 0.27
INTENSITY BODY x2
COMPONENT ENERGY
1.3E4 6.4E5 3.0E6 7.6E7 1.7E8
4.5E8 5.9E8 7.0E9 7.2E8
WEIGHTING AUTOMATIC
END
*****

```

This unified source is defined as a general source that non-separable function of space, energy and direction are applied. The source is defined reference to a part in the FG model. In our case, the first body in part one is modeled as the active fuel rod and replicated 4913 times (17x17x7) for 7 fuel assemblies. A set of line energies for production of sources and source intensity over a subset of possible energy dimension are also defined. For the weighting function, 'WEIGHTING AUTOMATIC' specifies that the important function used for splitting will also be used for the source weighting.

4.6. Variance Reduction Technique

Variance reduction technique is a part of the acceleration function. It is used to speed up the calculation or obtain more acceptable results. In a realistic shielding problem, up to 10^6 of attenuation factor may be involved due to the thick gamma and neutron shielding materials associated to a spent fuel flask. Typically, at least 100 particles must reach the scoring region to provide acceptable results. Thus, a direct analogue Monte Carlo calculation would involve simulating about 10^8 or even more particles. This will take too much CPU time and much CPU resources are wasted on tracking the 10^6 particles that cannot reach the score region and contribute to results. With the help of VR, efforts are only concentrated on those particles which contribute to the score. The Importance Map Unit is another part of acceleration function. 'IMPORTANCE' is a measure of the expected contribution to the score as a function of space, energy and direction (Serco, 1994).

One often used VR technique is Splitting/Russian Roulette(S/R). In this method, S/R planes are set with certain distance corresponding to the splitting mesh that employed in the 'SPLITTING GEOMETRY' unit. Particles heading towards the detector are split into multiple fragments with higher importance but less weight when they cross the S/R planes. Inversely, fragments move depart from the detector play Russian roulette at the S/R planes and the survivors pass through planes with higher weight but less importance.

In order to set up the S/R, an importance mesh must be defined to hold the importance map. The splitting (importance) mesh is independent of the material geometry and normally covers all the material geometry. There are two options to produce the splitting mesh, chose the splitting mesh intervals by users or adopt the automatic meshing function. When the splitting mesh is ready, the importance map values can be calculated using MAGIC adjoint diffusion calculation after defining FG geometric model and TARGET mesh region and response for acceleration. An example of the splitting mesh of Excellox 7 flask is given in Figure. (The corresponding input data can be found in Appendix 1)

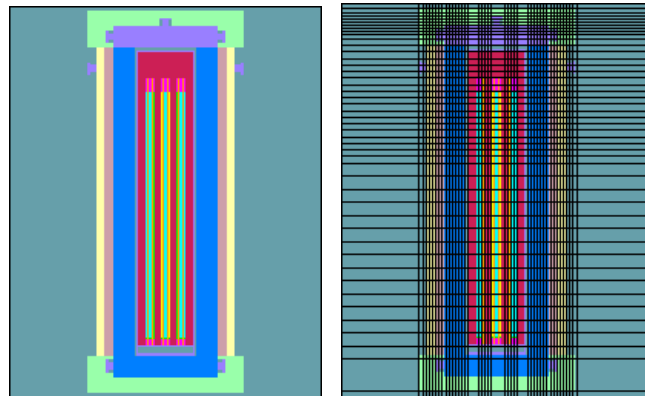


Figure 9. Excellox 7 flask with and without splitting mesh

```

*****
BEGIN IMPORTANCE MAP
CALCULATE
TARGETS 2
PART 24 ZONES 12 13
STRENGTHS 0.3 0.7
END
*****

```

In this input data, the particles are accelerated towards 2 detectors, in zone 12 and zone 13 of part 24 with weight of 0.3 and 0.7 respectively (zone 13 is more significant

than zone 12). The key word ‘CALCULATE’ indicate that the importance values are calculated by code using MAGIC adjoint diffusion calculation methods.

4.7. Scoring Function

MCBEND provide two options of scoring, one in FG region and the other one in splitting meshes. If scoring in FG region, suitable extra FG regions may have to be defined. Scoring in the splitting mesh can be useful for observing the variation of the results through thick material layers without having to introduce extra complexity in the geometry model (Serco, 1994).

The most important scored quantities are flux, responses, and sensitivity. Particles fluxes are scored in specified energy groups. The definition of scalar fluxes is shown in the expression below:

$$\phi_g = \int_{E_{g-1}}^{E_g} \int_{4\pi} N(E, \underline{\Omega}) d\underline{\Omega} dE$$

Response is the specified result of folding in supplied response cross sections included in the code with the estimated flux (Serco, 1994). It gives the gamma, neutron or other dose rate of detectors. The expression of response is:

$$R = \int_0^{\infty} \phi(E) \rho(E) dE$$

The sensitivities are the variation of flux or response due to the change of basic nuclear data cross section. Sensitivity of fluxes and responses to material cross sections can be scored. Both first and second order sensitivities are available (N.R.Smith et al., 2000). These may be used to calculate uncertainties in the result due to data uncertainties or due to uncertainties or perturbations of physical parameters such as density, porosity .etc. A geometrical sensitivity option also exists, which allows the effect of geometrical uncertainties or perturbations to be determined

(E.Shuttleworth, 2000). The expressions of flux and response sensitivities are given below.

$$\frac{\sigma}{R} \frac{\partial R}{\partial \sigma} = \frac{\sigma}{\phi_g} \frac{\partial \phi_g}{\partial \sigma}$$

There are two methods for estimating the fluxes, collision density method in which point flux estimator at a point is used and track length method which is more commonly used (Serco, 1994) in the track length method, the flux is calculated through a track length estimator, all the particles tracks within the score region are collected, and all the contributions are summed up, and then divided by the score region volume (S. Portugal, 2002). The estimate calculation expression is:

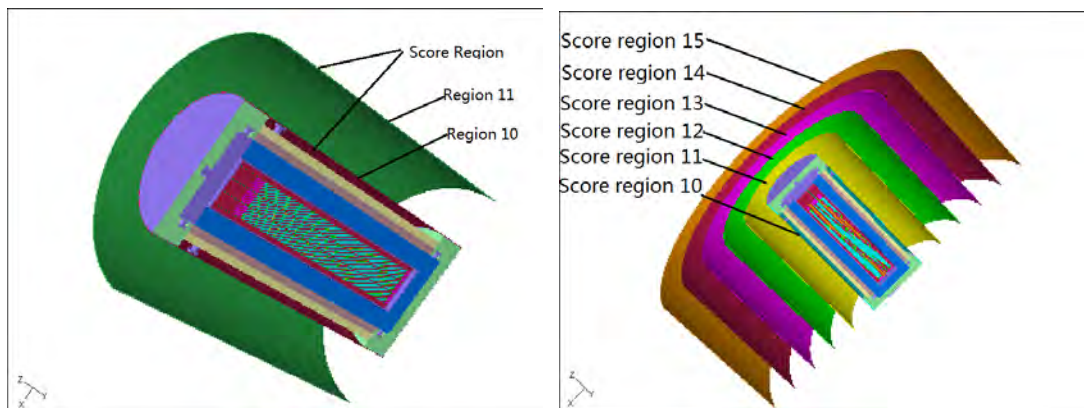
$$\bar{\phi} = \frac{S \sum X_i}{PV}$$

Where,

S= total source strength

P=particles started

X_i=the ith simulated particle have track length in the score region.



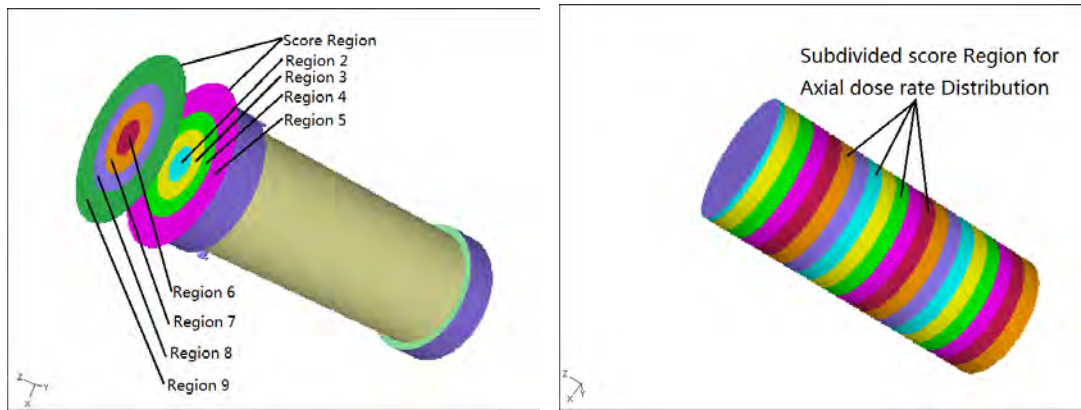


Figure 10. Illustration of score region in modeling

In our flask model case, the former option is chosen. Figure10 shows the different score region of various functions. The upper left one is used for normal side face scoring with two distances (14 cm and 1m), the upper right defines 6 score region with different distance to indicate the dose rate variation with distance in side face of flask. The lower two snapshots in Figure10 are the scoring regions with four subdivided concentric O-rings at the shock absorber surface and 1 meter away from the shock absorber surface and well-proportioned subdivided scoring regions along the axial of the flask. They help to calculate the axial and radius distribution of dose rate respectively. Scoring data, response data, sensitivity data, geometry sensitivity data .etc are included in the scoring function. In our flask model case, only the former two units are taken into consideration. The input data of them are given below.

```

*****
BEGIN SCORING DATA
FLUX ALL
RESPONSES
PART 24 SOME 2 3 4 5 6 7 8 9 10 11
END
*****

```

```
*****  
BEGIN RESPONSE DATA  
FUNCTION GAMMA DOSE  
END  
*****
```

5. MCBEND Result

The flag 'qx' in the MCBEND output data indicate errors of the program. In the flask shielding code programmed in this paper, zero volumes are found due to the use of array geometry but will disappear if cluster geometry is used in place of the array geometry with a price that a great complexity of input data in material geometry unit will be introduced. In other words, zones associated with array part are not corresponding to scoring. Thus, the warning show in Figure11 is ignored in our calculation.

```
qx: WARNING: Zero or negative volumes found.  
qx  Inspect the FG printout to ensure that these do not  
qx  correspond to scoring regions.
```

Figure 11. A warning in MCBEND output

5.1. Neutron Dose Rate Varying With the Shielding Thickness

The major part of the neutron source is produced from spontaneous fission of the heavy nuclides. A significant part of the neutron source is also produced from ^{17}O (alpha, n) and ^{18}O (alpha, n) reactions in the UO_2 in the spent fuel (O. W. Hermann et al., 1998). Neutrons from the sources in spent fuel are usually born with significant energy and can pass fairly easily through many materials and neutron particles cannot be sufficiently shielded by typical high mass density material due to their electrically neutral property. In other words, neutrons do not interact with the electrons of materials through which they pass like photons but interact with the nuclei of the

atoms (G. Chabot, 2011). For this reason, the neutron attenuation mechanism in a typical shielding material is mostly relevant to the neutron slow down process by collision with other nucleus. And after neutrons have been slowed down they finally disappear by being absorbed into the nuclei of materials. A non dimensional unit called Average Lethargy is introduced in order to measure average energy loss due to one collision process. The expression of Average Lethargy is:

$$\xi = 1 + \frac{(A-1)^2}{2A} \ln\left(\frac{A-1}{A+1}\right)$$

Where, A is the atomic mass of the collision nuclei.

From this formula we can readily know that light nuclei are better for neutron shielding because the neutrons transfer larger amounts of their energy to the light nuclei through each elastic collision. The closer in mass the nucleus is to that of the neutron, the more efficient is the energy transfer. Hydrogen is the closest nuclei in mass to the neutron and has a quiet large and even cross section (left snapshot in Figure12.) of elastic scattering so it is the best chose for slowing down neutron. In addition, hydrogen also has a moderate propensity for absorbing slow neutrons. (right snapshot in Figure12.) Thus, material with high hydrogen content is desirable for shielding energetic neutrons (G. Chabot, 2011).

Examples of good and cheap neutron shields are water, many plastics and concrete which are all high hydrogen content shielding material. However, the process of absorbing slow neutrons of hydrogen leads to excitation of the nucleus and emission of the excitation energy as a rather high-energy gamma ray which may also require shielding (G. Chabot, 2011). This is the so called secondary gamma rays which are not discussed in this paper. In order to reduce the secondary gamma ray production, Excellox 7 flask adopt boron silicon rubber as the neutron shielding material in which boron, particularly the isotope ^{10}B , undergoes a nuclear reaction when it captures a neutron and produces an alpha particle instead of photons (G. Chabot, 2011).

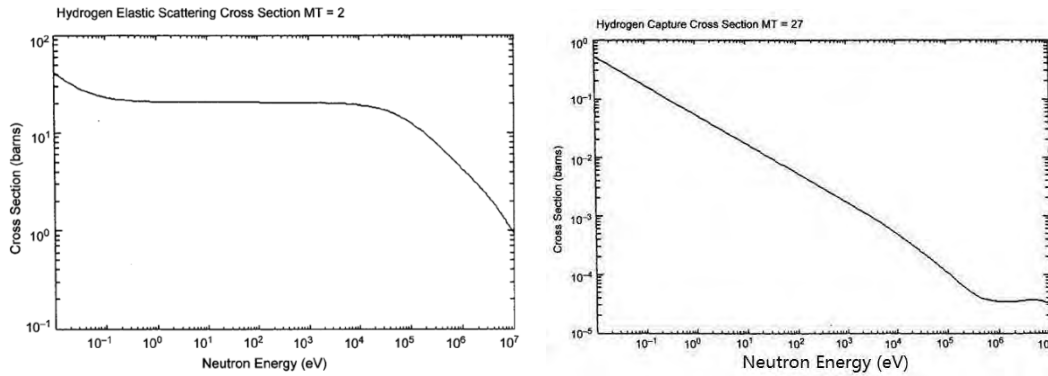


Figure 12. Elastic and radioactive capture cross section for ^1H . (Sources From: <http://www.dne.bnl.gov/CoN/index.html>.)

In order to help to understand the neutron attenuation mechanism, the neutron attenuation formula is derived below. Assume the neutron source is small enough. Consider a bunch of neutrons with intensity I bombard a very thin layer of neutron shielding material dx with area of 1 cm^2 , the experiment result gives:

$$dI \propto -INdx$$

Where N is the atom density of shielding material. Or

$$dI = -\sigma INdx$$

Where σ is the microscopic cross-section.

Integrate with a boundary condition of $I(0) = I_0$, we get:

$$I(x) = I_0 e^{-\Sigma_T x} \dots\dots(2)$$

Where Σ_T is the total macroscopic cross-section which indicates the probability of neutron interacting with nuclei when it passes through a shielding material per unit length. The detailed form is:

$$\Sigma_T = \Sigma_{scatter} + \Sigma_{rad-capture} + \Sigma_{fission} + \dots$$

Because the intensity is proportional to the dose rate, so we have:

$$D(x) = D_0 e^{-\Sigma_T x}$$

Table 7. Excellox 7 flask side face neutron dose rate varying with Neutron shielding thickness¹

Thickness	Dose at 14cm from cooling fins	COEF of VAR	Dose at 1 m from cooling fins	COEF of VAR
4	1.709E+01	0.2	7.760E+00	0.2
6	1.046E+01	0.2	4.750E+00	0.2
8	6.564E+00	0.2	2.982E+00	0.2
10	4.207E+00	0.2	1.910E+00	0.2
12	2.743E+00	0.2	1.246E+00	0.2
14	1.822E+00	0.2	8.267E-01	0.2
16	1.233E+00	0.2	5.603E-01	0.2
18	8.445E-01	0.2	3.837E-01	0.2
20	5.937E-01	0.2	2.695E-01	0.2
22	4.229E-01	0.2	1.920E-01	0.2
24	3.027E-01	0.2	1.375E-01	0.2

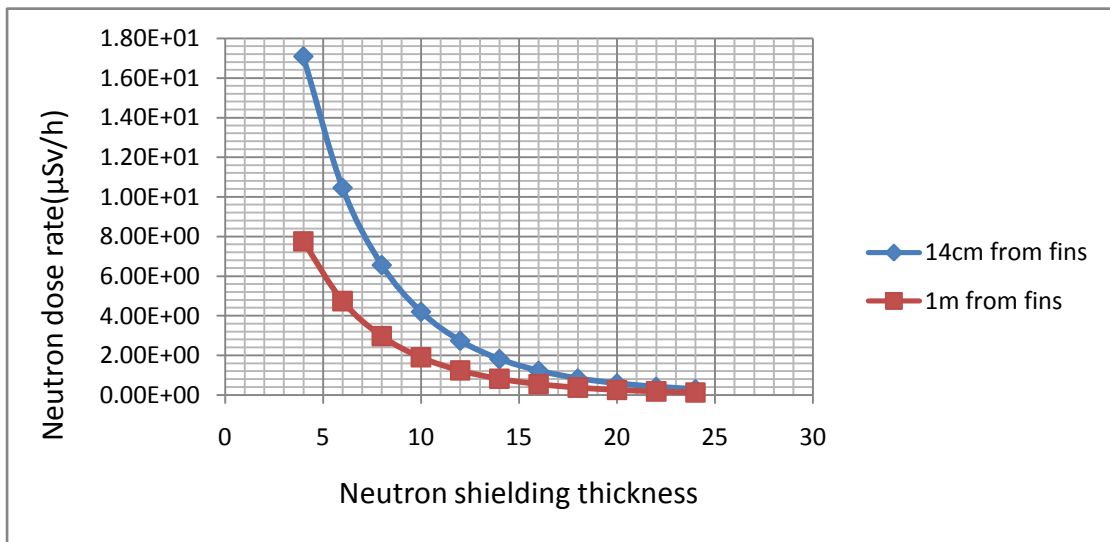


Figure 13. Neutron dose rate varying with Neutron shielding thickness in normal coordinate

¹ Detailed data with Sample numbers and variations are given in Table from 28 and 29 in Appendix 4.

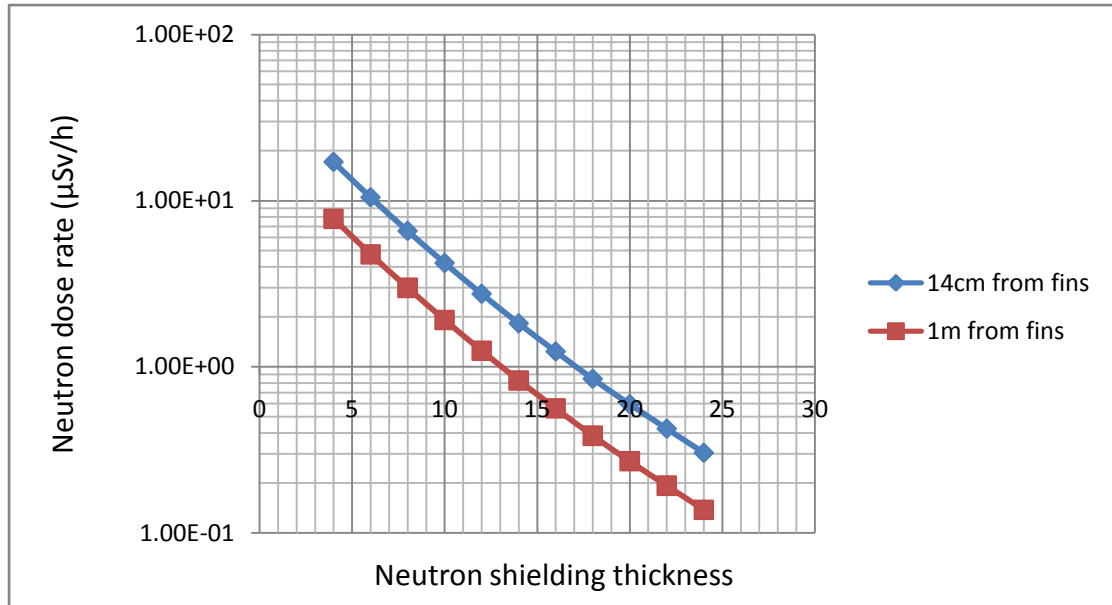


Figure 14. Neutron dose rate attenuated with Neutron shielding thickness in logarithmic coordinate

Table7 gives the calculation result with COEF of VAR of 0.2% scored 14 cm and 1m from the cooling fins around the flask. Figure14 indicate that our calculation result is close to this theoretical derivation but not exactly follow the exponential relationship. This is because that the complicated varying neutron cross-section respect to neutron energy which can't be meticulously modeled plus the non-point source effect. It is notes that the neutron dose rate attenuated close to zero when the shielding thickness is about 25 cm. In other words, 25 cm thick neutron shielding material is sufficient and there is no further requirement for more shielding thickness. Take the dose rate scored 14 cm from the cooling fins, the Attenuation shielding formula can be obtained through Eviews by using Least Square Method:

The Fitting result is: $LNY = 3.50282116931 - 0.201001415401 * X$, in normal coordinate axes:

$$D(x) = 33.209e^{-0.2010x}$$

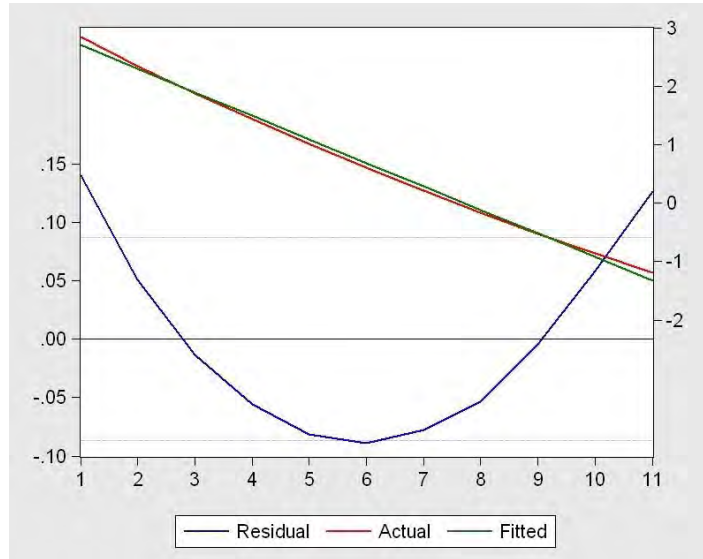


Figure 15. Eviews fitting result of neutron dose rate variation

This fitted result has a good agreement with the actual MCBEND calculation result with a residual (error) of range between -0.10 and 0.15. Another important physical quantity in shielding calculation called mean free path which is the average distance of a penetrating particle travels in the absorber before interacting is derived below. Deforming equation (2) to:

$$e^{-\Sigma_T x} = \frac{I(x)}{I_0}$$

$e^{-\Sigma_T x}$ is the ratio of non-interact neutrons pass through a length of x to the incident neutrons. Consider a neutron that does not have any interaction during the penetrating process in a shielding material of thickness of x, but interact with nuclei in a thin layer having a thickness of dx, according to the law of the probability of two independent random events occur at the same time, the probability of this process is:

$$e^{-\Sigma_T x} \times (\Sigma_T dx)$$

The average distance of a neutron traveling in the absorber before its first interaction is the so called mean free path (λ). It is the reciprocal of the macroscopic cross section $1/\Sigma_T$.

$$\lambda = \int_0^{\infty} x e^{-\Sigma_T x} \Sigma_T dx = \frac{1}{\Sigma_T}$$

In our case,

$$\lambda = \frac{1}{\Sigma_T} = \frac{M}{\sigma_T \rho N_A} = \frac{1}{0.2010} = 4.975 \text{ cm} \dots \dots (3)$$

From Equation (3) we know, for incident neutron with certain energy, the mean free path only relevant to the property of the shielding material (σ_T and M relevant to the material kinds, ρ is the density of this material and N_A is Avogadro constant). Excellox 7 adopts boron silicon rubber as neutron shielding material. Equation (3) tells that, averagely, neutrons interaction (including scattering, fission, radioactive capture.etc) occurs each time when it travelling 4.975 cm in boron silicon rubber.

In addition, HVT (Half Value Thickness) is also introduced to express the attenuation of dose rate in a shielding material. The Half Value Thickness which depends on the energy of radioactive particles indicates the shielding ability of a specified material.

$$HTV = \frac{\ln 2}{\Sigma_T} = \frac{\ln 2}{0.2010} = 3.45 \text{ (cm)}$$

Neutron intensity or dose attenuated to 50% of the original value when they pass through every 3.45 cm in boron silicon rubber. As we discussed before, almost all neutrons fall off after pass through 25cm thick boron silicon rubber. Thus, we prove that boron silicon rubber is a befitting neutron shielding material.

5.2. Gamma Dose Rate Varying With Shielding Thickness

Before the discussion of the calculation result, some basic understanding of gamma rays and its attenuation is required. First of all, gamma rays interact with matters by three major processes, photoelectric absorption, Compton scattering, and pair production. In the photoelectric absorption process, the gamma ray loses all of its energy in one interaction. The photon disappears and an energetic photo-electron is

ejected by the atom from one of its bound shells. The probability for this process depends very strongly on gamma-ray energy and atomic number Z^2 . This process predominates when the gamma energy is between 0 and a few hundred KeV. In Compton scattering, the incoming gamma ray photon is deflected through a certain angle and transfers part of its energy to the recoil electron. The probability for this process is weakly dependent on energy and atomic number. Pair production process is relatively unimportant for fissile material since it has a threshold above 1MeV.

Two kinds of attenuation coefficient for gamma attenuation are discussed in our case, linear attenuation coefficient and linear energy absorption attenuation coefficient. The linear attenuation coefficient can be considered as the fraction of photons that interact with the shielding medium per centimeter of shielding. This coefficient assumes that all photons that interact are removed and ignores Compton scatter and pair production photons (underestimates the shielded dose rate and the shielding required) (G. Chabot, 2001). The linear energy absorption attenuation coefficient can be considered the fraction of energy removed from the photons by the shielding medium per centimeter of shielding or the fraction of energy absorbed. This coefficient takes into account Compton scatter and pair production photons but it assumes that all scattered photons reach the detector (overestimates the shielded dose rate and the shielding required). It is also known as broad beam conditions because the source and detector are assumed to be uncollimated (G. Chabot, 2001).

A point gamma source of estimating dose rate by hand calculation method is introduced in order to help for understanding of gamma attenuation mechanism. Formula (1) in unified source unit gives the dose rate at the spent fuel assembly. Then the dose rate follows an exponential reduction within the shielding material. The expression of gamma attenuation for a point source is given below. (The derivation of this formula is similar with the neutron case so it is omitted here)

² G. Nelson and D. Rely, Gamma-Ray Interactions with Matter.

$$D(r) = \frac{ME}{6R^2} \times e^{-\mu x} \times B(E, \mu x)$$

Where,

D is the dose rate in $\mu\text{Sv}/\text{hour}$

M is the activity of the source in MBq

E is the total gamma energy per Bq in MeV

R is the source/detector distance in m

μ is the linear attenuation coefficient = $\ln 2/\text{HVT}$

B is the buildup factor

The buildup factor (usually written $B(E, \mu x)$) is a correction factor which depends on gamma energy, shield material, shielding thickness and the overall geometry.³ It provides a compromised result between the values obtained from linear attenuation coefficient and linear energy absorption attenuation coefficient. Buildup factors are usually measured experimentally – and then tabulated in terms of E and μx .⁴ With the help of buildup factor, dose rate for point source can be properly estimated. However, in real cases, the sources are always complicated in shape, intensity and with several energy groups. For extended sources, two approaches can be adopted. The first one is Monte Carlo techniques discussed in this paper. The other method is called ‘Point kernel numerical integration models’. In the latter model, the source is described as a lot of point sources. The model calculates the distance of each contributing dose point and the attenuation of any source material and shield layers. Then integrate over the whole point source. Commonly used software is called Micro-shield technique.

As we discussed in the gamma rays interact with matter mechanism in the first paragraph, photoelectric absorption strongly depends on gamma-ray energy. Thus, energy effect of the linear attenuation coefficient must be discussed. Figure16

³ John L Robertson, 2011. Nuclear Fuel Cycle, NTEC notes

⁴ John L Robertson, 2011. Nuclear Fuel Cycle, NTEC notes

illustrates exponential attenuation for three different gamma ray energies and shows that the transmission increases with increasing gamma ray energy and decreases with increasing absorber thickness.⁵

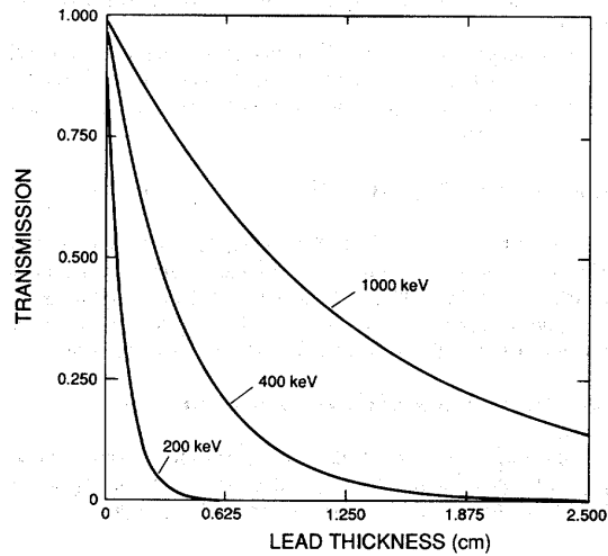


Figure 16. Different energy gamma-ray exponential attenuation in lead

The ratio D/D_0 is called the gamma ray transmission. Photoelectric absorption predominates when the gamma energy is between 0 and a few hundred KeV, thus, low energy photons have shorter mean free path which means more sharp attenuation (Figure16).

The results obtained from calculation of MCBEND take all the relevant factors into account including the buildup factor, different energy groups of source and extend shape of source. The Table8 below gives the calculation result of gamma dose rate varying with the gamma shielding thickness varying from 7.5 cm to 57.5 cm at four different score regions (14 cm from cooling fins, 1 m from cooling fins, shock absorber surface and 1 m away from the shock absorber lid). Figure17 associate the variation respect to shielding thickness for all the four cases.

⁵ G. Nelson and D. Rely, Gamma-Ray Interactions with Matter.

Table 8. Gamma dose rate varying with the gamma shielding thickness⁶

Thickness	14cm Dose Side Face	1m Dose Side Face	Sa Surface Dose ⁷	1m From Sa Surface Dose ⁸
7.5	7.812E+03	3.893E+03	5.960E+01	2.384E+01
12.5	1.336E+03	6.684E+02	1.468E+01	5.299E+00
17.5	2.481E+02	1.245E+02	3.477E+00	1.283E+00
22.5	4.826E+01	2.421E+01	7.977E-01	2.727E-01
27.5	9.594E+00	4.825E+00	1.935E-01	6.870E-02
32.5	1.943E+00	9.772E-01	4.564E-02	1.629E-02
37.5	3.989E-01	2.009E-01	1.006E-02	3.386E-03
42.5	8.359E-02	4.220E-02	2.482E-03	8.140E-04
47.5	1.765E-02	8.905E-03	4.113E-04	1.501E-04
52.5	3.684E-03	1.865E-03	8.415E-05	2.863E-05
57.5	7.727E-04	3.916E-04	1.880E-05	6.964E-06

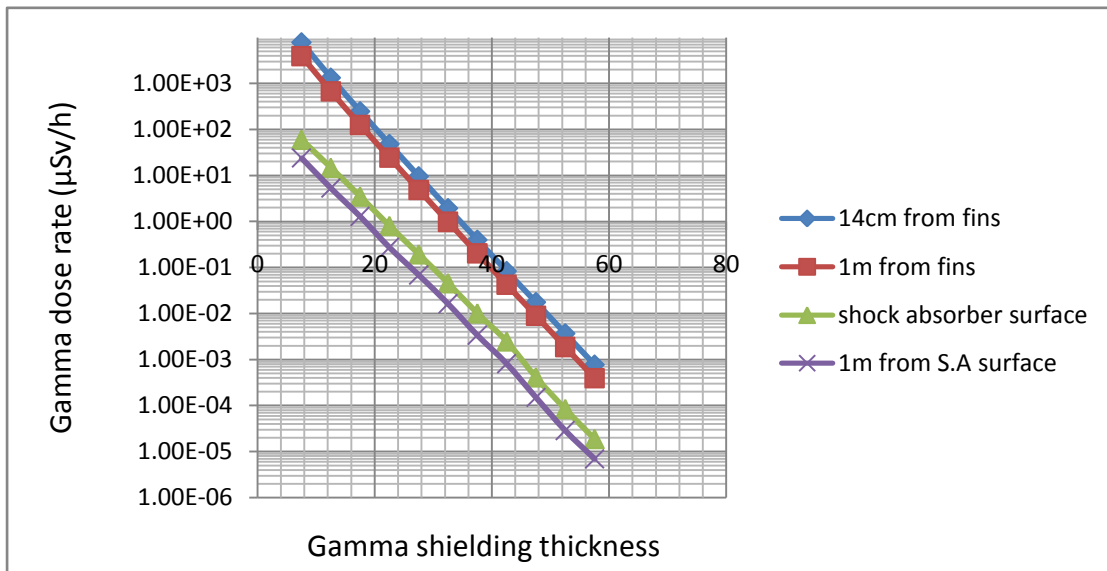


Figure 17. Gamma dose rate attenuated with Neutron shielding thickness in logarithmic coordinate

⁶ Detailed data with Samples and variations are given in Table from 24 to 27 in Appendix 4.

⁷ Gamma dose rate in score region 2.

⁸ Gamma dose rate in score region 6

The calculation results indicate a quite accurate exponential reduction within the shielding material. From Figure17 we know, dose rate at side face is higher than that at the area of shock absorber. The distance effect is also indicated that dose rates scored 1 meter away are slightly lower. Further discussion about the distance effect will be given in later chapter.

Take the dose rate scored 14 cm from the cooling fins, the Attenuation shielding formula for integral gamma energy of spent fuel and normal shape of the fuel assembly (extend source) in carbon steel (gamma shielding material used in Excellox 7 flask) can be obtained through Eviews by using Least Square Method:

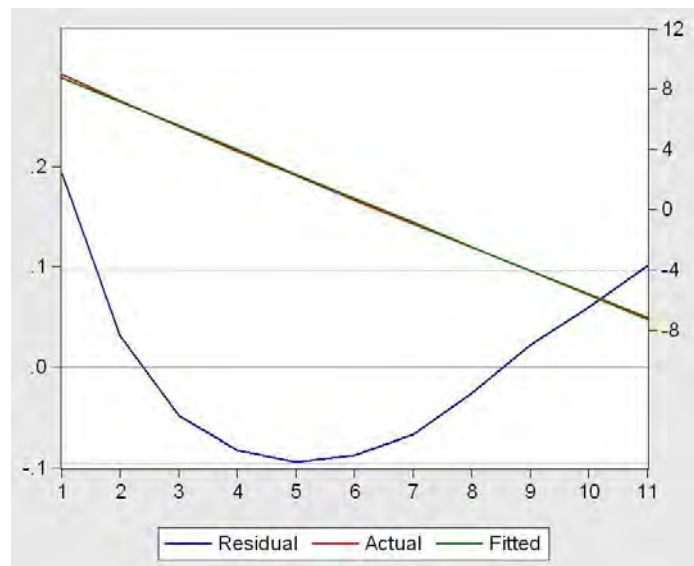


Figure 18. Eviews fitting result of photon dose rate variation

The Fitting result is: $LNY = 11.1753722582 - 0.320726457096 * X$. In normal coordinate axes:

$$D(x) = 7.135 \times 10^4 e^{-0.3207x}$$

This fitted result also has a good agreement with the actual MCBEND calculation result with a residual within the range (-0.10, 0.2).

The Half Value Thickness for carbon steel is

$$HTV = \frac{\ln 2}{\mu} = \frac{\ln 2}{0.3207} = 2.1614(\text{cm})$$

Gamma dose attenuated to 50% of the original value when they pass through every 2.1614 cm in carbon steel and almost all photons fall off after pass through 32.5 cm thick carbon steel shielding. It is noticed that photon is easier shielded compare with neutrons. (Compare these two values of HTV). Thicker shielding thickness is required for gamma shielding due to the larger initial dose. One of the most important properties of a material for shielding against gamma rays is its electron and mass density because of that gamma rays interact primarily with atomic electrons. This is the major difference between neutron and gamma rays shielding mechanism.

5.3. Radius and Axial Dose Rate Distribution

Knowing the radius and axial dose rate distribution around spent fuel flask are sometime useful for radiation protection. Basic spatial dose rate distribution regularities around Excellox 7 flask are discussed in this chapter. Table 9 and 10 give the calculation results of gamma and neutron dose rate distribution scored at the shock absorber surface and 1 meter away from the shock absorber surface along the radius of score region center with an average confidence of variation around 4.1%. Figure19 associate the distribution of these 4 cases together for comparison. From Figure19 we notice that the dose rates in the flask end area present unimodal distribution with the peak in the center of flask ends for all the four cases. Neutrons emission from spent fuel falls off at the ends, (the dose rate scored at the surface of shock absorber is below 0.015) so there is no neutron shielding requirement on the two ends of flask. Although 32.5 cm thick gamma shielding is adopted at the lid and base of flask in our model, the gamma dose is still higher than the neutron dose.

Table 9. Gamma dose distribution at lid surface and 1m away from lid surface of 32.5 cm thickness of gamma shielding

Distance from center of Score regions	Dose rate	COEF of VAR. (%)	Dose rate 1m from lid surface	COEF of VAR. (%)
-115	2.421E-03	5.2	3.409E-03	3.4
-75	7.739E-03	3.8	7.612E-03	3.3
-45	3.235E-02	3.2	1.319E-02	3.8
0	4.564E-02	4.6	1.629E-02	4.5
45	3.235E-02	3.2	1.319E-02	3.8
75	7.739E-03	3.8	7.612E-03	3.3
115	2.421E-03	5.2	3.409E-03	3.4

Table 10. Neutron dose distribution at lid surface and 1m away from lid surface of 14 cm thickness of neutron shielding

Distance from center of Score regions	Dose rate at lid surface	COEF of VAR. (%)	Dose rate 1m from lid surface	COEF of VAR. (%)
-115	4.454E-03	1.8	1.610E-03	3.1
-75	4.138E-03	3.8	1.930E-03	2.3
-45	1.108E-02	3.2	3.105E-03	2.4
0	1.302E-02	2.8	3.604E-03	2.8
45	1.108E-02	2.4	3.105E-03	2.4
75	4.138E-03	2.1	1.930E-03	2.3
115	4.454E-03	1.8	1.610E-03	3.1

Table 11. Axial gamma and neutron dose rate distribution along the flask for 32.5cm Gamma shielding and 14 cm neutron shielding

Axial height of flask	Axial gamma Dose rate	COEF of VAR. (%)	Axial neutron Dose rate	COEF of VAR. (%)
585	1.827E-01	17.7	4.677E-02	14.7
555	3.586E+00	8.0	2.521E+00	3.8
525	3.608E+01	2.9	1.669E+02	0.5
495	2.799E+02	1.4	5.384E+02	0.4
465	1.188E+03	0.9	1.284E+03	0.3
435	2.012E+03	0.6	2.550E+03	0.2
405	2.776E+03	0.6	3.371E+03	0.2
375	2.274E+03	0.6	3.600E+03	0.2
345	3.171E+03	0.7	3.310E+03	0.3
315	2.927E+03	0.9	3.777E+03	0.3
285	3.042E+03	1.0	3.386E+03	0.3
255	3.126E+03	1.1	3.204E+03	0.4
225	2.642E+03	1.1	3.641E+03	0.4
195	2.936E+03	1.6	3.754E+03	0.5
165	2.282E+03	1.4	3.644E+03	0.6
135	3.026E+03	1.9	3.085E+03	0.6
105	2.386E+03	2.3	2.885E+03	0.7
75	1.321E+03	4.4	1.654E+03	1.0
45	3.978E+02	11.1	4.001E+02	1.8
0	4.370E+01	15.7	3.388E+00	18.2

Table 12. Axial gamma and neutron dose rate distribution along the flask for 22.5cm Gamma shielding and 24 cm neutron shielding

Axial height of flask	Axial gamma Dose rate	COEF of VAR. (%)	Axial neutron Dose rate	COEF of VAR. (%)
585	4.347E+00	12.4	2.000E-02	14.6
555	1.030E+02	5.0	6.131E-01	3.8
525	8.994E+02	2.2	2.704E+01	0.9
495	6.837E+03	1.1	8.864E+01	0.6
465	2.932E+04	0.7	2.118E+02	0.5
435	5.009E+04	0.5	4.216E+02	0.4
405	6.844E+04	0.5	5.500E+02	0.4
375	5.484E+04	0.4	5.894E+02	0.4
345	7.728E+04	0.6	5.471E+02	0.4
315	7.156E+04	0.6	6.133E+02	0.5
285	7.525E+04	0.7	5.561E+02	0.5
255	7.837E+04	0.9	5.306E+02	0.6
225	6.580E+04	0.9	6.112E+02	0.7
195	7.046E+04	1.2	6.142E+02	0.9
165	5.500E+04	1.1	5.899E+02	1.0
135	7.467E+04	1.5	5.056E+02	1.0
105	6.024E+04	1.6	4.560E+02	1.2
75	3.500E+04	2.6	2.709E+02	1.7
45	8.386E+03	4.8	6.751E+01	3.1
0	1.254E+03	13.0	2.230E+00	18.8

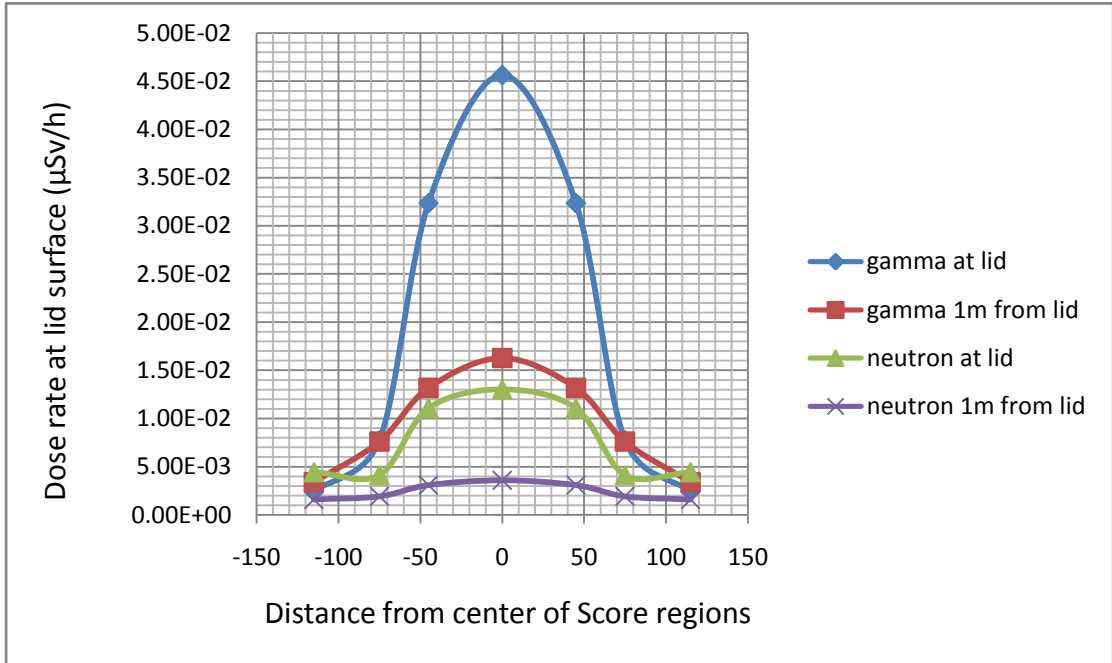


Figure 19. Radius dose rate distribution at the upper shock absorber

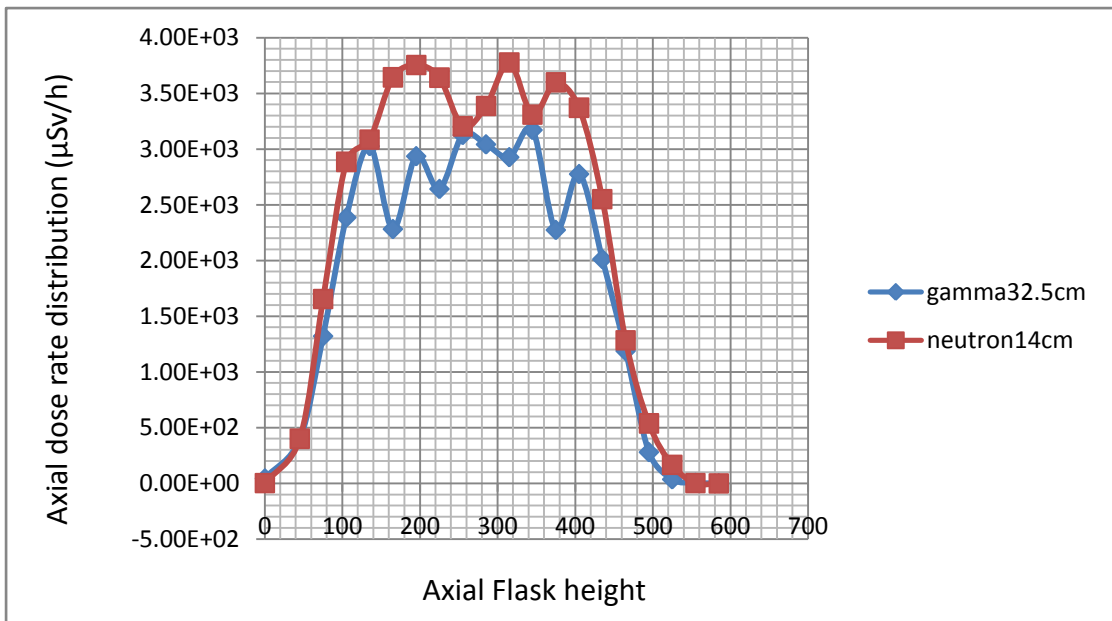


Figure 20. Axial dose rate distribution around Excellox 7 flask in normal coordinate

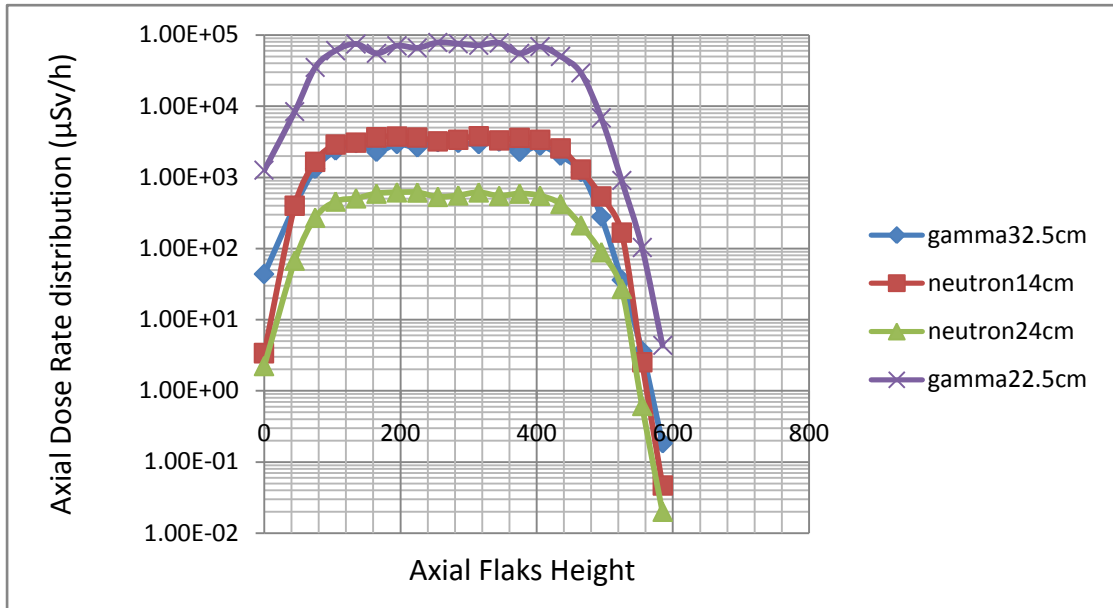


Figure 21. Axial dose rate distribution around Excellox 7 flask in logarithmic coordinate

Table 11 and 12 give the calculation results of gamma and neutron dose rate distribution scored at 14 cm and 1 meter away from cooling fins along the axial of flask with an average COEF of VAR around 2.6%. The COEF of VAR values at two ends of flask are much higher than the average level due to less samples in the end region. Figure 20 shows the high resolution gamma and neutron distribution with shielding thickness of 32.5 cm and 14 cm respectively. (Small range fluctuations exist due to errors) Figure 21 shows the neutron and gamma dose rate distribution along flask with different shielding thickness (32.5 cm and 22.5 cm for gamma, 24 cm and 14 cm for neutron) with relatively lower resolution. Figure 22 shows the gamma activity or neutron particles emitted number distributions along a single typical PWR fuel rod (Only major gamma emitter Cs134 and Ru106 distribution are given).

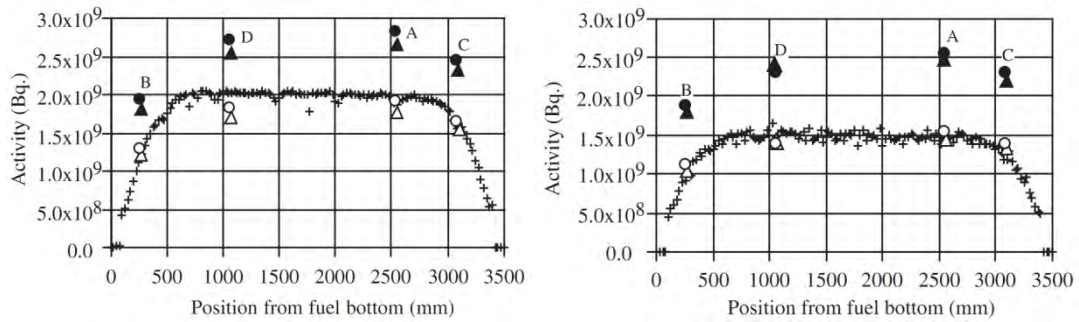


Figure 22. Measured and calculated gamma ray source distributions along fuel rod for Cs134 and Ru106 distribution

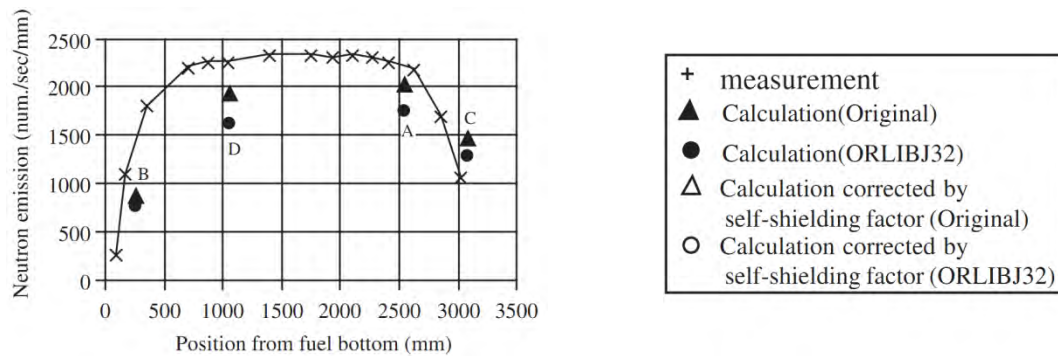
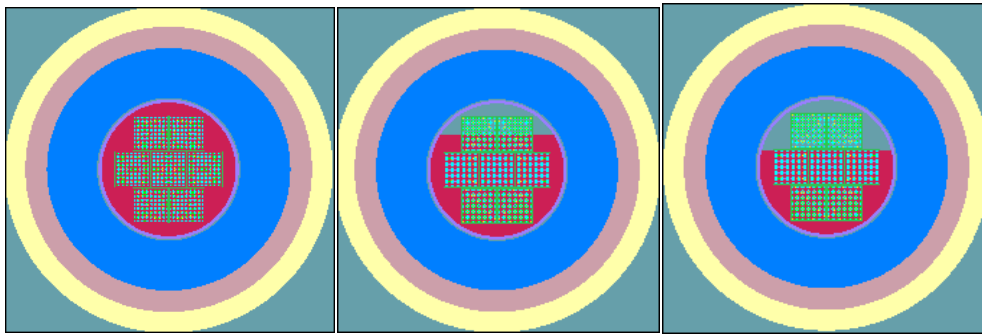


Figure 23. Measured and calculated neutron emission distributions along fuel rod (Sources from: Akihiro Sasahara et al., 2004. Neutron and gamma ray source evaluation of LWR high burn-up UO₂ and MOX spent fuels)

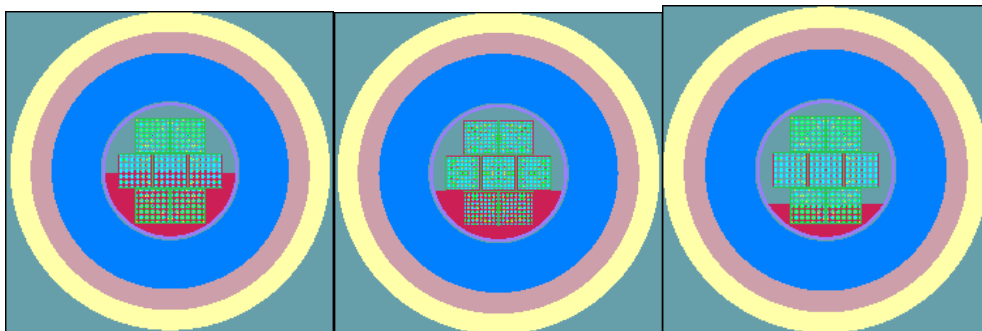
Compare these figure we can know that the dose rate distribution of the whole flask from 71.25cm to 480.5 cm agrees quite well agree with the single fuel rod dose rate distribution because this is the position where fuel assembly stayed in MEB. There is a flat distribution along the main part of the flask and gradually attenuated at the two ends in the above-mentioned region. Similar distribution is found in a single fuel rod. This is corresponding to the unit intensity of the gamma or neutron emitter along main part of the finite fuel rod. In Figure21, regions from the bottom to 71.25 cm and from 480.5cm to 521.25 cm are corresponding to the ullage chamber plus base shock absorber and the void of fuel chamber in MEB plus the upper shock absorber (see Figure8) respectively. The dose rates continue to attenuate in these two regions with increasing gradient.

5.4. Water Level

This unit is introduced to discuss the water level effect within the spent fuel flask. The flask is placed horizontally in transportation. Thus, only the horizontal case of flask is modeled. The flask cut views of six different water levels are illustrated in Figure 24. In addition, the new Excellox 7 design tightly fit the MEB in the flask cave, so the space between them is ignored in our modeling.



Case 1: water level 91cm Case 2: water level 69cm Case 3: water level 57.25cm



Case 4: water level 45.5cm Case 5: water level 33.75cm Case 6: water level 22cm

Figure 24. Flask cut views of water levels change for modeling

Table 13. Gamma dose rate varying with water level in the Excellox 7 Flask

Water level	Dose rate ^a	Samples	COEF of VAR	+ST.DEV.	+ST.DEV.
91	1.734E+00	247855	0.4	1.74E+00	1.73E+00
69	1.944E+00	443446	0.4	1.95E+00	1.94E+00
57.25	2.100E+00	456497	0.4	2.11E+00	2.09E+00
45.5	2.212E+00	271375	0.4	2.22E+00	2.20E+00
33.75	2.300E+00	471620	0.3	2.31E+00	2.29E+00
22	2.444E+00	476249	0.3	2.45E+00	2.44E+00

a: scoring at 14cm from the cooling fins

Table 14. Neutron dose rate varying with water level in the Excellox 7 Flask

Water level	Dose rate ^a	Samples	COEF of VAR	+ST.DEV.	+ST.DEV.
91	7.914E-01	561812	0.3	7.94E-01	7.89E-01
69	1.822E+00	1439762	0.2	1.82E+00	1.82E+00
57.25	2.616E+00	1381777	0.2	2.62E+00	2.61E+00
45.5	3.367E+00	801282	0.2	3.38E+00	3.36E+00
33.75	4.010E+00	1410788	0.2	4.02E+00	4.00E+00
22	4.699E+00	978723	0.2	4.71E+00	4.69E+00

a: scoring at 14cm from the cooling fins

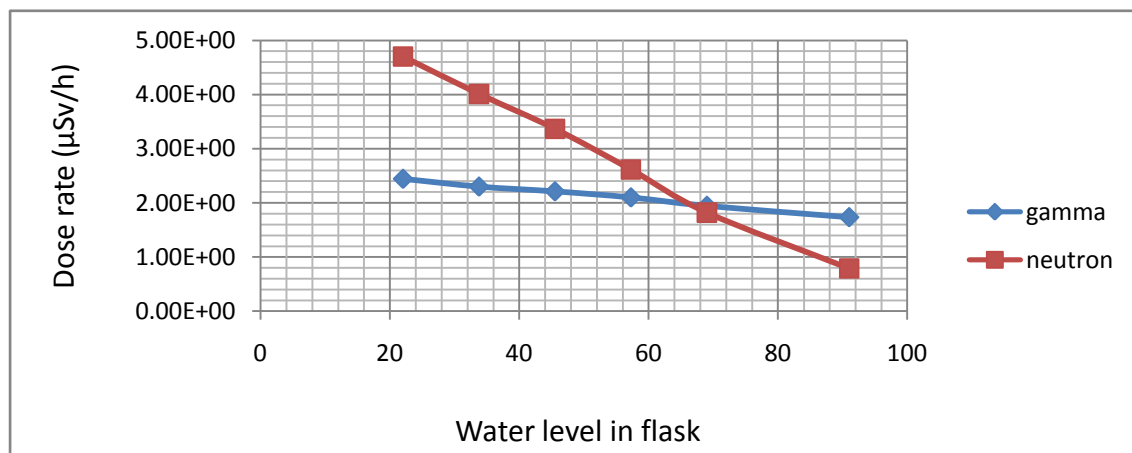


Figure 25. Dose rate variation with respect to water levels in flask

Table 13 and 14 show the results of MCBEND calculated dose rate varying with water level in the flask. The samples, COEF of VAR values are also given. Figure 25 presents the variation of both gamma and neutron case. The line represents neutron dose rate decrease more sharply than that stands for gamma dose rate. In other words, the water level has a larger influence to neutron dose rate than to photon dose rate. As we discussed in the neutron attenuation chapter, the neutron attenuation mechanism in a typical shielding material is mostly relevant to the neutron slow down process by collision with other nucleus. Water is a very good neutron moderator due to its high hydrogen content. However, water is not a good shielding material for gamma photons due to its low electron density and 'Z' number. Thus, water level change has less influence on gamma dose than on neutron dose.

In a transportation accident, both gamma and neutron dose increase when water leaked out of the flask. Strengthen of the radiation protection, especially the neutron protection, is necessary when handling the flasks in an accident environment. In addition, a certain volume of water contained in the flask is crucial also because water is the coolant of decay heat which mainly because the alpha and beta decay of fission products and actinides in the irradiated fuel. Due to space limitations in this article, the discussion of decay heat is not included here.

5.5. Burnup, Cooling Time and Initial Enrichment Effect to Spent Fuel Dose Rate

In nuclear power technology, burnup (also known as fuel utilization) is a measure of how much energy is extracted from a primary nuclear fuel source.⁹ It is closely relevant to the spent fuel composition and, of course, to the dose rate. Thus, the relationship between spent fuel dose and burnup is discussed in this chapter.

PWR Spent fuel radioactivities versus time after discharge for six cases of different burnup with different initial enrichment are shown in Figure 26. The detail values and

⁹[Wikipedia, Definition of Burnup](#)

description are listed in Table 15. From Figure 26 we know the radioactivity of recent discharge fuel become slightly larger as the burnup increase. However, the difference values of radioactivity between different burnup non- continuously increases as the cooling time increase and the difference peaked at 100 years and 0.2 million years.

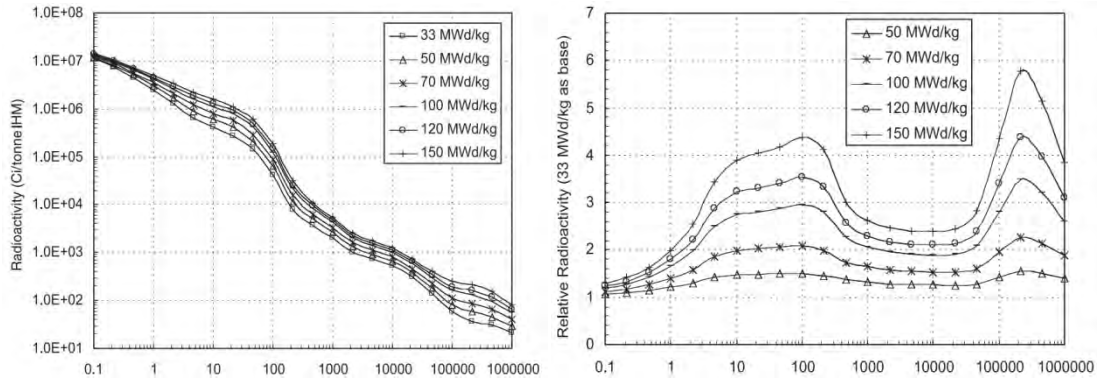


Figure 26. Radioactivity per ton initial heavy metal (IHM) versus time after discharge

Sources from: Zhiwen Xu et al., 2005. Impact of High Burnup on PWR Spent Fuel Characteristics.

Table 15. High burnup PWR spent fuel case

Case No.	Burnup (MWd/kg)	Enrichment (wt%)	Description
1	33	3.1	Early-days discharge burnup
2	50	4.5	Contemporary burnup level
3	70	6.3	Foreseeable future
4	100	9.1	Future burnup level
5	120	11.2	Far-future burnup
6	150	14.3	Remote future

Sources from: Zhiwen Xu et al., 2005. Impact of High Burnup on PWR Spent Fuel Characteristics.

The radioactivity of spent fuel decrease continuously as the cooling time goes by. Generally speaking, the actinides have very long half-lives, on the order of tens of thousands of years, and long decay chains. In contrast, most fission products have short half-lives (tens of years) and short decay chains. Therefore, the short-term

spent-fuel characteristics are governed by fission products while the long-term behavior is governed by actinides. Combined together, the spent nuclear fuel remains highly radioactive for many thousands of years (Zhiwen Xu et al., 2005).

Table 16 below gives the MCBEND calculation results of four different burnup (5, 25, 45 and 60 GWd/MTU). The spent fuel composition used for modeling is 4.0% enriched after 2 years-cooling time. Figure 27 displays a visual representation of the relationship between dose rate and fuel burnup. Both gamma and neutron dose rate slightly increased as the fuel burnup became deeper. Just like it is mentioned before, there is a small difference of radioactivity values between different fuel burnup. This difference will become larger as the cooling time increase. Detailed dose rate distribution of variation with cooling time is not discussed in this paper but it can be reasonably deduce that the distribution will be quite similar to that illustrated in Figure 26.

Table 16. Gamma and neutron dose rate scoring at 14 cm from cooling fins for different burnup¹⁰

Burnup	Gamma Dose rate	COEF of VAR. (%)	Neutron Dose rate	COEF of VAR. (%)
5 GWd/MTU	1.929E+00	0.3	1.823E+00	0.2
25 GWd/MTU	1.961E+00	0.3	1.829E+00	0.2
45 GWd/MTU	2.000E+00	0.4	1.831E+00	0.2
60 GWd/MTU	2.029E+00	0.4	1.843E+00	0.2

¹⁰ Detailed table are shown in Table 30 and 31 in Appendix 4

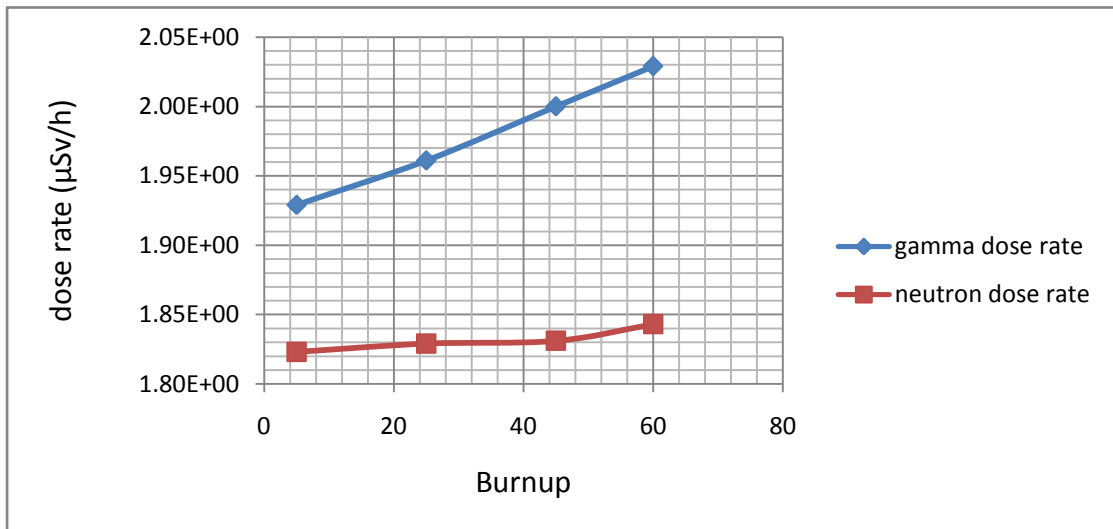


Figure 27. Neutron and gamma dose rate varying with spent fuel Burnup

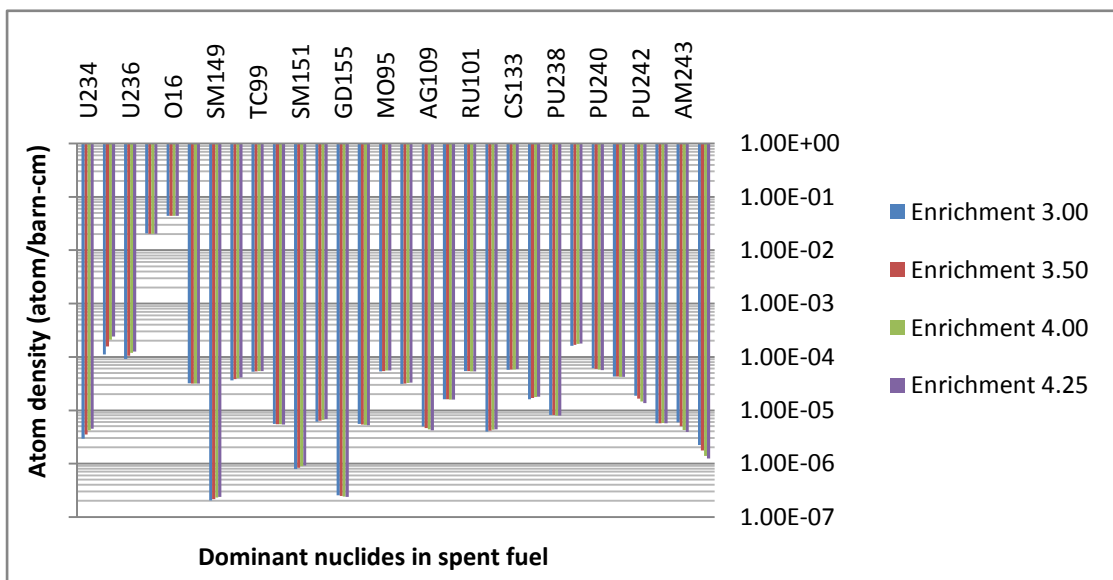


Figure 28. Change of predominant nuclides in typical PWR spent fuel with respect to different initial enrichment

Figure 28 gives comparison of the predominant nuclides in spent fuel with different initial enrichment. These data are collected from a typical PWR fuel with burnup of 45 GWd/MTU after 2 years-cooling. Most nuclides don't have any distinct change as the initial enrichment increase. Thus we can reasonably deduce that the initial enrichment don't have large influence on the spent fuel dose rate, especially for low initial enrichment.

5.6. Distance Effect

As we know, the dose rate is inversely proportional to the square of the distance from a point source. Figure 29 shows the dose rate distribution nearby the flask. The scored regions are illustrated in Figure 10 in the scoring function unit. Although the source cannot be treated as ‘point source’, the distribution still roughly obeys the inverse square law. If the distance is far enough, until the whole flask can be treated as a ‘point’, the dose rate will preferably agree with the distance law.

Table 17. Gamma and neutron dose rate scored at side face of different distance¹¹

Distance from cooling fins (m)	Gamma dose rate	COEF of VAR. (%)	Neutron dose rate	COEF of VAR. (%)
0.14	2.005E+00	0.3	1.835E+00	0.1
1.0	1.008E+00	0.3	8.332E-01	0.1
2.0	6.432E-01	0.3	4.981E-01	0.1
3.0	4.513E-01	0.3	3.322E-01	0.1
4.0	3.344E-01	0.3	2.363E-01	0.1
5.0	2.572E-01	0.3	1.759E-01	0.1

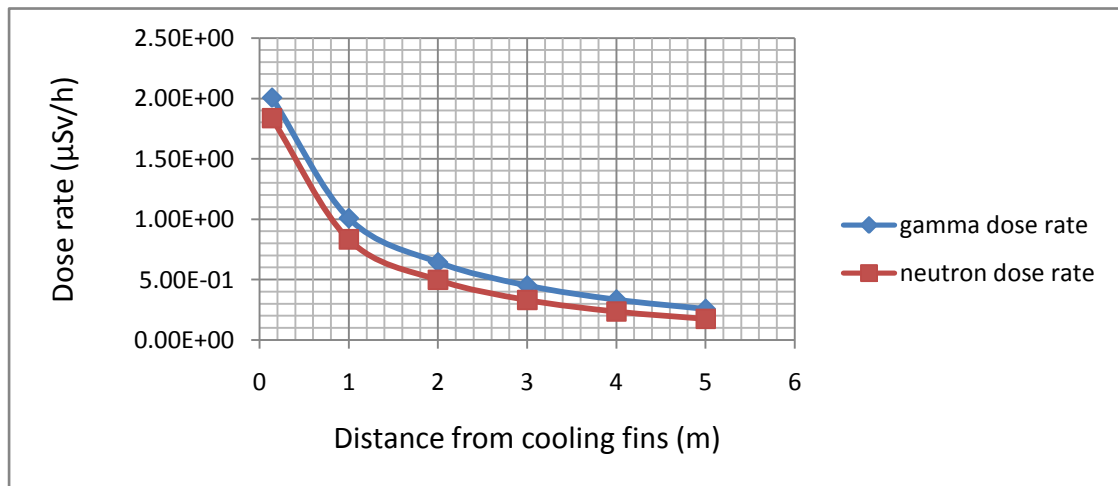


Figure 29. Dose rate varying with distance from flask in normal coordinate axes

¹¹ Detailed table available in Table 32 and 33 in Appendix 4

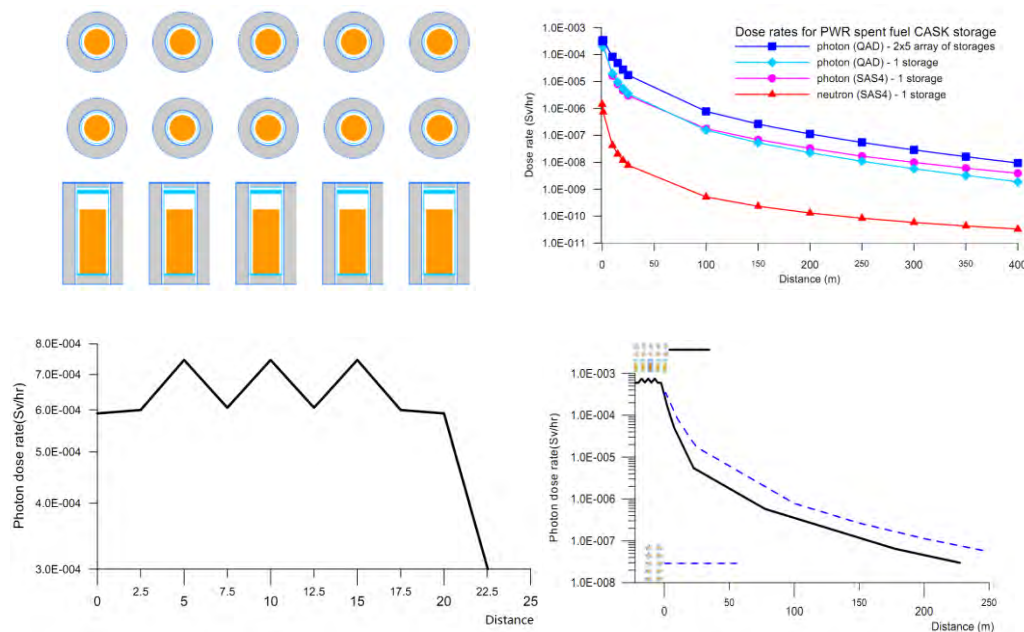


Figure 30. Simplified Cask Geometry Modeling of 2 x 5 array and Photon dose rates within the array (left); Photon dose rates for the array (right) (Byeong-Soo Kim et al., 2007)

In Figure30, simplified geometry modeling of the flask array (upper left), in-array dose rate distribution(lower left), 2x5 array integral dose rate(lower right) and the comparison of different cases (upper right) are illustrated. For a case of the single flask, dose rates are calculated by SAS4 (SCALE 5.0) (SCALE, 2005) and QAD-CGGP-A (K.A. Litwin et al., 1994). For multiple flasks in an array of 2x5, QAD-CGGP-A code is utilized due to its array function. Homogenization of the spent fuels, three-dimensional geometry modeling and the dose conversion factor of ANSI/ANS-6.1.1-1977¹² are applied for both these two cases.

¹² ANSI/ANS-6.1.1-1977, American National Standard Neutron and Gamma-Ray Flux-to-Dose-Rate Factors, American Nuclear Society, March 1977.

6. TRISO Type Fuel Utilized in PWR

TRIStructural-ISOtropic fuel is a type of micro fuel particle. It consists of a fuel kernel composed of UO_2 (sometimes UC or UCO) in the center, coated with four layers of three isotropic materials.¹³ TRISO type fuel used in a small size pressurized water reactor is a new conceptual design. The presence of TRISO fuel in PWR technology improves the integrity of design due to its fission fragments retention ability as this fuel provides first containment boundary within fuel itself against the release fission fragments and can retain the fission products at elevated temperatures (Anwar. Hussain et al., 2010). A basic comparable study of the normal and TRISO type PWR spent fuel dose rate property in Excellox 7 flask is discussed in this unit.

6.1. TRISO Type Fuel Rod Geometrical Description

It is assumed in our modeling that the new TRISO fuel rod has an identical diameter and length with the regular PWR fuel rod. The difference is that, in the TRISO fuel rod, millions of TRISO fuel particles are filled in a zircaloy sheathed fuel tube with empty spaces occupied by helium gas (Anwar. Hussain et al., 2010). The TRISO fuel particles consist of a UO_2 fuel kernel surrounded by four layers. A low-density porous buffer layer being the first layer provides the retention space for released fission fragments from the fuel during irradiation. The other three layers made up of a highly dense pyrolytic carbon (PyC) and a ceramic layer of silicon carbide (SiC) provide the structural integrity and contain the fuel at elevated temperatures (Anwar. Hussain et al., 2010). The illustration of TRISO particles and TRISO PWR fuel rod are in Figure31.

¹³ [Wikipedia Definition of TRISO fuel](#)

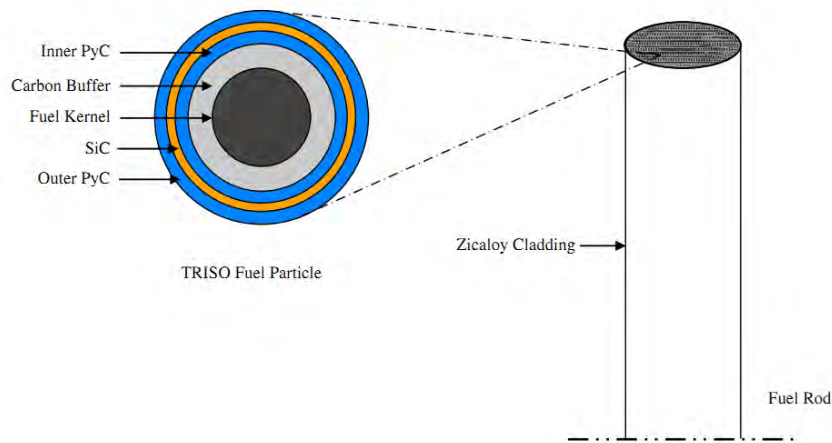


Figure 31. Illustration of TRISO particles and TRISO PWR fuel rod

6.2. Material Specification

UO₂ fuel is still adopted in the TRISO particle kernels except a small amount of Pu-240 with 5.0 w/o has been added in TRISO fuel particle composition in the place of U-238 (Anwar, Hussain et al., 2010). Together with the higher enrichment utilized (9%), the spent fuel composition will be slightly different with the ordinary PWR fuel. Although bias is introduced, in our MCBEND calculation, both of these two changes are excluded in the model set up procedure. The main purpose of this modeling is to discuss the structural influence of the new TRISO PWR fuel design to the spent fuel dose rate. Table 18 and 19 give the basic parameters of TRISO type and normal fuel relevant to modeling and description of TRISO fuel particle used for modeling.

Table 18. Comparison of TRISO PWR fuel and normal PWR fuel

Parameter	TRISO fuel	Normal fuel
Fuel composition	UO ₂	UO ₂
Lattice type	PWR shape	PWR shape
Coolant/Moderator	Light water	Light water
Fuel enrichment	9%	4%
Addition	Pu240 replace of U238	NONE
Cladding material	Zircaloy	Zircaloy

Table 19. Description of TRISO fuel particle for modeling

Material	Density (g/ cm ³)	Outer diameter (cm)	Diameter in modeling case 1	Diameter in modeling case 2
UO ₂ fuel kernel	10.88	0.04	0.14	0.04
buffer layer	1.0	0.06	0.18	0.06
Inner PyC	1.9	0.07	0.2	0.07
SiC coating	3.2	0.077	0.24	0.077
Outer PyC	1.9	0.087	0.26	0.086

6.3. The Building up of Model

In reality, the diameter of the TRISO fuel particle is 0.087 (Table19), in modeling, the number of TRISO fuel particles in a single fuel rod is about 4.0E+05, in a single assembly is 1.1E+08 and in the whole flask is 8.0E+08. However, the maximum space allocated to the modeling is 1.0E+08. It is impossible to modeling the whole flask, not even a single fuel rod with TRISO fuel particles in real dimension (See Figure32). The modeling Material geometry input is given in Appendix 2.

Two measures are adopted in order to get a reasonable result:

1. Case 1-simplify the modeling by enlarge the diameter of the TRISO fuel particles. In this case, fewer particles are contained in one fuel rod, thus reduce the CPU space used for calculation. So 9 fuel rods constitute one fuel assembly are modeled and only the center fuel assembly is stayed in the flask cave. The fuel cladding shape is changed in order to apply the Hexagonal Array. The other parts (including moderator and other fuel assembly) in the flask cave are occupied by void to make sure a certain quantity of neutrons or gamma photos can reach the scoring region. For the ordinary fuel type, same numbers of fuel rods in the same condition are also modeled as a comparison (Figure33).
2. Case 2-calculation implemented only on a part of a single fuel rod with a length of 43.5cm adopting the real TRISO particle size. The fuel cladding shape is changed in order to apply the Hexagonal Array. The other parts (including moderator, other

fuel assembly and the non-modeling part of the centre fuel rod) in the flask cave are occupied by void. For the ordinary fuel type, same length and position of modeling fuel rod in the same condition are also modeled as a comparison (Figure33).

DATA GROUP AREA USED BY MA31	
TOTAL SPACE USED	: 81286724
INPUT/OUTPUT DATA	: 81200836
WORK AREA	: 28160
FWD/ADJ FLUXES	: 57728
SPACE NOW REMAINING	: 2

Figure 32. Space remaining when modeling a single fuel rod with TRISO fuel particles in real dimension

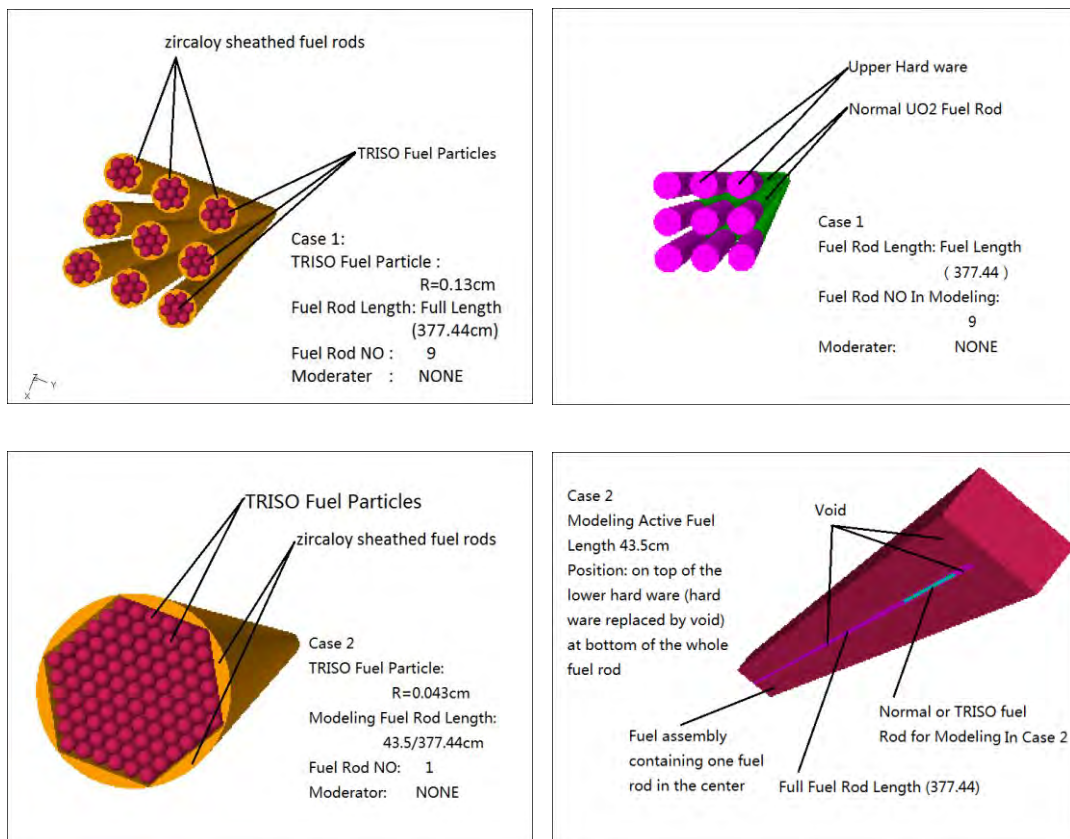


Figure 33. Illustration of geometrical details for two modeling cases (Left for TRISO type fuel and right for ordinary type fuel; upper for case 1 and lower for case 2)

6.4. Calculation Result

Normal UO₂ fuel, TRISO type PWR fuel and Normal UO₂ fuel of the same mass of that in TRISO type fuel for modeling are calculated by MCBEND. The score region is 14 cm from the cooling around the flask. In the modeling, the difference of spent fuel composition between normal and TRISO fuel due to the initial enrichment of U235 does not taken into consideration. This will introduce bias but not significant because the initial enrichment of fuel have little influence on the spent fuel composition and further on the neutron or gamma dose rate (See Figure36 in Appendix 5). The addition of PU240 in TRISO fuel is also ignored in the modeling. This simplification is reasonable because only a small amount of Pu240 is added into the fresh fuel replacing U238 (5.0 w/o).

Table 20. Calculation results for two cases¹⁴

	Normal	TRISO	Normal same mass
Case 1 gamma	1.272E-01	1.055E-02	8.312E-03
Case 1 neutron	1.139E-01	6.982E-03	6.453E-03
Case 2 gamma	1.889E-03	1.343E-04	1.239E-04
Case 2 neutron	1.344E-03	7.603E-05	8.239E-05

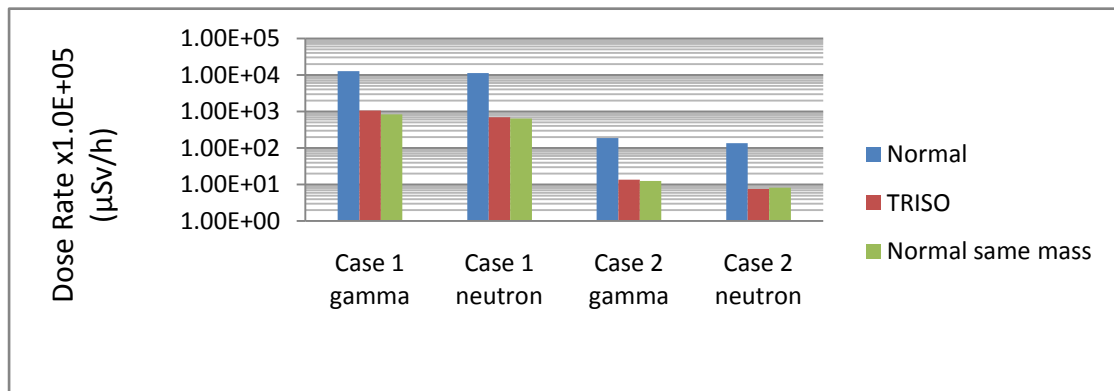


Figure 34. Comparison of TRISO PWR and Normal PWR spent fuel dose rate outside flask

¹⁴ Detailed table with COEF of VAR are available in appendix

Despite the bias mentioned above, for both gamma and neutron dose rate in these two cases, the TRISO type spent fuel dose rates are one order of magnitude lower than the normal PWR fuel. The utilization of TRISO type of PWR fuel can significantly reduce the shielding protection and distance restrict during transportation (Figure34). The aim of introducing the normal UO₂ fuel of the same mass of that in TRISO type fuel into modeling is to illustrate that the using of TRISO type fuel in PWR assembly significantly reduced both the neutron and photon dose rate not because the special multi-layer structure of TRISO fuel, but due to the less mass contained in one fuel rod. This also explains why higher fuel enrichment (9%) is applied in TRISO type fuel.

Although the multi-layer structure of TRISO fuel can't reduce the dose rate of spent fuel, it is an excellent engineered barrier for containing radionuclide in a spent fuel transport condition and long term geological repository environment. Leaching tests were performed on the coated waste particles and more conventional glassified waste forms. For the coated waste particles, radionuclides were not detected in the leachate using sensitive analytical techniques. In contrast, radionuclides leached from glassified waste form were readily detected (C. Rodriguez et al., 2003).

7. MCBEND Calculation Error

Like all the other calculation system, two kinds of errors are produced during the calculation of MCBEND. One is system errors and the other is statistical errors. System errors of MCBEND come from the uncertainties of the known nuclear data. Statistical errors are because that it is only possible to simulate the fate of a finite number of source particles (Serco, 1994). However, it is possible to estimate the magnitude of the statistical errors for a given MCBEND calculation. Calculation errors produced in this paper are kept under 5% except in case that excessive shielding thickness is adopted, in places where the volumes of score region or sample number in boundary region of flask are limited.

8. Conclusion

Neutron and gamma dose rate outside of Excellox 7 flask of various study cases are presented in this paper. The utilization of MCBEND code provides accurate calculation results as follows. Firstly, neutron and gamma attenuation roughly follow an exponential relationship in certain shielding material, which may helpful for the flask shielding design. Secondly, Lower dose rates are detected in boundary of flask when discuss the dose rate distribution around flask, contributing a lot to radiation protection. Thirdly, water level may change in a transportation accident; therefore, neutron protection is especially important compared to gamma rays when handling the accident spot. In addition, burnup, cooling time and initial enrichment of spent fuel don't have much influence to the spent fuel activity in short time. What's more, utilize of TRISO type fuel can significantly reduce the spent fuel activity and provide an excellent containment of radioactive material. Those conclusions above are basically in accordance with their experimental and theoretical findings.

9. Reference

Akihiro Sasahara, Tetsuo Matsumura, Giorgos Nicolaou and Dimitri Papaioannou, 2004. Neutron and gamma ray source evaluation of LWR high burn-up UO₂ and MOX spent fuels, Journal of Nuclear Science and Technology, Vol. 41, No. 4, p. 448-456.

Anwar. Hussain, and Cao. Xinrong, 2010. Small PWR core design with coated particle based fuel with a novel composition, Progress in Nuclear Energy, 52 (2010) 531-535.

Anne BARREAU, 2006. Burn-up Credit Criticality Benchmark, Nuclear Energy Agency Organisation for Economic Co-Operation and Development, France, NEA No. 6227.

Ayodeji. B. Alajo, 2007. Impact of PWR Spent Fuel Variations on TRU-Fueled VHTRs, Master's thesis of Science, Texas A&M University.

Byeong-Soo Kim, Jae-Hak Jeong, and Chan-Woo Jeong, 2007. Pre-conceptual study on the review Framework for the radiation shielding safety of the PWR spent fuel cask interim storage in Korea, Korea Institute of Nuclear Safety, 19 Kusong-Dong, Yusong-Ku, Daejeon, 305-338, Republic of Korea.

C. J. Edney and R. L. Rutter, 1977. Some UK experience and practice in the packaging and transport of irradiated fuel, International conference on nuclear power and its fuel cycle, Salzburg, Austria 2-13.

C. Rodriguez, A. Baxter, D. McEachern, M. Fikani, and F. Venneri, 2003. Deep-Burn: making nuclear waste transmutation practical, Nuclear Engineering and Design 2805, 1-19.

Edward G. Nisbett, and Albert S. Melilli, 1987. Steel Forgings, American Society for Testing and Materials. Committee A-1 on Steel, Stainless Steel, and Related Alloys

E.Shuttleworth, 2000. The Geometrical Sensitivity Option in MCBEND Proc. Monte Carlo 2000 Conference.

Glenn. Ellcock, E. Port, 1981. Container for irradiated nuclear fuel, British Nuclear Fuel Limited, Warrington, England, Appl. No.: 420,348.

George. Chabot, 2001. Shielding Equations and Buildup Factors Explained,
<http://hps.org/publicinformation/ate/faqs/gammaandexposure.html>

George. Chabot, 2011. Radiation Shielding, Health physics society,
<http://www.hps.org/publicinformation/ate/q1094.html>

IAEA, 1996. Food and agriculture organization of the United Nations, International atomic energy agency, international Labour Organisation, OECD nuclear energy agency, pan American health organization, world health organization, International Basic Safety Standards for Protection against Ionizing Radiation and for the Safety of Radiation Sources, Safety Series No. 115, IAEA, Vienna.

- IAEA, 1997. Further analysis of extended storage of spent fuel, IAEA, Vienna, IAEA-TECDOC-944,ISSN 1011-4289.
- IAEA, 2007. Radiation protection programmes for the transport of radioactive material, International Atomic Energy Agency, Austria, Vienna,11-31
- J. H. Hubbel, 1969. Photon Cross Sections, Attenuation Coefficients, and Energy Absorption Coefficients from 10 keV to 100 GeV, National Bureau of Standards report NSRDS-NSB 29.
- J.R. Guzmán, G. Espinosa-Paredes, J.L. François, and C. Martín-del-Campo, 2010. A novel method for transuranic fuel design, *Progress in Nuclear Energy* 52 (2010) 689-697.
- K.A. Litwin, I.C. Gauld, and G.R. Penner,1994. Improvements to the Point Kernel Code QAD-CGGP: A Code Validation and User's Manual, RC-1214, COG-94-65, AECL Research.
- Lance Snead, Francesco Venneri, Jim Tulenko, Charles Forsberg, and Per Peterson, 2011. Microencapsulated fuels-a transformational technology for next generation reactors, Presented at the 15th ICENES San Francisco.
- M Coeck, F Vermeersch, and F Vanhavere, 2002. Neutron shielding evaluation for a small fuel transport case. *Nuclear Instruments and Methods in Physics Research Section A: Accelerators, Spectrometers, Detectors and Associated Equipment* Volume 476, Issues 1-2, Pages 273-276.
- M.Q. Huda, M.M. Rahman, M.A. Imtiaz, and K.C. Nguyen, 2011. Design studies of a typical PWR core using advanced computational tools and techniques, *Annals of Nuclear Energy* 38 (2011) 1939-1949.
- NDA, 2010. Geological Disposal Feasibility studies exploring options for storage, transport and disposal of spent fuel from potential new nuclear power stations, NDA Report No. NDA/RWMD/060.
- N.R.Smith, E.Shuttleworth, S.J.Carter and M.Evans, 1994. Geometry Modelling and Visualisation for the Monte Carlo Code MCBEND. Proc. 8th International Conference on Radiation Shielding.
- N.R.Smith, E.Shuttleworth, M.J.Grimstone, J.L.Hutton, M.J.Armishaw, A.J.Bird, N.J.France and S.M.Connolly, 2000. The Current Status and Future Plans for the Monte Carlo Codes MONK and MCBEND Proc. Monte Carlo 2000 Conference
- O. W. Hermann and C. W. Alexander, A review of spent-fuel photon and neutron source spectra, ORNL/CSD/TM-205.
- R. Gowing, J. Emmison, T. Roberts, F. Siddall and P.C. Purcell, 1994. Introduction of new flasks for high burnup spent fuel, Nuclear Technology Publishing, RAMTRANS Vol.5, Nos 2-4, pp.181-187.
- Robert M. Versluis, Francesco Venneri, David Petti, Lance Snead, and Donald McEachern, 2008. Project deep-burn: development of transuranic fuel for high-temperature helium-cooled reactors, Proceedings of the 4th international topical meeting on high temperature reactor technology.

Sacavem, Portugal, 2002. Nuclear Science Computing Radiation Dosimetry - CRD 2002, Organisation for Economic Co-operation and Development, Nuclear Energy Agency.

SCALE, 2005. A Modular Code System for Performing Standardized Computer Analyses for Licensing Evaluations, ORNL/TM-2005/39, Version 5, Vols. I–III.

Serco, 1994. MCBEND User Guide Version 10, ANSWERS Software Service.

S. P. Cerne, Q. W. Hermann and R. M. Westfall, 1987. Reactivity and isotopic composition of spent PWR fuel as a function of initial enrichment, burnup, and cooling time, ORNL/CSD/TM-244.

Svensk Kärnbränslehantering AB, 2010. Spent nuclear fuel for disposal in the KBS-3 repository, Technical Report, TR-10-13.

Zhiwen Xu, Mujid S. Kazimi, and Michael J. Driscoll, 2005. Impact of High Burnup on PWR Spent Fuel Characteristics, Nuclear Science and Engineering: 151, 261–273.

10. Appendixes

10.1. Appendix 1 Input Data for 32.5 cm thick gamma shielding¹⁵

BEGIN CONTROL DATA

RUN

TIME LIMIT 3600

SEEDS 12345 54321

END

BEGIN OUTPUT CONTROL

SUPPRESS INFLOWS

END

BEGIN MATERIAL GEOMETRY

PART 1 NEST

							!fuel rod
ZROD	M1	0.63	0.63	11.75	0.4095	377.45	!active fuel length
ZROD	M2	0.63	0.63	11.75	0.418	377.45	!gap filled with helium
ZROD	M3	0.63	0.63	11.75	0.475	377.45	!fuel clad
ZROD	M3	0.63	0.63	10.00	0.475	379.20	!upper and lower end plug
ZROD	M4	0.63	0.63	0.00	0.475	409.20	!Upper and lower hardwares

VOLUMES UNITY

PART 2 NEST

ZROD	P1	0.63	0.63	0.00	0.475	409.20	
BOX	M5	0.00	0.00	0.00	1.26	1.26	409.20 !moderator

VOLUMES UNITY

PART 3 NEST

ZROD	P1	0.63	0.63	0.00	0.475	409.20	
BOX	M0	0.00	0.00	0.00	1.26	1.26	409.20 !VOID

VOLUMES UNITY

PART 4 NEST

							!guide tube with absorber
ZROD	M6	0.63	0.63	0.00	0.436	409.20	!absorber rod
ZROD	M7	0.63	0.63	0.00	0.486	409.20	!absorber clad
ZROD	M5	0.63	0.63	0.00	0.573	409.20	!gap (control rod & guide tube)
ZROD	M3	0.63	0.63	0.00	0.613	409.20	!guide tube

VOLUMES UNITY

¹⁵ Not all calculation input data are given due to space constraints. (including the varying of Neutron shielding thickness, water level changes, Burnup, Cooling Time And Initial Enrichment Effect)

PART 5 NEST

ZROD	P4	0.63	0.63	0.00	0.613	409.20		
BOX	M5	0.00	0.00	0.00	1.26	1.26	409.20	!moderator

VOLUMES UNITY

PART 6 NEST

ZROD	P4	0.63	0.63	0.00	0.613	409.20		
BOX	M0	0.00	0.00	0.00	1.26	1.26	409.20	!void

VOLUMES UNITY

PART 7 NEST

ZROD	M5	0.63	0.63	0.00	0.573	409.20		!guide tube without absorber
ZROD	M3	0.63	0.63	0.00	0.613	409.20		!modertor in guide tube
								!guide tube

VOLUMES UNITY

PART 8 NEST

ZROD	P7	0.63	0.63	0.00	0.613	409.20		
BOX	M5	0.00	0.00	0.00	1.26	1.26	409.20	!moderator

VOLUMES UNITY

PART 9 NEST

ZROD	P7	0.63	0.63	0.00	0.613	409.20		
BOX	M0	0.00	0.00	0.00	1.26	1.26	409.20	!void

VOLUMES UNITY

PART 10 ARRAY

17 17 1

!17*17 typical PWR fuel assembly

```

2 2 2 2 2 2 2 2 2 2 2 2 2 2 2 2 2
2 2 2 2 2 2 2 2 2 2 2 2 2 2 2 2 2
2 2 2 2 2 5 2 2 5 2 2 5 2 2 2 2 2
2 2 2 5 2 2 2 2 2 2 2 2 2 5 2 2 2
2 2 2 2 2 2 2 2 2 2 2 2 2 2 2 2 2
2 2 5 2 2 5 2 2 5 2 2 5 2 2 5 2 2
2 2 2 2 2 2 2 2 2 2 2 2 2 2 2 2 2
2 2 2 2 2 2 2 2 2 2 2 2 2 2 2 2 2
2 2 5 2 2 5 2 2 8 2 2 5 2 2 5 2 2
2 2 2 2 2 2 2 2 2 2 2 2 2 2 2 2 2
2 2 2 2 2 2 2 2 2 2 2 2 2 2 2 2 2
2 2 5 2 2 5 2 2 5 2 2 5 2 2 5 2 2
2 2 2 2 2 2 2 2 2 2 2 2 2 2 2 2 2
2 2 2 5 2 2 2 2 2 2 2 2 2 5 2 2 2
2 2 2 2 2 5 2 2 5 2 2 5 2 2 2 2 2

```

2 2 2 2 2 2 2 2 2 2 2 2 2 2 2 2
 2 2 2 2 2 2 2 2 2 2 2 2 2 2 2 2

PART 11 ARRAY

!fuel assembly

17 17 1

!17*17 typical PWR fuel assembly with ullage

2 2 2 2 2 2 2 2 2 2 2 2 2 2 2 2
 2 2 2 2 2 2 2 2 2 2 2 2 2 2 2 2
 2 2 2 2 5 2 2 5 2 2 5 2 2 2 2 2
 2 2 2 5 2 2 2 2 2 2 2 2 5 2 2 2
 2 2 2 2 2 2 2 2 2 2 2 2 2 2 2 2
 2 2 5 2 2 5 2 2 5 2 2 5 2 2 2 2
 2 2 2 2 2 2 2 2 2 2 2 2 2 2 2 2
 2 2 2 2 2 2 2 2 2 2 2 2 2 2 2 2
 3 3 6 3 3 6 3 3 9 3 3 6 3 3 6 3 3
 3 3 3 3 3 3 3 3 3 3 3 3 3 3 3 3
 3 3 3 3 3 3 3 3 3 3 3 3 3 3 3 3
 3 3 6 3 3 6 3 3 6 3 3 6 3 3 6 3 3
 3 3 3 3 3 3 3 3 3 3 3 3 3 3 3 3
 3 3 3 6 3 3 3 3 3 3 3 3 6 3 3 3
 3 3 3 3 6 3 3 6 3 3 6 3 3 3 3 3
 3 3 3 3 3 3 3 3 3 3 3 3 3 3 3 3
 3 3 3 3 3 3 3 3 3 3 3 3 3 3 3 3

PART 12 NEST

!Separate compartment in MEB

BOX P10 1.04 1.04 0.0 21.42 21.42 409.20

!fuel assembly

BOX M5 0.5 0.5 0.0 22.5 22.5 450.0

!Bounded sheet inner dimension

BOX M8 0.0 0.0 0.0 23.5 23.5 450.0

!Bounded sheet outer dimension

VOLUMES UNITY

PART 13 NEST

BOX P11 1.04 1.04 0.0 21.42 21.42 409.20

!fuel assembly with ullage

BOX M5 0.5 0.5 0.0 22.5 22.5 450.0

!Bounded sheet inner dimension

BOX M8 0.0 0.0 0.0 23.5 23.5 450.0

!Bounded sheet outer dimension

VOLUMES UNITY

PART 14

!combination of 7 fuel assembly

BOX 1 -11.75 -11.75 0.0 23.5 23.5 450

!fuel assembly with Fixed plate 1

BOX 2 -35.25 -11.75 0.0 23.5 23.5 450

!fuel assembly with Fixed plate 2

BOX 3 11.75 -11.75 0.0 23.5 23.5 450

!fuel assembly with Fixed plate 3

BOX 4 -23.5 11.75 0.0 23.5 23.5 450

!fuel assembly with Fixed plate 4

BOX 5 0.0 11.75 0.0 23.5 23.5 450

!fuel assembly with Fixed plate 5

BOX 6 -23.5 -35.25 0.0 23.5 23.5 450

!fuel assembly with Fixed plate 6

BOX 7 0.0 -35.25 0.0 23.5 23.5 450

!fuel assembly with Fixed plate 7

IHS 8 0.0 23.0 0.0 0.0 1.0 0.0
CONTAINER
ZROD 9 0.0 0.0 0.0 43.5 450 !cavity dimension filled with water
ZONES

/assembly1/ P12 +1
/assembly2/ P12 +2
/assembly3/ P12 +3
/assemblyU1/ P13 +4
/assemblyU2/ P13 +5
/assembly4/ P12 +6
/assembly5/ P12 +7
/felwater/ M5 +9 -1 -2 -3 -4 -5 -6 -7 -8
/felvoid/ M0 +9 -1 -2 -3 -4 -5 -6 -7 +8

VOLUMES UNITY

PART 15 NEST !MEB
ZROD P14 0.0 0.0 15.0 43.5 450.0 !fuel chamber
ZROD M7 0.0 0.0 13.0 43.5 452.0 !Fixed plate
ZROD M0 0.0 0.0 3.0 43.5 462.0 !Additional chamber
ZROD M7 0.0 0.0 0.0 45.5 468.0 !entire MEB vessel

VOLUMES UNITY

PART 16 NEST !lifting pintle and
ZROD M7 0.0 0.0 0.0 5.5 9.0 !lifting trunnion and
ZROD M0 0.0 0.0 0.0 9.5 9.0 !secondary trunnion
ZROD M7 0.0 0.0 0.0 9.5 13.0

VOLUMES UNITY

PART 17 NEST !MEB in flask cave
ZROD P15 0.0 0.0 0.0 45.5 468.0 !entire MEB vessle
ZROD M0 0.0 0.0 0.0 46.5 472.5 !flask cave
ZROD M9 0.0 0.0 0.0 79.0 472.5 !gamma shielding
ZROD M10 0.0 0.0 0.0 93.0 472.5 !neutron shielding
ZROD M11 0.0 0.0 0.0 106.5 472.5 !smearred region of cooling fins

VOLUMES UNITY

PART 18 CLUSTER !middle part of the flask
ZROD P17 0.0 0.0 0.0 106.5 472.5
ZROD P16 -106.5 0.0 440 9.5 13.0 YROT 90 !secondary trunnion
ZROD P16 106.5 0.0 440 9.5 13.0 YROT -90
ZROD M0 0.0 0.0 0.0 120.5 472.5

VOLUMES UNITY

PART 19 CLUSTER !lid inner part

ZROD M7	0.0 0.0 0.0	79.0	32.5		
ZROD P16	-79 0.0 16.25	9.5	13.0	YROT 90	!lifting trunnion
ZROD P16	79 0.0 16.25	9.5	13.0	YROT -90	
ZROD P16	0.0 0.0 32.5	9.5	13.0		!lifting pintle
ZROD M12	0.0 0.0 0.0	120.0	56.25		
VOLUMES UNITY					
PART 20 NEST					
ZROD P19	0.0 0.0 0.0	120.0	56.25		!lid and upper shock absorber
ZROD M7	0.0 0.0 0.0	120.5	56.75		
VOLUMES UNITY					
PART 21 CLUSTER					
ZROD M9	0.0 0.0 23.75	79.0	32.5		!base inner part
ZROD P16	-79 0.0 40.75	9.5	13.0	YROT 90	!lifting trunnion
ZROD P16	79 0.0 40.75	9.5	13.0	YROT -90	
ZROD M12	0.0 0.0 0.5	120.0	56.25		
VOLUMES UNITY					
PART 22 NEST					
ZROD P21	0.0 0.0 0.5	120.0	56.25		!base and lower shock absorber
ZROD M7	0.0 0.0 0.0	120.5	56.75		
VOLUMES UNITY					
PART 23 CLUSTER					
ZROD P18	0.0 0.0 0.0	120.5	472.5		!flask globe part
ZROD P20	0.0 0.0 472.5	120.5	56.75		
ZROD P22	0.0 0.0 -56.75	120.5	56.75		
ZROD M0	0.0 0.0 -56.75	120.5	600.0		
VOLUMES UNITY					
PART 24					
ZROD 1	0.0 0.0 -5.5	120.5	600.0		!scoring region
ZROD 2	0.0 0.0 594.5	140	1		!flask wall
ZROD 3	0.0 0.0 693.5	140	2		
ZROD 4	0.0 0.0 -200.0	240	1200		
ZROD 5	0.0 0.0 450.0	30.0	400		
ZROD 6	0.0 0.0 450.0	60.0	400		
ZROD 7	0.0 0.0 450.0	90.0	400		
ZROD 8	0.0 0.0 600.0	110.0	88.0		
ZROD 9	0.0 0.0 -5.5	121.5	586.0		
ZROD 10	0.0 0.0 -5.5	221.5	586.0		
ZROD 11	0.0 0.0 -5.5	223.5	586.0		

ZONES

/FLASKWALL/	P23	+1	!zone1
/LIDSCORE1/	M0	+2 +5	!zone2
/LIDSCORE2/	M0	+2 +6 -5	!zone3
/LIDSCORE3/	M0	+2 +7 -6	!zone4
/LIDSCORE4/	M0	+2 -7	!zone5
/1MSCORE1/	M0	+3 +5	!zone6
/1MSCORE2/	M0	+3 +6 -5	!zone7
/1MSCORE3/	M0	+3 +7 -6	!zone8
/1MSCORE4/	M0	+3 -7	!zone9
/FINSCORE/	M0	+9 -1	!zone10
/1MFINSORE/	M0	+11 -10	!zone11
/DUMMYZONE1/	M0	+8	!zone12
/DUMMYZONE2/	M0	+10 -9	!zone13
/OUTERVOID/	M0	+4 -1 -2 -3 -8 -11	!zone14
/EXTVOID/	M-2000	-4	!zone15

VOLUMES

1.0 2.826E3 8.478E3 1.696E4 4.459E4 5.652E3 1.696E4 3.391E4
8.918E4 4.453E5 1.638E6 1.0 1.0 1.0 1.0

END

BEGIN MATERIAL SPECIFICATION

TYPE

GAMMA

NORMALISE

!revise so all PROP=1.0

WEIGHT

MIXTURE 1

!Mixture define: Balsa Wood

H 0.06545
O 0.40175
C 0.5328

ATOMS

MIXTURE 2

!Mixture define: Borated water

H 2.00
O 1.00
B10 0.00018

WEIGHT

MIXTURE 3

!Mixture define: Carbon steel

FE 0.9926
C 0.002

MN 0.0045
P 0.0004
S 0.0005

WEIGHT

MIXTURE 4

!Mixture define:stainless steel

MN 0.01
NI 0.09
CR 0.175
FE 0.725

WEIGHT

MIXTURE 5

!Mixture define:air

N 7.65172E-1
O 2.34828E-1

NUMDEN

MATERIAL 1

!spent PWR fuel

U235 3.403E-4
U236 1.005E-4
U238 2.111E-2
PU238 2.050E-6
PU239 1.240E-4
PU240 4.103E-5
PU241 2.453E-5
PU242 6.292E-6

ATOMS

MATERIAL 2 DENSITY 1.786E-4
HE PROP 1.0

!Helium

NUMDEN

MATERIAL 3

!fuel Cladding material

FE 1.383E-4
CR 7.073E-5
O 2.874E-4
ZR 3.956E-2

NUMDEN

MATERIAL 4

!Upper and lower hardware

CR 8.714E-03
MN 8.682E-04
FE 2.968E-02
NI 3.860E-03

H	3.338E-02			
O	1.669E-02			
VOLUME				
MATERIAL 5	MIXTURE 2	DENSITY 0.79	PROP 1.0	!Water/Boron Water
ATOMS				
MATERIAL 6	DENSITY 7.41			!control rods/ Absorber
GD	2.00			
O	3.00			
NUMDEN				
MATERIAL 7				!stainless steel
CR	1.743E-02			
MN	1.736E-03			
FE	5.936E-02			
NI	7.721E-03			
NUMDEN				
MATERIAL 8				!Borated stainless steel (1 wt.% boron)
CR	1.691E-02			
MN	1.684E-03			
FE	5.758E-02			
NI	7.489E-03			
B10	7.836E-04			
B11	3.181E-03			
WEIGHT				
MATERIAL 9	DENSITY 7.872	MIXTURE 3	PROP 1.0	!Carbon steel
NUMDEN				
MATERIAL 10				!Boro-silicone
H	4.49E-2			
B	9.40E-4			
VOLUME				
MATERIAL 11				!smearred region of cooling fins
MIXTURE 4	DENSITY 7.905		PROP 0.3	
MIXTURE 5	DENSITY 0.001225		PROP 0.7	
VOLUME				
MATERIAL 12				!Balsa Wood
MIXTURE 1	DENSITY 0.64		PROP 1.0	

END

BEGIN ENERGY DATA

GAMMA

SPLITTING GROUPS 17 4.0 3.0 2.5 2.0 1.66 1.44 1.22 1.0 0.8
0.6 0.511 0.4 0.3 0.2 0.1 0.05 0.02 0.01

SCORING GROUPS 8 4.0 3.0 2.0 1.5 1.0 0.5 0.2 0.1 0.01

UNIFIED SOURCE

END

BEGIN UNIFIED SOURCE DATA

GEOMETRY

FGBODY x2 1 IN PART 1

!source body

ENERGY LINES

3.5 2.9 2.5 2.2 1.55 1.0 0.76 0.51 0.27

INTENSITY BODY x2

COMPONENT ENERGY

1.3E4 6.4E5 3.0E6 7.6E7 1.7E8

4.5E8 5.9E8 7.0E9 7.2E8

WEIGHTING AUTOMATIC

!source weighting

END

BEGIN SPLITTING GEOMETRY

R 22 0.0 10.0 15.0 20.0 25.0 30.0 45.0 50.0 55.0 60.0 65.0

70.0 75.0 80.0 85.0 90.0 95.0 100.0 105.0 110.0 115.0 120.5 240.0

Z 64 -200.0 -5.5 44.5 64.5 84.5 104.5 124.5 144.5 164.5 184.5 204.5 224.5

244.5 264.5 284.5 304.5 324.5 344.5 354.5 364.5 374.5 384.5 394.5 404.5

414.5 424.5 434.5 444.5 454.5 464.5 474.5 484.5 494.5 504.5 514.5 524.5

526.5 528.5 530.5 532.5 534.5 536.5 538.5 540.5 542.5 544.5 546.5 548.5

550.0 552.5 554.5 556.5 558.5 560.5 562.5 564.5 566.5 568.5 570.5 572.5

574.5 576.5 578.5 580.5 1200.0

BEGIN IMPORTANCE MAP

CALCULATE

TARGETS 2

PART 24 ZONES 12 13

STRENGTHS 0.3 0.7

END

BEGIN SCORING DATA

FLUX ALL

RESPONSES

PART 24 SOME 2 3 4 5 6 7 8 9 10 11

END

BEGIN RESPONSE DATA

FUNCTION GAMMA DOSE

END

10.2. Appendix 2 Partial input Data for TRISO PWR fuel¹⁶

BEGIN MATERIAL GEOMETRY

PART 1 NEST

SPHERE	M1	0.0	0.0	0.0	0.0	0.02			!TRISO fuel particle
SPHERE	M14	0.0	0.0	0.0	0.0	0.03			!Carbon Buffer
SPHERE	M13	0.0	0.0	0.0	0.0	0.035			!Inner Pyretic Carbon
SPHERE	M15	0.0	0.0	0.0	0.0	0.0385			!SiC
SPHERE	M13	0.0	0.0	0.0	0.0	0.043			!outer Pyretic Carbon
ZHEX	M2	0.0	0.0	-0.0435	0.0435	0.087			

VOLUMES UNITY

PART 2 ZHEXARRAY

M2 0.427 0.087 6

91*1

PART 3 NEST

ZHEX	P2	0.0	0.0	0.0	0.427	0.087			
ZROD	M3	0.0	0.0	0.0	0.495	0.087			!fuel cladding
BOX	M0	-0.63	-0.63	0.0	1.26	1.26	0.087		

VOLUMES UNITY

PART 4 ARRAY

1 1 500

500*3

PART 5 NEST

BOX	P4	10.08	10.08	11.75	1.26	1.26	43.5		
BOX	M0	0.0	0.0	0.0	21.42	21.42	409.2		

¹⁶ Other parts of input data are similar with the normal PWR case.

10.4. Appendix 4 Detailed Tables

Table 21. Atom densities for dominant absorbers in spent fuel, atom/barn-cm (PWR typical irradiation history 4.0% enrichment, 2 years cooling)¹⁸

Isotope	Fresh fuel	5 GWd/MTU	25 GWd/MTU	45 GWd/MTU	60 GWd/MTU
U234	8.0703E-6	7.5573E-6	5.6947E-6	4.2338E-6	3.3970E-6
U235	8.9287E-4	7.6753E-4	4.1457E-4	2.1064E-4	1.2123E-4
U236	4.0008E-6	2.7941E-5	9.1280E-5	1.1956E-4	1.2567E-4
U238	2.1146E-2	2.1071E-2	2.0737E-2	2.0357E-2	2.0049E-2
O16	4.4102E-2	4.4102E-2	4.4102E-2	4.4102E-2	4.4102E-2
RH103		4.0538E-6	1.9618E-5	3.1746E-5	3.8788E-5
SM149		1.0605E-7	1.8203E-7	2.3211E-7	2.7587E-7
ND143		6.5941E-6	2.7107E-5	4.0254E-5	4.6425E-5
TC99		7.1306E-6	3.2812E-5	5.4041E-5	6.7337E-5
SM152		5.8207E-7	3.3122E-6	5.4754E-6	6.9481E-6
SM151		2.9445E-7	6.4058E-7	8.9419E-7	1.0839E-6
SM147		1.2892E-6	4.8901E-6	6.6844E-6	6.9200E-6
GD155		1.0909E-8	8.3253E-8	2.4304E-7	3.8764E-7
EU153		2.7307E-7	2.5309E-6	5.3183E-6	7.2657E-6
MO95		7.2935E-6	3.3402E-5	5.5642E-5	7.0429E-5
ND145		4.4822E-6	2.0015E-5	3.2533E-5	4.0317E-5
AG109		1.6852E-7	1.9938E-6	4.3723E-6	6.1231E-6
SM150		1.2800E-6	8.2746E-6	1.5928E-5	2.2224E-5
RU101		6.0969E-6	3.0408E-5	5.3962E-5	7.0924E-5
PM147		1.1635E-6	3.6120E-6	4.3233E-6	4.7149E-6
CS133		7.8292E-6	3.5843E-5	5.8632E-5	7.2611E-5
NP237		9.2000E-7	8.6287E-6	1.7799E-5	2.3519E-5
PU238		4.2529E-8	2.0775E-6	8.0020E-6	1.3789E-5
PU239		5.3333E-5	1.4792E-4	1.7469E-4	1.8097E-4
PU240		3.8582E-6	3.3823E-5	5.7846E-5	6.9227E-5
PU241		9.2101E-7	2.2540E-5	4.2571E-5	5.1756E-5
PU242		2.8180E-8	3.9882E-6	1.4628E-5	2.4385E-5
AM241		1.1178E-7	2.9786E-6	5.7685E-6	6.6701E-6
AM243		7.3625E-10	6.4303E-7	4.2610E-6	8.9440E-6
CM244		1.8136E-11	1.0051E-7	1.3958E-6	4.2626E-6

¹⁸ S. P. Cerne, Q. W. Hermann and R. M. Westfall, 1987. Reactivity and isotopic composition of spent PWR fuel as a function of initial enrichment, burnup, and cooling time, ORNL/CSD/TM-244.

Table 22. Atom densities for dominant absorbers in spent fuel, atom/barn-cm (PWR typical irradiation history 4.0% enrich, 45 GWd/MTU)¹⁹

ISOTOPE	AT. DENSITY 2 year cool	AT. DENSITY 10 year cool	AT. DENSITY 20 year cool
U234	4.2338E-6	4.7253E-6	5.2979E-6
U235	2.1064E-4	2.1068E-4	2.1073E-4
U236	1.1956E-4	1.1961E-4	1.1967E-4
U238	2.0357E-2	2.0357E-2	2.0357E-2
O16	4.4102E-2	4.4102E-2	4.4102E-2
RH103	3.1746E-5	3.1746E-5	3.1746E-5
SM149	2.3211E-7	2.3211E-7	2.3211E-7
ND143	4.0254E-5	4.0254E-5	4.0254E-5
TC99	5.4041E-5	5.4040E-5	5.4038E-5
SM152	5.4754E-6	5.4758E-6	5.4761E-6
SM151	8.9419E-7	8.4076E-7	7.7843E-7
SM147	6.6844E-6	1.0485E-5	1.0970E-5
GD155	2.4304E-7	7.2628E-7	9.0299E-7
EU153	5.3183E-6	5.3183E-6	5.3183E-6
MO95	5.5642E-5	5.5645E-5	5.5645E-5
ND145	3.2533E-5	3.2533E-5	3.2533E-5
AG109	4.3723E-6	4.3723E-6	4.3723E-6
SM150	1.5928E-5	1.5928E-5	1.5928E-5
RU101	5.3962E-5	5.3962E-5	5.3962E-5
PM147	4.3233E-6	5.2219E-7	3.7182E-8
CS133	5.8632E-5	5.8632E-5	5.8632E-5
NP237	1.7799E-5	1.7964E-5	1.8360E-5
PU238	8.0020E-6	7.5391E-6	6.9688E-6
PU239	1.7469E-4	1.7465E-4	1.7461E-4
PU240	5.7846E-5	5.8165E-5	5.8430E-5
PU241	4.2571E-5	2.9193E-5	1.8218E-5
PU242	1.4628E-5	1.4628E-5	1.4628E-5
AM241	5.7685E-6	1.8981E-5	2.9560E-5
AM243	4.2610E-6	4.2578E-6	4.2538E-6
CM244	1.3958E-6	1.0276E-6	7.0086E-7

¹⁹ S. P. Cerne, Q. W. Hermann and R. M. Westfall, 1987. Reactivity and isotopic composition of spent PWR fuel as a function of initial enrichment, burnup, and cooling time, ORNL/CSD/TM-244.

Table 23. Atom densities for dominant absorbers in spent fuel, atom/barn-cm (PWR typical irradiation history 2 years cooling, 45 GWd/MTU)²⁰

ISOTOPE	AT. DENSITY Enrichment 3.00	AT. DENSITY Enrichment 3.50	AT. DENSITY Enrichment 4.00	AT. DENSITY Enrichment 4.25
U234	2.9311E-6	3.5125E-6	4.2338E-6	4.5489E-6
U235	1.1123E-4	1.5709E-4	2.1064E-4	2.3998E-4
U236	9.1868E-5	1.0618E-4	1.1956E-4	1.2607E-4
U238	2.0492E-2	2.0428E-2	2.0357E-2	2.0319E-2
O16	4.4097E-2	4.4100E-2	4.4102E-2	4.4104E-2
RH103	3.2128E-5	3.1928E-5	3.1746E-5	3.1661E-5
SM149	2.0420E-7	2.1746E-7	2.3211E-7	2.3991E-7
ND143	3.6373E-5	3.8399E-5	4.0254E-5	4.1113E-5
TC99	5.2793E-5	5.3446E-5	5.4041E-5	5.4317E-5
SM152	5.5748E-6	5.5247E-6	5.4754E-6	5.4513E-6
SM151	7.9642E-7	8.4370E-7	8.9419E-7	9.2029E-7
SM147	6.1313E-6	6.4141E-6	6.6844E-6	6.8137E-6
GD155	2.5627E-7	2.4973E-7	2.4304E-7	2.3970E-7
EU153	5.5590E-6	5.4386E-6	5.3183E-6	5.2589E-6
MO95	5.3571E-5	5.4671E-5	5.5642E-5	5.6083E-5
ND145	3.1156E-5	3.1883E-5	3.2533E-5	3.2831E-5
AG109	5.0013E-6	4.6728E-6	4.3723E-6	4.2325E-6
SM150	1.6087E-5	1.6016E-5	1.5928E-5	1.5880E-5
RU101	5.4146E-5	5.4047E-5	5.3962E-5	5.3923E-5
PM147	4.0210E-6	4.1738E-6	4.3233E-6	4.3957E-6
CS133	5.7231E-5	5.7961E-5	5.8632E-5	5.8943E-5
NP237	1.6136E-5	1.7070E-5	1.7799E-5	1.8126E-5
PU238	8.2035E-6	8.1449E-6	8.0020E-6	7.9224E-6
PU239	1.6284E-4	1.6883E-4	1.7469E-4	1.7751E-4
PU240	6.1837E-5	5.9870E-5	5.7846E-5	5.6827E-5
PU241	4.2903E-5	4.2861E-5	4.2571E-5	4.2339E-5
PU242	1.8834E-5	1.6599E-5	1.4628E-5	1.3738E-5
AM241	5.7140E-6	5.7598E-6	5.7685E-6	5.7591E-6
AM243	5.9277E-6	5.0226E-6	4.2610E-6	3.9288E-6
CM244	2.2503E-6	1.7661E-6	1.3958E-6	1.2448E-6

²⁰ S. P. Cerne, Q. W. Hermann and R. M. Westfall, 1987. Reactivity and isotopic composition of spent PWR fuel as a function of initial enrichment, burnup, and cooling time, ORNL/CSD/TM-244.

Table 24. Excellox 7 flask 14cm away from side face gamma dose rate varying with gamma shielding thickness

thickness	Dose	Samples	COEF of VAR. (%)	+ST.DEV.	+ST.DEV.
7.5	7.812E+03	1854820	0.3	7.84E+03	7.79E+03
12.5	1.336E+03	792892	0.3	1.34E+03	1.33E+03
17.5	2.481E+02	729290	0.3	2.49E+02	2.47E+02
22.5	4.826E+01	552408	0.3	4.84E+01	4.81E+01
27.5	9.594E+00	421758	0.3	9.63E+00	9.56E+00
32.5	1.943E+00	442659	0.4	1.95E+00	1.94E+00
37.5	3.989E-01	212762	0.5	4.01E-01	3.97E-01
42.5	8.359E-02	172388	0.6	8.41E-02	8.31E-02
47.5	1.765E-02	135346	0.7	1.78E-02	1.75E-02
52.5	3.684E-03	108633	0.8	3.71E-03	3.66E-03
57.5	7.727E-04	92434	0.9	7.80E-04	7.66E-04

Table 25. Excellox 7 flask 1 meter away from side face gamma dose rate varying with gamma shielding thickness

thickness	Dose	Samples	COEF of VAR	+ST.DEV.	+ST.DEV.
7.5	3.893E+03	1818076	0.4	3.91E+03	3.88E+03
12.5	6.684E+02	781460	0.3	6.70E+02	6.67E+02
17.5	1.245E+02	720894	0.3	1.25E+02	1.24E+02
22.5	2.421E+01	547060	0.3	2.43E+01	2.41E+01
27.5	4.825E+00	418370	0.3	4.84E+00	4.81E+00
32.5	9.772E-01	439694	0.4	9.81E-01	9.74E-01
37.5	2.009E-01	211575	0.5	2.02E-01	2.00E-01
42.5	4.220E-02	171530	0.6	4.24E-02	4.20E-02
47.5	8.905E-03	134756	0.7	8.96E-03	8.85E-03
52.5	1.865E-03	108250	0.8	1.88E-03	1.85E-03
57.5	3.916E-04	92098	0.9	3.95E-04	3.88E-04

Table 26. Excellox 7 flask shock absorber surface gamma dose rate varying with gamma shielding thickness

thickness	Dose rate ^a	Samples	COEF of VAR. (%)	+ST.DEV.	+ST.DEV.
7.5	5.960E+01	2015	3.6	6.17E+01	5.75E+01
12.5	1.468E+01	1150	4.7	1.54E+01	1.40E+01
17.5	3.477E+00	1375	5.0	3.65E+00	3.30E+00
22.5	7.977E-01	1325	4.9	8.37E-01	7.59E-01
27.5	1.935E-01	1152	5.5	2.04E-01	1.83E-01
32.5	4.564E-02	1523	4.6	4.77E-02	4.35E-02
37.5	1.006E-02	877	6.3	1.07E-02	9.43E-03
42.5	2.482E-03	927	6.8	2.65E-03	2.31E-03
47.5	4.113E-04	708	7.1	4.40E-04	3.82E-04
52.5	8.415E-05	566	7.3	9.03E-05	7.80E-05
57.5	1.880E-05	614	8.2	2.03E-05	1.73E-05

a: gamma dose rate in region 2.

Table 27. Excellox 7 flask 1 meter away from lid surface gamma dose rate varying with gamma shielding thickness

thickness	Dose rate ^b	Samples	COEF of VAR. (%)	+ST.DEV.	+ST.DEV.
7.5	2.384E+01	1563	3.9	2.48E+01	2.29E+01
12.5	5.299E+00	896	5.4	5.58E+00	5.01E+00
17.5	1.283E+00	1104	5.6	1.35E+00	1.21E+00
22.5	2.727E-01	1021	5.1	2.87E-01	2.59E-01
27.5	6.870E-02	986	5.5	7.24E-02	6.49E-02
32.5	1.629E-02	1299	4.5	1.70E-02	1.56E-02
37.5	3.386E-03	944	5.8	3.58E-03	3.19E-03
42.5	8.140E-04	977	6.3	8.65E-04	7.63E-04
47.5	1.501E-04	729	6.7	1.60E-04	1.40E-04
52.5	2.863E-05	619	7.1	3.07E-05	2.66E-05
57.5	6.964E-06	660	7.6	7.49E-06	6.43E-06

b: gamma dose rate in region 6.

Table 28. Excellox 7 flask 14 cm away from side face neutron dose rate varying with Neutron shielding thickness

thickness	Dose	Samples	COEF of VAR	+ST.DEV.	+ST.DEV.
4	1.709E+01	1119635	0.2	1.71E+01	1.71E+01
6	1.046E+01	1793908	0.2	1.05E+01	1.04E+01
8	6.564E+00	1719495	0.2	6.57E+00	6.55E+00
10	4.207E+00	1616762	0.2	4.21E+00	4.20E+00
12	2.743E+00	1104955	0.2	2.75E+00	2.74E+00
14	1.822E+00	1052075	0.2	1.83E+00	1.82E+00
16	1.233E+00	962040	0.2	1.24E+00	1.23E+00
18	8.445E-01	1204855	0.2	8.46E-01	8.43E-01
20	5.937E-01	1105142	0.2	5.95E-01	5.92E-01
22	4.229E-01	993052	0.2	4.24E-01	4.22E-01
24	3.027E-01	847718	0.2	3.03E-01	3.02E-01

Table 29. Excellox 7 flask 1 meter away from side face neutron dose rate varying with Neutron shielding thickness

thickness	Dose	Samples	COEF of VAR	+ST.DEV.	+ST.DEV.
4	7.760E+00	1105973	0.2	7.78E+00	7.74E+00
6	4.750E+00	1774767	0.2	4.76E+00	4.74E+00
8	2.982E+00	1701446	0.2	2.99E+00	2.98E+00
10	1.910E+00	1601128	0.2	1.91E+00	1.91E+00
12	1.246E+00	1094383	0.2	1.25E+00	1.24E+00
14	8.267E-01	1042003	0.2	8.28E-01	8.25E-01
16	5.603E-01	953360	0.2	5.62E-01	5.59E-01
18	3.837E-01	1192933	0.2	3.85E-01	3.83E-01
20	2.695E-01	1094893	0.2	2.70E-01	2.69E-01
22	1.920E-01	983190	0.2	1.92E-01	1.92E-01
24	1.375E-01	839287	0.2	1.38E-01	1.37E-01

Table 30. Gamma dose rate varying with spent fuel burnup

Burnup	Gamma Dose rate	Samples	COEF of VAR. (%)	+ST.DEV.	+ST.DEV.
5 GWd/MTU	1.929E+00	441696	0.3	1.94E+00	1.92E+00
25 GWd/MTU	1.961E+00	433905	0.3	1.97E+00	1.95E+00
45 GWd/MTU	2.000E+00	444275	0.4	2.01E+00	1.99E+00
60 GWd/MTU	2.029E+00	390807	0.4	2.04E+00	2.02E+00

Scoring at 14 cm from cooling fins

Table 31. Neutron dose rate varying with spent fuel burnup

Burnup	Neutron Dose rate	Samples	COEF of VAR. (%)	+ST.DEV.	+ST.DEV.
Fresh fuel	1.827E+00	1061351	0.2	1.83E+00	1.82E+00
5 GWd/MTU	1.823E+00	1054345	0.2	1.83E+00	1.82E+00
25 GWd/MTU	1.829E+00	1243072	0.2	1.83E+00	1.83E+00
45 GWd/MTU	1.831E+00	1233335	0.2	1.83E+00	1.83E+00
60 GWd/MTU	1.843E+00	1430098	0.2	1.85E+00	1.84E+00

Table 32. Gamma dose rate varying with distance

Distance ²¹	Dose rate	Samples	COEF of VAR. (%)	+ST.DEV.	+ST.DEV.
0.14	2.005E+00	400787	0.3	2.01E+00	2.00E+00
1.0	1.008E+00	398921	0.3	1.01E+00	1.00E+00
2.0	6.432E-01	392279	0.3	6.45E-01	6.41E-01
3.0	4.513E-01	382472	0.3	4.53E-01	4.50E-01
4.0	3.344E-01	371000	0.3	3.35E-01	3.33E-01
5.0	2.572E-01	358718	0.3	2.58E-01	2.56E-01

Table 33. Neutron dose rate varying with distance

Distance	Dose rate	Samples	COEF of VAR. (%)	+ST.DEV.	+ST.DEV.
0.14	1.835E+00	1389123	0.1	1.84E+00	1.83E+00
1.0	8.332E-01	1384233	0.1	8.34E-01	8.32E-01
2.0	4.981E-01	1369126	0.1	4.99E-01	4.97E-01
3.0	3.322E-01	1348113	0.1	3.33E-01	3.32E-01
4.0	2.363E-01	1323477	0.1	2.37E-01	2.36E-01
5.0	1.759E-01	1296254	0.1	1.76E-01	1.76E-01

²¹ Distance from cooling fins.

Table 34. TRISO PWR fuel case 1 dose rate scoring at 14cm from the cooling fins

Gamma Dose rate	Samples	COEF of VAR. (%)	+ST.DEV.	+ST.DEV.
Normal UO ₂ fuel				
1.272E-01	1074080	0.2	1.28E-01	1.27E-01
TRISO UO ₂ fuel				
1.055E-02	146215	0.6	1.06E-02	1.05E-02
Normal UO ₂ fuel of the same mass of that in TRISO type fuel for modeling				
8.312E-03	872602	0.2	8.33E-03	8.30E-03
Neutron Dose rate	Samples	COEF of VAR. (%)	+ST.DEV.	+ST.DEV.
Normal UO ₂ fuel				
1.139E-01	1407440	0.1	1.14E-01	1.14E-01
TRISO UO ₂ fuel				
6.982E-03	504879	0.3	7.00E-03	6.96E-03
Normal UO ₂ fuel of the same mass of that in TRISO type fuel for modeling				
6.453E-03	1393887	0.1	6.46E-03	6.44E-03

Table 35. TRISO PWR fuel case 2 dose rate scoring at 14cm from the cooling fins

Gamma Dose rate	Samples	COEF of VAR. (%)	+ST.DEV.	+ST.DEV.
Normal UO ₂ fuel				
1.889E-03	1192764	0.2	1.89E-03	1.89E-03
TRISO UO ₂ fuel				
1.343E-04	137850	0.5	1.35E-04	1.34E-04
Normal UO ₂ fuel of the same mass of that in TRISO type fuel for modeling				
1.239E-04	1399863	0.1	1.24E-04	1.24E-04
Neutron Dose rate	Samples	COEF of VAR. (%)	+ST.DEV.	+ST.DEV.
Normal UO ₂ fuel				
1.344E-03	1563678	0.1	1.35E-03	1.34E-03
TRISO UO ₂ fuel				
7.603E-05	719739	0.2	7.62E-05	7.59E-05
Normal UO ₂ fuel of the same mass of that in TRISO type fuel for modeling				
8.239E-05	1411594	0.1	8.25E-05	8.23E-05

10.5. Appendix 5 Extra Figures

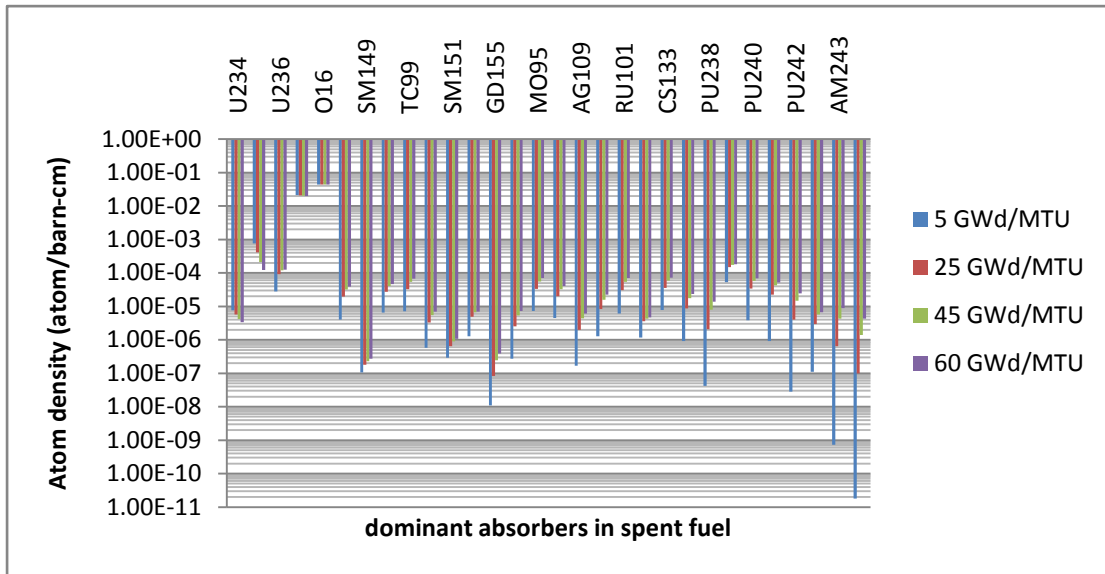


Figure 35. Burnup effect to spent fuel composition

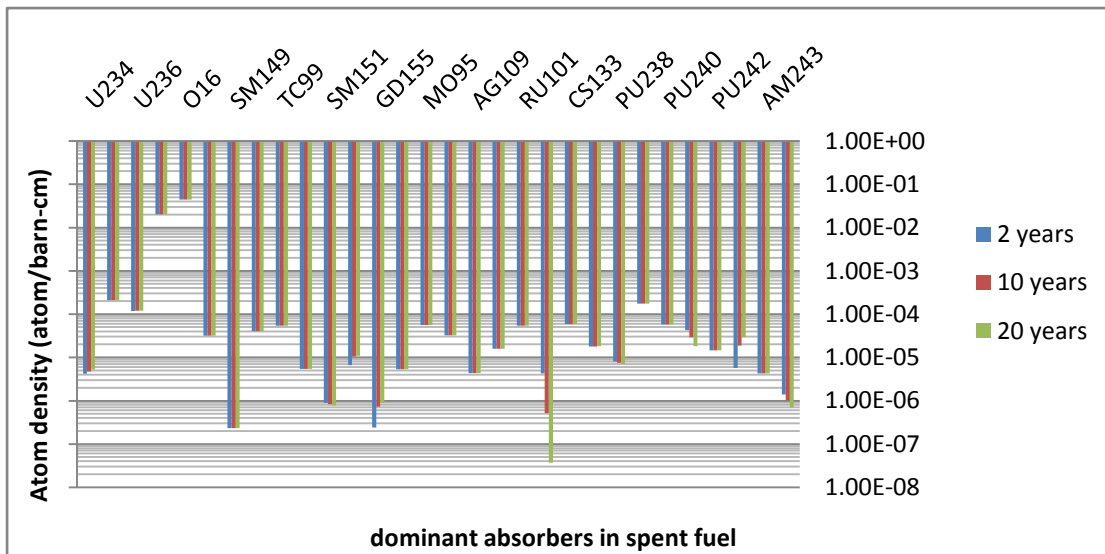


Figure 36. Cooling time effect to spent fuel composition

Appendix D

Economic Analysis of the U-Battery

November 2011

Prepared by
Theo Kooijman
Rik Linssen

Delft University of Technology

D.1 Introduction

So far, most reactors have been built with economies of scale as the leading principle by increasing the power output of the reactor: most new reactors are 1000MWe and above nowadays. There might be a good case for micro reactors, where the economy of number will dominate to achieve a similar power output. Our purpose therefore is to devise an economically feasible micro reactor (20MWth). To achieve this reactor has to be failsafe and with virtually no operating or maintenance expenses.

Based on the Cost Estimating Guidelines for Generation IV Nuclear Energy Systems we adopted a top-down approach. The model is described in the Gen IV guideline as:

“For projects early in their life cycle, top-down estimating techniques can be used. Many of the Generation IV systems will likely use these methods because these systems are at an early stage of development. At this stage, the design/development/estimating staff is usually small, and financial resources are limited. The first task is to develop a reference design to which cost estimating techniques can be applied. The cost estimating part of this task generally is accomplished by considering the costs of systems and equipment used for similar projects and then increasing or decreasing the scale of the system or equipment. As an example, one might start cost estimating on the VHTR by scaling reactor plant equipment from a project for which detailed estimates are available, such as the General Atomics HTGR.

Indirect and supplementary costs are often calculated with standardized factors or formulas. For example, design costs can be calculated as a fixed percentage of construction costs, based on historical experience. These formulas are sometimes accompanied by cost-scaling equations; however, at this time no set of equations can be used for all projects. These equations are equipment specific and must be developed by the designers and cost estimators working jointly.”

To estimate the gain by building more of a kind the Gen IV guideline says following:

“Two factors drive costs: (1) the recovery of deployment costs over the transitional units; and (2) the decline in BCC from learning-by-doing (and other cost-saving effects such as scale economies in commodity purchasing) during the construction of transitional units. (...) The decline in BCC from FOAK to NOAK units can be modeled as follows. For an approximation, when account costs are not detailed to equipment, labor, and bulk material, cost estimators can assume that direct construction costs (...) decline at the rate equivalent to 0.94”.

This approach is used together with the example worked out for the South African PEPER case. Our analysis consists of an input-throughput-output model to assess the economic parameters of a the 20 MWth and a 2*10 MWth U-Battery reactors.

D.2 Model description

At the start the Potchefstroom Experimental Pebble Bed Reactor (PEPER-Plant – Brits et al.) was set as a reference case and a list of the relevant cost items in Cost Estimating Guidelines for Generation IV Nuclear Energy Systems (e.g. Code of Accounts – COA).

In order to make an economic evaluation of our case studies of the U-battery possible, we devised an economic model in a spreadsheet. The model consists basically of an input-throughput-output sequence in which the input variables are set for the different cases¹ and calculated results are shown separately. For convenience you will find the in- en output in the Parameter sheet of the model (spreadsheet); while the throughput is put in a separate Calculation sheet.

Apart from this main sequence, we added some additional features in the economic model:

- Scenarios in order to compare different make-ups of the U-Battery.
- To answer the question which input variable has a high - and which variable has a low impact on the results a Sensitivity Analysis is added to calculate the impact of changing input parameters.

¹ The term case refers to the sequence FOAK to NOAK, while the term business case refers to different sets of parameters, i.e. a different state of the worksheet. Scenarios are used to model the different business cases of the U-Battery.

Components of the model

Parameters section (the input section of the model)

Our case uses as starting point the needed cost information for our equipment designs some bottom-up and some by searching for the scaling factors for a top down approach. These figures ended up in the Parameter sheet of the worksheet. Financial parameters are recalculated – where needed – to the same currency; which in this model is set at the euro. The actual values in this model for each parameter (calculation included) are shown in paragraph D3.

The parameters are the source for more detailed calculations for each case in the calculation sheet, where the cash flow is calculated for the duration of the project (preparation phase plus 60 years).

Calculations (the throughput section of the model)

The Calculation section of the model raises the question whether this project should be evaluated on its own merits (a separate business case) or whether this project should be treated as part of a company, with a separate balance sheet and profit & loss statement. We departed from the situation that the business case is a single project, but the model can easily be extended to a business case involving a company.

Results (the output section of the model)

Starting point in the Results table is the First-of-a-kind (FOAK) situation, which is then extrapolated to the Nth-of-a-kind (NOAK) situation, in which N is set at 8 based on the Cost Estimating Guidelines for Generation IV Nuclear Energy Systems. Each next-of-a-kind situation means an improvement of F to the prior situation:

$$IC^{\text{noak}} = F * IC^{\text{noak-1}}$$

Where

- F = Factor for improvement,
- IC = Investment Costs and
- NOAK = Nth-of-a-kind.

The Factor for improvement (F) is shown as a variable in the Parameter sheet and is set on 94% according to the guideline.

When analyzing the results of a business case, there are several measures in order to reach an optimum choice and assessment. The time value of money is of course an essential factor in the calculations, because the business cases stretch over a period of 60 years. For any investor, the profitability is important, but also the time necessary to regain the investment. The height of an investment is also of major importance.

We choose the following assessment criteria for the U-Battery business cases:

- Net Present Value (NPV, in euro)
- Total Investment (TI, in euro)
- Return on Investment [NPV/Investment] (ROI, in %)
- Nominal Pay Back Period (PBP, in years)
- Investment per KWe/h (in euro)

A positive value for the NPV indicates that the (financial) return on the U-Battery project exceeds the firm's cost of capital. By using the Firms Cost of Capital (FCOC) as percentage to calculate the present value of the cash inflow and the cash outflow, the time-value of money and the requirements of an organization for the return on investment are taken into account.

The NPV only partly shows the degree in which a project is profitable. Although the NPV shows whether a positive cash flow results, this is not related to the amount invested in the project. There's a difference between a NPV of 1 euro obtained with an investment of 10 euro's or an investment of 100 euro's.

By defining the ROI as NPV/TI we assure the relationship between both measures. While the firm's cost of capital is the base for the calculation of the NPV; a positive ROI implicitly means, that the profitability of the project exceeds the firm's cost of capital.

Because the firm's cost of capital is incorporated in the NPV, a positive ROI automatically means, that the return on the project exceeds the firm's cost of capital. Thus, a positive ROI is one of the criteria for a go/no-go decision for the project.

Thereby we established the Total initial costs of the project (TI), the net present value (NPV) and the profitability of the investment (ROI) and are able to compare these measures with the requirements of an organization.

The question remains in how many years the investment will be recovered. The Pay Back Period (PBP) is added to the model to be able to assess the business cases along this dimension.

Each of the mentioned criteria on its own makes it difficult to assess the U-Battery business cases, but taking them all together gives us a perspective from which an adequate assessment is possible. Offsetting the calculated values of these criteria against the requirements of the organization gives a financial view on the desirability of the cases.

Tools for further analysis in the model

Sensitivity Analysis

For each input parameter on the one side and for each Nth-OAK on the other side a dynamic cross table for Sensitivity Analysis was created in order to establish relations between input parameters and output in the model. By varying the input parameter with step of 10% from the original value in a range between -100% and +100% we were able to discover the impact of each variable on each case.

Both for Construction Costs as for Personnel Costs a feature is built in the model which facilitates calculating the sensitivity not only the individual parameters, but also of the group of parameters.

Comparison sheet

In the Comparison Sheet both U-Battery scenarios are compared with each other and the PEPER-case. The PEPER-case is recalculated in euro. The sheet can be used to check whether all investment costs are taken into account. A byproduct is the information about the structure of the investments per scenario.

Pivot Table & Pivot Graph

For analytical purposes a pivot table and a pivot graph are added. The pivot table is a very powerful tool with mainly two features: filtering the different dimensions of the model and/or using the different dimensions to create a cross-table.

D.3 Input Data

Introduction

The model consists of a section Input Data in which variables can be defined to make the model dynamic. The input data are grouped in six categories:

- General Data
- Financial General
- Sales Price Electricity
- Investment
- Reactor
- Running Costs

General Data

To compute the different scenarios for the U-Battery, eight financial parameters are added to the model:

Return on equity (RoE in %)	12,00
Return on debt (RoD in %)	4,00
Equity/(Total Balance sheet) (E/TB in %)	20,00
Cost of Capital (CoC in %)	5,60
Exchange rate \$→€	1,38
Exchange rate £→€	0,64
Return on Savings in %	4,00
Inflation rate in %	2,00

For the calculation of the NPV an interest percentage is needed to transfer the nominal values to present values the cost-of-capital (CoC). The variables RoE, RoD and E/TB are created in the model to arrive at the COC². In our model the CoC is calculated as³:

$$(\text{RoE} * \text{E/TB}) + (\text{RoD} * \text{D/TB})$$

In which

- E = equity,
- D= debt en
- TB = Total Balance Sheet

The conversion rates (dollar vs. euro or pound vs. euro) to calculate the scenarios in this model are kept modest to avoid the risk of underestimating the costs of the project. The chosen conversion rate for the dollar is 1.38 \$/€, while the conversion rate for the English pound is 0.64 £/€. Return on Savings is set at 4% and the inflation rate is set at 2%. These percentages are fixed over the lifetime of the project which is 60 years.

Sales Price Electricity

The Sales Price of Electricity is defined as a variable, because the selling price varies over countries and markets. In the model the selling price increase over the years with an index representing the inflation rate.

The variable Selling Price Electricity is used in the model to calculate the turnover of the U-Battery. The turnover of any year is:

$$\text{Number of hours per year} * \text{eurocents per MWh}$$

In which

$$\text{MWh} = \text{MWth} * \text{Efficiency of the U-Battery} * \text{Availability of the U-Battery}.$$

The assumption is that the U-Battery can generate electricity on full capacity immediately after Construction and testing.

Investment

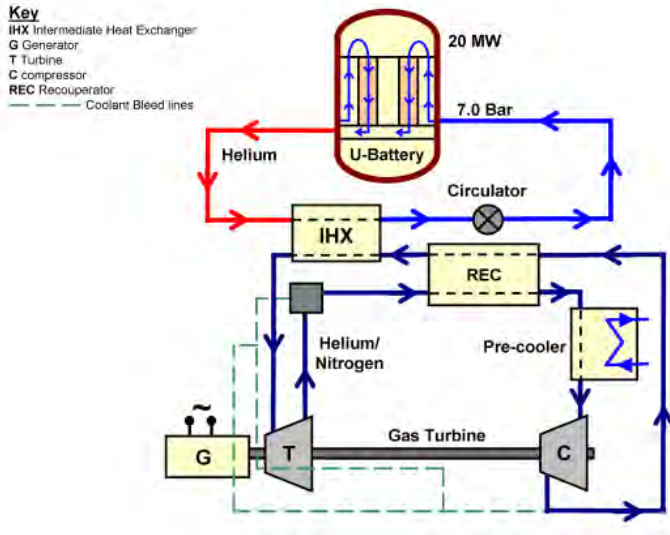
Introduction

The U-Battery contains a primary circuit, which consists of the nuclear island, and the conventional parts in which heat is converted to electricity. With the top-down approach in mind, first the Cost of Major Equipment (FOAK) is calculated; in the primary circuit this means the RPV, the Reflector Material and the Control Rods; in the secondary

² Debt/Total Balance Sheet (D/TB) is not defined as a separate input variable: it is the complement of E/TB: D/TB = 100- E/TB

³ For a more advanced calculation of the cost of equity we defer to Capital Asset Pricing Model of W.F. Sharp et al.

circuit this is the Power Generation Module. The Cost of Major Equipment in the primary and secondary circuits is then complete with an amount for Other Miscellaneous Costs.



The Costs of Major Equipment is the base for 3 Markups:

- Markup for Direct Field Costs,
- Markup for Indirect Field Costs and
- Markup for Contingency.

Finally, adding the Working Capital Costs leads to the Total Investment Costs.

Cost of Major Equipment

The weight of the reactor pressure vessel (in tons of steel, grade SA-508) is the base for calculating the costs. Next, the needed amount of reflector material is calculated. In the case of the 20MWth U-Battery the reflector material consists of nuclear grade graphite; while in the 2*10 MWth U-Battery we opted for a combination of Graphite en Beryllium Oxide (BeO). Finally an amount is added for the necessary control rods.

Costs of Primary Circuit	20 MWth	2*10 MWth
Reactor Pressure Vessel	3.4	1.7
Reflector material	8.7	4.7
Control Rods	3.6	4.0
Total	15.7	10.4

Cost of Major Equipment; primary circuit in million euro, FOAK

RPV

In the case of the 20MWth U-Battery we calculated from our hydraulic calculations a mass of 111.9 tons for the RPV. At a price of 42\$/kg this resulted in 4.7 M\$_{FOAK} or 3.4 M€_{FOAK} at a conversion rate of 1.38.

For the U-Battery of 2*10 MWth scenario we calculated the mass of the RPV at 28 tons, which means 2 vessels*28.000 kg each at a price of 42\$/kg is 2.4 M\$_{FOAK} or 1.7 M€_{FOAK} at a conversion rate of 1.38.

Reflector Material

The Reflector Material for the 20MWth U-Battery consists of nuclear grade graphite, which can be bought at the market at approximately €65/kg. SGL Carbon roughly estimated the mass of graphite for the U-Battery at 133 ton also based on the hydraulic calculations and the example of the existing HTR10.

Graphite:
NBC07: 53.12 ton
NBG17: 28.73 ton
NBG18: 51.33 ton
Total 133.17 ton

The cost of the graphite thus amounts to 133 ton times €65/kg = 8.7 M€

For the 2*10 MWth we need graphite (mass calculated at 8 ton per vessel) and Beryllium oxide (BeO), which can be bought at the market at about 230 €/kg. For the BeO reflectors we calculated a mass of 7.9 ton per vessel. Overall this results in $2 * [(65 * 8) + (230 * 7.9)] = 4.7 \text{ M€}_{\text{FOAK}}$.

Control Rods

The AP600 CRDMs are estimated at 10 M\$ (= 3.6 M€) . The mode of operation for PWR CRDMs is significantly different from gas-cooled reactor control rods (with three independently movable control banks plus a shut-down bank, and both black and grey rods). The costs of the Control Rods are scaled down for the U-Battery at 50%. This amounts to 5.0 M€_{FOAK} or 3.6 M€_{FOAK} for the 20MWth U-Battery and 4.0 M€_{FOAK} for the 2*10 MWth U-Battery.

Power Generation Module

Rolls Royce have published estimated production costs for a 600 MWth/300 MWe indirect gas turbine power generation module based on a mixed HE/N2 secondary circuit. The total cost installed was \$140M and comprised:

Turbo compressor	\$20M
Heat exchangers	\$80M
Vessel	\$30M
Gearbox and intercooler/precooler	\$10M

We scaled this down to approx. 10% and calculated the FOAK value (not installed) at 4.5 M€.

Other Miscellaneous Costs

The remaining Other Miscellaneous Costs are guestimated at 10.0 M€_{FOAK} for both U-Battery-cases. These Costs represent civil (buildings), cooling-tower/heat sink, residual heat removing RCCS (natural circulation), Helium Make-up system, spent fuel storage etc.

Mark-up for Other Direct Field Costs

We used markups on top of the major equipment costs for direct field costs, indirect cost and contingencies. For the direct field costs the markup is 100%, and contains field costs like mechanical and civil costs, electrical systems, instrumentation etc.

Mark-up for Indirect Field Costs and Contingencies

The markup for indirect cost is estimated at 50% on top of the sum of cost of major equipment and (other) direct field costs; thus for the 20MWth and the 2*10 MWth case respectively 30.1 M€_{FOAK} 24.8 M€_{FOAK}. With the markup for contingency at 30% on top of the total field costs, the total fixed capital expenditures amounts to 117.6 M€_{FOAK} for the 20 MWth case and 96.9 M€_{FOAK} for the 2*10 MWth case.

Working Capital

Fuel, fuel-handling and Construction Costs

With the fixed capital investment set at 117.6 and 96.7 M€_{FOAK} and for the 20 MWth and 2*10 MWth case respectively, we have to calculate the expenditures which contain the fuel costs (first load incl handling) and the construction costs.

For 17% enrichment in the 20 MWth case and a price (excl. final disposition) per 1,000 kg set at 15,831.50\$ we arrive at 15.8 M\$ or 11.5 M€⁴. Adding handling cost for 0.5 M€ this amounts tot 11.9 M€ for the 20 MWth case for a load which will last about 10 years. Along the same line of reasoning we arrive for the 2*10 MWth at 6.1 M€ (20% enrichment, 208 kg, 0.5 M€ handling costs and 2 initial loads – one per vessel). This will be used up in approximately 5 years.

⁴ Urenco

For both business cases the labor costs during construction are set at 4 M €.

Decommissioning

Based upon calculations for the decommissioning of the RID reactor at Delft we estimated that for both U-Battery business cases a nominal value of 20 M€ is needed. This amount should be guaranteed at the start of the project. We assumed a deposit in a savings account with an interest of 4% and calculated the required yearly cash outflow by assuming an inflation rate of 2%. Finally, these yearly amounts (provision) is recalculated to NPV by using de COC (5.6%).

Reactor

In both business cases is the thermal power of the micro-reactor is set at 20MWth. Due to the configuration the lifetime of the fuel in case of the 2*10 MWth U-Battery was calculated to be 5 years, while the lifetime for the 20 MWth U-Battery is 10 years. At an efficiency rate of 40%, the micro-reactor will yield 8 MWe during its lifetime. We estimated the Availability of both micro-reactors at 96% uptime; the downtime will be needed to change the fuel.

Running Costs

The input data for the cash outflow for each year consists of direct labor (e.g. operating, maintenance and security) and direct materials and was set as shown:

Personnel security (# of persons)	5,00
Yearly income security personnel	€50.000,00
Personnel operations & maintenance (# of persons) ⁵	10,00
Yearly income O&M personnel	€75.000,00

These cash flows occur for each year in the lifetime of the U-Battery (set at 60 years) and are accrued with the inflation rate of 2%/year. This applies to the other Operational Expenses as well, which are set at 350 K€ per year initially, with an additional cost for the changing of the fuel each 10 (20 MWth U-Battery) or 5 (2*10 MWth U-Battery) years.

D.4 Analysis

Cash Flows

The basis for evaluating both U-Battery business cases lies in the cash in- and cash outflows. The cash inflow consists of the turnover of the U-Batteries, while the cash outflow consists of the investment (up front) and the operational expenses during the lifetime of the U-Batteries.

Taxes are not incorporated in the model because the different tax systems in different countries are numerous, e.g. income taxes, V.A.T., environment taxes, tax shields, (local) permits etc.

Cash Inflow - Revenues

For the first year the revenues of de both cases are depended on the availability of the battery, the efficiency and of course the selling price per KWh. At 96% availability and 40% efficiency, the battery produces 7,680 KW per year. At a selling price of 0.10 €/KWh and 8.766 hours /year this gives a cash inflow of 6.9 M€ for the first productive year. This amount is accrued with the inflation rate (2%) each year.

Cash Outflow - Total Investment Costs

The preparation and building phase of the U-Battery is 2 years in which the cash outflow consists mainly of capital expenditures. From FOAK to NOAK we assumed this period to be constant, although one could argue that the length of the building phase would diminish while nearing the 8th OAK.

⁵ The maintenance cost of the U-Battery is estimated as an annually 3% of Replacement Asset Value (RAV) being the best practices in industry. This amounts to 433 K€ and consists of personnel and material.

There is no need to calculate depreciation figures while dealing with cash flows and using the Cash Flow Statement as the sole means of evaluating the project. This would be different when the Profit & Loss Statement was chosen as foundation for our model. Based on the input variables and the model for this business case, the cash outflow (Total Investment) for both U-Batteries (FOAK and 8th-OAK) is calculated:

Cash outflow in M€	FOAK	FOAK	8th OAK	8th OAK
	20 MWth	20 MWth	2*10 MWth	2*10 MWth
Vessel	3,4	2,2	1,7	1,1
Reflector Material	8,7	5,6	4,7	3,0
Control Rods	3,6	2,3	4,0	2,6
Power Conversion Module	4,5	2,9	4,4	2,9
Miscellaneous Equipment	10,0	6,5	10,0	6,5
Cost of Major Equipment	30,1	19,5	24,8	16,1
Markup for other Direct Costs	30,2	19,5	24,8	16,1
Direct Field Costs	60,3	39,0	49,6	32,2
Markup for Indirect Field Cost	30,2	19,5	24,8	16,1
Markup for Contingencies	27,1	17,7	22,4	14,5
Initial Fuel Core Load	12,0	12,0	6,1	6,1
Labor during Construction	4,0	4,0	4,0	4,0
Decommissioning Costs	10,3	10,3	10,3	10,3
Working Capital	26,3	26,3	20,4	20,4
Total Investment (TI)	143,9	102,5	117,2	83,2

From FOAK to NOAK

NOAK and FOAK	20 MWth	2* 10 MWth
Module number	Total Investment	Total Investment
1	M€ 144	M€ 117
2	M€ 137	M€ 111
3	M€ 130	M€ 106
4	M€ 124	M€ 101
5	M€ 118	M€ 96
6	M€ 113	M€ 91
7	M€ 107	M€ 87
8	M€ 103	M€ 83

Cash Outflow - Operational Expenses

From the input data the operational yearly expenses can be calculated, consisting of personnel for security and maintenance and miscellaneous expenses. This amount is accrued for the following years with the inflation rate (2%)

Assessment

Introduction

To assess both business cases, the Net Present Value (NPV), the Total Investment (TI), the Return on Investment (ROI, defined as the NPV/TI) and the Pay-Back Period (PBP) are selected as decision criteria.

Though the capital investment for a U-Battery is much lower compared to the expenditure for a large reactor; there is still a timing difference between the manufacturing of the battery (the investment phase -up front), and the cash inflows - during the lifetime of 60 years. This would be a problem for a stand-alone situation, in which one or a

relatively small number of batteries are produced. By applying serial production the producer can divert part of this economic risk. Alternatively, the timing difference could be a smaller problem for an end-user buying a secure energy solution at a fixed price for the next 60 years. The economic risk of building U-Batteries can thus be shared between producer and end-user.

Assessment of both cases – End User

In paragraph D3 the firms cost of capital was calculated at 5.6%. Starting point for the evaluation of the 20 MWth and the 2*10 MWth is the 8th OAK situation, after which a steady state occurs.

While the NPV_{FOAK} of both business cases is negative (-11 M€ and -34 M€ for the 2*10 and 20 MWth business cases respectively), due to the efficiency factor in building the U- batteries, they are positive for the NPV_{8-OAK} (resp. +23M€ and +7 M€) as shown in tables z1 and z2.

20 MWth	NPV (M€)	Investment (M€)	ROI	PBP
8thOAK	7.1	-102.5	7%	18

2*10 MWth	NPV (M€)	Investment (M€)	ROI	PBP
8thOAK	23.0	-83.2	28%	16

From the viewpoint of an end user the 2*10 MWth U-Battery business case gives better (financial) results than the 20 MWth business case. However, bear in mind that the fuel in the 2*10 MWth business case lasts (only) 5 years, while the fuel in the 20 MWth business case lasts 10 years. Financially this is taken into account in both cases, but the wish to attain a less attended or even an unattended situation is best reached in the 20 MWth business case.

In both business cases the investment per KWh is approximately 2 euro cent. The U-Battery producing electricity of 20MWth would be enough for a community of 20.000 families, consisting of an average of 2.3 persons per family and using on average 3,500 KWh per family.

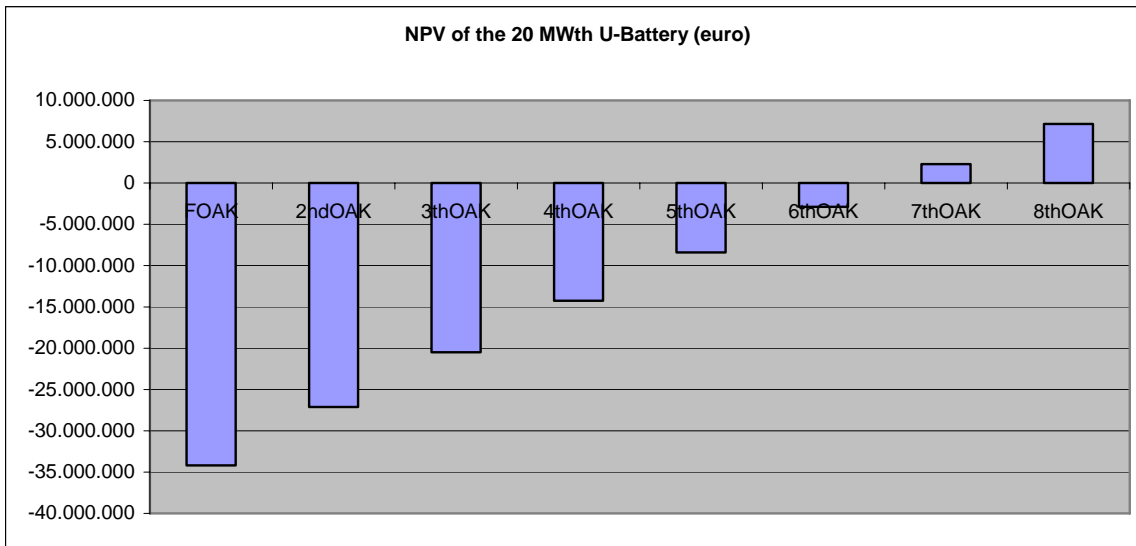
20 MWth U-Battery in M€			NPV	Preparation Phase	Year 1-10	Year 11-20	Year 21-30	Year 31-40	Year 41-50	Year 51-60	
CF Investment	Field Cost	RPV	-2,2	-2,2							
		Reflector Material	-5,6	-5,6							
		Control Rods	-2,3	-2,3							
		Power Conversion Module	-2,9	-19,5							
		Miscellaneous Equipment	-6,5	-2,9							
		Markup for other Direct Costs	-19,5	-6,5							
		Indirect Field Cost	-19,5	-19,5							
	Total Field Cost			-58,6	-58,6						
	Base Construction Cost		Contingency on Investment Costs	-17,6	-17,6						
	Other Construction Costs	Initial Fuel Core Load		-12,0	-12,0						
Labor during Construction		-4,0	-4,0								
Decommissioning Costs		-10,3		-3,3	-4,9	-7,3	-10,7	-15,9	-23,5		
Total Other Construction Costs			-26,3	-16,0	-3,3	-4,9	-7,3	-10,7	-15,9	-23,5	
Total CF Investment			-102,5	-92,2	-3,3	-4,9	-7,3	-10,7	-15,9	-23,5	
CF operational	Turnover	Produced Electricity	166,9	0,0	75,2	91,7	111,7	136,2	166,0	202,4	
	Operation & Maintenance	Fuel Costs	-23,8	0,0	-14,6	-17,8	-21,7	-26,4	-32,2	0,0	
		Auxiliary Materials	-8,7	0,0	-3,9	-4,8	-5,8	-7,1	-8,6	-10,5	
		Security	-6,2	0,0	-2,8	-3,4	-4,1	-5,1	-6,2	-7,5	
		Maintenance & Operating	-18,6	0,0	-8,4	-10,2	-12,4	-15,2	-18,5	-22,5	
Total O&M			-57,3	0,0	-29,7	-36,2	-44,1	-53,7	-65,5	-40,6	
Total CF operational			109,7	0,0	45,5	55,5	67,6	82,4	100,5	161,8	
End total			7,1	-92,2	42,2	50,6	60,4	71,7	84,6	138,3	

Note that in the period 51-60 years the NPV rises significantly because at the end of the project (year 60) no fuel change will be needed.

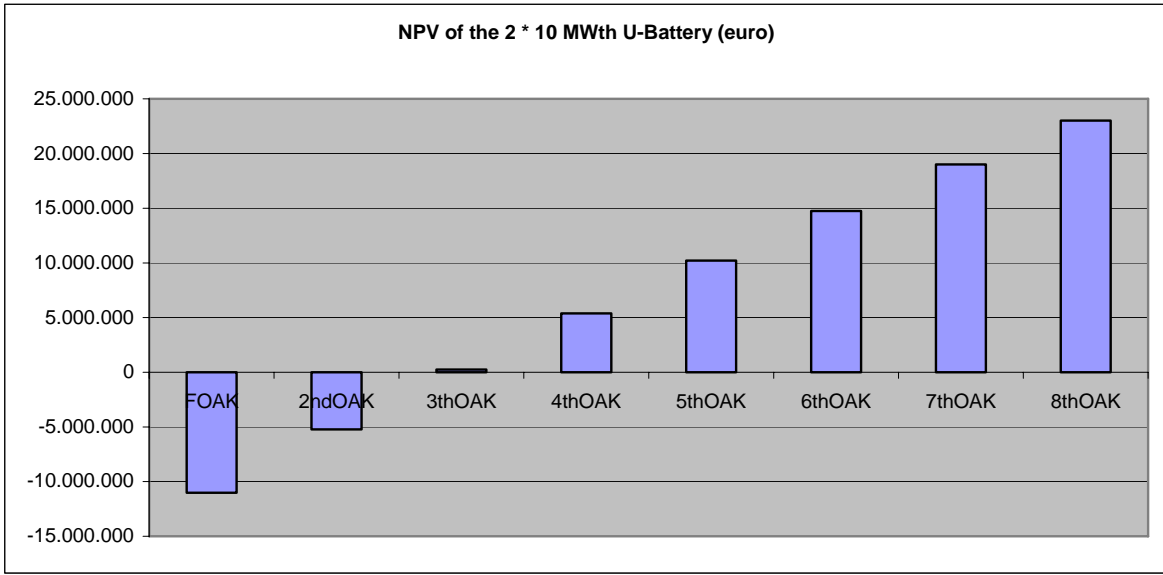
2*10 MWth U-Battery in M€			NPV	Preparation Phase	Year 1-10	Year 11-20	Year 21-30	Year 31-40	Year 41-50	Year 1-60	
CF Investment	Field Cost	RPV	-1,1	-1,1							
		Reflector Material	-3,0	-3,0							
		Control Rods	-2,6	-2,6							
		Power Conversion Module	-2,9	-2,9							
		Miscellaneous Equipment	-6,5	-6,5							
		Markup for other Direct Costs	-16,1	-16,1							
		Indirect Field Cost	-16,1	-16,1							
	Total Field Cost			-48,3	-48,3						
	Base Construction Cost			-14,5	-14,5						
	Other Construction Costs	Initial Fuel Core Load		-6,1	-6,1						
Labor during Construction			-4,0	-4,0							
Decommissioning Costs			-10,3	0,0	-3,3	-4,9	-7,3	-10,7	-15,9	-23,5	
Total Other Construction Costs			-20,4	-10,1	-3,3	-4,9	-7,3	-10,7	-15,9	-23,5	
Total CF Investment			-83,2	-72,9	-3,3	-4,9	-7,3	-10,7	-15,9	-23,5	
CF operational	Turnover		166,9		75,2	91,7	111,7	136,2	166,0	202,4	
	Operation & Maintenance	Fuel Costs	-27,2		-14,1	-17,2	-20,9	-25,5	-31,1	-18,0	
		Auxiliary Materials	-8,7		-3,9	-4,8	-5,8	-7,1	-8,6	-10,5	
		Security	-6,2		-2,8	-3,4	-4,1	-5,1	-6,2	-7,5	
		Maintenance&Operating	-18,6		-8,4	-10,2	-12,4	-15,2	-18,5	-22,5	
Total O&M			-60,7		-29,2	-35,5	-43,3	-52,8	-64,4	-58,6	
Total CF operational			106,2		46,0	56,1	68,4	83,4	101,7	143,8	
CF Financial			0,0								
End total			23,0	-72,9	42,7	51,2	61,2	72,7	85,8	120,3	

Assessment of both business cases – From the viewpoint of a producer

The FOAK for both U-Battery business cases show a negative NPV. The learning curve stipulates the advantages of serial production: in the 20 MWth business case the NPV is not positive until the 7th OAK while in the 2*10 MWth business case the NPV is positive in the 3rd OAK (both with a cash inflow calculated at 10 cents per MWe).



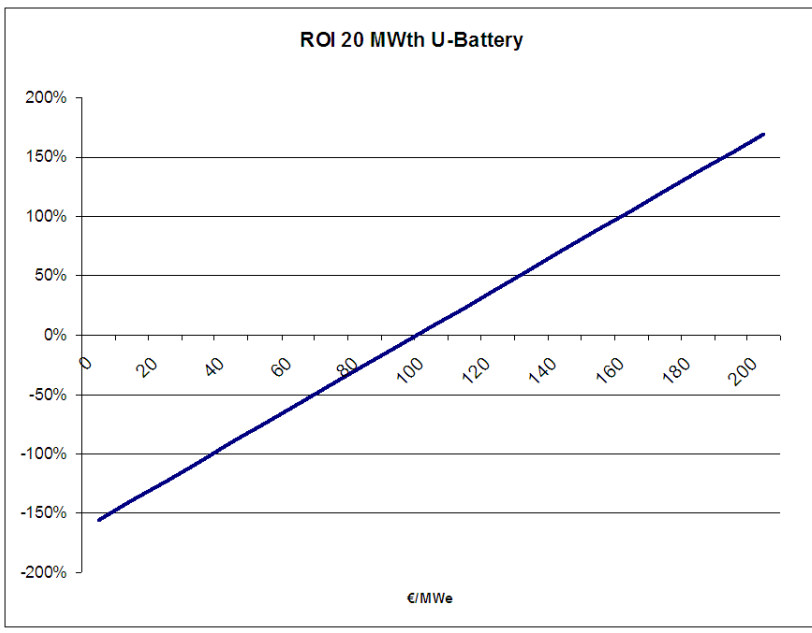
In the business case of the 20 MWth U-Battery, the cumulative NPV (the sum of FOAK till 8th OAK) is -98 M€, which of course would be very dissatisfying. In fact, assuming a steady state after the 8th OAK, the producer would not break even until the 22nd OAK.

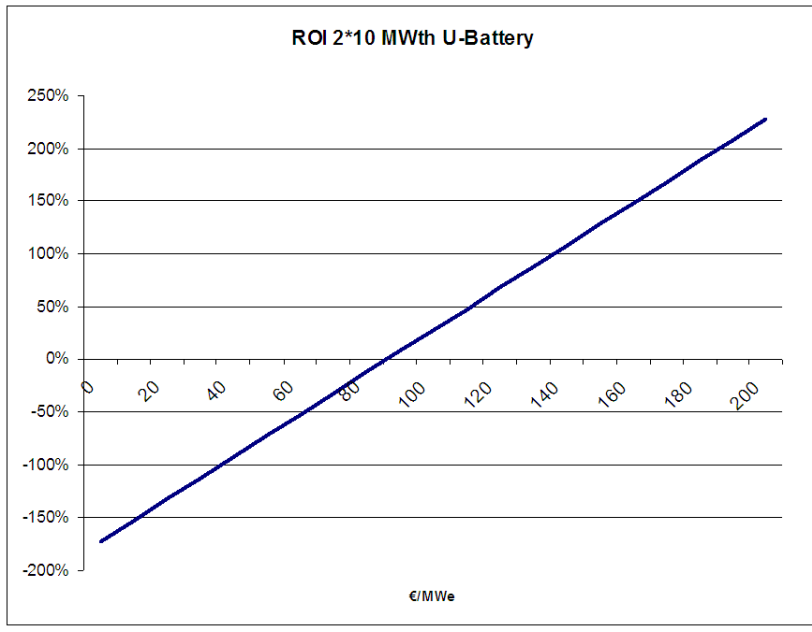


The graphs show that for a producer the 2*10 MWth U-Battery is clearly the better business case, with the break-even point just after the 5th OAK.

Sensitivity Analysis – From the viewpoint of an end user

By changing the variables between -100% and +100% we were able to discover the impact of each variable in the end result. Most sensitive for the end result is the price at which a KWh is sold, in our business case initially set at 10 euro cent. This is the lower limit with a positive margin for the 20 MWth U-Battery. A price of 9 euro cent would result in a loss of -9% ROI in the steady state. However for the 2*10 MWth U-Battery 9 cent/KWh seems to be still feasible but is the lower limit with a positive margin of 8% ROI.





D.5 Conclusions and recommendations

The calculations in the economic model show that the 2*10 MWth U-Battery business case is economically feasible from a KWh price of 9 cent, whereas the 20 MWth U-battery business case is feasible from a KWh price of 10 cent. This result shows that there are opportunities in designing tailor made reactors for large industries or (small) towns. These opportunities lie in modularity and standardization, simple design, serial fabrication of components and building multiple units at one site.

The economic risk in building and operating the U-Batteries in real life would be shared between a producer and an end-user, ultimately by means of negotiating the price for the U-Battery transaction.

For the end-user as a buyer both business cases are feasible as they show a positive NPV in steady state, although economically they would prefer the 2*10 MWth U-Battery.

For a producer on the other hand the 2*10 MWth U-Battery is by far the better business case. Our model indicates that the producer is breaking even after producing only five U-Batteries, which is before the production reaches the maturity stage. In the 20 MWth U-Battery business case the producer reaches the break-even point only after the 22nd delivery, which is not an appealing business case.